Valorization of biomass derived platform molecule *via* catalytic hydrogenation and oxidation

by

Bhanupratap Singh Solanki
10CC14A26024

A thesis submitted to the
Academy of Scientific & Innovative Research
for the award of the degree of
DOCTOR OF PHILOSOPHY
in
SCIENCE

Under the supervision of
Dr. Santosh B Mhaske (Admin)
Dr. Chandrashekhar V Rode

CSIR-National Chemical Laboratory, Pune

Academy of Scientific and Innovative Research AcSIR
Headquarters, CSIR-HRDC campus
Sector 19, Kamla Nehru Nagar,
Ghaziabad, U.P. – 201 002, India

May-2022

Certificate

This is to certify that the work incorporated in this Ph.D. thesis entitled, "*Valorization of biomass derived platform molecule via catalytic hydrogenation and oxidation*", submitted by *Bhanupratap Singh Solanki* to the Academy of Scientific and Innovative Research (AcSIR) in fulfillment of the requirements for the award of the Degree of *Doctor of Philosophy in Science*, embodies original research work carried-out by the student. We, further certify that this work has not been submitted to any other University or Institution in part or full for the award of any degree or diploma. Research material(s) obtained from other source(s) and used in this research work has/have been duly acknowledged in the thesis. Image(s), illustration(s), figure(s), table(s) etc., used in the thesis from other source(s), have also been duly cited and acknowledged.

(Signature of Student)	(Signature of Co-Supervisor)	(Signature of Supervisor)
Bhanupratap Singh Solanki	Chandrashekhar V Rode	Santosh B Mhaske (Admin)
Date: 06/05/2022	Date: 06/05/2022	Date: 06/05/2022

STATEMENTS OF ACADEMIC INTEGRITY

I Bhanupratap Singh Solanki, a Ph.D. student of the Academy of Scientific and Innovative Research (AcSIR) with Registration No. 10CC14A26024 hereby undertake that, the thesis entitled "Valorization of biomass derived platform molecule *via* catalytic hydrogenation and oxidation" has been prepared by me and that the document reports original work carried out by me and is free of any plagiarism in compliance with the UGC Regulations on *"Promotion of Academic Integrity and Prevention of Plagiarism in Higher Educational Institutions (2018)"* and the CSIR Guidelines for "*Ethics in Research and in Governance (2020)".*

Signature of the Student
Date : 06/05/2022
Place : Pune

It is hereby certified that the work done by the student, under my/our supervision, is plagiarism-free in accordance with the UGC Regulations on *"Promotion of Academic Integrity and Prevention of Plagiarism in Higher Educational Institutions (2018)"* and the CSIR Guidelines for "*Ethics in Research and in Governance (2020)".*

Signature of the Co-supervisor
Name : Chandrashekhar V Rode
Date : 06/05/2022
Place : Pune

Signature of the Supervisor
Name : Santosh B Mhaske (admin)
Date : 06/05/2022
Place : Pune

Dedicated to my family, friends and Mother Nature

Acknowledgement

It was a dream for me to pursue the Ph. D. until I started the initial steps towards it and today when I am about to complete it, I would like to pen down the emotion of gratitude to all the special support I received in my tenure.

First and foremost I would like to thank my research supervisor ***Dr. Chandrashekhar V Rode*** *for continuously encouraging, supporting and boosting me throughout my journey. He is the prime reason for successful completion of this thesis. His firm hands on my shoulder pushed me beyond my limit in order to get skills. His vigorous evaluation of my work, vital intellect inputs and consistent supervision helped me a lot in the entire Ph. D. I would like to thank again specially Dr. Rode for helping me out of the way.*

I would like to show gratitude to my DAC members Dr. Prakash P. Wadgaonkar, Dr. Manohar V Badiger and Dr. Suresh P Gokhale for critical review of my work during every DAC presentations. Their valuable inputs groomed my work style a lot. I would also like to specially thank Dr. Rajeev C Chikate for evaluating my JRF to SRF upgradation and imparting some of his vast knowledge. A very special thanks to ***Dr. Sanjay P. Kamble*** *for helping me on several crucial points. I am extremely grateful to all the present and former head of the CEPD departments and directors of CSIR NCL for providing great atmosphere and world class facilities for conducting my research work.*

My special words of thanks should also go to Dr. C P Vinod, Dr. Mahesh Kulkarni, Dr. B L V Prasad, Dr. C.G. Suresh, Dr. Chetan Gadgil, Dr. M. S. Shashidhar, Mr. P V Iyer, Mrs. P. Kolhe, Ms. Komal, Ms. Vaishali and SAO staff for their cooperative assessment of AcSIR documents. I am also grateful to CMC division for providing excellent instrumental facilities and especially Mr. R K Gholap, Chetan, Sheetal, Tushar, Venkatesh, Megha, Pankaj (For SEM and TEM), Dr. C.S. Gopinath, Mr. S. S. Deo (For XPS) for their help and support. I also thank the staffs from administration, accounts, Glass blowing, medical, Engineering Section, DIRC, Stores and Purchase for providing excellent facility. The entire library staffs for providing excellent facilities are gratefully acknowledged.

I would like to take this opportunity to thank all of my helping and kind labmates starting with Dr. Amol Hengne, Dr. Ajay Jha, Dr. Narayan Biradar, Mrs. Aparna Potdar, Dr. Sharda Kondawar, Dr. Rasika Mane, Dr. Rajan Pandya, Mrs. Shobha Birajdar, Dr. Chetana Patil, Dr. Sachin Sakate, Dr. Suhash Shinde, Dr. Sumit Kamble, Dr, Virendra Patil, Dr. Gayatri Kasar, Dr. Nandan Date, Dr. Sanjay Jadhav, Dr. Dnyanesh Vernekar, Mr. Sagar More, Mr. Harish Joshi, Mr. Rameshwar K. Swami, Mr. Shivanand Balu, Mr. Mahesh Patil, Mr. Shankar Dengale, Mr. Subhash Magar, Mr. Shrinivas Charate, Mr. Anil Patil, Ms. Komal Tarade, Ms. Samrin Sheikh and Ms. Geetanjali Ratrey.

I was constantly tolerated, encouraged and sustained by some of my dearest friends which include Mr. Padam Singh Negi, Mrs. Roopa Parate Madkaikar, Dr. Ruchi Jain, Dr. Rajan Pandya, Dr. Virat Pandya, Mr. Rohit Shetty and Mrs. Himanshu Sharma. I was fortunate enough to blessed with company of great individuals like Dr. Vijay Beniwal, Dr. Manoj Ghosalya, Dr. Amit Yadav, Dr. Sandeep Sharma, Dr. Bhavna Pandey, Dr. Praveen Jangid and Dr. Vinita Yadav. I want to extend my special love to Dr. Virat Pandya, Dr. Rajan

Pandya, Dr. Rajesh Bisht and Dr. Manikchandra Shil for organising weekend special "Banna's drinking diary conferences". I also want to thank my hostel cooks Mr. Sujeet Da and Chhotu who always served delicious food.

A brief timespell of this journey was affected by Wuhan Corona Virus (COVID-19). I would like to express my sincere gratitude to immensely kind family of my colleague Mr. Rohit Shetty. Their support and utmost care in that tough time helped me to survive. I want to extend my special respect to Mrs. Renu Shetty and Mr. Ravi Shetty for showering their affection on me. I would also like to thank my spiritual brothers and sisters Mr. Avi Raina, Mr. Rakesh Jamwal, Mr. Navroop Singh, Mrs. Maneeza Ahuja and Mrs. Priyanka Pathak for guiding me in the tough phase.

Family is the strongest support system for completing a great achievement. I was consistently endorsed by my family during this journey. I am thankful to my uncle Dr. Parmal Singh Solanki and Er. Chhatrasal Singh Solanki for seeding the dreams of higher education in me. While writing this thesis, I deeply miss the warmth and love of my grandfather late. Shri Shivraj Singh Solanki. He was the source of constant support for me and I will never be able to recover from his loss. This journey could not been started without the initial support of my parents ***Smt. Pushpa Devi*** *and* ***Shri Tilak Singh Solanki****. Their deep affection and care encouraged me to pursue this degree. I would also like to thank both of my lovely sisters* ***Mrs. Bharti Singh Rajput*** *and* ***Ms. Arti Kanwar Solanki*** *for taking care of family in my absence. This journey became more beautiful with my wife* ***Mrs. Navita Walia****. I want to thank her for showing unshakable faith and love to me.*

I would also like to express my deep respect to all of my teachers who prepared me for different levels of my life. The work ethics and learning I got from them is the foundation of this work. Lastly, I bow down to ***Bhagwan Shiva*** *and* ***Adishakti Amba*** *for blessing me the courage, patience and wisdom to carry out my work.*

Thank You

Bhanupratap Singh Solanki

Table of Contents

List of Contents

Section No	Title	Page No.

Chapter 1. Introduction

Chapter 3. Selective hydrogenolysis of 5-(hydroxymethyl)furfural to 2,5-dimethylfuran over Pd/C catalyst

Chapter 4. Selective hydrogenation of 5-HMF to 2,5-DMF over a magnetically recoverable non-noble metal catalyst

Chapter 6. Highly efficient bimetallic synergism of Cu-Co on x-GO for selective aerial oxidation of 5-HMF to FDCA

List of Tables

Chapter 3

Chapter 4

Chapter 5

Chapter 6

List of Figures

Chapter 3

Chapter 4

Chapter 5

Chapter 6

List of Schemes

Chapter 3

Chapter 4

Chapter 5

Chapter 6

Abbreviations

%	Percentage
°C	Degree Celsius
K	Kelvin
h	Hour
min	Minutes
psig	Pressure Square Inch per gauge
µ	Specific growth rate
µg	Microgram
µL	Microlitre
mg	Miligram
KJ	KiloJule
PJ	PicoJule
mL	MiliLitre
mm	Milimeter
Mt	Metric ton
B. E.	Binding Energy
eV	Electron Volt
K. E.	Kinetic Energy
LCB	Lignocellulosic Biomass
5-HMF	5-(Hydroxymethyl) fufural
PAN	Polyacrylo Nitrile
PVC	Polyvinyl chloride
USDOE	United States Department of Energy
BAC	Business Analytics Centre
LBAE	Lobry deBruyn-Alberda van Ekenstein
H^1-NMR	Proton Nuclear Magnetic Resonance
DMF	2, 5-Dimethyl furan
EMF	5-(ethoxymethyl) furan

BHMF	2, 5-(bishydroxymethyl) furan
BHMTHF	2, 5-(bishydroxymethyl) tetrahydrofuran
HCPN	3-(hydroxymethyl) cyclopentanone
DFF	2, 5-Diformyl furan
FDCA	2, 5-Furandicarboxyllic acid
PEF	Polyethylenefuranoate
HMFCA	5-(hydroxymethyl) Furan-2-Carboxylic acid
MAD	Maleic anhydride
LHV	Latent Heat of Vaporization
RON	Research Octane Number
GDI	Gasoline Directed Injection Engine
pX	*para*-Xylene
PET	Poly ethylene terephthalate
HDO	Hydrodeoxygenation
CMF	5-(chloromethyl) furfural
MIBK	Methyl isobutyl ketone
ACN	Acetonitrile
THF	Tetrahydrofuran
CNT	Carbon Nanotubes
HT	Hydrotalcite
MWC NT	Multiwall Carbon Nanotubes
FDCC	Furan-2,5-dicarbonyl chloride
TEMPO	2,2,6,6-tetramethylpiperidine-1-oxide
BAIB	[bis-(acetoxy)-iodo] benzene
OMS-2	Octahedral Mesoporous Silica-2

MA	Maleic acid
PBT	Poly Butylenes Terephthalate
x-GO	Exfoliated Graphene Oxide
FFCA	5-Formyl-2-furan carboxylic acid
t-BuOOH	Tertiary butyl hydrogen peroxide
XRD	X-ray Diffraction Spectroscopy
XPS	X-ray Photoelectron Spectroscopy
TEM	Transition Electron Microscopy
FE-SEM	Field Emission-Scanning Electron Microscopy
FTIR	Fourier Transformation Infra red Spectroscopy
TPM	Temperature Programmed Method
TPD	Temperature Programmed Desorption
TPR	Temperature Programmed Reduction
TPO	Temperature Programmed Oxidation
BET	Brunauer Emmett Teller Surface Area
BJH	Barrett-Joyner-Halenda
GC	Gas Chromatography
UHPLC	Ultra High Performance Liquid Chromatography
GC-MS	Gas Chromatography coupled with Mass Spectrometry
LC-MS	Liquid Chromatography coupled with Mass Spectrometry
TGA	Thermogravimetric Analysis
DSC	Differential Scanning Calorimetry
DTA	Differential Thermal Analysis
TGA-MS	Thermogravimetric Analysis coupled with Mass Spectrometry
ESCA	Electron Spectroscopy for Chemical Analysis

APPES	Ambient Pressure Photoelectron Spectrometer
BSE	Back Scattered Electron
SE	Scattered Electron
EDX	Electron Dispersive X-ray
FID	Flame Ionization Detector
TCD	Thermo Coupled Detector
LA	Lewis Acidity
BA	Brönsted Acidity
TLA	Total Lewis Acidity
TBA	Total Brönsted Acidity
ICP-AES	Inductively Coupled Plasma-Atomic Emission Spectroscopy
MWD	Multi Wavelength Detector
MFFR	5-methyl-2-Furfural
MFAL	5-methyl-2-furfuryl alcohol
IPA	Isopropyl alcohol
2G	Second Generation
MF	2-methyl Furan
GVL	Gamma Valerolactone
EL	Ethyl Levulinate
MeOH IR	Methanol Infra red Spectroscopy
FWHM	Full Width at Half Maxima
FCC	Face Cubic Centred
TON	Turn Over Number
TOF	Turn Over Frequency

Chapter 1

Introduction

Introduction

1.1 Biomass and its Potential

With an exponential increase in world population in conjunction with modernization of the life style, energy demand has also been growing up tremendously. According to various forecast models the world population is expected to be 8-10 billion by 2050 ultimately leading to rapid and complete consumption of natural energy resources like oil, coal and gas [1].

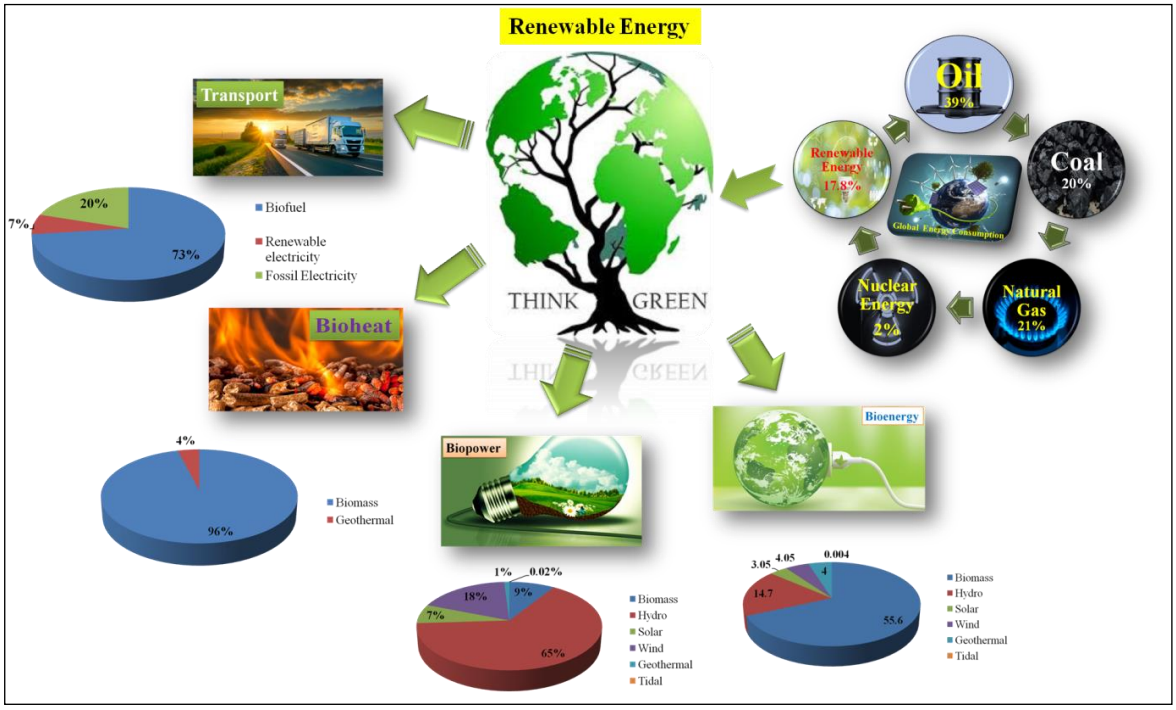

Figure 1.1: Potential of biomass (Source of Data: World Biomass Energy Report 2019)

The rapid and unorganised consumption of these non renewable fossil fuels is further deteriorating pre-existing environmental problems like enhanced global temperature, increased green house gas emission and carbon footprints etc. For sustainable future and environmental protection Paris agreement (*L'accord de Paris*) was accepted in 2015 according to which every country was given target of reduction of carbon footprint by 2025 so that global temperature can be kept well below 2°C above pre-industrial time and

endeavour to limit them even more to 1.5°C [2]. To maintain these standards of global environmental index scientific community is also searching for greener, economical and clean energy resources. In this regard, biomass proves to be one of the best options owing to its vast availability globally at very low cost. Biomass can be defined as whole organic matter of the biosphere originated from animal/plant or their natural/artificial transformative derivatives [3-6]. Biomass has tremendous energy potential as much as of 3 x 10^8 KJ attributed to its 1x10^{11} ton massive annual production [7]. Global Biomass Energy Statistics Report 2019 published by World Bioenergy Association states that out of 17.7% global renewable energy, share of biomass feedstock was 70%. Almost 25% of global electricity demand and 3% of transport sector was biomass derived. Similarly, 95% of end use sector and 96% of renewable heat market is produced by biomass derived bioenergy [8]. While biomass feedstock promises a large energy potential it is yet to be utilised with full capacity due to multiple issues.

1.2 Composition of Biomass

Biomass is largely composed of lignin, cellulose and hemicellulose and is also called as Lignocellulosic biomass (LCB). Triglycerides, oil, fat, proteins, lipids are some other components which are present in limited amount depending upon species of biomass. The major component of LCB is Cellulose which constitutes almost 40-50% share of LCB [9]. Cellulose is mainly composed of D-glucose unit which are interlinked with each other by β-1,4-glycosidic bonds. It is a linear polymer with complex polysaccharide whose structural base is cellobiose or 4-o-β-D-glucopyranosyl-D-glucopyranose [10].

Due to existing intermolecular H-bonding between –OH group of third carbon atom and oxygen atom of neighbouring glycosidic ring cellulose shows crystallinity from 30-80% [11].The density of this crystalline cellulose is little higher (1.588 g/cm^3) than the amorphous cellulose (1.50 g/cm^3) [10].

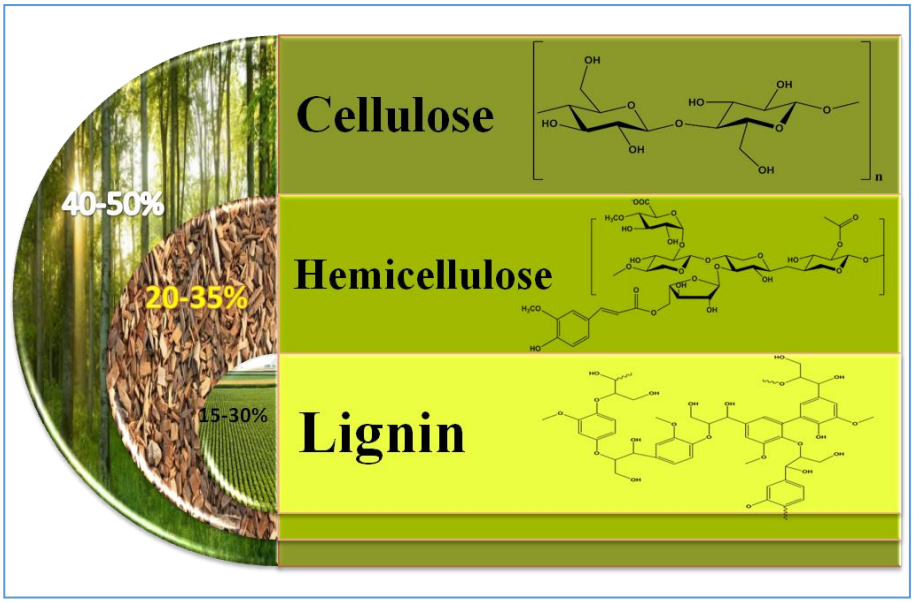

Figure 1.2: Composition of Lignocellulosic Biomass (LCB)

Amorphous form of cellulose is easily accessible by hydrolysis which ultimately yields into D-glucose whereas partial hydrolysis of cellulose forms a disaccharide unit. Hemicellulose shares 20-35% chunk of lignocellulosic biomass. It is a branched polysaccharide which is linked with surface of cellulose microfibrilles. It comprises of C5 and C6 sugars like xylose, arabinose and glucose, galactose, rhamnose, mannose respectively. Due to its non-linear nature it is an amorphous solid which acts as adhesive and can be easily hydrolysed [(12)]. Lignin is another major content of LCB which comprise almost 15-30% part of it. It provides the compactness and resistance to the plant by binding and cementing the fibres. Lignin is composed of 3D network of phenylpropane monomers which make it an intricate aromatic polymer with amorphous nature with 60-65% Carbon, 5-6% Hydrogen and remaining Oxygen. The compactness arises in lignin because of its various bonds and interaction within the structural framework. Lignin induces encrusting effect which covers cell fibres so, to obtain cellulose fibres lignin degradation is an essential process [(13)]. These different contents of LCB have different chemical and physical properties which require robust chemical treatment or procedures for their conversion into utility products and platform chemicals.

This whole concept of destructive upgradation of biomass is an elementary step used in 'Biorefinery'.

1.3 Biorefinery: A hope for sustainable future

The concept of biorefinery deals with the full scale utilisation of biomass which is a non-fossil carbon source. Two major objectives of biorefinery are to create the eco-sustainable channel to fulfil the energy demand by producing biofuels and enhancing the life index of mankind by generating commodity/utility chemicals in a cost effective process [(14)]. A brief concept of biorefinery is represented in **Figure 1.3**.

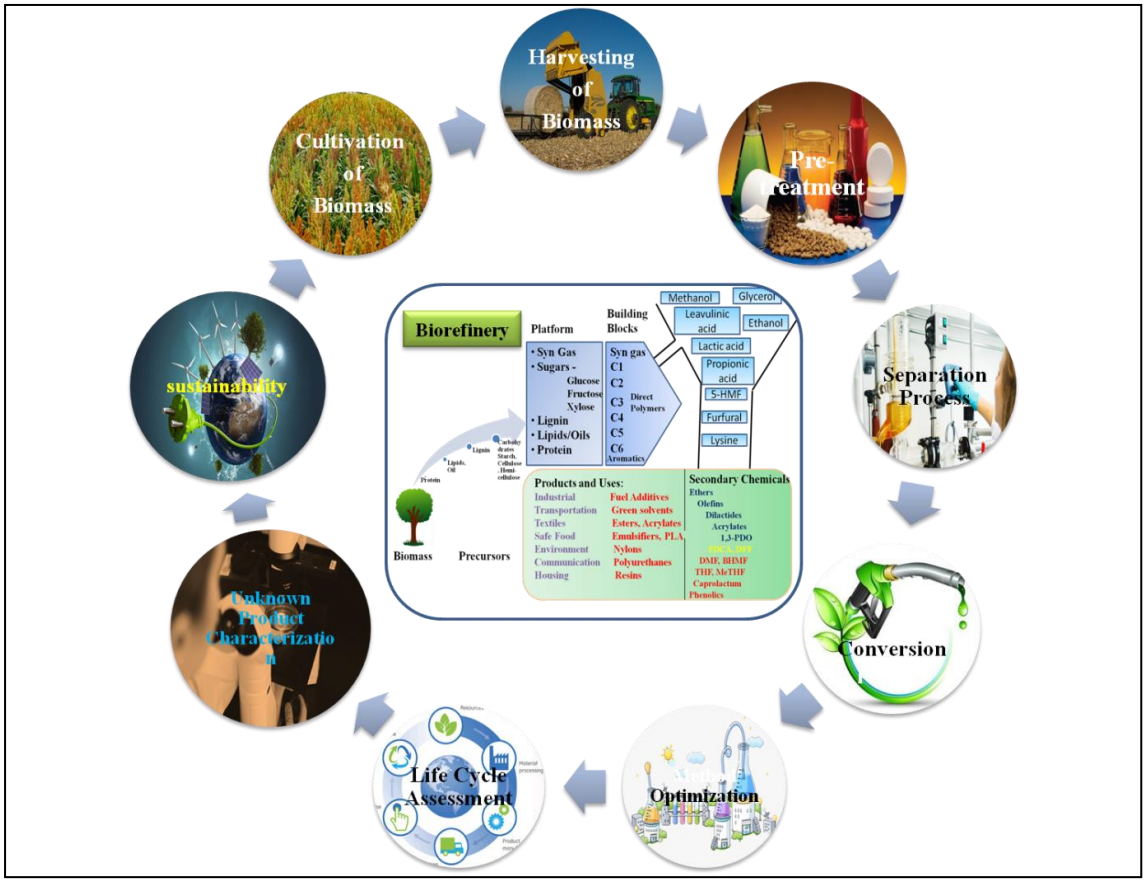

Figure 1.3: Biomass to utility chemicals: A concept of biorefinery and its challenges

A successful biorefinery aims towards reduction of carbon and water footprint by producing environmentally benign analogue molecules of petrochemical refinery at competitive price with equal or better properties thus achieving golden equilibrium [(15)]. Feasibility of

biorefinery can be achieved by low cost operation and efficient use of available resources. A typical biorefinery can be focussed on the production of one or more high value, low volume utility chemicals and low value, high volume biofuel molecules [16]. Biorefinery has extra advantages of reduced energy cost as they can generate their own electricity and heat with the help of combined heat and power technology. Overall performance and efficiency of biorefinery directly depends on type of conversion processes. There are three generic categories of biomass conversion process i.e. thermochemical, biochemical and chemo-catalytic. Aforementioned first step of destructive upgradation of biomass in liquid/gaseous platform chemicals is followed by second step of constructive upgradation of these platform molecules to value added chemicals and biofuels. In lignocellulosic biomass based biorefinery, most prominently used processes are thermochemical catalytic treatment and chemocatalytic process. In the first one, the feedstock is treated under harsh reaction conditions employing catalytic combustion, pyrolysis, liquefaction and gasification. This will generate various solids (biochar), liquid (bio-oil) and gaseous (syn gas) energy sources. Further catalytic treatment of these energy resources will produce refined fuels and synthesis gas. Chemocatalytic process can be operated under milder conditions of temperature and pressure in presence of either solid/liquid/mono or bifunctional catalyst [17]. Typically hydrolysis or hydrodeoxygenation or oxidative dehydrogenation, delignification, aqueous phase reforming took place in chemocatalytic process. These pathways mainly produce monosaccharide, polyols, Levulinic acid, carboxylic acid derivatives, and furan derivatives like furfural, 5-HMF *etc* in biomass based biorefineries [18].

1.4 Catalysis: A pillar of Biorefinery

Biomass derived molecules invariably contains several oxygen atoms in the form of different functional groups the conversion of which result into multiple products hence, the plays a pivotal role in biorefinery processes. Catalyst is a substance which increases the rate of reaction without altering cumulative Gibbs energy change in the reaction [19]. It is classified into heterogeneous, homogenous and biocatalysts out of which heterogeneous catalyst helped in revolutionary transformation of industrial, agriculture and chemical sectors.

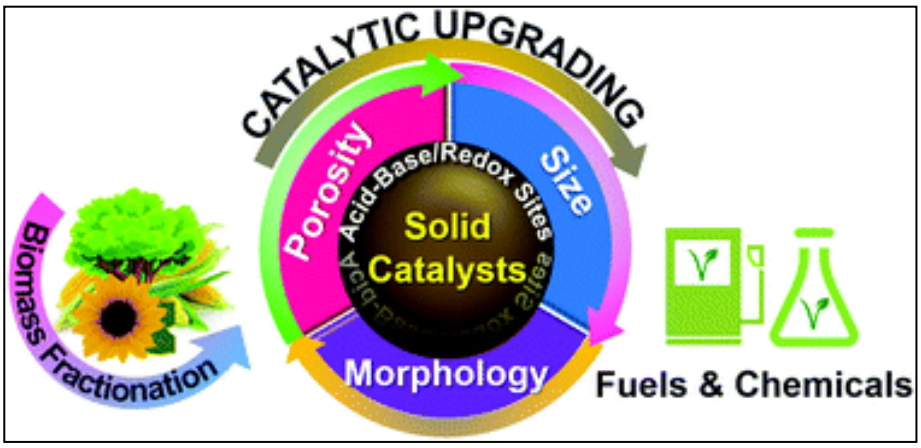

Figure 1.4: Catalytic upgrading in biomass based biorefinery (Source: ***Chem. Soc. Rev.,*** 2019, 48, 2366)[6]

Socioeconomic impact of catalyst is evident by the fact that it contributes about 35% in global gross domestic product market. Many significant reactions and technologies like NH_3 production, H_2SO_4 production, NH_3 oxidation, methanation, water gas shift reaction, alkylation, polymerisation, ethylene epoxidation, PAN and PVC production, catalytic cracking and hydrotreating of crude oil, gasoline production from naphtha and steam reforming of methane are dependent on heterogeneous catalyst today [20]. Heterogeneous catalysis flourished in conventional petrochemical refinery owing to its advantage of easy separation, reusability and excellent activity. Although heterogeneous catalysis in biorefinery is still in nascent stage compared to petrochemical refinery and requires massive development

drive it helped in bridging the transformation of biomass feedstock into the platform molecules and their upgradation into biofuels, fine chemicals and clean energy alternatives which was the main aim of biorefinery. The scope of this thesis highlights the importance of supported monometallic and bimetallic catalysts for the valorization of biomass derived furan based C6 platform molecule.

1.5 Biomass Valorization

In the processing of lignocellulosic biomass, the crystallinity and chemical complexity of feedstock imposes several challenges. High functionality due to presence of various high oxygen content in its chemical structure, is a major challenge in biorefinery processes as more functional groups lead to more side products and chemical intermediate which affects the selectivity of the desired products [(21)]. LCB is required pretreatment/destructive upgradation which can be chemical, biological, and thermal or combination of biological and chemical methods. Enzymatic saccharification, ionic liquid treatment, Ammonia fibre/freeze explosion, CO_2 (supercritical) explosion pretreatment, hot water treatment also known as hydrothermolysis, steam explosion, explosive decompression, steam/aqueous fractionation, aquasolvolysis, non-catalytic solvolysis, organosolvolysis like acetylsalicylic acid, salicylic acid and oxalic acid pretreatment in aqueous-organic solvents, Lime pretreatment, acid hydrolysis (H_2SO_4, HNO_3, HCl and H_3PO_4) and flow through acid pretreatment are some common method used for softening/enhancing the digestibility/delignification of the LCB feedstock [(22-29)]. Cellulose is a major constituent of LCB as stated earlier and it can only be used in biorefinery after segregation from LCB crust.

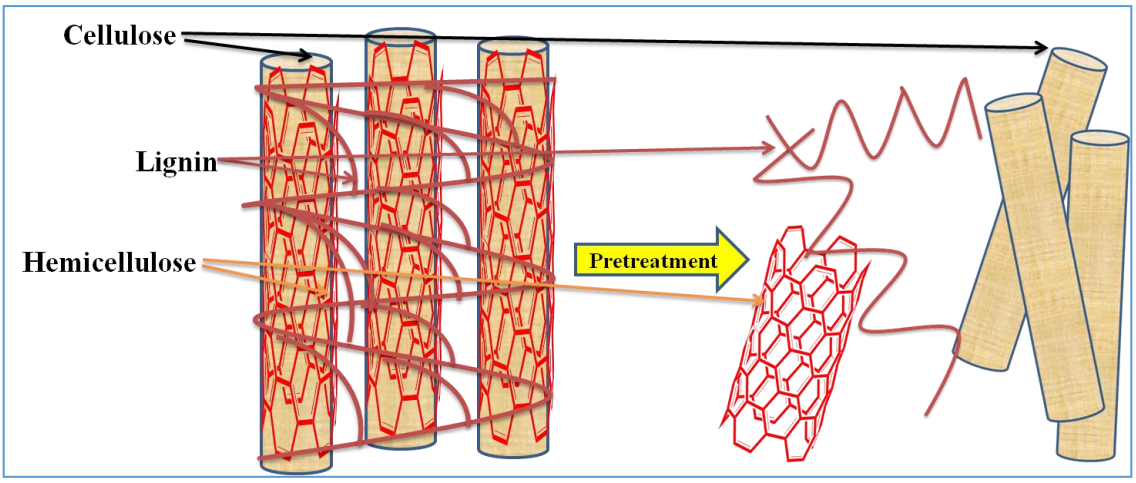

Figure 1.5: Arrangement and pretreatment of lignocellulosic biomass

Cellulose on acid hydrolytic pretreatment gives its monomeric C6 sugar D-glucose and fructose by cleavage of β-1, 4-glycosidic linkage. Similarly hemicellulose which is present on cellulose as shown in **Figure 1.5**, on hydrolysis liberates C5 sugar xylose and arabinose. Generation of various platform chemicals/building blocks. C6 sugar glucose on triple dehydration gives a C6 platform molecule 5-hydroxymethylfuraldehyde (5-HMF) whereas C5 sugar xylose on dehydration in acidic conditions liberates furfural which is a C5 platform molecule. These platform molecules are starting materials for many important commodity chemicals and biofuels. The USDOE enlisted 12 building block chemicals in 2004 as shown in **Figure 1.6** which can be obtained from chemical/biological treatment of platform like 5-HMF and furfural [(30)].

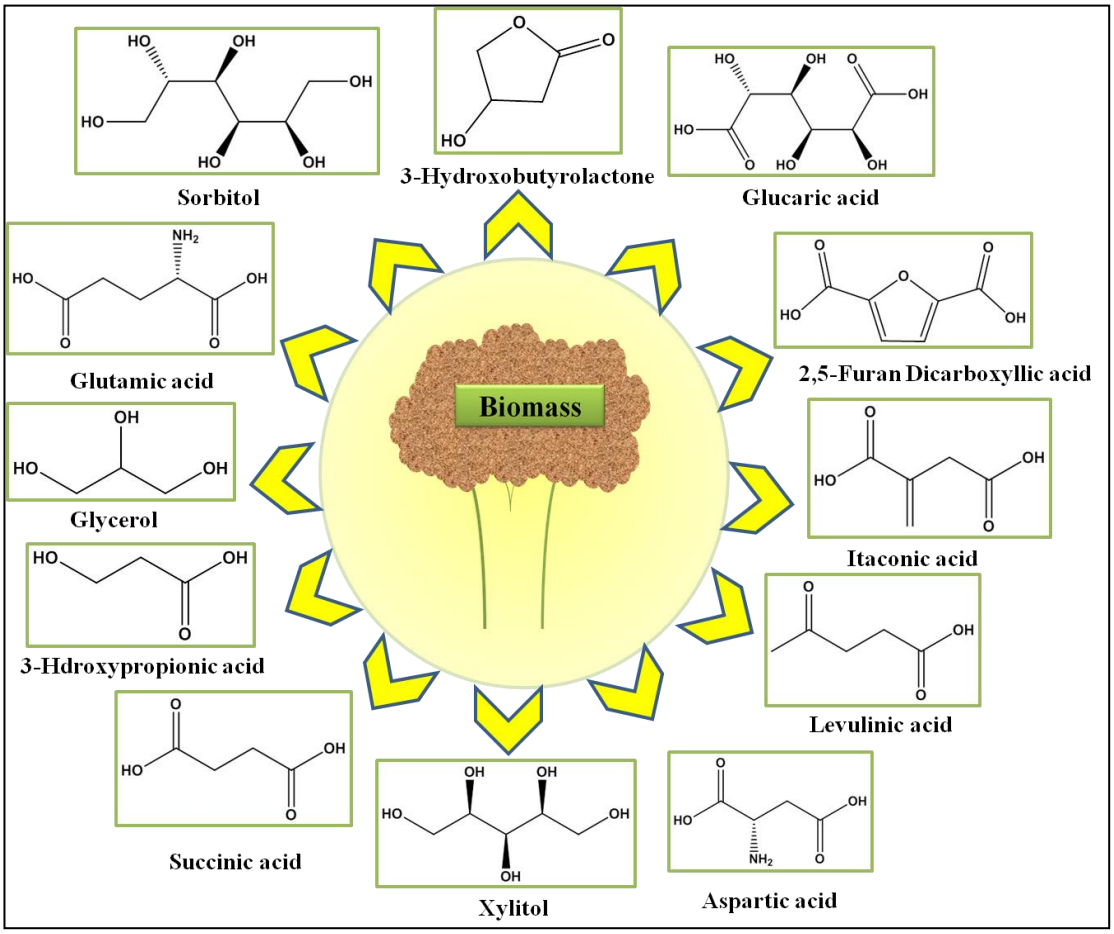

Figure 1.6: Top 12 biobased building blocks chemical enlisted by US DOE in 2004

1.6 5-HMF: A molecule of possibilities

One of the most important perspectives of sustainability and green chemistry is conversion of biomass derived platform molecules into value added chemicals which is considered as the expanded approach of lignocellulosic biorefinery. C6 platform molecule 5-(hydroxymethyl) furfural or 5-HMF obtained from hexose sugars of lignocellulosic biomass is a significant building block molecule in this context. It is a very distinctive molecule as it retains all 6 carbons of hexose sugar [31]. 5-HMF is an aromatic member of furan ring family with –C=O functional group at 2nd and –CH_2OH functional group on 5th position. Due to its multifunctionality and versatility, it is considered as "sleeping giant" or "petrochemical readily accessible from renewable resources" [32-33]. 5-HMF is considered as the connecting link between carbohydrate refinery and biobased products due to its immense chemical

potential [34]. Bozell updated the original DOE report of biobased molecules in his evaluation and included 5-HMF in "TOP 10+4" molecules [35]. According to Business Analytics Centre Report (BAC-2015) the annual global consumption of 5-HMF is 100 t/year emphasizing on the need of rational utilisation of 5-HMF [36]. The first report on 5-HMF was documented way back in 1895 by Düll and Kiermayer independently and termed it as "oxymethylfurfurol" [37]. Middendorp, later on in 1919 presented full scale synthesis, chemical behaviour and physical properties of 5-HMF in his study [38].

1.6.1 Properties of 5-HMF

Table 1.1: Physical and chemical properties of 5-HMF

Sr. No.	**Entries**	**Contents**
1	CAS No	67-47-0
2	EC Numbers	200-654-9
3	Chemical abstract name	5-(hydroxymethyl)-2-furancarboxyaldehyde
4	Molecular formula	C6H6O3
5	Smiles	C1=C(OC(=C1)C=O)CO
6	Molecular Weight	126.11
7	Description	Yellow Powder
8	Boiling Point	110 °C at 0.02 mmHg, 114-116 at 1hPa
9	Melting Point	31.5 °C
10	Solubility	freely soluble in water, methanol, ethanol, acetone, ethyl acetate, dimethylformamide; soluble in ether, benzene, chloroform; less soluble in carbon tetrachloride; sparingly soluble in petroleum ether

11	Density	1.243 g/cm^{-3} at 25°C
12	Flash Point	79 °C in close cup
13	Refractive Index	1.5627 at 18°C
14	Topological polar surface area	50.4 A°^{2}

1.6.2 Production of 5-HMF

There are three synthetic strategies reported for 5-HMF production *i.e.* (I) Maillard reaction of hexose which takes place in presence of amines/amino acids (II) Reverse aldol condensation reaction of C3 macromolecules. (III) Catalytic/ acidic dehydration of cellulosic hexoses [39-41]. The most popular and well studied route which also aligns with the scope of thesis research work is catalytic/acidic dehydration of cellulosic hexoses. A brief introduction to Maillard reaction and Aldol condensation is also presented below.

1.6.2.1 Maillard Reaction for 5-HMF synthesis

Presence of 5-HMF and its derivative in the food particles lead to the origin of Maillard reaction which occurs when reducing sugars reacts with an amino acid like glycine, lysine and proline. According to this reaction, reducing sugars react with amino acids and forms a chemical adduct known as Amadori compound. In many reports Amadori compound acts as a substrate for 5-HMF.Amadori compound undergoes chemical degradation and rearrangement to form 5-HMF as shown in **Scheme 1.1**. Many factors are responsible for synthesis of 5-HMF in Amadori rearrangement but the common understanding is the lower value of pH i.e. (pH<7) [42].

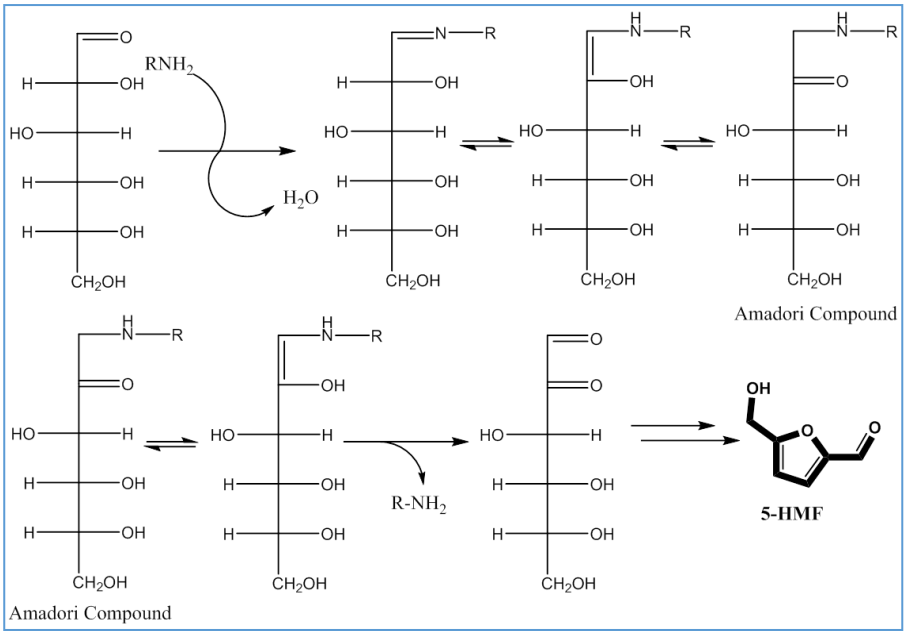

Scheme 1.1: Maillard Reaction for 5-HMF synthesis (Amadori Compound rearrangement)

1.6.2.2 Reverse aldol condensation of C3 macromolecules

Traces of 5-HMF (0.3%) was also observed in the degradation pathways of C3 sugars which was further investigated by retro aldol condensation of C3 sugars [43]. According to this reaction mechanism glyceraldehyde undergoes β-dehydration reaction and form pyruvaldehyde which further reacts with glyceraldehyde and form 5-HMF as shown in **Scheme 1.2**.

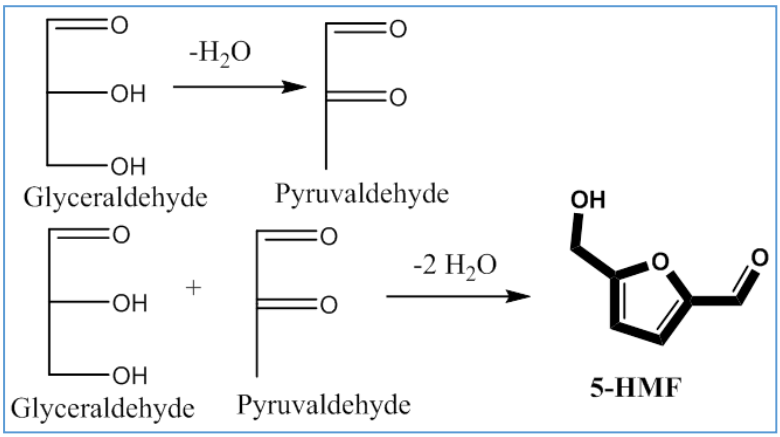

Scheme 1.2: Reverse aldol condensation of C3 sugars for 5-HMF synthesis

1.6.2.3 Catalytic/ acidic dehydration of cellulosic hexoses

Catalytic/acidic dehydration of cellulosic hexoses is the most worked out approach for 5-HMF production. First acidic dehydration of sugar (sucrose) was reported by Dutchman Mulder in 1840 where he got Levulinic acid but misinterpreted it as formic acid [(44)]. Since then the synthesis of 5-HMF from carbohydrate was reviewed regularly by number of researchers [(41, 45-53)]. 5-HMF synthesis was attempted using different starting carbohydrates like monosaccharide, oligosaccharides, polysaccharides, sucrose, inulin, glucose, mannose, fructose, cellulose and also from raw biomass like corn stover, sugarcane and wheat straw etc. [(31, 35, 54-60)]. Most efficient and well known route is dehydration of fructose because of its higher degree of enolisation. Fructose is a ketohexose whereas glucose and mannose are aldohexose which have stable ring structure and less degree of enolisation. The degree of enolisation is the rate determining step for 5-HMF formation which is also known as Lobry deBruyn-Alberda van Ekenstein (LBAE) transformation [(61-62)]. This 1,2-enediol intermediate undergoes 2 successive β-dehydration followed by ring closure with third elimination of water molecule to form 5-HMF as shown in **Scheme 1.3**. This mechanistic approach is given considering hexose sugar as acyclic.

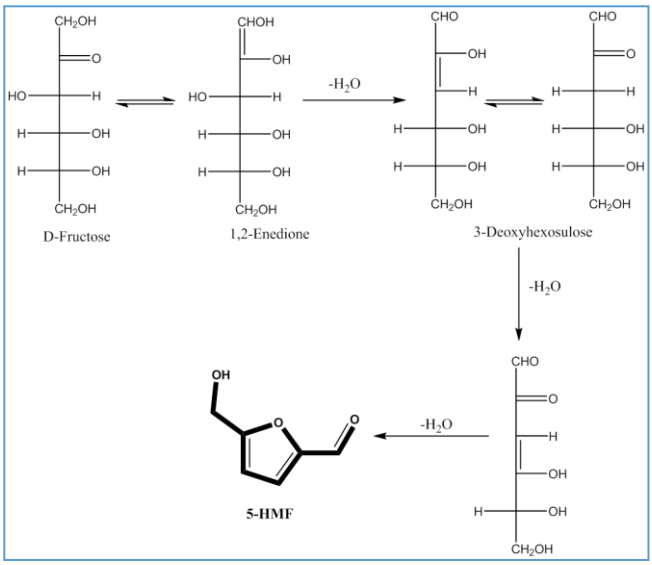

Scheme 1.3: Formation of 5-HMF from acyclic D-fructose

There are several reports on the proposed mechanism for the formation of 5-HMF [63-66]. The initial step of cyclic pathways is considered as formation of tertiary carbenium cation which is facilitated by dehydration of hemiacetal at 2nd position of fructose. Ketofuranose ring undergoes β-dehydration two times which leads to the formation of 5-HMF. Isotope labelling experiments and H^1-NMR studies suggested that all steps except first dehydration of ketofuranose are irreversible which further supported the cyclic pathways of 5-HMF synthesis. **Scheme 1.4** represents the cyclic pathway of 5-HMF production [67].

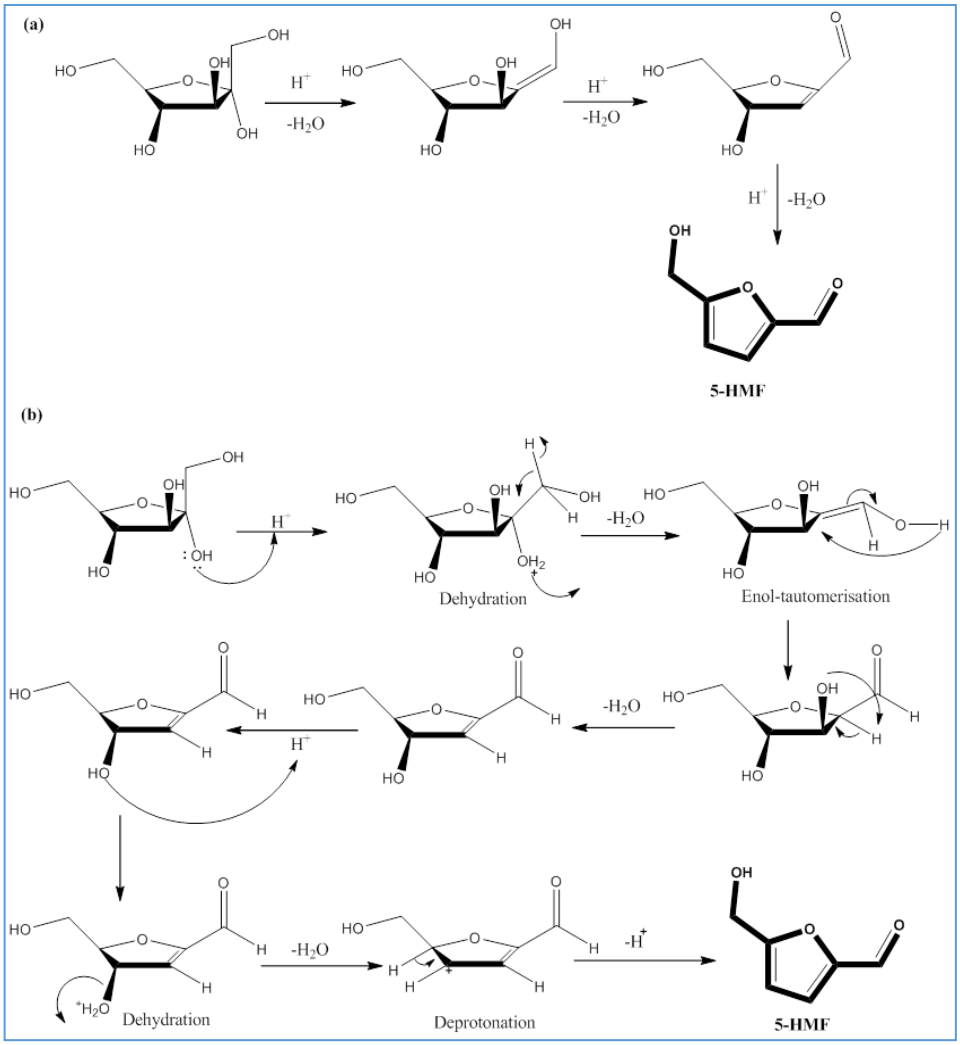

Scheme 1.4: 5-HMF synthesis pathway for cyclic fructose (a) Reaction pathway (b) Reaction mechanism

1.6.3 Versatility of 5-HMF

As 5-HMF is a multifunctional molecule, it can be converted into number of value added utility chemicals as shown in **Figure 1.7**. Hydrogenolysis of 5-HMF produces 2,5-dimethylfuran (DMF) which is a very competitive fuel additive [(68)]. Its detailed properties and synthetic approaches are described later in this thesis. Selective hydrogenation of 5-HMF can produce 2,5-(bishydroxymethyl)furan (BHMF) which is a symmetric diol and can act as monomeric unit for its polyurethane foam [(69)]. A good fuel additive for diesel, 5-ethoxymetylfurfural (EMF) can be obtained by etherification of 5-HMF [(70)]. Functional group hydrogenation followed by furan ring hydrogenation yields into 2,5-(bishydroxymethyl)tetrahydrofuran (BHMFTHF) and can be processed into bioplastic [(71)]. Hydrogenation and ring rearrangement reaction of 5-HMF lead to the formation of 3-(hydroxymethyl)cyclopentanone (HCPN) which is a starting material for pharmaceutical, solvent and fragrance industry [(72)]. Long chain (C7-C15) alkanes can be obtained from 5-HMF by its aldolization/crotonization reactions [(73)]. Similarly oxidation pathway of 5-HMF can be very fruitful in terms of value addition. Partial oxidation and complete oxidation of 5-HMF produces symmetric 2,5-diformyl furan (DFF) and 2,5-furandicarboxyllic acid (FDCA) which acts as building blocks for polyethylenefuranoate (PEF) polymers [(74-75)]. This oxidation pathways also generates one intermediate known as 5-(hydroxymethyl)lfurancarboxylic acid (HMFCA) which is a significant chemical interleukin for the treatment of leukaemia [(76)]. 5-HMF on oxidation can also be converted into maleic anhydride (MAD) which is clinical for the unsaturated polyester resins [(77)]. Ring opening hydrogenation forms 1,6-hexandiol which converted into caprolactum and caprolcatone [(78)]. All these processes describe huge chemical potential of 5-HMF for commodity chemicals and renewable energy. An important and significant aspect of 5-HMF based bioplastic is improved biodegradation which also fulfil the long term goal of reducing environmental carbon footprint.

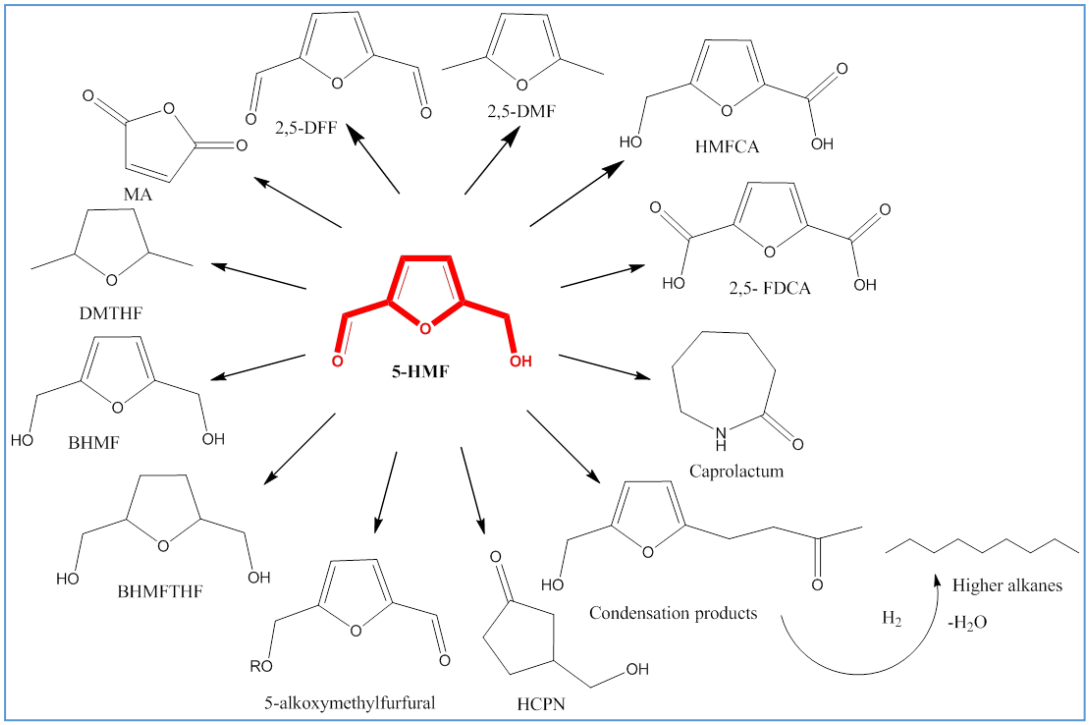

Figure 1.7: Value addition of 5-HMF

1.7 DMF: A promising fuel additive

As shown in **Figure 1.7** hydrogenolysis of 5-HMF results in DMF which is an excellent candidate for fuel additive in C6 lignocellulosic biorefinery.

1.7.1 Properties and application of DMF

DMF has outstanding combustion and emission properties as shown in **Table 1.2**. It has higher value of LHV than bioethanol which is very cost effective for transportation fuels. Its volumetric energy density is almost equals to gasoline and 40% higher than bioethanol [(62)]. Its research octane number is 119 which are higher than bioethanol (110), biobutanol (98) and gasoline (100). Higher value of RON facilitates the use of high engine compression ratios for enhanced fuel economy [(79)]. DMF is stable and easy to store because its solubility in water is very less (0.26% at 20°C) as compared to bioethanol (7.7% at 20°C) [(80)]. Similarly DMF production is also cost effective than bioethanol as it consumes only 1/3rd energy of

bioethanol production [81]. The boiling point of DMF is also highly suitable for suppression of vapour lock of inlet as well as cold starting performance at optimum temperature [82]. Similarly its lower kinematic viscosity (0.57 cSt at 20°C) matches with gasoline (0.37-0.44 cSt at 20°C) and helps both in controlling the injection pressure and protecting the movement of engine [81]. Moreover it has the lower oxygen content (O/C= 0.16) and auto ignition temperature (286°C) than bioethanol (423°C) [83]. The practical application of a fuel additive is only possible if it is not harmful for mankind while use. DMF was not detected in alveolar air while use but it was found in urine sample [84]. It contained moderate aquatic toxicity but no bioaccumulation was observed in various experiments [85]. The fuel characteristics of blending of DMF with gasoline were also tested in single cylinder, spark ignition, Gasoline Directed Injection (GDI) engine [86]. Promising results were obtained for combustion, emission and ignition properties similar to gasoline. Based on above combustion properties and similarity to gasoline, DMF can be a highly suitable automotive energy carrier.

Table 1.2: Fuel properties of Gasoline, DMF and Bioethanol

Sr. No.	**Molecules** **Properties**	**Gasoline**	**DMF**	**Bioethanol**
1	Boiling point (°C)	35	92	77
2	Solubility in Water (% at 20°C)	Insoluble	0.26	7.7
3	Kinematic viscosity (cSt at 20°C)	0.37-0.44	0.57	1.5
4	Lower Heating Value (MJ/Kg)	43.44	32.89	26.95

5	Research Octane Number	100	119	110
6	Volumetric Energy Density (MJ/L)	32.2	31.5	23
7	Gravimetric Oxygen Content (%)	0	34.8	16.7
8	Oxygen Content (O/C)	0	0.16	0.5
9	Autoignition Temperature (°C)	257	423	286

DMF also serves as an adduct for Diels Alder reaction/cycloaddition reaction with ethylene as shown in **Scheme 1.5** and can be upgraded to p-xylene (pX) [87]. pX is a significant commodity chemical currently obtained by Naptha fraction of petroleum with annual global production of 22 million metric tons [88]. The main application of pX is in the manufacturing of polyethylene terephthalate (PET) plastic which is important ingredient of packaging materials, film and fibres [89]. Hence provided its adequate production, DMF can be a highly useful utility chemical as well as potential biofuel additive.

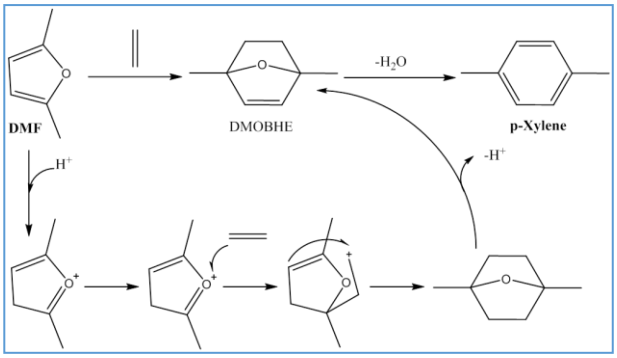

Scheme 1.5: Reaction pathway and mechanism of synthesis of p-Xylene (pX) from DMF

1.7.2 Production of DMF

2,5-dimethyl furan (DMF) was first synthesized by Shunichi in 1980 by reduction of 5-HMF followed by hydrodeoxygenation (HDO) [90]. N_2H_4 was used as reducing agent, in cyclohexene and Pd/C was catalyst for HDO. It can also be produced from lignocellulosic biomass by 2 step process of dehydration followed by HDO of fructose/glucose. Though most common route for DMF production is by HDO/hydrogenolysis of 5-HMF. Both these routes are explained in the following section.

1.7.2.1 Direct production of DMF from raw biomass and Lignocellulosic Sugar

Synthesis of DMF from lignocellulosic sugars is a complex process. It was attempted from raw biomass like sugarcane bagasse, corn stover, wheat straw, cellulose, starch, sucrose, glucose and fructose [91-93]. Direct conversion of lignocellulosic biomass in DMF attempted by Saha *et al*. in 2012 used multicomponent catalyst $[DMA]^+[CH_3SO_3]^-$, Ru/C and formic acid. 32% yield of DMF was achieved using fructose at mild reaction conditions *i.e.* 75°C and 1h whereas at higher temperature (150°C) and longer reaction time gave 14% DMF from α-cellulose, 9.8% and 27% DMF obtained from sugarcane bagasse and agar, respectively [94]. Citing the poor yield of DMF from biomass, two step processes was designed by many researchers involving cellulosic sugars conversion to 5-(chloromethyl) furfural (CMF) and subsequent conversion to DMF [84]. Another option involves raw biomass dehydration to 5-HMF followed by its HDO to produce to DMF.

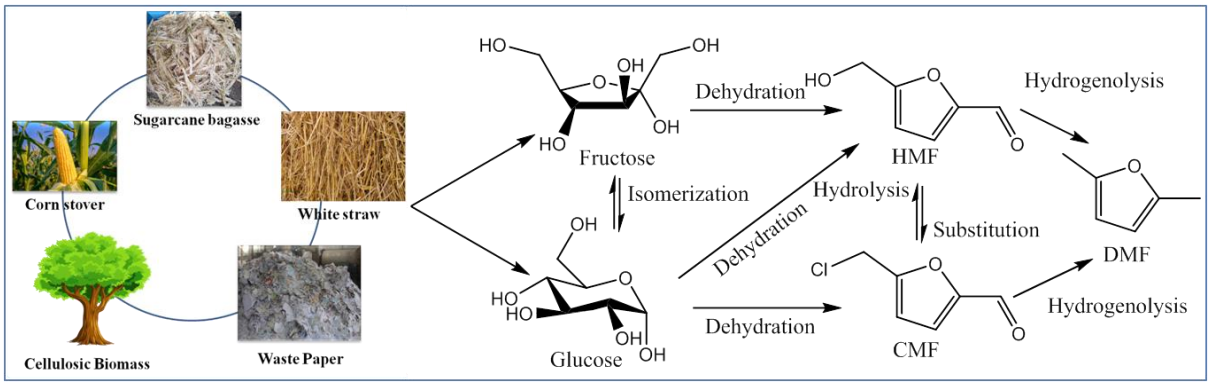

Figure 1.8: Synthetic route of DMF directly from lignocellulosic biomass

CMF is treated as an important biomass derived chemical plant oil in biofuel precursor as it can be converted into suitable fuels by reacting with alcohols [95]. Mascal and Nikitin synthesized CMF from a number of biomass sources like corn stover (80.2%), cellulose (83.5%), sucrose (89.7%) and glucose (81.2%). They used aqueous HCl and dichloromethane in presence of LiCl at high temperature and obtained excellent yield of CMF (above 80%) from all the sachharides [95]. Due to its easy production from raw biomass like corn stover, and wheat straw, CMF is attractive starting material for synthesizing DMF. Utilising strategy of mixed homogeneous (5-50% NH_4Cl or conc. HCl) and heterogeneous catalysts (5% Pd/C) in aqueous conditions 25% of CMF was produced from cellulose which further undergoes HDO to produce 96% yield of DMF [96]. Similar mixed catalytic systems were identified by Dutta and Mascal where they used N,N-Dimethylformamide/ acetic acid and Pd/C catalyst for corn stover derived CMF (65% yield) at 3 atm H_2 and obtained 76% yield of DMF after 1.25 h of reaction [97]. To enhance the productivity and cost effectiveness of raw biomass to DMF production, 5-HMF pathway was also explored.

1.7.2.2 DMF via 5-HMF route

Emphasis on production of 5-HMF in recent years been a hot topic in biomass valorization. It also is an intermediate in DMF production starting from Lignocellulosic biomass. In the first step, biomass is dehydrated to 5-HMF with the help of any mineral acid, ionic liquid or saline

biphasic solution. 5-HMF is then extracted and undergoes hydrogenolysis over heterogeneous catalysts to obtain DMF. Dumesic *et al.* used Cu-Ru/C along with biphasic saline solution for 71% yield of DMF directly from fructose in 2 step process [68]. Employing saline solution improved the partitioning of HMF during extraction by enhancing the extraction ratio of organic phase (1-butanol). A brief literature search of DMF production from biomass via 5-HMF is given in **Table 1.3**.

Table 1.3: DMF production from biomass via 5-HMF

Sr.No.	**Starting Material and Catalysts**	**Reaction Conditions**				**Efficiency (%) (DMF production)**			**Ref**
		T (°C)	**P (bar)**	**Rt (h)**	**Solvent**	**C (%)**	**S (%)**	**Y (%)**	
1	Fructose, HCl-NaCl 5-HMF, Cu-Ru/C	180 220	-- 6.8	3 m 10	Water and 1-butanol 1-butanol	88 100	82 71	71 71	68
2	Fructose, DMA-KI, H_2SO_4 Glucose, $CrCl_2$, DMA-NaBr Cellulose,$CrCl_2$, [EMIM]Cl LCB, $CrCl_2$, [EMIM]Cl 5-HMF, Cu-Ru/C	100 100 140 140 220	-- -- -- -- 6.8	5 2 2 1 10	DMA DMA DMA DMA 1-butanol	-- -- -- -- --	-- -- -- -- --	33 69 9 19 49	62

3	LCB, Conc HCl, PS-NH_3Cl 5-HMF, 5%Pd/C	120 25	-- PM HS	2 1	Cyclohexane 1-butanol	-- 81	-- --	19 1	96
4	Fructose, Formic Acid (FA) 5-HMF, Pd/C, H_2SO_4	150 70	-- FA	2 15	DMSO THF	-- --	-- --	93 51	98
5	Glucose, 12-MPA 5-HMF, Pd/C	120 120	-- 62	3 1	[EMIM]Cl, ACN [EMIM]Cl, CAN	71 47	89 32	63 16	99
6	Glucose, Amberlyst-70, Sn-β Zeolite 5-HMF, Sn-Ru/C	170 200	-- H_2	40 min 4	GVL:H_2O (9:1) GVL	88 --	70 --	59 27	100
7	Fructose, Amberlyst-15 5-HMF, Ru-Sn/ZnO	100 240	-- 1	5 100	1-butanol 1-butanol	96 100	97	93 99	101
8	Glucose, Pd/UiO-66@SGO Fructose, Pd/UiO-66@SGO	180 160	10 10	3 3	THF THF	87 91	63	45 70	102
9	Fructose,	110	--	40m	Ethanol and	--	38	48	103

	Amberlyst-15 5-HMF, 10%Ni@WC	150	30	3	FA Ethanol	100	--	39	

1.7.2.2.1 Nobel metal catalysts for hydrodeoxygenation of 5-HMF

Noble metals are known to be highly active for hydrogenation due to their partially filled d orbitals, ease of reduction from their metal precursors, redox nature etc [104-105]. 5-HMF hydrodeoxygenation is vastly explored on supported Pd, Pt, Ru and Ir catalysts. Mixture of supercritical CO_2 (100 bar) and water was screened for 5%Pd/C at mild temperature of 80°C and 10 bar of H_2 with complete conversion and yield of DMF [106. Same catalyst was also investigated with formic acid as additive in THF solvent and 95% DMF was achieved after 15 h of reaction at 120°C [107]. Pd was also screened on different supports like Cs doped polytungstic acid, vulcanised CNT and other metals like Au, Fe and Co as bimetallic combinations with moderate Substrate/catalyst ratio and mineral acids like HCl [110,121,107 and 119]. Ru was extensively explored on various supports for 5-HMF hydrodeoxygenation like activated C, CNT, industrial carbon source like MSC-20, hydrotalcites (HT), zeolites like NaY, ZSM-5 and K doped mesoporous Silica (K-OMS2) [109, 117, 124, 112, 113, 123 and 111]. Bimetallic combinations of Ru with Co and Mo were also reported at very high temperature [115 and 118]. Some highly efficient Ru catalysts with excellent TON were designed by Nagpure *et al.* (Ru/NaY) owing to very high dispersion. Gao *et al.* (Ru-Co) provided its surface defects due to Oxygen vacancy at metal support interface enhancing Hydrogen spillover effect and Zeng *et al.* (Ru@MSC-30) because of excellent interaction between Ru species and microporous carbon support [113, 118, 124]. Few reports of Monometallic and bimetallic catalysts of Pt supported over carbonaceous material are also documented. Temperature of

hydrodeoxygenation was observed to be dependent on the type of supports. It was 120°C for Pt/r-GO where 73.2% DMF obtained at 30 bar of external H_2 pressure [114]. When Pt was combined with Co and supported on MWCNT 92.3% DMF was obtained at 160°C and 10 bar of external H_2 pressure [116]. Higher temperature of 180°C required in case of hollow carbon sphere supported Pt where excellent yield of 98% towards DMF was achieved [125]. SiO_2 impregnated Ir was also reported by R J Chimentao *et al* where they used mineral acids like H_2SO_4 and HCl for better yield but use of mineral acids lead to deactivation of catalysts [122].

Table 1.4: Literature survey for 5-HMF hydrogenolysis to DMF by noble metal catalysts

Sr. No.	**Catalysts**	**Reaction Conditions**					**Efficiency (DMF production) (%)**			**Ref**
		5-HMF/ Cat. Ratio	**T (°C)**	**P (bar)**	**Rt (h)**	**Solvent**	**C (%)**	**S (%)**	**Y (%)**	
1	5%Pd/C	5	80	100 CO_2 10 H_2	2	$ScCO_2$: H_2O	100		100	106
2	Pd-Au/C (50:50)	1	60	1	6	THF/ HCl	99		99	107
3	5%Pd/C	20	120	2	15	1,4-dioxane Formic acid	100		95	108

4	5%Ru/C	2	200	20	2	THF	100		95	109
5	2%Pd-20%$Cs_{2.5}H_{0.5}PW_{12}O_{40}$	30	90	10	2	THF	98	81		110
6	2%Ru-KOMS-2	3	220	10	6	1-butanol	100		33	111
7	0.56%Ru/HT	2	220	10	4	2-propanol	100		58	112
8	2%Ru-NaY	200	220	15	1	THF	100		78	113
9	2%Pt/r-GO	100	120	30	2	1-butanol	100		73	114
10	5%Ru-10%MoO_x/C	5	180	15	1	1-butanol	100	72		115
11	3%Pt-25%Co/MWNT	2	160	10	8	1-butanol	100		92	116
12	5%Ru/CNT	84	150	15	1	1,4-dioxane	100		84	117
13	3%Ru-Co	252.7	200	5	2	1,4-	100		97	118

						dioxane				
14	20%Fe-1%Pd/C	13	150	20	3	THF	100	85		119
15	4%Ru-8%Co/SiO_2	2.5	120	15	8	THF	100		99	120
16	Pd-CoS_8/S-CNT	2.5	120	3	13	THF	96	84		121
17	1%Ir/SiO_2	100	50	10	5	THF/HCl	97	100		122
18	1%Ru/ZSM-5	2	180	17	3	Ethanol	98	97		123
19	2.5%Ru@MSC-30	252	125	5	1	IPA	100		70	124
20	2%Pt-1%Co@HCS	5	180		2	1-butanol	100		98	125

1.7.2.2.2 Non-Noble metal catalysts

Though Noble metals are well known and much explored for catalytic hydrogenation, their poor abundance and higher cost is a limiting factor for their full scale utilisation as catalysts. To counter this problem, non-noble transition metals were investigated for 5-HMF hydrodeoxygenation. Promising results were shown by many Co, Cu, Ni and bimetallic non-noble catalytic combinations as shown in **Table 1.5**. Supported Ni is most explored non-noble transition metal for HMF hydrogenolysis reaction as it enhanced the reusability and

hydrogenolysis efficiency of catalytic entity. It was screened on activated charcoal, WO_3, Co_3O_4, Al_2O_3, zeolites like ZSM-5 as well as in form of bimetallic combination like Ni-W_2C/AC and Ni-Cu/SBA-16 etc [133, 135, 129, 130, 143, 127 and 140]. Efficient supports and bimetallic synergism imparted bifunctional acidic sites to enhance multiple steps of hydrodeoxygenation. Similarly robust alloy combinations like Cu-Zn and supported Ni-Fe/CNT were also investigated [128 and131]. Porous mesoporous oxide supported Cu was screened for 5-HMF hydrogenolysis in supercritical methanol by Hansen et al but they suffered from poor yield [126]. But highly active and efficient synergism was observed when Cu was introduced with other metals. Co driven by its excellent nature of absorbance of hydrogenation adducts and acidic sites on CoO_x species and metallic species also proved sustainable alternative to noble metal hydrogenation [134].

Table 1.5: Literature survey for non-Noble metal hydrodeoxygenation of 5-HMF

Sr. No.	**Catalyst**	**Reaction Conditions**					**Efficiency (%) (DMF production)**			**Ref**
		HMF/ Cat. Ratio	T (°C)	P (bar)	Rt (h)	Solvent	C (%)	S (%)	Y (%)	
1	Cu-PMO	1	300	Sc-MeOH	0.75	CH_3OH	100		34	126
2	Ni-W_2C/AC	1	180	40	3	THF	100		96	127
3	Cu-Zn	5	220	20	5	CPME	100		97*	128

4	Ni/Co_3O_4	2.5	130	10	24	THF	99		76	129
5	Ni/Al_2O_3	15	180	12	4	1,4-dioxane	100		92	130
6	Ni-Fe/CNT	10	200	30	3	1-butanol	100		91.3	131
7	Cu-Co(1:3)/C	12.5	180	50	8	Ethanol	100		99.4	132
8	Ni/C	2.30	180	100	2	THF	100	87		133
9	Co_3O_4	5	170	10	12	1,4-dioxane	100		83.3	134
10	Ni/W_2O_3	7	180	10	6	H_2O	99	95		135
11	Cu-ZnCox	3.3	210	EtOH	5	Ethanol	100	99		136
12	Co/β-Zeolite	5	150	15	3	THF	100		83.1	137
13	Co-NC/NiAl	2.5	170	15	6	THF	99.9	99.9		138
14	Cu/Al_2O_3	42	150	20	10	THF	100		90	139

15	Ni-Cu/SBA 16	0.2	210	20	6	THF	100		60.7	140
16	FeCoNi/ h-BN	1.2	180	20	5	THF	100		94	141
17	Ni-Fe/TiO_2	6.67	220	30	3	1,4-dioxane	100		75	142
18	40%Ni/ZSM-5	2.5	180	2.5	7	THF	96.2		91.2	143

1.7.3 Reaction Pathways of 5-HMF hydrodeoxygenation

Catalytic hydrodeoxygenation of 5-HMF proceed via two step process of hydrogenation and hydrogenolysis as shown in **Scheme 1.6**. During hydrogenation of 5-HMF the –C=O group is converted into $–CH_2OH$ and hence BHMF is formed. Due to high activity of catalytic entity sometimes hydrogenation of C2 aldehydic group and hydrogenolysis of C5 $–CH_2OH$ group involved in competitive reaction. In such instances delocalisation of electron over furan ring plays an important role as this conjugation stabilises the ring but due to electron withdrawing nature of Oxygen both functional groups remain labile [(144)]. Hence hydrogenation of -C=O occurs predominantly despite the fact that C=C hydrogenation is thermodynamically more favourable process. In second step BHMF undergo hydrogenolysis on both side of the ring subsequently and 2,5-DMF is formed. This DMF can also undergo to ring hydrogenation and form DMTHF whereas ring opening of DMF lead to formation of 2-hexanol. Ring opening can also occur at BHMF step leading to the formation of 1,2,6-hexantriol. The hydrogenolysis instead of hydrogenation in first step leads to the formation of MFFR. MFFR

hydrogenation results into MFAL which further undergo hydrogenolysis to from DMF. Hydrogenation or hydrogenolysis as primary steps is decided by geometries of absorption species on metal surface, nature of Hydrogen species and acidic properties of catalytic systems [145, 146]. This fact gave the ample amount of space to study in the area of support study and bimetallic synergism.

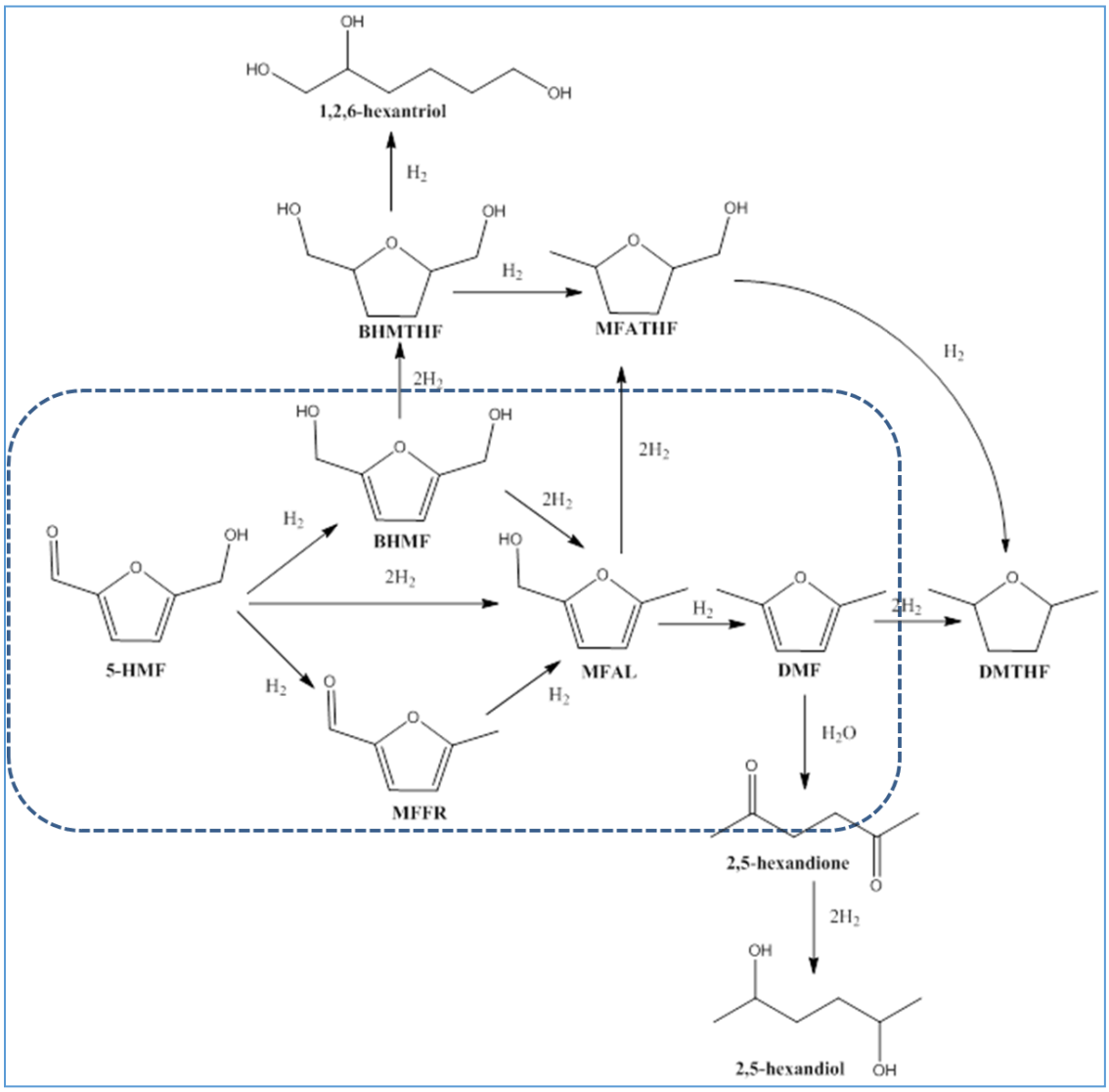

Scheme 1.6: Detailed Hydrodeoxygenation pathway of 5-HMF

1.8 Catalytic Hydrogenation

In biomass refineries most important task to obtain clean, efficient and qualitative fuel alternative is reducing the abundant Oxygen species present in platform molecules.

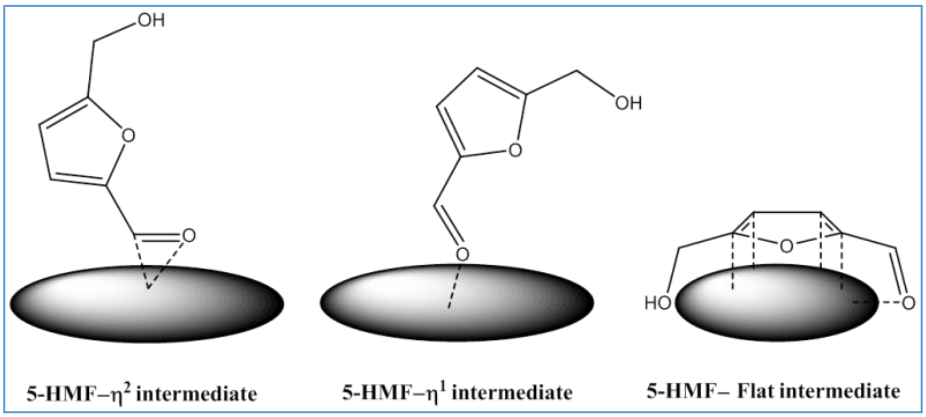

Scheme 1.7: Various adsorption geometry of 5-HMF on catalytic surface

The surface of metallic nanoparticles provides the platform for the adsorption and activation of Hydrogen molecule which attacks on the unsaturated centre of target molecule. It also acts as adsorption site for reactant molecule via different atom of reactants. Transition metals have vacant d orbitals which are clinical in performing the hydrogenation reaction as more will be the number of vacant d orbitals stronger will be the bond strength of metal-hydrogen bond [(148)]. But in order to perform hydrogenation activity Metal-Hydrogen bond should not be very strong so maximum activity is performed by transition metals containing one vacant d orbital [(149)]. Aforementioned hydrogenation process largely depends on adsorption geometry of molecule on surface, nature of Hydrogen species and acidic or basic properties of catalytic surface. Reports are available for 5-HMF where fate of the reaction decided by the η^1 or η^2 geometry of intermediate (**Scheme 1.7**) [(150-151)].

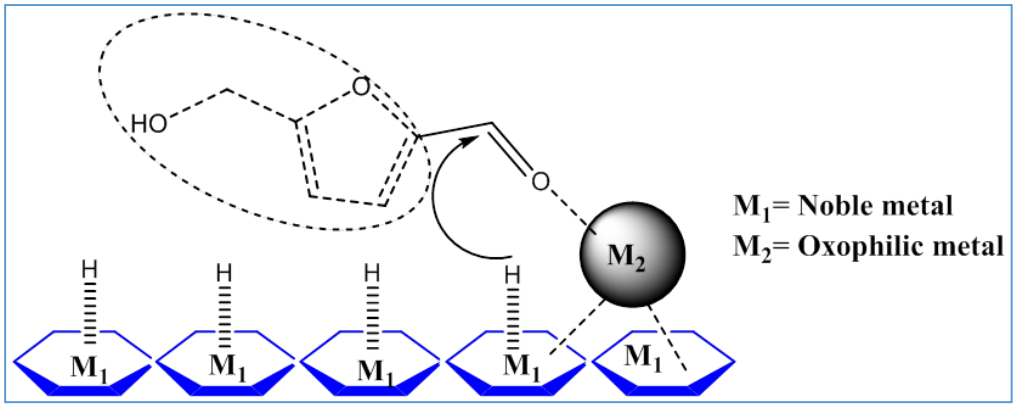

Scheme 1.8: Effect of oxophilic metal addition on 5-HMF hydrogenation

Many oxophillic metals having acidic properties are investigated with the combination of noble metals as well as non-noble metals. This promotional effect induced by oxophilicity was found to provide a significant push to H-transfer property of noble metals and also adsorption geometry of molecules as shown in **Scheme 1.8** [(152-153)]. This provides the fine tunability and high selectivity while synthesizing selectively efficient catalysts.

1.9 2,5- diformyl furan (DFF): Oxidative value addition of 5-HMF

The oxidative treatment of 5-HMF can also produce numerous value added chemicals. 2,5-diformyl furan (DFF) is one of those highly value added fine chemical which has huge market potential because of its ability to convert into plenty of useful products. DFF is highly useful for polyurethane industry as it can acts as monomeric unit for polymeric-urea resin, polymeric Schiff's base with primary amines, polyamines. It has application in pharmaceutical industry, composite, adhesive, foams, binders, sealants, solvents and organic conductors [(154-156)]. It can be converted into numerous fluorescent chemicals, antifungal agents, sapphyrin based macrocyclic ligands, surfactants and vitrimers [(157-158)]. Considering its vast scope and ability catalytic oxidation of 5-HMF becomes a significant process in C6 biorefinery.

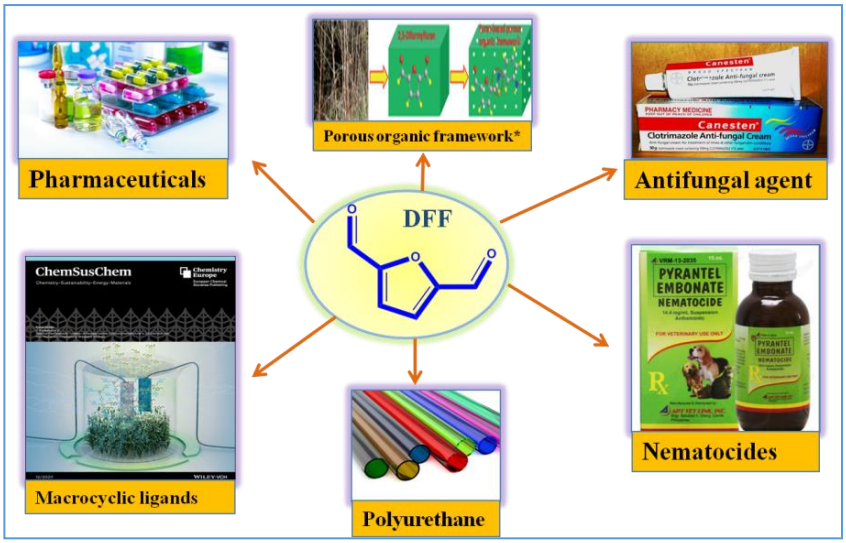

Figure 1.9: Industrial application of DFF

1.9.1 Properties and scope of DFF

DFF contains two highly active aldehydic groups at 2nd and 5th position of furan ring. This make it highly symmetric and aromatic as conjugation of ring is also remain uninterrupted in side chains. It is an odourless solid white powder at room temperature with molecular weight of 124.094 g/mol. **Table 1.6** shows its detail physical and chemical properties.

Table 1.6: Physical and chemical properties of DFF

Sr. No.	**Entries**	**Contents**
1	CAS No	823-82-5
2	EC Numbers	212-520-7
3	Chemical abstract name	2,5-furandicarbaldehyde
4	Molecular formula	$C_6H_4O_3$
5	Smiles	C1=C(OC(=C1)C=O)C=O
6	Molecular Weight	124.094
7	Description	White solid

8	Boiling Point	276.8 °C at 760 mmHg
9	Melting Point	110 °C
10	Solubility	Partially soluble in water and soluble in few organic solvents like ethyl acetate, chloroform and alcohols
11	Density	1.298 g/cm^{-3}
12	Flash Point	124.1 °C
13	Refractive Index	1.585
14	Topological polar surface area	47.3 $A^{\circ 2}$

DFF can undergo multiple chemical transformations due to its unique structural properties. Some of them are shown in **Figure 1.10**. Furan-2,5-dicarbonyl chloride (FDCC) which is an important chemical intermediate for furoate ester biofuel production can be obtained by oxidation of DFF in presence of t-butyl hypochlorite [(159)]. Reductive Amination of DFF generates monomeric units of poly methyl amines whereas dehydration and hydrogenation generates 2,5-dicyanofuran and 2,5-bis(aminomethyl) furan [(160]. Similarly high demand molecule like maleic acid and monomers for resins and artificial fibres like BHMF can be obtained by simple oxidation and hydrogenation process respectively [(161)].

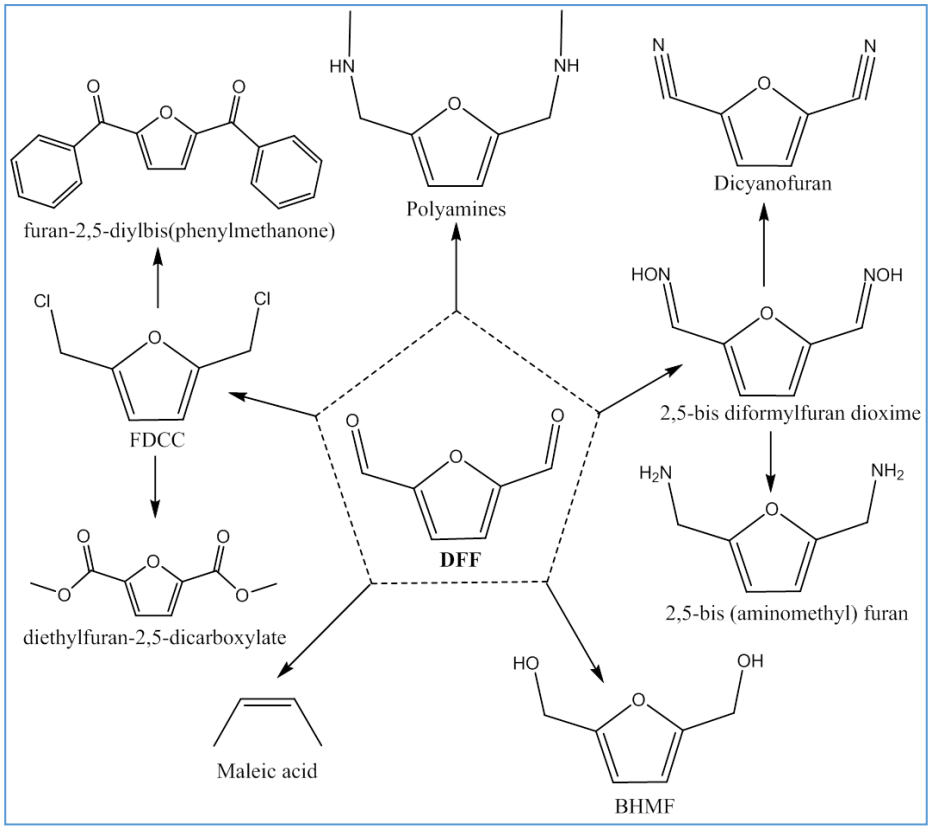

Figure 1.10: Chemical transformation of DFF into fine chemicals

1.9.2 Literature survey

Significant research was devoted since early 19th century for production of DFF from HMF due to its immense market potential and high utility. Different method including stoichiometric oxidation, homogeneous catalysts and heterogeneous catalysts were explored for the HMF oxidation. Earlier chemical oxidants like $Pb(OAc)_4$/Pyridine, $BaMnO_4$, 2,2,6,6-tetramethylpiperidine-1-oxide (TEMPO), CrO_3/Pyridine, Pyridinium chlorochromate-aluminium oxide and lately Mn-salen/NaOCl, $K_2Cr_2O_7$-DMSO, 4-hydroxy-TEMPO radical with [bis-(acetoxy)-iodo] benzene (BAIB) with acetic acid as co-oxidant and Fe_3O_4@ SiO_2-TEMPO and t-butyl nitite/acetic acid in toluene were used [163-169]. But these chemical oxidants generate lots of hazardous material which are not coherent with the principals of green chemistry. Homogeneous catalysts like CuCl, Lewis acids like $AlMe_3$, Co/Mn/Zn in presence of Br^- ion, $CuNO_3$/$VOSO_4$ and other Vanadium complexes are designed to obtain

good yield of DFF [170-174]. High efficiency, sustainable extraction/ separation and elimination of harmful oxidant were major challenges in front of heterogeneous catalysts which were addressed by many researchers as described below.

Many noble as well as non-noble metal heterogeneous catalytic systems were screened for selective oxidation of 5-HMF with a major emphasis on Ru, V and Mn variants. Ru/C proved efficient for longer reaction time although selectivity towards DFF was always high [175, 176]. Functionalised materials like zirconium phosphate, covalent triazine framework and N-containing mesoporous-polymelamine-formaldehyde were also investigated for a longer reaction time but suffered from poor yield of DFF [177-179]. Ru nanoparticles on ϒ-Al_2O_3 proved highly efficient catalyst at relatively milder conditions of 40 psig Oxygen pressure, 120°C temperature and with 5-HMF/Catalyst= 1.2. After 4h of reaction in toluene Antonyraj *et al.* obtained 97.3% selectivity to DFF with 100% conversion [180]. Ag-NP incorporated over octahedral molecular sieves (OMS-2) were found highly efficient with 100% selectivity to DFF and 99% conversion in 2-propanol at 120°C and 220 psig external pressure of O_2 after 4h [181]. **Table 1.7** highlights the major noble metal catalysts for HMF oxidation.

Table 1.7: Noble metal catalytic oxidation of 5-HMF to DFF (*= starting material was Fructose)

Sr. No.	**Catalyst**	**Reaction Conditions**					**Efficiency (%) (DMF production)**			**Ref**
		5-HMF/ Cat. Ratio	T (°C)	P (bar)	Rt (h)	Solvent	C (%)	S (%)	Y (%)	
1	Ru/C	3	110	20	2	Toluen	30	96.2		175

						e				
2	Ru/C	3	110	20	0.3-7	Toluene	100	95.8		176
3	Ru/ZrP	1	110	20 ml min^{-1}	12	Toluene	91	66		177
4	Ru/Triazine	40*	80	20 (air)	6	MTBE	86.3	63.6		178
5	Ru/Mes_N	5	105	20	12	Toluene	99.6	85		179
6	Ru/ϒ-Al_2O_3	31.5	120	3	4	Toluene	100	97.3		180
7	Ag/OMS-2	1	120	15	4	IPA	99	100		181

V and Mn are some non-noble metals which are studied extensively for DFF production from 5-HMF. V- based catalyst in particular were explored because of their high surface density and acidic properties. V_2O_5/C was found highly active at very low pressure of external O_2 (3 bar). 98% selectivity to DFF was achieved with 95.1% conversion of HMF at 100°C in toluene after 4h of reaction [182]. Intercalated VOPO were designed by Grasset *et al.* for DFF production at atmospheric pressure of O_2 in toluene at 110°C. 83% yield of DFF was obtained after 6 h of reaction with 99% conversion [183]. $VOPO_4$ based catalysts were synthesized by

Carlini et al. where they substituted VO^{3+} species by various cation and it was observed that Mg/VPO was most active variant with 74% conversion and 85% selectivity to DFF [184]. Immobilised Vanadyl-pyridine complex on polymeric and organofunctionalized mesoporous support was prepared by O. C. Navarro et al with moderate selectivity to DFF (75%) after very long reaction time [185]. Tendency to cross polymerise and decarbonylation limits the use of Vanadium based catalysts. Mn based catalyst remain efficient even at relatively lower pressure of external O_2. They were explored in bimetallic combination with Cu, Al and Fe in organic as well as aqueous solvent but energy consumption was a major concern due to longer reaction time [186, 187, 191 and 193]. Mo, Zr, Ce and Co showed bimetallic constructive synergism generating excellent yield of DFF [188-190 and 192]. **Table 1.8** represents the non-noble metal literature for selective oxidation of 5-HMF in DFF.

Table 1.8: Non-noble metal explored for 5-HMF oxidation to DFF

Sr. No.	**Catalyst**	**Reaction Conditions**					**Efficiency (%) (DMF production)**			**Ref**
		5-HMF/ Cat. Ratio	T (°C)	P (bar)	Rt (h)	Solvent	C (%)	S (%)	Y (%)	
1	V_2O_5/C	2	100	3	4	Toluene	95.1	98		182
2	Intercalated VPO	420	110	1	6	Toluene	99		83	183
3	VPO based Catalyst	2.52	100	1	6	DMF	84	95		184

4	V-Py_Meso	30	130	10	24	Toluene	75	82		185
5	Mn/OMS-2	2	120	10ml/Min	8	DMSO	100		94	186
6	Cu/MnO_2	5	140	20ml/Min	17	DMSO	99	86		187
7	$Bi(NO_3)_3$ Cellulose/Cu	200	90	8	24	Water	90	87		188
8	Ce-Mo	60	100	10	6	Toluene Na_2CO_3	100		99	189
9	Mo-Zr(S)	6.3	120	20ml/Min	4	N,N-DMF	100		82.1	190
10	Cu:Mn:Al	2	120	10ml/Min	8	DMSO	100		94	191
11	MOF_Co-Fe	20	140	20ml/Min	17	DMSO	99	86		192
12	Mn-Fe	0.79	90	8	24	Water	90	87		193

1.10 2,5-furandicarboxyllic acid (FDCA): A sleeping giant

Many fine chemicals can be produced by oxidation of 5-HMF like HMFCA, MA, DFF and FDCA. Complete oxidation of both functional groups of 5-HMF produces 2,5-furandicarboxyllic acid. The importance of this fine chemical can be understood by the fact that it was included in the TOP 12 biobased molecules list issued by US Department of Energy.

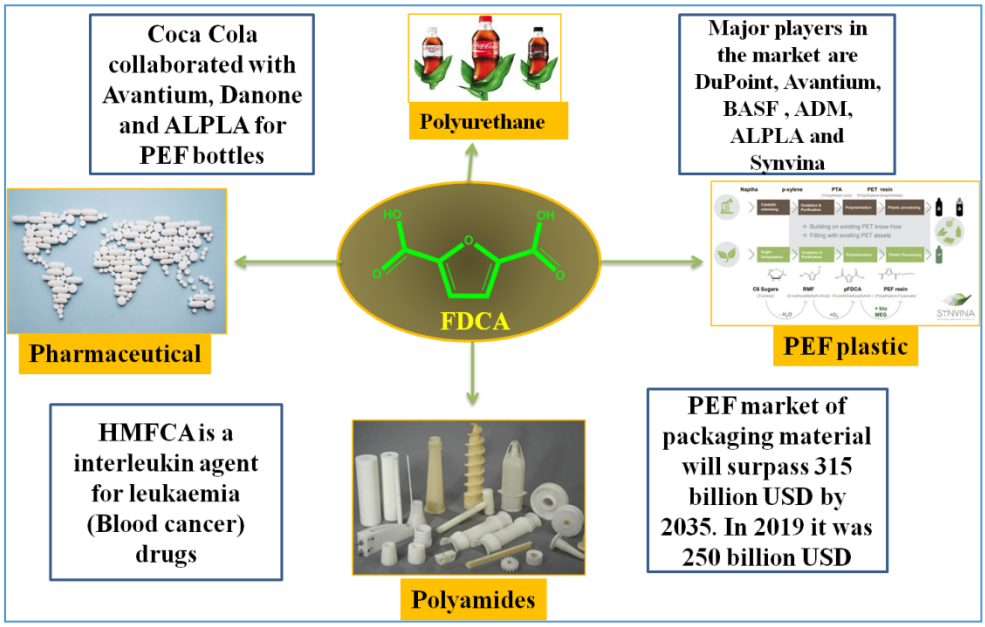

Figure 1.11: Market potential of FDCA

It can significantly reduce the Carbon footprints and almost eliminate the "white pollution" generated by petroleum based plastics. Estimated production of plastic around the world is 1124 million metric ton/year generated by conventional terephthalate polymers like Poly ethylene terephthalate (PET) and Poly butylenes terephthalate (PBT) [(194)]. Almost 12 million metric ton of biobased aliphatic plastic is generated by biorefineries as a part of renewable industry but they suffer from poor performance. Its main reason is lack of aromatic characteristics compared to traditional petrochemical derived plastics [(195)].

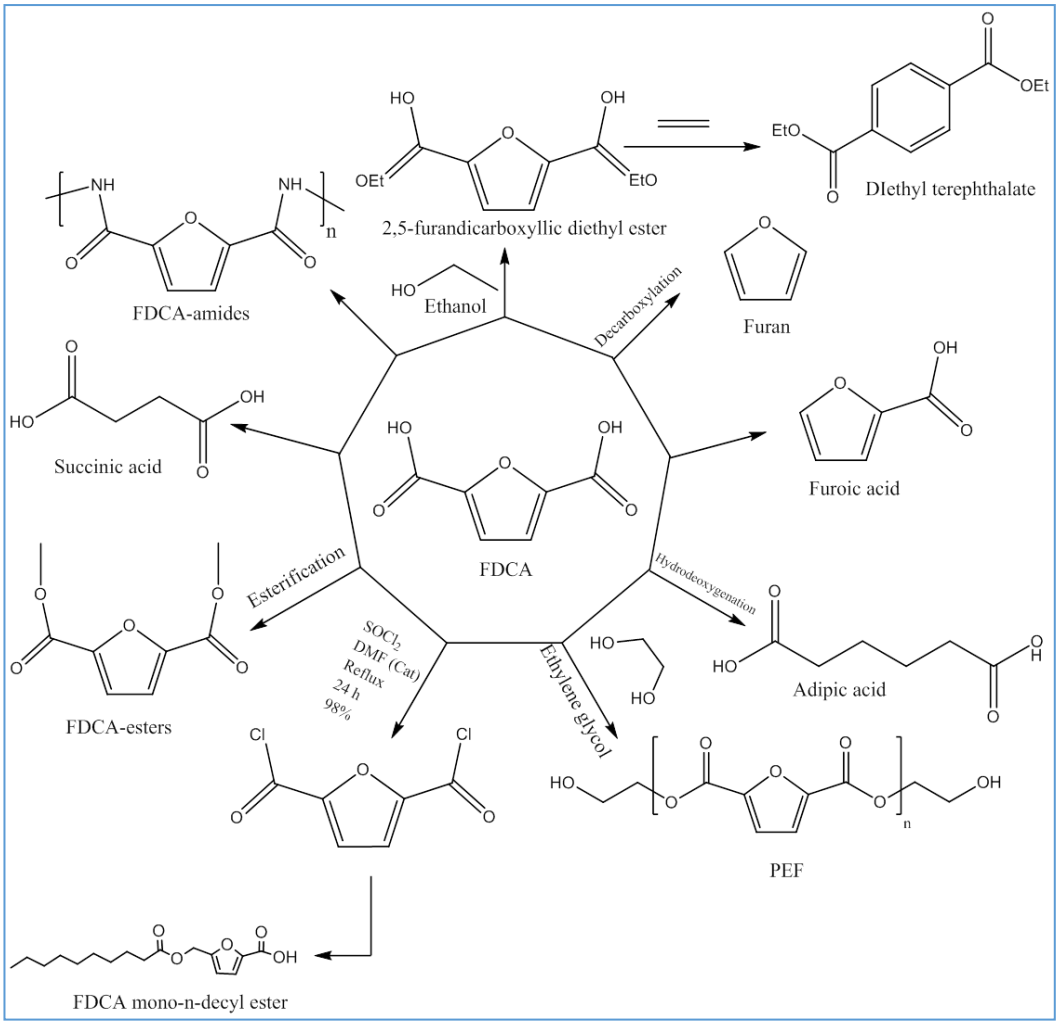

Figure 1.12: Chemical transformation routes of FDCA

Hence, FDCA is considered as a "sleeping giant" because of its structural analogy with terephthalic acid which can open the gate for extra efficient polymeric properties [53]. FDCA has immense applications in pharmacology, organic synthesis, MOF designing and polymers like polyamides, polyesters and polyurethanes [196-200]. FDCA derived polyethylene furanoate (PEF) has shown remarkable polymeric properties and has ability to overcome the drawbacks of PET plastics. It was estimated that approximately 50% (440-520 PJ) reduction of non-renewable energy and 45-55% (20-35 Mt of CO_2 equivalent) reduction in green house gases are possible with complete replacement of PET by FDCA derived PEF which will further require generation of approximately 15 million metric ton PEF/year [201]. PEF has higher

glass transition temperature (82-87°C) compared to PET (71-75°C) and lower melting point (40°C) which not only make it heat resistant but also enhance the ability of blow molding and extrusion process [202-204]. This generates thinner wall of PEF with higher strength and modulus and has excellent gas barrier property, reduction of CO_2 and O_2 several fold than PET [205-206]. High biodegradability, easy mechanical as well as chemical recycling, least environmental risk and genotoxicity make it highly suitable for packaging material industry [207-209]. Taking note of all these immaculate, proficient and economic aspects corporate ventures like Avantium, ADM, DuPoint, BASF, Mitsui, Coca Cola and Synvina invested in production of FDCA [210]. **Figure 1.11** gives an elementary idea about the market potential of FDCA.

1.10.1 Properties of FDCA

As name suggested FDCA is a symmetric diacid with aromatic furan ring. It is a white solid with molecular weight of 156.09 g/mol. Due to its unique chemical structure it is considered as most promising molecule out of all 12 biobased building block chemicals which can replace around 300 petrochemical derived molecules [54]. Detailed chemical and physical properties of FDCA are given in **Table 1.9**.

Table 1.9: Chemical and physical properties of FDCA

Sr. No.	Entries	Contents
1	CAS No	3238-40-2
2	EC Numbers	21-800-8
3	Chemical abstract name	Furan-2,5-dicarboxyllic acid
4	Molecular formula	$C_6H_4O_5$
5	Smiles	C1=C(OC(=C1)C(=O)O)C(=O)O

6	Molecular Weight	156.09 g/mol
7	Description	White solid
8	Boiling Point	420°C
9	Melting Point	342°C
10	Solubility	DMSO, 1mg/mL in H_2O at 18°C
11	Density	1.604 g/cm^3
12	Flash Point	207°C
13	Refractive Index	~ 1.6400
14	Topological polar surface area	87.7 $A^{\circ 2}$

1.10.2 Synthetic strategy for FDCA production

There are 4 different synthetic strategies are known to produce FDCA based on availability of starting materials. In very first type of strategy furfural derived furoic acid can be converted into FDCA via furoate. This approach of disproportionation of furoate into FDCA is basically well known Henkel reaction (**Scheme 1.9**) [211].

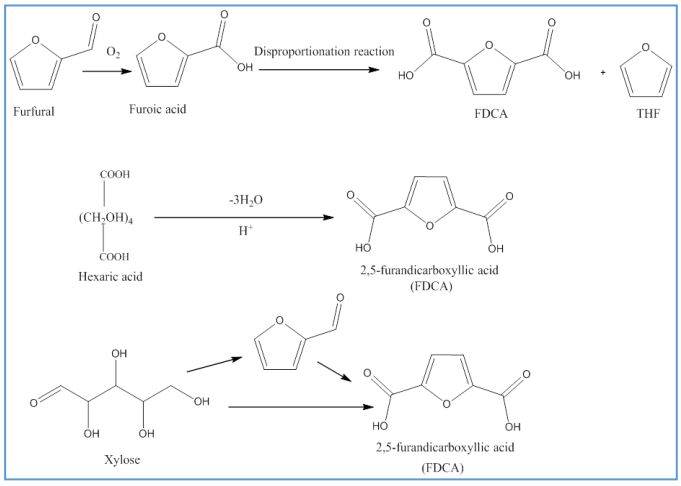

Scheme 1.9: Synthetic strategy of production of FDCA other than HMF

Second pathway is cyclodehydration of hexaric/mucic acid in acidic conditions which can also lead to formation of FDCA [212]. This was the first synthetic route discovered for FDCA production. Third chemical strategy to produce FDCA is cyclodehydration of xylose via furfural [213]. But extensively worked chemical route for FDCA production is oxidation of HMF. HMF oxidation proceeds via intermediates like HMFCA, FFCA and DFF. HMFCA is a monocarboxyllic acid which contains primary alcohol on its 5th position. It is very useful in pharmaceutics as it is building block of interleukin inhibitor due to its anticarcinogenic properties [74]. HMFCA on oxidation produces FFCA which is very stable in this reaction due to deactivated furan ring and its oxidation finally produces FDCA. Alternatively HMF can undergo oxidative dehydrogenation to produce DFF. The importance of DFF is already discussed in earlier section. **Scheme 1.10** shows these two pathways of HMF oxidation.

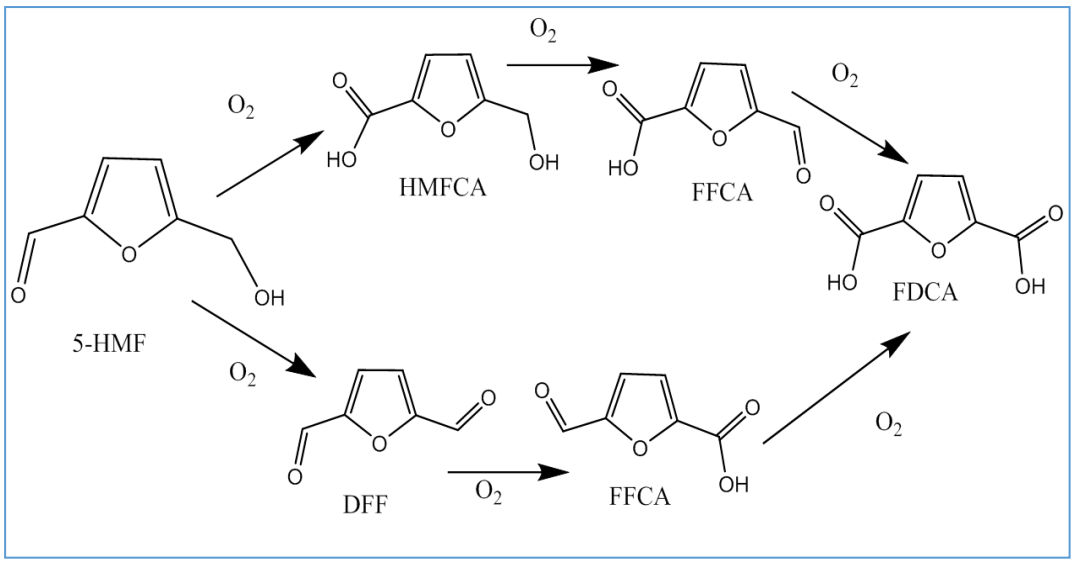

Scheme 1.10: Reaction pathways of Oxidation of 5-HMF

1.10.3 Literature survey

Due to its immense market potential and application in various renewable industries FDCA always remained a topic of interest since late 1800s. It was first reported by Fittig and

Heinzelman in 1876. They made it by the dehydration of mucic acid with the help of 48% HBr as a catalyst and solvent, that's why it is also called as dehydromucic acid [214].

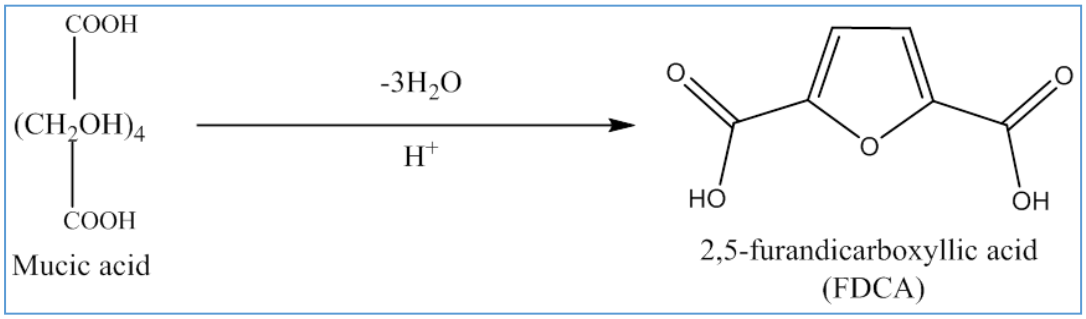

Scheme 1.11: Synthesis of FDCA from mucic acid

First heterogeneous catalytic evidence on HMF oxidation to FDCA was reported by Verdeuger and co workers where they used Pt/C and observed that addition of Pb enhanced the activity of catalyst [215]. Since then lot of research were devoted on production of FDCA from HMF via its complete oxidation which majorly include noble metals like Au, Pd, Pt and Ru. Similar effect of Bi doping on Pt catalyst was observed as it increased the oxygen resistance of Pt and stopped the leaching of Pt. It was observed that HMFCA and DFF were readily oxidised to FFCA but oxidation of FFCA in FDCA was the rate determining step of HMF oxidation as it was slow [216]. Pt was also investigated on reduced graphene oxide (r-GO) in which only HMFCA was formed as an intermediate [217]. Metal oxide support like TiO_2, ZrO_2 and Υ-Al_2O_3 and CeO_2 were also tested for with incorporation of Pt on their surface. Pt/Υ-Al_2O_3 was found highly efficient at very mild conditions but higher activity of Pt lead to chemisorptions of O_2 on Υ-Al_2O_3 which deactivated it [220]. Similarly it was concluded by Sahu and Dhepe that the Oxygen storage capacities of non-reducible oxides like Υ-Al_2O_3, ZrO_2 and carbonaceous support is very low which activates the required active site but for reducible oxides like CeO_2 and TiO_2 the oxygen storage capacity is very high due to presence of redox couple in them [221]. Modified support of CeO_2 and Bi was investigated

by Yang and co-workers in form of $Pt/Ce_{0.8}Bi_{0.2}O_{2-\delta}$. They observed that Bi doped Ceria facilitated the oxygen reduction process and due to presence of abundant O_2 vacancies. They proposed that reaction is conducted by Pt-alkoxide intermediate of HMF followed by β-H elimination [(222)]. Pt based catalysts are enlisted in **Table 1.10**. In order to get rid of saline solution generated by use of base Pt /PVP was also screened but higher reaction time and higher metal loading could not make it cost effective [(76)].

Table 1.10: Pt based catalysts for 5-HMF oxidation

Sr. No.	**Catalyst**	**Reaction Conditions**					**Efficiency (%) (DMF production)**			**Ref**
		Base used	T (°C)	P (bar)	Rt (h)	Solvent	C (%)	S (%)	Y (%)	
1	Pt-Pb/C	NaOH	25	1	2	H_2O	100		99	215
2	Pt/C	NaOH	25	1	2	H_2O	100		81	215
3	Pt-Bi/C	Na_2CO_3	100	40	6	H_2O	100		99	216
4	Pt/C	Na_2CO_3	100	40	6	H_2O	99		69	216
5	Pt-Bi/TiO_2	Na_2CO_3	100	40	6	H_2O	99		99	217
6	Pt/TiO_2	Na_2CO_3	100	40	6	H_2O	90		84	217
7	Pt/r-GO	NaOH	25	1	24	H_2O	100		84	218

8	Pt/C	NaOH	22	6.9	6	H_2O	100		79	219
9	Pt/ϒ-Al_2O_3	Na_2CO_3	60	0.2	6	H_2O	100		99	220
10	Pt/ϒ-Al_2O_3	Na_2CO_3	75 140	1	12	H_2O	96		96	221
11	Pt/ZrO_2	Na_2CO_3	75 140	1	12	H_2O	100		94	221
12	Pt/C	Na_2CO_3	75 140	1	12	H_2O	100		89	221
13	Pt/TiO_2	Na_2CO_3	75 140	1	12	H_2O	96		2	221
14	Pt/CeO_2	Na_2CO_3	75 140	1	12	H_2O	100		8	221
15	Pt/CeBiO	NaOH	23	10	0.5	H_2O	100		98	220
16	Pt/CeO_2	NaOH	23	10	0.5	H_2O	100		20	220
17	Pt/PVP	No Base	80	1	24	H_2O	100		94	76

Aerobic oxidation of HMF was also tested on Pd based catalysts (**Table 1.11**). Pd/C was found moderately active at room temperature with 71% yield of FDCA. Supported Pd

catalysts were found very active at atmospheric pressure of O_2 and at lower base equivalents [219]. PVP stabilised Pd was developed by DaSiyo *et al* which resulted 90% yield of FDCA with complete conversion because of their smaller nanoparticles size (1.8nm). Smaller size facilitated higher number of surface atoms and enhanced unsaturated active sites of metal which lead to increase in catalytic efficiency [223]. Pd was also investigated on several metal oxides like ϒ-Al_2O_3, TiO_2 and ZrO_2-La_2O_3 and it was observed that non-substantial change in electronic properties of Pd and non aggregation made the Pd/ZrO_2-La_2O_3 efficient [75]. Further addition to the sustainability was done by introducing magnetism in heterogeneous Pd/C catalysts [224-226].

Table 1.11: Pd based catalysts for HMF oxidation to FDCA

Sr. No.	**Catalyst**	**Reaction Conditions**					**Efficiency (%) (DMF production)**			**Ref**
		Base used	T (°C)	P (bar)	Rt (h)	Solvent	C (%)	S (%)	Y (%)	
1	Pd/C	NaOH 2	23	6.9	6	H_2O	100		71	219
2	Pd/PVP	NaOH 1.25	90	1	6	H_2O	99		90	223
3	Pd/ZrO_2/ La_2O_3	NaOH 1.25	90	1	6	H_2O	99		90	75
4	Pd/Al_2O_3	NaOH 1.25	90	1	6	H_2O	99		78	75
5	Pd/Ti_2O_3	NaOH 1.25	90	1	6	H_2O	99		53	75

6	ϒ-Fe_2O_3@HAP-Pd	K_2CO_3 0.5	100	1	6	H_2O	97		92.9	224
7	C-Fe_3O_4-Pd	K_2CO_3 0.5	80	1	4	H_2O	98.1		91.8	225
8	Pd/C@Fe_3O_4	K_2CO_3 0.5	80	1	6	H_2O	98.4		86.7	226

HMF oxidation in aquatic solvent was also extensively explored on various supported Gold catalysed systems (**Table 1.12**). Au/CeO_2 and Au/TiO_2 was investigated differently and it was observed that HMFCA was the sole intermediate formed in course of reaction. Missing of other intermediates can be because of hemiacetal formation in reaction. Ce^{3+} Lewis acid centres and Oxygen vacancies activated the O_2 and reaction was supposed to take place by superoxide species of Cerium ($CeOO^{\cdot}$) [(227)]. Bi^{3+} doped CeO_2 was investigated like Pd as it can enhance the activation of O_2 and hydride transfer. It was found that though conversion was almost same but the yield of FDCA increased to 75% from 39% of Au/CeO_2 [(228)]. Au nanoclusters were incorporated on HY zeolites supercage which limited their growth and strong interaction between acidic –OH group of supercage and Au nanoclusters lead to significant increase in the activity of Au/HY in compare to Au/TiO_2, Au/CeO_2, Au/$Mg(OH)_2$, Au/H-MOR and Au/ZSM-5 [(229,230)]. Au containing bimetallic catalysts were also screened and proved highly efficient because of alloy formation. Au-Cu/TiO_2 at 95°C, 4 equivalent of NaOH and 10 bar of external O_2 pressure produced 99% FDCA with complete conversion of HMF after 4h. Strong bimetallic synergism in terms of stability, activity was observed along with least leaching and agglomeration of catalyst [(231)]. Similar effect of alloying on enhanced activity and stability was also observed in Au-Pd bimetallic combination [(232)]. In order to

design the environmentally benign catalysts baseless oxidation of HMF was tried on hydrotalcite supported Au and CNT supported Au-Pd bimetallic combination [234]. Though this approach gave good results but increased reaction time remain a major concern.

Table 1.12: Au catalysed oxidation of 5-HMF in FDCA

Sr. No.	**Catalyst**	**Reaction Conditions**					**Efficiency (%) (DMF production)**			**Ref**
		Base used	T (°C)	P (bar)	Rt (h)	Solvent	C (%)	S (%)	Y (%)	
1	Au/CeO_2	NaOH 4	130	10	5	H_2O	100		96	227
2	Au/TiO_2	NaOH 4	130	10	8	H_2O	100		84	227
3	Au/CeBiO	NaOH 4	65	1	2	H_2O	100		99	228
4	Au/HY	NaOH 5	60	0.3	6	H_2O	99		99	229
5	Au/CeO_2	NaOH 5	60	0.3	6	H_2O	99		73	229
6	Au/TiO_2	NaOH 5	60	0.3	6	H_2O	99		85	229
7	$Au/Mg(OH)_2$	NaOH 5	60	0.3	6	H_2O	99		76	229
8	Au/H-	NaOH	60	0.3	6	H_2O	96		15	229

	MOR	5								
9	Au/Na-ZSM-5-25	NaOH 5	60	0.3	6	H_2O	92		1	229
10	Au/TiO_2	NaOH 20	30	20	18	H_2O	100		71	230
11	Au-Cu/TiO_2	NaOH 4	95	10	4	H_2O	100		99	231
12	Au-Pd/C	NaOH 2	60	30	2	H_2O	99		99	232
13	Au/HT	No Base	95	1	7	H_2O	99		99	233
14	Au-Pd/CNT	No Base	100	5	12	H_2O	100		94	234
15	Au-Pd/CNT	No Base	100	10	12	H_2O	100		96	234

Ru was also explored for complete oxidation of HMF due to its excellent activity to DFF production. Ru/C was screened in high pH alkaline solvent by Vuyurru and Starsser and it was observed that higher alkalinity destroys the stability of HMF with very poor yield of FDCA [(235)]. The performance of Ru/C was tested in various bases by Yi et al and it was observed that $CaCO_3$ was the best alkaline material for the production of FDCA. But it acts as neutraliser rather than enhancing oxidation which lead to deactivation of catalyst. So emphasis turned to Ru based catalysts which can catalyse the reaction without any base. Ru/C

without base proved highly efficient with quantitative yield of 88% for FDCA. It was observed that FDCA was synthesised by DFF route in absence of base [236]. Ru(OH)x species were incorporated on hydrotalcite (HT) and in presence of ionic liquids they were tested for HMF oxidation without addition of base with good proficiency but at larger scale they suffered by activity loss [237]. Metal oxides and their various phases were investigated for Ru nanoparticles and shape dependent oxidation of HMF was observed. Lewis and Brönsted acidity of surface of Ru/$MnCo_2O_4$ proved significant for exceptionally high yield. But the efficiency of catalyst decreased when $MnCo_2O_4$ was replaced by $CoMn_2O_4$. The change in crystalline structure of support i.e. BCC from cubic structure distorted the spinel phase of material which further lead to low surface area and decreased surface adsorption capacity for O_2 [238]. Ru was also incorporated on metal oxide with higher surface area like ZrO_2 but catalytic efficiency was not improved [239. New support like hydroxyappetite with basic properties was designed by T Gao et al and Ru was anchored on it. It proved highly efficient with 99.6% yield of FDCA at higher temperature of 140°C and 10 bar O_2 pressure but higher reaction time was the major drawback [242]. Like Ru another noble metal Rh was also tested for FDCA production but it showed very poor activity [235]. **Table 1.13** summarise the supported Ru catalysts for HMF oxidation.

Table 1.13: Ru based catalysts for 5-HMF oxidation

Sr. No.	**Catalyst**	**Reaction Conditions**					**Efficiency (%) (DMF production)**			**Ref**
		Base used	T (°C)	P (bar)	Rt (h)	Solvent	C (%)	S (%)	Y (%)	
1	Ru/C	pH=13	50	10	4	H_2O	98.5		6.48	235

2	Ru/C	NaOH 1	120	2	5	H_2O	100		69	236
3	Ru/C	K_2CO_3 1	120	2	5	H_2O	100		80	236
4	Ru/C	Na_2CO_3 1	120	2	5	H_2O	100		93	236
5	Ru/C	HT 1	120	2	5	H_2O	100		90	236
6	Ru/C	$CaCO_3$ 1	120	2	5	H_2O	100		95	236
7	Ru/C	Base free	120	2	10	H_2O	100		88	236
8	$Ru(OH)_x$/ MgO	Base free	140	2.5	20	H_2O	100		96	237
9	$Ru(OH)_x$/ $MgAl_2O_4$	Base free	140	2.5	42	H_2O	100		60	237
10	$Ru(OH)_x$/ HT	Base free	140	2.5	6	H_2O	100		100	237
11	$Ru(OH)_x$/ HT	Base free	140	1	38	H_2O	100		98	238
12	$Ru/MnCo_2O_4$	Base free	120	24	10	H_2O	100		99.1	238

13	$Ru/CoMn_2O_4$	Base free	120	24	10	H_2O	100		82.2	238
14	$Ru/MnCo_2CO_3$	Base free	120	24	10	H_2O	99.9		69.9	238
15	Ru/ZrO_2	Base free	120	10	16	H_2O	100		71	239
16	Ru/C	Na_2CO_3 1	75	35% H_2O_2	6	H_2O	100		91.3	240
17	Ru/C	$NaHCO_3$ 4	100	40	2	H_2O	100		75	241
18	Ru/AC-NaOCl	$NaHCO_3$ 4	100	40	4	H_2O	100		55	241
19	Ru/HAP	Base free	140	10	24	H_2O	100		99.6	242
20	Ru/HAP	Base free	140	10	24	H_2O	100		99.9	242

Given their high price, rare abundance and deactivation tendency noble metals don't fit in the catalytic sustainability. Some stable, active and inexpensive non-noble transition metal catalysts were explored for many applications including 5-HMF oxidation to FDCA. Chemical oxidants like t-BuOOH and H_2O_2 were used with Co-Fe, merrified Co-Py

combination, various Mo complexes and Co-Mn/SiO_2 catalysts for base free oxidation of 5-HMF [244, 246, 250 and 252]. Continuous flow of O_2 was also implemented with non-metallic N_2 doped nanoporous carbon derived by zeolitic imidazole framework (ZI-8/NNC) [251]. Mixed metal oxides like Fe-ZrO_2, Fe-CeO_2, CeO_2-ZrO_2 and Ce-Fe-ZrO_2 were tried in presence of ionic liquids but all suffered from poor yield and longer reaction time [247-248]. A brief literature survey of use of non-noble metal catalyst is given in **Table 1.14**.

Table 1.14: Non-noble metal catalysts for 5-HMF oxidation

Sr. No.	**Catalyst**	**Reaction Conditions**					**Efficiency (%) (DMF production)**			**Ref**
		Base used	T (°C)	P (bar)	Rt (h)	Solvent	C (%)	S (%)	Y (%)	
1	Fe-POP	Base free	100	10	10	H_2O	100		79	243
2	Merrified resin-Co-Py	Base free	100	t-BuOOH	24	ACN	95.6		90.4	244
3	$Li_2CoMn_3O_8$/NaBr	Base free	150	55	8	Acetic acid	100		80	245
4	Fe_3O_4-CoO_x	Base free	80	t-BuOOH	12	DMSO	97.2		68.6	246
5	$Fe_{0.6}Zr_{0.4}O_2$	[Bmim]Cl	160	20	24	IL	99.7		60.6	247

6	$Ce_{0.5}Fe_{0.5}O_2$	[Bmim]Cl	140	20	24	IL	98.4		13.8	248
7	$Ce_{0.5}Zr_{0.5}O_2$	[Bmim]Cl	140	20	24	IL	96.1		23.2	248
8	$Ce_{0.5}Fe_{0.15}Zr_{0.35}O_2$	[Bmim]Cl	140	20	24	IL	99.9		44.2	248
9	$MnCo_2O_4$	$KHCO_3$	100	20	24	H_2O	99.5		70.9	249
10	Mo Compelx	NaOH	50	H_2O_2	2	H_2O	100		99.5	250
12	ZI-8-NNC	K_2CO_3	80	Cont flow 100 ml/min	48	H_2O	100		80	251
13	Mn_xFe_y	NaOH	90	8	24	H_2O	93		32	74
14	Co-Mn/SiO_2	Base Free	120	t-BuOOH	12	ACN	100		72.4	252
15	Tio_2-Funct C	Base Free	85	1	22	H_2O	100		23	253

Non-noble metal transition metal catalysts suffered from poor activity, longer reaction time and deactivation due to hazardous material. They are also not explored to their full extent for 5-HMF oxidation. All these open the gates for ample amount of work in this field.

1.11 Catalytic Oxidation

Discovery of Oxygen by Carl Wilhelm Sheele (1772), Joseph Priestley (1774) and its identification as major oxidant in combustion process by Antoine Laurent Lvaoisier (1777) opened the vast area of research by exploring its chemical properties [254-255]. Currently it is considered as one of the best terminal oxidant for many useful industrial oxidative processes. Its highest active Oxygen content (100%), best atom economy, minimum production of hazardous side products, rapid reaction rate, lower cost and least energy consumption are certain points which favour the use of O_2 as most suitable oxidising agent [256]. Many Oxygen species are created during oxidation, out of which superoxo species ($O_2^{\bullet-}$) and peroxo species (O_2^{2-}) are very reactive because of their lower dissociation energy and longer bond length as shown in **Scheme 1.12** [257].

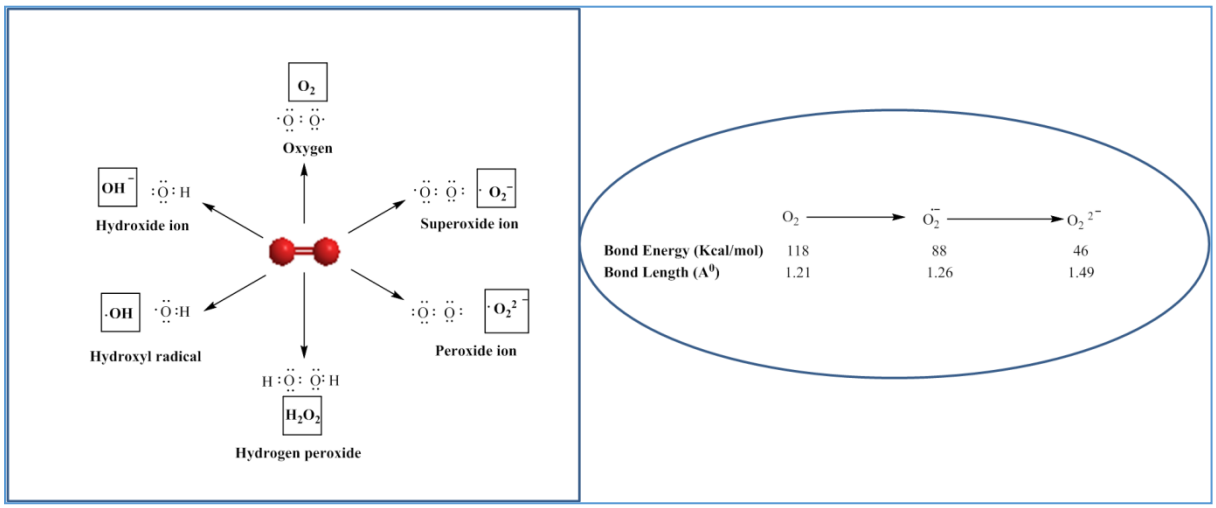

Scheme 1.12: Various Oxygen species and their activity

Heterogeneous catalysts facilitated oxidation due to their capacity to activate O_2 based on their surface properties. To understand the need of a metal catalyst it's necessary to

understand the physiochemical nature of Oxygen [258]. Generally in ground state diradicle O_2 molecule is present in triplet state whereas most of the reactants molecules are present in singlet state in ground state [259]. The triplet energy state if O_2 is because of presence of 2 unpaired electrons in its higher energy ABMOs (**Scheme 1.13**). Thus the oxidation reactions are denied citing Wigner's spin rules [260].

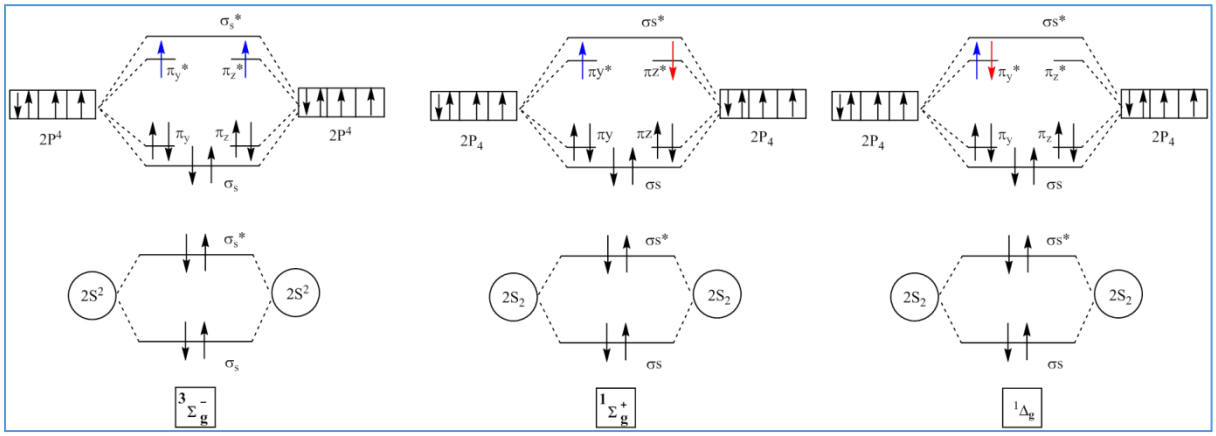

Scheme 1.13: Different spin state of Oxygen molecule (a) Triplet ground state $^3\Sigma^-_g$ (b) Singlet excited state with each electron in both ABMOs $^1\Sigma^+_g$ (c) Singlet excited state with paired electron in single ABMO $^1\Delta_g$.

The activation of this paramagnetic O_2 can be done by introducing another paramagnetic transition metal which can induce the spin inversion by donating its electron of d orbitals [261]. This will activate the O_2 due to spin-orbital coupling. Fe^{+2}, Fe^{+3}, Cu^{+2}, Mo^{+3}, Mo^{+5}, Co^{+2}, Co^{+3}, Ni^{+1}, Ni^{+2},Ni^{+3}, Mn^{+2}, Mn^{+3} and Mn^{+4} are common example of such type of paramagnetic metals [262]. Donation of one electron from metal will produce superoxide species and neutral superoxo metal complex [263]. Once it formed there will be an array of different metal oxo species as shown in **Scheme 1.14** [264]. Super oxo complex can generate monomeric peroxo metal species by its second electron donation which can further converted into bridged dimers like η or μ peroxo species [265]. Metal centred Oxygen transfer reactions are the final point of this propagation in which 4 electrons are donated to molecular Oxygen [266].

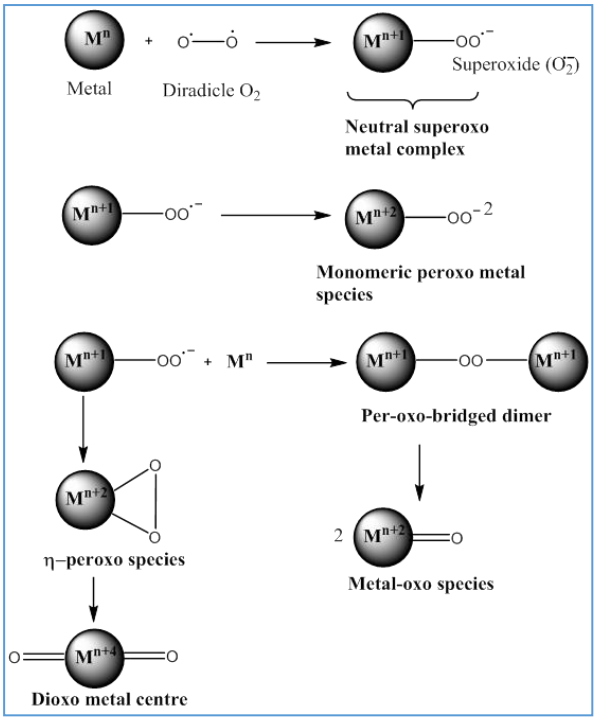

Scheme 1.14: Generation of various Oxygen species on metal surface during catalytic oxidation

Metal catalysed oxidation largely depends on the dissociation pattern of O_2 on the surface of catalyst. It can be dissociate on the catalytic surface in two ways (i) Homolytic dissociation and (ii) Heterolytic dissociation [(267)]. Different mechanistic approach occur while oxidation in both the cases.

(I) Haber- Weiss mechanism

This reaction is mostly occurs while auto-oxidation and classic example of homolytic activation of O_2 by metals [(268)]. In this approach radicals and surface oxo species are generated during the reaction due to homolytic dissociation of ROOH on the catalytic surface [(269)]. Radical initiator generally starts the oxidative reaction. In this type of reaction oxidation propagates via radical chain mechanism due to which many side products are formed. This mechanism is prominent even at mild reaction conditions like lower reaction temperature and pressure [(270)]. This reaction is quite common in first row transition metals due to single

electron redox couple formation tendency like Cu^{I}/Cu^{II}, Co^{II}/Co^{III} and Mn^{II}/Mn^{III} [271]. Uncontrolled chain radicals due to catalytic surface lead to poor selectivity to the desired product in this reaction especially in liquid phase oxidation.

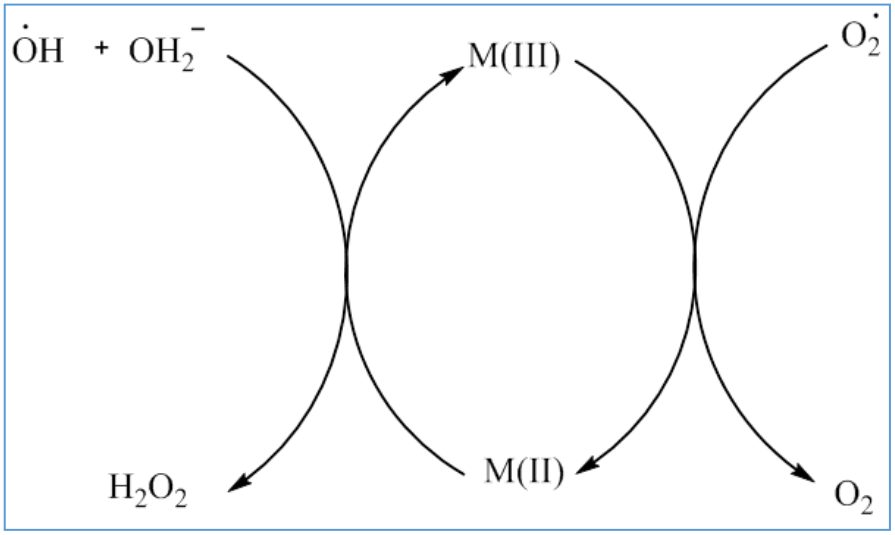

Scheme 1.15: Haber –Weiss mechanism of catalytic oxidation

(II) Mars- Van- Krevelen mechanism

This mechanism proceeds by heterolytic mode of activation of O_2 molecule. In this strategy metal oxides or mixed metal (bimetallic) oxides utilise their lattice oxygen species for oxidation [272]. This type of reaction mechanism can be operated at higher reaction temperature. As shown in **Scheme 1.16** central metal atom in this mechanistic approach has easy access to lower oxidation states. External O_2 resaturates the vacancies created during the course of reaction. Oxidation reactions occurring via Mars-Van-Krevelen approach are highly selective due to more control on lattice Oxygen bounded on metallic surface [273].

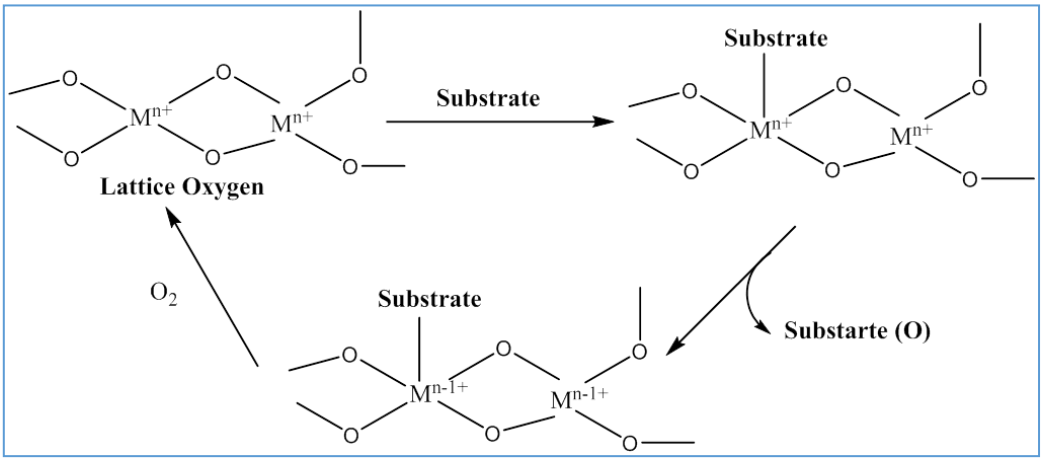

Scheme 1.16: Mars-Van-Krevelen mechanism for oxidation

Objective and Scope of thesis

Considering the various challenges in the efficient value addition of 5-HMF after extensive literature study focus was shifted on 3 major objective (i) Catalytic hydrodeoxygenation of 5-HMF to DMF (ii) Chemoselective oxidation of 5-HMF to DFF and (iii) Complete oxidation of 5-HMF to FDCA. The hydrodeoxygenation process was conducted over noble metal as well as non-noble metal catalyst to improve the economic viability of the catalytic hydrodeoxygenation of 5-HMF. Designing an efficient non-Noble metal catalyst for oxidation of 5-HMF was a major challenge. Alkali doped transition metal catalyst with good reusability was developed for high production of DFF. Catalytic application of metallic nanoparticles and graphene oxide was explored for 5-HMF oxidation to FDCA under very mild conditions which served the aspect of green chemistry. The major objective of this thesis are given below

- Understanding the challenge and developing a state of art of **active catalysts** for 5-HMF value addition
- Designing the highly selective **noble and non-noble metal catalyst** for efficient **hydrodeoxygenation** of 5-HMF

- Developing various catalysts to learn the **catalytic synergism** for efficient oxidation of 5-HMF
- Coherent study of reaction parameters and catalyst characterization to link the **structure-activity correlation**
- Studying the **surface and subsurface structural properties** by using different techniques like XRD, XPS, SEM, TEM, Raman spectroscopy, FTIR, TPD, TPR, TPO and BET surface area.
- Proposing the reaction pathways and **plausible mechanisms** based on observation of controlled reaction studies
- Exploring the possibilities of regeneration of catalytic activity, recovery of catalyst and their reusability
- Generating the **analytical methodology** for analysis of molecules of interest during the course of reaction using GC and UHPLC

References

1. W. Lutz, K. C. Samir, *Philos Trans R Soc Lond B Biol Sci.*, **2010**, 365, 2779–2791

2. Paris Agreement to the United Nations Framework Convention on Climate Change, **2015**, Dec. 12, T.I.A.S. No. 16-1104

3. A. Mehedintu, M. Sterpu and G.Soava, *Sustainability*, **2018**, 10, 1515-1536

4. A. A. Muresan and S. Attia, *Renew. Sustain. Energy Rev*, **2017**, 74, 349–363

5. C.I. Contescu, S.P Adhikari, N.C. Gallego, N.D. Evans and B.E. Biss, *C J. Carbon Res.*, **2018**, 4, 51-66

6. P. Sudarsanam, E. Peeters, E. V. Makshina, V. I. Parvulescu and B. F. Sels, *Chem. Soc. Rev.*, **2019**, 48, 2366-2421

7. Z. Zhang and Z. K. Zhao, *Bioresour. Technol.*, **2010**, 101, 1111–1114

8. Global Bioenergy Statistics 2019, World Bioenergy Association

9. B. M. Upton, A. M. Kasko, *Chem. Rev.* **2016**, 116, 2275−2306

10. A. Tursi, *Biofuel Research Journal*, **2019**, 22, 962-979

11. H. Chen, **2014**, Chemical composition and structure of natural lignocellulose, in: Chen, H. (Ed.), Biotechnology of Lignocellulose. Springer, Dordrecht, pp. 25-71

12. J.D. Bala, J. Lalung, A.A.S. Al-Gheethi, I. Norli, **2016**, A Review on Biofuel and Bioresources for Environmental Applications, in: Ahmad, M., Ismail, M., Riffat, S. (Eds.), Renewable Energy and Sustainable Technologies for Building

13. J. Fromm, B. Rockel, S. Lautner, E. Windeisen, G. Wanner, Lignin distribution in wood cell walls determined by TEM and backscattered SEM techniques. *J. Struct. Biol.* **2003**, 143, 77-84

14. A. J. Ragauskas, C. K. Williams, B. H. Davison, G. Britovsek, J. Cairney, C. A. Eckert, W. J. Frederick, J. P. Hallett, D. J. Leak, C. L. Liotta, J. R. Mielenz, R. Murphy, R. Templer, T. Tschaplinski, *Science*, **2006**, 311, 484–489

15. M. Aresta, A. Dibenedetto, F. Dumeignil, Biorefineries: An Introduction, Walter de Gruyter GmbH, Germany, (2015)

16. B. Kamm, *Angew Chemie - Int Ed*, **2007**, 46, 5056–5058

17. J.C. Serrano-Ruiz, R. Luque, J.H. Clark, The Role of Heterogeneous Catalysis in the Biorefinery of the Future, Elsevier, UK, (2013)

18. F. Frusteri, D. Aranda, G. Bonura, Sustainable Catalysis for Biorefineries, The Royal Society of Chemistry, UK, (2018)

19. A. D. McNaught and A.Wilkinson, IUPAC Compendium of Chemical Terminology, 2nd Ed. Blackwell Scientific Publications, Oxford (1997)

20. Chorkendorff and J.W. Niemantsverdriet, Concepts of Modern Catalysis and Kinetics, Wiley-VCH, Weinheim (2003)

21. J.K. Nørskov, T. Bligaard, J. Rossmeisl, C.H. Christensen, *Nat Chem*, **2009**, 1, 37–46

22. C. W. Forsberg, H. E. Schellhorn, L. N. Gibbons, F. Maine, C.E. Mason, *Biotechnology and Bioengineering*, **1986**, 28, 176–184

23. H. H. Brownell, J. N. Saddler, *Biotechnology and Bioengineering Symposium*, **1984**, 14, 55–68

24. K. Grohmann, R. Torget, M. Himmel, *Biotechnology and Bioengineering Symposium*, **1985**, 15, 59–80

25. V.S. Chang, M. Nagwani, M.T. Holtzapple, *Applied Biochemistry and Biotechnology*, **1998**, 74, 135–159

26. B. Bals, C. Rogers, V. Balan and B. Dale, *Biotechnology for biofuels*, **2010**, 3, 1-11

27. X. Zhao, K. Cheng, and D. Liu, *Applied microbiology and biotechnology*, **2009,** 82, 815-827

28. V. B. Agbor, N. Cicek, R. Sparling, A. Berlin and D. B. Levin, *Biotechnology advances*, **2011**, 29, 675-685

29. A. Brandt, M. J. Ray, T. Q. To, D. J. Leak, R. J. Murphy and T. Welton, *Green Chemistry*, **2011**, 13, 2489-2499

30. U.S. Department of Energy, Report Top Value Added Chemicals from Biomass, **2004**

31. R. J. Putten, J. C. Waal, E. Jong, C. B. Rasrendra, H. J. Heeres, and J. G. Vries, *Chem. Rev.*, **2013**, 113, 1499−1597

32. M. Bicker, D. Kaiser, L. Ott, H. Vogel, *J. Supercrit. Fluids*, **2005**, *36*, 118-126

33. F. W. Lichtenthaler, E. Cuny, D. Martin, S. Ro¨nninger, In *Carbohydrates as Organic Raw Materials*; F. W. Lichtenthaler, Ed.; VCH Publishers: Weinheim/NewYork, **1991**; p 214

34. F. W. Lichtenthaler, E. Cuny, D. Martin, S. Ro¨nninger, In *Carbohydrates as Organic Raw Materials*; Lichtenthaler, F. W., Ed.; VCH Publishers: Weinheim/NewYork, **1991**; p 80

35. J. J. Bozell, G. R. Petersen, *Green Chem.*, **2010**, 12, 539- 554

36. F. Yang, Q. Liu, X. Bai, Y. Du, *Bioresour Technol*, **2011**, 102, 3424–3429

37. Kiermayer, *J. Chem.-Ztg.*, **1895**, 19, 1003-1006

38. Middendorp, *J. A. Rec. Trav. Chim.Pays-Bas*, **1919**, 38, 1-71

39. S. I. F. S. Martins, M. A. J. S. V. Boekel, *Food Chem.* **2005**, 92, 437-448

40. B Cämmerer, B. L. Wedzicha, L. W. Kroh, *Eur. Food Res. Technol.* **1999**, 2099, 261-265

41. F. H. Newth, *Adv. Carbohydr. Chem.*,**1951**, 6, 83-106

42. P. Y. Nikolov, V. A. Yaylayan, *J. Agric. Food Chem.* **2011**, 59, 6099- 6107

43. M. Murkovic, M. A. Bornik, *Mol. Nutr. Food Res.* **2007**, 51, 390- 394

44. G. J. Mulder, *J. Prakt. Chem. (Leipzig)* **1840**, 21, 203-240

45. J. Lewkowski, *ARKIVOC* **2001**, 1, 17-54

46. A. Corma, S. Iborra, A. Velty, *Chem. Rev.* **2007**, 107, 2411-2502

47. C. Moreau, M. N. Belgacem, A. Gandini, *Top. Catal.* **2004**, 27, 11-30

48. X. Tong, Y. Ma, Y. Li, *Appl. Catal. A*, **2010**, 385, 1-13

49. A. A Rosatella, S. P. Simeonov, R. F. M. Frade, and C. A. M. Afonso, *Green Chem.*, **2011**, 13, 754-793

50. A. Stark, B. Ondruschka, In Ionic Liquids, Handbook of Green Chemistry, Vol. 6; P. Wasserscheid, A. Stark, Eds.; WILEY-VCH Verlag GmbH & Co. KGaA: Weinheim, Germany, 2010;

51. T. Ståhlberg, W. Fu, J. M. Woodley, A. Riisager, *ChemSusChem*, **2011**, 4, 451-458

52. S. Lima, M. M. Antunes, M. Pillinger, A. A. Valente, *ChemCatChem*, **2011**, 3, 1686-1706

53. M. E. Zakrzewska, E. Bogel-Łukasik, R. Bogel-Łukasik, *Chem. Rev.*, **2011**, 111, 397-417

54. T. Werpy, G. Petersen, A. Aden, J. Bozell, J. Holladay, J. White, A. Manheim, D. Eliot, L. Lasure and S. Jones, Top value added chemicals from biomass. Volume 1-Results of screening for potential candidates from sugars and synthesis gas, DTIC Document, 2004

55. Z. Fang, R. L. Smith Jr. and X. Qi, Production of Platform Chemicals from Sustainable Resources, Springer, Singapore, 1st edn, 2017

56. D. E. Resasco, S. Sitthisa, J. Faria, T. Prasomsri and M. P. Ruiz, in Solid Waste as a Renewable Resource: Methodologies, Apple Academic Press, 2015, pp. 103–144

57. L. Yang, X. Yan, S. Xu, H. Chen, H. Xia and S. Zuo, *RSC Adv.*, **2015**, 5, 19900–19906

58. H. Xia, S. Xu, X. Yan and S. Zuo, *Fuel Process Technol.*, **2016**, 152, 140–146

59. C. Li, Z. Zhang and Z. K. Zhao, *Tetrahedron Lett.*, **2009**, 50, 5403-5405

60. H. Xia, S. Xu and L. Yang, *RSC Adv.*, 2017, 7, 1200–1205

61. Y. Su, H. M. Brown, X. Huang, X. D. Zhou, J. E. Amonette and Z. C. Zhang, *Appl. Catal. A*, **2009**, 361, 117–122.

62. J. B. Binder and R. T. Raines, *J. Am. Chem. Soc*., **2009**, 131, 1979–1985

63. M. S. Feather, J. F. Harris, *Adv. Carbohydr. Chem.* 1973, 28, 161-224

64. Kuster, B. F. M. Starch/Staerke 1990, 42, 314

65. C. Moreau, R. Durand, S. Razigade, J. Duhamet, P. Faugeras, P. Rivalier, P. Ros, G. Avignon, *Appl. Catal. A* **1996**, 145, 211-224

66. E. F. L. J. Anet, *Adv. Carbohydr. Chem.* **1964**, 19, 181-218

67. M. J. Antal, W. S. L. Mok, G. N. Richards, *Carbohydr. Res.*, **1990**, 199, 91-109

68. Y. Román-Leshkov, C. J. Barrett, Z. Y. Liu and J. A. Dumesic, *Nature*, **2007**, 447, 982-985

69. P. Gallezot, *Chem. Soc. Rev.* **2012**, 41, 1538−1558

70. P. Lanzafame, D. Temi, S. Perathoner, G. Centi, A. Macario, A. Aloise and G. Giordano, *Catal. Today*, **2011**, 175, 435-441

71. C. M. Cai, N. Nagane, R. Kumar, C. E.Wyman, *Green Chem.* **2014**, 16, 3819−3829

72. J. Ohyama, Y. Ohira, A. Satsuma, *Catal. Sci. Technol.*, **2017**, 7, 2947− 2953

73. A. Boisen, T. B. Christensen, W. Fu, Y. Y. Gorbanev, T. S. Hansen, J. S. Jensen, S. K. Klitgaard, S. Pedersen, A. Riisager, T. Ståhlberg, J. M. Woodley, *Chem. Eng. Res. Des.* **2009**, 87, 1318-1327

74. F. Neatu, R. S. Marin, M. Florea, N. Petrea, O. D. Pavel and V. I. Pˆarvulescu, *Appl. Catal. B*, **2016**, 180, 751–757;

75. B. Siyo, M. Schneider, J. Radnik, M. M. Pohl, P. Langer and N. Steinfeldt, *Appl. Catal. A*, **2014**, 478, 107–116

76. S. Siankevich, G. Savoglidis, Z. Fei, G. Laurenczy, D. T. L. Alexander, N. Yan and P. J. Dyson, *J. Catal.*, **2014**, 315, 67-74

77. Z. Du, J. Ma, F. Wang, J. Liu and J. Xu, *Green Chem.*, **2011**, 13, 554–557

78. T. Buntara, S. Noel, P. H. Phua, I. Melián-Cabrera, J. G. de Vries and H. J. Heeres, *Angew. Chem. Int. Ed.*, **2011**, 50, 7083-7087

79. L. Hu, Y. Sun and L. Lin, *Prog. Chem.*, **2011**, 23, 2079–2084

80. X. Wu, Z. Huang, T. Yuan, K. Zhang, L. Wei, *Combust Flame*, **2009**, 156, 1365-1376

81. M. Mascal, E. B. Nikitin, *Angew. Chem. Int. Ed.*, **2008**, 47, 7924–7926

82. B. Saha and M. M. A. Omar, *ChemSusChem*, **2015**, 8, 1133– 1142

83. J. L. da Silva and M. Aznar, *Fuel*, **2014**, 136, 316–325

84. L. Perbellini, A. Princivalle, M. Cerpelloni, F. Pasini, F. Brugnone, *Int Arch Occup Environ Health*, **2003**, 76, 461–466

85. J. Phuong, S. Kim, R. Thomas, L. Zhang, *Environ Mol Mutagenesis*, **2012**, 53, 478–87

86. W. Yang, A. Sen, *ChemSusChem*, **2011**, 4, 349 –352

87. T. A. Brandvold, **2010**, US 20100331568A1

88. H. O'Neil, P. Wantanachaisaeng, Capturing Opportunities for para-Xylene Production: A Report from the Aromatics (Thailand) Public Co., Ltd. And UOP LLC, **2007**

89. Y. Yoshino, Y. Hayashi, I. Iwahama, S. Sakaguchi, Y. Ishii, *J. Org. Chem.*, **1997**, 62, 6810 –6813

90. M. Shunichi, *Noguchi Kenkyusho Jiho*, **1980**, 23, 39– 44

91. S De, B. Saha, R. Luque, *Bioresour. Technol.* **2015,** 178, 108−118

92. V. Menon, M. Rao, *Prog. Energy Combust. Sci.*, **2012**, 38, 522−550

93. M. J. Climent, A. Corma, S. Iborra, Green Chem. **2014**, 16, 516−547

94. S. De, S. Dutta, and B. Saha, *ChemSusChem*, 2012, 5, 1826–1833

95. M. Mascal and E. B. Nikitin, *ChemSusChem*, **2009**, 2, 859–861

96. H. Li, C. Wang, Y. Xu, Z. Yu, S. Saravanamurugan, Z. Wu, S. Yang and R. Luque, *Green Chem.*, **2020**, 22, 637-645

97. S. Dutta and M. Mascal, *ChemSusChem*, **2014**, 7, 3028 – 3030

98. T. Thananatthanachon and T. B. Rauchfuss, *Angew. Chem. Int. Ed.*, **2010**, 49, 6616–6618

99. M. Chidambaram and A. T. Bell, *Green chem.*, **2010**, 12, 123-1262

100. J. M. R. Gallo, D. M. Alonso, M. A. Mellmer and J. A. Dumesic, *Green Chem.*, **2013**, 15, 85-90

101. P. P. Upare, D. W. Hwang, Y.K Hwang, U.W. Lee, D.Y. Hong and J. S. Chang, *Green chem.*, **2015**, 17, 3310-3313

102. R. Insyani, D. Verma, S.M. Kim and J. Kim, *Green Chem.*, **2017**, 19, 2482-2490

103. M. Barun and M. Antoniettti , *Green Chem.*, **2017**, 19, 3813-3819

104. A. S. Crampton, M. D. Rötzer, F. F. Schweinberger, B. Yoon, U. Landman, U. Heiz, *Journal of Catalysis*, **2016**, 333 51–58

105. W. Zang, G. Li, L. Wang and X. Zhang, *Catal. Sci. Technol.*, **2015**, 5, 2532-2553

106. M. Chatterjee, , T. Ishizaka, and H. Kawanami, *Green Chem.*, **2014**, 16, 1543-1551

107. S. S. Nishimura, N. Ikeda, K. Ebitani, *Catal. Today*, **2014**, 232, 89–98

108. J. Mitra, X. Zhou and T. Rauchfuss, *Green Chem.*, **2015**, 17, 307–313

109. L. Hu, X. Tang, J. Xu, Z. Wu, L. Lin, and S. Li, *Ind. Eng. Chem. Res.* **2014**, 53, 3056−3064

110. A. B. Gawade, M. S. Tiwari and G. D. Yadav, *ACS Sustainable Chem. Eng.*, **2016**, 4, 4113-4123

111. N. Lucas, N. R. Kanna, A. S. Nagpure, G. Kokate and S. Chilukuri, *J. Chem. Sci.*, **2014**, 126, 403–413

112. A S. Nagpure, A. K. Venugopal, N. Lucas, M. Manikandan, T. Raja and S. Chilukuri. *Catal. Sci. Technol.*, **2015**, 5, 1463-1472

113. A. S. Nagpure, N. Lucas, and S. V. Chilukuri, *ACS Sustainable Chem. Eng.* **2015**, 3, 2909−2910

114. J. Shi, Y. Wang, X. Yu, W. Du, Z. Hou, *Fuel*, **2016**, 163, 74–79

115. Y. Yang, Q. Liu, D. Li, J. Tan, Q. Zhang, C. Wang and L. Ma, *RSC Adv.*, **2017**, 7, 16311-16318

116. X. Wang, Y. Liub and X. Liang, *Green Chem.*, **2018**, 20, 2894–2902

117. P. Priecel, N. A. Endot, P. D. Carà, and J. A. Lopez-Sanchez, *Ind. Eng. Chem. Res.*, **2018**, 57, 1991−2002

118. Z. Gao, G. Fan, M. Liu, L. Yang and F. Li, *Applied Catalysis B: Environmental*, **2018**, 237, 649–659

119. A. D. Talpade, M. S. Tiwari and G. D. Yadav, *Molecular Catalysis*, **2019**, 465 1–15

120. M. Esen, S. Akmaz, S. N. Koç and M. A. Gürkaynak, *Journal of Sol-Gel Science and Technology*, **2019**, 91, 664–672

121. W. Liaoa, Z. Zhua, N. Chena, T. Sua, C. Denga, Y. Zhaob, W. Renb, and H. Lü, *Molecular Catalysis*, **2020**, 482, 110756

122. R. J. Chimentão, H. Oliva, J. Belmar, K. Morales, P. M. Arvela, J. Wärnå, D.Yu. Murzin, J. L. G. Fierro, J. Llorca and D. Ruiz, *Applied Catalysis B: Environmental*, **2019**, 241, 270–283

123. L. Feng, X. Li, Y. Lin, Y. Liang, Y. Chen and W. Zhou, *Renewable Energy*, **2020**, 160, , 261-268

124. T.W. Tzeng, C.Y. Lin, C. W. Pao, J. L. Chen, R. J. G. Nuguid and P. W. Chung, *Fuel Processing Technology*, 2020, 199, 106225

125. G. H. Wang, J. Hilgert, F. H. Richter, F. Wang, H. J. Bongard, B. Splietho, C. Weidenthaler and F. Schüth, *Nat. Mater.*, **2014**, 13, 293-300

126. T. S. Hansen, K. Barta, P. T. Anastas, P. C. Fordc and A. Riisager, *Green Chem.*, **2012**, 14, 2457–2461

127. Y. B. Huang, M. Y. Chen, L. Yan, Q. X. Guo, and Y. Fu, *ChemSusChem*, **2014**, 7, 1068–1070

128. G. Bottari, A. J. Kumalaputri, K. K. Krawczyk, B. L. Feringa, H. J. Heeres, and K. Barta, *chemSusChem* **2015**, 8, 1323 –132

129. P. Yang, Q. Cui, Y. Zu, X. Liu, G. Lu, Y. Wang, *Catalysis Communications*, **2015**, 66, 55–59

130. X. Kong, R. Zheng, Y. Zhu, G. Ding, Y. Zhu and Y. W. Li, *Green Chem.*, **2015**, 17, 2504–2514

131. L. Yu, L. He, J. Chen, J. Zheng, L. Ye, H. Lin, and Y. Yuan, *Chemcatchem*, **2015**, 7, 1701-1707

132. B. Chen, F. Li, Z. Huang, and G. Yuan, *Applied Catalysis B: Environmental*, **2017**, 200, 192–199

133. M. S. Gyngazova, L. Negahdar, L. C. Blumenthal and R. Palkovits, *Chemical Engineering Science*, **2017**, 173, 455–464

134. D. Li , Q. Liu , C. Zhu , H. Wang , C. Cui , C. Wang , L. Ma, *Journal of Energy Chemistry*, **2019**, 30, 34-41

135. N. Siddiqui, A. S. Roy, R. Goyal, R. Khatun, C. Pendem, A. N. Chokkapu, A. Bordoloi and R. Bal, *Sustainable Energy Fuels*, **2018**, 2, 191–198

136. Z. Zhang, S. Yao, C. Wang, M. Liu, F. Zhang, X. Hu, H. Chen, X. Gou, K. Chen, Y. Zhu, X. Lu, P. Ouyang and J. Fu, *Journal of Catalysis*, **2019**, 373, 314–321

137. N. Chen, Z. Zhu, H. Ma, W. Liao, H. Lü, *Molecular Catalysis*, **2020**, 486, 110882

138. N. Ma, Y. Song, F. Han, G. I. N. Waterhouse, Y. Li and S. Ai, *Catal. Sci. Technol.*, **2020**, 10, 4010–4018

139. L. M. Esteves, M. H. Brijaldo, E. G. Oliveira, J. J. Martinez, H. Rojas, A. Caytuero and F. B. Passos, *Fuel*, **2020**, 270, 117524-117537

140. S. Umasankar, P. Tamizhdurai, P. Santhana krishnan, S. Narayanan, V.L. Mangesh, K. Shanthi, *Biomass and Bioenergy*, **2020**, 143, 105868

141. N. Chen, Z. Zhu, T. Su, W. Liao, C. Deng, W. Ren, Y. Zhao, H. Lü, *Chemical Engineering Journal*, **2020**, 381, 122755

142. M. Przydacz, M. J˛edrzejczyk, J. Rogowski, M. Szynkowska-Jó´zwik and A. M. Ruppert, *Energies*, **2020**, 13, 4660-4673

143. D. Guo, X. Liu, F. Cheng, W. Zhao, S. Wen, Y. Xiang, Q. Xu, N. Yu, D. Yin, *Fuel*, **2020**, 274, 117853-117860

144. J. March, *Advanced Organic Chemistry*, **1985**, 3, 173-176

145. K. M. Bratlie, H. Lee, K. Komvopoulos, P. Yang and G. A. Somorjai, *Nano Lett.*, **2007**, 7, 3097‑3101

146. V. Vetere, A. B. Merlo, J. F. Ruggera, M. L. Casella, *Journal of the Brazilian Chemical Society*, **2010**, 21, 914-920

147. H.S. Fogler, *Elements of chemical reaction engineering*. **1992**: Prentice-Hall

148. R. A. Sheldon, I.W.C.E. Arends, and U. Hanefeld, *Introduction: Green Chemistry and Catalysis*, in *Green Chemistry and Catalysis*. 2007, Wiley-VCH Verlag GmbH & Co. KGaA. p. 1-47

149. F. Delbecq, and P. Sautet, *Journal of Catalysis*, **2002**. 211, 398-406

150. N. Z. Ming, X. M. Yu. S. Wei and Q. P. Ping, *Acta Physico-Chimica Sinica*, **2013**, 29, 1916-1922

151. J. Haubrich, D. Loffreda, F. Delbecq, P. Sautet, Y. Jugnet, A. Krupski, C. Becker and K. Wandlet, *The Journal of Physical Chemistry C*, **2008**, 112, 3701-3718

152. M. A. Aramendıa, V. Borau, C. Jiménez, J. M. Marinas, A. Porras andF. J. Burrano, *Journal of Catalysis*, **1997**, 172, 46-54

153. A. Vicente, G. Lafaye, C. Especel, P. Marécot and C. T. Williams, *Journal of catalysis*, **2011**, 283, 133-142

154. A. S. Amarasekara, D. Green, L. D. Williams, *Eur.Polym. J.*, **2009**, 45, 595–598

155. T. Xiang, X. Liu, P. Yi, M. Guo, Y. Chen, C. Wesdemiotis, J. Xu, Y. Pang, *Polym. Int.*, **2013**, 62, 1517–1523

156. Y. Xu, X. Jia, J. Ma, J. Gao, F. Xia, X. Li, J. Xu, *Green Chem.* **2018**, 20, 2697–2701

157. K. T. Hopkins, W. D. Wilson, B. C. Bender, D. R. McCurdy, J. E. Hall, R. R. Tidwell, A. Kumar, M. Bajic, D. W. Boykin, *J. Med. Chem.*, **1998**, 41, 3872–3878

158. M. D. Poeta, W. A. Schell, C. C. Dykstra, S. K. Jones, R. R. Tidwell, A. Kumar, D. W. Boykin, J. R. Perfect, *Antimicrob. Agents Chemother*, **1998**, 42, 2503–2510

159. S. Dutta, L.L. Wu, M. Mascal, *Green Chem.*, **2015**, 17, 3737-3739

160. J. J. Roylance, K.S. Choi, *Green Chem.*, **2016**, 18, 5412-5417

161. X. K. Li, B. Ho, D. S. W. Lim, Y. G. Zhang, *Green Chem.*, **2017**, 19, 914-918

162. C. Li, G. Xu, X. Liu, Y. Zhang, Y. Fu, *Ind. Eng. Chem. Res.*, **2017**, 56, 8843-8849

163. J. W. Reijendam, G. J. Heeres and M. J. Janssen, *Tetrahedron*, **1970**, 26, 1291-1301

164. L. Cottier, G. Descotes, J. Lewkowski and R. Skowronski, *Pol. J. Chem.*, **1994**, 68, 693-698

165. L. Cottier, G. Descotes, J. Lewkowski, R. Skowronski and E. Viollet, *J. Heterocycl. Chem.*, **1995**, 32, 927-930

166. L. Cottier, G. Descotes, J. Lewkowski and R. Skowronski, *Org. Prep. Proced. Int.*, **1995**, 27, 564-566

167. A. S. Amarasekara, D. Green and E. McMillan, *Catal. Commun.*, **2008**, 9, 286-288

168. W. Partenheimer and V. V. Grushin, *Adv. Synth. Catal.*, **2001**, 343, 102-111

169. N. Mittal, G. M. Nisola, L. B. Malihan, J. G. Seo, S. P. Lee, and W. J. Chung, *Korean J. Chem. Eng.*, **2014**, 31,1362-1367

170. G. Li, Z. Sun, Y. Yan, Y. Zhang, and Y. Tang, *ChemSusChem*, **2017**, 10, 494–498

171. T. S. Hansen, I. Sadaba, E. J. Garcia-Suarez and A. Riisager, *Appl. Catal. A: Gen.*, **2013**, 456, 44– 50

172. J. Ma, Z. Du, J. Xu, Q. Chu, and Y. Pang, *ChemSusChem*, **2011**, 4, 51–54

173. G. A. Halliday, R. J. Young, Jr., and V. V. Grushin, *Org. lett.* **2003**, 5, 2003-2005

174. S. K. Hanson, R. Wu, and L. A. "Pete" Silks, *Org. lett.*, **2011**, 13, 1908-1911

175. J. Nie, J. Xie and H. Liu, *Journal of Catalysis*, **2013**, 301, 83–91

176. N. Junfang, X. Jiahan, L. Haichao, *Chinese J. Catal.*, **2013**, 34, 871-875

177. F. Yang, Z. Yuan, B. Liu, S. Chen and Z. Zhang, *JIEC*, **2016**, 38, 181-185

178. J. Artz, S. Mallmann, and R. Palkovits, *Chemsuschem*, **2015**,8,672-679

179. K. Ghosh, R. A. Molla, M. A. Iqubal, S. S. Islam and S. k. M. Islam, *Applied Catalysis A: General*, **2016**, 520, 44–52

180. C. A. Antonyraj , J. Jeong , B. Kim , S. Shin , S. Kim , K. Y. Lee and J. K. Cho, *JIEC*, **2012**, 19, 1056-1059

181. G. D. Yadav and R. V. Sharma, *Appl. Catal. B: Env*, **2014**, 147, 293-301

182. C. A. Antonyraj, B. Kima, Y. Kima, S. Shin, K. Y. Lee, I. Kimd, J. K. Cho, *Catalysis Communications*, **2014**, 57, 64–68

183. F. L. Grasset, B. Katryniok, S. Paul, V. N. Rataj, M. Pera-Titus, J. M. Clacens, F. de Campo and F. Dumeignil, *RSC Adv.*, **2013**, 3, 9942-9948

184. C. Carlini, P. Patrono, A. M. R. Galletti, G. Sbrana and V. Zima, *Appl. Catal. A: Gen*, **2005**, 289, 197-204

185. O. C. Navarro, A. Corma and S. I. Chornet, Top Catal. **2009**, 52, 304–314

186. J. Nie and H. Liu, *Journal of Catalysis*, **2014**, 316, 57–66

187. X. Tong, L. Yu, H. Chen, X. Zhuang, S. Liao and H. Cui, Catal. Commun. **2017**, 90, 91-94

188. D. Baruah, F. L. Hussain, M. Suri, U. P. Saikia, P. Sengupta, D. K. Dutta and D. Konwar, *Catal. Commun.* **2016**, 77, 9-12

189. Z. Yang, W. Qi, R. Su, and Z. He, *ACS Sustainable Chem. Engg.*, **2017**, 5, 4179-4187

190. J. Zhao, A. Jayakumar, and J. M. Lee, *ACS Sustainable Chem. Engg.*, **2018**, 6, 2976-2982

191. F. Neatu, N. Petrea, R. Petre, V. Somoghi, M. Florea, V.I. Parvuescu, *Catal. Today*, **2016**, 278, 66-73

192. R. Fang, R. Luque and Y. Li, *Green Chem.*, **2016**, 18, 3152-3157

193. B. Liu, Z. Zhang, K. Lv, K. Deng and H. Duan, *Appl. Catal. A: Gen*, **2014**, 472, 64-71

194. L. Dammer, A. Raschka, and L. Scholz, Market developments of and opportunities for bio-based products and chemicals. N.-I.f.E.a.Innovation (Ed.), **2013**

195. X. Fei, J. Wang, J. Zhu, X. Wang, and X. Liu, *ACS Sustainable Chem. Eng.* **2020**, 8, 8471–8485

196. N. Jacquel, R. Saint-Loup, J. P. Pascault, A. Rousseau and F. Fenouillot, *Polymer*, **2015**, 59, 234−2421973. S. Rajendran, R. Raghunathan, I. Hevus, R. Krishnan, A. Ugrinov, M. P. Sibi, D. C. Webster, J. Sivaguru, *Angew. Chem., Int. Ed*, **2015**, 54, 1159−1163

198. C. H. R. M. Wilsens, N. J. M. Wullems, E. Gubbels, Y. F. Yao, S. Rastogi, B. A. Noordover, *Polym. Chem.*, **2015**, 6, 2707−2716

199. S. S. Nagarkar, A. K. Chaudhari, S. K. Ghosh, *Cryst. Growth Des.*, **2012**, 12, 572−576

200. M. Rose, D. Weber, B. V. Lotsch, R. K. Kremer, R. Goddard, and R. Palkovits, *Microporous Mesoporous Mater.*, **2013**, 181, 217−221

201. A. Eerhart, A. P.C. Faaij, and M. K. Patel. *Energ. Environ. Sci.*, **2012,** *5*, 6407-6422

202. R. J. I. Knoop, W. Vogelzang, J. V. Haveren, *J. Polym. Sci., Part A: Polym. Chem.*, **2013,** 51, 4191-4199

203. M. Jiang, Q. Liu, Q. Zhang, C. Ye and G. Zhou, *J. Polym. Sci., Part A: Polym. Chem.*, **2012,** *50*, 1026-1036

204. J. Wang, X. Liu, J. Zhu, Y. Jiang, *Polymers* **2017,** *9*, 305- 319

205. G. Z. Papageorgiou, D. G. Papageorgiou, Z. Terzopoulou, and D. N. Bikiaris, *Eur. Polym. J.* **2016**, *83*, 202-229

206. J. G. Berkel, N. Guigo, J. J. Kolstad, L. Sipos, B. Wang, M. A. Dam, N. Sbirrazzuoli, *Macromol. Mater. Eng.* **2015,** *300*, 466-474

207. G. Q. Chen, N. M. Straalen, D. Roelofs, *Green Chem.* **2016,** *18*, 4420-4431

208. C. M. Rochman, *The Complex Mixture, Fate and Toxicity of Chemicals Associated with Plastic Debris in the Marine Environment*. In: Bergmann M., Gutow L., Klages M. (eds) Marine Anthropogenic Litter. Springer, Cham, **2015**

209. J. E. De, M. A. Dam, L. Sipos, G. J. M. Gruter, *Furandicarboxylic acid (FDCA), a versatile building block for a very interesting class of polyesters*. Polymers and Materials, **2012**

210. Avantium. Avantium Technology & Markets Day: "Entering the Commercialization Phase for PEF". https://www.avantium.com/press-releases/avantium-technology-markets-day-entering-thecommercialization- phase-for-pef/

211. T. Pan, J. Deng, Q. Xu, Y. Zuo, Q.-X. Guo and Y. Fu, *Chemsuschem* **2013,** *6*, 47-50

212. Y. Taguchi, A. Oishi and H. Iida, *Chem. Lett.* **2008,** 37, 50-51

213. H. B. Yuan, H. L. Liu, J. K. Du, K. Q. Liu, T. F. Wang and L. Liu, *Appl. Microbiol. Biotechnol.* **2019,** 104, 527-543

214. R. Fittig and H. Heinzelmann, *Chem. Ber.* **1876**, 9, 1198-1199

215. P. Verdeguer, N. Merat and A. Gaset, *J. Mol. Catal.* **1993**, 85, 327− 344

216. H. A. Rass, N. Essayem, and M. Besson, *Green Chem.*, **2013**, 15, 2240−2251.

217. H. A. Rass, N. Essayem and M. Besson, ChemSusChem, **2015**, 8, 1206−1217.

218. W. Q. Niu, D. Wang, G. H. Yang, J. Sun, M. B. Wu, Y. Yoneyama and N.Tsubaki, *Bull. Chem. Soc. Jpn.* **2014**, 87, 1124−1129.

219. S. E. Davis, L. R. Houk, E. C. Tamargo, A. K. Datye, R. J. Davis, *Catal. Today*, **2011**,160, 55−60.

220. P. Vinke, H. E. Dam and H. Bekkum, Studies in Surface Science and Catalysis; Elsevier: Amsterdam, **1990**; Vol. 55, pp 147− 157

221. R. Sahu, P. L. Dhepe, *React. Kinet. Mech. Catal.* **2014**, 112, 173−187.

222. Z. Z. Miao, T. X. Wu, J. W. Li, T. Yi, Y. B. Zhang, X. G. Yang, *RSC Adv.* **2015**, 5, 19823−19829

223. B. Siyo, M. Schneider, M. M. Pohl, P. Langer and N. Steinfeldt, Catal. Lett., **2014**, 144, 498−506.

224. Z. H. Zhang, J. D. Zhen, B. Liu, K. L. Lv and K. J. Deng, *Green Chem.* **2015**, 17, 1308−1317

225. B. Liu, Y. S. Ren and Z. H. Zhang, *Green Chem.* **2015**, 17, 1610−1617

226. N. Mei, B. Liu, J. D. Zheng, K. L. Lv, D. G. Tang and Z. H. Zhang, *Catal. Sci. Technol.* **2015**, 5, 3194−3202

227. O. Casanova, S. Iborra, and A. Corma, *ChemSusChem*, **2009**, 2, 1138−1144

228. Z. Z. Miao, Y. B. Zhang, X. Q. Pan, T. X. Wu, B. Zhang, J. W. Li, T. Yi, Z. D. Zhang, and X. G. Yang, *Catal. Sci. Technol.* **2015**, 5, 1314−1322

229. J. Y. Cai, H. Ma, J. J. Zhang, Q. Song, Z. T. Du, Y. Z. Huang and J. Xu, *Chem. Eur. J.* **2013**, 19, 14215−14223

230. Y. Y. Gorbanev, S. K. Klitgaard, J. M. Woodley, C. H. Christensen, A. Riisager, *ChemSusChem*, **2009**, 2, 672−675

231. T. Pasini, M. Piccinini, M. Blosi, R. Bonelli, S. Albonetti, N. Dimitratos, J. A. Lopez-Sanchez, M. Sankar, Q. He, C. J. Kiely, G. J. Hutchings, and F. Cavani, *Green Chem.* **2011**, 13, 2091−2099

232. A.Villa, M. Schiavoni, S. Campisi, G. M. Veith and L. Prati, *ChemSusChem*, **2013**, 6, 609−612

233. N. K. Gupta, S. Nishimura, A. Takagaki, K. Ebitani, *Green Chem.*, **2011**, 13, 824−827

234. X. Y. Wan, C. M. Zhou, J. S. Chen, W. P. Deng, Q. H. Zhang, Y. H. Yang and Y. Wang, *ACS Catal.* **2014**, 4, 2175−2185

235. K. R. Vuyyuru and P. Strasser, *Catal. Today*, **2012**, 195, 144–154

236. G. Yi, S. P. Teong and Y. Zhang, *Green Chem.*, **2016**, 18, 979–983

237. T. Ståhlberg, E. Eyjólfsdóttir, Y. Y. Gorbanev, I. Sádaba and A. Riisager, *Catal. Lett.*, **2012**, 142, 1089–1097

238. D. K. Mishra, H. J. Lee, J. Kim, H.-S. Lee, J. K. Cho, Y.-W. Suh, Y. Yi and Y. J. Kim, *Green Chem.*, **2017**, 19, 1619–1623

239. C. M. Pichler, M. G. Al-Shaal, D. Gu, H. Joshi, W. Ciptonugroho and F. Schüth, *ChemSusChem*, **2018**, 11, 2083–2090

240. C.T. Chen, C. V. Nguyen, Z. Y. Wang, Y. Bando, Y. Yamauchi, M. T. S. Bazziz, A. Fatehmulla, W. A. Farooq, T. Yoshikawa, T. Masuda and K. C. W. Wu, *ChemCatChem*, **2018**, 10, 361–365

241. F. Kerdi, H. Ait Rass, C. Pinel, M. Besson, G. Peru, B. Leger, S. Rio, E. Monflier and A. Ponchel, *Appl. Catal., A*, **2015**, 506, 206–219

242. T. Gao, Y. Yin, W. Fang and Q. Cao, *Mol. Catal.*, **2018**, 450, 55–64

243. B. Saha, D. Gupta, M. M. Abu-Omar, A. Modak and A. Bhaumik, *J. Catal.*, **2013**, 299, 316–320

244. L. Gao, K. Deng, J. Zheng, B. Liu and Z. Zhang, *Chem. Eng. J.*, **2015**, 270, 444–449

245. A. Jain, S. C. Jonnalagadda, K. V. Ramanujachary and A. Mugweru, *CATCOM*, **2015**, 58, 179–182.

246. S. Wang, Z. Zhang and B. Liu, *ACS Sustainable Chem. Eng.*, **2015**, 3, 406–412

247. D. Yan, J. Xin, Q. Zhao, K. Gao, X. Lu, G. Wang and S. Zhang, *Catal. Sci. Technol.*, **2018**, 8, 164–175

248. D. Yan, J. Xin, C. Shi, X. Lu, L. Ni, G. Wang and S. Zhang, *Chem. Eng. J.*, **2017**, 323, 473–482

249. S. Zhang, X. Sun, Z. Zheng and L. Zhang, *Catal. Commun.*, **2018**, 113, 19–22

250. S. Li, K. Su, Z. Li and B. Cheng, *Green Chem.*, **2016**,18, 2122-2128

251. C. V. Nguyen, Y.T. Liao, T. C. Kang, J. E. Chen, T. Yoshikawa, Y. Nakasaka, T. Masudab and K.C.W. Wu, *Green Chem.*, **2016**, 18, 5957-5961

252. F. Yang, Y. Ding, J. Tang, S. Zhou, B. Wang and Y. Kong, *Molecular Catalysis*, **2017**, 435, 144–155

253. D. Gupta, K. K. Pant and B. Saha, *Molecular Catalysis*, 2017, 435, 182–188

254. G. F. Rodwell *Nature*, **1882**, 27, 8–11

255. Richard Myers, *The Basics of Chemistry*, **2003**

256. D.L. Gilbert, (ed.). Oxygen and Living Processes. *An Interdisciplinary Approach.* New York: SpringerVerlag, **1981**, 1-43

257. C. L. Hill and I.A. Weinstock, *Nature*, **1997**, 388,332-333

258. X. Liu, Y. Ryabenkova and M. Conte, *Phys.Chem.Chem.Phys.*, **2015**, 17, 715-7317

259. R. Prabhakar, P. E. M. Siegbahn, B. F. Minaev and H. Agren, *J. Phys. Chem. B*, **2002**, 106, 3742‑3750

260. C. Carbogno, J. Behler, A. Gros and K. Reuter, *Phys. Rev. Lett.*, **2008**, 101, 96104-96107

261. N. Jin and J. T. Groves, *J. Am. Chem. Soc.*, **1999**, 121, 2923‑2924

262. A. Brückner, *Chem. Soc. Rev.*, **2010**, 39, 4673‑4684

263. M. H. Dickman and M. T. Pope, *Chem. Rev.*, **1994**, 94, 569‑584

264. M. Zhou and R. H. Crabtree, *Chem. Soc. Rev.*, **2011**, 40, 1875‑1884

265. J. M. Mayer, *Inorg. Chem.*, **1988**, 27, 3899-3903

266. R. H. Holm, *Chem. Rev.*, **1987**, 87, 1401-1449

267. K. P. Jensen and U. Ryde, *J. Biol. Chem.*, **2004**, 279, 14561-14569

268. J. Weinstein and B. H. J. Bielski, *J. Am. Chem. Soc.*, **1979**, 101, 58-62

269. Y. S. Duh, C. S. Kao, H. H. Hwang and W. W. L. Lee, *Trans. IChemE.*, **1998**, 76, 271-276

270. M. Y. Sinev, *J. Catal.*, **2003**, 216, 468-476

271. N. Lehnert, R. Y. N. Ho, L. Que Jr. and E. I. Solomon, *J. Am. Chem. Soc.*, **2001**, 123, 8271-8290

272. P. Mars and D. W. Krevelen, *Chem. Eng. Sci.*, **1954**, 3, 41-59

273. A. M. Khenkin, L. Weiner, Y. Wang and R. Neumann, *J. Am. Chem. Soc.*, **2001**, 123, 8531-8

Chapter 2

Experimental, Characterization and Analytical methodology

Experimental, Characterization and Analytical methodology

2.1 Introduction

Heterogeneous catalyst and its activity and efficiency largely affected by the experimental conditions in which it is synthesized. Textural properties and chemical properties of heterogeneous catalyst can be tailored by reaction parameters like pH, centrifugation, precipitating agent, nature of solvent, temperature etc. Similarly to understand the nature of catalysts, quantitative and qualitative estimation of its active sites characterization techniques proved vital instrument. Important catalytic properties like porosity, surface area, crystal planes and their structural characteristics, surface acidity and basicity, size of particles and active phases can be find out by different characterization techniques like BET surface area, XRD, XPS, micrographic images, temperature programmed desorption profile etc. Final goal of any catalytic reaction is formation of desired product efficiently. Identification, quantification, extraction and qualitative examination is done by various analytical techniques like gas chromatography (GC), high performance liquid chromatography (HPLC), integrated instruments like GC-MS or LC-MS and Nuclear Magnetic Resonance spectroscopy (NMR). Understanding the experimental and calculation aspects of all these terminologies and techniques is of prime importance for one catalytic system to be successful. In this section all the used methodologies are discussed and in detail.

2.2 Materials used

5-(hydroxymethyl)furfural (99.98%), 5-methyl furfural (98%), 2,5-dimethyl furan (98.5%) and 2,5-DMTHF (96%), 2,5-furandicarboxyllic acid (98.5%), $Mn(NO_3)_2.4H_2O$ (97%), $Ca(NO_3)_2.4H_2O$ (99.0%), ϒ-Al_2O_3, Cs_2CO_3 (99.0%) and activated charcoal were purchased from Sigma–Aldrich, Bangalore, India. $Cu(NO_3)_2{\cdot}3H_2O$ (95%), $Fe(NO_3)_3{\cdot}9H_2O$ (97%), $Co(NO_3)_2{\cdot}6H_2O$ (99%), $La(NO_3)_3.xH_2O$ (99.0%), ZrO_2, K_2CO_3 (99.5%), CH_3OH (99.8%),

MIBK (99.0%), toluene (99.0%), CH_3CN (99.9%), 2-propanol (99.7%), NaOH (97.5%) and $NaBH_4$ (96%) were procured from Thomas Bakers. $PdCl_2$ was purchased from chemlab-India. Hydrogen, Oxygen, Nitrogen and air of high purity (99.99 %) were obtained from Inox-India. $CsNO_3$ (99.8%), $(NH_4)_6Mo_7O_{24}$ (99.0%), $Mg(NO_3)_2.6H_2O$ (98.0%) were purchased from Loba-Chemie. $SrNO_3$ (99.0%) was obtained from Merck whereas $Ba(NO_3)_2$ was procured from S. D. Fine-Chem Pvt. Ltd. HPLC grade acetic acid with 99.9% purity was purchased from SRL Chem. 2,5-diformylfuran (98%), 5-formyl furan-2-carboxyllic acid (98%) and 5-hydroxymethyl furan-2-carboxyllic acid (99%) were purchased from TCI ltd.

2.3 Synthesis of catalysts

2.3.1 Synthesis of 3% Pd/C

Pd/C was prepared by modified wet impregnation method [(1)]. In a typical synthesis of 3% Pd/C calculated amount of $PdCl_2$ was dissolved in minimum amount (~15mL) of diluted HCl. In this homogeneous solution, 2g aqueous slurry of activated charcoal was added. This mixture was vigorously stirred for 2h at room temperature. After 2h, 10M solution of NaOH was added to maintain the pH of the solution in the range of 8–9 and the stirring was again continued for 0.5h. After that $NaBH_4$ was added as reducing agent to the solution. The reaction mixture was further stirred for 0.5h. After that as obtained slurry was washed with deionised water till the pH of the mother liquor becomes neutral and dried at 383K for 24h. Similarly, other Pt, Ir, Ru, and Re supported catalysts were prepared. The prepared catalysts were nominated as 3%M/C where M stands for metals. Catalysts on different support systems like ZrO_2, CeO_2 and Al_2O_3 were also synthesised by the same method.

2.3.2 Synthesis of Cu-Fe (1:2)

A bimetallic Cu–Fe catalyst was prepared by a co-precipitation method. Calculated amounts of $Cu(NO_3)_2 \cdot 3H_2O$ and $Fe(NO_3)_3 \cdot 9H_2O$ (100mL each) in 1:2 ratio were taken in a 500mL three neck round bottom flask along with 2M solution of NaOH. All three solutions were mixed dropwise with continuous stirring for 10h at room temperature. The as-obtained precipitate was washed with deionised H_2O until the pH became 7. This cake was dried at 383K and calcined at 723K for 4h with a rate of $10°Cmin^{-1}$. The calcined catalyst was activated using hydrogen at 523K for 3h with a rate of $2°Cmin^{-1}$. The flow of hydrogen was maintained at $2mLmin^{-1}$. All the metal catalysts were prepared by the same method.

2.3.3 Synthesis of Mn-Cs (80:20)

2.3.3.1 Synthesis of Mn-Cs nanocomposite: Calculated amount of $Mn(NO_3)_2.4H_2O$ was taken in the aqueous solution in a round bottom flask and stirred for 0.5h. After that 100 mL solution of calculated amount of $CsCO_3$ was added to the solution which leads to precipitation of $Mn(NO_3)_2.4H_2O$. After complete addition of $CsCO_3$ solution the mixture was stirred for 6h in a Nitrogen environment at room temperature. After that obtained slurry was filtered and washed by 2L deionised water till the pH of filtrate becomes neutral. The wet cake of material was heated at 110°C for drying purpose followed by calcination at 450°C for 5h with the heating ramp of 10°C/min.

2.3.3.2 Impregnation of Mn over various supports: Different loading of Mn over various supports like ZrO_2, CeO_2, Al_2O_3 were prepared by incipient wet impregnation method. Here the calculated amount of $Mn(NO_3)_2.4H_2O$ was taken in 100mL of methanol which lead to the formation of a homogeneous mixture in a few minutes. After 15 minutes calculated amount of supports was added and stirred for 6h at room temperature. The solvent was evaporated at rotavapour after that heated at 110°C for drying purpose followed by calcination at 450°C for 5h with the heating ramp of 10°C/min.

2.3.4 Synthesis of exfoliated Graphene oxide

Modified Hummer's method was used for synthesis of graphene oxide [(2)]. 1g of $NaNO_3$ was dissolved in 50mL concentrated H_2SO_4 containing beaker which is present in ice bath and temperature is maintained below 20°C. After complete dissolution of $NaNO_3$, 2g of graphite powder added step by step in the mixture and stirred for 1.5h while keeping the temperature well below 35°C. After that slow addition of $KMnO_4$ was performed and slurry was set at vigorous agitation. After 1.5h of agitation 80mL water was added dropwise into the slurry. Since it is an exothermic step due to oxidation of Graphene the temperature mandatorily should be below 20°C. After complete addition of 80mL water again add 120mL of water into the solution. This solution was stirred for another 1.5h and after that the apparatus transferred in hot oil bath at the temperature of 95°C. It was digested for 2h at this temperature and after that again placed at room temperature. After cooling down it was transferred to ice bath and stirred for 15 minutes. 20mL of 50% H_2O_2 was added in a controlled manner after 15 minutes which stopped the reaction. After another 15 minutes agitation the as obtained slurry was washed with 1L of 5% HCl solution to remove the metal impurity if any. Further washing was given with 5L deionised water and neutral graphene oxide was separated by centrifugation at 5000 rpm. Hence obtained graphene oxide was dried at 120°C in the oven.

2.3.5 Synthesis of Cu-Co/x-GO

CuCo/-GO nanocomposite was synthesised by a solvothermal method. In a typical synthesis, GO was dispersed into ethylene glycol (60mL) and sonicated for 1h, followed by the subsequent addition of aqueous NH_3 (1.6mL), and stirred again for 1h. Copper and cobalt nitrates were added in a 1:3 molar ratio and the solution was gradually heated to 160°C. As the temperature reached 160°C, a 0.3M aqueous solution of Na_2CO_3 (200mL) was added

dropwise and the slurry was further aged for 2h under a nitrogen atmosphere. The resulting product was filtered, thoroughly washed with distilled water until neutralisation, and dried overnight at 100°C, then calcined at 350°C for 4h.

2.4 Characterization techniques

2.4.1. Surface area measurement and N_2 sorption study

Textural properties of catalyst and metallic nanoparticles can be determined by N_2 sorption study. When size of particles minimised to the nano dimensions atoms per unit area becomes important for catalytic activity. Surface area can be measured by N_2 sorption study and applying BET theory which was developed by Stephen **Brunauer**, Paul **Emette** and Edward **Teller** in 1938. BET theory is basically extension of Langmuir theorem which suggested monolayer adsorption of gaseous adsorbate (one site-one adsorbate) at the solid surface [(3)].

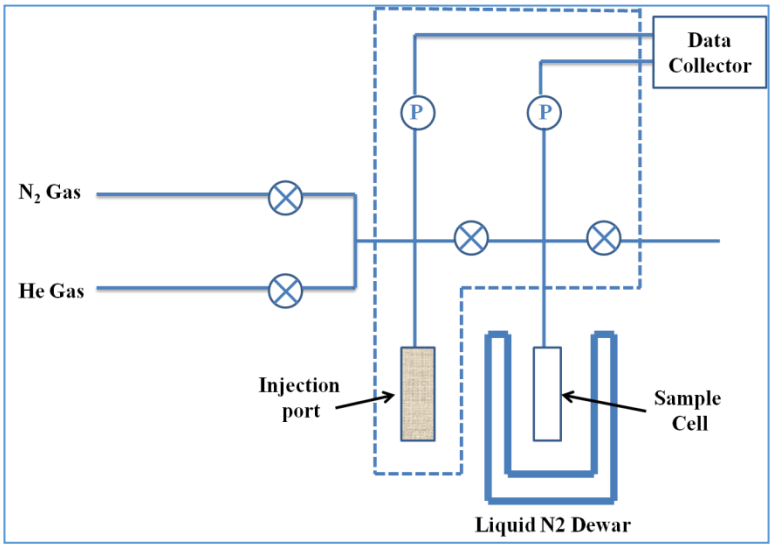

Figure 2.1: Schematic diagram of BET surface area instrument

Langmuir theory also proposed that adsorption energy (E_{ads}) is same for every surface site for all adsorbate and activity of these adsorbates was directly proportional to their concentration. Though BET theory considered that physiosorption of adsorbate on the solid surface takes place due to van der Waals forces. These gas-solid interactions occur in

multilayer which makes them short of adsorbent surface. So vapour phase interaction comes into play among gaseous molecules whose energies are almost equivalent to gas-solid interactions [4].

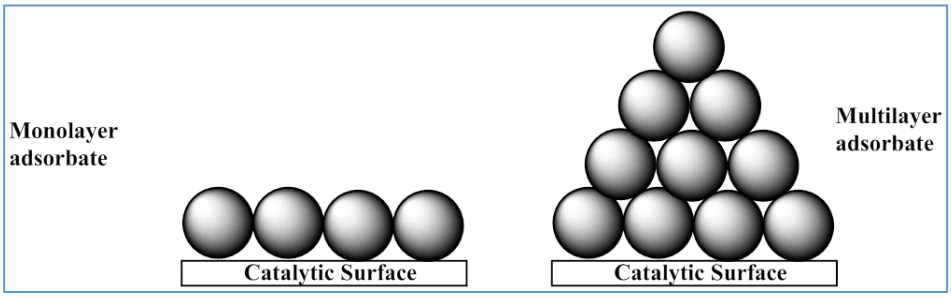

Figure 2.2: Langmuir theory of adsorption vs BET theory of adsorption mechanism

This phenomenon leads to the formation of multilayer of adsorbate on each other and condensation occurs into liquid. When temperature of adsorbent surface is lower than the critical temperature of gas (adsorbate) then monolayer adsorption takes place followed by the capillary condensation. Capillary condensation takes place below the saturation vapour pressure due to the limited space of pores hence enhanced van der Waals forces. Functioning of BET surface area application starts with adhesion of N_2 molecules on the surface of material because of its strong affinity with most of the solids. Aforementioned exposed surface sites will be directly proportional to quantity of adsorbate. Here it should also be noted that this concentration of adsorbate also depends on various parameters like pressure of gas, temperature and strength of solid-gas interaction [5]. Adsorbent surface is cooled by liquid N_2 for recordable adsorption followed by passing of known amount of N_2 in the sample cell under vacuum. At saturation pressure adsorption become static and difference in pressure is recorded by transducer. Post formation of adsorption step sample is transferred under heat from N_2 atmosphere and desorption is quantified with the help of data recorder. The data of BET isotherm is plotted between the amount of N_2 adsorbed v/s relative pressure (P/P_0) whereas the BET equation is defined as 2.1

$$\frac{P/Po}{N(1-{}^{P}/_{Po})} = \frac{1}{NmC} + \frac{C-1}{NmC}({}^{P}/_{Po}) \ldots\ldots\ldots\ldots\ldots\ldots\ldots\ldots\ldots\ldots (2.1)$$

Here N is the amount of adsorbed molecule at relative pressure P/P_o whereas N_m stands for monolayer capacity of adsorbed gas. P_o is the saturation pressure of adsorbate at constant temperature of adsorption process. C is the BET constant which is related to E_{ads} as shown in equation 2.2

$$C = e^{(Em-El/RT)} \ldots\ldots\ldots\ldots\ldots\ldots\ldots\ldots\ldots\ldots (2.2)$$

Where E_m is energy of adsorption of first layer and E_l is energy of adsorption of multilayers which are present over first layer. The value of C gives the shape of BET isotherm which is represented in **Figure 2.3**.

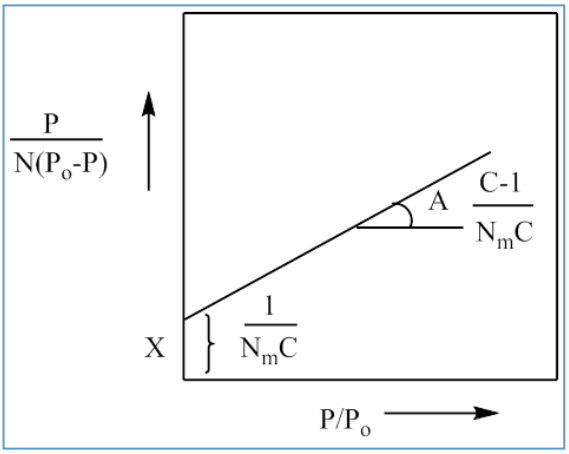

Figure 2.3: Graphical representation of adsorption isotherm

The linearity of BET equation can be maintained between the relative pressure ranges of 0.05-0.35 [(6)]. The value of monolayer capacity N_m, BET constant 'C', surface area and specific surface area can be calculated by equation 2.3, 2.4, 2.5 and 2.6 respectively.

$$Nm = \frac{1}{A+X} \ldots\ldots\ldots\ldots\ldots\ldots\ldots (2.3)$$

$$C = 1 + \frac{A}{X} \ldots\ldots\ldots\ldots\ldots\ldots\ldots\ldots\ldots\ldots (2.4)$$

$$S_{tot.} = \frac{NmNa\sigma}{N} \ldots\ldots\ldots\ldots\ldots\ldots\ldots\ldots (2.5)$$

$$[S] = \frac{Stot}{a} \ldots\ldots\ldots\ldots\ldots\ldots\ldots\ldots\ldots\ldots (2.6)$$

Where N_a= Avogadro's number

σ = Molecular cross-section area and

a= Mass of solid sample

BET isotherms also reveals about the porosity of material in terms of pore size, pore volume etc which is clinical for understanding the transportation phenomenon of reaction system. There are total 6 type of N_2 physiosorption isotherm according to IUPAC which provide significant information about the porous nature of catalyst [7]. Reversible type-I isotherm as shown in **Figure 2.4** is of two types. Reversible type-I.a isotherm comes for microporous materials having pore diameter less than 1 nm whereas I.b type isotherm obtained for microporous and smaller mesoporous materials having pore diameter of ~2 .5nm. Reversible type-II is evaluated for nonporous or macroporous materials whereas Reversible type-III and type-V isotherm achieved for those materials which have very week interaction with adsorbate molecules. In type-V isotherm hysteresis loop is observed at higher pressure which is the result of formation of molecular cluster after condensing of pores. This type of isotherm can not give any information regarding porosity. Like reversible type-I isotherm, reversible type-IV isotherm also have two classes. Appearance of type-IV.a isotherm suggests that pore diameter of the mesoporous material is higher than the critical diameter whereas type-IV.b isotherm achieved when pore diameter is smaller than critical width of pores. Type-VI isotherm is seen for highly uniform nonporous surface of material. Shape of this isotherm suggests multilayer adsorption of molecules on the surface of adsorbent.

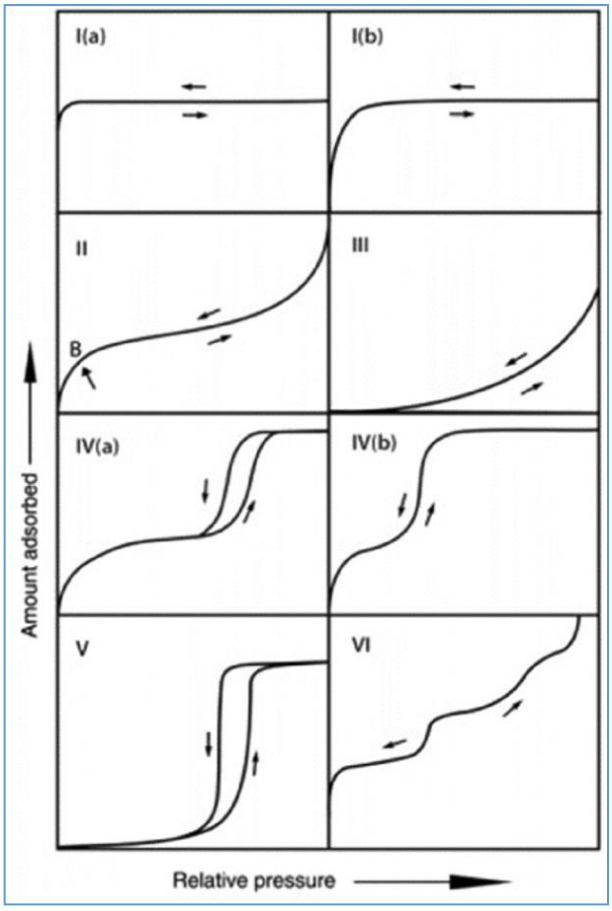

Figure 2.4: Type of N_2 adsorption isotherms according to IUPAC [7]

In this thesis N_2 adsorption was measured by Brunauer-Emmett-Teller (BET) equation at pressure (10^{-4} Torr) and temperature of N_2 (77 K) for determination of surface area, pore volumes and pore size distribution of catalysts. All these measurements were conducted on Chemisorb 2720 Micrometics instrument.

2.4.2 Thermal Analysis

Thermal behaviour of any material under physic-chemical dimension is explored by its Thermal Analysis (TA). According to International Confederation of Thermal Analysis and Calorimetry (ICTAC) thermal analysis is the investigation of change in chemical and physical properties of a sample with respect to time under a controlled temperature program which can be heating, cooling, isothermal holds or combination of all these. It is important to

understand the fact that thermal analysis determines properties not structure of the sample. It was Lavoisier who used thermal analyser techniques for mass change which later on modified for temperature change by Le-Chatelier [8]. Commonly used thermal analysis techniques are TGA, DSC, DTA and integrated TGA-MS based on physical parameters like mass, temperature/heat flux and dynamic as shown by **Figure 2.5**.

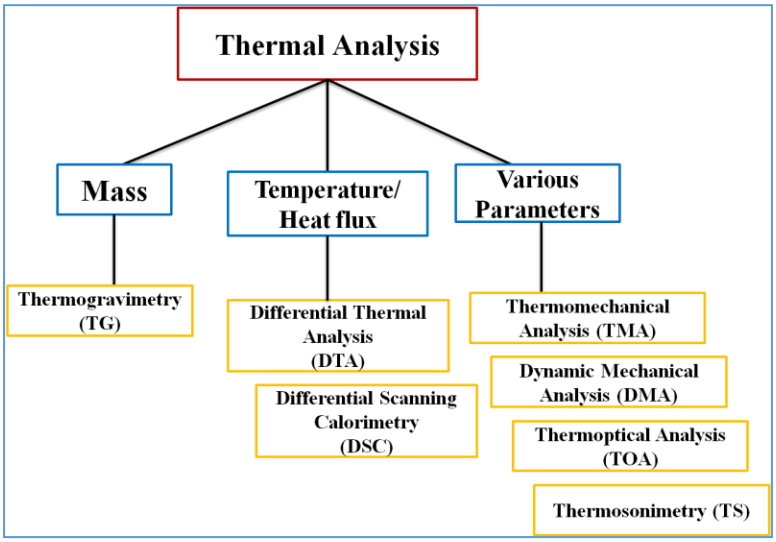

Figure 2.5: Classification of thermal analysis

2.4.2.1 Thermo Gravimetric Analysis (TGA)

Thermogravimetric analysis (TGA) deals with the change in mass with respect to controlled temperature and specific time. It operates in the range of 0°-2000°C. The change in the mass of analyte occurs due to various chemical (oxidation, reduction, chemisorption, water of crystallization, loss of drying and degradation) and physical transitions (adsorption, desorption, sublimation, evaporation and vaporisation).Based on various parameters it further can be of three types. (I) Dynamic TGA, (II) Isothermal/specific TGA and (III) Quasistatic TGA.

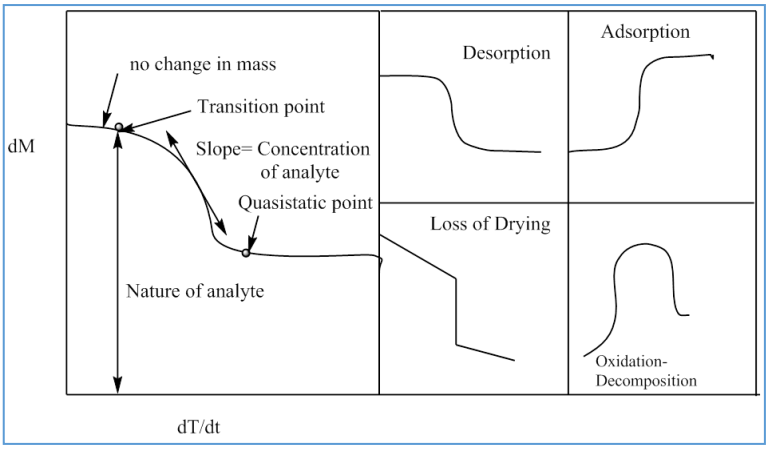

Figure 2.6: Various types of chemical/physical transitions curves in TGA

2.4.2.2 Differential Thermal Analysis (DTA)

In this thermal analysis difference of temperature between the analyte and reference is calculated against the time/temperature under specific program of temperature. It operates in the range of 150°-1600°C. DTA can identify and quantitatively analyse the chemical composition of analytes.

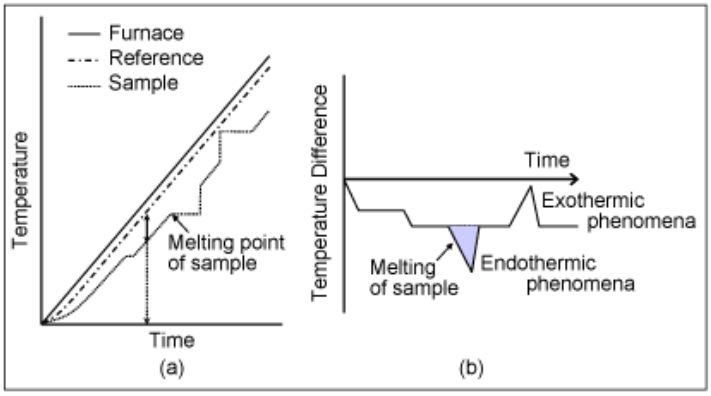

Figure 2.7: Typical DTA curves

2.4.2.3 Differential Scanning Calorimetry (DSC)

DSC is the calculation of extent of energy of analyte originated due to ongoing chemical and physical transitions owing to heat flux generated under a temperature program. It provides qualitative as well as quantitative estimation of analyte. During endothermic DSC curves

more heat flux required whereas for exothermic DSC curves less heat flux is needed for increasing the temperature.

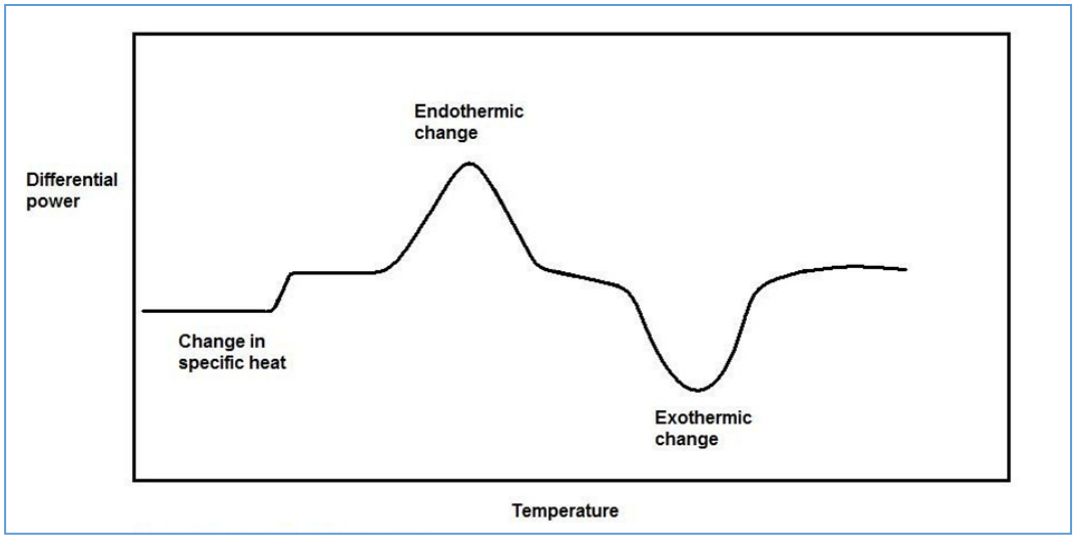

Figure 2.8: Example of typical curve for DSC

2.4.2.4 Thermo Gravimetric Analysis (TGA) –Mass Spectrometry (MS)

TGA-MS is Evolved Gas Analysis (EGA) kind of thermal analysis which integrates the mass spectrometer and thermogravimetry. This instrument is used for exact identification of evolved gaseous molecular fragments during thermogravimetric treatment of analyte. Information of analyte in TGA-MS curve is displayed in terms of ionic current vs mass fragment (m/z).

In the thesis work DTA/TGA-MS curves were obtained on a Simultaneous thermal analyzer SDT-Q600 Discovery series MS by heating the samples from room temperature to 600 °C under a N_2 atmosphere with a ramping rate of 10 °C min−1.

2.4.3 X-Ray Diffraction (XRD)

X-ray Diffraction Chromatography (XRD) is non-destructive technique which is used in identifying, quantifying and characterising the materials. In heterogeneous catalysts information about crystalline nature, crystal orientation, unit cell parameter, crystallite size,

phase synthesis and identification, crystal structure and crystal defects is obtained by XRD technique [9]. It is largely based on Bragg's law which correlate the electromagnetic radiation with the diffraction angle and lattice spacing of a crystal as

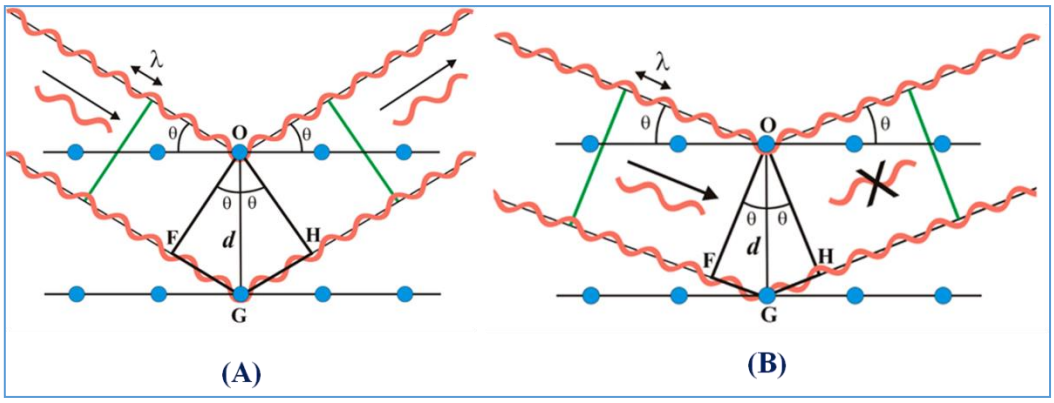

Figure 2.9: Demonstration of Bragg's law of diffraction (A) Constructive interference (B) Destructive interference

$n\lambda = 2dsin\theta$…… (2.7)

Here *n*= integer (n= 1,2,3,…….)

λ= wavelength of X-ray

Θ= Angle of diffraction

d= Interplananr spacing giving diffraction

The constructive interference between monochromatic x-ray source and analyte takes place when Bragg's law is satisfied [10]. X-ray diffractometer mainly composed of an X-ray tube, X-ray detector and sample holder. X-rays are produced in CRT (Cathode Ray Tube) by heating a filament to generate electrons. When these electrons have enough amount of energy to remove inner shell electron of the analyte then characteristic X-ray spectra originated which consists of K_α and K_β (most common component). These X-rays are monochromated by specific filters and directed towards crystal after collimation. With the movement of sample and detector intensity of reflecting X–rays are recorded. In order to get intense X-ray

pattern constructive interference aligned with Bragg's law geometry of incident X-rays needed to impinge the sample surface.

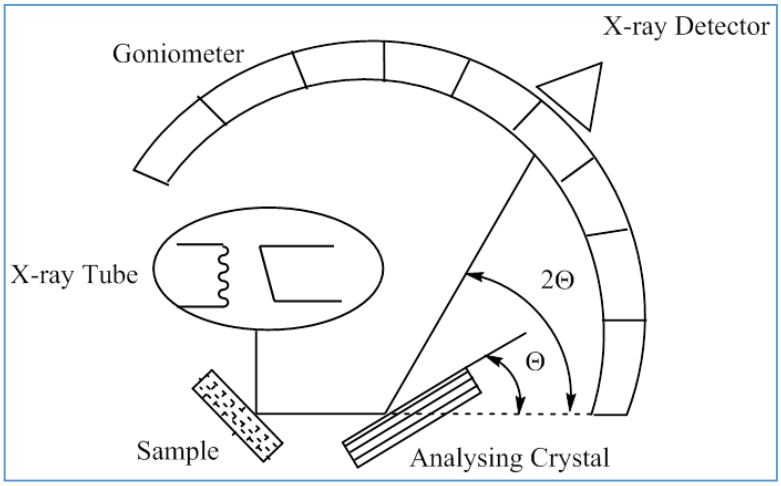

Figure 2.10: Schematic diagram of X-ray Diffractogram

In this thesis work X-ray diffraction (XRD) patterns were recorded on a PAnalytical PXRD system (Model X-Pert PRO-1712), using Ni filtered Cu Kα radiation (λ = 0.154 nm) as a source (current intensity, 30 mA; voltage, 40 kV) and X-celerator detector. The samples were scanned in the 2θ range of 10°–80°. The metal phases of the catalysts were identified by their characteristic 2θ values provided in Joint Committee on Powder Diffraction Standards (JCPDS). The software program X-Pert High Score Plus was used to subtract the contribution of the Cu Kα2 line prior to data analysis. Crystallite size of the materials used was calculated by Scherrer equation i.e.

$$L=\frac{K\lambda}{\beta Cos\theta} \dots\dots\dots\dots\dots\dots\dots\dots\dots\dots\dots\dots (2.8)$$

Where K= Dimensionless Shape factor and its value is 0.9

λ= X-ray Wavelength

β= Line broadening at FWHM and

Θ= Bragg's angle

2.4.4 X-ray Photoelectron Spectroscopy (XPS)

Developed by Kai Siegbahn X-ray Photoelectron Spectroscopy (XPS) is a powerful tool for qualitative and quantitative evaluation of elemental composition of catalyst [(11)]. Due to its surface sensitivity it is also known as Electron Spectroscopy for Chemical Analysis (ESCA). XPS is based on the photoelectric effect first observed by Hertz.

$$B.E. = h\upsilon - K.E \ldots\ldots\ldots\ldots\ldots\ldots\ldots (2.9)$$

Where B.E= Binding Energy of photoelectrons

h= Plank's Constant

υ= Frequency of irradiation

K.E. = Kinetic Energy of photoelectrons

In a typical XPS characterisation sample is treated with X-rays photons of known energy which eject out the core electrons from the surface (0-10nm) of sample. These emitted electrons (also termed as photoelectron) are measured for their kinetic energy (K.E.) by an electromagnetic analyser. The binding energy of the electronic orbit from which photoelectron has been emitted can be calculated by XPS experiment on applying Einstein's photoelectric equation. *i.e*

$$B.E. = h\upsilon - K.E. - \phi \ldots\ldots\ldots\ldots\ldots\ldots\ldots\ldots\ldots (2.10)$$

Here, hυ= X-ray Photon energy (Monochromatic Al Kα=1486.6eV and Mg Kα= 1253.6eV)

K.E. = Kinetic energy of photoelectron

Φ= Work function induced by analyser and can be eliminated. Hence equation 2.10 reduced to 2.9.

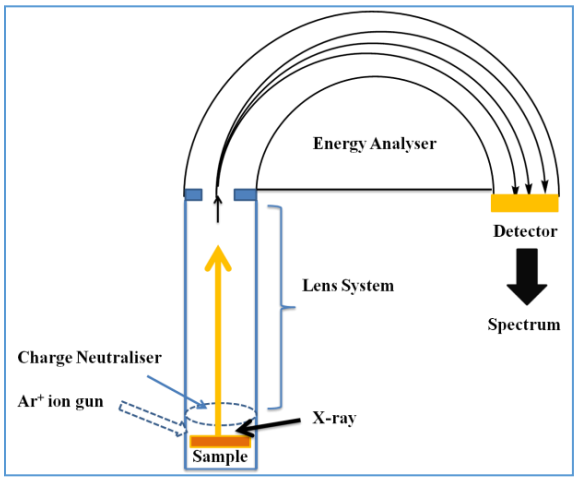

Figure 2.11: Schematic diagram of X-ray Photoelectron Spectrometer (XPS)

It is important to understand that the core level electron B. E. acts as fingerprint of specific atom. If this atom has different chemical environment or interaction with surrounding then prominent shift of (0.1eV-10eV) is observed in their B. E. This shift in binding energy is also termed as "chemical shift" which determine the chemical status of the sample [(12)]. Since the amount of photoelectron is directly proportional to the concentration of atom, quantification of chemical composition of surface can also be done by XPS by following equation

$$Ci = \frac{Ii/Si}{\Sigma Ii/Si} \quad \ldots\ldots\ldots\ldots\ldots\ldots\ldots\ldots \quad (2.11)$$

C*i*= Atomic concentration of element *i*

I_i= Peak intensity of element *i*

S_i= Sensitivity factor of peak *i*

In the present thesis X-ray photoelectron spectra were recorded using an ESCA-3000 (VG Scientific, Ltd, England) with a 9-channeltron CLAM4 analyzer under vacuum greater than 1 × 10−8 Torr, using Mg Kα radiation (1253.6 eV) and a constant pass energy of 50 eV. The binding energy values were charge-corrected to the C1s signal (284.6 eV). In one another work photoelectron spectra of the samples were recorded with a custom built ambient

pressure photoelectron spectrometer (APPES) (Prevac, Poland) at CSIR-NCL Pune. The instrument sis equipped with a VG Scienta R3000HP analyser and MX650 monochromator. Monochromatic Al K_α X-rays were generated at 200 W and used for measuring the X-ray photoelectron spectrum (XPS) of the catalysts. Base pressure in the analysis chamber was maintained in the range of 10^{-10} mbar. The energy resolution of the spectrometer was set at 0.5 eV at pass energy of 50 eV. Binding energy (BE) was calibrated with respect to Au 4f7/2 core level at 84.0 eV.

2.4.5 Electron Microscopy

Many features that control the various properties of material are present below light microscope scale. So, to understand these controlling features an alternate microscopic technique was needed. De Broglie in 1925 proposed the concept of dual nature of electron where he stated that electron can behave both particle as well as wave with wavelength lesser than visible light. This concept was transformed in "electron microscopy" first of all by Knoll and Ruska in 1932 [13]. Electron can be considered as a type of ionisation radiation which on interaction with material shows various phenomena as shown in **Figure 2.12**.

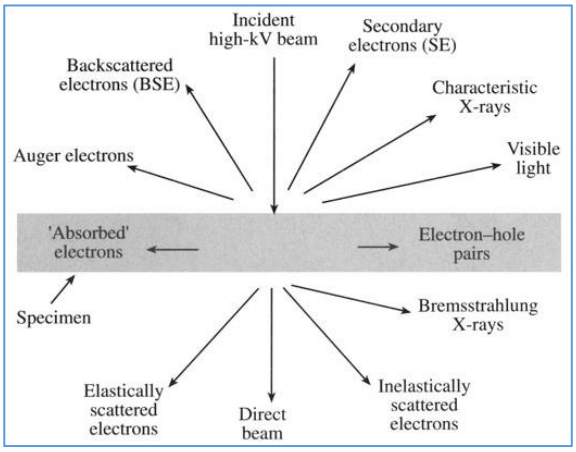

Figure 2.12: Type of transitions occur during interaction of material and ionised radiation

2.4.5.1 Scanning Electron Microscope (SEM)

Scanning Electron Microscope (SEM) deals with the morphological and topological aspect of analyte as it scan the surface of specimen by a focused electron beam in a raster pattern. When the incident electrons collide with specimen then lot of interactions occur as shown in **Figure 2.12**. These interactions can be classified into inelastic and elastic collision. Primary electrons are scattered by atomic nucleus or inner shell electron of similar energy in elastic collision with almost zero energy loss and wide angle direction change. If these electrons are scattered by more than 90° then Backscattered Electrons (BSE) generated which give compositional and topographical inputs of specimen [(14)]. In a typical elastic scattering 10-50% electrons are BSE with energy greater than 50 eV and 60-80% of their initial energy is retained. Primary electron ionise the specimen by transferring their part of energy to it. This will lead to the generation of loosely bound secondary electron (SE) in form of inelastic collision. Their energy is always less than 50 eV due to which they provide high resolution topographical contrast of specimen. Similarly when an inner shell electron is replaced by the incident electron an outer shell electron replace it to maintain the charge balance of orbital. Hence ionised specimen comes into the ground state by emitting characteristic X-rays. This provides Energy Dispersive X-ray Spectroscopy (EDS) which is a microanalytical technique to know about the elemental composition of specimen. It gives the information till the depth of 1-2 micron. The lateral resolution of BSE is 1μm whereas for SE it is 10nm. In the thesis work the particle morphology and elemental composition studies were carried out on silicon grid by Scanning Electron Microscopy (SEM) and Energy Dispersive X-ray Analysis (EDX), respectively. The analysis was performed on LEO-LEICA STEREOSCAN 440 at various magnifications using a Bruker detector.

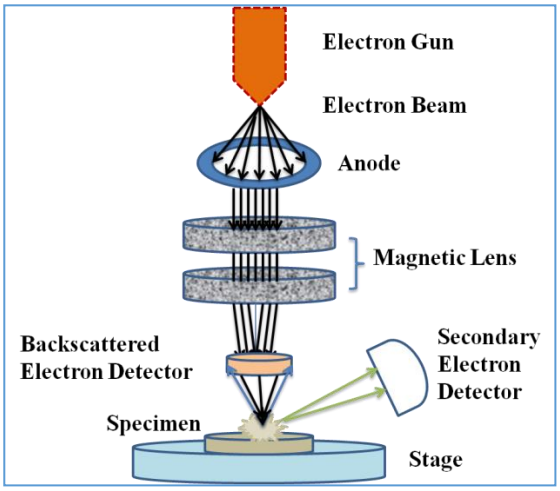

Figure 2.13: Schematic ray diagram of SEM instrument

2.4.5.2 Transmission Electron Microscopy (TEM)

Transmission Electron Microscopy (TEM) provides the information about the particle size, degree of aggregation, dispersion of nanoparticles on support and internal microstructure of catalysts. The ability of TEM instrument to do the spatial resolution of material equal to the atomic level plays vital role in getting these information [(15)]. Aforementioned TEM is also based on quantum mechanical behaviour of electron proposed by De-broglie. It utilise the imaging, spectroscopy and diffraction efficiently for microanalysis of specimen. Here scattered electron with small angle due to elastic collision cause contrast imaging. The contrast in TEM depends on geometry of illuminated electron, scattered electron within the specimen and the path of transmitted electron by lens, aperture and detection system. Electrons are accelerated by accelerating voltage of 80-300 kV which penetrate the specimen by atleast 1μm. As shown in **Figure 2.14** TEM transmitted and scattered electrons are recombined and focused by objective lens to perform a diffraction pattern whereas condenser lens focus the electron in to a beam of controlled diameter and convergence and finally projector lens magnify the image or diffraction pattern on the detector. In this thesis Particle size and distribution were studied using a transmission electron microscope (HR-TEM), model JEOL 1200 EX. A small amount of the solid sample was sonicated in 2-propanol for 1

min. A drop of the prepared suspension was deposited on a Cu grid coated with a carbon layer, and the grid was then dried at room temperature before analysis

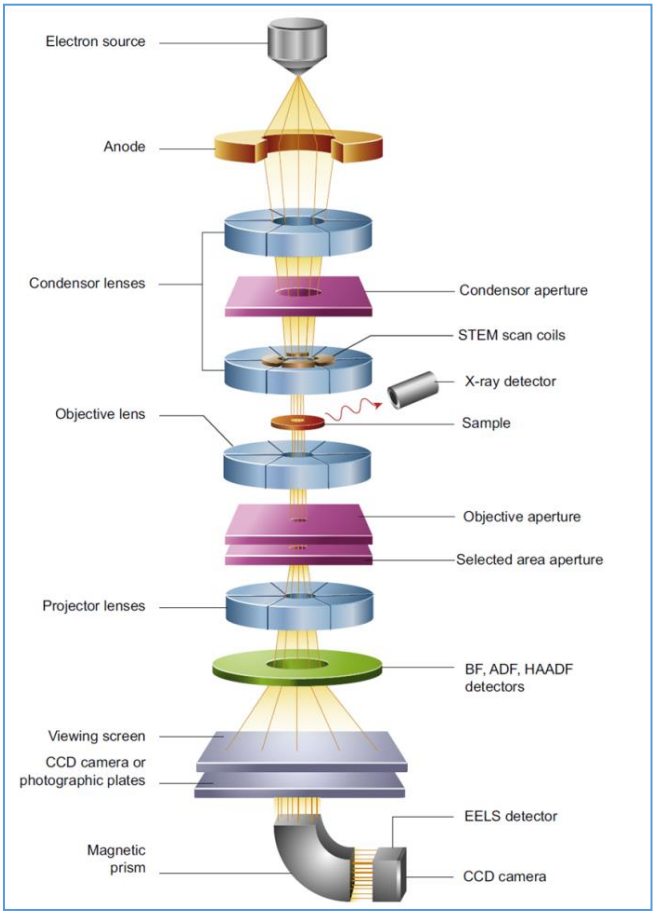

Figure 2.14: Schematic ray diagram and various part of TEM instrument

2.4.6 Temperature Programmed Methods (TPM)

Temperature Programmed Methods (TPM) can be defined as the event happening at the surface of solid under a controlled temperature programme where temperature of analyte (β) changes according to equation 2.12

$$\beta(t) = \frac{dT}{dt} \dots\dots\dots\dots\dots\dots\dots\dots\dots (2.12)$$

TPM is modified version of flash adsorption method invented by Amnenomiya and Cvetanović and it's applicable to porous materials as well as single crystalline structures [(16)].

When TPM is applied for the rate of desorption of adsorbed molecule as function of temperature then its called Temperature Programmed Desorption (TPD) which can provide vital information about the catalytic active site, binding energies, adsorption phases, desorption kinetics and surface concentration of material under investigation. TPD largely depends on the adsorption-desorption (chemisorption) phenomena on the surface of solid [(17)]. Chemisorption is a highly specific, active process where chemical interaction like overlapping of molecular orbitals takes place between adsorbate and adsorbent. This process is also characterised by high heat of adsorption, higher temperature range, exothermic and spontaneous process. TPD instrument composed mainly of three components (1) Gas panel for controlled experiment (2) Reactor/sample holder and (3) Detector. To investigate the sample controlled flow of probe gas is required which acts as adsorbate. TPD is classified on the basis of probe gas like NH_3, CO_2, SO_2, CO etc. The analyte which is to be investigated is placed in a reactor or sample holder which is generally a temperature controlled furnace. Probe molecule adsorbed evolutes at controlled temperature conditions which are recorded by a detector which can be FID, TCD (catharometer), conductometric titration and mass spectrometer. Either area under the curve is calculated to find out the amount of surface coverage or temperature maxima is observed to find out the strength of interactions. Various type of TPD/TPR/TPO used in this thesis are discussed in brief here.

2.4.6.1 NH_3-Temperature Programmed Desorption (NH_3-TPD)

As name suggest in this TPD probe gas is NH_3 and CO_2 which are basic and acidic respectively in nature. This desorption phenomena is used to determine the acidity and basicity of sample [(18)]. It is important to note that in TPD desorption of adsorbate is monitored with respect to temperature. So here after degassing/purity of sample under He atmosphere it is kept under the NH_3/CO_2 environment for adsorption at active sites of

material followed by desorption at controlled temperature programme. Desorption takes place when heat overcome the activation energy barrier of adsorbent-adsorbate interaction. The desorbed molecules are dragged to detector by flow of He environment where concentration of evolved gas is measured. NH_3-TPD experiments were carried out on a Micromeritics-2720 (Chemisoft TPx) instrument. In order to evaluate the acidity of the catalysts, ammonia TPD measurements were carried out by: (i) pre-treating the samples from room temperature to 200°C under a helium flow rate of 25 mLmin−1, (ii) adsorption of ammonia at 40°C and (iii) desorption of ammonia with a heating rate of 10°Cmin−1 starting from the adsorption temperature to 700°C. CO_2-TPD experiments were also carried out on a Micromeritics-2720 (Chemisoft TPx) instrument. In order to evaluate the surface basicity of the catalysts, CO_2-TPD measurements were carried out by: (i) pre-treating the samples from room temperature to 200°C under a helium flow rate of 25mLmin−1, (ii) adsorption of CO_2 at 40°C and (iii) desorption of CO_2 with a heating rate of 10°Cmin−1 starting from the adsorption temperature to 700°C.

2.4.6.2 Temperature Programmed Reduction and Temperature Programmed Oxidation (TPR/TPO)

The reducibility of the catalytic surface is calculated by H_2-TPR whereas the oxidation trend of material is calculated by O_2-TPO. In both the experiments the probe gas is mixed with inert gas and detected by catharometer.TPR and TPO analysis is clinical for the catalytic sites used in hydrogenation and oxidation respectively as it can find out the presence of one or more type of species that can be reduced or oxidise respectively. Exact amount of these species in the catalyst and their energy of activation for oxidation or reduction can also be calculated by the adsorbed probe adsorbent and T_{max} where rate of reduction or oxidation is highest [19]. H_2-TPR studies of the catalysts were carried out using a Micromeritics

Autochem-2920 instrument in the temperature range of 50–750 °C at a heating rate of 5 °C min−1 using 5% H_2 in He as the probe gas. The H_2 consumption in the TPR study was estimated quantitatively with a thermal conductivity detector that was calibrated before the TPR study

2.4.7 Fourier Transform Infra Red spectroscopy (FTIR)

Important aspect of catalyst like nature of surface site (acidic, basic, redox, surface defects) and their dynamic behaviour in certain reaction conditions can be determined by the use of Infra Red (IR) spectroscopy. IR spectroscopy based on the idea of change in dipole while vibration in the molecules [(20)]. Generally region of frequency of 400-4000 cm^{-1} of electromagnetic spectrum is considered as mid-IR region and considered in IR spectroscopy. In Fourier Transform Infra Red Spectroscopy (FTIR) spectrometer is a collimating optics where molecules are treated with the IR radiations which excite them at higher vibrational level and measured IR intensity is directly proportional to change in dipole moment. This change in dipole moment comes from the energy transferred from the photon energy of IR. While introducing probe molecule like Pyridine, NH_3, CO_2, CO and NO one can determine the nature of surface sites. Adsorption of such probe molecules can be vital for the identification and quantification of surface active sites. Pyridine is commonly used as to find out the type of surface acid sites like Brönsted acidity or Lewis acidity. Shift in the vibrational mode of material while adsorption can tell about the chemical properties which further can be quantified given that adsorption coefficient is known. Though pyridine is less sensitive in this technique but it is highly specific for acidic sites [(21)]. In the thesis work we did Pyridine-IR spectra and MeOH-IR spectra of the prepared catalysts on a PerkinElmer 2000 FTIR spectrometer in the wave number range of 4000–400 cm^{-1} using the KBr pellet

technique. 20µL of pyridine was injected step by step and scans were performed in the temperature range of 25–170°C.

2.4.8 Raman Spectroscopy

Raman spectroscopy deals with the concept of change in polarisibility of molecule under investigation. In this technique electromagnetic radiation irradiates molecule and induces an oscillating dipole which scatter the incident light. This induced dipole moment is an off-resonance interaction mediated by an external electric field [(22)]. During scattering of light maximum transitions are elastic collisions (10^{-3} of incident light) where frequency of incident and scattered light remain equal and is called as Rayleigh scattering. Only 10^{-6} of scattered light shows inelastic transitions and known as Raman scattering [(23)]. In it frequency of incident is either less than scattered light (Antistoke's line) or more than scattered light (Stoke's line).

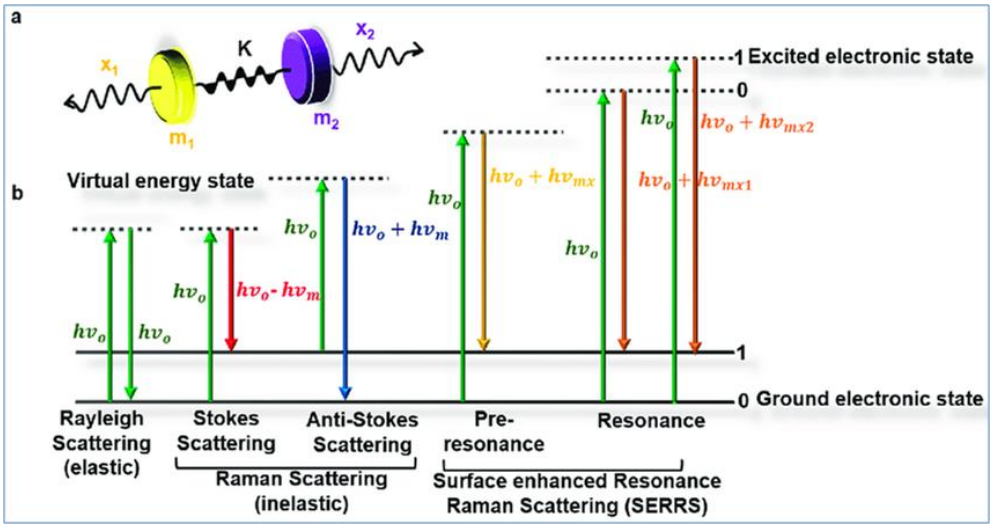

Figure 2.15: Representation of Raman Effect

Molecules present initially in the ground vibrational state shows Stoke's line whereas those present in vibrational excited state shows antistoke's line. As most of the molecules at ambient room temperature conditions remain in ground state the intensity of stoke's line is

always higher than the antistoke's line. Relative intensity ratio of stoke's and antitsoke's line depend on the absolute temperature of sample and energy difference of ground and vibrational energy level. The intensity of Raman scattering can be explained as

$$I \alpha \upsilon^4 I_o N(\Delta\alpha/\Delta Q)^2 \ldots\ldots\ldots\ldots\ldots\ldots\ldots\ldots (2.13)$$

Where I= Intensity of Raman scattering

I_o= Intensity of incident laser

N= No. of scattering molecule

υ = Frequency of exciting laser

α= Polarisibility of molecule

Q= Vibrational amplitude

Raman spectroscopy can provide chemical structure and nature of surface species of catalyst. Structure of crystalline phase, amorphous phase and nature of molecular species can also be determined by Raman spectrometer. In the thesis The Raman spectra of the samples were recorded on a Horiba JY Lab RAM HR800 micro-Raman spectrometer with 17mW, 632.8nm laser excitation.

2.4.9 Inductively Coupled Plasma-Atomic Emission Spectroscopy (ICP–AES)

Inductively Couple Plasma-Atomic Emission Spectroscopy (ICP-AES) is an atomic emission technique with combination of inductive and capacitive coupling. In heterogeneous catalysts it is particularly useful for the trace analysis of metal/atom/ions in the analyte. It is highly sensitive process with very less detection limit (ppm or ppb) and large dynamic range [(24)]. One of the major advantages is its reduced matrix effect due to use of high temperature of Argon plasma. In ICP-AES liquid samples are turned into aerosol and placed under plasma

where a deosolvation, vapourization, atomisation and excitation processes occur. Hence generated atoms/ions in the ICP process are excited at the extremely high temperature of Ar plasma (7000K). Each atom/ion has its own characteristic wavelength which is recorded and their concentration is detected given the number of photons. All the metals utilised in the best suited catalysts in thesis are investigated for their leaching by ICP with a Spectro 165 high resolution ICP-OES spectrophotometer (ARCOSFSH 12 model).

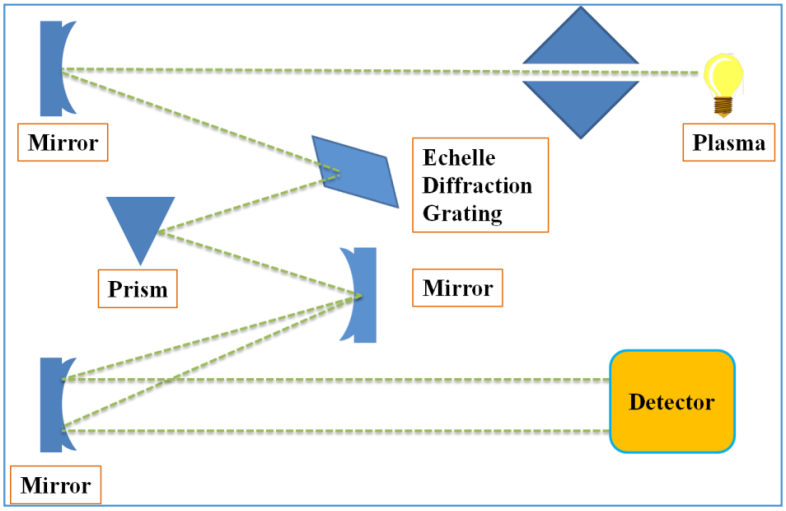

Figure 2.16: Ray diagram of ICP-AES instrument

2.5 Activity evaluation of catalysts

2.5.1 Hydrogenation of 5-HMF by 3%Pd/C

The hydrogenation of HMF was carried out in 300mL capacity autoclave supplied by Parr Instruments Co. USA at an agitation speed of 1000 rpm. The typical hydrogenation conditions were: temperature, 443K, H_2 pressure, 300psig, HMF, 0.1g, solvent, 2-propanol, 20g and catalyst loading, 0.01g. The reproducibility of results was confirmed by repeating three times. Liquid samples were withdrawn after specific time interval. The aliquots taken during the reaction were analysed using a Trace GC 700 series GC System (Thermo SCINTIFIC) coupled with FID detector and capillary column (HP-5 capillary column, 30m

length X 0.32mm id). The following temperature program method was used for GC analysis: 40°C (3 min), 1°C/min, 45°C (1 min), 10°C/min, 60°C (0 min), 20°C/min, and 250°C (1 min). The mass balance calculated by gas chromatogram calibration was found 96.17%.

2.5.2 Hydrogenation of 5-HMF by Cu-$CuFe_2O_4$

The hydrogenation of HMF was carried out in a 45mL capacity autoclave supplied by Parr Instruments Co. USA, at an agitation speed of 1000rpm. The typical hydrogenation conditions were as follows: temperature: 443K, H_2 pressure: 300psig, 5-HMF: 100mg, solvent, 2-propanol: 20g and catalyst loading: 50mg. Liquid samples were withdrawn after a specific time interval. The aliquots taken during the reaction were analysed using a Trace GC 700 series GC System (Thermo Scientific) coupled with an FID detector and capillary column (HP-5 capillary column, 30m length × 0.32mm id). The following temperature program method was used for GC analysis: 40°C (3 min), 1°Cmin^{-1}, 45°C (1 min), 10°Cmin^{-1}, 60°C (0 min), 20°C min^{-1}, and 250°C (1 min).

2.5.3 Oxidation of 5-HMF by Mn-Cs(80:20)

Catalysts were tested in 300mL Parr autoclave which was equipped with sample and pressure inlet valve. 100mg of 5-HMF and 50mg of catalyst was dissolved in 150mL of solvent and charged into reactor. The reactor was purged 5 times by N_2 after which reactor were heated at desired temperature with continuous stirring of 1000 rpm. After attaining desire temperature reactor was charged with 200psig of air and reaction was taken for 4h. Reaction aliquots were taken after every hour to analyse the reaction progress. The reaction samples were filtered by the help of 0.22 μ PTFE syringe filters and analysed on Agilent 1260 series UHPLC equipped with Multi Wavelength Detector (MWD) and Agilent Hi-Plex-H column at λ= 280nm, BW= 4, T= 45°C. The mobile phase used for analysis was 85% H_2O (0.1% CH_3COOH): 15% CH_3CN with 0.6ml/min flow rate.

2.5.4 Oxidation of 5-HMF by Cu-Co(1:3)/x-GO

Oxidation of 5-HMF was done in a 300mL Parr autoclave connected with the type 4842 controller. The reactor was equipped with sample valve, pressure inlet valve and thermocouple to control the temperature of reaction. Reactor was charged with 100mg 5-HMF in 100mL deionised water and 25mg of catalyst. The reactor was purged with Nitrogen to ensure the neutral environment before the reaction followed by heating. After attaining the desired temperature desire pressure of air was introduced in the reactor and reaction was started. After 1h reaction was stopped and reaction aliquots were taken after every 15 minutes to analyse the reaction progress. The reaction samples were filtered by the help of 0.22 μ PTFE syringe filters and analysed on Agilent 1260 series UHPLC equipped with Multi Wavelength Detector (MWD) and Agilent Hi-Plex-H column at λ= 280nm, BW= 4, T= 45°C. The mobile phase used for analysis was 85% H_2O (0.1% CH_3COOH): 15% CH_3CN with 0.6 mL/min flow rate.

2.6 Analysis of catalytic activity

2.6.1 Gas Chromatography (GC)

Hydrogenation products of 5-HMF like BHMF, DMF, MFFR, MFAL etc along with solvent like IPA, methanol, ethanol and 1-butanol were detected by Trace GC 600 series (Thermo Scientific) Gas Chromatograph (GC) equipped with Flame Ionisation Detector (FID). The detail of analysis, identification and material is given below

- GC : Thermo Scientific Trace GC 700 series
- Column: Capillary HP-5
- Column details: 30m length x 0.32mm ID x 1 μm film thickness
- Column stationary phase: (5% Phenyl)-methylpolysiloxane

- Carrier gas: He
- Detector: FID
- Injector temperature: 250°C
- Detector temperature: 300°C
- Total run time: 19.50 min
- Injection volume: 1µL
- Oven temperature program is according to **Table 2.1**

Table 2.1: Oven temperature of GC

Sr. No.	**Temperature (°C)**	**Ramp (°C/min)**	**Hold time (minutes)**
1	40	1	3
2	45	10	1
3	60	20	0
4	250	0	1

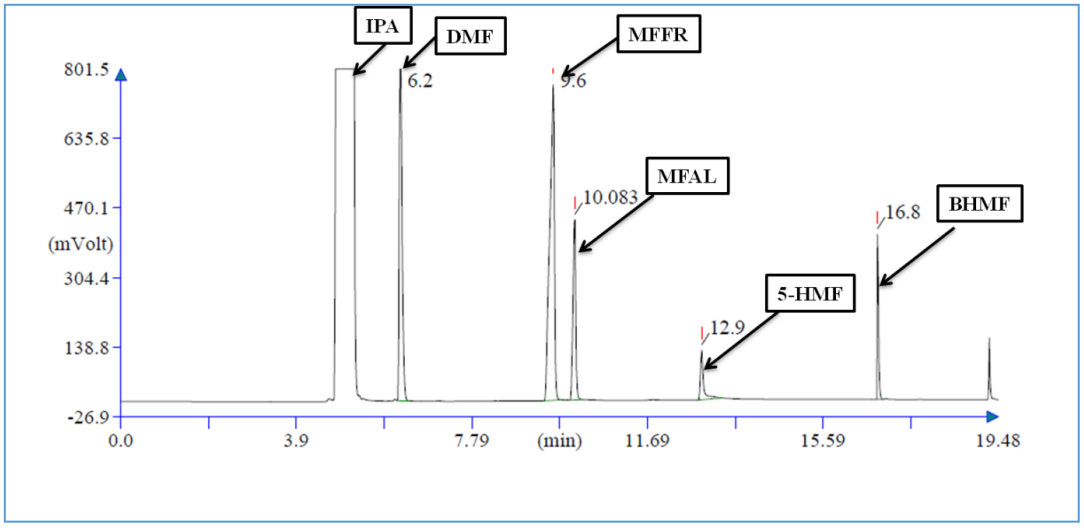

Figure 2.17: Gas chromatogram of 5-HMF hydrogenation products

Table 2.2: Retention time of all the standards

Sr. No.	Compound	Retention time
1	5-HMF	12.9
2	BHMF	16.8
3	MFFR	9.6
4	MFAL	10.08
5	DMF	6.2
6	IPA (solvent)	5.05

2.6.2 High Performance Liquid Chromatography (HPLC)

Agilent 1260 infinity series quaternary pump Ultra High Performance Liquid Chromatography (UHPLC) was used for the detection of oxidation products of 5-HMF. Analysis of 5-HMF oxidation products such as HMFCA, FFCA, FDCA and DFF was done on Multi Wavelength Detector (MWD). The analysis conditions were

- UHPLC : Agilent 1260 infinity series
- Column: Hi-Plex-H
- Column details: 7.7 x 300mm, 8 μm
- Column stationary phase: Strong cation-exchange resin consisting of sulfonated, crosslinked styrene-divinylbenzene copolymer in Hydrogen form
- Detector: MWD
- Flow rate: 0.6 mL/min
- Column temperature: 45°C
- Wavelength (Band): 280 nm (4)

- Sample run time: 15 min
- Injection volume: 10µL
- Mobile phase: 85% H_2O (0.1% CH_3COOH): 15% acetonitrile

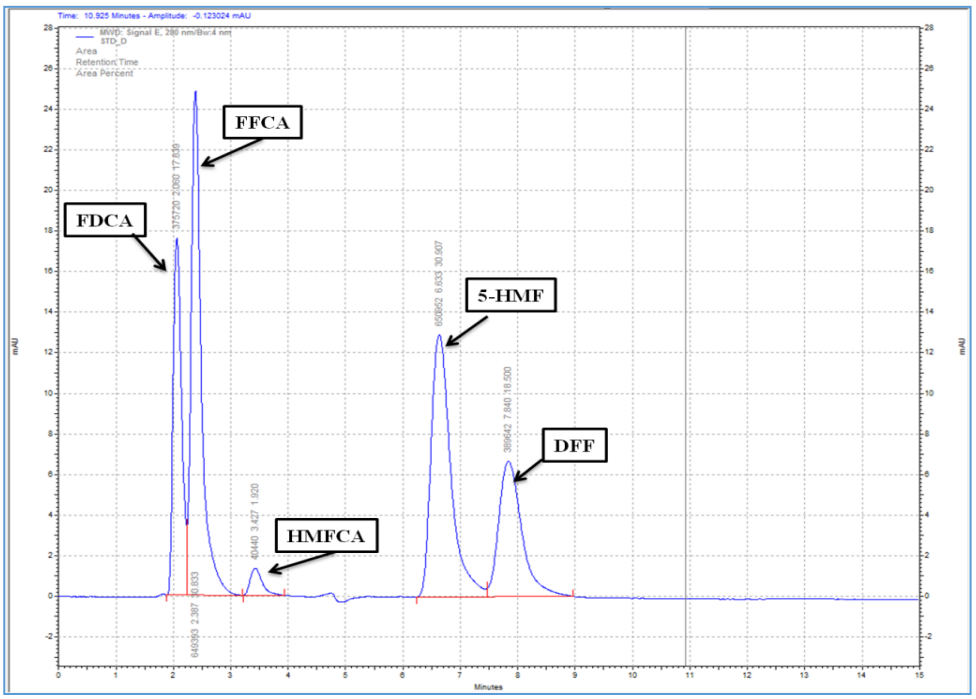

Figure 2.18: High performance liquid chromatogram of 5-HMF oxidation

Table 2.3: Retention time of 5-HMF oxidation products

Sr. No.	Compound	Retention time
1	5-HMF	6.63
2	HMFCA	3.42
3	FFCA	2.38
4	DFF	7.84
5	FDCA	2.00

2.7 Various formulas and terms used

For quantitative estimation and calculation of analytes many formula and terms were used in this thesis which are defined as follow

$$\boldsymbol{Conversion}\ (\%) = \frac{\boldsymbol{initial\ concentration\ of\ 5{-}HMF - final\ concentrtion\ of\ 5{-}HMF}}{\boldsymbol{initial\ concentration\ of\ 5{-}HMF}} \times \mathbf{100} \ldots\ldots\ldots\ldots\ldots (\mathbf{2.14})$$

$$\boldsymbol{Selectivity}\ (\%) = \frac{\boldsymbol{Moles\ of\ desired\ product\ formed}}{\boldsymbol{moles\ of\ 5{-}HMF\ consumed}} \times \mathbf{100} \ldots\ldots\ldots\ldots \mathbf{(2.15)}$$

$$\boldsymbol{Yield}\ (\%) = \frac{\boldsymbol{Conversion} \times \boldsymbol{Selectivity}}{\mathbf{100}} \ldots\ldots\ldots\ldots\ldots (\mathbf{2.16})$$

$$\boldsymbol{Tunr\ Over\ Number}\ (\boldsymbol{TON}) = \frac{\boldsymbol{moles\ of\ substrate\ consumed}}{\boldsymbol{catalytic\ active\ sites\ of}\ (\boldsymbol{catalyst})\boldsymbol{in\ moles}} \ldots\ldots\ldots\ldots (\mathbf{2.17})$$

$$\boldsymbol{Turn\ Over\ Frequency}\ (\boldsymbol{TOF}) = \frac{\boldsymbol{moles\ of\ substrate\ consumed}}{\boldsymbol{catalytic\ active\ sites\ of\ catalyst\ in\ moles} \times \boldsymbol{reaction\ time}\ (\boldsymbol{h})} \ldots\ldots\ldots\ldots \mathbf{(2.18)}$$

$$\boldsymbol{Carbon\ Balance}(\boldsymbol{for\ 5-HMF\ hydrogenation}) = \frac{\begin{array}{c}\boldsymbol{moles\ of\ DMF} \times \mathbf{6} + \boldsymbol{moles\ of\ BHMF} \times \mathbf{6} + \\ \boldsymbol{moles\ of\ MFFR} \times \mathbf{5} + \boldsymbol{moles\ of\ MFAL} \times \mathbf{5} + \boldsymbol{remaining\ moles\ of\ 5-HMF} \times \mathbf{6}\end{array}}{\boldsymbol{moles\ of\ HMF} \times \mathbf{6}} \times \mathbf{100} \ldots\ldots\ldots (\mathbf{2.19})$$

References

1. N.S. Biradar, A.A. Hengne, S.N. Birajdar, R. Swami and C.V. Rode, *Org. Process Res. Dev.*, **2014**, 18, 1434–1442

2. A. Jha, S. H. Patil, B. P. Solanki, A. P. C. Ribeiro, C. A. N. Castro, K. R. Patil, A. Coronas and C. V. Rode, *ChemPlusChem*, **2015**, 80, 1164-1169

3. S. Lowell, J. E. Shields, *Powder Surface Area and Porosity*, **2013,** Springer Science & Business Media, New York, NY

4. W. A. Steele, G. Zgrablich, W. Rudzinski, *Equilibria and Dynamics of Gas Adsorption on Heterogeneous Solid Surfaces*, **1996,** Elsevier

5. B. Crittenden, W. J. Thomas, *Adsorption Technology and Design*, **1998,** Elsevier

6. M. D. LeVan, *Fundamentals of Adsorption: Proceedings of the Fifth International Conference on Fundamentals of Adsorption*, **2012,** Springer Science & Business Media

7. M. Thommes, K. Kaneko, A. V. Neimark, J. P. Olivier, F. R. Reinoso, J. Rouquerol, K. S. W. Sing, *Pure Appl. Chem.* **2015**, *87*, 1051-1069

8. LeChatelier H, *Z Phys Chem*, **1887**, 1, 396–402

9. W. H. Bragg, W. L. Bragg, *The Crystalline State*, **1949**, Vol. 1, McMillan, New York

10. R. W. G. Wyckoff, *Crystal Structures*, **1964**, 2nd ed., Wiley, New York

11. K. Siegbahn, C. Nordling, A. Fahlman, R. Nordberg, K. Hamrin, J. Hedman, G. Johansson, T. Bergmark, S. E. Karlsson, Lindgren, and B. Lindberg, *'ESCA-Atomic, Molecular and Solid State Structure Studied by Means of Electron Spectroscopy'*, **1967**, Nova Acta Regiae Soc. Sci., Upsaliensis, Ser.IV,Vol.20

12. D. J. O'connor, B. A. Sexton and R. St. C. Smart, *Surface analysis method in materials science*, **1992**, Springer-Verlag, Heidelberg

13. Ruska E, *The early development of electron lenses and electron microscopy*, **1980**, (Trans Mulvey T) S Hirzel Verlag, Stuttgart

14. W. Zhou and Z. L.Wang, *Scanning microscopy for nanotechnology: Techniques and application*, **2006**, Springer, New York

15. G. H. Michler, Electron microscopy of polymers, **2008**, Springer-Verlag Berlin, Heidelberg

16. R.J. Cvetanovi´c, Y. Amenomiya, *Adv. Catal.*, **1967**, 17, 103–149

17. F. Rouquerol, J. Rouquerol, K. Sing, *Adsorption by Powders and Porous Solids, Principles Methodology and Applications*, **1999**, Academic Press, San Diego

18. E. Selli, L. Forni, *Microporous Mesoporous Mater.*, **1999**, 31, 129– 140

19. D.A.M. Monti and A. Baiker, *J. Catal.*, **1983**, 83, 323–335

20. P. Larkin, *Infrared and Raman spectroscopy: Principles and Spectral interpretation*, **2011**, Elsevier, The Boulevard, Langford Lane, Kidlington, Oxford, OX5 1GB, UK

21. F. Zaera, *Chem. Soc. Rev.*, **2014**, 43, 7624-7663

22. D. A. Long, *Raman Spectroscopy*, **1977**, McGraw-Hill: New York, NY

23. E. B. Wilson, J. C. Decius and P. C. Cross, *Molecular Vibrations: The Theory of Infrared and Raman Vibrational Spectra*, **1955**, McGraw-Hill: New York, NY

24. M. L. Fernández-Sánchez, *Atomic Emission Spectrometry | Inductively Coupled Plasma*, Editor(s): Paul Worsfold, Colin Poole, Alan Townshend, Manuel Miró, *Encyclopedia of Analytical Science (Third Edition)*, **2019**, Academic Press, Pages 169-176

Chapter 3

Selective hydrogenolysis of 5-(hydroxymethyl)furfural to 2,5-dimethylfuran over Pd/C catalyst

Selective hydrogenolysis of 5-(hydroxymethyl)furfural to 2,5-dimethylfuran over Pd/C catalyst

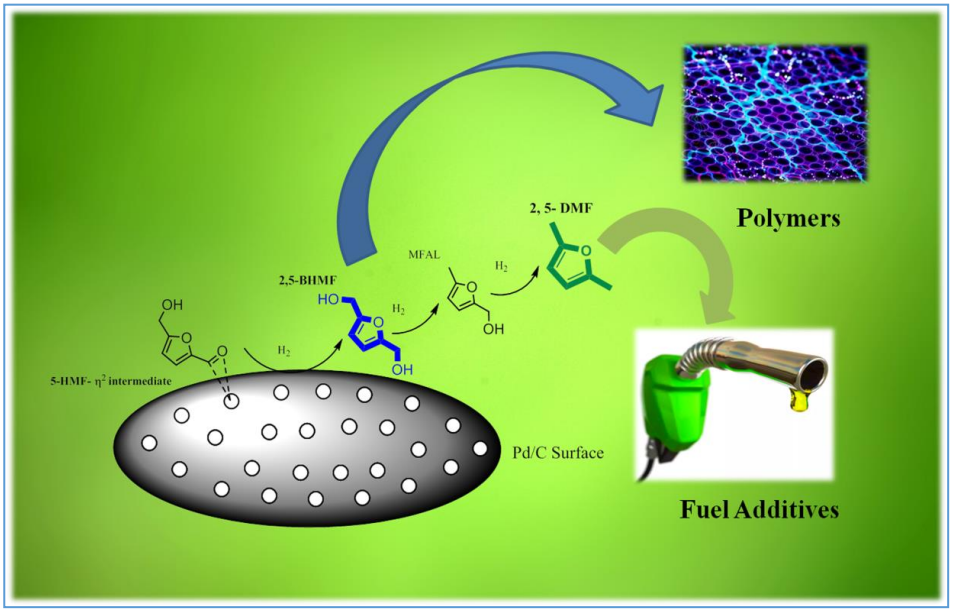

***Journal of Saudi Chemical Society*, 2019, 23, 439–451**

2, 5-dimethyl furan (DMF) is a potential renewable fuel additive which can be obtained by the hydrogenolysis of 5-HMF. Several noble metal catalysts were prepared by wet impregnation method to explore their activity for catalytic hydrogenolysis of 5-HMF. 3% Pd/C proved highly efficient and selective owing to its excellent physic-chemical properties characterised by various techniques like XRD, XPS, BET surface area, N_2-desorption isotherm and SEM-TEM analysis. 99% of DMF was obtained after 4 h of reaction at 443 K and 300 psig of external pressure of H_2. Extensive characterisation and detailed parameter optimisation studies were conducted to find out the structure-activity correlation of catalyst and reaction system. Homogeneous distribution, Pd-PdO nanohybrid synergism, high surface area and microporous nature of support proved instrumental for catalytic efficiency. At optimum reaction conditions and 5-HMF/catalyst= 10 complete conversion of 5-HMF was obtained.

3.1 Introduction

Deoxygenation of oxygen rich biomass derived platform molecules into biofuel additives has been a hot topic of research recently due to rapid shrinkage of traditional energy resources [1-2]. Scientific community is exploring various economically viable alternatives for energy sources. Reducing the overdependence on fossil fuels is the prime aim of renewable chemistry which leads to evolution of second generation (2G) biofuel [3]. Bioethanol, methanol, butanol, furan derivatives like furan, 2-methyl furan (2-MF), DMF, ethyl levulinate (EL), 5-ethoxymethyl furfural (EMF) and ϒ-valerolactone (GVL) are major identified 2G fuel molecules [4-5]. The blending of these 2G fuel additives can reduce the engine emission and enhance the fuel quality. Bioethanol is the most used and attractive biofuel currently as it can greatly shrivel the contribution to the greenhouse gas emission by automotive industry [6]. It has certain disadvantage like its Lower Heating Value (LHV) which enhances the transportation cost. It is highly soluble in water which adds extra cost for distillation and dehydration since in a typical aqueous stream of sugar fermentation only about 6 weight % of ethanol is present. It also has very high oxygen content i.e. (O/C= 0.5) which poses many operative challenges to engine [7]. These entire drawbacks of bioethanol pave the way for next generation-non-ethanol based liquid biofuels and DMF comes out as one of the best alternatives due to its excellent fuel properties [8]. It can be obtained by hydrodeoxygenation of 5-HMF (**Table 1.1**). The hydrogenation of 5-HMF can produce BHMF by reducing formyl group of furan ring. This symmetric diol molecule further undergoes hydrogenolysis in which reductive dehydration occurs and DMF is formed. The catalytic hydrodeoxygenation of 5-HMF was attempted in the past over several supported noble metal catalysts like Ru, Pt, Pd and Au as shown in **Table 1.4** [9-12]. Considering the high-priced nature of noble metals, cheap supporting material like carbon has a significant place in catalytic hydrogenation reactions as there is paramount role of supporting material in order to synthesize an efficient

catalyst. Activated carbon is considered as best suitable material for noble metal catalysed hydrogenation reactions. The major reasons are its higher surface area which leads to higher metal dispersion, its surface porosity which can be changed into various shape and size, chemical inertness; alleviate recovery of active phase from used catalyst and lastly its economic viability due to less price [(13)]. In catalytic hydrodeoxygenation of 5-HMF, carbon supported noble monometallic as well as bimetallic catalysts were screened. 5% Ru/C was used by Li *et al.* at 200 °C to achieve 94.7% yield of DMF with complete conversion within 2 h of reaction [(14)]. Ru was also tested in bimetallic combination with MoO_x on carbon but only 71.3% DMF was obtained in butanol after 1h of reaction at 180 °C [(15)]. 5% Pd/C and Pd-Au/C were also studied for 5-HMF hydrodeoxygenation at mild temperature but use of mineral acids, longer reaction time, use of corrosive reagents and higher external pressure hampered its catalytic efficiency [(16-17)]. Bimetallic combination of supported Pd with Fe and Co was also investigated but they suffered with lower selectivity of DMF and longer reaction time [(18-19)]. Though Pd was used earlier for hydrodeoxygenation of 5-HMF but very less catalytic insight is available about it.

Although, there have been several reports on hydrogenolysis of 5-HMF using various catalysts systems, but use of harsh reaction conditions like high temperature (473 K), high metal loading (50%), high pressure (as high as 900 psig), long reaction time (15 h), involvement of mineral acids (H_2SO_4) *etc.* are the major drawbacks which necessitates scope for improved catalyst systems. In the present work, we report 3% Pd/C catalyst for the conversion of 5-HMF to DMF at 443 K temperature under 300 psig H_2 pressure in 4 h of reaction time to give 99.9% 5-HMF conversion with 99% DMF selectivity. Various parameter effects such as pressure, temperature, stirring effect, reaction time, substrate loading, support study and metal loading on 5-HMF conversion as well as DMF selectivity were studied in batch reactor.

3.2 Experimental

Carbon supported metal catalysts (M/C; M= Pd, Ru, Rh, Ir and Pt) of specific loading percentage were synthesized by the wet impregnation as described in chapter 2 (section 2.3, subsection 2.3.1). 3% Pd/C was found most suitable catalysts after detail activity testing performed in Parr reactor as described in section 2.5, subsection 2.5.1 of chapter 2. Detailed catalytic characterization was performed using XRD, XPS. FTIR, BET surface area, NH_3-TPD, TEM and E-SEM as depicted in section 2.4 of chapter 2 (subsections 2.4.3, 2.4.4, 2.4.7, 2.4.1, 2.4.6.1, 2.4.5.2 and 2.4.5.1). The activity analysis was conducted on GC as mentioned in section 2.6, subsection 2.6.1 of chapter 2.

3.3 Result and Discussion

Major objectives of this work was (i) to design an efficient catalyst for mild reaction conditions (ii) extensive study of reaction parameters for the catalyst (iii) to find out the structure- activity correlation by in depth study of catalyst characterisation.

3.3.1 Catalyst characterisation

3.3.1.1 BET surface are analysis

Textural properties of various metal supported carbon catalysts are presented in **Tables 3.1 - 3.3**. High surface area value of activated carbon (954 m^2/g) decreased as soon as metals were loaded on it. From 1% to 5% loadings of Pd almost 26.83% loss of surface area of bare activated carbon was observed (**Table 3.2**).

Table 3.1: BET surface area of catalysts supported on activated C

Sr. No.	**Catalyst**	**Surface area (m^2/g)**
1	Activated C	954

2	3% Pd/C	826
3	3% Ir/C	364
4	3% Rh/C	359
5	3% Ru/C	546
6	3% Re/C	291
7	3% Pd/Al_2O_3	208
8	3% Pd/ZrO_2	101
9	3% Pd/CeO_2	67

For 3% Pd/C, surface area decreased to 826 m^2/g suggesting fine dispersion of metal particles on activated C. This pattern of decline in surface area for various metals continued in the following order: Pd/C (826 m^2/g) > Ru/C (546 m^2/g) > Ir/C (364 m^2/g) > Rh/C (359 m^2/g) > Re/C (291 m^2/g). Size of parent metals in respective metallic precursors also influenced surface area of catalyst. Pd was also loaded on different supports for comparison purpose and surface area was found to vary according to the nature of supporting materials. Activated carbon was found superior than other supports in terms of surface area as shown in **Table 3.1**

Table 3.2: Comparative BET surface area of activated C and Pd/C with different metal loading

Sr. No.	**Catalyst**	**Surface area (m^2/g)**
1	Activated C	954
2	1% Pd/C	902
3	2% Pd/C	858
4	3% Pd/C	826
5	4% Pd/C	748

6	5% Pd/C	698

This change in surface area was also monitored for fresh and used catalyst after every recycle run and it was observed that after fifth recycle the active surface area decreased to almost 35.84% of fresh catalyst (**Table 3.3**). This may be due to the continuous deposition of carbonaceous matter of reaction media on the surface of catalyst after each recycle run.

Table 3.3: BET surface area comparison of fresh and spent catalyst after each recycle

Sr. No.	**Catalyst**	**Surface area (m^2/g)**
1	Activated C	954
2	3% Pd/C-Fresh	826
3	3% Pd/C- First recycle	771
4	3% Pd/C- Second recycle	702
5	3% Pd/C-Third recycle	617
6	3% Pd/C-Fourth recycle	557
7.	3% Pd/C-Fifth recycle	429

Decrease in surface area, among fresh and used catalyst might also be due to agglomerization which was also evidenced by TEM and SEM images, as discussed later. Similarly, the comparative N_2 adsorption isotherm (**Figure 3.1.a**) of fresh and spent 3% Pd/C showed type-I isotherm which is characteristics of microporous material [20]. Average pore diameter was found to be almost equal (5.1 A°) in both the cases though the pore volume decreased from 0.32 cc/g of fresh catalyst to 0.21 cc/g of used catalyst which may be due to the deposition of unstable carbonaceous matter of reaction media. Very narrow pore size area distribution was

observed for fresh and used 3% Pd/C as shown in **Figure 3.1.b**. These findings revealed that though material was qualitatively intact but quantitative loss was observed in the textural properties.

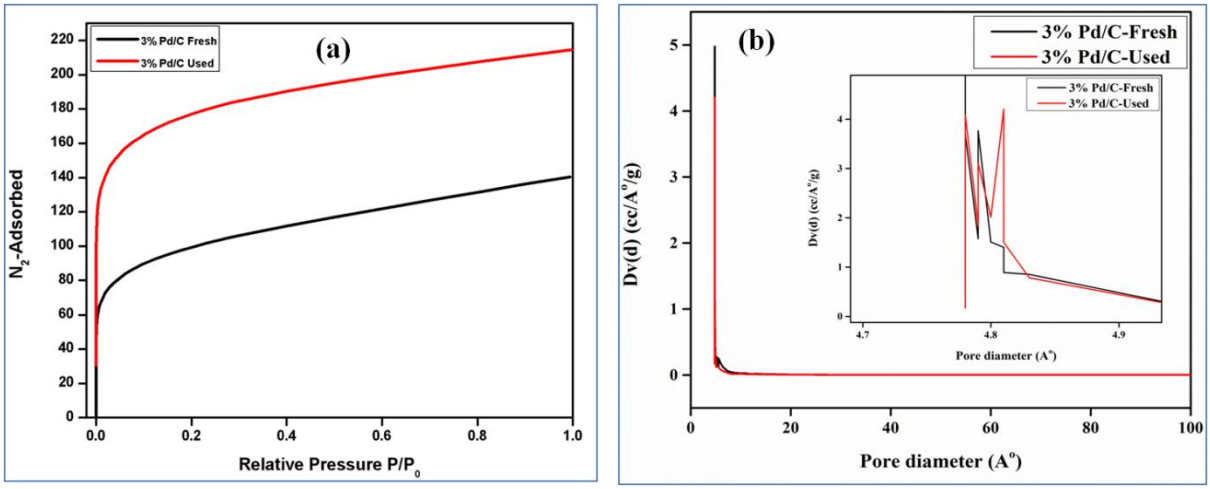

Figure 3.1: (a) N_2-adsorption isotherm of fresh and used 3% Pd/C catalyst (b) Pore size distribution of fresh and used 3% Pd/C (INSAT: Zoomed image for pore size distribution)

3.3.1.2 XRD

XRD patterns of fresh and used carbon supported Pd catalysts are shown in **Figure 3.2**. Both fresh and used catalysts showed almost similar XRD patterns suggesting catalytic stability after its use. The FWHM of characteristic peak of metallic Pd *i.e.* 2θ = 39.10° decreased in spent catalyst compared to fresh Pd/C suggesting increased size and enhanced intensity of metallic content due to reduction environment of reaction. This was also confirmed by micrograph pattern and quantitative estimation of Pd/PdO in XPS analysis. Characteristic impressions of graphitic nature of carbon were observed at 2θ =24.21°, 79.33°, and 43.70° [21-22]. The presence of graphitic nature can enhance the rate of catalytic hydrogenation of 5-HMF due to strong π-π stacking. These π-π stackings can be instrumental for adsorption of reactant and easy access of the metal active sites [23]. Both fresh and spent 3%Pd/C showed

Pd(0) impressions at 2θ = 39.10° and 68.33° corresponding to (111) and (220) planes of FCC structure, respectively (JCPDS No #46-1043) [24].

Other metals (Ru, Rh, Pt, and Ir) were found devoid of any kind of reflections corresponding to respective metals except Pt. In Pt, 2θ = 39.71°, 46.66° and 67.99° corresponding to its (111), (200) and (220) planes were observed. Rest of the metals didn't show any specific peaks which might be due to either overlapping of peaks with carbon or by formation of fine layer over carbon support (**Figure 3.3**). Similarly, as shown in **Figure 3.2.b** after impregnation of Pd on various supports, no characteristic peaks of Pd were observed.

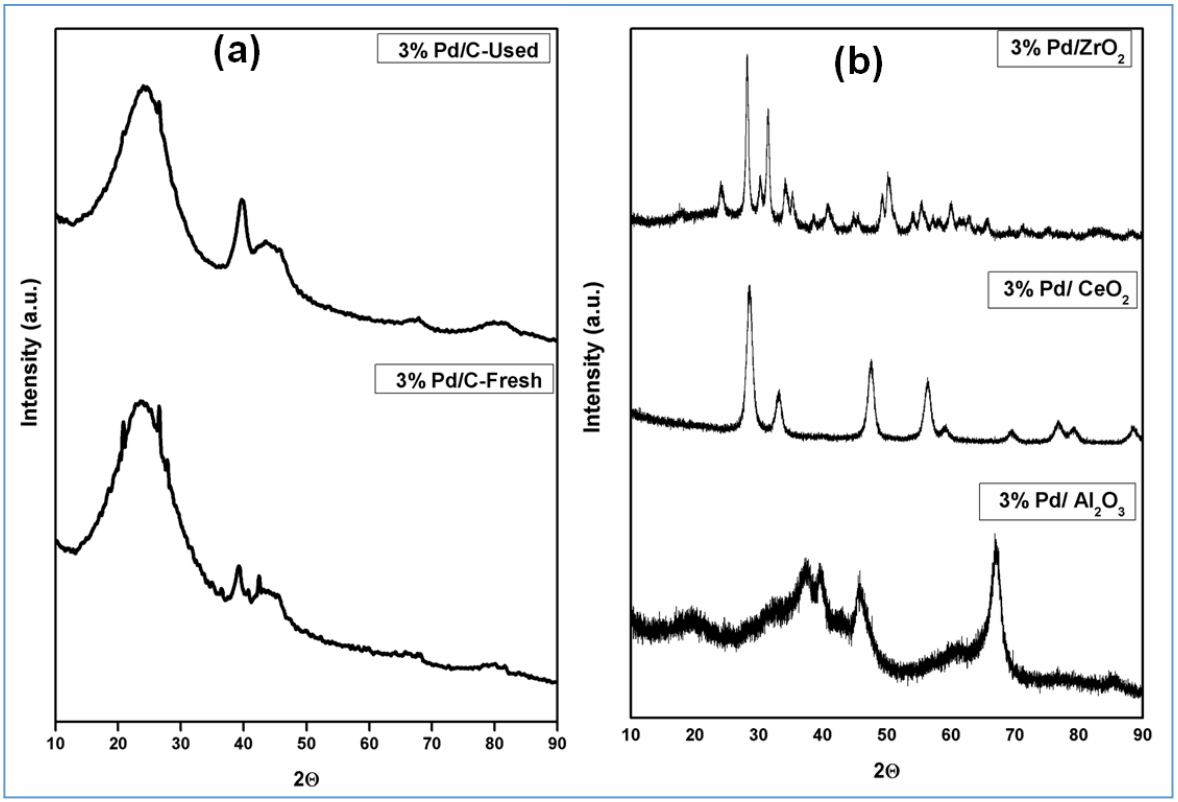

Figure 3.2: XRD pattern of (a) fresh and spent 3% Pd/C (b) 3% Pd loaded on various supports

3% Pd/Al_2O_3 showed characteristic peaks of ϒ-Al_2O_3 at 2θ = 37.55°, 39.85°, 45.95°, 67.04°, and 84.85°. Different phases of Pd overlapped with observed phases of ϒ-Al_2O_3 due to low metal loading of Pd and cannot be cited [25]. Fluorite nature of CeO_2 was observed in its XRD

pattern with major peaks at 2θ = 28.60°, 33.7°, 47.55°, 56.29° and few minor peaks at 2Θ values of 59.59°, 69.59°, 76.78°, 79.08° and 88.32° lacking any specific information of Pd phases [26]. Similarly monoclinic phase of ZrO_2 was spotted for 3% Pd/ZrO_2 combination irrespective of metal loading.

Table 3.4: Various textural parameters of fresh and used 3% Pd/C

Sr. No.	**Catalysts**	**Dspacing (nm)**	**BJH Pore diameter (nm)**	**Pore Volume (cc/g)**	**Crystallite Size (nm) XRD**
1	3% Pd/C-Fresh	0.345	0.51	0.32	6.09
2	3% Pd/C-Used	0.349	0.50	0.21	7.23

Table 3.4 presents the crystallite size along with various surface properties of both fresh and used 3% Pd/C. Crystallite size of 3% Pd/C was calculated by comparing the FWHM at 2θ=39.10° which correspond to (111) plane metal lattice. Increase in crystallite size was observed for obvious reason of deposition of organic reaction crude.

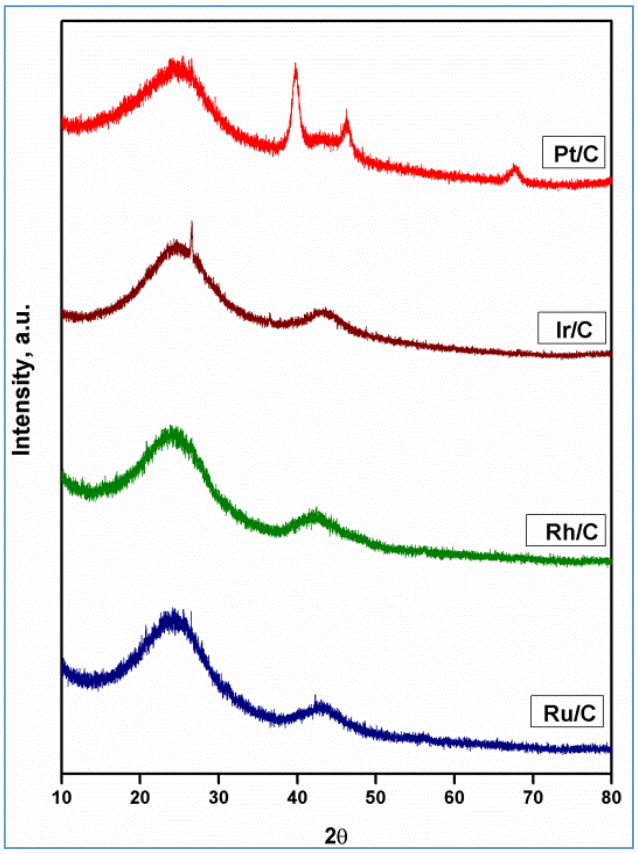

Figure 3.3: XRD pattern of various metals supported on activated C

3.3.1.3 XPS

Figures 3.4.a and **3.4.b** present the deconvoluted XPS pattern of fresh and used 3% Pd/C. In the fresh 3% Pd/C two asymmetric maxima were observed with a signature B.E. difference of 5.40 eV due to spin orbital coupling of $Pd3d_{3/2}$ and $Pd3d_{5/2}$ [(27)]. The presence of bimodal asymmetry is indication of partially reduced Pd species which are in the form of various oxides of Pd. Detailed species of oxygen were also interpreted with the help of O1s pattern. In both fresh and spent catalyst sample, the value of binding energy with respect to metallic Pd and PdO_x are consistent suggesting concise amount of stability in the catalyst. A peak at B.E. of 335.3 eV in $Pd3d_{3/2}$ was ascribed to Pd(0) whereas satellite peaks at 337 eV was

attributed to Pd(+2) whereas these values were 340.70 eV and 342 eV for $Pd3d_{5/2}$ respectively [28].

Table 3.5: Relative peak intensity of Pd/PdO species in 3% Pd/C

Catalyst	**3% Pd/C-Fresh**	**3%Pd/C-Used**
Phase / **Peaks**	**Pd/PdO**	**Pd/PdO**
$3d_{3/2}$	2.55	212611
$3d_{5/2}$	1.87	24.88

To understand the influence of metallic and oxide species on catalytic hydrogenation their quantitative estimation was done as shown in **Table 3.5**. It was observed that Pd/PdO ratio in various energy levels *i.e.* in Pd $3d_{3/2}$ were higher (2.55) than $Pd3d_{5/2}$ (1.87) which may be due to the higher degree of reduction on surface than in bulk metal.

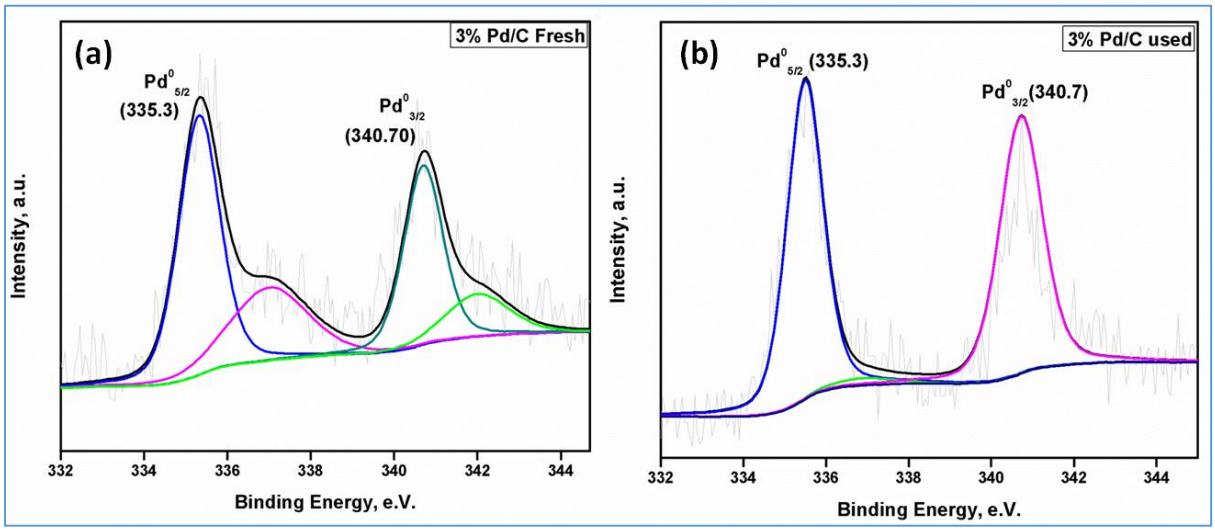

Figure 3.4: XPS analysis of (a) $Pd3d_{3/2}$ of Fresh 3% Pd/C (b) $Pd3d_{5/2}$ of Used 3% Pd/C

XPS pattern of O1s revealed information about the nature of oxygen present in the catalyst (**Figures 3.5.a** and **3.5.b**). Three O1s bands were observed at B. E. of 530.13, 531.72 and 533.14 eV. Most intense peak was 531.72 eV which constituted 49.89% of total oxide

species. This peak was correlated with surface O-H bonds and unsaturated –C=O species supporting graphitic nature of activated C as seen in XRD analysis [29].

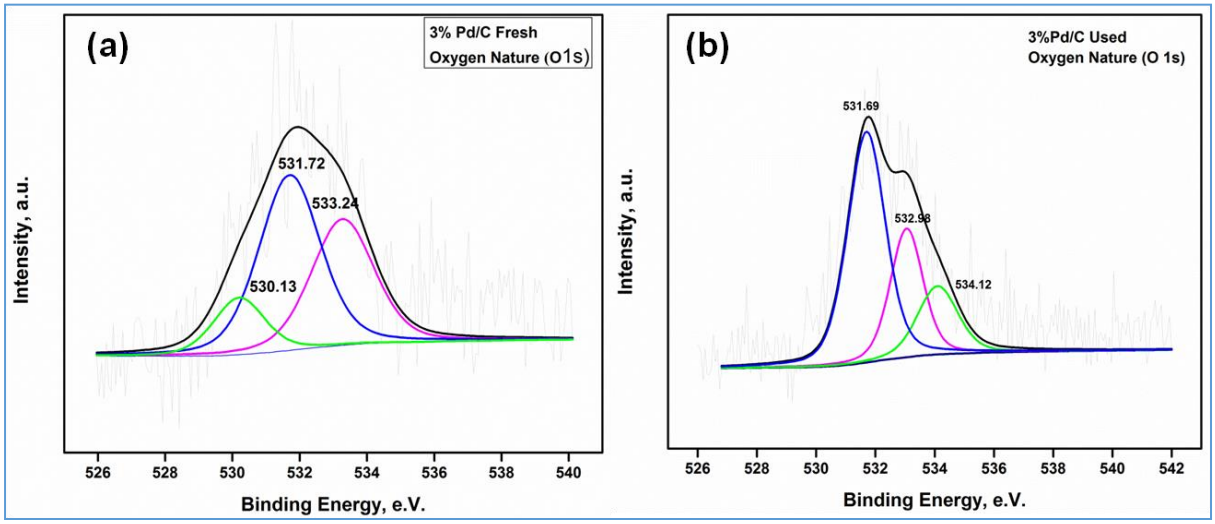

Figure 3.5: O1s XPS deconvolution in (a) Fresh 3% Pd/C and (b) Used 3% Pd/C

Shoulder peak was observed at B. E. of 530.13 eV with only 13.50% share can be attributed to lattice oxygen suggesting aforementioned partial reduction of Pd. Second most intense peak with 36.60% share was at B. E. of 533.14 eV which may be correlated with surface adsorbed oxide species [30]. In the spent 3%Pd/C, O 1s XPS spectra, lattice oxygen almost vanished which may be due to complete reduction of Pd during the hydrogenation. Here also three peaks were observed at B. E. of 531.69, 532.96 and 534.12 eV.

Table 3.6: Relative intensity of different species of oxygen in O1s of fresh and used 3% Pd/C

Contents / **Catalyst**	**Binding Energy (eV)**	**Area Percentage (%)**	**FWHM**	**Nature**
3% Pd/C-Fresh	530.13	13.50	1.8	O^{2-} of Pd-O (Lattice Oxygen)
	531.72	49.89	2.16	Surface –OH groups
	533.24	36.60	2.2	Chemisorbed H_2O ($O^-/O_2^{2-}/O_2^-$)

	531.69	55.57	1.5	Surface –OH groups
3% Pd/C-Used	532.96	26.87	1.3	Chemisorbed H_2O ($O^-/O_2^{2-}/O_2^-$)
	534.12	17.55	1.6	-C-O species

The peak at higher binding energy of 534.12 eV with 17.55% amount appeared correspond to saturated -C-O species of reaction media whereas increased relative intensity of 531.69 eV suggested increased surface –O-H groups which can be due to reduction of lattice O^{2-} species or deposition of reaction crude. These observations reveal the presence of Pd-PdO nanohybrid in the catalyst. Although the major active site is metallic Pd, the presence of PdO can enhance the activity of the catalyst due to the complex mutual electron interaction between Pd and PdO and also it is known that hydrogenation reactions proceed smoothly on the phase boundary of Pd-PdO rather than Pd alone [31]. **Table 3.6** represent the quantitative estimation of different O1s species.

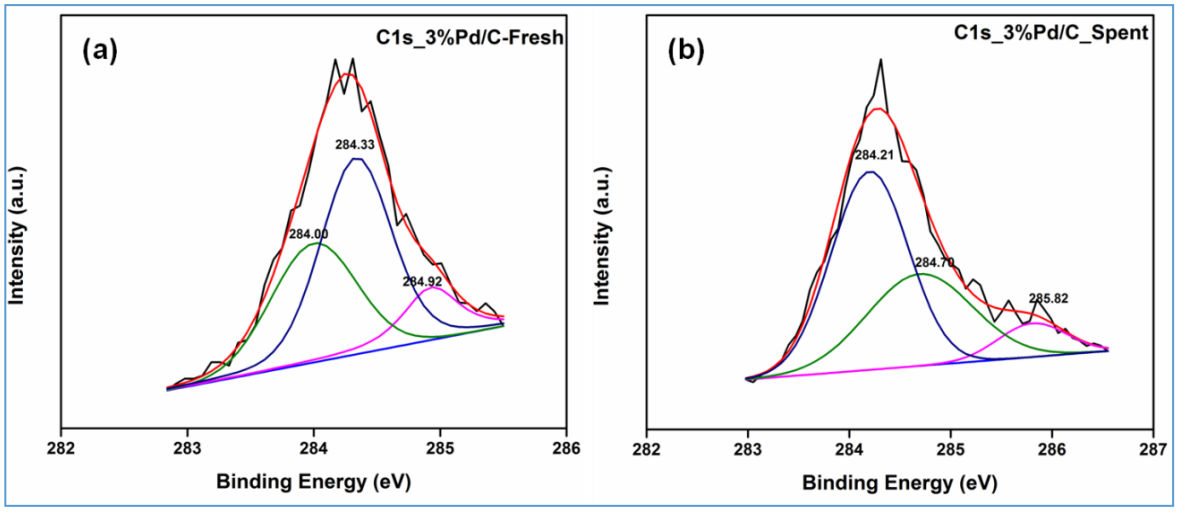

Figure 3.6: XPS interpretation of C1s in (a) 3% Pd/C-fresh and (b) 3% Pd/C-used

Graphitic carbon species are confirmed by the XPS deconvolution of C1s spectra of fresh 3% Pd/C catalyst. A considerable relative amount of sp^2 carbon (34.76%) was observed at 284.00 eV along with its typical sp^3 backbone C-C (51.60%) nature at 284.33 eV [32]. Peak at higher

binding energy i.e. 284.92 eV can be attributed to adventitious C-C species [33]. The spent 3% Pd/C was devoid of sp^2 carbon species in it C1s spectra obviously due to its use in reductive reaction. The typical C-C backbone and adventitious C species were continuous along with carbonaceous ether deposition observed at 285.92 eV with relative intensity of 8.47%. Hence graphitic nature of support and Pd-PdO nanopair observed in XRD were also supported by XPS analysis. **Table 3.7** shows quantitative estimation of different C1s species in both fresh and used catalyst.

Table 3.7: Relative intensity of various carbon species calculated by XPS interpretation of C1s spectra of fresh and used 3% Pd/C

Contents / **Catalyst**	**Binding Energy (eV)**	**Area Percentage (%)**	**FWHM**	**Nature**
3% Pd/C-Fresh	284.00	34.76	0.79	SP^2 –C=C species
	284.33	51.60	0.66	SP^3 –C-C backbone
	284.92	13.67	0.52	Adventitious C-C species
3% Pd/C-Used	284.21	56.00	0.89	SP^3 -C-C backbone
	284.70	35.52	1.22	Adventitious C-C species
	285.82	8.47	0.79	Reaction crude deposition –C-OR

3.3.1.4 SEM and TEM analysis

The morphology, metal dispersion and particle size of most active catalyst *viz.* 3% Pd/C were determined by TEM and E-SEM analysis (**Figure 3.7 and 3.8**). Uniform particle distribution

of round shape Pd on activated C was observed (**Figures 3.7.a and 3.7.b**). The average size on comparing 50 nanoparticles was found between 2.6-3.0 nm range (**Figure 3.7.d**).

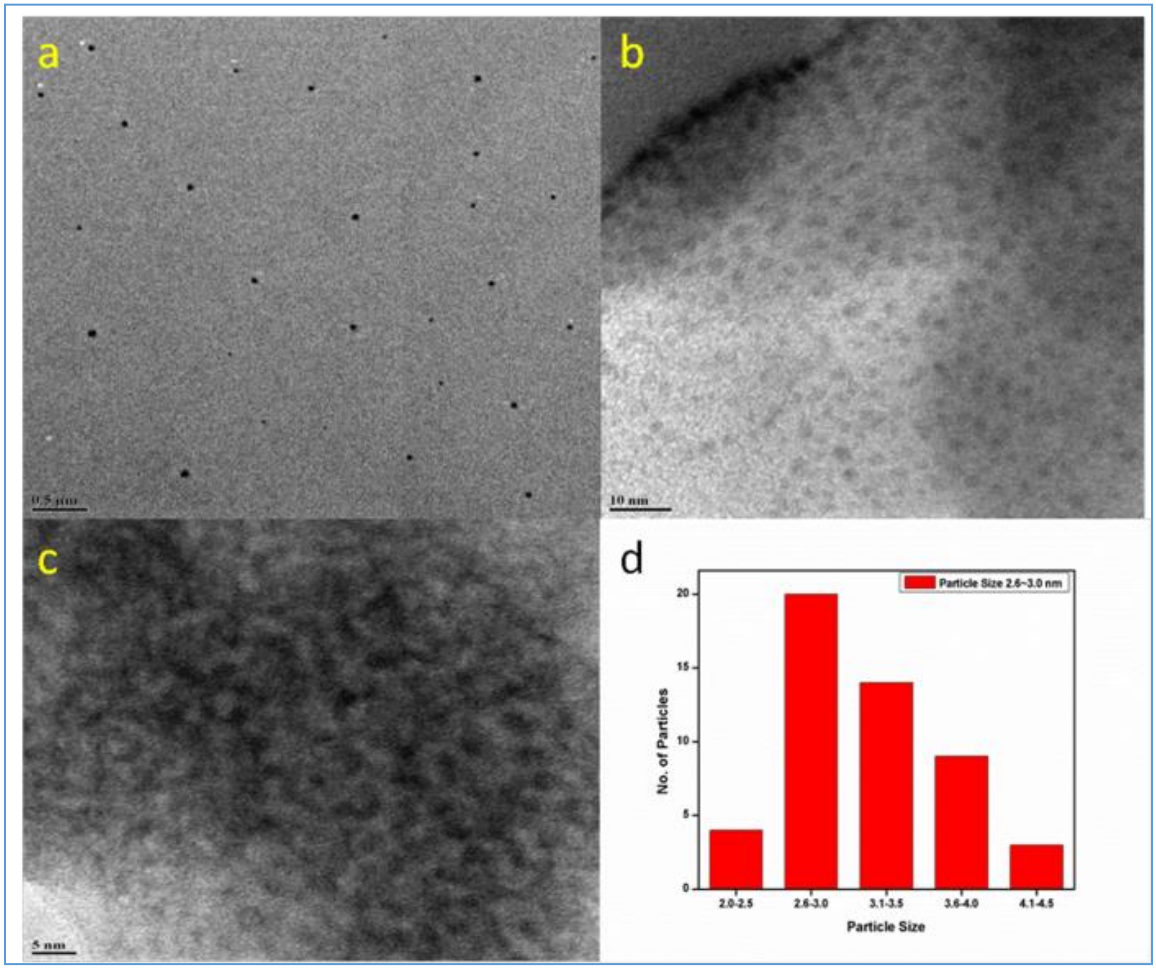

Figure 3.7: TEM images of (a) fresh 3% Pd/C at 0.5 μm scale (b) 10 nm scale (c) 3% Pd/C-used at 5 nm scale and (d) particle size distribution histogram of 3% Pd/C- fresh

As evident from TEM and SEM images (**Figures 3.7.c and 3.8.b**) spent 3% Pd/C clearly showed agglomeration of nanoparticles and deposition of carbonaceous matter which limits the access to active sites of the catalyst for reactant molecules resulting in less activity. Porous nature was also visible in the SEM images of the same (**Figure 3.8.d**)

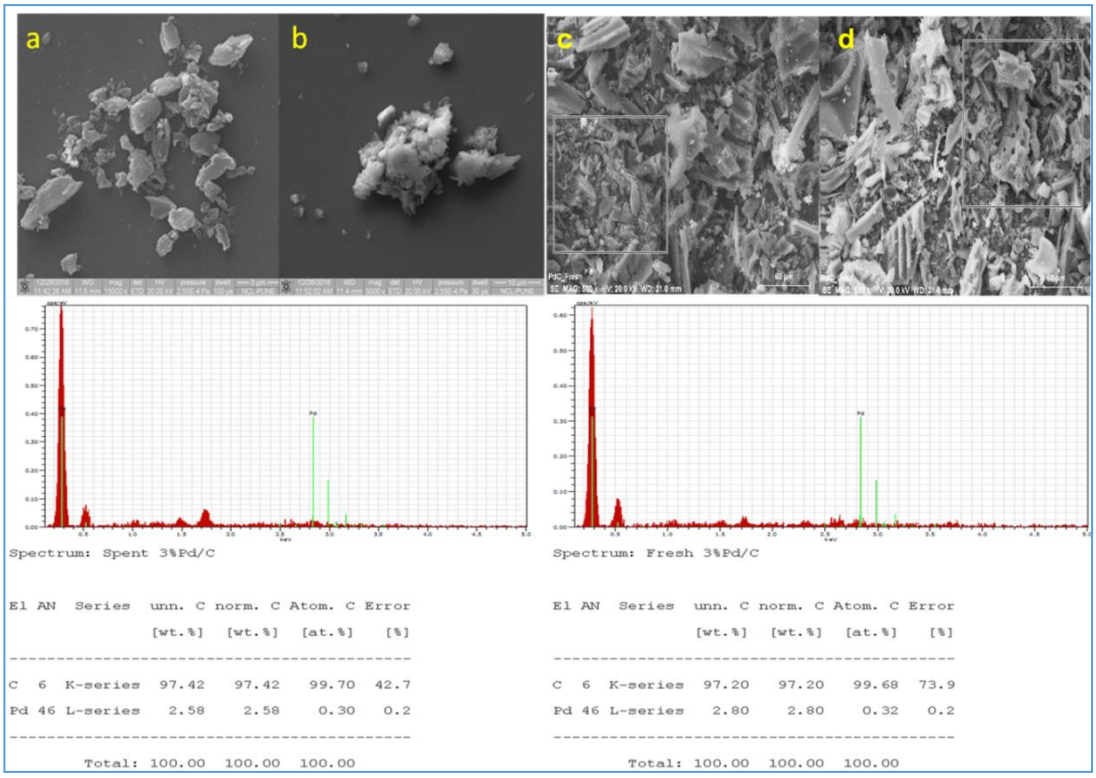

Figure 3.8: SEM images if fresh (a) 3% Pd/C (b) used 3% Pd/C, E-SEM images of (c) 3% Pd/C fresh and (d) 3% Pd/C- used followed by EDX outcome of used (LHS) and fresh (RHS) 3% Pd/C

EDX patterns of fresh and spent 3% Pd/C samples is shown in **Figure 3.8 (LHS and RHS)** and it confirmed that the actual Pd on activated C was approximately the same (2.80%) as used during synthesis. Fig 3.8 (LHS) shows that the Pd loading for the spent catalyst was nearly same as that of fresh 3% Pd/C (2.58%). These results were in well agreement with our hot filtration test which revealed that no metal leaching was observed under the optimum reaction conditions.

3.3.1.5 FTIR Analysis

To explore the nature and various phase of carbonaceous matter deposited on fresh and spent catalyst samples, these were analysed by FTIR. As shown in **Figure 3.9**, a major IR band was present at 1738 cm^{-1} (Θ) which was assigned to DMF (confirmed with standard FTIR of

DMF and reaction crude after reaction, **Figures 3.9.c** and **3.9.b**). A spike at the wave number 2860 cm^{-1} (μ) was observed for the C-H stretching vibration of -CHO group (5-HMF) as suggested by literature [34]. Our analysis (**Figure 3.9.a**) shows a tiny band at 2860 cm^{-1} in 4th hour suggesting almost complete conversion of 5-HMF (99.9%). Some perturbation related to conjugated C=C unsaturation (5-HMF) were observed at 1572 cm^{-1} (α) in first hour of reaction and almost vanished at the end of 4th hour [35]. An enhanced spike appeared at the end of reaction around 2973 cm^{-1} (η). It was attributed to the aliphatic C-H bands of asymmetric and symmetric -CH_2 and -CH_3 stretching mode.

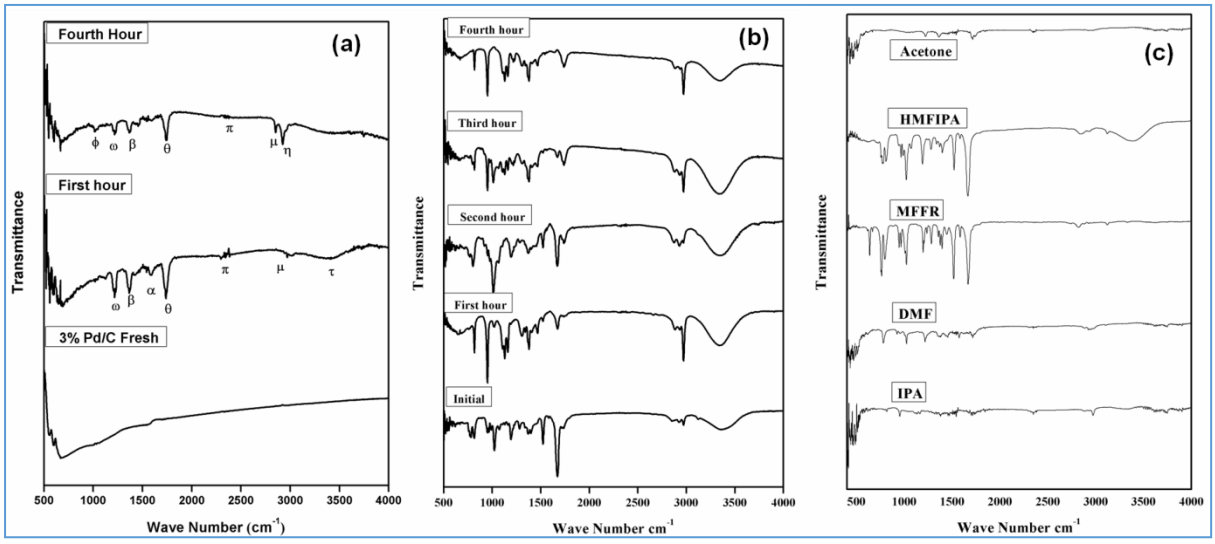

Figure 3.9: FTIR of (a) 3% Pd/C (b) reaction crude of 5-HMF hydrogenolysis (c) standard molecules

The peaks near 1369 cm^{-1} (β) and 1225 cm^{-1} (ω) are attributed to C-H deformation modes whereas a small band near 1020 cm^{-1} (ϕ) is claiming a minute presence of hydrogenated furan ring oligomer in the system [36]. A clear trough was seen at 3410 cm^{-1} (τ) in first hour of analysis which is associated with -OH group of 5-HMF. This trough was not observed in fourth hour due to almost complete conversion of 5-HMF. A perturbed area was seen at 2347 cm^{-1} (Π) in FTIR spectra of catalyst which can be assigned to O-H stretching of the reaction media i.e. 2-propanol though some reports also related it with atmospheric CO_2. Hence it was

also evident and supported by FTIR study that there was almost complete conversion of 5-HMF on 3%Pd/C which was also revealed by reaction analysis as discussed in further sections.

3.4 Activity testing

3.4.1 Catalysts screening

Table 3.8 presents various catalysts investigated for hydrogenolysis of 5-HMF to DMF. Initially, reaction was conducted without any catalyst (blank run) to confirm that reaction does not proceed homogeneously. (**Table 3.8, entry 1**) In order to understand the activity of support, activated charcoal was also tested for hydrogenation of 5-HMF but only 10% conversion with major product as BHMF (12%) and 2% of MFAL was obtained (**Table 3.8, entry 2**). It may be due to the surface activity along with enhanced temperature [37]. To understand the strength of surface acidity of activated C, NH_3-TPD was conducted as shown in **Figure 3.10**.Total acidity in terms of NH_3-desorped per unit weight of activated carbon was found to be 1.1356 mmol/g. For comparison purpose NH_3-TPD of 3% Pd/C was also taken (**Figure 3.10**)

Pd, Pt, Ru and Rh catalysts supported on activated C showed promising results in terms of 5-HMF conversion among all the investigated catalysts (**Table 3.8, entry 3, 4, 6 and 7 respectively**). 3% Pd/C was found to be the most suitable catalyst in terms of 99.9% conversion of 5-HMF with almost 99% selectivity to 2, 5-DMF (**Table 3.8, entry 3**). 3% Pt/C and 3% Rh/ C showed 87% and 88% conversion respectively whereas for 3% Rh/C it was 60%. Though for 3% Ir/C conversion was very poor i.e. 30% but the selectivity towards DMF was on the higher side like Pt (70%), Ru (89%) and Rh (84%). For 3% Ir/C the selectivity to DMF was 87% (**Table 3.8, entry 5**).

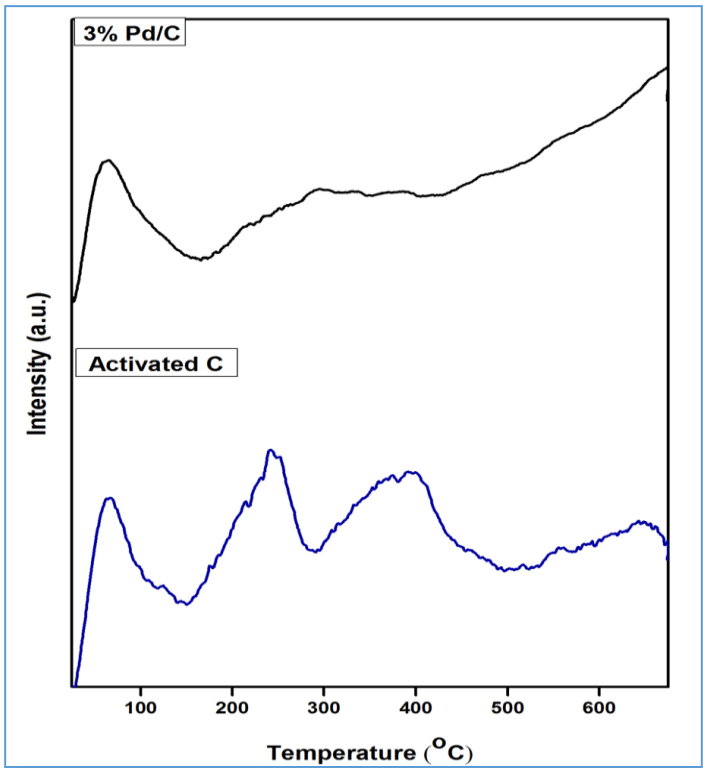

Figure 3.10: NH_3 TPD analysis of activated C and fresh 3% Pd/C

For almost all the catalysts, the second major product was BHMF except 3% Rh/C and 3% Pd/CeO_2 where it was MFAL. Formation of BHMF during 5-HMF hydrogenolysis suggested that first step may be hydrogenation followed by its hydrogenolysis. Some control runs were taken to find out this aspect of reaction mechanism and are discussed later. Excellent performance of 3% Pd/C catalyst for 5-HMF hydrogenation might be due to combined outcome of fine and homogeneous dispersion of microporous Pd nanoparticles on the surface of activated C, surface acidity of the catalyst and formation of small sized Pd-PdO nanopair and Pd-PdO synergism in hydrodeoxygenation mechanism as evident by BET surface area analysis, NH_3-TPD, electronic micrograph images, XRD and XPS studies respectively. The higher activity of 3% Pd/C can also be attributed to the tendency of metallic Pd to form intermediates with –C=O functional group.

Table 3.8: Hydrogenolysis of 5-HMF over different catalyst, **Reaction Conditions:** HMF= 100 mg, IPA= 20g, catalyst= 10 mg, T= 443K P= 300 psi, agitation=1000 rpm, t= 4h

Entry	**Catalyst**	**Conversion (%)**	**Selectivity (%)**				
			DMF	**MFAL**	**MFFR**	**BHMF**	**UnK**
1	Blank Run	-	-	-	-	-	-
2	Activated C	10	3	2	0	12	-
3	3%Pd/C	99.9	99	0.3	0	0.7	0
4	3%Pt/C	87	70	7	6	15	2
5	3%Ir/C	30	87	4	3	6	0
6	3%Ru/C	88	89	3	2	6	0
7	3%Rh/C	60	84	6	2	2	6
8	3% Pd/Al_2O_3	53	47	13	16	21	3
9	3% Pd/ZrO_2	42	41	10	13	30	6
10	3% Pd/CeO_2	25	32	22	18	18	10

It was proposed that Pd shows affinity towards both C and O of –C=O group of furan ring which is known as η^2 intermediate [38, 39]. Appearance of this η^2 intermediate during course of reaction favours the hydrogenation of reactant molecule. If Pd shows affinity to only C of –C=O group them it is termed as η^1 intermediate which favours decarbonylation at elevated temperature [40]. We didn't find furfural alcohol and 2-methyl furan but appearance of 5-methyl-2-furfural (MFFR) in our reaction products suggested domination of hydrogenation route while 5-HMF hydrogenolysis. Due to the presence of –OH group on 5^{th} position of

furan ring in 5-HMF, another possibility of formation of Pd--OH-CH_2 complex exists due to accessible sites at catalytic surface. This will create a flat or sideways adsorption of 5-HMF on the surface of Pd. In this condition, vacant d orbitals of Pd and delocalised electron of conjugated furan ring system can enhance the extent of hydrogenation due to dπ–Pπ interactions [41]. The catalytic activity of Pd may be outstanding due to presence of graphitic nature of C which also provide surface for such interaction due to considerable amount of sp^2 -C=C share in its skeleton as observed by XRD and XPS study.

The effect of metal loading on the surface of activated C was investigated and the results are shown in **Figure 3.11**. The lesser the loading lesser was the catalytic activity suggesting absence of enough active sites on Pd/C surface. Value of conversion varied from moderate to excellent from 1% to 5% loading of Pd. It was 47% and 69% for 1% Pd/C and 2% Pd/C with 61% and 73% of DMF respectively. As the loading increased above 3%, ring hydrogenation was observed along with complete conversion due to enhanced catalytic active sites on catalyst.

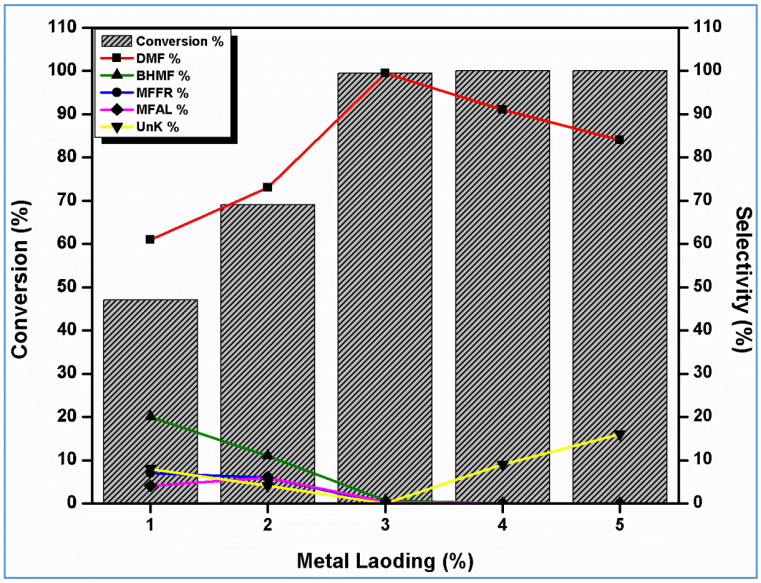

Figure 3.11: Effect of metal loading on 5-HMF hydrogenolysis, **Reaction conditions:** 5-HMF= 100 mg, IPA= 20 g, catalyst= 10 mg, T= 443 K P= 300 psig, agitation=1000 rpm, t= 4 h

Optimum loading for 5-HMF hydrogenolysis was 3% where 99% DMF was achieved with complete conversion at optimum reaction conditions. 5-HMF hydrogenation was also investigated using different supports like ZrO_2, Al_2O_3 and CeO_2 for 3% Pd catalyst but they proved to be far less efficient due to their poor surface areas and lower metal dispersion. Also there was no active adsorption contribution was available for 5-HMF like carbon due to its specific textural properties. The activity order for the screened support was found to be Pd/C> Pd/Al_2O_3 >Pd/ZrO_2 > Pd/CeO_2.

3.4.2. Effect of temperature

Temperature studies on 5-HMF hydrogenation were conducted for 3% Pd/C catalyst, in the range of 353– 443 K. Lower temperature showed lower conversion and selectivity whereas, higher temperature increased catalytic efficiency as shown in **Figure 3.12**. At 353 and 383 K conversion of 5-HMF was only 2% and 13% with 15% and 32% selectivity to DMF, respectively. It was observed that BHMF appears as major product at lower temperature units suggesting hydrogenation of –C=O functional group as initial pathway. The conversion and selectivity profile exponentially increased as the temperature was raised further. It was observed that at 413 K, conversion enhanced up to 6 times from 13% to 75% and selectivity to DMF also showed significant increase up to 72% from 32%. The increase in the DMF was observed at the expense of other side products like BHMF, MFAL and MFFR. Their decline continued further at most up to 443 K, where 99% selectivity to DMF was achieved with complete consumption of 5-HMF. Hence, optimum reaction temperature was 443 K and further study was done at this temperature.

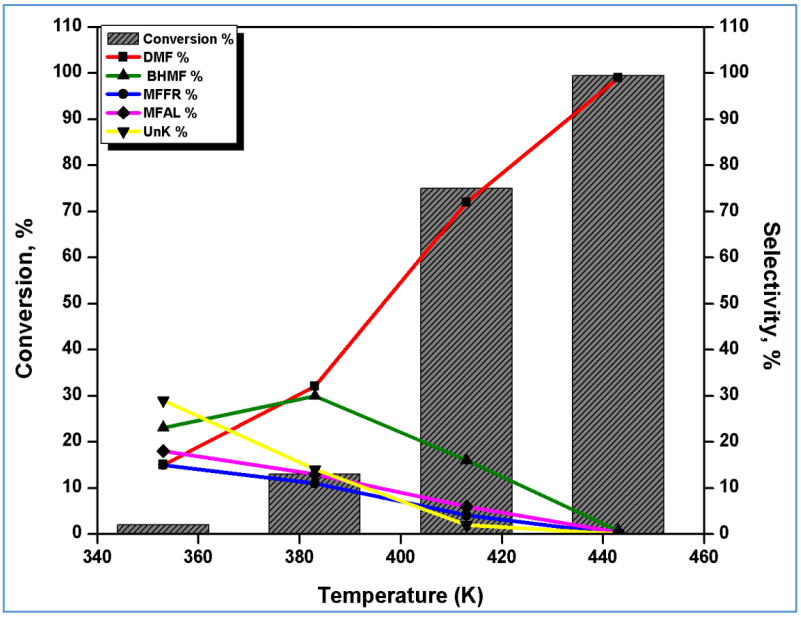

Figure 3.12: Temperature effect on 5-HMF hydrogenolysis, **Reaction conditions:** 5-HMF= 100 mg, IPA= 20 g, catalyst= 10 mg, P= 300 psig, agitation=1000 rpm, t= 4 h

3.4.3. Effect of H_2 pressure

Effect of external pressure of H_2 on the catalytic activity was seen in the range if 100-500 psig. **Figure 3.13** suggested that more than half of 5-HMF was consumed even at lower pressure like 100 psig. Similar results were obtained for the selectivity of DMF where it was 63% at 100 psig and 81% for 200 psig. The conversion also increased to 77% after doubling the amount of H_2. Mechanistic observations were very much similar like temperature parameter where BHMF was the second major product suggesting dominance of hydrogenation over hydrogenolysis. 300 psig was found best suitable pressure for 5-HMF hydrogenolysis giving the excellent selectivity to DMF (99%) with complete conversion. Above 300 psig over hydrogenated products like DMTHF and ether oligomer started to appear which significantly reduced the selectivity of DMF. Hence at 443 K the optimum H_2 pressure was 300 psig.

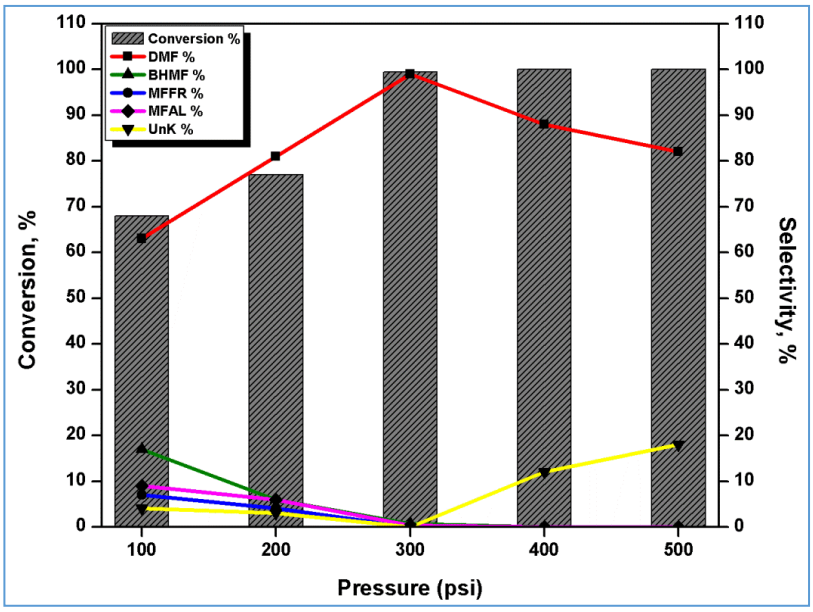

Figure 3.13: Effect of external H_2 pressure on 5-HMF hydrogenolysis, **Reaction conditions:** 5-HMF= 100 mg, IPA= 20 g, catalyst= 10 mg, T= 443 K, agitation=1000 rpm, t= 4 h

3.4.4. Effect of catalyst loading

Reaction was monitored for various loadings of 3% Pd/C but most suitable 5-HMF/catalyst ratio was found to be 10 mg of catalyst. **Figure 3.14** presents the catalyst loadings study for 5-HMF hydrogenolysis where it is quite evident that as the loading many side products started to appear. This led to decline in the selectivity of DMF till 71% at 50 mg loading of 3% Pd/C. Dimeric oligomers of 5-HMF, ether combinations of various alcoholic reactants and IPA, ring hydrogenated products like DMTHF and BHMTHF were observed as identified by GC-MS analysis at higher catalyst loadings.

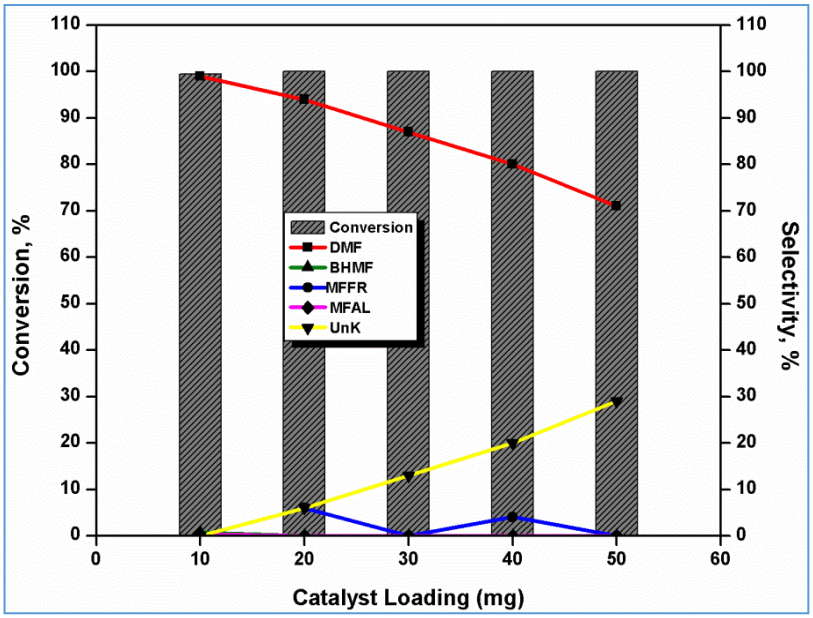

Figure 3.14: Effect of catalyst loading on 5-HMF hydrogenolysis, **Reaction conditions:** 5-HMF= 100 mg, IPA= 20 g, T= 443 K, P= 300 psig, agitation=1000 rpm, t= 4 h

3.4.5. Effect of substrate loading

Substrate loading studies of 5-HMF hydrogenolysis were conducted at variable 5-HMF concentrations by keeping catalyst amount constant. As shown in **Figure 3.15**, conversion-selectivity profile drifted downwards with increase in substrate concentration in reaction due to less availability of catalytic active surface sites. Approximately 10 mol% decline in the conversion were observed when moles of HMF were doubled. This also led to almost 16 mol% reduction in the selectivity of DMF. Aforementioned decline in catalytic efficiency was consistent with every fold increase in the concentration of 5-HMF. Three fold increase in the amount of 5-HMF reduced conversion and selectivity to 16 mol% and 24 mol% whereas 4 time increase in HMF amount of 20 mmol, this decline in conversion and selectivity reached to 22 mol% and 26 mol% than that of original value. It was observed that hydrogenated intermediates like BHMF, MFAL and MFFR appeared at higher concentration during this increase in concentration of 5-HMF and it was also observed in further

enhancement of 5-HMF amount. 4 mmol of 5-HMF concentration at constant catalytic concentration gave selectivity of 30 mol% to DMF. Similarly consumption of 5-HMF reduced to 22 mol%. Hence after analysing all the results, we concluded that 0.8mmole (100mg) is the optimum substrate concentration for the optimum catalyst concentration of 10mg.

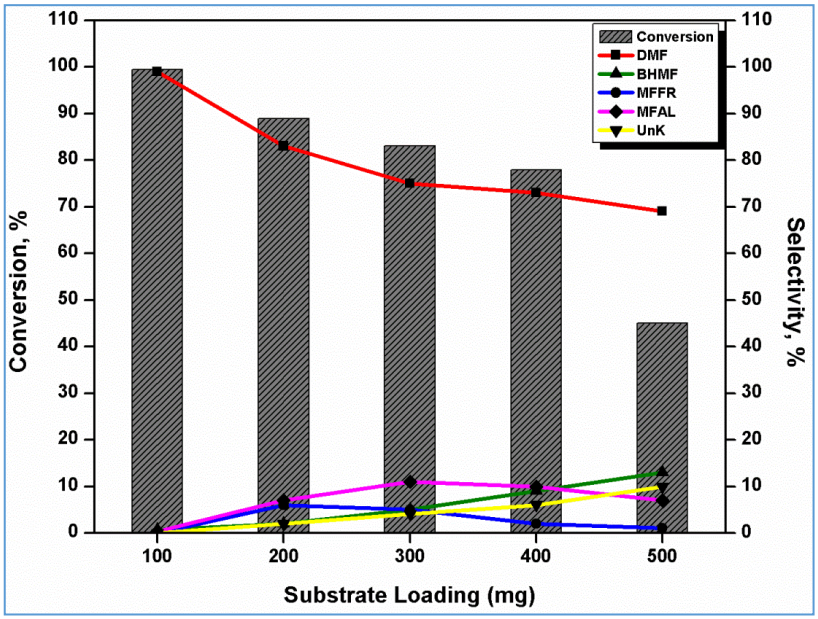

Figure 3.15: Effect of substrate loading on 5-HMF hydrogenolysis, **Reaction conditions:** IPA= 20 g, catalyst= 10 mg, T= 443 K, P= 300 psig, agitation=1000 rpm, t= 4 h

3.4.6. Solvent study

In order to understand the effect of reaction medium on hydrogenolysis of 5-HMF reaction was monitored in various solvents as shown in **Figure 3.16**. Initially to explore the green chemistry aspect, the reaction was taken in water and it was observed that 92% of 5-HMF was consumed with 70% selectivity to DMF and 27% BHMF. Further non-aqueous polar protic solvent like methanol, 2-propanol and 1-butanol were also studied and it was observed that best reaction medium for 5-HMF hydrogenation was 2-propanol. It may be due to its lower value of dielectric constant which in turn provides higher affinity to the solubility of

hydrogen [42]. Reaction results were poor with 1-butanol even though it has almost similar hydrogen solubility to 2-propanol. The probable reason for this may be due to its bulky nature and solvation effect [43]. As stated earlier the formation of Pd-η^2- acyl intermediate in the reaction led to the formation of BHMF. The polarity of BHMF can interact with the alcoholic solvents but given the steric hindrance of 1-butanol due to its bulky nature, BHMF (67%) auto- limits its accessibility to the catalytic active sites available on surface of catalyst by interacting with 1-butanol. This restricted further hydrogenolysis of BHMF in DMF and reflected in terms of poor selectivity to DMF (16%) for 1-butanol. Here it must be noted that with similar relative polarity 2-propanol due to its smaller size and ability to donate hydrogen, higher selectivity to DMF (99%) was achieved [44]. In a control experiment, transfer hydrogenation ability of 2-propanol was tested by conducting a run without external hydrogen which led to 48% conversion of 5-HMF along with 22% DMF selectivity. In case of CH_3OH, only 38% DMF was obtained with many etherified side products. Overall study of various solvents as the reaction media concluded that best suitable solvent for hydrogenation of 5-HMF was 2-propanol.

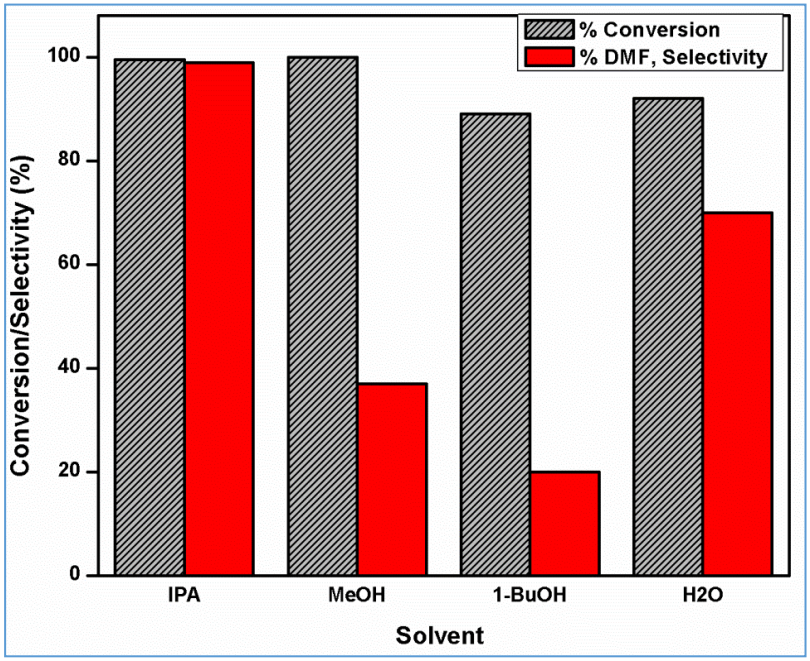

Figure 3.16: Effect of solvent for 5-HMF hydrogenolysis, **Reaction conditions:** 5-HMF= 100 mg, catalyst= 10 mg, T= 443 K, P= 300 psig, agitation=1000 rpm, t= 4 h

3.4.7. C-t profile

In order to understand the reaction pathway of 5-HMF hydrogenation over 3% Pd/C catalyst, conversion-selectivity profile was observed. In the first hour of 5-HMF hydrogenation, 41% of 5-HMF was consumed resulting in 45% of DMF. Other reaction intermediates like BHMF (29%), MFAL (9%) and MFFR (14%) were also observed suggesting higher activity of 3% Pd/C. Appearance of MFFR suggested initial hydrogenolysis whereas MFAL can be its hydrogenated product. In the second hour of reaction, conversion of 5-HMF jumped to 66% whereas, in third hour it was 87%. On careful evaluation of reaction profile it was observed that concentration of BHMF was continuously decreasing after first hour suggesting initial hydrogenation pathway was followed by hydrogenolysis resulting DMF via MFFR and MFAL. 99.9% 5-HMF was consumed at the end of reaction in four hour giving 99% of desired product DMF whereas traces of MFFR and MFAL were also observed.

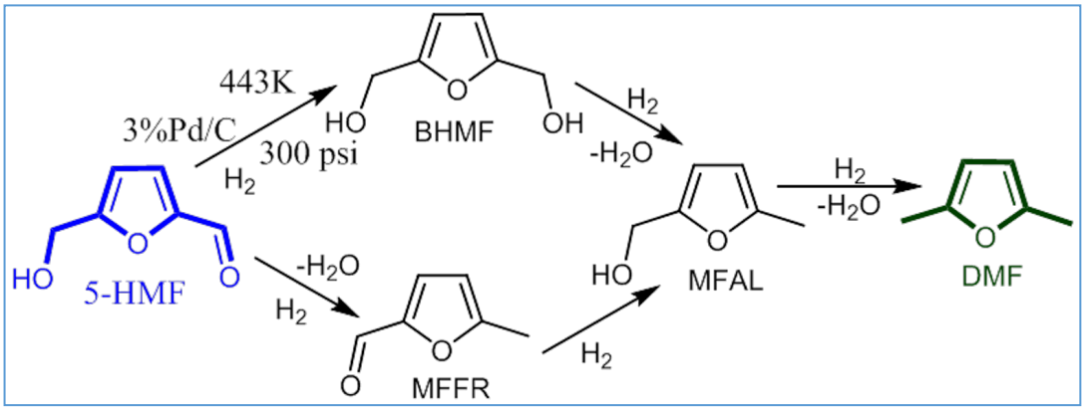

Reaction Scheme 3.1: Reaction pathway of 5-HMF hydrogenolysis

Various control experiments were conducted based on which reaction pathway for 5-HMF hydrogenolysis shown in **Reaction Scheme 3.1**. When MFFR was taken as starting material within 2 h of reaction under optimised reaction conditions, 94% DMF was obtained with complete 5-HMF conversion. MFAL was also detected in the reaction analysis. After 2 h of reaction, ring hydrogenation led to decline in the selectivity of DMF. BHMF was also tested as a substrate and the only product other than DMF after 2.5 h of reaction was MFAL. When MFAL was taken as a substrate, within 1h of the reaction itself, DMF was observed (98%). These observations were in well accordance with our previous work in which strong activity of Pd was attributed to the interaction of Π electrons of furan ring and Pd metal [(45)].

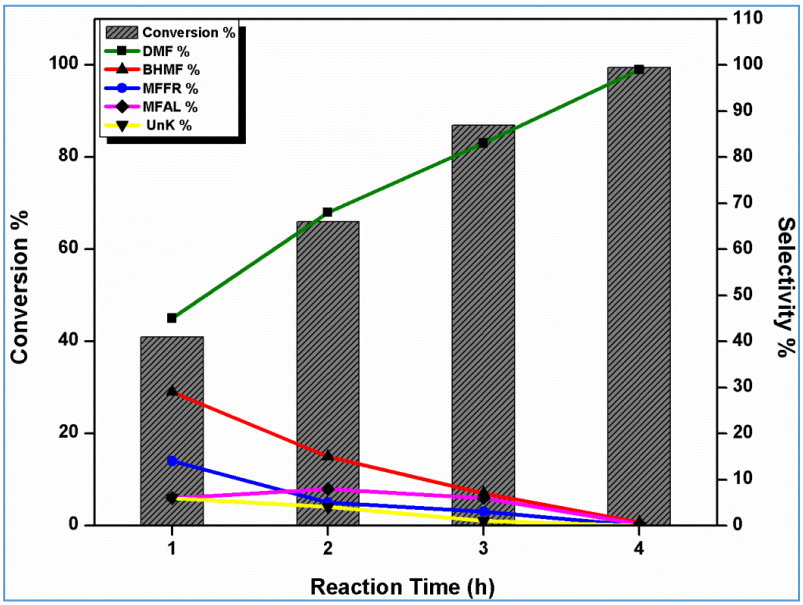

Figure 3.17: Reaction c-t profile of 5-HMF hydrogenolysis, **Reaction conditions:** 5-HMF= 100 mg, IPA= 20 g, catalyst= 10 mg, T= 443 K P= 300 psig, agitation=1000 rpm, t= 4 h

3.4.8. Catalyst recycle study

The stability and reusability of the catalyst was investigated by conducting recyclability test after 1.5 h at 50% conversion of 5-HMF. Reaction was stopped after 1.5 h and the catalyst was separated from reaction crude. In order to reuse it for next run it was washed and dried at 383K. The catalyst was found to be reusable up to 4 recycle runs with complete conversion of 5-HMF and slight decline in selectivity as shown in **Figure 3.18**. Conversion of 5-HMF was 55% and 52% in first two recycle runs, respectively, whereas the selectivity to DMF was 53% and 50%, respectively. A mild drop was observed in the activity of catalyst in the third run where conversion remained 47% with 45% selectivity to DMF. In 4^{th} recycle, significant loss of almost 14% in the conversion of 5-HMF (41%) was observed and selectivity also decreased to 39%. This loss in catalytic activity was revived by following a standard reduction protocol where after heating the catalyst at 383 K it was treated with H_2 flow of 3.0 mL/min at 523K for 2 h. It was interesting to observe that the catalytic efficiency of this

rejuvenated 3% Pd/C was almost identical to that of the original catalyst. 57% selectivity to DMF was observed in this catalytic run with56% conversion of 5-HMF.

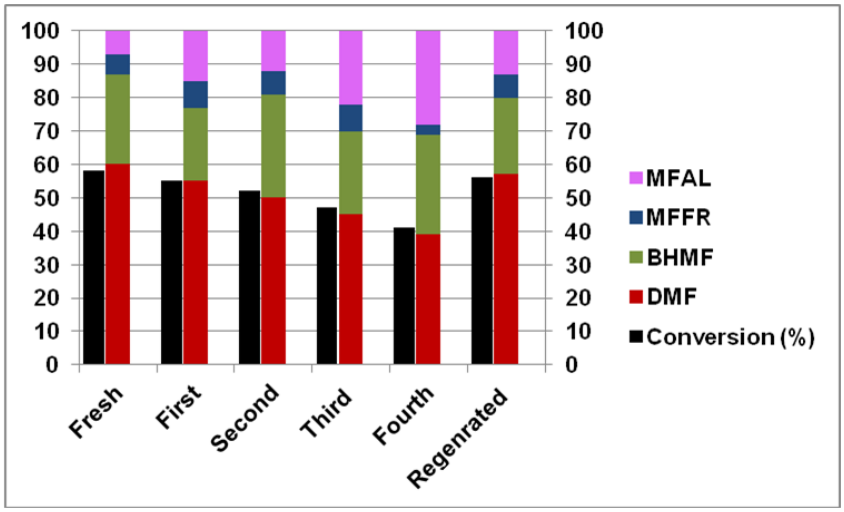

Figure 3.18: Catalyst recyclability for 5-HMF hydrogenolysis, **Reaction conditions:** 5-HMF= 100 mg, IPA= 20 g, catalyst= 10 mg, T= 443 K P= 300 psig, agitation=1000 rpm, t= 4 h

Hot filtration test was also conducted to rule out the possibility of any kind of catalyst leaching. Accordingly, test reaction was stopped after 2 h and catalyst was isolated from mother liquor of the reaction. The reaction was continued without catalyst till 4 h in after recharging the reactor with reaction crude. No change in the conversion and selectivity was observed as shown in **Figure 3.19** suggesting no reaction took place in absence of catalyst. This also proved that Pd was not leached in reaction medium indicating its stability under the reaction conditions.

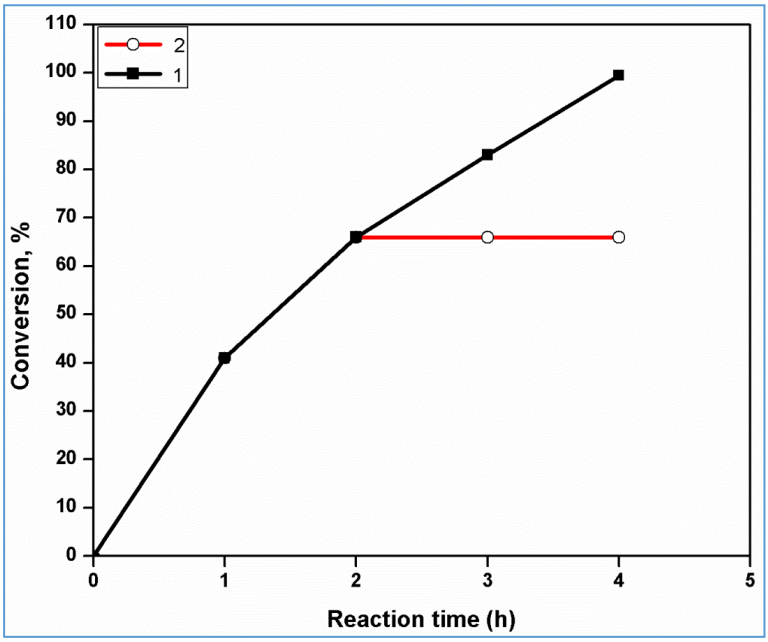

Figure 3.19: Hot filtration test for 5-HMF hydrogenolysis (1) Reaction with catalyst (2) Reaction continued after isolation of catalyst in 2 h. **Reaction conditions:** 5-HMF= 100 mg, IPA= 20 g, catalyst= 10 mg, T= 443 K P= 300 psig, agitation=1000 rpm, t= 4 h

3.5 Reaction Mechanism

3% Pd/C contains certain amount of PdO along with metallic Pd as shown in XPS whereas activated C has graphitic characteristics. The complex dΠ-PΠ mutual electronic exchange between Pd and C surface can enhance the adsorption and activity of Pd on C. Introduction of 5-HMF on the surface of catalyst led to generation of Pd-η^2 acyl intermediate (step-A). Formation of this transition state will yield BHMF as shown in **Reaction Scheme 3.2**. This process of hydrogenation should be more passive on the facet of Pd-PdO as suggested by earlier report [31]. Surface acidity possessed by PdO enhances the dehydration assisted by adsorbed hydride species of Pd(0). This process of hydrogenolysis will be repeated twice to yield DMF (step-B and step-C). Similar sequence of reaction can happen with MFFR via MFFR based η^2 acyl intermediate with Pd (step-D and step-E).

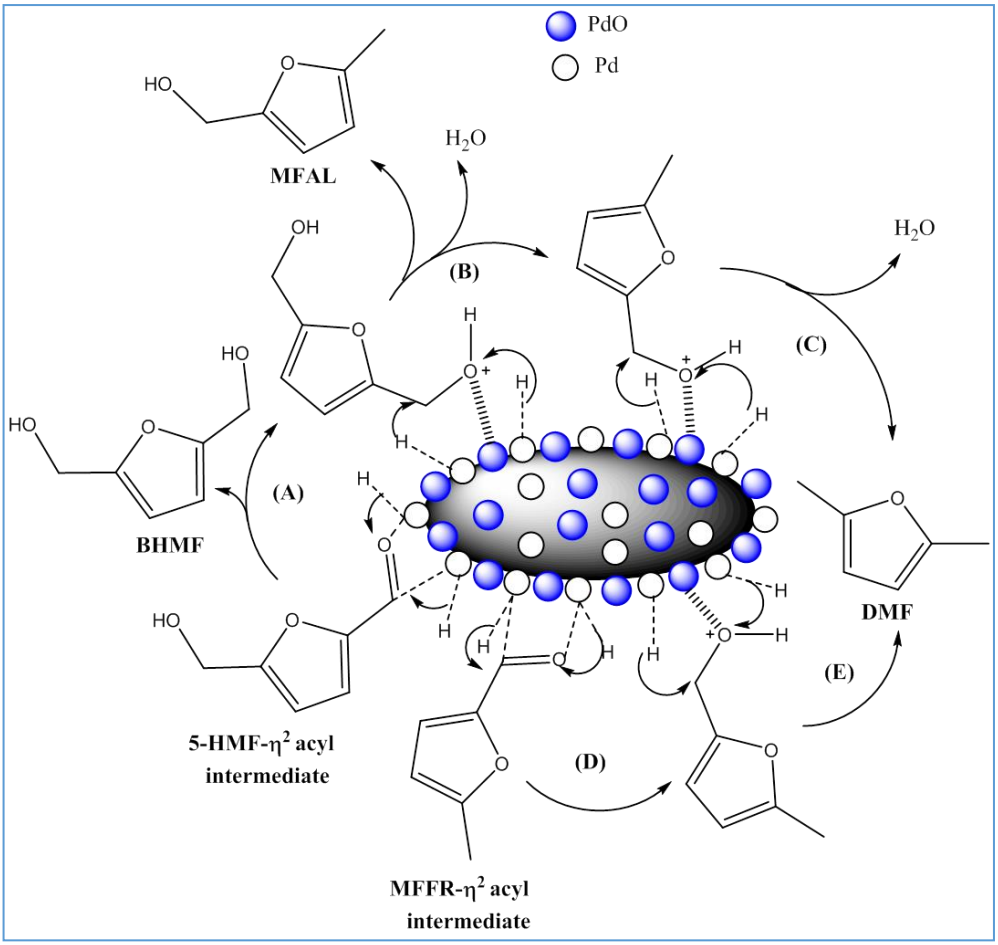

Reaction scheme 3.2: Plausible reaction mechanism of 5-HMF hydrogenolysis

3.6. Conclusion

3% Pd/C proved to be highly efficient catalyst for hydrogenation of 5-HMF with very high selectivity to DMF (99%) and complete conversion of 5-HMF within 4h of reaction. Parameter optimisation studies were conducted on 3% Pd/C with excellent recyclability up to 4 times. It was observed that increase in both temperature and pressure leads to reach almost complete conversion (99.5%) whereas temperature played predominant role for tuning the selectivity from HMF to DMF.

Reduction protocol was successfully designed to revive the lost activity of spent catalyst. Extensive characterisation studies revealed that microporous nature, high surface area, homogeneous distribution, small particle size of 2.6-3.0 nm and Pd-PdO nanohybrid

synergism played conclusive role in excellent activity of 3% Pd/C. TON and TOF of 3% Pd/C for 5-HMF hydrogenolysis were found to be 280.42 and 70.10 h^{-1} respectively.

All these properties cumulatively made 3% Pd/C superior catalyst over the earlier reports in terms of efficiency, reaction time (energy consumption) and recyclability without addition of any other reagent like formic acid, hence which was also environment friendly. Brief studies of reaction medium revealed that 2-propanol was the best suitable solvent for 5-HMF hydrogenation.

References

1. J. C. Serrano, R. Luque and A. Sepulveda-Escribano, *Chem. Soc. Rev.*, **2011**, 40, 5266–5281

2. J. Deng, T. Pan, Q. Xu, M. Y. Chen, Y. Zhang, Q. X. Guo, and Y. Fu, *Sci. Rep.*, **2013**, 3, 1244–1250

3. P. S. Nigam and A. Singh, *Prog Energy Combust Sci*, **2011**, 37, 52–68

4. S. N. Dodić, S. D. Popov, J. M. Dodić, J. A. Ranković and Z. Z. Zavargo, *Renew. Sustain. Energy Rev.*, **2009**, 13, 2197–2200

5. W. Coyle, In Next-Generation Biofuels: Near-Term Challenges and Implications for Agriculture, U.S. Department of Agriculture, Economic Research Service, May **2010**, 1-26

6. L. P. Wyszynski, C. R. Stone and G. T. Kalghatgi, The volumetric efficiency of direct and port injection gasoline engines with different fuels. *SAE Tech. Pap.* **2002**, 2002-01-0839

7. S. Zhong, R. Daniel, H. Xu, J. Zhang, D. Turner, M. L. Wyszynski and P. Richards, *Energy Fuels*, **2010**, 24, 2891– 2899

8. Y. Zu, P. Yang, J. Wang, X. Liu, J. Ren, G. Lu and Y. Wang, *Appl. Catal. B*, **2014**, 146, 244 – 248

9. A S. Nagpure, A. K. Venugopal, N. Lucas, M. Manikandan, T. Raja and S. Chilukuri. *Catal. Sci. Technol.*, **2015**, 5, 1463-1472

10. X. Wang, Y. Liub and X. Liang, *Green Chem.*, **2018**, 20, 2894–2902

11. A. B. Gawade, M. S. Tiwari and G. D. Yadav, *ACS Sustainable Chem. Eng.*, **2016**, 4, 4113-4123

12. S. Li, M. Dong, J. Yang, X. Cheng, X. Shen, S. Liu, Z. Q. Wang, X. Q. Gong, H. Liu and B. Han, *Nature Communications*, **2021**, 12, 584-592

13. V. B. Ukraintsev and K. A. Khokhryakov, *Ross. Khim. Zh*., **2006**, 50, 154–156

14. L. Hu, X. Tang, J. Xu, Z. Wu, L. Lin, and S. Li, *Ind. Eng. Chem. Res.* **2014**, 53, 3056−3064

15. Y. Yang, Q. Liu, D. Li, J. Tan, Q. Zhang, C. Wang and L. Ma, *RSC Adv*., **2017**, 7, 16311-16318

16. S. S. Nishimura, N. Ikeda and K. Ebitani, *Catal. Today*, **2014**, 232, 89–98

17. J. Mitra, X. Zhou and T. Rauchfuss, *Green Chem.*, **2015**, 17, 307–313

18. A. D. Talpade, M. S. Tiwari and G. D. Yadav, *Molecular Catalysis*, **2019**, 465, 1–15

19. W. Liaoa, Z. Zhua, N. Chena, T. Sua, C. Denga, Y. Zhaob, W. Renb, and H. Lü, *Molecular Catalysis*, **2020**, 482, 110756

20. H. Zhang, B. Dai, X. Wang, W. Li, Y. Han, J. Gu and J. Zhnag, *Green Chem.*, **2013**, 15, 829–836

21 X. Li, Y. Wang, L. Kang, M. Zhu and B. Dai, *J. Catal.*, **2014**, 311, 288–294

22. N. S. Date, N. S. Biradar, R. C. Chikate and C.V. Rode, *Chem. Sel.*, **2017**, 2, 24–32

23. Z. Wei, R. Pan, Y. Hou, Y. Yang and Y. Liu, *Sci. Rep.*, **2015**, 5, 15664-15672

24. B. Qi, L. DI, W. Xu and X. Zhang, *J. Mater. Chem. A*, **2014**, 2, 11885-11890

25. M. Magureanu, D. Dobrin, N. B. Mandache, B. Cojocaru and V. I. Parvulescu, *Front. Chem.*, **2013**, 1, 1-6

26. K. Deori, D. Gupta, B. Saha, S. K. Awasthi and S. Deka, *J. Mater. Chem. A*, **2013**, 1, 7091-7099

27. W. Yu, H. Hou, Z. Xin, S. Niu, Y. Xie, X. Ji and L. Shao, *RSC Adv.*, **2017**, 7, 15309-15314

28. L. P. A. Guerrero-Ortega, E. Ramirez-Meneses, R. Cabrera-Sierra, L. Palacios-Romero, K. Philippot, C. Santiago-Ramírez, L. Lartundo-Rojas and A. Manzo-Robledo, *Journal of Materials Science*, **2019**, 54, 13694-13714

29. D. Yang, A. Velamakanni, G. Bozoklu, S. Park, M. Stoller, R. D. Piner, S. Stankovich, I. Jung, D. A. Field, C. A. Ventrice Jr. and R. S. Rouff, *Carbon*, **2009**, 47, 145-152

30. M. Korzec, P. Bartczak, A. Niemczyk, J. Szade, M. Kapkowski, P. Zenderowska, K. Balin, J. Lelatko and J. Polanski, *J. Catal.*, **2014**, 313, 1–8

31. C. Wang, F. Yang, W. Yang, L. Ren, Y. Zhang, X. Jia, L. Zhang and Y. Li, *RSC Adv.*, **2015**, 15, 27526–27532

32. A. Morais, J. P. C. Alves, F. A. S. Lima, M. Lira-Cantu and A. F. Nogueira, *J. Photon. Energy*, **2015**, 5, 057408

33. A. M. Soliman, S. A. A. Elsuccary, I. M. Ali and A. I. Ayesh, *Journal of Water Process Engineering*, **2017**, 17, 245–255

34. J. R. McManus and J. M. Vohs, *Surf. Sci.*, **2014**, 630, 16–23

35. J. Ryczkowski, IR spectroscopy in catalysis, *Catal. Today*, **2001**, 8, 263–38

36. S. Barsberg and L. G. Thygesen, *Vib. Spectrosc.* **2009**, 49, 52–63

37. J. Jae, W. Zheng, R. F. Lobo and D. G. Vlachos, *ChemSusChem*, **2013**, 6, 1158–1162

38. R. Shekhar, R.V. Plank, J. M. Vohs and M. A. Barteau, *J. Phys. Chem. B*, 1997, 101, 7939–7951

39. J. L. Davis and M. A. Barteau, *J. Am. Chem. Soc.*, **1989**, 111, 1782–1792

40. S. Sitthisa and D. E. Resasco, *Catal. Lett.* **2011**, 141, 784–791

41. S. Chen, R. Wojcieszak, F. Dumeignil, E. Marceau and S. Royer, *Chem. Rev.*, **2018**, 118, 11023-11117

42. N. S. Biradar, A. M. Hengne, S. S. Sakate, R. K. Swami and C. V. Rode, *Catal. Lett.*, **2016**, 146, 1611–1619

43. E. Toukoniitty, J. Kuusisto, V. Nieminen, M. Hotokka and T. Salmi, *J. Mol. Catal. A*, **2003**, 192, 135–151

44. R. L. Augustine and P. Techasauvapak, *J. Mol. Catal.*, **1994**, 87, 95–105

45. N. S. Biradar, A. M. Hengne, S. N. Birajdar, P. S. Niphadkar, P. N. Joshi and C. V. Rode, *ACS sustainable, Chem. Eng.* **2014**, 2, 272–281

Chapter 4

Selective hydrogenation of 5-HMF to 2,5-DMF over a magnetically recoverable non-noble metal catalyst

Selective hydrogenation of 5-HMF to 2,5-DMF over a magnetically recoverable non-noble metal catalyst

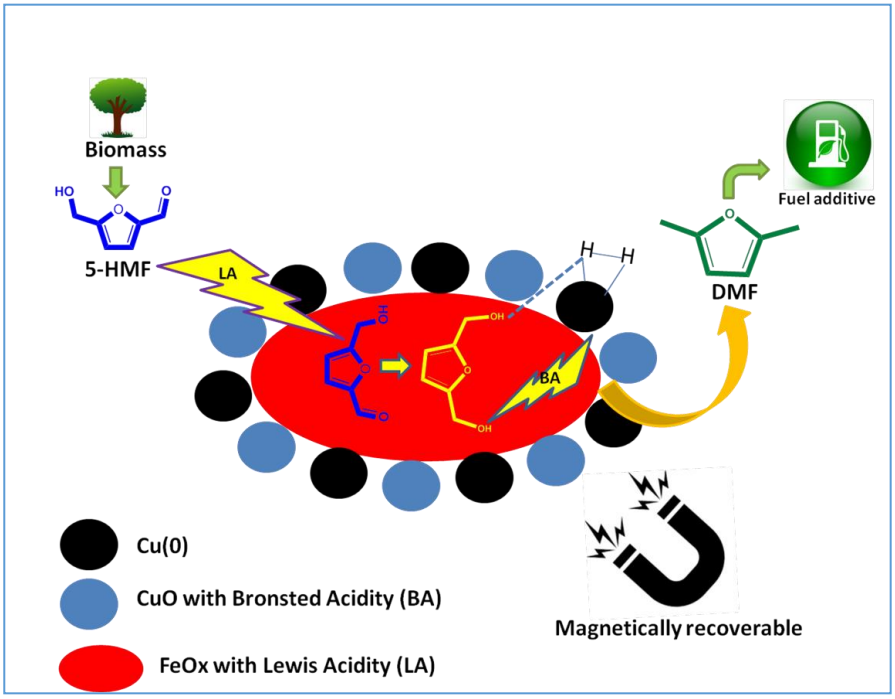

Green Chem., 2019, 21, 6390–6406

Cu-Fe nanomorph with the ratio of 1:2 was designed for efficient hydrodeoxygenation of 5-HMF in DMF. The catalyst was magnetically separable and highly selective under optimised reaction conditions of reaction temperature: 443 K, 300 psig H_2 pressure, S/C= 2 in 20 g of 2-propanol for 4 h. Cu-Fe (1:2) was characterized extensively with the help of XRD, XPS, TEM, FESEM, BET surface area, N_2-adsorption, NH_3-TPD, pyridine-IR and H_2-TPR measurements. Cu(0)-$CuFe_2O_4$ nanopair of the size of 15.4-17.6 nm was observed with mesoporous nature of particles. Lewis acidity of Fe and its oxophilicity played a key role in hydrogenation process whereas the surface Brönsted acidity of CuOx particles and affinity towards –C-O bond promoted synthesis of DMF with 93% selectivity. Detail parameter optimisation studies were conducted and 97% conversion of 5-HMF was obtained for which a plausible reaction mechanism was also proposed.

4.1 Introduction

To overcome the limited stock of conventional fossil fuel resources is going to be the one of the biggest challenges for the society in coming years [(1)]. This inevitable energy crisis needs to be addressed as soon as possible by sustainable energy alternatives with much better economical viabilities [(2-3)]. Biomass derived multiple platform chemicals can be best option given their renewable nature and availability globally [(4)]. C6 carbohydrates derived building block molecules like BHMF, DMF, FDCA, DMTHF and DFF have the huge potential to change the dynamics of fuel, utility chemicals and polymer markets [(5)]. 5-HMF is a C6 sugar derived molecule which can be converted into a highly efficient potential fuel additive DMF by its catalytic hydrodeoxygenation. **Table 1.2** shows some of the exceptional and superseding fuel properties of DMF over other biofuel alternatives like bioethanol and bio-butanol [(6-8)].

Multi-oxygenate nature of 5-HMF can be reduced by catalytic hydrogenation for which various noble metal catalysts were investigated earlier but their rare availability and higher price are major hurdles in their economic viability [(9)]. To overcome these problems, catalysts based on abundant Earth metal were explored recently as shown in **Table 1.5**. Mainly supported Ni, Cu and Co based catalysts were screened by various researchers due to their interesting surface properties. Bare metal oxides and various combinations of metals were also examined for 5-HMF hydrodeoxygenation like Co where bare CoO_x was able to produce 83.3% of DMF in 12 h of reaction whereas its combination with Fe and Ni showed improved efficiency at 180 °C in 5 h with complete conversion of 5-HMF [(10 -11)]. Co was also studied on different supports like carbon nitride and β-zeolites where significant improvement in the reaction conditions was observed [(12 -13)]. Ni is one of the most exploited metals on various supports like carbon, Al_2O_3, Co_3O_4 and W_2O_3 but higher external pressure (100 bar), poor

recyclability, higher energy consumption were certain drawbacks in this case [14-17]. Like other metals, it was also screened in combination of other metals like Fe, Cu, and W_2C but here also elevated reaction temperature (200 °C) very high reaction pressure and poor yield were matter of concerns [18-20]. Similarly, Cu was also explored with mesoporous oxide support in supercritical methanol where very poor yield of DMF (30.6%) was achieved [21]. Cu-Zn alloy at 220 °C, tuneable Cu-Co combination on activated C and at 50 bar H_2 pressure and Cu/Al_2O_3 for 10 h were tested for 5-HMF hydrodeoxygenation with more than 90% selectivity to DMF [22-24]. Though, a small amount of metal variants are reported in non-noble metal catalysts but limited information about their catalytic pathway and harsh reaction conditions provide an ample scope for further investigation. Based on the literature search we chose Cu and Fe as our metals of interest and designed various catalyst compositions for efficient 5-HMF hydrodeoxygenation. After detailed study we found that Cu-Fe(1:2) as one of the most efficient catalysts with 97% conversion and 93% selectivity to DMF. Cu-Fe(1:2) was comprehensively characterized by various techniques like XPS, XRD, TEM, SEM, BET, CO_2-TPD and NH_3-TPD to understand its structural and electronic attributes for its excellent activity. The catalyst was found magnetically recoverable with 5 times recyclability. Efforts were devoted for rejuvenation of catalytic activity of used catalysts and a plausible reaction mechanism was proposed based on interpretation of parameter study and catalytic properties.

4.2 Experimental

4.2.1 Catalyst Preparation

All different variants of Cu and Fe were prepared by the co-precipitation method as described in subsection 2.3.2. The catalytic run for 5-HMF hydrodeoxygenation was conducted in Parr reactor as mentioned in subsection 2.5.2 of chapter 2. Activity testing and selectivity calculation were done by GC method also described in subsections 2.6.1 and 2.7 of chapter 2.

Catalytic properties were evaluated by different characterisation techniques mentioned in section 2.4 of chapter 2.

4.3 Results and Discussion

Major objectives of this work were to (1) design a non-noble metal, efficient, reusable and recoverable metal catalyst and (2) to understand the structure–activity correlation to explain the observed catalytic activity performance.

4.3.1 BET Surface Area

Results of BET surface area analysis and observation of adsorption isotherm are summarised in **Table 4.1**.

Table 4.1: Surface area analysis and crystallite sizes by XRD for all the components of catalysts used in this work

Sr. No.	Catalysts	Surface Area (m^2/g)	BJH Pore Size diameter (nm)	Pore Volume cc/g	Crystallite Size (nm) from XRD
1	CuO_x	65	3.38	0.136	56.4
2	FeO_x	137	9.88	0.238	45.3
3	Cu-Fe (1:1)	85	10.16	0.192	63.4
4	Cu-Fe (2:1)	61	9.50	0.145	25.2
5	Cu-Fe (1:2)	109	11.40	0.147	42.8

BJH parameters were taken into account for pore size diameter calculation which revealed that both monometallic catalyst possessed narrow pore than bimetallic catalysts. The pore size of most active variant Cu-Fe(1:2) was 11.40 nm whereas crystallite size calculated by Scherer equation was 42.8 nm. Surface area also varied among all the catalysts. Apparently

highest surface area was found for monometallic FeO_x (137 m^2/g) whereas in the case of Cu-Fe(1:2) it was 109 m^2/g.

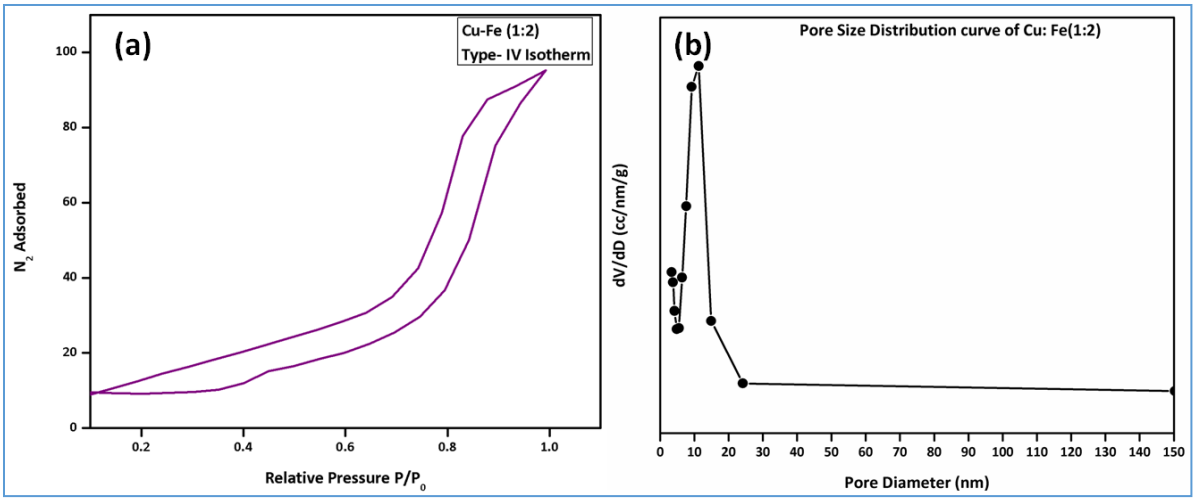

Figure 4.1: (a) N_2- adsorption isotherm for Cu-Fe(1:2) **(b)** Pore size distribution of Cu-Fe(1:2)

Type –IV isotherm plot with H4 type of low pressure hysteresis loop obtained in N_2-adsorption isotherm of Cu-Fe(1:2) suggested mesoporous nature of surface (**Figure 4.1.a**) [25]. H4 type loop was clearly visible well before 0.4 value of relative pressure which may be due to the unbalanced meniscus of liquid N_2 in the narrow slit shaped pores [26]. Narrow pore size distribution was observed in the Cu-Fe (1:2) as shown in **Figure 4.1.b**.

4.3.2 TGA Analysis

In order to understand the thermal stability of Cu-Fe(1:2) TG-DTA was conducted as shown **in Figure 4.2.a**. Overall only 8.27% loss in weight of catalyst was observed in the range of 25°C- 1000°C. The first endothermic valley was observed between 30 °C 182°C where the catalyst mass reduced to 95.34% suggesting a loss of almost 4.65%. This may be due to the loss of surface aqueous species or hydroxyl group of lattice [27]. To confirm it, catalyst was subjected to TGA-MS analysis and m/z value of 18 in the similar range supported our observation. From 200°C to 800°C, a continuous gradient kind of decline was observed in

TG-DTA of Cu-Fe(1:2) which may be due to the phase transition of Cu and Fe above 450 °C and exclusion of nitrate rudiments of the precursor from the surface [28]. This hypothesis was also supported by a signal of mass fragment m/z=30 in TGA-MS plot of Cu-Fe(1:2). Till 800°C, almost 5.87% loss in original weight was observed. A sharp signal of small weight (2.4%) loss was observed post 800 °C which may be due to the loss of lattice Oxygen.

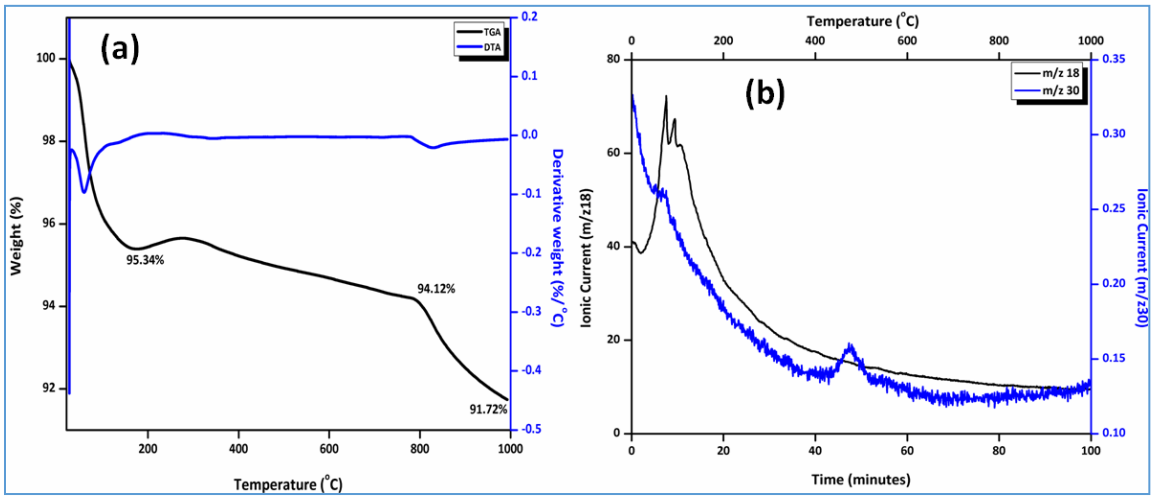

Figure 4.2: (a) TGA-DTA analysis of Cu-Fe(1:2) **(b)** TG-MS plot of Cu-Fe(1:2)

4.3.3 XRD Analysis

XRD patterns were recorded to find out the various surface species in the catalyst as shown in **Figure 4.3.a** showing bare CuO_x with FCC lattice with Cu(0) and CuO (+2) species in it.

Figure 4.5 shows the reflections at 2θ= 43.70° (111), 50.64° (211) and 74.23° (220) with JCPDF# 85-1326 which were related to metallic nature of Cu whereas those at 2θ = 35.25° and 38.60° having JCPDF# 01-1242 were corresponding to monoclinic CuO attributed to its thermodynamic stability over metastable $Cu(OH)_2$ which could be formed before calcination [29-31]. Wustite (FeO) at 2θ= 30.11° (220), magnetite (Fe_3O_4) at 2θ= 35.76° (220), 62.69° (440) and 53.95° (422) and haematite phase (α-Fe_2O_3) at 2θ= 57.54° (511) and 43.45° (400) were observed in XRD pattern of bare FeO_x (BCC lattice) [32-34].

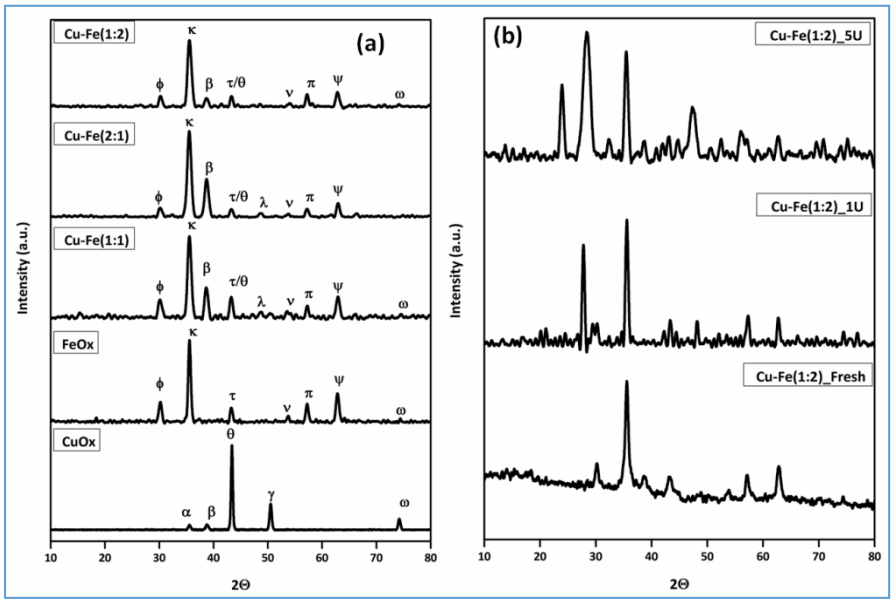

Figure 4.3: (a) XRD patterns of the catalysts: α = 35.25°, β = 38.60, θ = 43.70°, γ = 50.64°, ω = 74.23°, φ = 30.11°, κ = 35.76°, τ = 43.45°, ν = 53.95°, π = 57.54°, Ψ = 62.69°, λ = 48.71° (τ/θ are overlapped) **(b)** Comparative XRD analysis of the textural properties of fresh and spent Cu–Fe (1 : 2) catalysts.

The presence of spinel phase of Cu and Fe *i.e.* $CuFe_2O_4$ were evident in Cu-Fe(1:1) at 2θ= 35.50° (311), 38.85° (222) with JCPDF # 77-0010. Metallic Cu (2θ= 43.20°) and all three phases of Fe (ϕ, π and ψ) were also observed in all the bimetallic Cu-Fe variants along with spinel $CuFe_2O_4$ [35-36]. The presence of Cu(0)-$CuFe_2O_4$ nanopair was evident by XRD pattern of Cu-Fe(1:2) which can be vital for selectivity of hydrodeoxygenation of 5-HMF reaction due to propensity of Cu to catalyse the C-O bond cleavage and catalytic synergism of Cu and Fe as oxides of Fe became indispensible to prevent sintering of Cu(0) due to their inclusion ($CuFe_2O_4$) [33]. These initial results of mutual catalytic synergism were further investigated by XPS. The stability of Cu-Fe(1:2) in due course of reaction and recyclability were also examined by XRD analysis as shown in **Figure 4.3.b**. Cu(+2) of spinel phase (2θ= 35.50° and 38.85°) was found common in fresh as well as every spent catalyst. After consecutive recycle runs 2θ= 28.51° which shifted from 2θ= 30.11° in first recycled catalyst was found

dominant peak with spinel phase suggesting enhanced metallic nature of Cu due to reductive reaction medium. Continuous use of spent catalyst led to deposition of organic matter on its surface which led to generation of some mixed phase diffraction at 2θ= 24.01° in 5th recycle run. All these facts revealed that Cu-Fe(1:2) retained its certain phase and quite stable on optimised reaction conditions.

4.3.4 TEM

Cu-Fe(1:2) was subjected to TEM analysis to find out particle size, morphology and dispersion. **Figure 4.4.d** shows the fringe pattern value of 0.239 nm and 0.476 nm correspond to the 222 and 322 miller indices. Good dispersion of mainly round shaped particles with small aggregation was also seen in TEM images (**Figure 4.4.a**). Plane arrangements were well established in SAED pattern as shown in **Figure 4.4.e**. Average particle size was calculated by taking almost 100 different nanoparticles and it was found it ranged between 15.4-17.6 nm as shown in **Figure 4.4.c**.

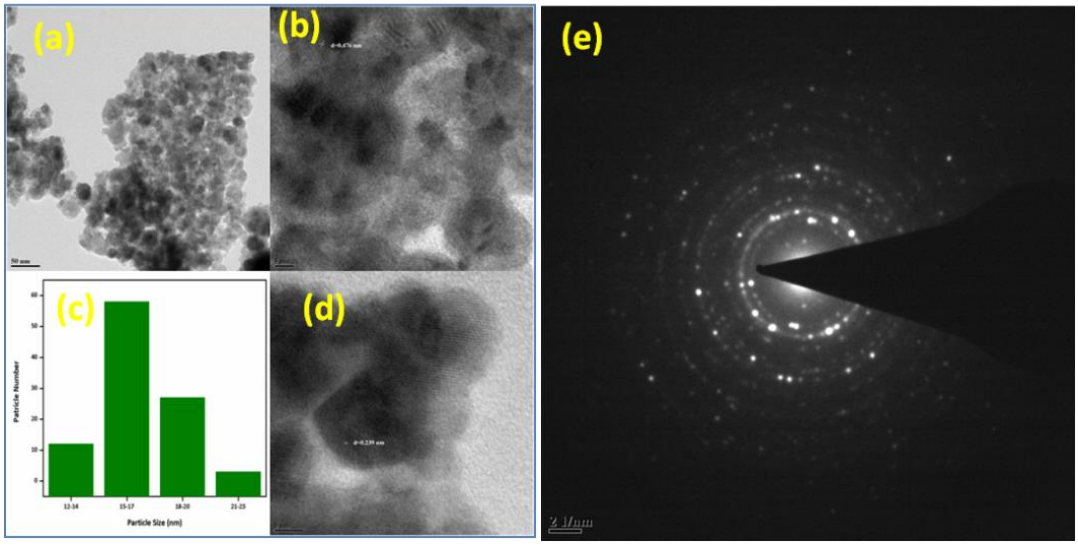

Figure 4.4: HR-TEM analysis of **(a)** the distribution of Cu–Fe(1 :2) at a 50 nm scale **(b)** Fringe width of Fe **(c)** Particle size distribution **(d)** Fringe width of Cu **(e)** SAED pattern of Cu-Fe(1:2)

4.3.5 SEM- EDX Analysis and Elemental Mapping

Morphology and elemental percentage of Cu-Fe(1:2) was studied by their epitaxial scanning in SEM and EDX, respectively. As seen in TEM images particles were round shaped with different size in SEM also. Larger particles were observed with different layer arrangement at their edges as shown in **Figure 4.5.b**. Elemental mapping and EDX of Cu-$CuFe_2O_4$ nanohybrid was also done to find out the relative position and amount of Cu, Fe and O as shown in **Figures 4.5.c and 4.5.d**. The EDX pattern revealed that almost 26% Cu and 51% of Fe was present in catalyst showing synthesis of Cu: Fe in exact 1:2 ratio.

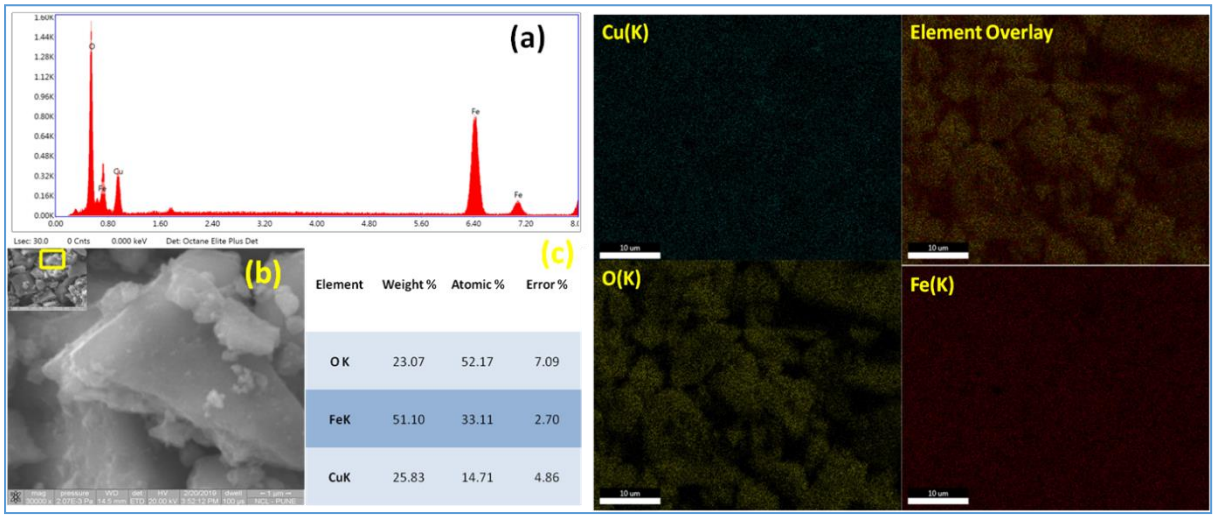

Figure 4.5: SEM of Cu–Fe(1:2) **(a)** EDAX pattern of Cu–Fe(1:2) **(b)** Morphology of Cu–Fe(1:2) **(c)** Elemental % of Cu, Fe and O in Cu–Fe(1:2) (d) Elemental mapping of Cu, Fe and O in Cu-Fe(1:2)

4.3.6 XPS Analysis

The identification and interpretation of various oxidation states of catalysts were done by XPS analysis. Cu and Fe XPS scan survey profiles of all the catalyst are shown in **Figures 4.6.a** and **4.6.b**. Cu $2p_{3/2}$ showed a dominant peak at B.E. of ~933 eV along with strong satellite peak at around B.E. of ~943 eV showing absence of any Cu (+1) [37-38]. Similarly at higher binding energies of ~953 eV and ~962 eV, two peaks were observed for Cu $2p_{3/2}$ with

almost equal intensity [39]. Fe $2p_{3/2}$ was observed at around B.E. of ~710-711 eV with very weak satellite peak at B.E. of ~718 eV indicating absence of any metallic Fe species but strongly suggesting presence of α-Fe_2O_3 and Fe_3O_4 phases as observed in XRD pattern [40-42]. These trends related to surface composition and valence states of Cu and Fe were consistent in all the catalysts.

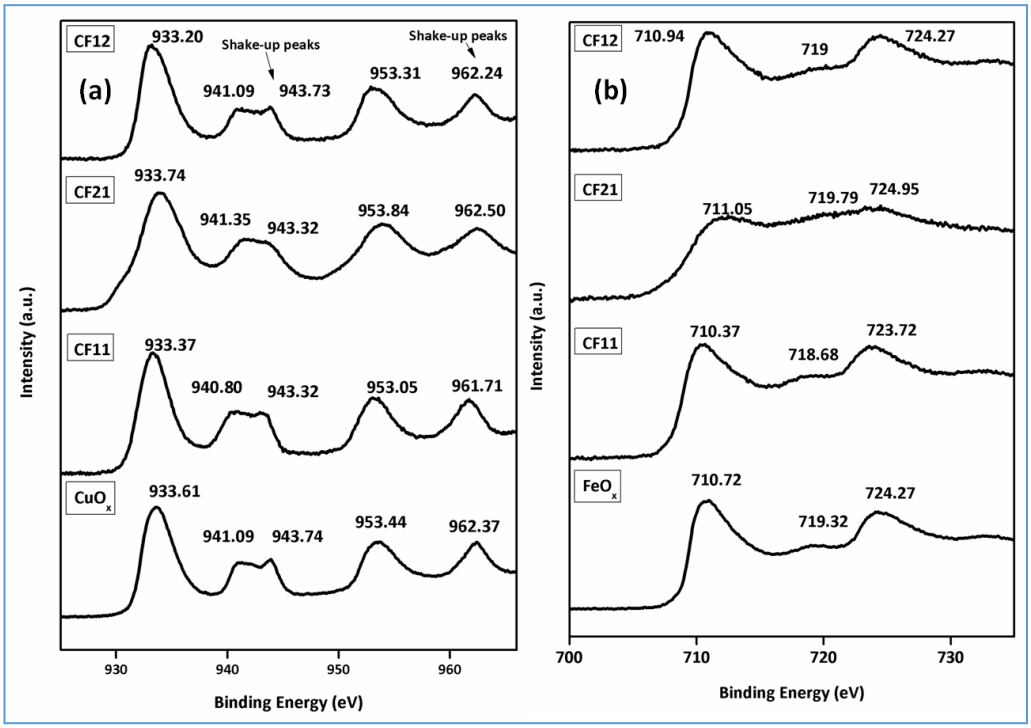

Figure 4.6: XPS scan survey profile of **(a)** Cu and **(b)** Fe

In order to understand various phase formation in catalyst as observed in XRD Cu $2p_{3/2}$, Fe $2p_{3/2}$ and O 1s XPS spectra of every variant of Cu-Fe were extensively interpreted along with monometallic Cu and Fe. **Figure 4.7** presents the detailed deconvolution of XPS peaks for Cu $2p_{3/2}$. In bare CuO_x three peaks were observed at B.E. of 932.79, 933.89 and 935.64 eV, representing Cu(0), CuO and $Cu(OH)_2$ species. Presence of these $Cu(OH)_2$ species were also observed by satellite peaks of Cu $2p_{3/2}$ and O 1s spectra of CuO_x. Also the presence of metallic Cu was supported by presence of string satellite peaks as mentioned earlier ruling

out the possibility of Cu_2O. Even H_2 TPR described later also supported the absence of Cu(+1) [43-45].

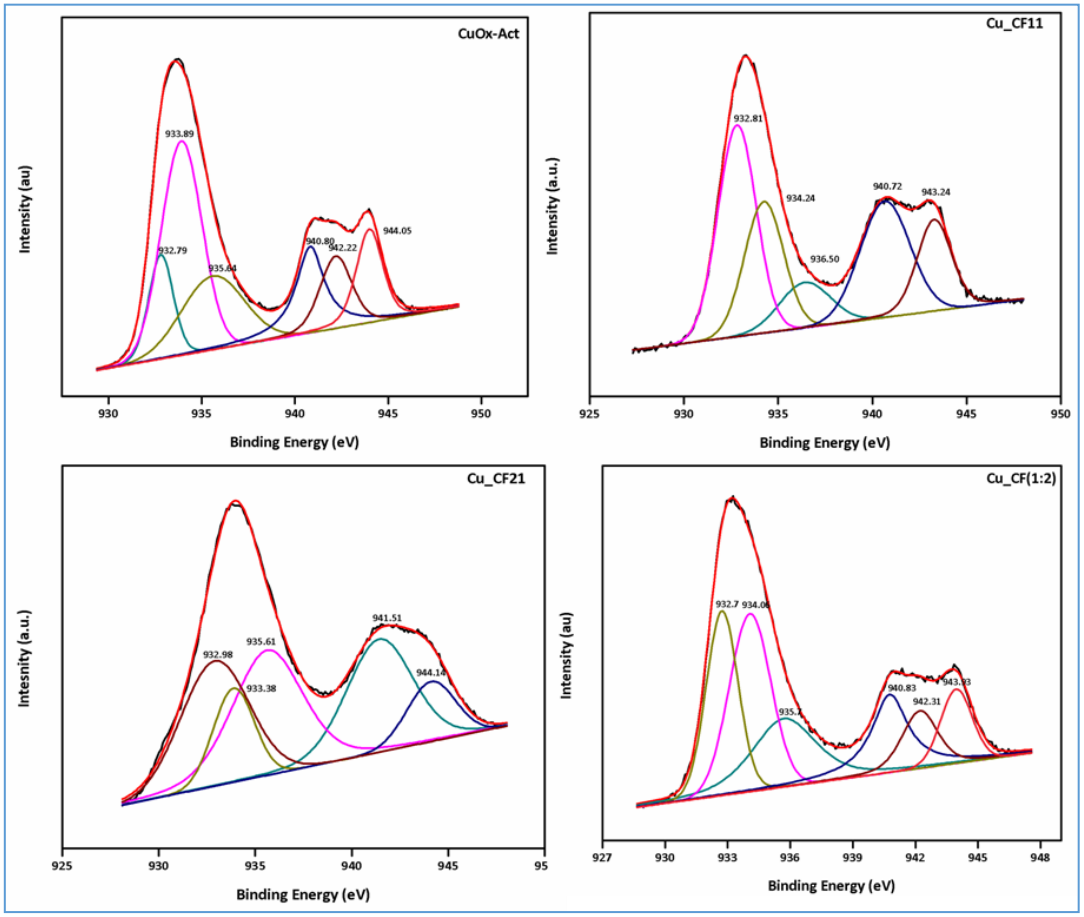

Figure 4.7: Phases of Cu $2p_{3/2}$ determined by XPS analysis in all the screened catalysts: **(a)** Cu in CuOx-Act, **(b)** Cu in Cu–Fe(1 : 1), **(c)** Cu in Cu–Fe (2 : 1) and **(d)** Cu in Cu–Fe (1 : 2)

The satellite peaks at B.E. of 940.80, 942.22 and 944.05 eV represented different oxide peaks of Cu. Similar trends were seen in other catalysts also with bimetallic combination but with varying intensity. In Cu-Fe(1:1) Cu $2p_{3/2}$ showed increased metallic nature at B.E. of 932.81 eV whereas relative intensity of other peaks decreased significantly indicating our successful reduction protocol at 523 K. But clear indication of catalytic synergism and new phase formation was visible due to shift of binding energy towards higher value *i.e.* 936.50 eV suggesting presence of Cu(+2) species in different chemical environment (tetrahedral CuO in $CuFe_2O_4$) than monometallic Cu [46]. Second major peak at B.E. of 934.24 eV can be assigned

to octahedral CuO as mentioned elsewhere [47]. When Cu was taken in excess Cu-Fe(2:1), these CuO species in different environment was found in slightly higher intensity than metallic Cu whereas, a considerable amount of native CuO was also present. Almost equal amounts of Cu(0) at B.E. of 932.7 eV and octahedrally coordinated CuO at B.E. of 934.04 eV was seen in most efficient Cu-Fe(1:2). Tetrahedrally coordinated CuO was also observed in the form of broad hump at 531.7 eV. Analysis of Cu $2p_{3/2}$ revealed that there is certainly catalytic synergism occurring between Cu and Fe in form of $CuFe_2O_4$ along with Cu(0) which can be the reason of excellent catalytic activity of our catalyst. The surface composition of Fe is shown in **Figure 4.8**.

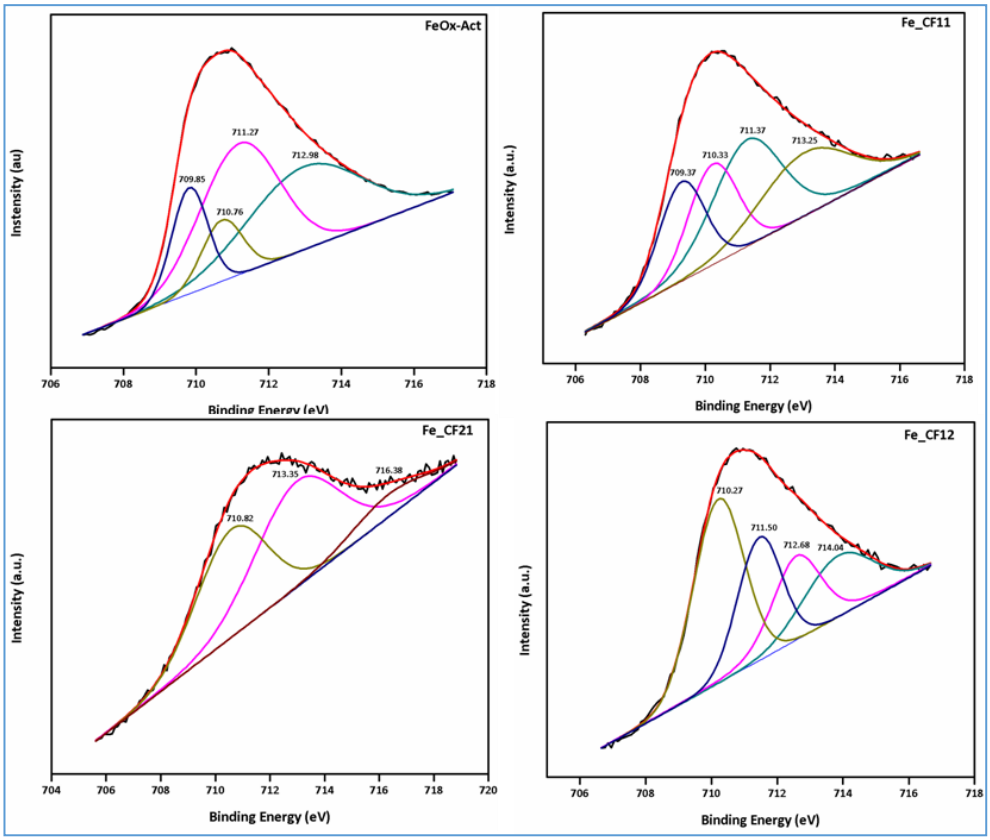

Figure 4.8: XPS analysis of different Fe $2p_{3/2}$ phases in all the screened catalysts: **(a)** Fe in FeO_x, **(b)** Fe in Cu–Fe(1 : 1), **(c)** Fe in Cu–Fe(2 : 1) and **(d)** Fe in Cu–Fe(1 : 2)

Fe $2p_{3/2}$ deconvolution in **Figure 4.8** clearly shows various oxide phases of Fe as its difficult to reduce the Fe below 873 K. In the monometallic FeO_x mixture of phase *i.e.* magnetite

(Fe_3O_4), haematite (α-Fe_2O_3) and wustite (FeO) were observed at binding energies of 710.76, 711.27 and 709.85 eV. The presence of Fe_3O_4 was further supported by the broad hump observed at B.E. of 712.98 eV [48-49]. All these results were in accordance with the observation of our XRD studies. Like Cu, here also shifting towards higher binding energy was observed after bimetallic combination suggesting onset of mutual catalytic synergism. In equimolar Cu-Fe(1:1) the shift in binding energy of Fe_3O_4 was seen from 712.98 to 713.25 eV indicating new phase formation [50]. This shift continued to increase in excess Cu and Fe variants due to appearance of $CuFe_2O_4$ though most intense peak was due to α-Fe_2O_3 at B. E. of 710.98eV. Two XPS impressions were also observed in Cu-Fe(1:2) at B.E. of 714.04 and 716.38 eV which could be assigned to the modified FeO species due to different chemical vicinity of $CuFe_2O_4$ [51-52]. Since oxides of both the metals were present, the nature of oxygen species can reveal significant information related to nanohybrid pair and Fe species and their respective roles in hydrogenation of 5-HMF to DMF. O 1s of all the catalysts was analysed and shown in **Figure 4.9**.

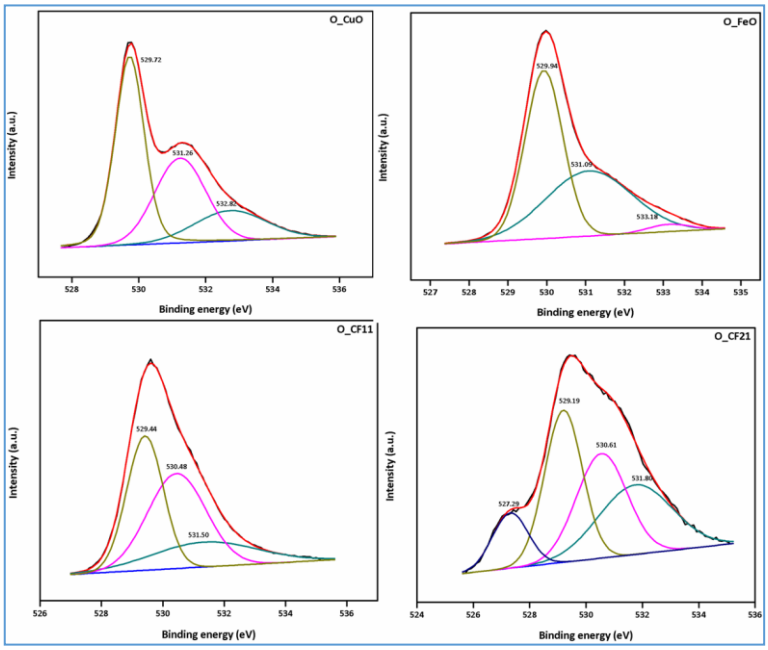

Figure 4.9: Nature of oxygen in all screened catalysts as determined by XPS analysis: (a) O in CuO_x, (b) O in FeO_x, (c) O in Cu–Fe(1:1) and (d) O in Cu–Fe(2:1).

It was observed that except Cu-Fe(2:1), all the other variants showed three type of species in the form of lower binding energy (~ 529 eV) medium binding energy (~531 eV) and higher binding energy (~533 eV). On careful evaluation of relative intensity of various peaks, it was observed that monometallic CuO_x and FeO_x showed almost similar pattern. Lower binding energy corresponding to lattice oxygen was observed at B.E. of 529.72 eV for CuO_x and at B.E. of 529.94 eV for FeO_x whereas subsurface –OH groups or lateral oxide species showed its presence at 531.60 eV for CuO_x and at 531.09 eV for FeO_x [(53)].

Table 4.2: Relative intensity and summary of various oxide species observed in O1s of catalysts

Contents / **Catalyst**	**Binding Energy (eV)**	**Area Percentage (%)**	**FWHM**	**Nature**
CuO	529.72 531.60 533.82	47.63 34.66 17.70	1.01 1.79 2.52	O^{2-} of M-O (Lattice Oxygen) Subsurface –OH groups/lateral Oxygen Chemisorbed H_2O ($O^-/O_2^{2-}/O_2^-$)
FeO	529.94 531.09 533.18	52.23 45.17 2.59	1.15 2.62 1.3	O^{2-} of M-O (Lattice Oxygen) Subsurface –OH groups/ lateral Oxygen Chemisorbed H_2O ($O^-/O_2^{2-}/O_2^-$)
Cu-Fe(1:1)	529.44 530.48 531.50	37.56 42.44 19.99	14 2.24 4.03	O^{2-} of M-O (Lattice Oxygen) O coordinated in dual environment Subsurface –OH groups/ lateral

				Oxygen
Cu-Fe(2:1)	527.29 529.19 530.61 531.80	10.90 31.68 29.24 28.33	1.49 1.57 2.11 3.07	Surface Oxide defects of crystal O^{2-} of M-O (Lattice Oxygen) O coordinated in dual environment Subsurface –OH groups/ lateral Oxygen
Cu-Fe(1:2)	529.93 531.16 532.20	52.85 24.63 22.50	1.25 1.59 2.48	O^{2-} of M-O (Lattice Oxygen) O coordinated in dual environment Subsurface –OH groups/ lateral Oxygen

Similarly, satellite peak related to oxide species of chemisorbed H_2O with very low intensity was seen at higher binding energy (533.84 eV and 533.18 eV) for both CuO_x and FeO_x respectively [(54)]. In case of bimetallic combinations of Cu and Fe oxygen species with different chemical environment were observed around B.E. of ~530 eV suggesting formation of new phase *i.e.* $CuFe_2O_4$ at 530.48 eV for Cu-Fe(1:1), 530.61 eV for Cu-Fe(2:1) and 531.16 eV for Cu-Fe(1:2). Exceptionally surface oxide defects were observed in the form of a tiny spike at B.E. of 527.09 eV for Cu-Fe(2:1) which can also be the reason for its good catalytic activity [(55)]. Comparative analysis of fresh and used catalyst was also done to get the idea of stability and structural changes in the catalyst (**Figure 4.10** and **Table 4.3**). In spent catalyst, amount of metallic Cu was clearly visible due to the obvious reason of reductive reaction environment.

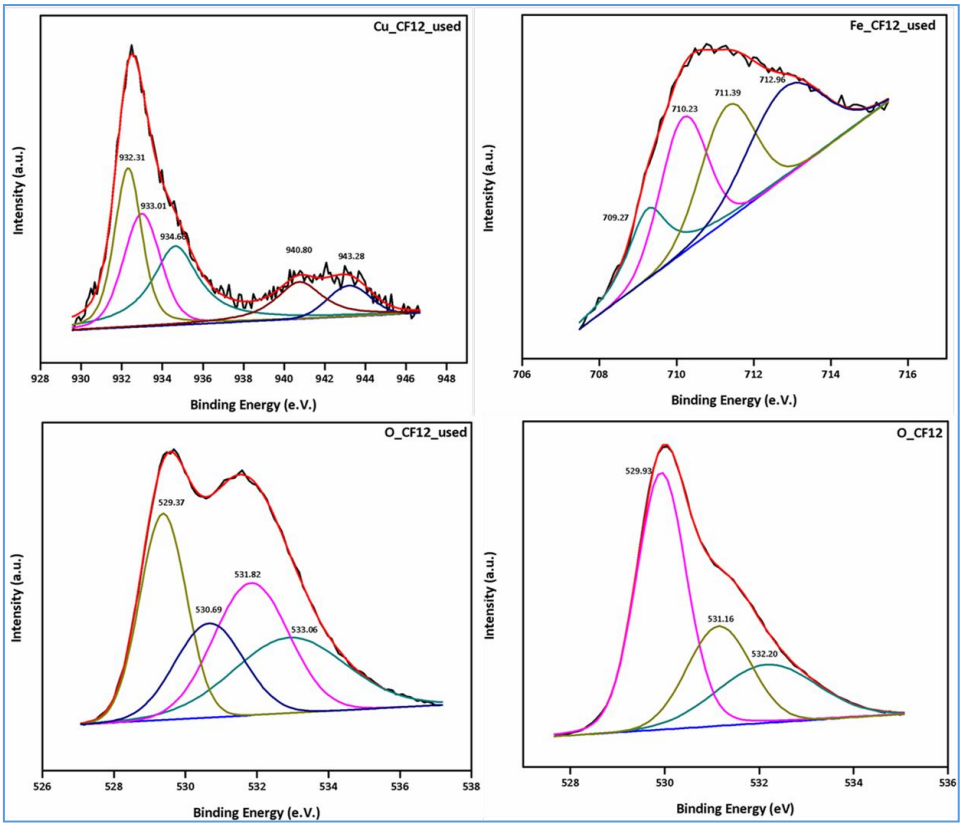

Figure 4.10: XPS of spent Cu–Fe(1:2) and the nature of Cu, Fe and O: (a) Cu in Cu–Fe(1:2)-used, (b) Fe in Cu–Fe (1:2)-used, (c) O in Cu–Fe(1:2)-used and (d) O in Cu–Fe(1:2)-fresh.

It was also observed that native CuO species decreased significantly at the cost of mixed CuO species and $Cu(OH)_2$. Decreased FWHM of higher binding energy is also revealing the quantitative increase of later. Similar decline of FWHM was also observed in the various species of Fe in spent Cu-Fe(1:2) which suggested increase in the oxide species of Fe due to its oxophillic nature in reaction media. Hydrogenation environment led to significant decline in the lattice oxygen species of the catalyst. Various oxygen species like ether derivatives and –OH group and organic matter deposition led to the appearance of less intense, weak multiple peaks with enhanced FWHM as shown in **Table 4.3** [(56)]. The presence of carbonaceous deposition was also examined and supported by C1s deconvolution of spent Cu-Fe(1:2) as shown in **Figure 4.11**. Various carbonaceous species related to unstaurated –C=C, saturated sp3 C-C, carbon bonded to hydroxyl group (C-OH), etherified carbonaceous array (C-O-C)

and ester group (O-C=O) were observed at B.E. of 284.19, 284.75, 285.51, 286.57 eV and 288.85 eVs respectively [57]. This carbon deposition decreased the catalytic activity in the catalyst recycle run which was also detected by Raman and TEM images, discussed later in this chapter.

Table 4.3: Summary of comparative analysis of various phase of Cu, Fe and O in Cu-Fe(1:2)-fresh and Cu-Fe(1:2)-used

Contents / **Catalyst**		**Binding Energy (eV)**	**Area Percentage (%)**	**FWHM**
Cu-Fe(1:2)-Fresh	**Cu $2p_{3/2}$**	932.7	32.06	1.79
		934.04	39.27	2.34
		935.1	28.67	3.62
	Fe $2p_{3/2}$	710.27	39.61	1.80
		711.50	23.06	1.57
		712.68	19.33	1.73
		714.04	17.99	2.47
	O 1s	529.93	52.85	1.25
		531.16	24.63	1.49
		532.20	22.50	2.48
	Cu $2p_{3/2}$	932.31	33.83	1.59
		933.01	30.47	2.16
		934.68	35.77	2.75

Cu-Fe(1:2)-Used	**Fe $2p_{3/2}$**	709.27	17.31	1.23
		710.23	27.05	1.42
		711.39	26.34	1.63
		712.96	29.29	2.30
	O 1s	529.37	27.45	1.52
		530.69	18.48	2.25
		531.82	28.55	2.48
		533.06	25.51	3.71

Thus, $Cu/CuFe_2O_4$ pair evidenced in XPS studies, have an excellent synergism including different oxide defects on the surface that strongly accelerated 5-HMF hydrogenation to 2, 5-DMF. All these results were also commensurate with our XRD analysis. Since Cu played a significant role in enhancing the selectivity to DMF, the quantitative composition of each phase of Cu in each catalyst based on relative peaks intensity are also given in **Table 4.4**.

Table 4.4: Relative intensity of Cu/CuO in all the catalysts

Sr. No.	**Catalysts**	**Cu/CuO**
1	CuOx	0.2052
2	Cu-Fe(1:1)	1.0911
3	Cu-Fe(2:1)	0.6210
4	Cu-Fe(1:2)	0.4720

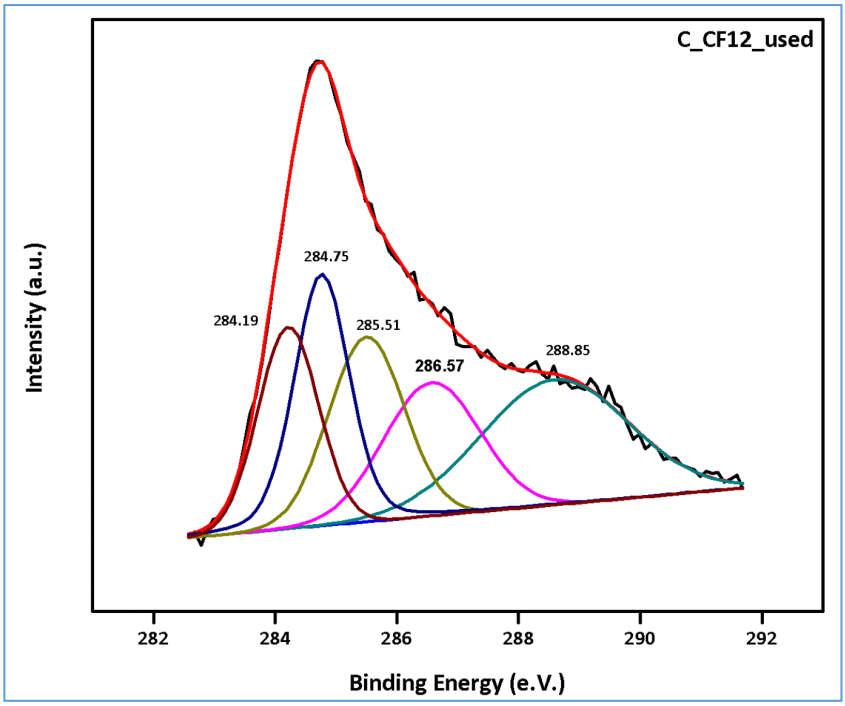

Figure 4.11: XPS of C 1s peak deconvolution in Cu-Fe(1:2)-Spent

4.3.7 CO_2-TPD

Surface chemisorbed properties of Cu and Fe were studied by various temperature programmed desorption studies.

Table 4.5: Basicity by CO_2-TPD analysis

Sr. No.	**Catalysts**	**Temperature Range (ºC)**			**Total CO_2 desorbed**
		25-250	**250-500**	**500-750**	
1	CuO_x	0.368	0.0346	0.0097	0.4123
2	FeO_x	0.1574	0	0	0.1574
3	Cu-Fe(1:1)	0.1665	0.1592	0.0377	0.3634
4	Cu-Fe(2:1)	0.2996	0	0.0023	0.3019

5	Cu-Fe(1:2)	0.1068	0.0141	0.0035	0.1244

It was reported that excess of Cu impart surface basicity which in 5-HMF hydrodeoxygenation can reduce the selectivity of DMF because of increase amount of oligomers whereas Fe is known for its surface acidity which played a vital role in efficient catalytic activity [58].

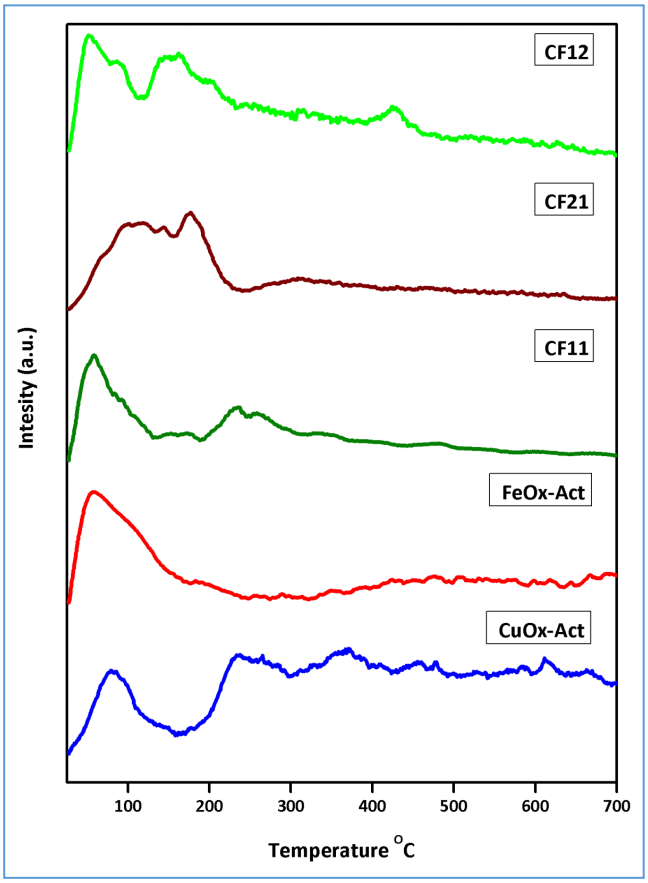

Figure 4.12: CO_2-TPD analysis of all the screened catalyst for 5-HMF hydrodeoxygenation

The quantification of surface basic properties of the catalyst was estimated by CO_2 TPD as shown in **Figure 4.12** and the basicity was calculated in form of total CO_2 desorbed (**Table 4.5**). It was very clear from **Table 4.5** that Cu contained higher number of basic sites which is the probable reason of its limited catalytic oligomerization property whereas Fe showed very

less basicity (**Table 4.5**, **entries 1 and 2**). Bimetallic catalysts were devoid of any clear trend which can be due to the phase transitions in catalytic lattice. Most efficient catalyst Cu-Fe(1:2) showed least surface basicity which can be another reason for its higher selectivity.

4.3.8 NH_3-TPD and Py-IR Analysis

As mentioned earlier surface acidic properties can prove extremely vital for catalytic efficiency hence, NH_3-TPD analysis of our catalysts was also done (**Figure 4.13.a** and **Table 4.6**).

Table 4.6: Acidity by NH_3-TPD analysis

Sr. No.	**Catalysts**	**Temperature Range (°C)**			**Total NH_3 desorbed (mmol/g)**
		25-200	**200-400**	**400-750**	
1	CuO_x	0.0280	0.1640	0.0203	0.2123
2	FeO_x	0.3788	0.0228	0.0752	0.4768
3	Cu-Fe(1:1)	0.2495	0.5149	0.0457	0.8101
4	Cu-Fe(2:1)	0.0429	0.0679	0.0783	0.1891
5	Cu-Fe (1:2)	0.1126	0.0563	0.0765	0.2454

The nature of acidity and its quantitative estimation was later determined by Pyridine adsorbed IR analysis (**Figure 4.13** and **Tables 4.7** and **4.8**). As mentioned earlier higher amount of NH_3 was desorbed by FeO_x compared to CuO_x suggesting good amount of surface acidic properties. Maximum acidity was shown by equimolar Cu-Fe whereas in case of

excess metal content variants *i.e.* Cu-Fe(2:1) and Cu-Fe(1:2) the value decreased suggesting higher amount of interaction of both metals compared to Cu-Fe(1:1).

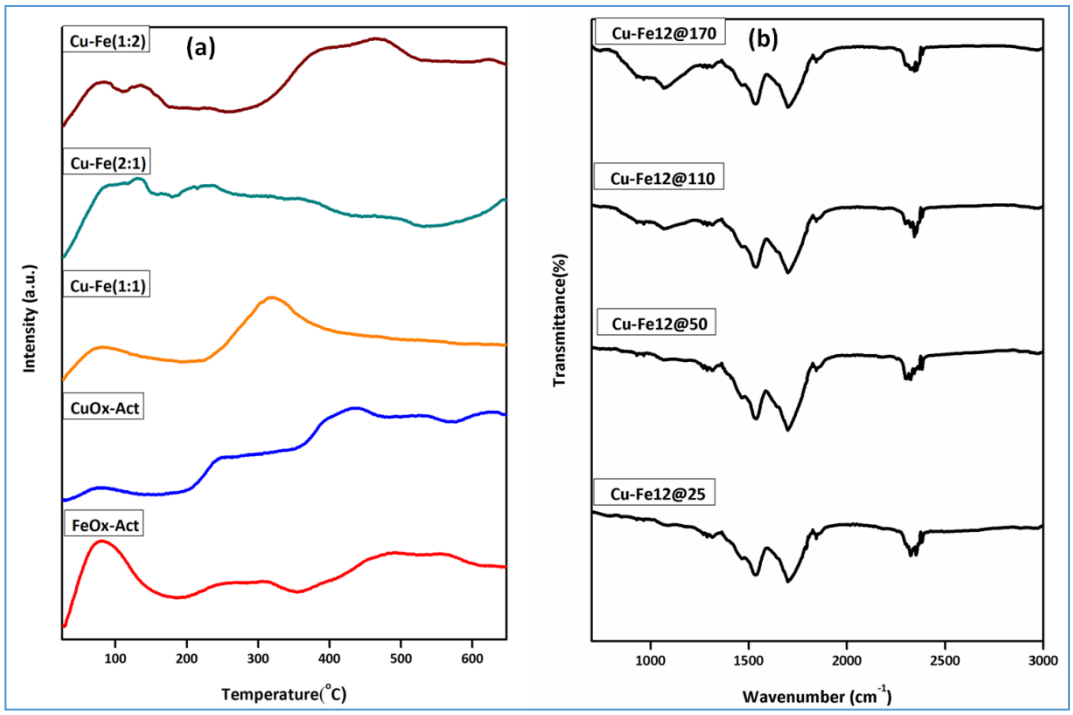

Figure 4.13: (a) NH_3-TPD profile of all the catalysts **(b)** Estimation of various acidic sites on Cu-Fe(1:2) at different temperature by Pyridine-IR

Amount of strong acidity observed was also higher in bimetallic Cu-Fe(1:2) and Cu-Fe(2:1) than in monometallic Cu and Fe. This also suggested that well dispersed acidity was desirable for the hydrodeoxygenation rather than unorganised higher acidity.

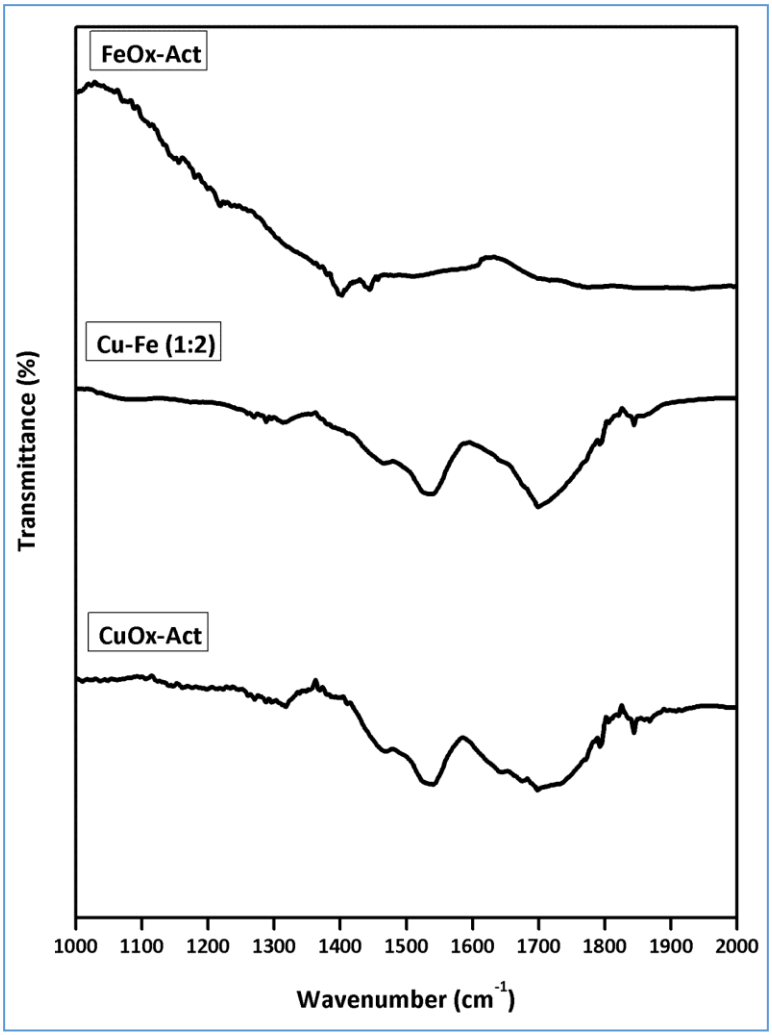

Figure 4.14: Pyridine-IR of different catalyst

Py-IR of the catalyst revealed that Fe was the source of Lewis acidity (BA/LA=0.5294) whereas Brönsted acidic sites were present in Cu (BA/LA= 6.8226) as shown in **Table 4.7** though, the Brönsted acidic value was only slightly higher for Fe than Cu. BA/LA value also decreased in bimetallic variants where Cu-Fe(1:2) had minimum value of BA/LA whereas the Cu-Fe(1:1) had the highest value. This was due to the high amount of Lewis acidic sites of Fe in Cu-Fe(1:2). Similarly almost double Brönsted acidic sites than Lewis acidic sites were found in Cu-Fe(2:1). All these observation obtained from NH_3-TPD and Py-IR revealed that there is certain Cu-Fe synergism and interaction is going on which concluded as Cu(0)-

$CuFe_2O_4$ from XRD and XPS studies. Given its higher catalytic efficiency Cu-Fe(1:2) was subjected to Py-IR analysis at various temperature (**Figure 4.13.b**).

Brönsted acidic sites and mixture of Brönsted and Lewis acidic sites were observed at 1540 cm^{-1} and 1698 cm^{-1}, respectively [59]. On careful evaluation of these two broad humps further two peaks related to Lewis acidity at 1455 cm^{-1} and Brönsted acidity at 1640 cm^{-1} was found embedded [60]. In comparative analysis with monometallic catalysts, peaks at 1440 cm^{-1} and 1630 cm^{-1} in FeO_x and 1540 cm^{-1} were seen in CuO_x corresponding to inherent Lewis and Brönsted acidity, respectively. The Lewis acid centre of Cu-Fe catalyst can activate –C=O group of 5-HMF which further can lead to sideways binding between catalytic surface and electron rich oxygen of carbonyl group which enhances the synthesis of BHMF and neutralise the decarbonylation activity of Cu whereas Brönsted acidity of Cu-Fe catalyst enhances the dehydration of BHMF which proves decisive in determining selectivity of hydrogenolysis pathway [61-62]. Hence, both the acidic properties play an important role in the hydrogenation as well as dehydration step of the reaction mechanism as discussed later.

Table 4.7: BA/LA of all the catalysts by Py-IR analysis

Sr. No.	**Catalysts**	**Types of Acidity**		**TBA/TLA**
		Total Lewis Acidity (TLA)	**Total Brönsted Acidity (TBA)**	
1	CuOx	0.0344	0.2347	6.8226
2	FeOx	0.4743	0.2511	0.5294
3	Cu-Fe(1:1)	0.0196	0.0656	3.3469
4	Cu-Fe(2:1)	0.1519	0.3268	2.1514

5	Cu-Fe (1:2)	0.3195	0.2337	0.7314

4.3.9 H_2-TPR

In order to understand the reductive nature and course of hydrogenation, all the Cu-Fe variant salong with monometallic were subjected to H_2-TPR studies (**Figure 4.15**). An asymmetric bimodal peak was observed at 234 °C with first mode at 195 °C which can be assigned to the complete reduction of CuO species to metallic Cu [(63)]. Bimodal nature may be due to the different size of Cu nanoparticles eliminating any possibility of any other oxidation state of Cu. This was in well accordance with the results of XRD and XPS analysis which suggested that reduction of Cu_2O to metallic Cu requires elevated temperature and that powdered CuO_x tends to reduce directly to the metallic Cu instead of any kind of intermediate phases like Cu_2O or Cu_4O_3 [(64)].

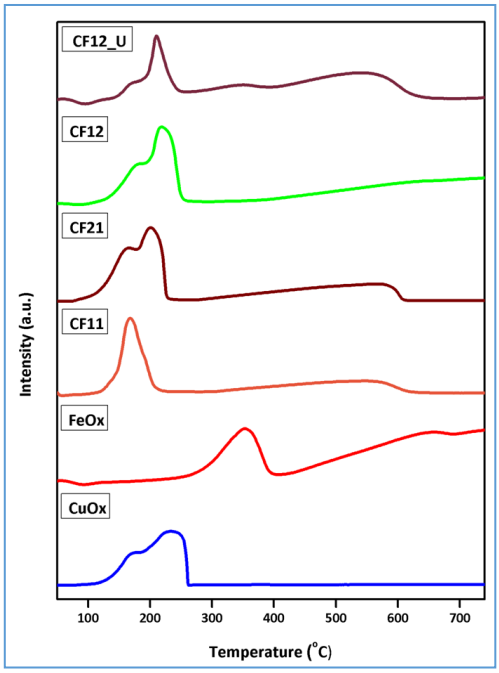

Figure 4.15: H_2-TPR of the screened catalysts: Cu–Fe(1:1) is represented as CF11, Cu–Fe(1:2) as CF12, Cu–Fe (2:1) as CF21 and spent Cu–Fe (1:2) as CF12_U

The H_2 treatment of FeO_x showed three major peaks at 301.47°C, Fe_3O_4 to FeO at 552.68°C corresponding to conversion of α-Fe_2O_3 to Fe_3O_4 and finally appearance of metallic Fe at very high temperature of 698.16°C [65]. The lower temperature bimodal maxima related to variable sizes of nanoparticles and interaction of Cu ad Fe in Cu-Fe(1:2) ad Cu-Fe(2:1) whereas it was unclear in Cu-Fe(1:1) with perturbations at higher temperature as a result of reduction activities of sequential reduction of different Fe species as described earlier [66]. Cu-Fe(1:2) showed dissimilar reduction profile compared to earlier catalyst where appearance of two shoulder peaks revealed the presence deposition of carbonaceous oxides on the surface. Similar interaction of organic medium was observed with Fe in the form of a maxima at 458.86°C [67]. Another usual peak at higher temperature was related to complete reduction of Fe. First reduction of all the catalysts was at relatively lower temperature of 170-230 °C and was due to their mesoporous nature which was also evident in our BET surface area studies. The presence of mesoporous nature is known to reduction of the T_m in case of copper ferrites [68].

4.4 Activity Evaluation

Table 4.8 presents screening of various catalysts for 5-HMF hydrodeoxygenation. Monometallic catalysts like CoO_x, CuO_x and FeO_x were investigated initially to understand the catalytic efficiency of individual metals and it was found that CuO_x and FeO_x showed better result than CoO_x for which 47% conversion observed without any hydrogenation product (**Table 4.8, entry 1**). Though FeO_x showed very less conversion *i.e.* 39% but promising product distribution was found without any side reaction unlike CuO_x where decarbonylation was also observed with hydrogenation process.

Table 4.8: Catalyst screened for 5-HMF hydrogenation into DMF; **Reaction Conditions:** 5-HMF=100 mg; Solvent (IPA)=20 g; Catalyst = 50 mg; temperature = 443 K; H2 pressure = 300 psig, reaction time = 4 h; agitation speed = 1000 rpm

Sr. No.	**Catalysts**	**Conv (%)**	**Selectivity (%)**				
			DMF	**BHMF**	**MFFR**	**MFAL**	**2-MF +FAL**
1	CoO_x-NP	47	0	0	0	0	0
2	CuOx-NP	80	59	6	6	10	19
3	FeOx-NP	39	16	38	10	25	0
4	Cu-Fe(1:1)	85	72	8	3	7	10
5	Cu-Fe(2:1)	95	84	3	1	1	11
6	Cu-Fe(1:2)	97	93	4	1	2	0

In case of FeO_x, BHMF (38%) and MFAL (25%) were major products with only 16% of the desired product, DMF whereas CuO_x showed an excellent conversion of 80% with 59% selectivity to DMF. Other intermediates like BHMF, MFAL and MFFR were also present in low amount but most importantly, 17% of 2-methyl furan (2-MF) and traces of furfuryl alcohol (FA) were showing competitive reaction between hydrodeoxygenation and decarbonylation. Considering all these results, Cu and Fe were considered as metals of interest and several variants having their different molar ratios were prepared and screened for 5-HMF hydrogenolysis. Cu:Fe(1:1) led to 85% conversion of 5-HMF with 72% selectivity to DMF suggesting catalytic synergism but still 10% decarbonylation products were hampering the DFF selectivity. Since decarbonylation was more prominent, Fe was

taken in double amount than Cu and it was found that there was no decarbonylation for Cu-Fe(1:2) with very high selectivity of 93% to DMF and 97% conversion whereas variant with excess Cu produced almost 11% of decarbonylation though consumption of 5-HMF was almost similar to Cu-Fe(1:2) *i.e.* 95%. 84% DMF was observed in the Cu-Fe(2:1) with 3% BHMF and equal amount of MFFR and MFAL (1% each) (**Table 4.8, entry 5**). The formation of 4% BHMF as well as c-t profile (**Figure 4.22**) that the hydrogenation route of 5-HMF initiated via hydrogenation of –C=O group (**Reaction Scheme 4.1**). This may be attributed to the oxophillic nature and Lewis acidity of Fe. The excellent conversion of BHMF into DMF is because of Brönsted acidity of Cu/$CuFe_2O_4$ as observed by various characterisation techniques earlier.

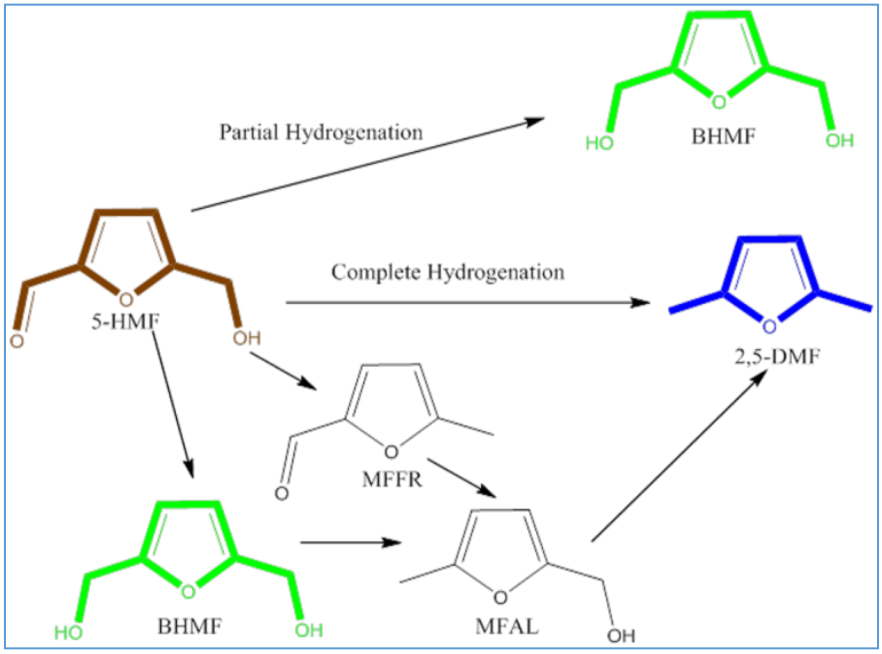

Reaction Scheme 4.1: Reaction pathway of 5-HMF hydrodeoxygenation

4.4.1 Temperature Effect

Effect of temperature on the reaction profile was studied as shown in **Figure 4.16**. Limited catalytic efficiency was observed at lower temperature and a steep rise in it was seen with rise in temperature.

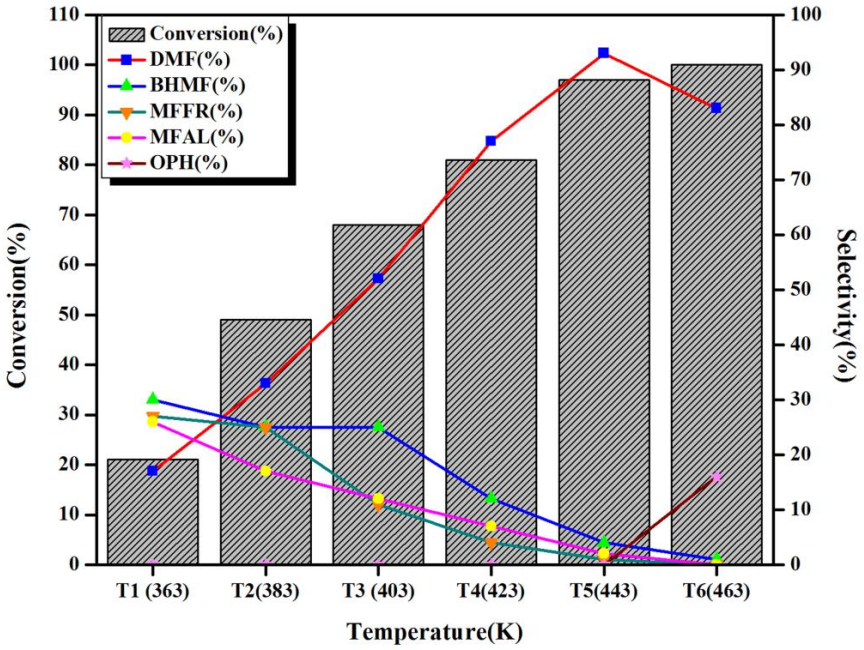

Figure 4.16: Temperature effect on 5-HMF hydrogenation; **Reaction conditions:** 5-HMF = 100 mg; catalyst = 50 mg; solvent (IPA) = 20 g; H2 pressure = 300 psig; reaction time = 4 h; agitation speed = 1000 rpm

At 363 K hydrogenation reaction was more dominant on hydrogenolysis with poor conversion (21%) as 30% BHMF and only 17% DMF appeared along with 27% MFFR and 26% MFAL. Further 20 K rise in temperature triggered the hydrogenolysis activity of Cu(0)-CuFe2O4 as almost half of 5-HMF consumed (49%). The major product was DMF with 33% share whereas other reaction intermediate like BHMF and MFFR have selectivity of 25% each. Another 20 K increase in temperature brought the conversion of 5-HMF to 68% and first time more than half of consumed 5-HMF appeared as DMF (52%). It was interesting to note that BHMF was still the second major product in the reaction products suggesting first step as partial hydrogenation. When reaction was studied at 423 K conversion jumped to 81% with 77% selectivity towards DMF. Here also 12% BHMF appeared as second major product along with 4% MFFR and 7% MFAL. Best catalytic activity was witnessed at 443 K where almost 97% of 5-HMF get consumed with excellent 93% selectivity to DMF. Reaction profile

was also investigated at 463 K but ring hydrogenation products appeared in reaction aliquots reducing the selectivity of DMF to 83%.

4.4.2 H_2 Pressure Effect

Effect of pressure of external H_2 was studied in the range of 100-500 psig and it was found that 300 psig was the most suitable pressure for 5-HMF hydrodeoxygenation.

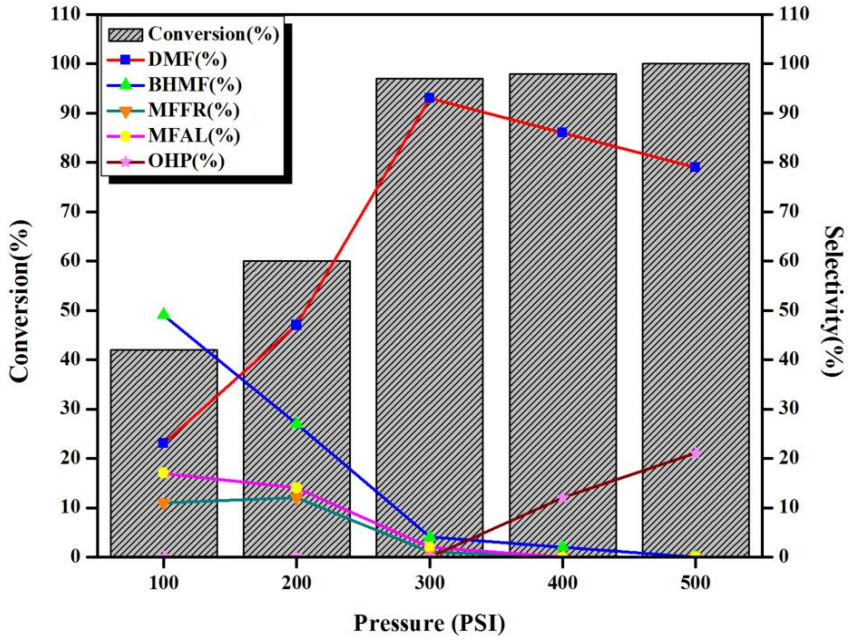

Figure 4.17: Effect of H_2 pressure on the hydrogenation of 5-HMF; **Reaction conditions:** 5-HMF = 100 mg; catalyst = 50 mg; solvent (IPA) = 20 g; temperature = 443 K; reaction time = 4 h; agitation speed = 1000 rpm

Lower pressure conditions were more suitable for hydrogenation of 5-HMF as BHMF appeared as major product (49%) and DMF only 23% with 41% conversion. Just like temperature effect, here also increase in pressure was beneficiary for DMF selectivity. After 2 fold increase in external pressure the selectivity increased to 47% with 59% conversion. This rise in both the catalytic activity parameters was consistent at 300 psig where 97% 5-HMF consumed with 93% selectivity to DMF As shown in **Figure 4.17**. Further increase in pressure led to decline in selectivity of DMF to 84% though conversion was always

complete. At 400 psig, ring hydrogenated product like HMFTHF, DMTHF and ether derivatives of various alcoholic group starts to appear which enhanced to 21% from 12% in case of 500 psig suggesting threshold peak of Cu(0)/$CuFe_2O_4$ at 300 psig of H_2. This sharp decline in the selectivity to DMF was due to the ring opening of 5-HMF which led to the formation of 2, 5-hexanediol.

4.4.3 Catalyst Loading Effect

Figure 4.18 presents effect of different catalyst loadings on 5-HMF hydrodeoxygenation and it was revealed that the best 5-HMF/catalyst ratio is 2 at optimum reaction conditions.

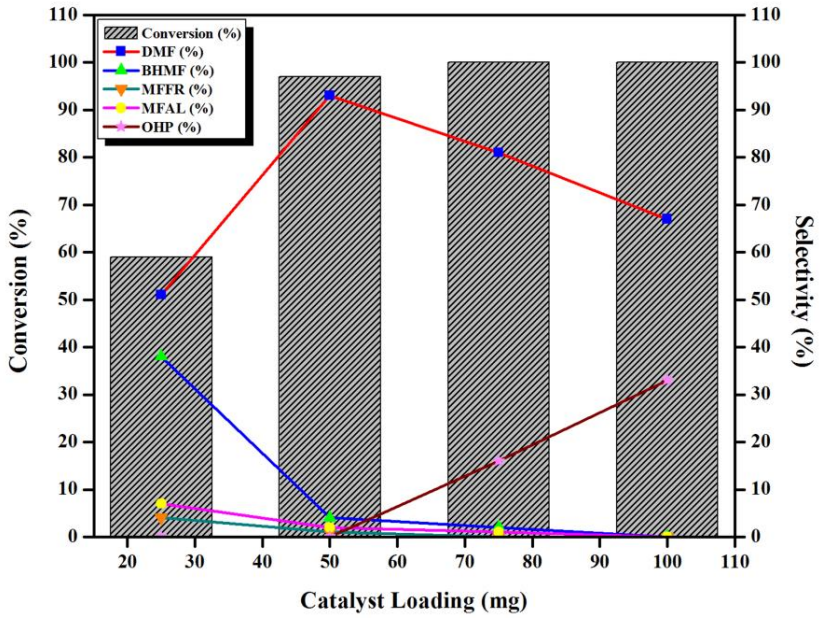

Figure 4.18: Effect of catalyst loading on 5-HMF hydrogenation; **Reaction conditions:** 5-HMF = 100 mg; solvent (IPA) = 20 g; temperature = 443 K; H_2 pressure = 300 psig; reaction time = 4 h; agitation speed = 1000 rpm

Catalyst loading effect was studied in the range of 25 to 100 mg and it was found that even at lower loading value (20 mg) conversion was moderate (59%) but giving lower selectivity of 51% to DMF. A good amount of hydrogenation intermediate, BHMF (38%) was observed with traces of MFFR and MFAL at lower loading of 20 mg. The best catalytic activity with

97% conversion of 5-HMF and DMF selectivity of 93% was observed at 50 mg loading of catalyst. Consumption of 5-HMF further increased on 3 fold increase of catalytic amount but selectivity of DMF took a dip to 80% due to appearance of DMTHF (14%). Similar observation repeated in 5-HMF/Catalyst=1 where ring hydrogenated products and other side product raised to 33% with 100% conversion. Hence, 50 mg of catalyst amount was taken as standard loading of the catalyst in the present work.

4.4.4 Agitation Speed Effect

Effect of agitation speed on the 5-HMF conversion and product distribution was also studied in the range of 600 to 1200 rpm and the results are given in **Figure 4.19**. 5-HMF conversion as well as DMF selectivity increased with increase in agitation speed from 600 to 1000 rpm. Complete conversion of 5-HMF as well as DMF selectivity was achieved at 1000 rpm hence it was considered as the standard agitation parameter.

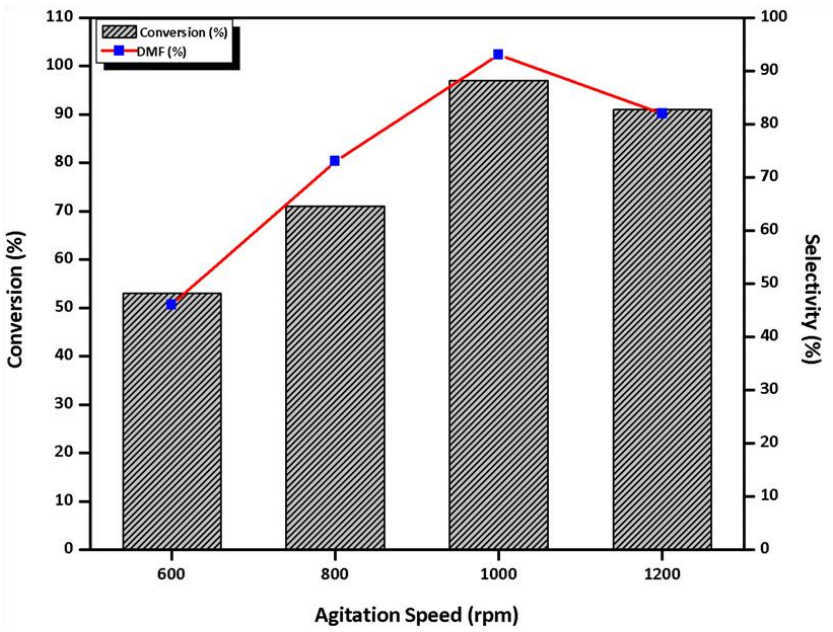

Figure 4.19: Effect of agitation speed on 5-HMF hydrogenation; **Reaction conditions:** 5-HMF = 100 mg; catalyst = 50 mg; solvent (IPA) = 20 g; temperature = 443 K; H_2 pressure = 300 psig; reaction time = 4 h

4.4.5 Solvent Effect

Solvents have a significant effect on the reaction profile as the solubility of both liquid and gaseous reactants viz. 5-HMF and H_2 play an important role. Hence various solvents screened were water, methanol, isopropyl alcohol and n-butanol for 5-HMF hydrogenation and the results are shown in **Figure 4.20**. Among various solvents studied, 2-propanol proved to be the best solvent due to its tendency to donate hydrogen, moderate boiling point, less polarity, low dielectric constant and less bulky nature [(70)]. Less solubility of 5-HMF and steric hinderance originated due to its bulky nature, n-butanol yielded only 67% DMF with 74% conversion of 5-HMF [(71)].

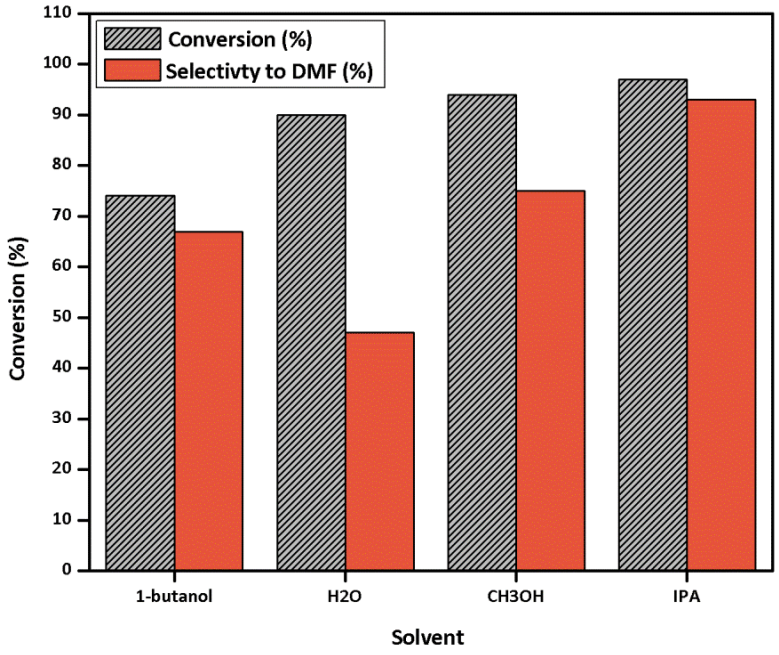

Figure 4.20: Effect of the solvent on 5-HMF hydrogenation; **Reaction conditions:** 5-HMF = 100 mg; catalyst = 50 mg; solvent = 20 g; temperature = 443 K; H2 pressure = 300 psig; reaction time = 4 h; agitation speed = 1000 rpm

Aqueous reaction media led to poor selectivity of DMF (47%) and 90% conversion of 5-HMF which may be due to lower H_2 solubility. Formation of significant amount of BHMF (32%) can be attributed to the solvolysis effect of H_2O [(72)]. High conversion of 5-HMF (94%)

was seen in case of methanol but the selectivity of DMF reduced to 75% only. Lower alcohols are known for etherification reaction and hemiketal formation at higher temperature with other alcoholic counterpart [73]. Here also we observed some methoxy ethers of 5-HMF and BHMF during GC-MS analysis which can be responsible for its low efficiency as reaction media for 5-HMF hydrogenation.

4.4.6 Reaction Time Effect

Figure 4.21 presents the effect of reaction time on 5-HMF hydrogenation. The reaction was monitored for maximum of 8 h. For longer reaction duration, higher extent of over hydrogenated products was formed.

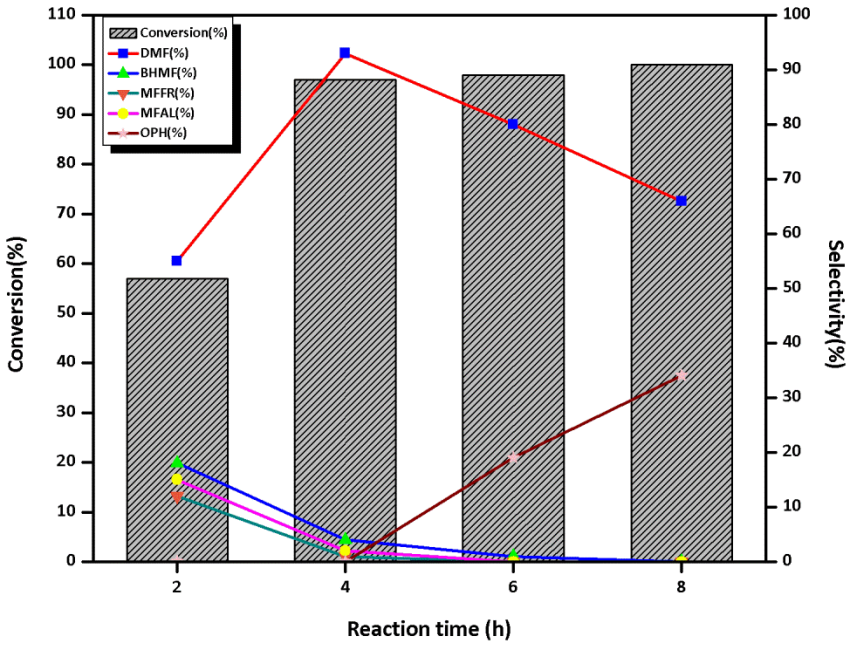

Figure 4.21: Effect of reaction time on 5-HMF hydrodeoxygenation; **Reaction conditions:** 5-HMF = 100 mg; catalyst = 50 mg; solvent (IPA) = 20 g; temperature = 443 K; H_2 pressure = 300 psig; agitation speed = 1000 rpm

When reaction was extended to 8 h, considerate amount of DMTHF (34%) was observed which reduced the selectivity of DMF to 66%. This observation suggested that catalyst was also capable of hydrogenation of delocalised C=C bond of 5-HMF ring. For reaction time of

6 h, 19% mixture of BHMTHF and DMTHF was observed. During initial 2 h of reaction time, C-O bond hydrogenation was in progress as total 33% (15% MFFR and 18% MFAL) hydrogenolysis products were observed. The best reaction time was found to be 4 h for 5-HMF hydrogenation to give DMF in high selectivity of 93%,

4.4.7 C-t Profile

In order to understand the course of catalytic reaction and efficiency of catalyst, conversion/selectivity profile was plotted as a function of time as shown in **Figure 4.22**. First hour of reaction showed 38% consumption of 5-HMF and the first step hydrogenation product, BHMF as the major product (33%). The selectivities of DMF and MFAL were 32% and 22%, respectively, whereas 13% MFFR was also seen indicating that the hydrogenation as the initial step (1 h) was in progress rather than hydrogenolysis of 5-HMF. In the second hour of reaction, DMF took over as a major product with 55% selectivity indicating the acceleration of hydrogenolysis activity of the catalyst along with BHMF (18%), MFAL (15%) and MFFR (12%) as other minor products. A significant increase in the conversion of 5-HMF from 38 to 57% also occurred in first 2 h. Hydrogenolysis nature of Cu-Fe(1:2) dominated clearly in third hour where 74% conversion of 5-HMF took place with remarkable increase in selectivity of DMF to 79%. With the progress in reaction time, BHMF further hydrogenolysed to DMF and at the end of 4^{th} hour selectivity of DMF increased to 93%. Here products other than DMF were MFAL (2%), BHMF (4%) and MFFR (1%) with 97% conversion of 5-HMF.

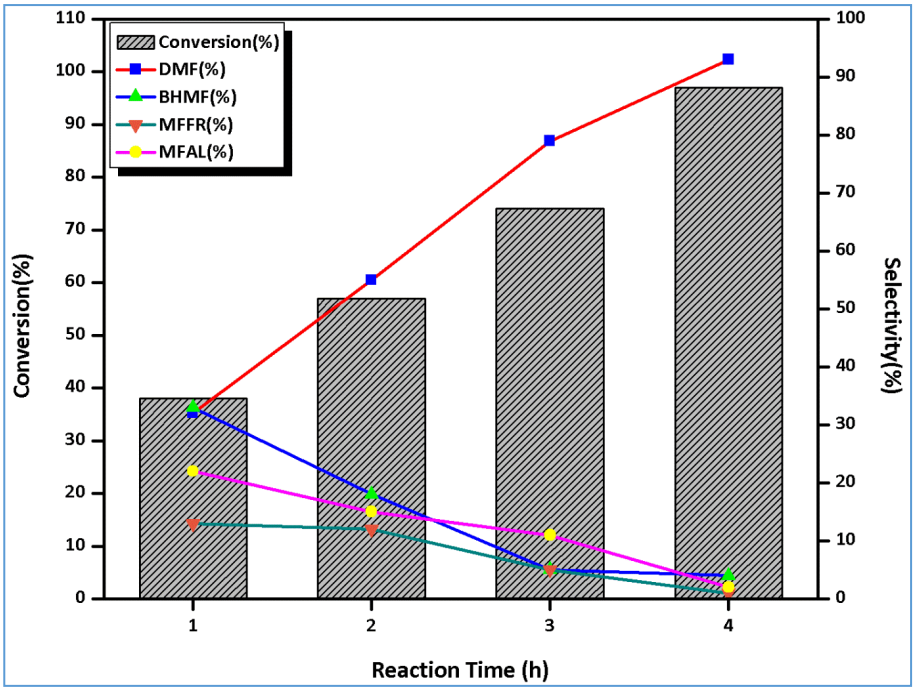

Figure 4.22: (a) C–t profile of 5-HMF hydrodeoxygenation; **Reaction conditions:** 5-HMF = 100 mg; catalyst = 50 mg; solvent (IPA) = 20 g; temperature = 443 K; H_2 pressure = 300 psig; reaction time = 4 h; agitation speed = 1000 rpm

4.4.8 Catalyst stability

Hot filtration test was conducted for Cu-Fe(1:2) during 5-HMF hydrodeoxygenation to ensure absence of any metal leaching. In a conventional protocol, reaction was stopped after 2 h and catalyst was separated from the reactor by a magnet and reaction was carried out without any catalyst further for 4 h. (**Figure 4.23.a**)

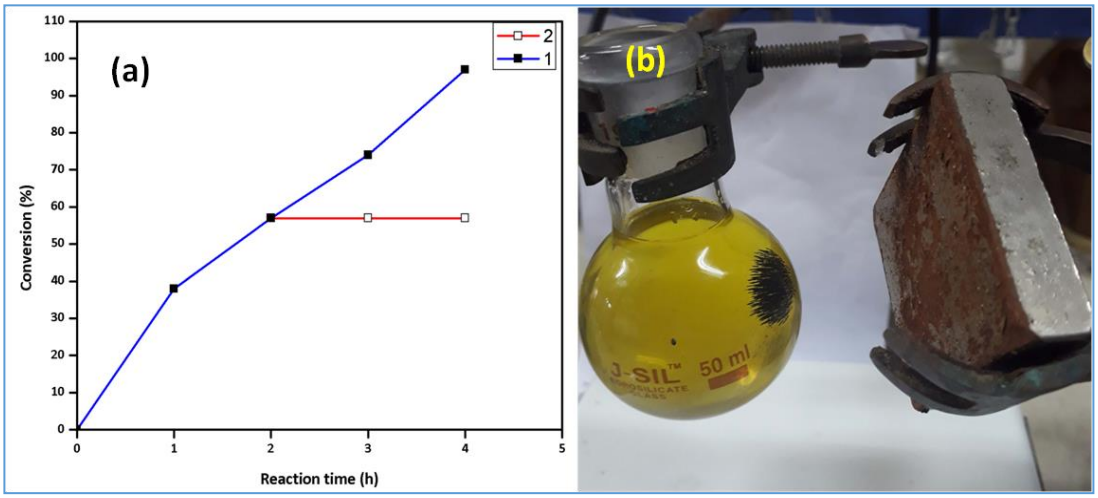

Figure 4.23: (a) Metal leaching study of 5-HMF hydrodeoxygenation**; Reaction conditions:** 5-HMF = 100 mg; catalyst = 50 mg; solvent = 20 g; temperature = 443 K; pressure = 300 psig; reaction time = 4 h; agitation speed = 1000 rpm; (1) with Cu–Fe (1 : 2) and (2) without Cu–Fe (1 : 2) **(b)** Magnetic recoverability of Cu–Fe (1 : 2)

As shown in **Figure 4.23.a** conversion showed coordinates parallel to X–axis indicating that no conversion occurred which confirmed that no any kind of metal leaching for Cu-Fe(1:2) catalyst occurred during reaction.

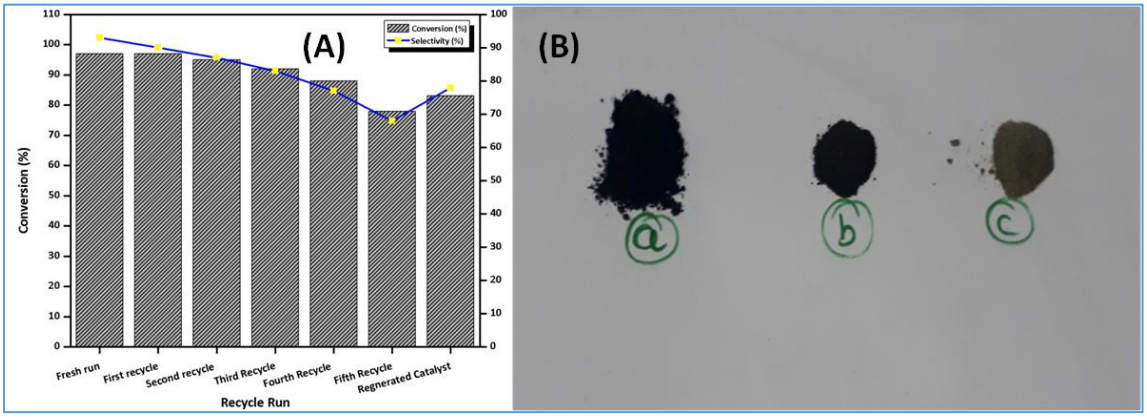

Figure 4.24: (a) Catalyst recycling study of 5-HMF hydrogenation; **Reaction conditions:** 5-HMF = 100 mg; catalyst = 50 mg; solvent = 20 g; temperature = 443 K; pressure = 300 psig; reaction time = 4 h; agitation speed = 1000 rpm **(b)** Colour changes during recycling

Observations of hot filtration test were supported by the SEM-EDX of spent Cu-Fe(1:2) where Cu and Fe showed almost similar concentration as that of fresh Cu-Fe(1:2) (**Figure 4.25**). Magnetic recoverability of Cu-Fe(1:2) was clearly visible from **Figure 4.23.b** and it remained active in all the recycle run. The recycle run of most efficient Cu-Fe(1:2) were also conducted to examine its reusable efficacy and its stability in the reaction medium. The catalyst was recyclable successfully with good efficiency till 4 recycles as shown in **Figure 4.24.a**.

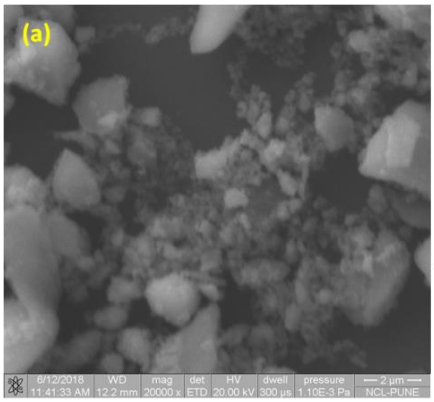

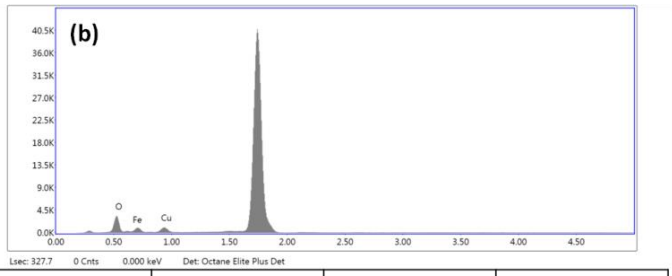

Element	Weight %	Atomic %	Error %
O K	36.04	67.33	6.60
FeK	39.81	21.31	2.42
CuK	24.16	11.37	4.02

Figure 4.25: (a) E-SEM of spent Cu-Fe(1:2) (b) EDX pattern of Cu-Fe(1:2)_spent

It was observed that selectivity of Cu-Fe(1:2) reduced earlier than conversion of 5-HMF. The conversion was similar for 1st recycle run whereas it decreased slightly for 2nd and 3rd recycle run *i.e.* 95% and 92% respectively. Consumption of 5-HMF decreased faster during 4th and 5th recycle run where it went 88% and 78% from 92% of 3rd recycle run. On the other hand selectivity to DMF was consistently decreasing after first recycle run. It was 90% for first recycle run and declined to 87% in second recycle. Similar rate of reduction in selectivity was observed for 3rd recycle run which witnessed 83% selectivity to DMF. The rate of decline in selectivity of DMF intensified from 4th recycle where it was 77% and remained only 68% for 5th recycle run. This categorical loss of catalytic efficiency was assigned to deposition of carbonaceous matter of reaction crude which made catalytic sites hard to access for 5-HMF.

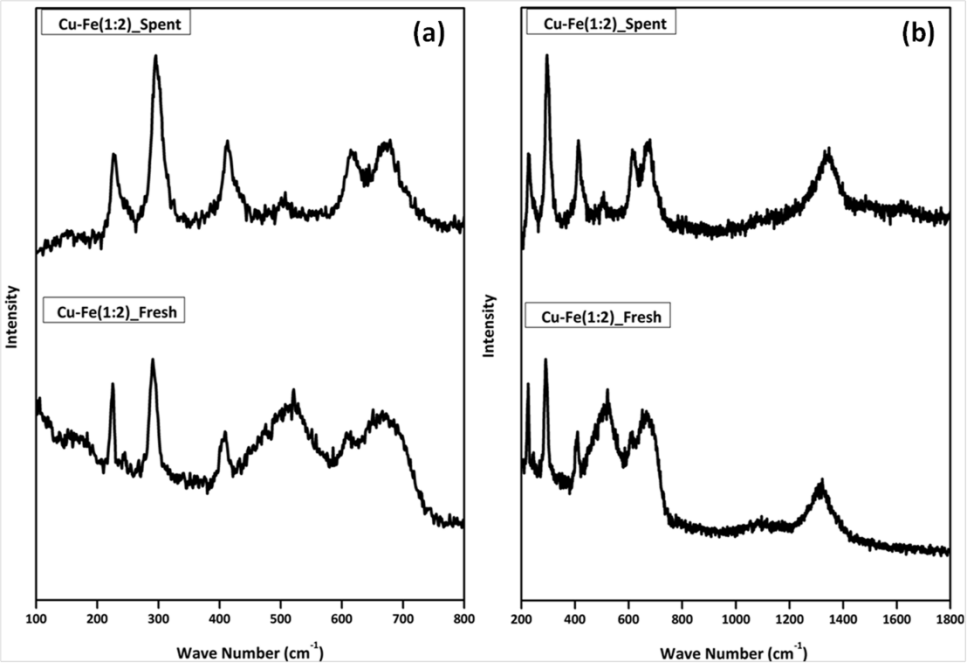

Figure 4.26: Raman spectra of fresh and spent Cu–Fe(1:2) ranging between **(a)** 100–800 cm^{-1} and **(b)** 200–1800 cm^{-1}.

The same fact was supported by the colour changes of our fresh and spent Cu-Fe(1:2) catalyst, comparative analysis of Raman spectroscopy (**Figure 4.26)** and TEM images (**Figure 4.27**) of the spent catalyst. Raman spectroscopy results of fresh and spent catalysts are shown in **Figure 4.26**. **Figure 4.26.a** showed the results in range of 100-800 cm^{-1} where F_{2g} phonon were observed at 226 cm^{-1}, 411 cm^{-1} and 508 cm^{-1}, A_{1g} phonon at 606 cm^{-1}, 693 cm^{-1} and 290 cm^{-1} were attributed to E_{1g} phonon of fresh Cu-Fe(1:2) [74]. These results showed the cubical inverse spinel phase of $CuFe_2O_4$ in which peak at 411 cm^{-1} revealed the octahedral position of metal cation whereas 606 cm^{-1} is attributed to the intrinsic stretching vibration of tetrahedral occupancy of metal cation. The broad hump nature of a peak at 508 cm^{-1} can be assigned to a mixture of different peaks which were related to secondary phase of haematite as shown in **Figure 4.26.b** with a peak at 1312 cm^{-1} [75]. This pattern was repeated in Cu-Fe(1:2) spent catalyst with obvious shifting of Raman peak because of biomass char

deposition. Pattern revealed from **Figure 4.26.b** confirmed it as it shows the spectra from 200 to 1800 cm^{-1}. It shows peaks of biomass char at 1622 cm^{-1} and 1347 cm^{-1} which are related G peaks of disordered coke and sp^2 C-C skeleton bands associated with organic material, respectively [76, 77]. The broadness of peak at 1347 cm^{-1} is attributed to its overlapping with haematite peak. This fact was also confirmed by TEM of spent catalyst.

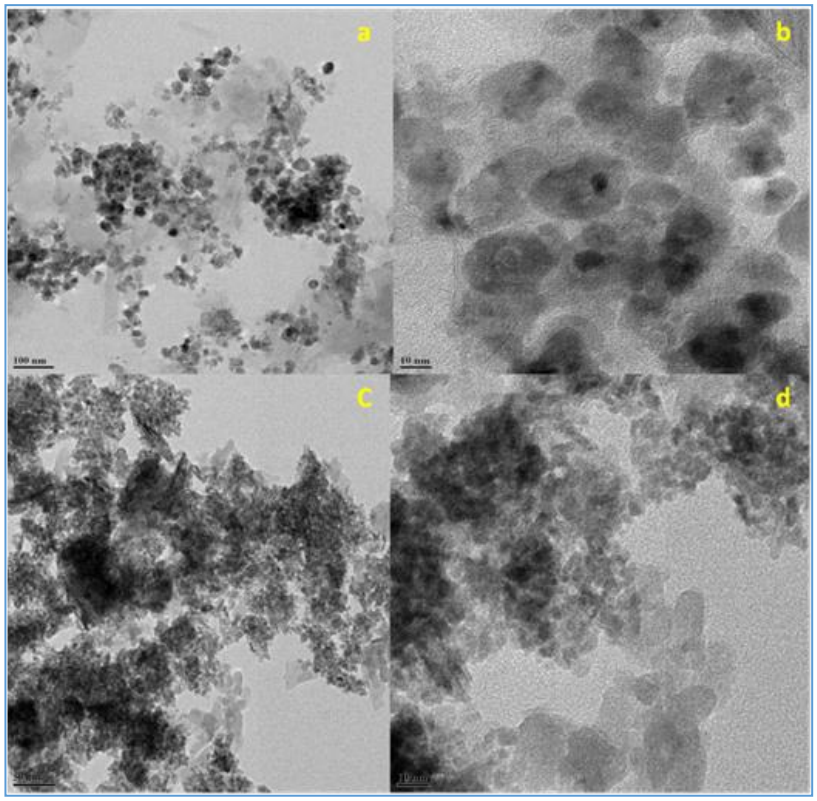

Figure 4.27: TEM pattern of spent Cu–Fe (1 : 2): **(a)** Cu–Fe (1 : 2)_1U at 100 nm; **(b)** Cu–Fe (1 : 2)_1U at 10 nm; **(c)** Cu–Fe (1 : 2)_5U at 50 nm and **(d)** Cu–Fe (1 : 2)_5U at 10 nm.

In the first recycle of catalyst deposition of carbonaceous matter was seen (**Figures 4.27.a** and **4.27.b**) whereas in the 5th recycle, growth of branched chain organic matter was clearly observed which indicate continuous deposition of on catalytic surface leading to inability of reactant to access catalytic active sites (**Figures 4.27.c** and **4.27.d**). An attempt to revive its activity was done by again treating it with the standard reduction protocol. The reaction with

the regenerated catalyst resulted into 83% conversion of 5-HMF with 78% DMF selectivity (**Figure 4.24.a**).

4.5 Plausible Reaction Pathway

A plausible reaction pathway for 5-HMF hydrodeoxygenation over Cu-Fe (1:2) is proposed in **Scheme 4.2**. 5-HMF hydrodeoxygenation was started by the initial activation of –C=O group due to the inherent Lewis acidity and oxophillic nature of Fe by attacking electron rich oxygen of the carbonyl group [78].

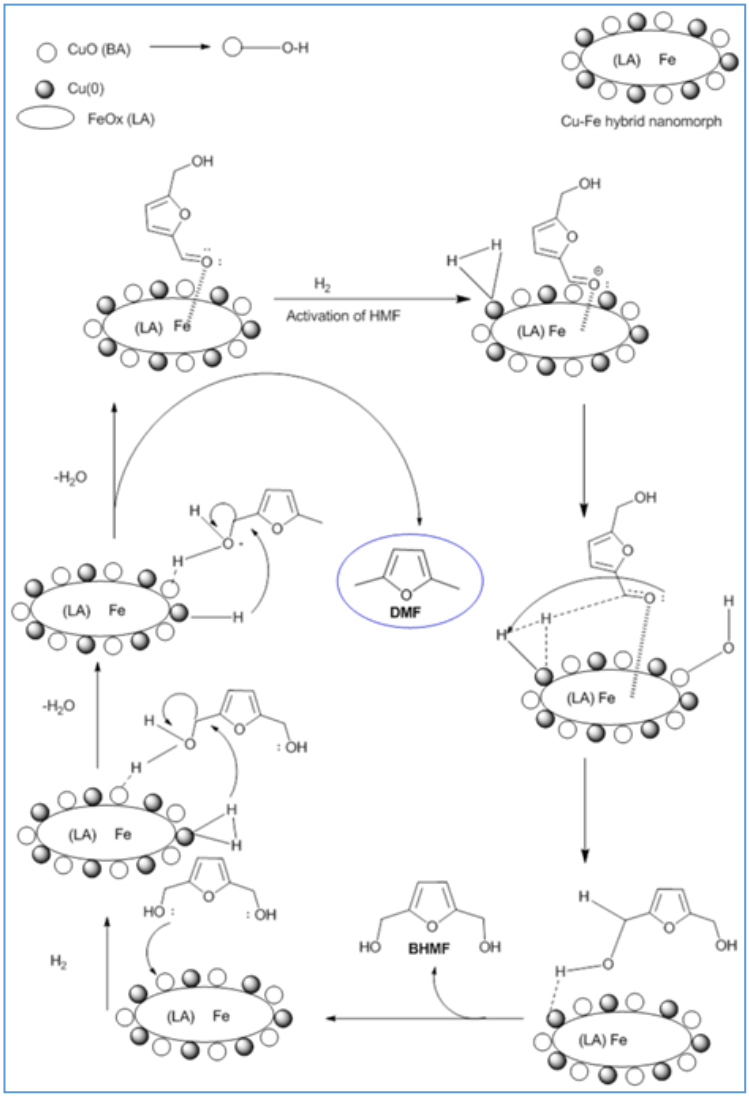

Reaction Scheme 4.2: Plausible reaction mechanism of 5-HMF hydrodeoxygenation

As a result of this, H_2 molecule which dissociates on the metallic Cu of Cu-Fe nanomorph attacked the electrophillic carbon of –C=O group giving BHMF as an initial reaction intermediate. This enhanced the rapid dehydration of BHMF into the DMF *via* MFAL. The O 1s spectra of Cu and Fe were showing O-H nature as observed during XPS analysis (**Figure 4.10.d**). This can be the reason why the Cu and Fe shows higher Brönsted acidity as by Py-IR and NH_3-TPD discussed earlier. The combined Brönsted acidity of Cu and Fe species activated the hydroxymethyl group of BHMF for dehydration as shown in **Reaction Scheme 4.2**. This leads to the formation of 2,5-dimtehylfuran (DMF) as the sole product. Some control experiments were also performed to deduce the reaction pathway for 5-HMF hydrodeoxygenation. For example, when BHMF was used as a substrate; within 2 h, complete conversion of BHMF took place to give DMF. On further continuation of the reaction, presence of MFAL and traces of BHMTHF and DMTHF were also observed indicating ring hydrogenation of DMF. MFFR as a substrate showed complete conversion and selectivity towards DMF in about 2.5 h. This indicated that initial hydrogenation step of –C=O is slower while further step of dehydration was very fast. When MFAL was taken as a starting material, within just 1 h complete conversion into DMF was observed.

4.6 Conclusions

The magnetically retrievable bimetallic Cu-Fe(1:2) catalyst was found to be highly selective (93%) for 5-HMF hydrodeoxygenation to DMF because of its specific structural properties in the form of a hybrid nanomorph ($Cu(0)/CuFe_2O_4$) confirmed by XRD, XPS and SEM. It was found that Lewis acidity of Fe activated the 5-HMF for hydrogenation whereas, the combined Brönsted acidity of Cu and Fe species catalyzed the dehydration of BHMF and MFAL which was responsible for higher selectivity to DMF by hydrogenolysis. Studies of various reaction parameters were conducted to obtain the optimized reaction conditions for highest 5-HMF

conversion and DMF selectivity. It was found that at 443 K temperature, 5-HMF/catalyst=2 and 300 psig H_2 pressure, 97% conversion of 5-HMF took place within 4 h of reaction time. Based on our experimental work we can say that due to high affinity of Cu towards C-O bond and oxophillic nature of Fe, 5-HMF was efficiently converted into DMF.

References

1. J. C. Serrano-Ruiz and J. A. Dumesic, *Energy Environ. Sci.*, **2011**, 4, 83–99

2. G. W. Huber, S. Iborra and A. Corma, *Chem. Rev.*, **2006**, 106, 4044–4098

3. F. H. Isikgor and C. R.Becer, *Polym. Chem.*, **2015**, 6, 4497–4559

4. F. Rosillo-Calle, *J Chem Technol Biotechnol,* **2016**, 91, 1933–1945

5. P. Lauri, P. Havlík, G. Kindermann, N. Forsell, H. Böttcher and M. Obersteiner, *Energy Policy*, **2014**, 66, 19-31

6. Barlow M, Smith D, Steward D. Fuel composition. *European patent EP0082689*; **1983**

7. P. Zhang, X. Su, H. Chen, L. Geng and X. Zhao, *Sci Rep*, **2020**, 10, 1427-1428

8. K. Alexandrino, A. Millera, R. Bilbao and M. U. Alzueta, *Energy Fuels,* **2019**, 33, 9851–9858

9. Q. Zhang, J. Zuo, L. Wang, F. Peng, S. Chen and Z. Liu, *ACS Omega,* **2021**, 6, 10910–10920

10. D. Li , Q. Liu , C. Zhu , H. Wang , C. Cui , C. Wang , L. Ma, *Journal of Energy Chemistry*, **2019**, 30, 34-41

11. N. Chen, Z. Zhu, T. Su, W. Liao, C. Deng, W. Ren, Y. Zhao, H. Lü, *Chemical Engineering Journal*, **2020**, 381, 122755

12. N. Ma, Y. Song, F. Han, G. I. N. Waterhouse, Y. Li and S. Ai, *Catal. Sci. Technol.*, **2020**, 10, 4010–4018

13. N. Chen, Z. Zhu, H. Ma, W. Liao, H. Lü, *Molecular Catalysis*, **2020**, 486, 110882

14. M. S. Gyngazova, L. Negahdar, L. C. Blumenthal and R. Palkovits, *Chemical Engineering Science*, **2017**, 173, 455–464

15. X. Kong, R. Zheng, Y. Zhu, G. Ding, Y. Zhu and Y. W. Li, *Green Chem.*, **2015**, 17, 2504–2514

16. P. Yang, Q. Cui, Y. Zu, X. Liu, G. Lu, Y. Wang, *Catalysis Communications*, **2015**, 66, 55–59

17. N. Siddiqui, A. S. Roy, R. Goyal, R. Khatun, C. Pendem, A. N. Chokkapu, A. Bordoloi and R. Bal, *Sustainable Energy Fuels*, **2018**, 2, 191–198

18. L. Yu, L. He, J. Chen, J. Zheng, L. Ye, H. Lin, and Y. Yuan, *Chemcatchem*, **2015**, 7, 1701-1707

19. S. Umasankar, P. Tamizhdurai, P. Santhana krishnan, S. Narayanan, V.L. Mangesh, K. Shanthi, *Biomass and Bioenergy*, **2020**, 143, 105868

20. Y. B. Huang, M. Y. Chen, L. Yan, Q. X. Guo, and Y. Fu, *ChemSusChem*, **2014**, 7, 1068–1070

21. T. S. Hansen, K. Barta, P. T. Anastas, P. C. Fordc and A. Riisager, *Green Chem.*, **2012**, 14, 2457–2461

22. G. Bottari, A. J. Kumalaputri, K. K. Krawczyk, B. L. Feringa, H. J. Heeres, and K. Barta, *ChemSusChem* **2015**, 8, 1323 –132

23. B. Chen, F. Li, Z. Huang, and G. Yuan, *Applied Catalysis B: Environmental*, **2017**, 200, 192–199

24. L. M. Esteves, M. H. Brijaldo, E. G. Oliveira, J. J. Martinez, H. Rojas, A. Caytuero and F. B. Passos, *Fuel*, **2020**, 270, 117524-117537

25. K. Zhao, K. Lyu, S. Liu, Q. Gan, Z. He and Z. Zhou, *Journal of material science*, **2017**, 52, 446-457

26. M. Sharma, B. Das, M. Sharma, B. K. Deka, Y. B. Park, S. K. Bhargava and K. K. Bania, *ACS Appl. Mater. Interfaces*, **2017**, 9, 3453–3462

27. R. B. Mane, S. E. Kondawar, P. S. Niphadkar, P. N. Joshi, K. R. Patil and C. V. Rode, *Catal. Today*, **2012**, 198, 321–329

28. E. Agouriane, B. Rabi, A. Essoumhi, A. Razouk, M. Sahlaoui, B. F. O. Costa and M. Sajeiddin, *J. Mater. Environ. Sci.*, **2016**, 7, 4116–4120

29. R. B. Mane, A. A. Hengne, A. A. Ghalwadkar, S. Vijayanand, P. H. Mohite, H. S. Potdar and C. V. Rode, *Catal. Lett.*, **2010**, 135, 141–147

30. R. B. Mane and C. V. Rode, *Green Chem.*, **2012**, 14, 2780– 2789

31. Y. Cudennec and A. Lecerf, *Solid State Sci.*, **2003**, 5, 1471– 1474

32. Y. Deng, D. Qi, C. Deng, X. Zhang and D. Zhao, *J. Am. Chem. Soc.*, **2008**, 130, 28–29

33. R. Han, W. Li, W. Pan, M. Zhu, D. Zhou and F. S. Li, *Sci. Rep.*, **2014**, 4, 7493–7497

34. K. Faungnawakij, Y. Tanaka, N. Shimoda, T. Fukunaga, R. Kikuchi and K. Eguchi, *Appl. Catal., B*, **2007**, 74, 144– 151

35. K. Yan, X. Wu, X. An and X. M. Xie, *J. Alloys Compd.*, **2013**, 552, 405–408

36. K. Yan and A. Chen, *Fuel*, **2014**, 115, 101–108

37. G. Avgouropoulos and T. Ioannides, *Appl. Catal., A*, **2003**, 244, 155–167

38. X. M. Liu, W. D. Yin, S. B. Miao and B. M. Ji, *Mater. Chem. Phys.*, **2009**, 113, 518–522

39. R. B. Mane, S. E. Kondawar, P. S. Niphadkar, P. N. Joshi, K. R. Patil and C. V. Rode, *Catal. Today*, **2012**, 198, 321–329

40. B. J. Tan, K. J. Klabunde and P. A. Sherwood, *Chem. Mater.*, **1990**, 2, 186–191

41. P. Mills and J. L. Sullivan, *J. Phys. D: Appl. Phys.*, **1983**, 16, 723–732

42. T. Yamashita and P. Hayes, *Appl. Surf. Sci.*, **2008**, 254, 2441– 2449

43. C. C. Chusuei, M. A. Brookshier and D. W. Goodman, *Langmuir*, **1999**, 15, 2806–2808

44. J. Ghijsen, L. H. Tjeng, J. van Elp, H. Eskes, J. Westerink, G. A. Sawatzky and M. T. Czyzyk, *Phys. Rev. B: Condens. Matter Mater. Phys*, **1988**, 38, 11322–11330

45. J. P. Espinós, J. Morales, A. Barranco, A. Caballero, J. P. Holgado and A. R. González-Elipe, *J. Phys. Chem. B*, **2002**, 106, 6921–6929

46. C. Reitz, C. Suchomski, J. Haetge, T. Leichtwiess, Z. Jagličić, I. Djerdj and T. Brezesinski, *Chem. Commun.*, **2012**, 48, 4471–4473

47. J. L. Cao, Y. Wang, X. L. Yu, S. R. Wang, S. H. Wu and Z. Y. Yuan, *Appl. Catal. B*, **2008**, 79, 26–34

48. L. Dong, Z. Liu, Y. Hu, B. Xu and Y. Chen, *J. Chem. Soc., Faraday Trans.*, **1998**, 94, 3033–3038

49. S. J. Roosendaal, B. V. Asselen, J. W. Elsenaar, A. M. Vredenberg and F. H. P. M. Habraken, *Surf. Sci.*, **1999**, 442, 329–337

50. L. He, X. Li, W. Lin, W. Lia, H. Cheng, Y. Yu, S. I. Fujit, M. Arai and F. Zhao, *J. Mol. Catal. A: Chem.*, **2014**, 392, 143– 149

51. T. Schedeniedrig, W. Weiss and R. Schlogl, *Phys. Rev. B: Condens. Matter Mater. Phys*, **1995**, 52, 17449–17460

52. M. C. Biesinger, B. P. Payne, A. P. Grosvenor, L. W. M. Lau, A. R. Gerson and R. Smart, *Appl. Surf. Sci.*, **2011**, 257, 2717– 2730

53. A. P. Grosvenor, B. A. Kobe and N. S. McIntyre, *Surf. Sci.*, **2004**, 572, 217–227

54. C. R. Brundle, T. J. Chuang and K. Wandelt, *Surf. Sci.*, **1977**, 68, 459–468

55. B. R. Strohmeier, D. E. Levden, R. S. Field and D. M. Hercules, *J. Catal.*, **1985**, 94, 514–530

56. N. S. Date, A. M. Hengne, K. W. Huang, R. C. Chikate and C. V. Rode, *Green Chem.*, **2018**, 20, 2027–2037

57. A. Jha, D. W. Jeong, J. O. Shim, W. J. Jang, Y. L. Lee, C. V. Rode and H. S. Roh, *Catal. Sci. Technol.*, **2015**, 5, 2752–2760

58. Y. Zhou, S. Wang, M. Xiao, D. Han, Y. Lu and Y. Meng, *RSC Adv.*, **2012**, 2, 6831–6837

59. T. Mathew, B. B. Tope, N. R. Shiju, S. G. Hegde, B. S. Rao and C. S. Gopinath, *Phys. Chem. Chem. Phys.*, **2002**, 4, 4260–4267

60. K. Cheng, W. Song, Y. Cheng, H. Zheng, L. Wang, J. Liu, Z. Zhao and Y. Wei, *RSC Adv.*, **2018**, 8, 19301–19309

61. H. Li, H. Luo, L. Zhuang, W. Dai and M. Qiao, *J. Mol. Catal. A: Chem.*, **2003**, 203, 267–275

62. H. Y. Zheng, Y. L. Zhu, L. Huang, Z. Y. Zeng, H. J. Wan and Y. W. Li, *Catal. Commun.*, **2008**, 9, 342–348

63. H. Tan, M. N. Hedhill, Y. Wang, J. Zhang, K. Li, S. Sioud, Z. A. A. Talla, M. H. Amad, T. Zhan, O. E. Talla and Y. Han, *Catal. Sci. Technol.*, **2013**, 3, 3360–3370

64. J. Y. Kim, J. A. Rodriguez, J. C. Hanson, A. I. Frenkel and P. L. Lee, *J. Am. Chem. Soc.*, **2003**, 125, 10684–10692

65. G. Neri, A. M. Visco, S. Galvagno, A. Donato and M. Panzalorto, *Thermochim. Acta*, **1999**, 329, 39–46

66. K. Faungnawakij, Y. Tanaka, N. Shimoda, T. Fukunaga, R. Kikuchi and K. Eguchi, *Appl. Catal. B*, **2007**, 74, 144– 151

67. K. Faungnawakij, R. Kikuchi, T. Fukunaga and K. Eguchi, *Catal. Today*, **2008**, 138, 157–161

68. Y. Wang, H. Zhao, M. Li, J. Fan and G. Zhao, *Appl. Catal, B*, **2014**, 147, 543–545

69. L. Hu, X. Tang, J. Xu, Z. Wu, L. Lin and S. Liu, *Ind. Eng. Chem. Res.*, **2014**, 53, 3056–3064

70. N. S. Biradar, A. A. Hengne, S. S. Sakate, R. K. Swami and C. V. Rode, *Catal. Lett.*, **2016**, 146, 1611–1619

71. E. Toukoniitty, J. Kuusisto, V. Nieminen, M. Hotokka and T. Salmi, J. *Mol. Catal. A: Chem.*, **2003**, 192, 135–151

72. R. L. Augustine, R. W. Warner and M. J. Melnick, *J. Org. Chem.*, **1984**, 49, 4853–4856.

73. B. Minder, T. Mallat, P. Skrabal and A. Baiker, *Catal. Lett.*, **1994**, 29, 115–124.

74. B. J. Rani, B. Saravanakumar, G. Ravi, V. Ganesh, S. Ravichandran and R. Yuvakkumar, *J. Mater. Sci.: Mater. Electron.*, **2018**, 29, 1975–1984

75. B. K. Chatterjee, K. Bhattacharjee, A. Dey, C. K. Ghosh and K. K. Chattopadhyay, *Dalton Trans.*, **2014**, 43, 7930–7944

76. C Zhu, Q. Liu, D. Li, H. Wang, C. Zhang, C. Cui, L. Chen, C. Cai and L. Ma, *ACS Omega*, **2018**, 3, 7407–7417

77. A. Milani, M. Tommasini, V. Russo, A. L. Bassi, A. Lucotti, F. Cataldo and C. S. Casari, *Beilstein J. Nanotechnol.*, **2015**, 6, 480–491

78. H. Li, H. Luo, L. Zhuang, W. Dai and M. Qiao, *J. Mol. Catal. A: Chem.*, **2003**, 203, 267–275

Chapter 5

Selective oxidation of 5-HMF to DFF over alkali promoted Mn nanocomposite

Selective oxidation of 5-HMF to DFF over alkali promoted Mn nanocomposite

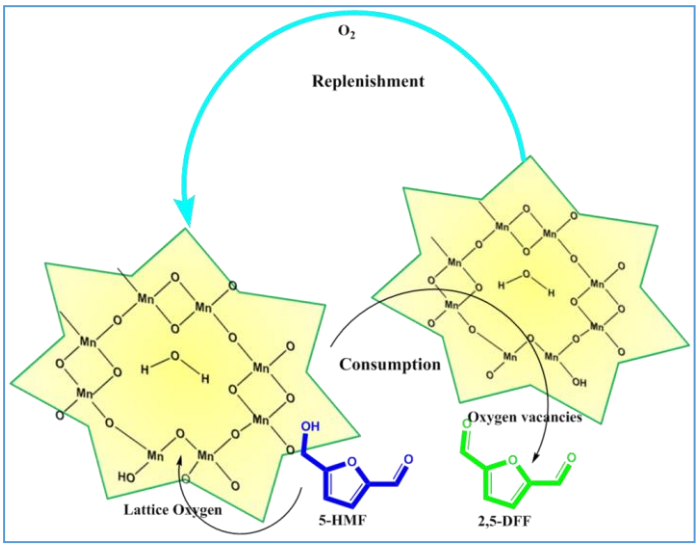

Various compositions of Cs promoted Mn were synthesized and investigated for selective oxidation of 5-HMF to DFF, among which Mn-Cs(80:20) was found to be most efficient giving 91% conversion of 5-HMF and 98% selectivity to DFF. Detail characterization like N_2-sorption, BET surface area, TG-DTA, XRD, XPS, FE-SEM-EDX, TEM, HR-TEM, CO_2-TPD, H_2-TPR, O_2-TPO, FTIR, Raman spectra and MeOH-IR were done to establish structure –activity correlation. Enhanced surface area, porosity, thermal stability, dual morphologies were observed due to inclusion of Cs in Mn lattice domain which further enhanced the crystallinity, and oxygen diffusion on the surface. Mixed morphologies comprising nanoparticles (4-5 nm) and nanorodes (50-60 nm) were observed with enhanced redox potential and reduced work function due to weakening of Mn-O bonds. Significant increase in the basicity of catalyst, interfacial redox properties, lattice oxygen led to highly efficient oxidation of 5-HMF to DFF *via* Mars-van Krevelen mechanism at relatively milder conditions *i.e.* T= 90 °C and pO_2= 200 psig. The catalyst was easily recyclable up to 7 times with minor loss in activity which was regenerated to certain extent by specific heat treatment protocol.

5.1 Introduction

Heretofore conventional fossil feedstock used to be the constant source of fine chemicals and fuel supplies for the world [1-2]. Although their bulk consumption and decreasing "supply to demand ratio" forcing scientific community to look for economically viable and sustainable routes [3]. Production of value added chemicals and fuel additives from biomass are drawing a great attention in recent times. Cellulosic biomass can easily be converted into various platform chemicals by acidic hydrolysis followed by triple dehydration. 5-hydroxymethylfurfural (5-HMF) in particular is the most attractive platform molecule and due to its immense potential it is considered as connecting link between biomass and fossil feedstock [4]. U.S. Department of Energy also listed it in "Top 10+4" list of bio-based chemicals [5]. 5-HMF promises different route to synthesize many value added chemicals like 2,5-dimethylfuran (DMF), 2,5-(bishydroxymethyl) furan (BHMF), 2,5-diformylfuran (DFF), 2,5-furandicarboxyllic acid (FDCA) etc [6-9]. Out of these, DFF is an important utility chemical due to its various applications. It is used as a precursor in various antifungal agents, nematocides, pharmaceutics, porous organic framework, polyurethane and macrocyclic ligands [10-13]. It also acts as starting material for various fluorescent materials, Poly-Schiff's bases, organic conductors and as a cross linking agent of poly vinyl alcohol (PVA) for battery separation [14-15]. DFF can be obtained by selective oxidation of less active hydroxymethyl group, rather than highly active α, β-unsaturated aldehyde group of 5-HMF which is a challenging task. Earlier DFF synthesis was attempted by the use of different sacrificial oxidants like 2,2,6,6-tetramethylpiperidine-1-oxide, NaOCl, $BaMnO_4$, pyridinium chlorochromate, pyridine-$Pb(OAc)_4$ trimethylammonium chlorochromate and CrO_3-Pyridine [16-22]. These oxidants pose an environmental threat due to their toxic and hazardous nature. To counter this problem, air or molecular oxygen is considered as a terminal oxidant which is environmentally benign. Reports on several homogeneous catalysts are also documented

which include Co/Mn/Zr/Br systems, Cu based catalysts like $CuNO_3/VOSO_4$, CuCl, vanadium phosphate complexes, and Lewis acid ($AlMe_3$) [23-28]. Other homogenous catalyst extensively explored is Mn-salen particularly, in buffer-DCM biphasic solvent [29]. But these processes suffer from use of harmful oxidants, low efficiency and separation issue which involves a tedious task to perform. Plenty of heterogeneous reports are also known where supported noble metals were used for DFF production. Ru was particularly explored on various supports like activated charcoal, ZrP, Υ-Al_2O_3, triazine and mesoporous Nitrogen framework [30-35]. Ru based catalysts were highly efficient for selective oxidation of 5-HMF but longer reaction times and their high price are limitation factor in their use. Kinetic study of chemoselective oxidation of 5-HMF over Pt/ZrO_2 was also conducted recently [36]. Among several non-noble metals used as heterogeneous catalysts, vanadium was proved to be highly efficient. For example, V_2O_5/C shows good efficiency at mild external pressure (40 psig) [37]. Similarly at atmospheric pressure of oxygen, vanadium phosphate intercalated with different metals shows good yield of 83-95% DFF in toluene and in N, N-DMF [38]. Corma *et al.* developed V-pyridine complex supported on polymeric mesoporous structure where they achieved 82% yield of DFF with only 75% conversion to HMF in 24h [39]. Although vanadium based catalysts showed promising results yet their toxic content and tendency to cross polymerize and decarbonylation reduces their efficiency. Many other non-noble metals like Fe, Co, Mn, Ce, Mo and Cu were also assessed for selective oxidation of 5-HMF. $Bi(NO_3)_3.5H_2O$ and cellulose mediated Cu-NP were developed by Baruah *et al.* where 82% yield of DFF was obtained at 80°C within 2h in oxygen atmosphere [40]. In another case, use of Cu/MnO_2 achieved 96.1% yield of DFF in ethanol with 86% conversion of 5-HMF in 5h [41]. A magnetically retrievable Mn-Fe combination tested in N, N-DMF with continuous flow of O_2 (20 ml/min) for 4h, gave 82.1% DFF with almost complete 5-HMF conversion [42]. Mn along with Cu and Al in aqueous solution provided 87% DFF with 90% conversion of HMF

but with a longer reaction time of 24h at 90°C and 120 psig external O_2 pressure [43]. A magnetic MOF derived Fe-Co hollow bimetallic catalyst showed 99% yield of DFF with complete conversion in toluene and alkaline medium at 100°C and 150 psig pressure of O_2 in 6h [44]. A cryptomelane type MnO octahedral molecular sieves (OMS-2) were also investigated for DFF in N, N-DMF to give 97.2% DFF with complete conversion of 5-HMF in 1h at 110°C and 75 psig of external O_2 pressure [45]. Interestingly, a bimetallic combination of Mo-Ce was examined for single as well as two pot conversion of fructose to DFF. At 120°C and continuous flow of O_2 fructose derived HMF could be completely converted to DFF with 94% yield [46]. Likewise sulphated Mo-Zr was tested at higher temperature (140°C) for fructose derived 5-HMF with continuous flow of O_2 till 17h to achieve 86% DFF with 99% conversion of 5-HMF in DMSO [47].

Out of several non-noble transition metals, Mn in particular proved to be an efficient catalyst because of its specific surface-lattice oxygen interaction. It is well documented that inclusion of other materials specifically alkali or alkaline metals in Mn structure increases its oxidative tendency because of multifunctional nature and enhanced redox properties in terms of lattice oxygen storage and release capacity (48-49). This particular aspect forms a strong background to investigate the doped/promoted Mn catalysts which can further improve the sustainability of 5-HMF oxidation to DFF. Here we report a non-noble alkali promoted metallic nanocomposite, Mn-Cs for 5-HMF oxidation as it provides a dual functionality *i.e.* oxidation as well as basicity. Various compositions of Mn-Cs were thoroughly screened and best one *i.e.* Mn-Cs (80-20) was optimised. At 90°C and 200 psig external air pressure, 91% conversion of 5-HMF was obtained with 98% selectivity and 86.8% yield of DFF. Catalyst was extensively characterised by various techniques to develop structure- activity correlation in a logical coherence.

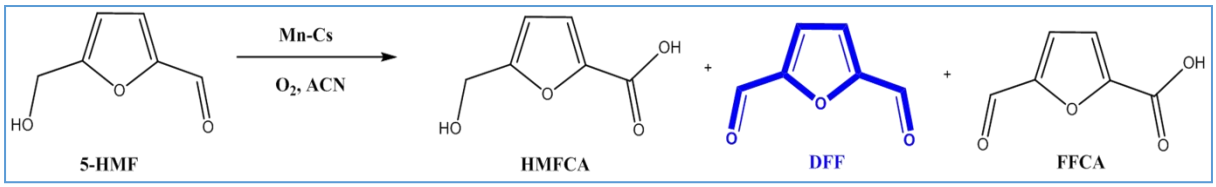

Reaction Scheme 1: Selective oxidation of 5-HMF into DFF

5.2 Experimental

5.2.1 Catalyst Preparation

Monometallic MnOx, different variants of Mn and Cs and supported Mn catalysts were prepared by the co-precipitation method as described in subsections 2.3.3, 2.3.3.1 and 2.3.3.2. The catalysts were tested on Parr reactor as mentioned in subsection 2.5.3 of chapter 2. Activity testing and selectivity calculations were done by HPLC method also described in subsections 2.6.2 and 2.7 of chapter 2. Catalytic properties were evaluated by different characterisation techniques mentioned in section 2.4 of chapter 2.

5.3 Results and Discussion

5.3.1 Objectives of this work

The main objectives of this work were (i) Designing a catalyst with enhanced surface properties like basicity, oxygen defects and oxygen mobility for efficient 5-HMF oxidation to DFF (ii) Extensive characterization of catalyst and parameter optimisation to establish structure activity correlation (iii) Elucidate the reaction pathway for 5-HMF oxidation to DFF.

5.3.2 Catalyst Characterization

5.3.2.1 N_2-desorption isotherm and BET surface area

Figure 5.1 presents the N_2-desorption isotherm and pore size distribution curves of monometallic MnO_x and most efficient Cs doped Mn catalyst. Both the catalysts showed type-IV isotherms suggesting mesoporous nature along with H3 kind of hysteresis loop which is because of change in the volume of the adsorbent *i.e.* pore size variation [50]. The N_2-sorption isotherm revealed that amount of N_2 desorbed was more in the case of Cs doped Mn compared to monometallic MnO_x suggesting significant increase in porosity of its surface and surface area as shown in **Table 5.1**, the pore size also increased and so the amount of N_2 in case of Cs doped Mn catalyst.

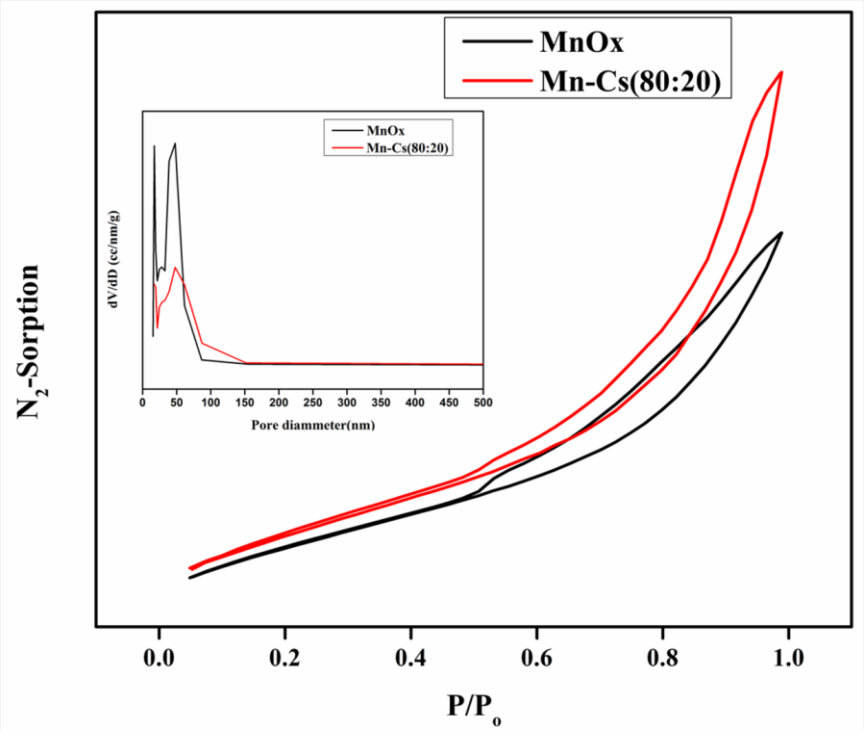

Figure 5.1: N_2-desorption isotherm and pore size distribution of MnO_x and Mn-Cs(80:20)

The BET surface area also showed increment after doping of Cs which may be due to morphological changes assisted by inclusion of Cs as shown in micrographic structural

analysis in FE-SEM and TEM. As shown in **Table 5.1**, the higher amount of porosity along with higher pore volume could be the reason of higher surface area of Mn-Cs(80:20) as its shows both spherical and rod shaped morphology whereas on the other hand, MnO_x contained only spherical nanoparticles with reduced porosity and multidimensional growth as shown later in **Figure 5.8**.

Table 5.1: Textural properties of MnO_x and Mn-Cs(80:20) by BET surface area analysis and BJH pore size distribution

Sr. No.	**Catalyst**	**Surface area (m^2)**	**<Pore size>$_{avg}$ (nm)**	**<Pore volume>$_{avg}$ (cc/g)**
1	MnO_x	190.72	4.53	0.25
2	Mn-Cs(80:20)	253.79	5.08	0.33

5.3.2.2 TGA-DTA

Figure 5.2 presents the TGA-DTA analysis of Mn-Cs(80:20). Aggregated weight loss of around 17.01% was observed in the broad temperature range of 25-800°C (**Figure 5.2.a**). Both pure MnO_x and Mn-Cs (80:20) show almost similar thermogravimetric characterisation suggesting absence of any major dopant related impurity [51]. The TGA curve also suggested that inclusion of Cs in Mn lattice increased the thermal stability of Mn-Cs(80:20). Starting from 25°C, there was continuous weight loss of around 5.81% till 289°C which may be due to surface adsorbed water or nitrate residue in MnO_2 [52]. Further two major endothermic peaks were observed at around 480°C and 704°C which may be corresponding to phase transformation of MnO_2 into Mn_2O_3 and subsequently to Mn_3O_4 [53]. Interestingly in MnO_x, more weight loss (20.12%) was observed than that in Mn-Cs (80:20) clearly suggesting

higher stability of Cs doped Mn than pure MnO_x. This may be due to the retention of phases of Mn by doping Cs ion at elevated temperature.

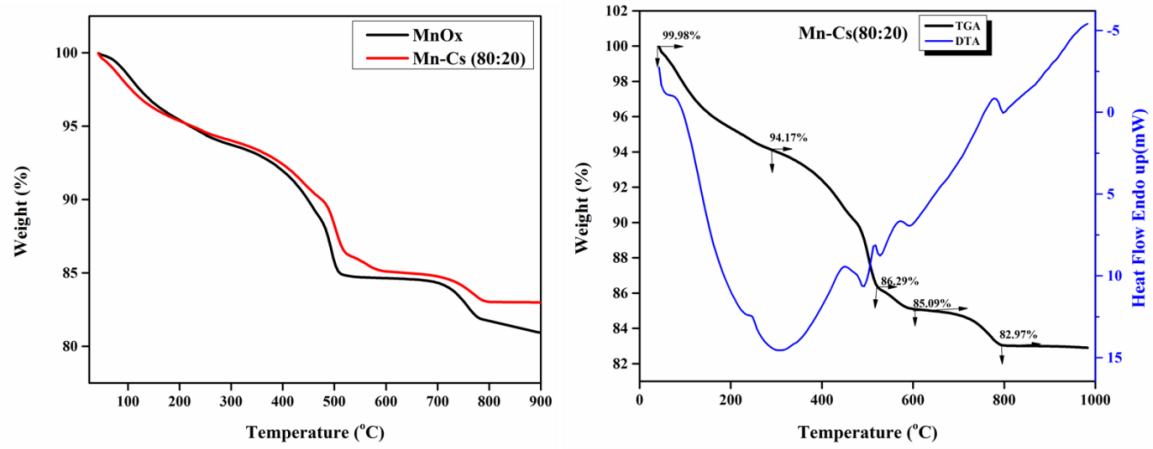

Figure 5.2: TG-DTA analysis of catalysts (a) Comparative TG analysis of MnOx and Mn-Cs (80:20) (b) TG-DTA profile of Mn-Cs (80:20)

5.3.2.3 XRD

XRD patterns were recorded to know the crystalline phases and chemical composition of various catalysts. Comparative XRD plots of different variant of Mn and Cs are shown in **Figure 5.3** in which the presence of mixture of orthorhombic MnO_2 and cubic Mn_2O_3 in the monometallic MnO_x are evidenced at 2θ value of β= 42.45° (222) and α= 36.99° (013) respectively with moderate crystalline nature [54]. The crystalline nature enhanced once Cs was introduced into the metal domain. The enhanced crystallite size of Mn-Cs(80:20) to 16.27 nm compared to MnO_x (9.81 nm) was also in coherence with increase in crystallinity. It is also known for enhanced diffusion of oxygen and higher mobility of oxygen in the lattice [55]. It was observed that increased Cs^+ content enhanced the appearance of XRD peaks of Mn^{+4} (2θ= 42.45°, 64.01° and 36.99°) and Mn^{+3} phases (2θ= 17.66°, 22.10°, 47.99° and 65.20°) [56]. Some peaks related to Mn_3O_4 phase were also detected at 2θ values of 29.66°, 32.10° and 49.52° [57]. This means that inclusion of Cs not only increased the crystallinity (43%) but also the valence state of Mn to some extent.

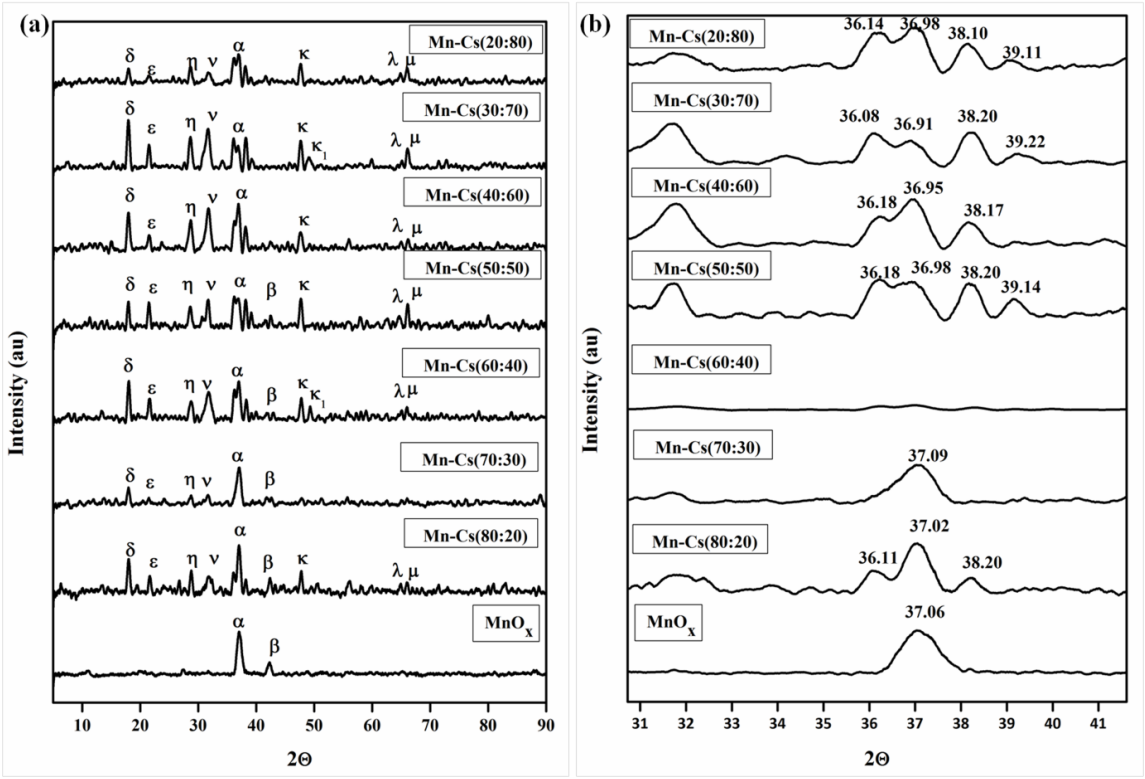

Figure 5.3: XRD Pattern of various catalysts for 5-HMF to DFF (a) comparative Mn xrd pattern of Mn and Cs doped variants of Mn where α= 36.99°, β= 42.45°, δ=17.66°, ε =22.10°, η=29.66°, ν=32.10°, κ=47.99°, λ=64.01°,μ=65.21° and κ_1=49.52° (b) Multiplets of 2θ= 36.99° on inclusion of Cs.

On careful evaluation of XRD patterns, it was found that 2θ reflection at 36.99° was divided into multiplet on Cs inclusion as shown in **Figure 5.3.b**. This clearly suggested the phase transformation process on Cs doping which further confirmed our observation of appearance of mixed phases in XRD pattern. The splitting of a reflection peak at 2θ = 36.99° into multiplets clearly suggested the presence of lattice strain and hence amorphous to crystalline phase transformation which is further visible in micrographic images in terms of morphological transformation from nanoparticles to nanorods [58]. As can be seen in **Figure 5.3.b**, a peak at 2θ =36.99° was broken into both higher 2θ as well as lower 2θ revealing presence of uniform compressive strain and uniform tensile strain respectively while phase

transformation [59]. FWHM also increased on Cs inclusion in Mn lattice suggesting peak broadening which is in accordance with the thermodynamics indicating about the presence of non-uniform strain too [59].

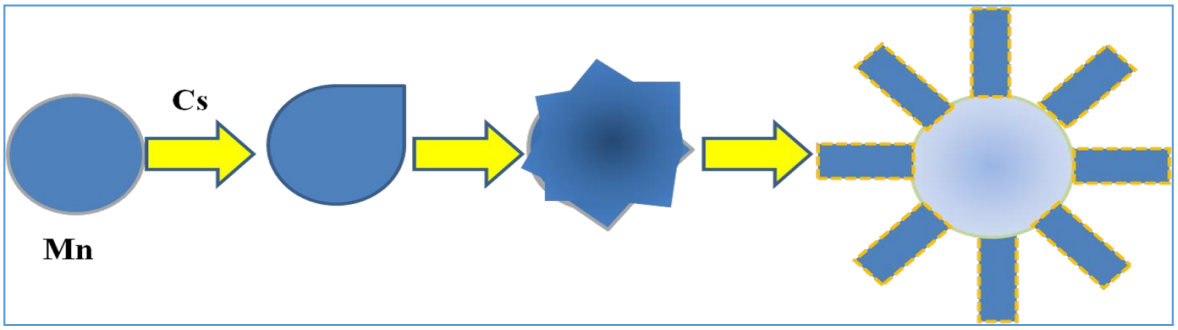

Scheme 5.2: Morphological changes in Mn ignited by Cs, transforming nanoparticles in nanorodes due to lattice strain

During phase transformation mass transfer takes place from nanoparticles to nanorods resulting in shrinking of nanoparticles which generate compressive strain at nanorods breeding site as shown in **Scheme 5.2** [60]. This compressive strain got released after complete formation of nanorods. A detail account of crystallite size, crystallinity and microstrain in the lattice of catalyst is given in **Table 5.2**.

Table 5.2: Crystalline size, microstrain and crystallinity of MnO_x and its Cs doped variants

Sr. No.	**Catalyst**	**Crystallinity (%)**	**Crystallite Size (nm)**	**Microstrain (*10^{-3})**
1	MnO_x	19.51	9.81	----
2	Mn-Cs(80:20)	43.06	16.27	7.04
3	Mn-Cs(70:30)	21.63	14.07	10.51
4	Mn-Cs(60:40)	33.77	13.58	9.95
5	Mn-Cs(50:50)	34.06	15.90	8.31
6	Mn-Cs(40:60)	38.61	13.37	10.21

7	Mn-Cs(30:70)	45.95	12.16	12.94
8	Mn-Cs(20:80)	33.46	11.75	11.80

5.3.2.4 XPS

Different active oxidation states of the screened catalysts were studied by XPS. **Figure 5.4** presents the Mn species in which signature binding energy difference of ~11.5-11.7 eV for Mn_2O_3 was observed between the Mn $2p_{1/2}$ and Mn $2p_{3/2}$ due to spin orbital coupling [61].

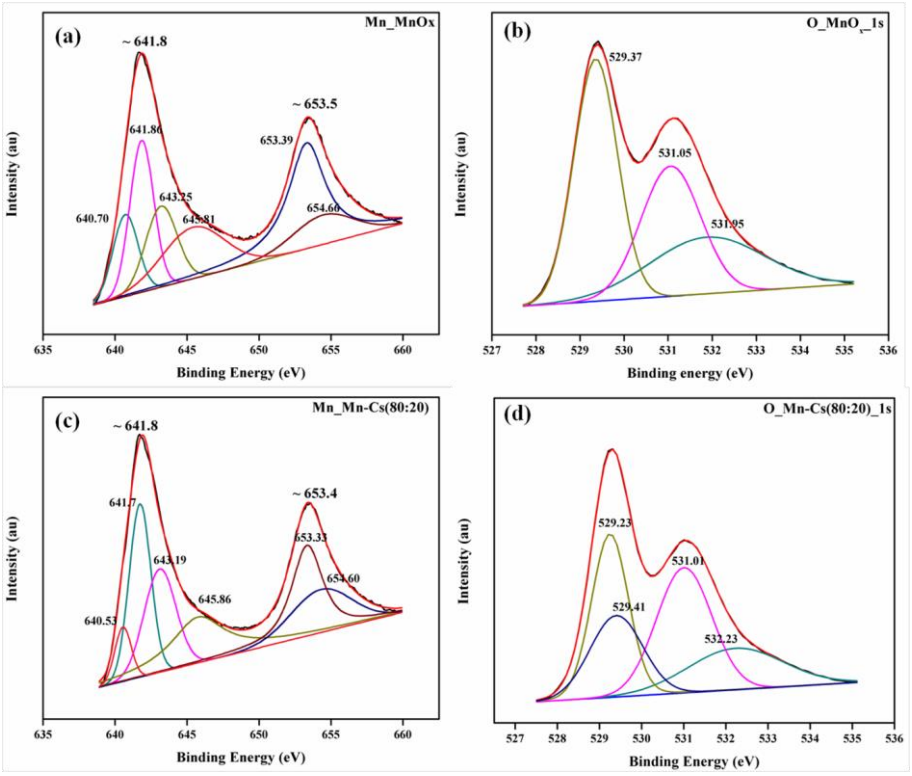

Figure 5.4: XPS analysis of (a) Mn 2p3/2 in MnOx (b) O1s in MnOx, (c) Mn2p3/2 in Mn-Cs(80:20) and (d) O 1s in used Mn-Cs(80:20)

Two XPS maxima were observed at B. E. of ~641.8 eV and ~653.5 eV corresponding to Mn $2p_{3/2}$ and Mn $2p_{1/2}$, respectively. Its deconvolution suggests the presence of Mn^{+2}, Mn^{+3} and Mn^{+4} species on the MnO_x surface at the binding energies of 640.7, 641.86 and 643.25 eVs,

respectively [62]. A broad satellite peak was also observed at higher B. E. of 645.81 eV due to charge transfer effect in Mn and again confirmed the existence Mn^{+4} species [63].

These trends were also observed after inclusion of Cs in Mn lattice with slight shift towards lower value of binding energies *i.e.* 640.53, 641.70, 643.19 and 645.75 eVs. This clearly suggested synergistic electronic interactions of Mn and Cs as it is well known that electron donation takes place from alkali metal to transition metal at their interface which reduces its work function and consequentially binding energy, too [64]. This lowering of binding energy enhances the redox properties of main metals significantly at interface of catalytic surface and reactants [65]. On detailed analysis, it was also observed that the Full Width at Half Maxima (FWHM) decreased in case of Mn-Cs (80:20) as shown in **Table 5.3**. This may be due to interaction between Mn and Cs and change in electronic properties with change in particle size [66].

Table 5.3: Detailed quantitative analysis of Mn2p3/2 peaks in MnO_x and Mn-Cs (80:20)

Sr. No.	**Contents**	**MnO_x**	**Mn-Cs (80:20)_Fresh**	**Mn-Cs (80:20)_Used**
1	Binding Energy (eV)	640.70	640.53	640.99
	Percentage (%)	17.96	7.63	27.82
	FWHM	2.04	1.34	2.04
	Oxidation state	Mn^{+2}	Mn^{+2}	Mn^{+2}
2	Binding Energy (eV)	641.86	641.70	642.22
	Percentage (%)	31.73	32.30	33.61

	FWHM	1.95	1.78	2.15
	Oxidation state	Mn^{+3}	Mn^{+3}	Mn^{+3}
3	Binding Energy (eV)	643.25	643.19	643.72
	Percentage (%)	22.29	28.21	15.85
	FWHM	2.56	2.51	2.58
	Oxidation state	Mn^{+4}	Mn^{+4}	Mn^{+4}
4	Binding Energy (eV)	645.81	645.75	646.09
	Percentage (%)	28.02	31.86	22.70
	FWHM	5.07	4.49	4.58
	Oxidation state	Mn^{+4}	Mn^{+4}	Mn^{+4}

Figures 5.4.b and **5.5** presents the O 1s deconvolution which represents oxygen species present in Mn and Cs doped Mn catalysts. Based on binding energy values oxygen species can be classified into three categories *viz.* (i) lattice oxygen (O^{2-}) showing peak at the lower Binding Energy (LBE) values ranging from 529-530 eVs, (ii) subsurface adsorbed O(OH) and O_2 vacancies showing peak at the medium Binding Energy (MBE) values ranging from 530- 532 eVs and (iii) oxygen of adsorbed water on catalytic surface showing peak in the Higher Binding Energy (HBE) beyond 532 eVs [67]. In monometallic MnO_x three XPS peaks were observed at B.E. values of 529.31, 531.05 and 531.95 eVs suggesting abundance of lattice oxygen followed by O_2 vacancy and adsorbed aqueous content. Similar peaks were observed in Mn-Cs (80:20) but with lower intensities. On detailed quantitative analysis it was observed that doping of Cs enhanced the extent of lattice oxygen. Splitting in main peak was

observed (**Figure 5.5.a and b**) may be because of different chemical environment of oxygen. Similarly amount of O_2 vacancies also increased at the cost of adsorbed H_2O. When compared with reused catalyst, a sharp increase of 17% was observed in O_2 vacancy accompanied by simultaneous with decrease of 12% in lattice oxygen. This reveals the redox nature of Mn-Cs(80:20) catalyst and indicates that reaction proceeded by Mars-Van-Krevelen mechanism due to enhanced lattice oxygen and availability of O_2 vacancies [68].

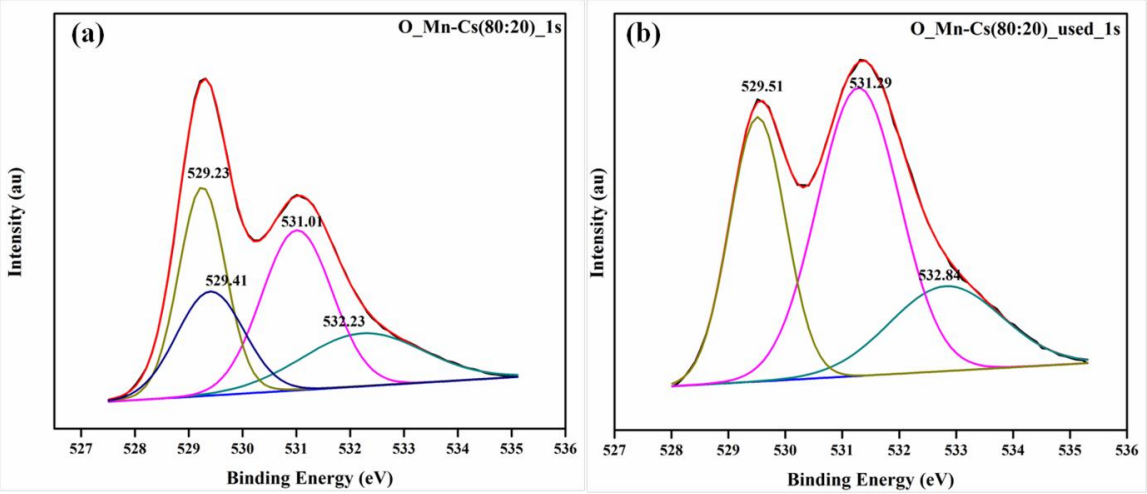

Figure 5.5: XPS deconvolution of O 1s in (a) Fresh Mn-Cs(80:20) and (b) Spent Mn-Cs(80:20)

Table 5.4 presents the binding energy, FWHM and relative percent of oxygen species in both Mn and Mn-Cs (80:20) catalyst. It was observed that binding energy values of Mn species slightly decreased in Mn-Cs (80:20) compared to those in MnO_x. This was due to high electro negativity of Mn and easy electron donating property of Cs which led to weak binding energy of Mn-O in doped Mn-Cs (80:20) and enhanced activity of lattice oxygen.

Table 5.4: O1s and its quantitative abundance in MnOx, Fresh Mn-Cs(80:20) and spent Mn-Cs(80:20)

Sr. No.	**Samples**	**MnOx**	**Mn-Cs(80:20)_Fresh**	**Mn-Cs (80:20)used**
1	Binding Energy (eV)	529.31	529.23	529.51
	Percentage (%)	42.64	28.97	30.78
	FWHM	1.16	1.03	1.16
2	Binding Energy (eV)	531.05	531.01	531.29
	Percentage (%)	31.24	32.46	49.47
	FWHM	1.59	1.54	1.7
3	Binding Energy (eV)	531.95	532.23	532.84
	Percentage (%)	26.12	18.46	19.73
	FWHM	3.05	2.6	2.32
4	Binding Energy (eV)	---	529.41	----
	Percentage (%)	---	20.11	----
	FWHM	---	1.47	----

5.3.2.5 FESEM-EDX and Elemental Mapping

Epitaxial morphology and element positions were detected by FE-SEM images associated with elemental mapping. **Figure 5.6.a** shows that MnO_x particles were showing spherical

globule type of morphology. On enhanced resolution, it was observed that these globules were made up of small sized subunits *i.e.* aggregation of several small size metal particles. The size of macroglobules was having the size of ~800 nm whereas their subunits were in the range of 5-8 nm (**Figure 5.6.b**). This was further confirmed by TEM analysis. The globules were of complete spherical shape in the fresh MnO_x case whereas spheres distorted on doping of Cs as shown in **Figures 5.6.d and 5.6.e**. The FE-SEM of Mn-Cs(80:20) also shows increase in the size of spherical globulates to ~1-1.5 μm. The elemental analysis was also performed by mapping of Mn (**Figure 5.6.c**) and Cs (**Figure 5.6.f**). The EDX is shown in **Figure 5.7** showing 17% Cs against our theoretical calculation of 20% Cs.

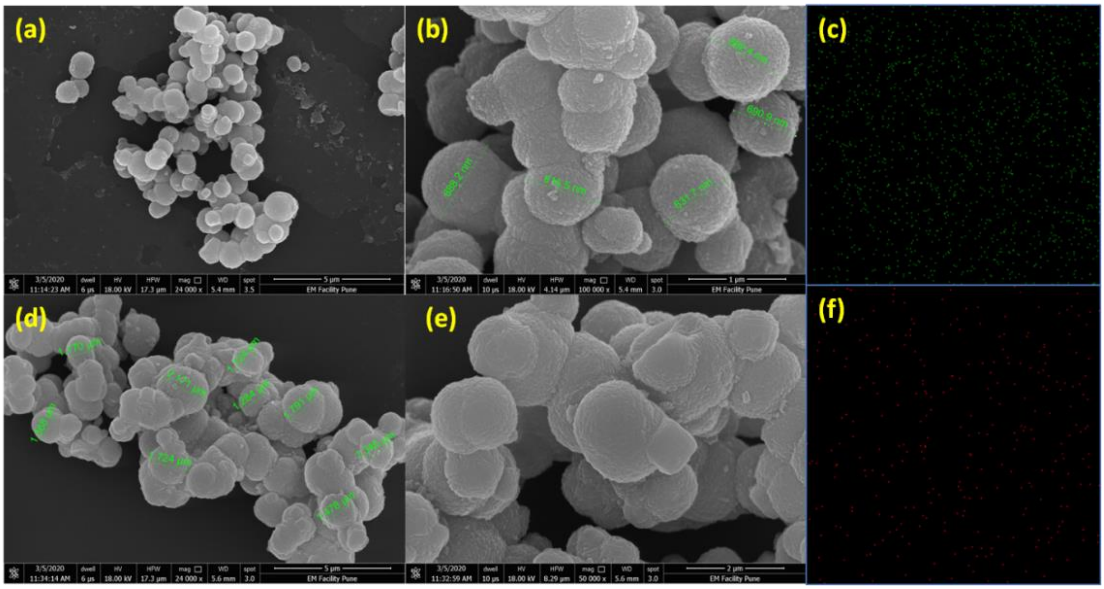

Figure 5.6: FESEM images of (a) MnOx at 5 μm scale (b) MnOx at 1 μm scale (c) Elemental mapping of Mn (d) FESEM of Mn-Cs(80:20) at 5 μm scale (e) Mn-Cs (80:20) at 1 μm scale and (f) Elemental mapping of Cs

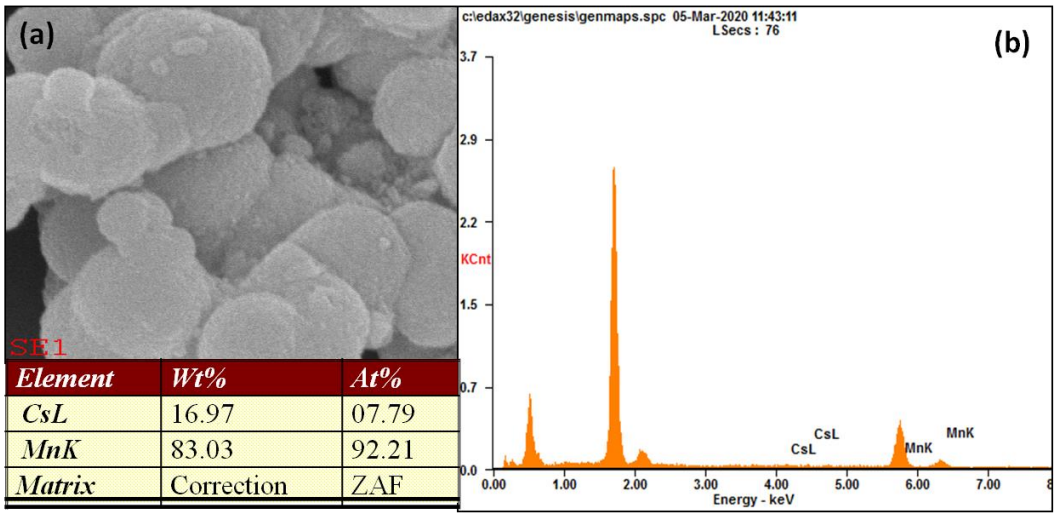

Element	Wt%	At%
CsL	16.97	07.79
MnK	83.03	92.21
Matrix	Correction	ZAF

Figure 5.7: EDX pattern of Mn-Cs (80:20) where (a) Area of EDX pattern and (b) EDX pattern of Mn-Cs (80:20)

5.3.2.6 TEM

TEM micrographs in **Figure 5.8** show the particle sizes and shapes of fresh and used Mn-Cs(80:20) catalyst. Interestingly, inclusion of Cs in MnO_x lattice shows dual morphology of round and cubical in both fresh and used Mn-Cs(80:20). It is well reported morphological feature attributed to inclusion of alkali metals in Mn lattice [69]. The average size of round shape particles in fresh Mn-Cs (80:20) were found to be in the range of 4~6 nm whereas for cubical rods, it was 55-60 nm. At higher resolution of 5 nm fringe pattern was observed with the'd' value of 0.303 nm which is related to (110) crystal plane of MnO_2. One more interesting finding was that the cubical rods were more profound on corners whereas core part was showing majority of round particles.

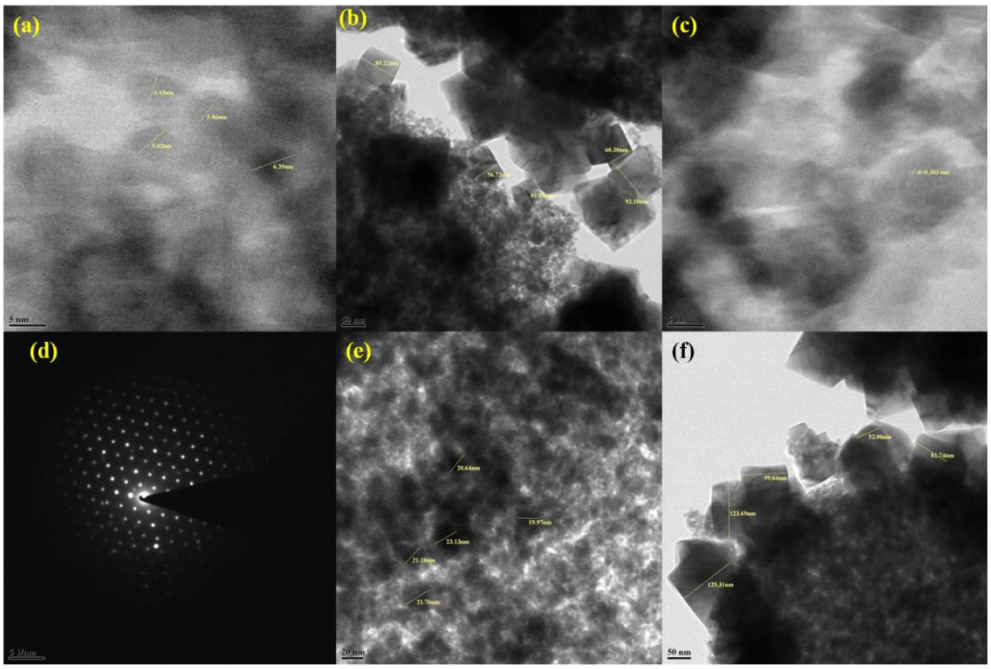

Figure 5.8: TEM analysis of (a) Mn-Cs (80:20)-Fresh round particle, (b) Mn-Cs (80:20)-Fresh cubicle particles, (c) Lattice fringe pattern in Mn-Cs (80:20), (d) SAED pattern of cubical Mn-Cs (80:20), (e) Mn-Cs (80:20)-Used round particles (f) Mn-Cs (80:20)-Used cubicle particles.

In the used Mn-Cs(80:20) catalyst sample, the round shaped particle size increased to 20-25 nm whereas the cubical rods showed increase in size up to 125 nm due to deposition of carbonaceous matter. SAED pattern of cubical rods as shown in **Figure 5.8.d** possessed uniform and fine lattice pattern while that of round shape particle was not uniform as shown in **Figure 5.9**.

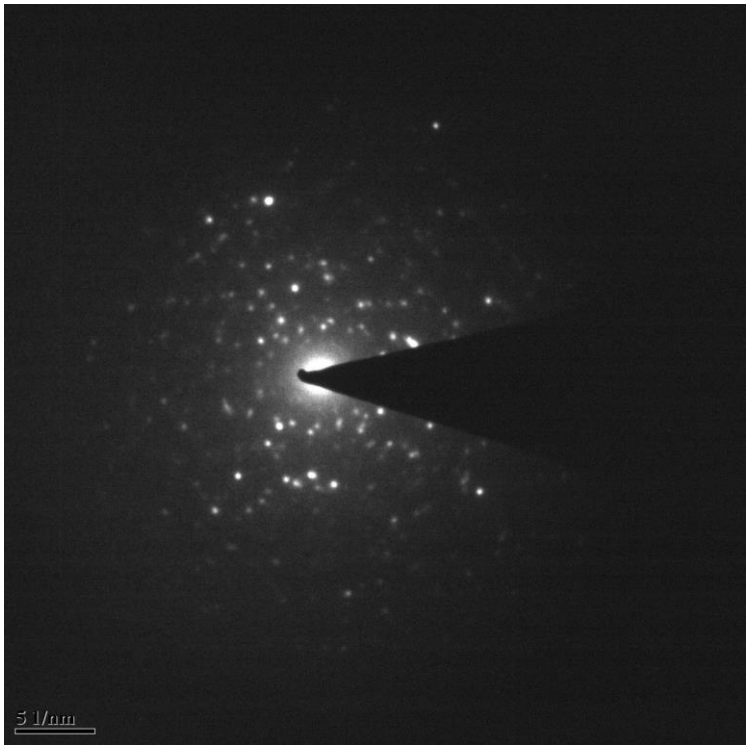

Figure 5.9: SAED pattern of used Mn-Cs(80:20) by TEM imaging

5.3.2.7 HR-TEM

HR-TEM imaging of Mn-Cs (80:20) revealed interesting fact about dual morphology of our catalyst. The inclusion of Cs induces the change in morphology from spherical to nanorodes as shown in **Figure 5.10.a**.

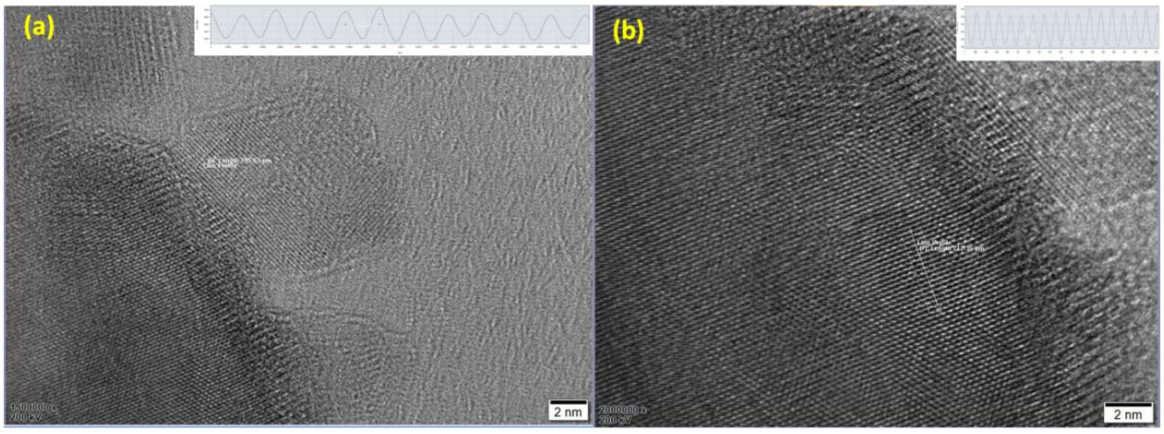

Figure 5.10: HR-TEM imaging of interface of Mn-Cs(80:20) on the scale of 2 nm having (a) d_{sp}= 0.1923 nm (420) and (b) d_{sp}= 0.2126 (222)

Figure 5.10.a shows d_{sp}= 0.1923 nm corresponding to (420) plane of newly generated lattice of nanorodes which is matching with the XRD reflection at 2θ= 47.49° of Mn-Cs (80:20). HR-TEM imaging of nanoparticles region in **Figure 5.10.b** shows 222 plane with d_{sp}= 0.2126 nm which was further supported by XRD peak at 2θ= 42.45° of Mn-Cs (80:20).

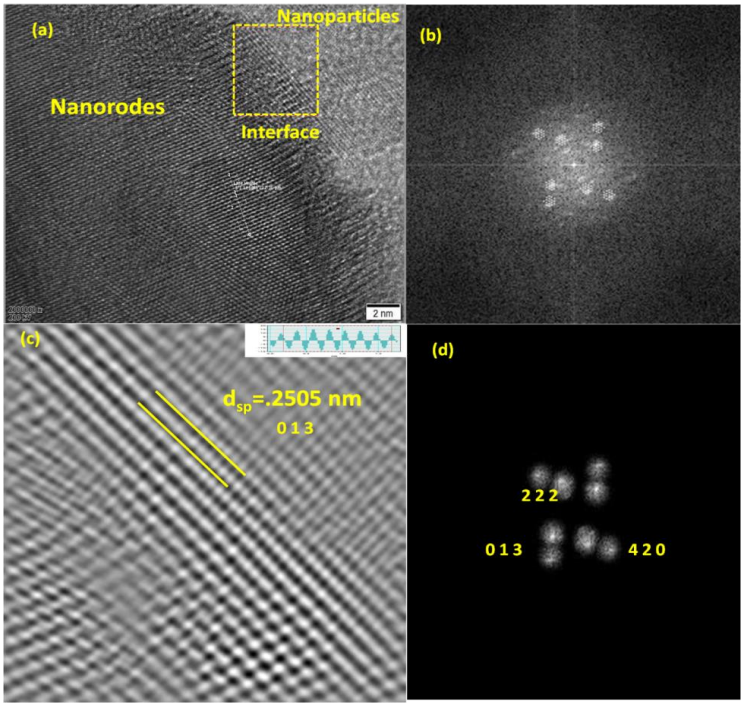

Figure 5.11: HR-TEM images of Mn-Cs(80:20) (a) on the interface of nanorodes and nanoparticles (b) Marked area for FFT pattern (c) d spacing calculation from IFFT fringe pattern (d) FFT pattern extracted from HR-TEM images of interface

Thus, the inclusion of Cs in the lattice of Mn initiates the formation of new crystalline surfaces evident by d_{sp}= 0.2574 nm of 013 plane (2θ= 36.99°) as shown by **Figure 5.11**. This process further generated a lattice strain in the Cs doped MnO_x which was quite evident by XRD of Cs doped Mn in which the peak at 2θ= 36.99° showed multiplets. The enhanced crystallinity due to doping of Cs seen in XRD was further confirmed by single atomic dot pattern of Mn-Cs (80:20) (**Figure 5.11.c, 5.12**).

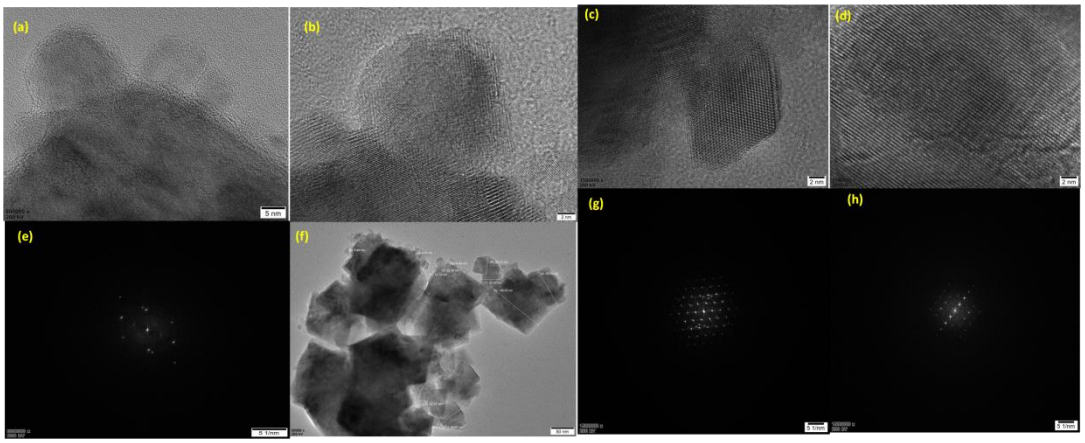

Figure 5.12: HR-TEM images of fresh Mn-Cs(80:20) depicting various fringe pattern and Single dot pattern

5.3.2.8 H_2-TPR

The reducibility of catalyst was analysed by H_2-TPR as shown in **Figure 5.13**. Two peaks were observed in all the catalyst samples; one at lower temperature around 270-320°C and the other at higher temperature in the range of 400-450°C.

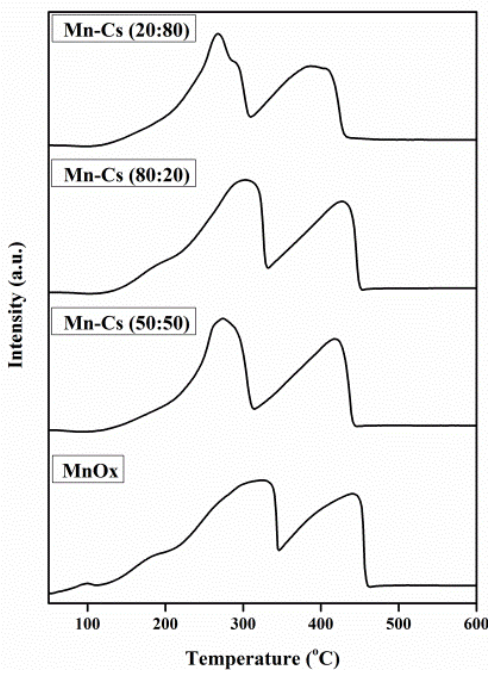

Figure 5.13: H_2 –TPR profile of MnOx and selected Cs doped variants for comparative purpose

It was observed that the lower temperature peaks of catalysts are not symmetric hence these were further deconvoluted as shown in **Figures 5.14**. Low temperature peaks correspond to reduction of MnO_2 in Mn_2O_3 whereas higher temperature could be correlated with Mn_2O_3 reduction to MnO [53]. In the bare MnO_x samples, peaks were observed at 287.11°C, 312.44°C and 424°C. When Cs was introduced in MnO_x decline in the reduction temperature was observed. For Mn-Cs (80:20) it reduced to 269.33°C, 300.66°C and 411.33°C. This decrease in reduction temperature was due to the fact that on introduction of Cs cation in metal, the strength of Mn-O bond weakened making the lattice oxygen highly mobile and available for desorption [70]. These facts were also supported by XPS investigation where the concentration of lattice oxygen increased and BE decreased to certain extent on introducing Cs ion. The desorption of oxygen occur from the interface present between Mn and Cs where Mn has lower valence sites [71].

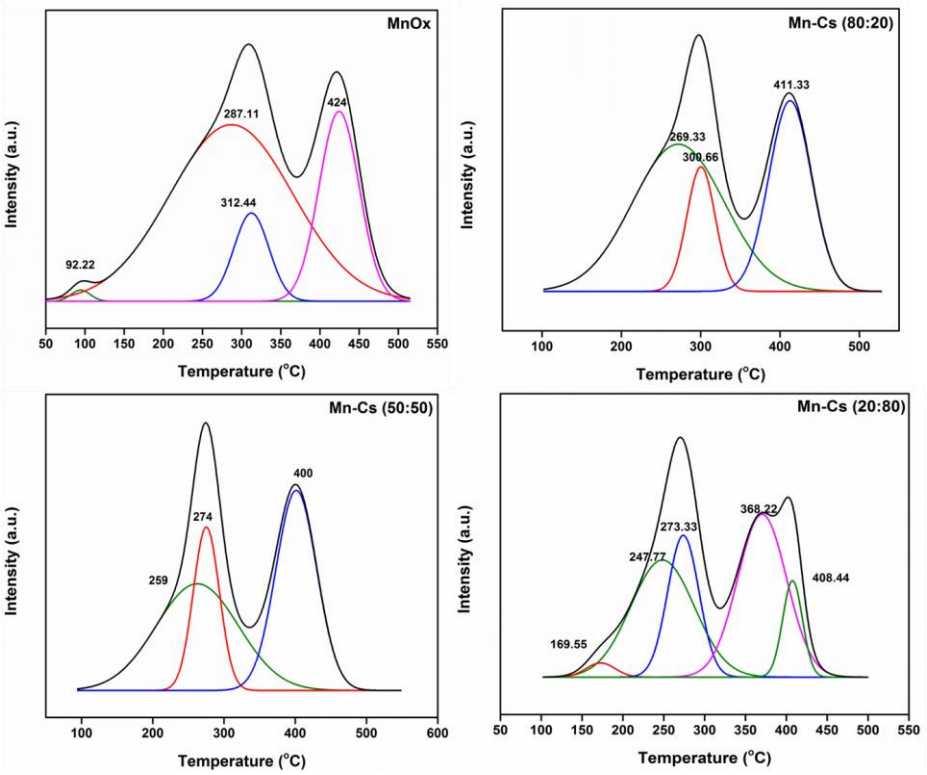

Figure 5.14: Deconvoluted temperature programmed reduction profile of MnO_x, Mn-Cs(80:20), Mn:Cs(50:50) and Mn-Cs(20:80)

5.3.2.9 TPO

To know the oxidizability and redox behaviour of Mn catalyst due to doping of Cs, TPO was performed and the results are shown in **Figure 5.15**. The onset of the oxidation of MnO_x started at 233°C whereas for the Cs doped Mn it get started at 227°C and maximum consumption of O_2 was recorded at 538°C and 526°C for MnO_x and Mn-Cs(80:20), respectively, suggesting strong interaction of Cs and Mn [72]. In the monometallic MnO_x, the TPO profile was asymmetric doublet whereas for Cs doped Mn it was triplet suggesting enhanced lattice oxygen in Mn-Cs(80:20) and was in accordance with XPS findings. Oxygen consumption for both the catalysts was almost similar suggesting minimal change in oxygen vacancies which was further supported by XPS.

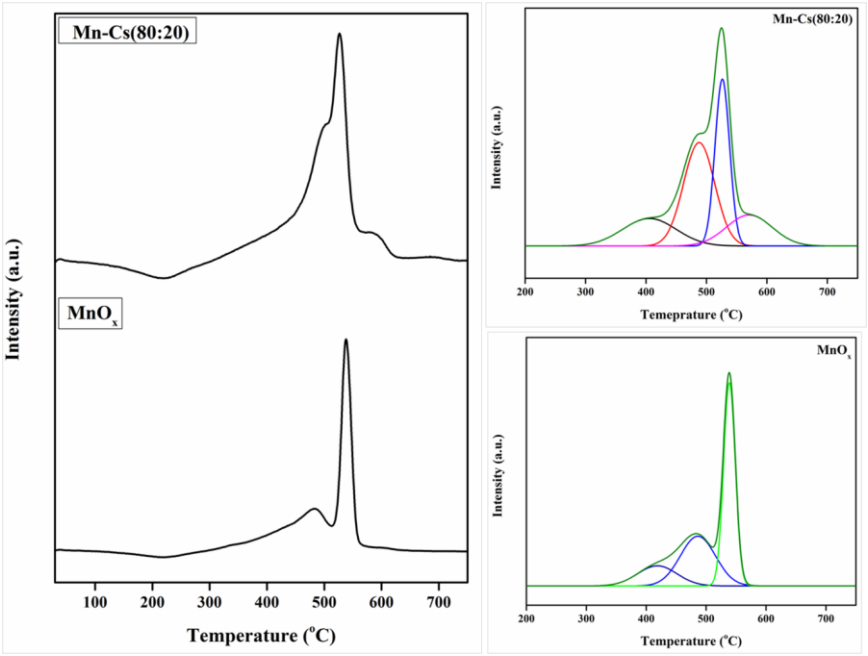

Figure 5.15: O_2 TPO profile of (a) MnOx and Mn-Cs (80:20) (b) Deconvoluted profile of MnO_x and Mn-Cs(80:20)

The deconvoluted TPO spectra of MnO_x showed peaks at 415°C, 486°C and 538°C whereas for Mn-Cs(80:20), four peaks were observed at 407°C, 487°, 525° and 573°C which can be assigned to Mn_2O_3 and MnO_2 species, respectively [73].

5.3.2.10 CO_2-TPD

Since alkali and alkaline earth metal are basic in nature and are known to increase the basicity of the catalyst, Temperature Programmed Desorption (TPD) using CO_2 as a probe molecule was carried out [74]. **Figure 5.16** represents the CO_2 TPD profile of the various Mn-Cs ratios. The observed graph and quantitative estimation revealed that inclusion of Cs in Mn lattice increased the basicity of catalyst significantly (**Table 5.5, Entries 1-2**). In case of bare MnO_x a small peak was observed at 80 °C due to linear interaction of CO_2 and surface –OH groups [75]. This peak was retained in almost all the variants except Mn-Cs (70:30). An intense hump was observed at 477 °C with tiny satellite impression at around 533 °C. This can be attributed to desorption of CO_2 from oxygen vacancy sites and termed as strong basicity [76]. It was observed that after introduction of Cs in MnO_x, these peaks at higher temperature appeared in the form of clear and intense bimodal symmetry suggesting enhanced strong basic properties in catalyst especially in Mn-Cs (80:20).

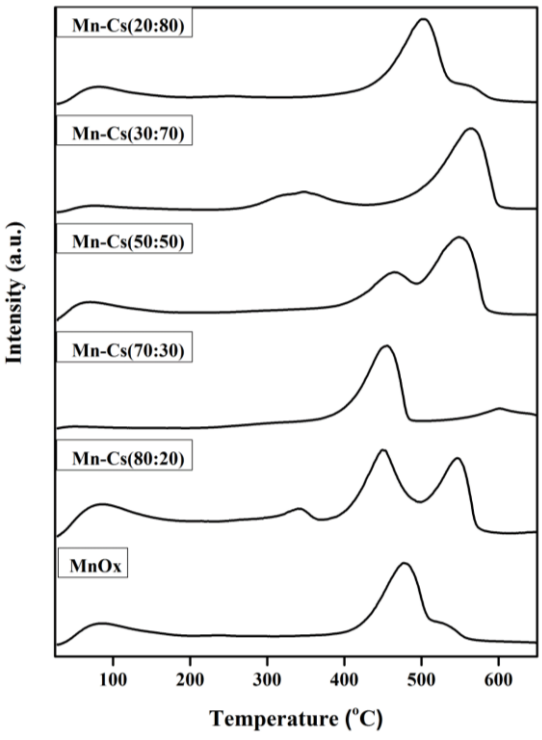

Figure 5.16: Comparative CO_2 TPD profile of Mn and its different variant of Mn-Cs

These results were well in accordance with increased oxygen vacancy observed in XPS. Like MnO_x, Mn-Cs(80:20) also showed peaks at 80°C, 451°C and 546°C. A tiny spike was also observed at 345 °C which can be because of decomposition of any monodentate/bidentate carbonate species (CO_3^{2-}) formed during adsorption of CO_2 on the surface [77]. Similar observations were made for Mn-Cs variants and quantitative estimation is given in **Table 5.5**.

Table 5.5: Quantitative estimation of basicity of MnO_x and Cs doped Mn variants by CO_2 TPD

Sr. No.	**Catalysts**	**Temperature Range (°C)**			**Total CO_2 desorbed (mmol/g)**
		25-250	**250-500**	**500-750**	
1	MnO_x	0.1766	0.2858	0.0094	0.4718
2	Mn-Cs(80:20)	0.1871	0.2093	0.1471	0.5435
3	Mn-Cs(70:30)	0.0074	-	0.2967	0.3041
4	Mn-Cs(50:50)	0.1111	0.0517	0.2054	0.3682
5	Mn-Cs(30:70)	0.0275	0.1064	0.4209	0.5548
6	Mn-Cs(20:80)	0.1913	0.4333	0.0151	0.6397

It was clear that Cs mainly enhanced the strong basicity as bimodal distribution of basic peaks appeared at higher temperature range of 400-650 °C in Cs doped Mn catalysts. It was also observed that with increase in Cs concentration, the strong basicity appeared in the catalyst (**Table 5.5, entries 5- 6**). This increase in overall basicity can be the region of non-selective oligomerization of 5-HMF since the conversion at this concentration of Cs was highest but no desired products formed while selective and target basic properties produced due to controlled Cs concentration were prolific for the desired product.

5.3.2.11 Raman spectra

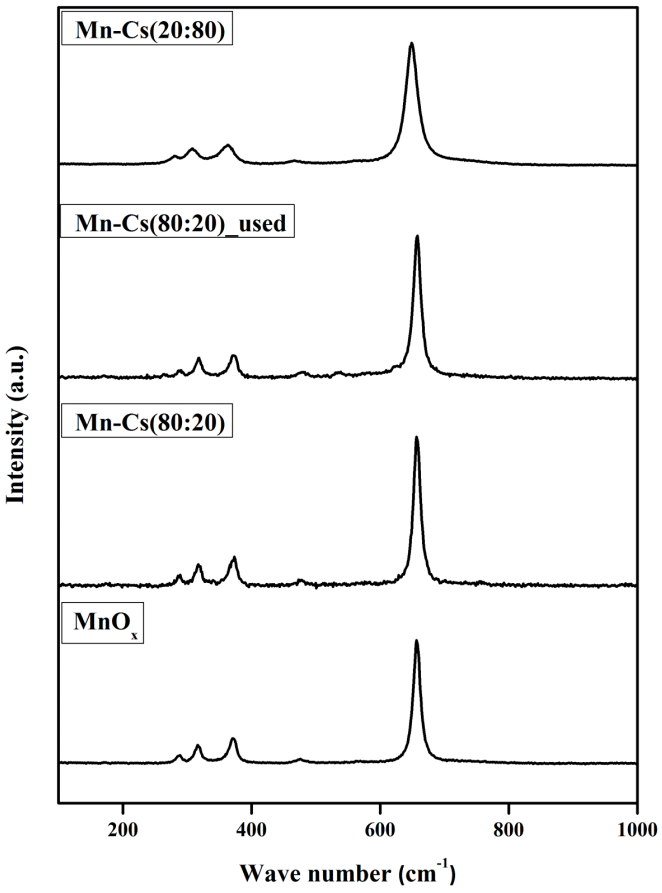

Figure 5.17: Raman spectroscopic analysis of MnO_x and various Cs doped variants of MnO_x

In order to find out the type of oxygen species and their role in the oxidation process of 5-HMF, Raman spectroscopic analysis of the catalysts was carried out (**Figure 5.17**). Monometallic MnO_x, various contents of Mn and Cs *i.e.*80:20, 80:20_used and 20:80 were analysed. Three major peaks based on different energy levels can be identified. Lower Energy Level (LEL) which ranges between 200- 450 cm^{-1}, Medium Energy Level (MEL) of 450-550 cm^{-1} and Higher Energy Level (HEL) of 550-750 cm^{-1}. In lower energy level three peaks were observed at (i) 287.90/287.90/287.90/281.80 cm^{-1} (ii) 316.69/318.10/317.82/308.07 cm^{-1} and (iii) 371.66/371.66/372.39/363.19 cm^{-1}. The LEL peaks represent the spectral domain of skeletal vibrations of Mn-O [78]. It was observed that

the intensity of these vibrational modes decreased drastically on inclusion of Cs which may be due to the morphological changes from nanoparticles to nanorodes as shown from SEM and TEM images. It may be due to formation of nanorods where the growth takes place in one dimension rather than 3D of nanoparticles which leads to significant decrease in vibrational degree of freedom [79]. One peak was observed in MEL region corresponding to 476.70/478.77/478.77/467.52 cm^{-1}. It is deformation mode of Mn-O bonds in Mn-O-Mn chains of MnO_2. Very less variation takes place in the intensity and position of these bands as the amount difference of MnO_2 was only +3% as shown in XPS profile (28% to 31%). A dominant peak was observed in HEL region around 657.37/657.37/657.37/648.82 cm^{-1}. This peak is corresponding to stretching mode vibrations of Mn-O bonds within the MnO_6 octahedral lattice [80]. Here also, the intensity decreased with zero variation in position suggesting mono-dimensional deformation of lattice which is limiting degree of freedom.

5.3.2.12 FTIR analysis

Figure 5.18 shows the FTIR pattern of Mn and its Cs doped variants. For comparison purpose, both Mn-Cs(80:20) and Mn-Cs(20:80) were analysed and very less difference was found in terms of peaks' shift. Transmittance peak at 475 cm^{-1} represents the Mn-O stretching vibration whereas a broad hump at 3330 cm^{-1} and 1623 cm^{-1} can be attributed to bending mode of surface –OH groups which can be due to adsorbance of H_2O on the surface [81]. A continuous groove and tiny perturbances were observed at 1365 cm^{-1} and 1075 cm^{-1} which can be due to the Mn-OH of various species of MnO_x [82]. A small but sharp valley was there at 849 cm^{-1}can be due to O-Mn-O vibrations of MnO_2 [83]. Appearance of weak vibrations and fewer peaks can be the sign of high structural symmetry of lattice [84].

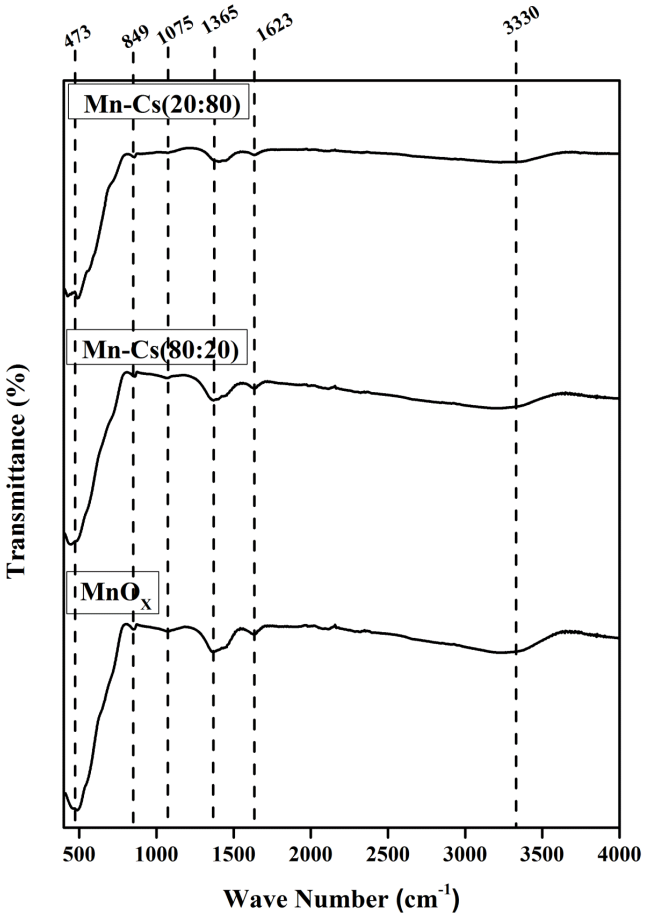

Figure 5.18: FTIR of MnOx, Mn-Cs(80:20) and Mn-Cs (20:80)

5.3.2.13 MeOH FTIR

In order to understand the basic nature of surface –OH group CH_3OH IR of MnO_x and most active variant Mn-Cs(80:20) were conducted. The difference of their fresh FTIR and CH_3OH IR is shown in **Figure 5.19** along with fine deconvolution of maxima of Mn-Cs(80:20).

Surface hydroxyl groups having Brönsted basic properties interact with methanol by forming monodentate or bidentate methoxy species as shown in **Reaction Scheme 5.3**. Both the catalysts, MnO_x and Mn-Cs(80:20) showed two bands but with enhanced intensity suggesting increased Brönsted basicity in the later.

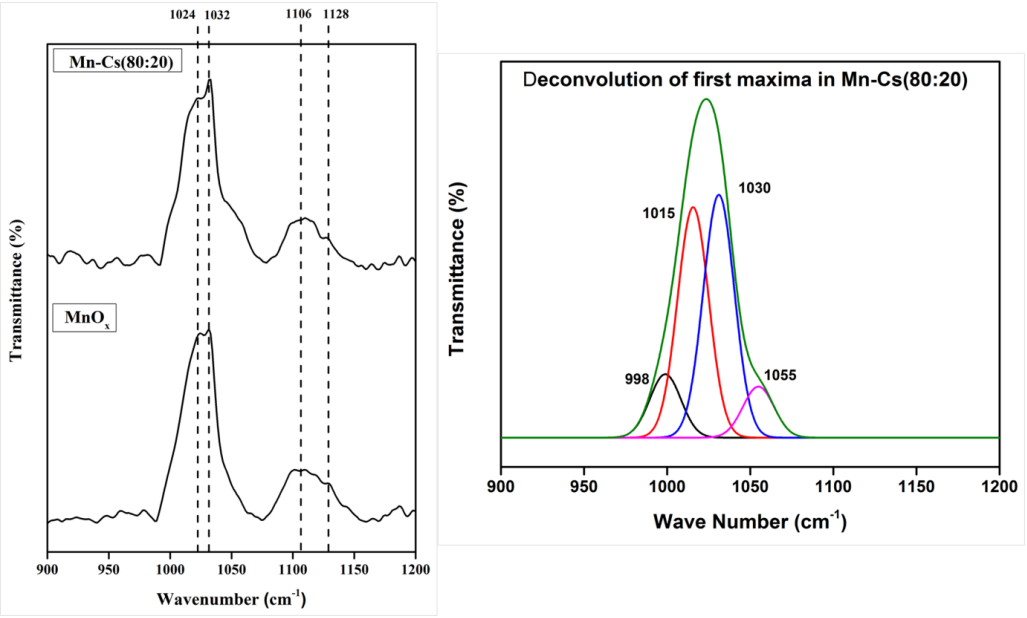

Figure 5.19: Pattern of CH_3OH-IR for (a) MnO_x and Mn-Cs(80:20) and (b) deconvoluted first maxima of Mn-Cs(80:20)

Asymmetric bimodal maxima were observed at around 1032 cm^{-1} corresponding to H-bonded molecularly adsorbed methanol [85]. Deconvolution of this maximum is also shown in **Figure 5.18.b** suggesting multiple chemical coordinations [86]. Two small peaks were seen at 1106 cm^{-1} and 1128 cm^{-1} which could be attributed to monodentate and bidentate methoxy species, respectively, evidencing presence of surface basicity due to O^-. Presence of this additional Brönsted basicity could be the reason of high DFF yield from 5-HMF [87].

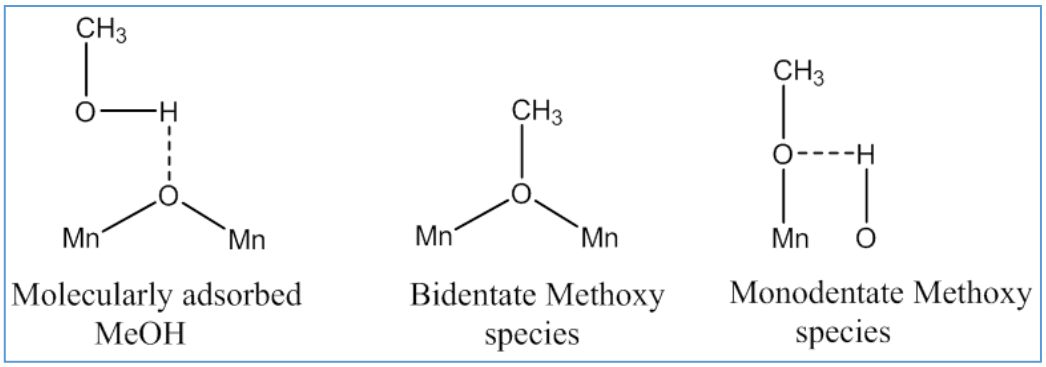

Scheme 5.3: Various species of methanol adsorbed on the surface of Mn during *insitu*-CH_3OH-IR

5.3.3 Activity evaluation

Table 5.6 lists the results screening of monometallic and alkaline metal doped variants of Mn catalysts for 5-HMF oxidation to DFF. Mo and Fe catalysts showed very less conversion and selectivity to DFF was also poor (**Table 5.6, entries 1 and 2**). In case of Co and Mn monometallic catalysts the conversion was only 25% and 33% but the selectivity increased significantly to 81% and 97%, respectively, suggesting their strong activity towards oxidative dehydrogenation (**Table 5.6, entries 3 and 4**). Mg and Ca doped Mn were not found much active as evident by their poor conversion, though Mn-Ba and Mn-Sr showed promising 60% and 74% conversion of HMF with 95% and 99% selectivity to DFF (**Table 5.6, entries 5-8**). Alkali metal doped Mn *i.e.* Mn-Cs proved highly efficient with 91% conversion and 98% selectivity to DFF hence, was used as a catalyst of interest for further studies (**Table 5.6, entry 9**). Considering the basic nature of La and Cs, Mn-La and Co-Cs were also tested but poor conversion was observed in this case (**Table 5.6, entry 10-11**).

Table 5.6: Catalytic screening for the oxidation of 5-HMF to DFF; **Reaction Conditions:** 5-HMF=100 mg, Catalyst= 50 mg , CH_3CN= 150 mL , T=90°C, P_{O2}= 200 Psig, Rt= 4h, Agitation speed= 1000 rpm

Sr. No.	**Catalysts**	**Conversion (%)**	**Selectivity (%)**
1	MoO_x	5	59
2	FeO_x	9	53
3	CoO_x	25	81
4	MnO_x	33	97
5	Mn-Mg	8	80
6	Mn-Ca	3	78

7	Mn-Ba	60	95
8	Mn-Sr	74	99
9	Mn-Cs	91	98
10	Mn-La	28	97
11	Co-Cs	57	93

Based on the primary catalyst screening results (**Table 5.6**), various combinations of Cs and Mn were screened for selective oxidation of 5-HMF in DFF and the results are shown in **Table 5.7**. Among these, Mn-Cs (80:20) proved to be highly efficient for 5-HMF oxidation to DFF (**Table 5.7, entry 8**). It was observed that amount of Cs higher than 20% led to higher conversion but selectivity of DFF decreased drastically with condensation product formation. The selectivity of DFF declined to 85% for Mn-Cs(70:30) from 98% of aforementioned Mn-Cs(80:20) and it continued to decrease as evident from **Table 5.7** (**entry 7**). Even conversion was decreased for Mn-Cs(50:50), Mn-Cs(60:40), Mn-Cs(70:30) (**Table 5.7, entry 5-7**) and though it again increased for Mn-Cs(40:60) onwards (**Table 5.7, entry 4**).

Table 5.7: 5-HMF oxidation to DFF over different combination of Mn and Cs **Reaction Conditions:** 5-HMF=100 mg, Catalyst= 50 mg , CH_3CN= 150 mL , T=90°C, P_{O2}= 200 Psig, Rt= 4h, Agitation speed= 1000 rpm

Sr. No.	**Loading Ratio (Mn-Cs)**	**C (%)**	**Selectivity (%)**	
			DFF	**FFCA**
1	10:90	95	2	2
2	20:80	95	10	7
3	30:70	90	29	7

4	40:60	78	35	10
5	50:50	66	48	15
6	60:40	70	67	10
7	70:30	78	85	5
8	80:20	91	98	1
9	90:10	55	80	20

Higher extent of interface between Cs and Mn is present for small amount of doping which are the active location for oxidative dehydration of 5-HMF [88]. This can be the reason for enhanced activity of Mn-Cs even at lower doping, whereas the excess amount of Cs can significantly reduce the interfaces between Cs and Mn leading to decreased activity of catalyst and according to Hedvall effect excessive migration of Cs in the Mn lattice and enhanced distribution in bulk of metal can also decline the catalytic activity [89].

Conversion selectivity profile for Mn-Cs(80:20) was studied for selective oxidation of 5-HMF to get insight of course of the reaction (**Figure 5.20).** Since first hour major product was DFF only which suggest the oxidation of hydroxyl group is preferred by Cs doped Mn rather than oxidation of aldehydic group. In the first hour, conversion was only 23% which increased to 39% after 2h with 100% selectivity to DFF. As the reaction progressed to longer duration, trace amount of FFCA was observed along with 99% DFF. In third hour of reaction, conversion was 66% which reached to 91% at optimised 4th hour of reaction.

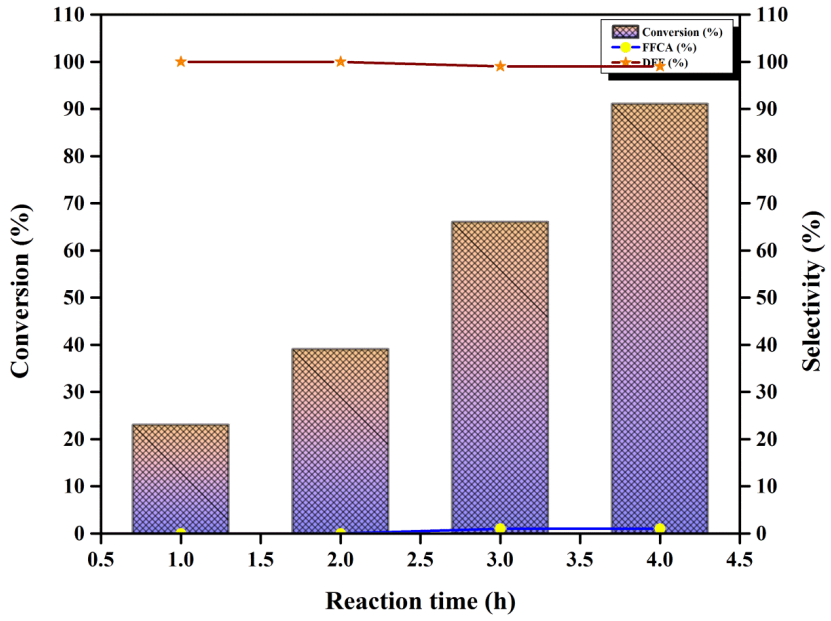

Figure 5.20: C-t profile of 5-HMF oxidation to DFF over Mn-Cs(80:20). **Reaction Conditions:** 5-HMF=100 mg, Catalyst= 50 mg , CH_3CN= 150 mL , T=90°C, P_{O2}= 200 Psig, Rt= 4h, Agitation speed= 1000 rpm

5.3.3.1 Effect of temperature

Effect of temperature on oxidation of 5-HMF was studied in the range of 60-120°C as shown in **Figure 5.21** and it was observed that higher reaction temperature led to further oxidation of DFF into FFCA. Though conversion of 5-HMF increased from 27 to 95% with increasing temperature from 60 to 120°C, selectivity to DFF reduced to 95% from 99% at 105°C which further dipped to 91% at 120°C. Trace amount of HMFCA was also detected at lower temperature of 60 and 75°C suggesting side oxidation of formyl group.

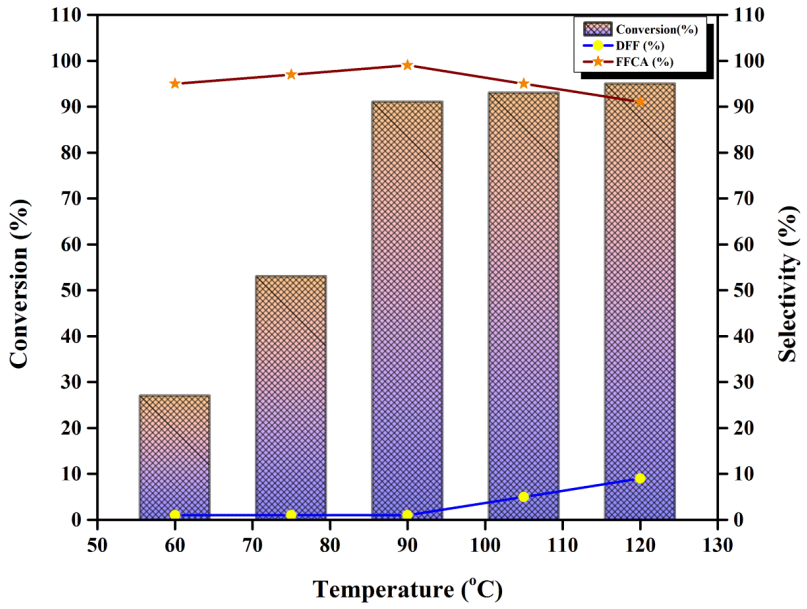

Figure 5.21: Temperature effect on the oxidation of 5-HMF to DFF, **Reaction Conditions:** 5-HMF=100 mg, Catalyst= 50 mg , CH_3CN= 150 mL , P_{O2}= 200 Psig, Rt= 4h, Agitation speed= 1000 rpm

5.3.3.2 Effect of pressure

5-HMF oxidation was also studied at different pressures of oxygen and the results are shown in **Figure 5.22**. At lower oxygen pressure of 50 psig, poor conversion of 5-HMF *i.e.* 18% was observed which increased to 32% for 100 psig oxygen pressure. As the pressure increased from 50 to 200 psig, a linear increase in conversion from 18 to 91% was observed. Interestingly, DFF selectivity was maintained more than 98%. However, further increase in pressure upto 300 psig, though conversion improved to 96%. DFF selectivity dropped to 90%, due to its further oxidation to FFCA.

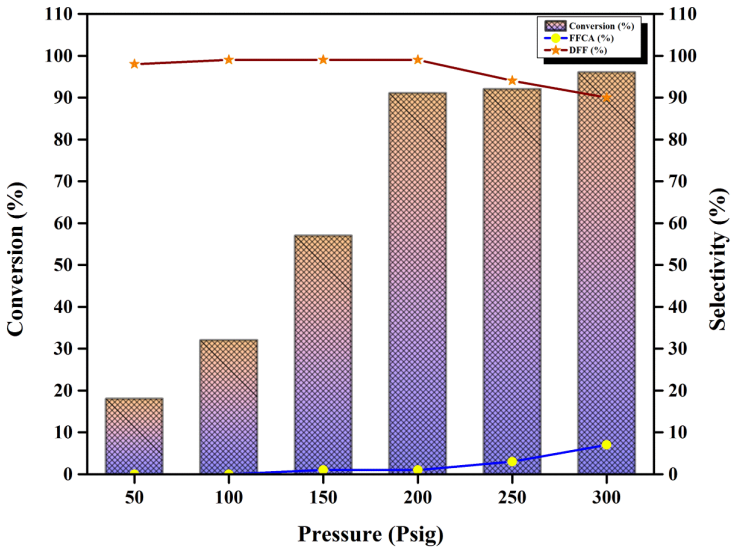

Figure 5.22: Effect of pressure on the oxidation of 5-HMF to DFF, **Reaction Conditions:** 5-HMF=100 mg, Catalyst= 50 mg , CH_3CN= 150 mL , T=90°C, Rt= 4h, Agitation speed= 1000 rpm

5.3.3.3 Catalyst loading effect

Figure 5.23 shows the effect of catalyst loading on conversion and selectivity in 5-HMF oxidation reaction. It was observed that at the lowest catalyst loading of 25 mg, DFF was selectively observed with only 31% conversion of 5-HMF. With increase in catalyst loading upto 100 mg, FFCA formation increased up to 35% along with 4% of FDCA and only 61% of DFF formation observed. Hence, catalyst loading of 50 mg was the most optimum value for 5-HMF oxidation where 91% conversion and 99% selectivity of DFF was observed.

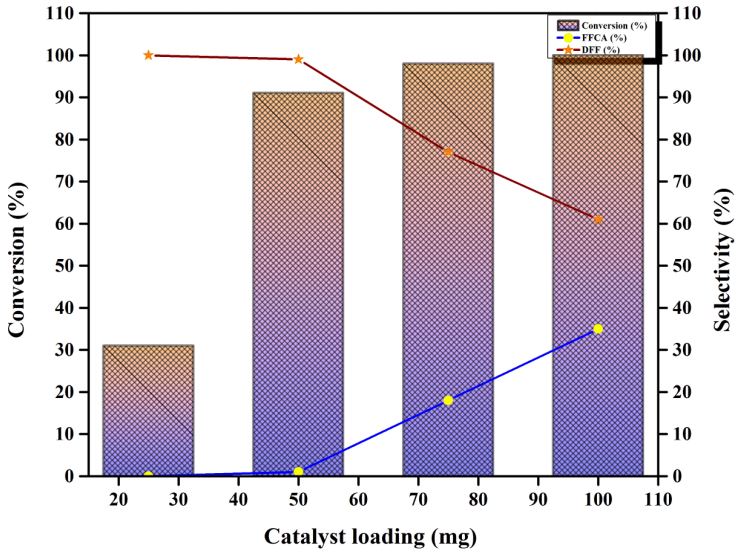

Figure 5.23: Effect of catalyst loading on the oxidation of 5-HMF to DFF, **Reaction Conditions:** 5-HMF=100 mg, CH_3CN= 150 mL , T=90°C, P_{O2}= 200 Psig, Rt= 4h, Agitation speed= 1000 rpm

5.3.3.4 Effect of reaction time

Selective oxidation of 5-HMF to DFF was monitored for 8 h of reaction time (**Figure 5.24**), in which conversion of 5-HMF increased from 39 to 100% with time. For 6 h, conversion increased to 98% but the selectivity to DFF remained at only 89% with 8% FFCA. This decline in selectivity of DFF continued (78%) when reaction was extended to 8 h, as concentration of FFCA increased to 17% with appearance of traces of FDCA (2%), with complete conversion of 5-HMF .

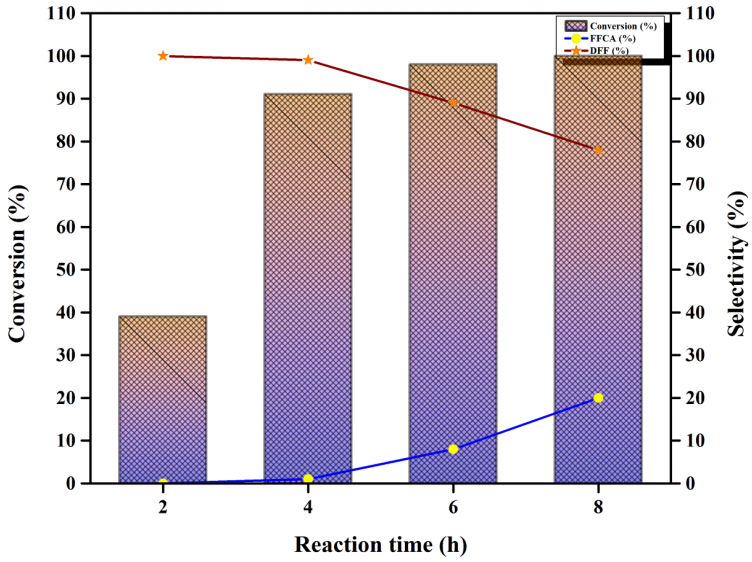

Figure 5.24: Effect of reaction time on 5-HMF oxidation to DFF, **Reaction Conditions:** 5-HMF=100 mg, Catalyst= 50 mg , CH_3CN= 150 mL , T=90°C, P_{O2}= 200 Psig, Rt= 4h, Agitation speed= 1000 rpm

5.3.3.5 Effect of solvent

Influence of reaction media was investigated thoroughly and acetonitrile was found best suitable solvent for selective formation of DFF (**Figure 5.25**). Several polar and protic solvents like H_2O, CH_3OH, polar aprotic solvents like acetonitrile and non polar toluene were screened for 5-HMF oxidation. It was observed that highly polar and protic solvent like water was gave only 47% conversion with 38% selectivity to DFF due to 5-HMF oligomerisation. On the other hand, methanol, due to its higher extent of adsorption on the catalytic surface rendered active sites inaccessible to the reactants. This behaviour can be explained by higher value of their Synder's eulotropic coefficient (ε°) which is 0.95 for CH_3OH [90]. For acetonitrile excellent solubility of molecular oxygen (8.1) and moderate value of Synder's eulotropic coefficient (0.65) prevented any kind of competition between reactant and solvent for the catalytic surface [43]. Moderate polarity (dielectric constant = 37) stabilised the active

metal cationic centre which could be the reason for higher conversion (91%) and selectivity (99%) in acetonitrile. In case of MIBK and toluene also the catalyst showed reasonable conversion of 62 and 58%, respectively but poor DFF selectivity of 70 and 67% which may be due to small value of ε° and less polarity, respectively.

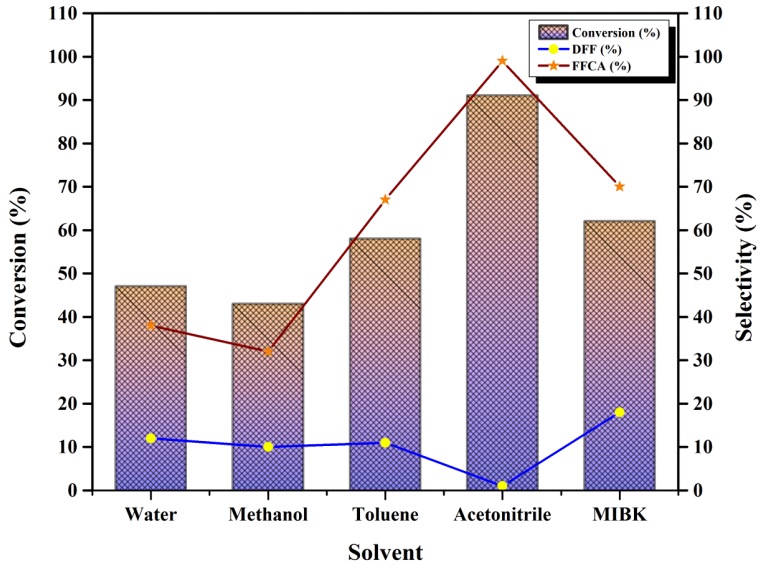

Figure 5.25: Effect of solvent on 5-HMF oxidation to DFF, **Reaction Conditions:** 5-HMF=100 mg, Catalyst= 50 mg , CH_3CN= 150 mL , T=90°C, P_{O2}= 200 Psig, Rt= 4h, Agitation speed= 1000 rpm

5.3.3.6 Stability of catalyst

Stability of our catalyst was investigated by hot filtration and recyclability tests. To exclude any kind of possibilities of metal leaching hot filtration was performed in which the reaction was stopped after 2 h and the catalyst was separated out from the reaction mixture. Then the reaction was resumed without any catalyst for next 2 h. There was no any increase in the conversion was observed as shown in **Figure 5.26**, ruling out any possibility of metal leaching.

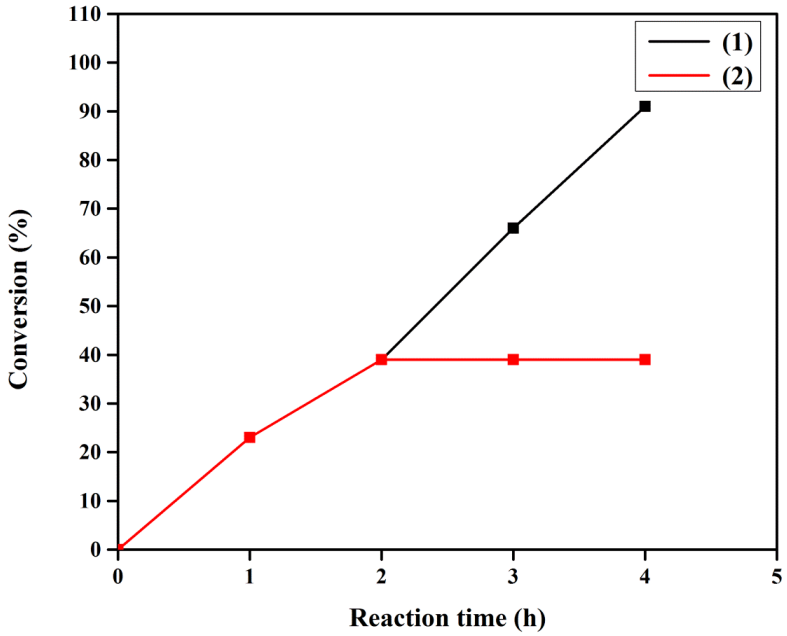

Figure 5.26: Hot filtration test for metal leaching (1) Normal reaction with catalyst (2) Reaction without catalyst after 2 h of reaction **Reaction Conditions:** 5-HMF=100 mg, Catalyst= 50 mg , CH_3CN= 150 mL , T=90°C, P_{O2}= 200 Psig, Rt= 4h, Agitation speed= 1000 rpm

The catalyst recycle efficiency of our catalyst was also evaluated (**Figure 5.27**). For the first 4 recycle runs the conversion marginally dropped from 91% to 85% with DFF selectivity remaining almost constant (95-99%). From 6^{th} recycle run onwards catalyst started to show rapid decline in catalytic activity with conversion decreasing to 64% whereas selectivity to DFF also dipped to 90%. The dramatic decrease in catalytic activity may be due to the deposition of carbonaceous mass as shown by TEM analysis of spent catalyst in **Figures 5.8.e and 5.8.f.**

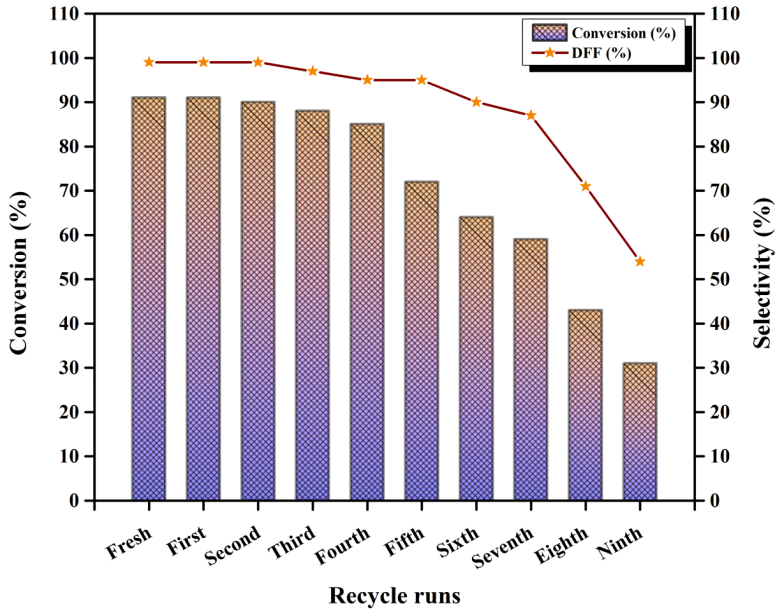

Figure 5.27: Catalyst recycle run for 5-HMF oxidation to DFF, **Reaction Conditions:** 5-HMF=100 mg, Catalyst= 50 mg , CH_3CN= 150 mL , T=90°C, P_{O2}= 200 Psig, Rt= 4h, Agitation speed= 1000 rpm

5.4. Plausible reaction mechanism

The characterization of the catalyst and the reaction studies suggested that efficient oxidation of 5-HMF to DFF proceeded by the assistance of lattice oxygen of the catalyst *via* Mars-van Krevelen mechanism. XPS studies revealed 6% increase in the amount of lattice oxygen after doping of Cs in Mn catalyst. Almost 18% decline in the lattice oxygen was further observed in used catalyst which indicates its role in 5-HMF oxidation to DFF. Similarly vacant oxygen sites also increased from 32% of fresh Mn-Cs(80:20) to 49% of used Mn-Cs(80:20) clearly showing stepwise consumption of lattice oxygen. These oxygen defects are replenished by external O_2 though it was observed that the rate of replenishment of oxygen defect is slightly lower which can limit the overall rate of reaction. These findings were also supported by the comparison of fresh and used Mn-Cs(80:20) where the amount of Mn^{+4} was found reduced to 39% whereas Mn^{+3} increased to 34% from 32% of fresh Mn-Cs(80:20). The higher

oxidation state of Mn *i.e.* Mn^{+4} which was catalytically active site found to increase to 60% on Cs doping from 50% of bare MnO_x. Higher oxygen mobility was also reported from the results of H_2-TPR and O_2-TPO which led to enhanced redox activity of Mn-Cs(80:20). In the first step of Mars-van Krevelen mechanism Mn^{+4} by its lattice oxygen gets converted to Mn^{+3}. This will simultaneously catalyse the oxidation of 5-HMF to DFF leaving oxygen vacancies behind which will be replenished by external O_2 pressure as shown in **Scheme 5.4**.

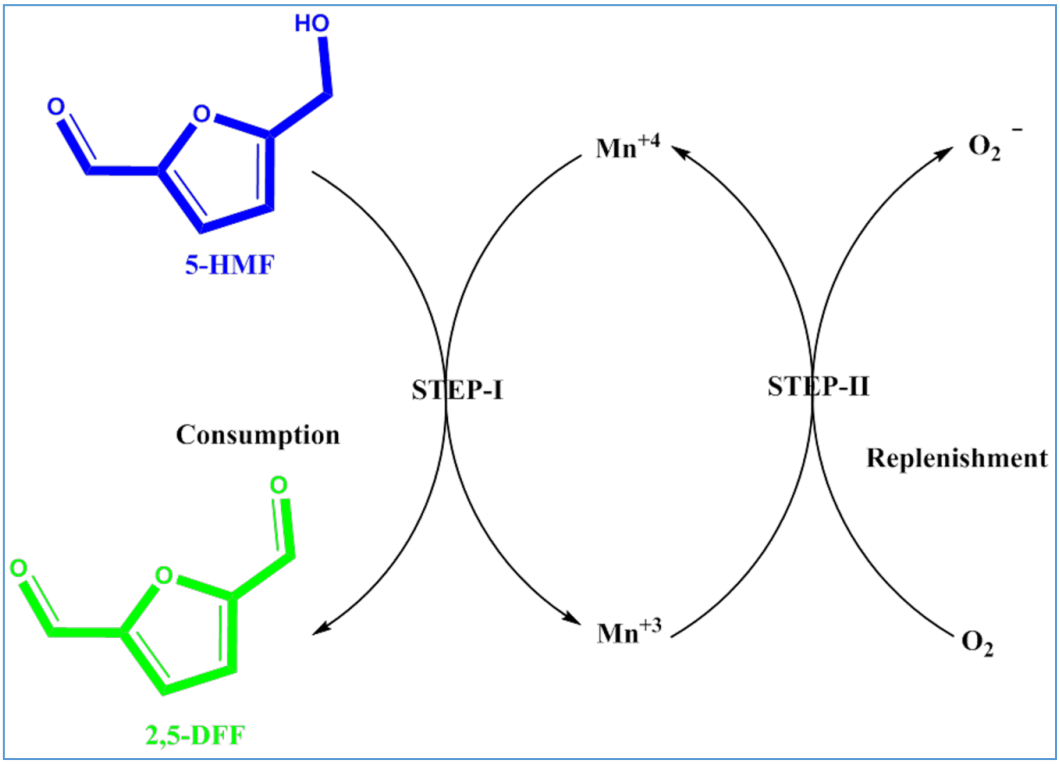

Reaction Scheme 5.4: Mars-van Krevelen mechanism for 5-HMF oxidation to DFF

5.5 Conclusion

Screening of Cs doped in the lattice of Mn created the best suitable Mn-Cs(80:20) catalyst for the selective oxidation of 5-HMF to DFF. XRD studies revealed that inclusion of Cs in Mn lattice domains increased the crystalline nature, mobility of oxygen and oxygen diffusion which were vital for selective oxidation of 5-HMF. Enhanced thermal stability, higher surface area, porosity was established by TG-DTA and N_2-sorption profile. Detailed qualitative and

quantitative analysis by XPS revealed lowered work function of Mn-Cs(80:20) and binding energy further suggesting mutual synergistic interaction of Mn and Cs. The comparative analysis of nature of O 1s of MnO_x, Mn-Cs(80:20)-Fresh and Mn-Cs(80:20)-spent by XPS established the role of lattice oxygen suggesting that the reaction took place by Mars-van Krevelen mechanism. FE-SEM, TEM, XPS and HR-TEM analysis showed dual morphologies and interfacial redox properties which were further confirmed by H_2-TPR and O_2-TPO profiles. Cs doping clearly enhanced the basicity of MnO_x due to increase in O_2 vacancy as found by CO_2 –TPD and XPS. MeOH-IR studies confirmed the strong Brönsted basicity due to different oxide species formed on the surface of Mn-Cs(80:20) which were responsible for 91% conversion and 98% selectivity with 86.8% yield of DFF formed under optimized reaction parameters of T=90°C, pO_2= 200 Psig, reaction time = 4h, agitation speed= 1000 rpm with 5-HMF/catalyst ratio of 2 in 150 mL acetonitrile solvent.

References

1. O. K. Lee, D. H. Seong, C. G. Lee and E. Y. Lee, *J. Ind. Eng. Chem.* **2015,** 29, 24-31

2. F. W. Lichtenthaler and S. Peters, *Comptes Rendus Chimie.* **2004**, **7**, 65–90

3. J. N. Chheda, G. W. Huber and J. A. Dumesic, *Angew. Chem. Int. Ed.,* **2007**, 46, 7164-7183

4. F. W. Lichtenthaler, E. Cuny, D. Martin and S. Rönninger, Carbohydrates as Organic Raw Materials, in: Lichtenthaler, F. W. (Eds.), VCH Publishers: Weinheim/NewYork, **1991**, pp. 80.

5. J. J. Bozell and G. R. Petersen, *Green Chem.,* **2010,** 12, 539- 554

6. Y. Román-Leshkov, C. J. Barrett, Z. Y. Liu and J. A. Dumesic, *Nature*, **2007**, 44, 982-985

7. R. Alamillo, M. Tucker, M. Chia, Y. Pagán-Torres and J. Dumesic, *Green Chem.,* **2012**, 14, 1413-1419

8. T. Ståhlberg, W. Fu, J.M. Woodley and A. Riisager *ChemSusChem*, **2011,** 4, 451-458

9. S. Albonetti, A. Lolli, V. Morandi, A. Migliori, C. Lucarelli and F. Cavani, *Appl. Catal. B: Environ.,* **2015,** 163, 520-530

10. M. del Poeta, W. A. Schell, C. C. Dykstra, S. Jones, R. R. Tidwell, A. Czarny, M. Bajic, A. Kumar, D. Boykin and J. R. Perfect, *Antimicrob. Agents Chemother.,* **1998,** 42, 2495-2502

11. K.T. Hopkins, W.D. Wilson, B.C. Bendan, D.R. McCurdy, J.E. Hall, R.R. Tidwell, A. Kumar, M. Bajic and D.W. Boykin, *J. Med. Chem.*, **1998,** 41, 3872-3878

12. A. S. Amarasekara, D. Green and L. D. Williams, *Eur. Polym. J.* **2009,** 45, 595-598

13. A. Gandini and M. N. Belgacem, *Prog. Polym. Sci.,* **1997,** 22, 1203–1379

14. D. Salgado-Chavarria and J. Palacios-Alquisira, *Chemistryselect,* **2020,** 5, 4826-4838

15. J. Dai, *Green Energy and Environment,* **2021,** 6, 22-32

16. L. Cottier, G. Descotes, E. Viollet, J. Lewkowski and R. Skowronski, *J. Heterocyclic Chem.,* **1995,** 32, 927-930

17. P. D. Hanke, Patent (USA), **2012,** 8, 183, 020 B2

18. H. Firouzabadi and E. Ghaderi, *Tetrahedron Letters*, **1978,** 19, 839-840

19. L. Cottier, G. Descotes, J. Lewkowski and R. Skowronski, *Pol. J. Chem.*, **1994,** 68, 693-698.

20. J. W. Reijendam, G. J. Heeres and M. J. Janssen, *Tetrahedron,* **1970,** 26, 1291-1301

21. L. Cottier, G. Descotes, J. Lewkowski and R. Skowronski, *Org. Prep. Proced. Int.*, **1995**, 27, 564-566

22. T. El-Hajj, J. C. Martin and G. Descotes, *J. Heterocyclic Chem.,* **1983,** 20, 233-235

23. W. Partenheimer and V. V. Grushin, *Adv. Synth. Catal.*, **2001,** 343, 102-111

24. J. Ma, Z. Du, J. Xu, Q. Chu and Y. Pang, *ChemSusChem*, **2011,** 4, 51–54

25. T. S. Hansen, I. Sàdaba, E. J. Gárcia-Suárej and A. Riisager, *Appl. Catal. A: Gen.,* **2013,** 456, 44– 50

26. G. A. Halliday, R. J. Young Jr. and V. V. Grushin, *Org. lett.,* 2003, **5**, 2003-2005

27. S. K. Hanson, R. Wu and L. A. "Pete" Silks, *Org. lett.*, **2011,** 13, 1908-1911

28. G. Li, Z. Sun, Y. Yan, Y. Zhang and Y. Tang, *ChemSusChem*, **2017**, 10, 494–498

29. A. S. Amarasekara, D. Green and E. Mcmillan, *Catal. Communi.*, **2008,** 9, 286–288

30. J. Nie, J.Xie and H. Liu, *J. Catal.*, **2013,** 301, 83–91

31. J. Nie, J. Xie and H. Liu, *J. Catal.*, **2013,** 34, 871-875

32. F. Yang, Z. Yuan, B. Liu, S. Chen and Z. Zhang, *J. Ind. Eng. Chem.*, **2016,** 38, 181-185

33. C. A. Antonyraj, J. Jeong, B. Kim, S. Shin, S. Kim, K. W. Lee and J. K. Chuo, *J. Ind. Eng. Chem.*, **2012,** 19, 1056-1059

34. J. Artz, S. Mallmann, R. Palkovits, *Chemsuschem*, **2015,** 8, 672-679

35. K. Ghosh, R. A. Molla, A. A. Iqubal, S. S. Islam and S. M. Islam, *Appl. Catal. A: Gen.*, **2016,** 520, 44–52

36. M. A. Lilga, R. T. Hallen and M. Gray, *Top. Catal.*, **2010,** 53, 1264–1269

37. C. A. Antonyraj, B. Kim, Y. Kim, S. Shin, K. W. Lee, I. Kim and J. K Chuo, *Catal. Commun.*, **2014,** 57, 64–68

38. F. L. Grasset, B. Katryniok, S. Paul, V. Nardello-Rataj, M. Pera-Titus, J. M. Clacens, F. D. Campo and F. Dumeignil, *RSC Adv.*, **2013,** 3, 9942-9948

39. O. C. Navarro, A. C. Canós and S. I. Chornet, *Top. Catal.*, **2009,** 52, 304–314

40. D. Baruah, F. L. Hussain, M. Suri, U. P. Saikia, P. Sengupta, D. K. Dutta and D. Konwar, *Catal. Commun.* **2016,** 77, 9-12

41. X. Tong, L. Yu, H. Chen, X. Zhuang, S. Liao and H. Cui, *Catal. Commun.*, **2017,** 90, 91-94

42. B. Liu, Z. Zhang, K. Lv, K. Deng and H. Duan, Appl. *Catal. A: Gen*, **2014,** 472, 64-71

43. F. Neatu, N. Petrea, R. Petre, V. Somoghi, M. Florea and V. I. Parvulescu, *Catal. Today,* **2016,** 278, 66-73

44. R. Fang, R. Luque and Y. Li, *Green Chem.,* **2016,** 18, 3152-3157

45. J. Lie and H. Liu, *J. Catal.*, **2014,** 316, 57–66

46. Z. Yang, W. Qi, R. Su and Z. He, *ACS Sustainable Chem. Engg.,* **2017,** 5, 4179-4187

47. J. Zho, A. Jaykumar and J. M Lee, *ACS Sustainable Chem. Engg.*, **2018,** 6, 2976-2982

48. W. Cen, Y. Liu, Z. Wu, H. Wang and X. Weng, *Phys. Chem. Chem. Phys.,* **2012,** 14, 5769-5777

49. A. Jha, K. R. Patil and C. V. Rode, *chempluschem,* **2013,** 78, 1384-1392

50. Y. Hou, J. Qi, J. Hu, Y. Xiang, L. Xin and X. Wei, *Processes,* **2020,** 8, 488-518

51. K. Nila Nandha and A. Nag, *Chem. Commun.,* **2018,** 54, 5205-5208

52. G. Jian, Y. Xu, L. C Lai, C. Wang and M. R. Zachariah, *J. Mater. Chem. A,* **2014,** 2, 4627–4632

53. E. R. Stobbe, B. A. d. Boer and J. W. Geus, *Catal. Today,* **1999,** 47, 161–167

54. X. Gu, J. Yue, L. Li, H. Xue, J. Yang and X. Zhao, *Electrochimica Acta,* **2015,** 184, 250–256

55. S. Liang, F. Teng, G. Bulgan, R. Zong and Y. Zhu, *J. Phys. Chem. C.,* **2008,** 112, 5307–5315

56. Z. Yuan, B. Liu, P. Zhou, Z. Zhang and Q. Chi, *Catal. Sci. Technol.,* **2018,** 8, 4430–4439

57. O. Jankovskýa, D. Sedmidubskýa, P. Šimeka, Z. Sofera, P. Ulbrichb and V. Bartůněka, *Ceram. Int.,* **2015,** 41, 595–601

58. Y. F. Shen, S. L. Suib, and C. L. O'Young, *J. Am. Chem. Soc.,***1994,** 116, 11020–11029

59. H. R. Barai, A. N. Banerjee, N. Hamnabard and S. W. Joo, *RSC Adv.*, **2016,** 6, 78887–78908

60. B. D. Cullity, Elements of X-ray Diffraction, Second ed., M A Reading, Addison-Wesley, CA, **1978**

61. S. K Apte, S. D. Naik, R. S. Sonawane, B. B. Kale, N. Pavaskar, A. B. Mandale and B. K. Das, *Mater. Res. Bull.*, **2006,** 41, 647-654

62. S. Ponce, M. A. Pena and J. L. G. Fierro, *Appl. Catal. B: Environ.*, **2000,** 24, 193–205

63. A. Jha, D. Mahamane, A. Suryawanshi, S. M. Joshi, P. Shaikh, N. Biradar, S. Ogale and C. V. Rode, *Catal. Sci. Technol.*, **2014,** 4, 1771–1778

64. K. Aika, H. Hori and A. Ozaki, *J. Catal.,***1972,** 27, 424-431

65. F. Zasada, P. Stelmachowski, G. Maniak, J.-F. Paul, A. Kotarba and Z. Sojka, *Catal. Lett.,* **2009,** 127, 126-131

66. Y. L. Lee, A. Jha, W. J. Jang, J. O. Shim and C. V Rode, B. H. Jeon, J. W. Bae and H. S, Roh, *Appl. Catal. A: Gen.*, **2018,** 551, 63–70

67. F. J. Shi, F. Wang, H. X. Dai, J. X. Dai, J. G. Deng, Y. X. Liu, G. M. Bai, K. M. Ji and C. T. Au, *Appl. Catal. A: Gen.*, **2012,** 433-434, 206–213

68. Y. Wang, K. Liu, J. Wu, Z. hu, L. Huang, J. Zhou, T. Ishihara and L. Guo, *ACS Catal.,* **2020,** 10, 10021−10031

69. L. C. Zhang, Z. H. Lio, X. H. Tang, J. F. Wang and K. Ooi, *Mater. Res. Bull.*, **2007,** 42, 1432–1439

70. H. Liu, X. Cao, J. Wei, W. Jia, M. Li, X. Tang, X. Zeng, Y. Sun, T. Lei, S. Liu and L. Lin, *ACS Sustainable Chem. Eng.*, **2019, 7,** 7812−7822

71. M. Atkins, J. Couves, M. Hague, B. H. Sakakini and K. C. Waugh, *J. catal.*, **2005,** 235, 103-113

72. Z. Xie, X. Zhou, H. Wu, H. Zhao, Y. Liu and H. Chen, *Catal. Lett.*, **2016,** 146, 1355–1360

73. N. D. Wasalathanthri, T. M. Santamaria, D. A. Kriz, S. L. Dissanayake, C. Hao-Kuo, S. Biswas and S. L. Suib, *Appl. Catal. B: Environ.*, **2017,** 201, 543–551

74. S. Biswas, A. S. Poyraz, Y. Meng, C. H. Kuo, C. Guild, H. Tripp and S. L. Suib, *Appl. Catal., B: Environ.*, **2015,** 165, 731–741

75. S. Rong, P. Zhang, F. Liu and Y. Yang, *ACS Catal.*, **2018,** 8, 3435−3446

76. X. Lin, Y. Yoon, N. G. Petrik, Z. Li, Z.-T. Wang, V.-A. Glezakou, B. D. Kay, I. Lyubinetsky, G. A. Kimmel, R. Rousseau and Z. Dohnálek, *J. Phys. Chem. C*, **2012,** 116, 26322−26334

77. S. Sun, M. Watanabe, J. Wu, Q. An and T. Ishihara, *J. Am. Chem. Soc.*, **2018,** 140, 6474–6482

78. B. H. Rita and J. P. Pereira-Ramos, *Chem. Rev.*, **2010,** 110, 1278–1319

79. H. R. Barai, A. N. Banerjee and S. W. Joo, *J. Ind. Eng. Chem.*, **2017,** 56, 212–224

80. S. H. Shim, D. LaBounty and T. S. Duffy, *Phys. Chem. Miner.*, **2011,** 38, 685–691

81. S. A. Moon, B. K. Salunke, B. Alkotaini, E. Sathiyamoorthi and B. S. Kim, *IET Nanobiotechnol*., **2015,** 9, 220-225

82. H. Chen, X. Dong, J. Shi, J. Zhao, Z. Hua, J. Gao, M. Ruan and D. Yan, *J. Mater. Chem.,* **2007,** 17, 855–860

83. D. Jaganyi, M. Altaf and I. Wekesa, *Appl. Nanosci.*, **2013,** 3, 329–333

84. H. Wang. Z. Lu, D. Qian, Y. Li and W. Zhang, *Nanotechnology,* **2007,** 18, 115616-115620

85. D. Vernekar, S. S. Sakate, C. V. Rode and D. Jagadeesan, *J. Catal.*, **2019,** 378, 80–89

86. M. Bensitel, O. Saur and J. C. Lavalley, *Mater. Chem. Phys.* **1991,** 28, 309-320

87. M. L. Bailly, C. Chizallet, G. Costentin, J. M Krafft, H. L. Pernot and M. Che, *J. Catal.*, **2005,** 235, 413–422

88. M. Haruta, *Catal. Surv. Jpn.*, **1997,** 1, 61-73

89. J. A. Hedvall, *Adv. Catal.*, **1956,** 8, 1-15

90. L. R. Snyder, J. J. Kirkland and J. W. Dolan, Introduction to Modern Liquid Chromatography, Wiley-Blackwell, Hoboken, NJ, **2009**.

Chapter 6

Highly efficient bimetallic synergism of Cu-Co on x-GO for selective aerial oxidation of 5-HMF to FDCA

Highly efficient bimetallic synergism of Cu-Co on x-GO for selective aerial oxidation of 5-HMF to FDCA

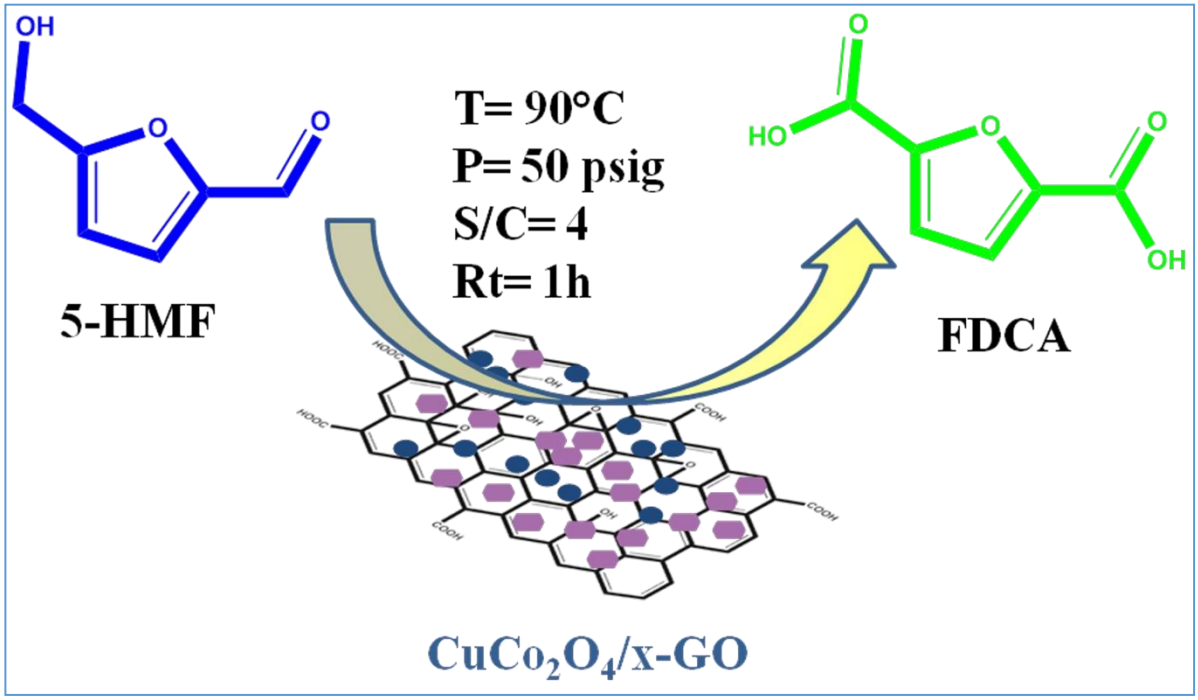

Exceptional catalytic activity of non-noble Cu-Co/x-GO catalyst was obtained for selective oxidation of 5-HMF to FDCA. Cu-Co(1:3)/x-GO proved to be the best catalyst due to its ultrafine size of 4-5 nm, uniform dispersion and high surface area. 98% selectivity to FDCA with complete conversion of 5-HMF was observed within 1 h of reaction in extremely mild conditions of 90°C with 50 psig external pressure of air. Surface Brönsted acidity of Cu and combined Lewis and Brönsted basicity of Cu+Co were found to be responsible for this excellent catalytic activity. XRD, XPS and FTIR revealed the role of spinel $CuCo_2O_4$ in 5-HMF oxidation. A plausible mechanism was proposed with the help of controlled experiments. Various reaction parameters and detailed characterization of catalyst was done to understand the catalytic insight.

6.1 Introduction

Rapid consumption of conventional fuel feedstock and corresponding price hikes of petrochemicals are growing concerns for an energy sustainable future [1-2]. This is also perturbing the supply chain of fine chemicals generated by the petrochemical refinery. Idiosyncratic pathways for efficient generation of adequate amount of commodity chemical feedstock from renewable resources are being explored since many decades. Considering the renewable resources, lignocellulosic biomass is getting much attention as it is attractive source of fixed renewable carbon which can be converted into various fine chemicals and it can immensely relieve pressure on traditional fossil fuel feedstock [3-5]. The humongous amount of biomass present all around the world is providing a gateway to fine chemicals, petrol derived commodities and polymer precursors. The average energy storage of annual 200 billion metric tons of biomass produced is $3x10^8$ KJ [6]. Biomass is full of oxygenated molecules/compounds which can be converted into various fine chemicals and polymeric precursors. 5-(hydroxymethyl)-2-furfural (5-HMF) is such kind of a platform molecule which can form various kinds of building block molecules having application as polyurethane, polyesters, pharmaceuticals and polyamide plastics [7-9]. 5-HMF can be converted into number of commodity chemicals like 2,5-dimethyl furan (DMF), 2,5-(bishydroxymethyl)furan (BHMF), 2,5-dimethyltetrahydrofuran (DMTHF), 5-(hydroxymethyl)furan-2-carboxyllic acid (HMFCA), 5-formyl-2-furancarboxyllic acid (FFCA), 2,5-diformylfuran (DFF) and 2,5-furandicarboxyllic acid (FDCA) *etc* [10-12]. Oxidation of 5-HMF gives oxy-rich compounds like DFF and FDCA which act as monomers for Polyethylenefuancarboxylate (PEF), a green alternative of current terephthalate (PET) polymeric plastics [13].

PET is currently produced for artificial polyester worldwide which in terms of volume *is* 26 million tonnes/yr [14]. From almost 60 million tons of medical devices to films and packaging materials, beverage bottles, textile fibres are made from this polyester due to its excellent durability, barrier properties, optical clarity and low productive cost [15]. But it is highly stable and non biodegradable chemical which is attributed to the presence of high ratio of aromatic content in its structure and corresponding limited mobility of polymeric chain [16]. These structural characteristics make this polyester very resistant to microbial attack and non-degradable [17]. As shown in **Reaction Scheme 6.1**, complete oxidation of 5-HMF yields symmetric FDCA which is enlisted in the top 12 value added chemicals derived from biomass by US Department of Energy [13]. The ethylene glycol derivative of FDCA is known as polyethylenefurancarboxylate (PEF) which is superior to PET due to its higher gas impermeability, glass transition temperature, low temperature formability, reduced chain mobility and biodegradable nature [18]. Taking account of all these advantages of PEF, selective and complete oxidation of 5-HMF into FDCA is highly desired.

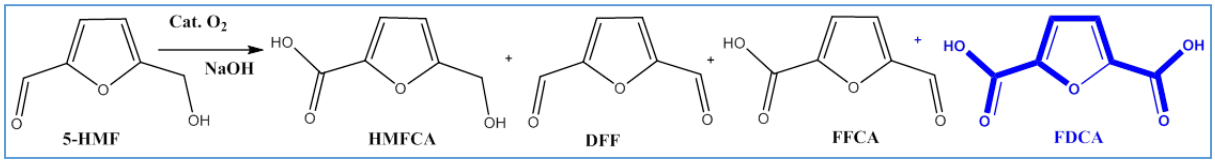

Reaction Scheme 6.1: Oxidation of 5-HMF to FDCA

Traditionally 5-HMF oxidation can be done by using stoichiometric amount of various oxidants like $Cr_2O_7^{2-}$, $KMnO_4$ and CrO_4^{2-} but it was highly toxic and hazardous route [19-20]. Homogenous Amoco Mild-Century (MC) catalyst used in presence of acetic acid as solvent by Partenheimer and Grushin whereas Saha *et al*. used acetate precursors of Co and Zn in NaBr and CF_3COOH for FDCA production form HMF but corrosive nature and no-recyclability made it unsuitable [21-22]. Combination of noble metal heterogeneous catalyst and molecular oxygen as oxidant attracted attention of many due to its high catalytic efficiency

and separable nature. Noble metals like Pd, Pt, Ru, Au and their alloys supported on various supports like Al_2O_3, CeO_2 TiO_2, hydroxyappetite (HAP), hydrotalcite (HT), ZrO_2, AC and zeolites were proposed out of which Au was found to be highly active due to higher resistance to H_2O and oxidative environment [23-28]. But end product, carboxylic acid and intermediates deactivates Au in the absence of alkaline medium. Higher substrate to catalyst ratio and high cost were few more reasons due to which it was not found economically viable. Focus then shifted on non-noble metal catalysts due to their cheap cost and easy availability. Saha *et al.* synthesized porphyrin based porous Fe catalyst and obtained complete conversion with 79% selectivity to FDCA at 120°C and 150 psig external pressure of oxygen in long 10 h of reaction time [29]. Bimetallic Co-Fe was investigated by Zhang *et al.* where t-BuOOH was used as an oxidant for 15 h and only 67.2% selectivity to FDCA was achieved at 80°C in DMSO solvent [30]. Another bimetallic combination of Mn-Fe(3:1) was tested by Pàrvulescu *et al.* in an aqueous medium [31] which gave only 32% selectivity to FDCA with 93% conversion of HMF after extensive reaction of 24 h at 90°C and 120 psig pressure of O_2. MnO_2 was applied for 5-HMF oxidation by Hara *et al.* where they achieved 91% yield of FDCA in presence of $NaHCO_3$ as base in 24 h of reaction at 100°C and 150 psig of external pressure [32]. While, physically mixed different earth crust abundant metals like CuO, MnO and CeO_2 claimed 99% selectivity to FDCA at higher temperature (130°C) and external pressure (300 psig) of oxygen in just 3 h [33]. Report also suggests use of various ionic liquids with heterogeneous catalyst with limitation of very high temperature (160°C) and poor selectivity (30-60%)[34]. Considering all theses shortcoming of previously reported catalytic systems, we designed a highly efficient non-noble bimetallic Cu-Co catalyst with ratio of 1:3 supported on x-Graphene oxide (x-GO) for 5-HMF oxidation. Under very mild reaction conditions of 90°C, 50 psig pressure of air and just 1 h of reaction time 98% selectivity with 90.1% yield of FDCA could be achieved with complete conversion of HMF.

This catalyst was found to be highly active up to 4 recycle studies with almost 84% selectivity of FDCA because of high surface area and uniformly dispersed metals.

6.2 Experimental

6.2.1 Catalyst synthesis and characterization methodology

x-GO and supported monometallic and bimetallic Cu-Co catalysts were synthesized by the method described in section 2.3.4 and 2.3.5 of Chapter 2. Activity evaluation and catalyst testing was conducted in 300 mL Parr reactor as mentioned earlier in subsection 2.5.4 of chapter 2 whereas the reaction progress was monitored by using HPLC as per analytical conditions of subsection 2.6.2 and 2.7 of chapter 2. The catalyst was extensively characterised by different techniques mentioned in section 2.4 of chapter 2.

6.3 Results and Discussion

6.3.1 Objective of this work

The main objective of this work are: (i) to develop and design an efficient reusable catalyst for 5-HMF oxidation to FDCA in relatively mild conditions (ii) In-depth characterization studies for catalyst to understand the surface properties responsible for efficient production of FDCA (iii) Detail parameter optimization study for establishing a structure-activity correlation

6.3.2 Characterisation of catalyst

6.3.2.1 BET Surface area analysis

BET surface area and BJH pore size analysis were conducted to reveal the surface distribution of metals on the support. **Table 6.1** describes the textural properties like surface area, pore size, pore volume and crystallite size of x-GO and all the x-GO supported

catalysts. Continuous decrease in the surface area was observed after loading of metals suggesting successful homogeneous distribution of nanoparticles on the support. Lowest surface area was observed for Cu:Co(1:3)/x-GO as shown in **Table 6.1, entry 5** suggesting highly uniform distribution of nanoparticles on support which was also confirmed by TEM and HR-TEM discussed later .

Table 6.1: Textural properties of x-GO supported metal catalysts screened for 5-HMF oxidation to FDCA

Sr. No.	**Catalyst**	**Surface area**	**Pore size (nm)**	**Pore volume (cc/g)**	**Crystallite size (nm)**
1	x-GO	797	11.5	4.61	3.02
2	Cu/x-GO	512	7.5	0.52	16.27
3	Co/x-GO	468	5.21	1.07	4.93
4	Cu:Co(1:1)/x-GO	440	10.91	0.43	7.77
5	Cu:Co(1:3)/x-GO	271	9.47	0.79	5.15

Crystallite size was also calculated by Scherer equation. The higher crystallite size of Cu/x-GO also reflected in its XRD pattern where the impressions were very sharp and intense but for other samples the amorphous peaks were observed due to lower crystallite size and uniform distribution. N_2 sorption isotherms were plotted to find out the porosity of surface, as shown in **Figure 6.1.a**. Type IV isotherm with H3 type of hysteresis loop suggested the mesoporous nature of surface along with slit shaped pores [(36)]. The open hysteresis loop can be because of unstable meniscus of liquid N_2 during analysis [(37)]. Pore volume drastically

reduced in the case of supported catalyst as compared to x-GO which can be because of occupancy of metal lattices on the porous domain of the surface of support. The same was observed by the amount of N_2 sorption that takes place during analysis where it decreased significantly for metal loaded x-GO rather than bare x-GO.

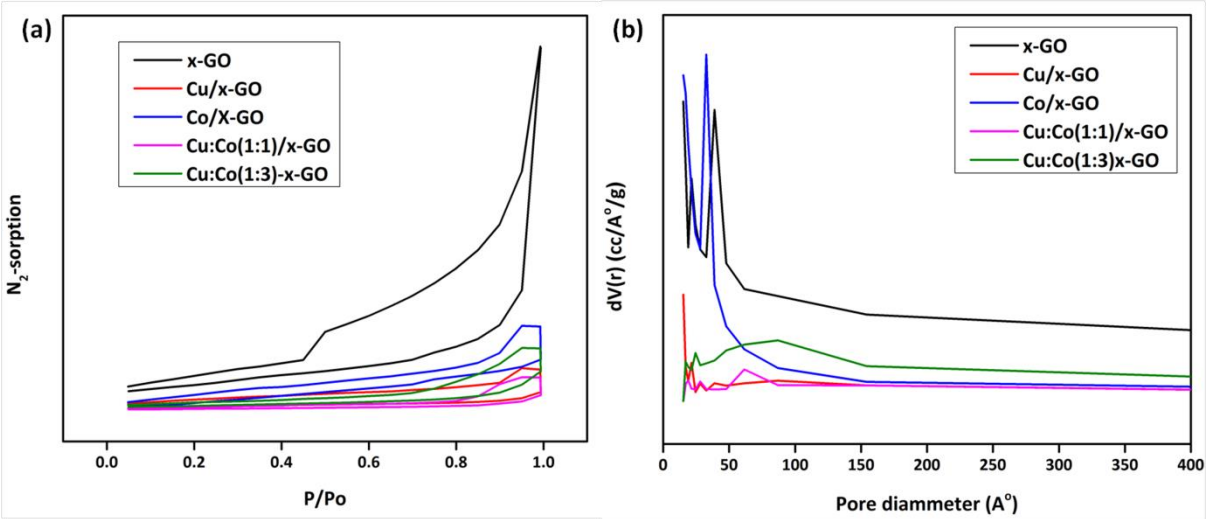

Figure 6.1: BET surface area analysis by (a) N_2 sorption isotherm and (b) pore size distribution of catalysts

6.3.2.2 XRD

Various chemical species and crystalline phases were identified by powder XRD of all the catalysts as shown in **Figure 6.2**. In case of exfoliated graphene oxide (x-GO) three peaks α, β and ϒ were observed at 2θ= 14.79°, 23.92° and 42.90° corresponding to (200), (002) and (100) planes, respectively. The appearance of α peak suggested presence of water molecules in the interlayer domains of x-GO with enhanced $d_{spacing}$ of 0.5879 nm [(38)]. Reflections at 2θ= 23.92° and 42.90° can be attributed to the reduction of oxygen groups of GO which led to the distorted stacking of crystal domains of x-GO in accordance with JCPDS #89-7213 [(39)]. The broadness of these peaks suggested presence of multilayered domains along with few monolayered x-GO sheets [(40)]. The number of layers of x-GO was calculated by using XRD parameters. The FWHM of (002) plane of x-GO was found to be 6.0960 which was divided

by interlayer distance calculated by Scherrer equation (0.3579 nm) which revealed about presence of total 17 layers in x-GO domain [41]. All impressions of Cu/x-GO indicated presence of monoclinic CuO with 2θ= 32.33° (110), 38.79° (111), 48.50° (202), 53.62° (020), 65.98° (311), 67.96° (220) having JCPDS #05-0661 whereas reflections at 2θ=29.82° (110), 35.56° (111) and 61.50° (113) were of Cu_2O (JCPDS #05-0667) [42]. Reflections at 2θ= 19.47° (ά), 31.45° (ξ), 36.81° (ψ), 44.87° (ϖ), 59.17° (υ) and 65.26° (λ) in Co/x-GO showed the presence of only cubic Co_3O_4 phase (JCPDS #74-1657) corresponding to (111), (220), (311), (400), (511) and (440) crystal planes, respectively [43]. Equimolar bimetallic combination of Cu and Co supported on x-GO found to be most crystalline in terms of XRD pattern where sharp intense bands corresponding to CuO and $CuCo_2O_4$ phases were observed along with x-GO. It is well documented that the distinction between Co_3O_4 and $CuCo_2O_4$ is very difficult based on the XRD impressions but observed d spacing of 0.477 nm in TEM images and observed peaks in XPS suggested the formation of spinel phase [44]. Apart from patterns of x-GO, reflections at 2θ= 18.75° (111), 31.07° (220), 35.56° (311), 36.47° (222), 44.50° (400), 58.64 (511) and 64.91° (440) can be assigned to $CuCo_2O_4$ according to JCPDS #78-2177 whereas reflections at 2θ= 38.81°, 48.79°, 66.61°, 68.49° and 61.68° were of CuO and Cu_2O, respectively as described earlier [45]. The intensity and amount of XRD peaks decreased in both excess Co variant of bimetallic catalyst suggesting better dispersion of the metals. Cu-Co(1:3)/x-GO showed better XRD impressions than Cu-Co(1:2)/x-GO like Cu-Co(1:1)/x-GO.

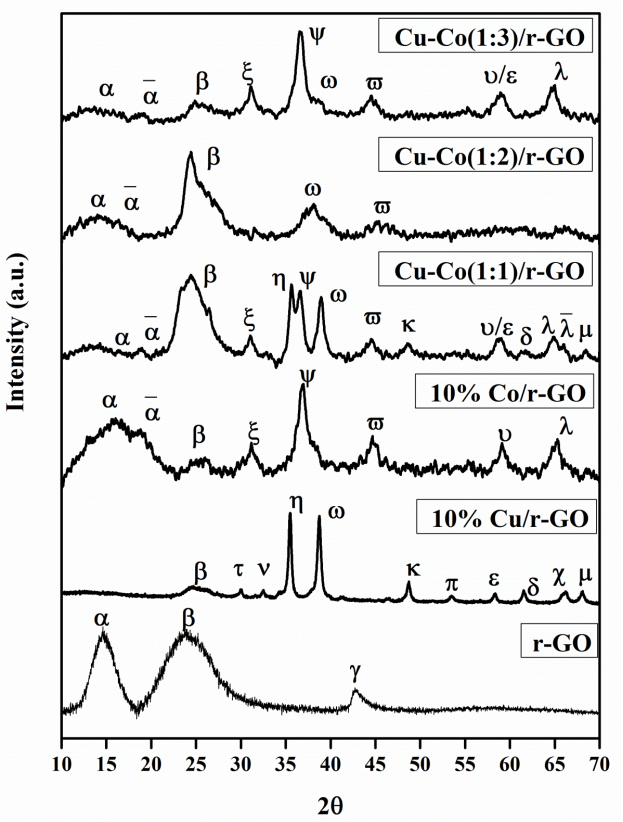

Figure 6.2: XRD pattern of x-GO and x-GO supported Cu, Co and their variants

6.3.2.3 XPS

Different surface valence states and composition of catalytic surface were identified by XPS studies. Scan survey of Cu and Co in monometallic and bimetallic catalyst was compared as shown in **Figures 6.3.a and b**. While there was negligible shift towards lower binding energy for Co in both the cases, binding energy of Cu was significantly perturbed suggesting definite mutual interactions between Cu and Co. Unimodal peaks of Cu in monometallic Cu/x-GO changed into bimodal asymmetric peaks in Cu:Co(1:3)/x-GO with significant shift in binding energies. For $Cu2p_{3/2}$ peak maxima was observed at BE of 935.04 eV which shifted to lower binding energy of 933.70 eV recommending phase transition in bimetallic combination. Difference in the binding energy due to spin orbit splitting was 14.91 eV and 15.14 eV in monometallic Co/x-GO and Cu:Co(1:3)/x-GO respectively which is the signature feature of

appearance of spinel Co_3O_4 [46]. Observing these important results, XPS deconvolution of $Cu2p_{3/2}$ and $Co2p_{3/2}$ was conducted in both monometallic as well as bimetallic catalysts.

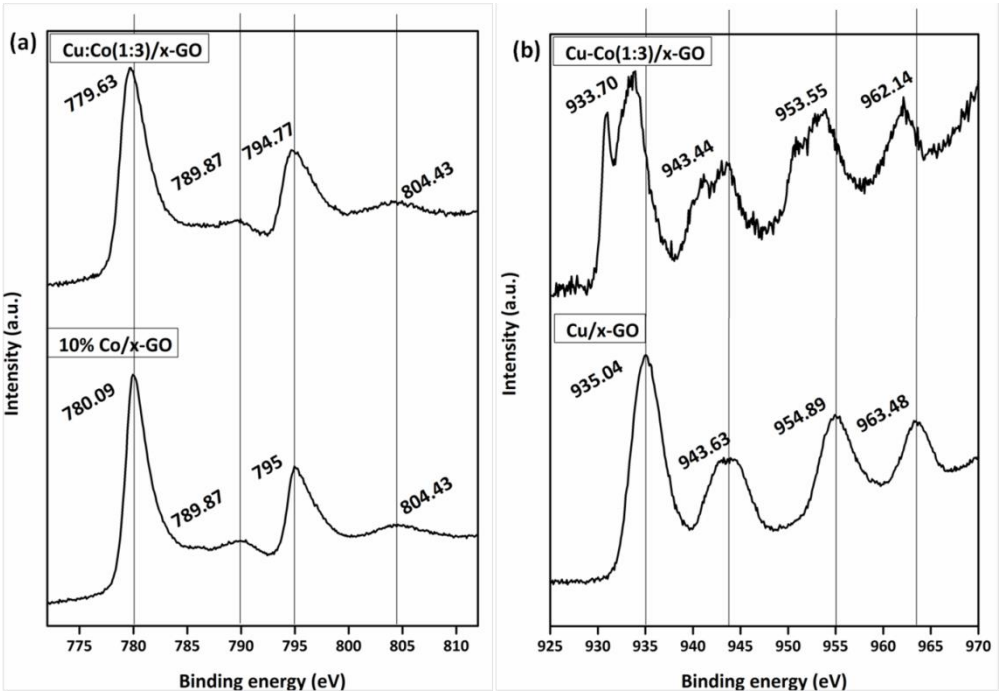

Figure 6.3: Comparative scan survey profiles of (a) Co in monometallic Co/x-GO and bimetallic Cu:Co(1:3)/x-GO (b) Cu in monometallic Cu/x-GO and bimetallic Cu:Co(1:3)/x-GO.

5 peaks were observed for $Co2p_{3/2}$ at the binding energies of 779.88 eV, 781.02, 782.29, 785.90 and 789.94 eVs for monometallic Co/x-GO (**Figure 6.4.a**). The most prominent and intense was a peak at BE of 779.88 eV corresponding to Co^{3+} whereas a peak at BE of 781.02 eV can be assigned to the Co^{2+} of Co_3O_4 phase (**Table 6.2**) [47]. A tiny impression at BE of 782.29 eV can be assigned to the Co^{2+} of CoO species whereas a satellite broad hump at BE of 785.90 eV can appear due to electronic transfer from 3d to 4s orbitals of Co^{2+} in CoO [48]. A characteristic satellite peak of Co_3O_4 was also observed at BE of 789.94 eV. Deconvoluted XPS spectra of Co2p3/2 for Cu:Co(1:3)/x-GO also showed 5 peaks with reduction in binding energy values (**Figure 6.4.b**).

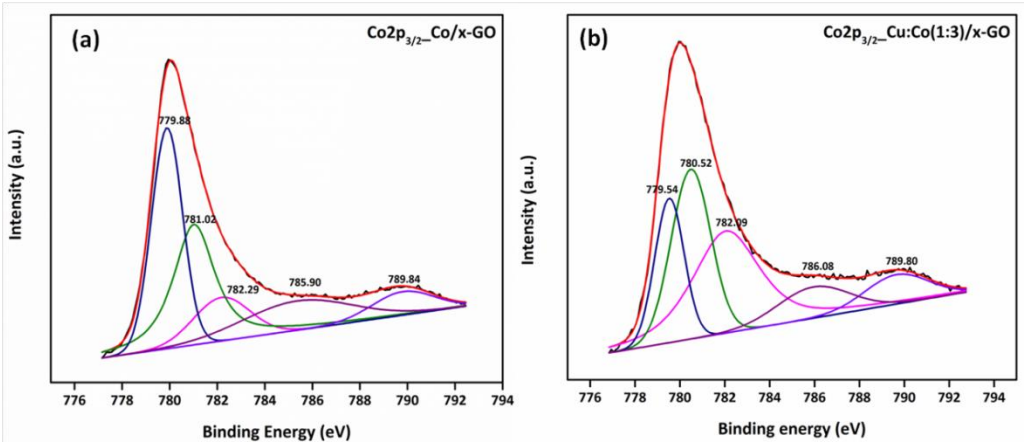

Figure 6.4: XPS spectra of Co2p3/2 in (a) Monometallic Co/x-GO (b) Bimetallic Cu-Co(1:3)/x-GO

The binding energy of peak due to Co^{3+} reduced from 779.88 eV to 779.54 eV with almost 15% decline in intensity whereas binding energy of Co^{2+} of CoO reduced to from 781.09 eV to 780.52 eV. There was significant rise in the relative quantity of Co^{2+} for which the peak was present at 782.09 eV (36.18%) which can be due to appearance of new spinel phase $CuCo_2O_4$ along with Co_3O_4 (**Table 6.4**).

Table 6.2: XPS Peak intensity calculation of Co2p3/2 in Co/x-GO

Species	**B. E.**	**FWHM**	**Area%**
Co 2p3/2	779.88	1.54	33
	781.02	2.04	33
	782.29	2.78	12
	785.36	5.37	15
	789.96	3.06	7
C 1s	284.50	1.02	46
	285.15	1.25	25
	286.34	1.37	17

	288.60	2.36	12
O1s	529	0.97	6
	529.76	1.28	25
	529.92	1.05	10
	531.13	2.05	35
	532.93	2.36	24

The appearance of new spinel phase was also observed by XPS pattern of Cu and TEM imaging. Presence of Co_3O_4 was again observed by its shoulder peak at BE of 789.80 eV.

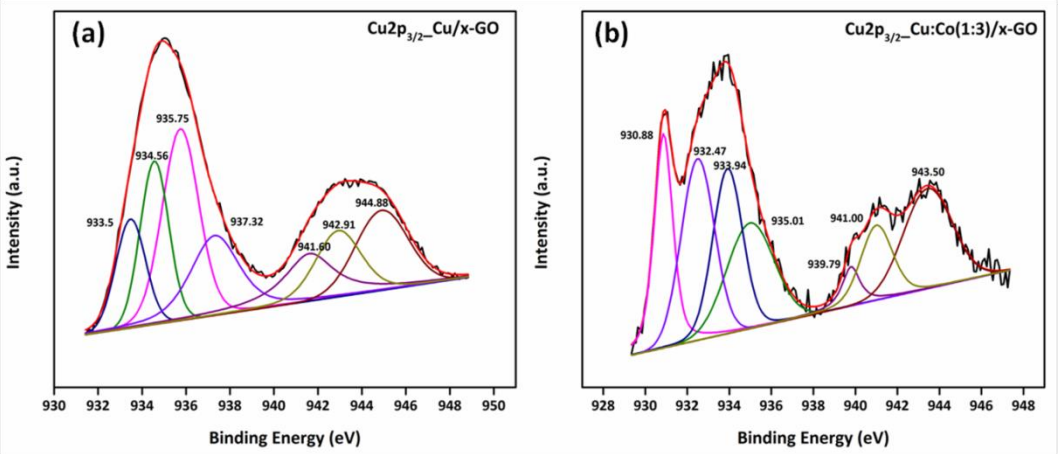

Figure 6.5: XPS pattern of Cu2p3/2 in (**a**) Monometallic Cu/x-GO and (**b**) Bimetallic Cu:Co(1:3)/x-GO

$Cu2p_{3/2}$ in monometallic Cu/x-GO (**Figure 6.5.a**) showed presence of only Cu^{2+} (BE of 933.50 eV) and was reconfirmed by the presence of strong satellite peaks from BE of 940-945 eVs which may have aroused due to metal ligand 3d charge transfer phenomenon [49-50]. The more intense peaks at BEs of 934.56 eV, 935.75 eV and 937.32 eV are generally assigned for the various surface Cu^{2+} species like $Cu(OH)_2$ and $Cu(OH)(CO_3)$ which appear due to the different coordination environment on the catalytic surface [51]. Significant

variation in the surface composition was observed in the XPS deconvolution pattern of $Cu2p_{3/2}$ of bimetallic Cu:Co(1:3)/x-GO as observed in **Figure 6.5.b** and **Tables 6.3** and **6.4**.

Table 6.3: XPS Peak intensity calculation for Cu/x-GO

Species	**B. E.**	**FWHM**	**Area%**
Cu 2p3/2	933.47	1.6	10
	934.55	1.53	15
	935.74	1.96	24
	937.30	2.60	15
	941.60	2.72	11
	942.92	2.44	11
	944.89	2.80	14
C 1s	284.54	0.97	32
	285.47	1.20	18
	286.35	1.42	17
	287.52	1.91	15
	290.07	3.17	14
	291.99	1.54	4
O 1s	530.33	1.3	8
	531.75	1.7	25
	532.96	1.42	22
	533.81	1.17	17
	534.7	1.22	14
	535.27	2.48	8

	535.01	0.88	1
	537.68	2.4	5

The unimodal maxima observed during monometallic Cu/x-GO bifurcated into bimodal spectra due to the formation of different valence state. A sharp intense peak was observed at BE of 930.88 eV which can be assigned to the formation of Cu^{+} occupying tetrahedral sites of spinel $CuCO_2O_4$ [(52)]. Due to this change in the nearby chemical environment shift towards lower binding energy was observed for CuO (932.47 eV) [(53)]. This also led to the almost 8% reduction in the shakeup satellite peak for CuO at BE of 939.79 eV. Various surface hydroxide species as mentioned earlier also showed considerable reduction in their relative quantity as shown by **Table 6.4**. Similar species were observed in spent Cu:Co(1:3)x-GO also where Cu_2O recued to 11% from 16% in fresh Cu:Co(1:3)/x-GO whereas 6% increase was observed in CuO species (**Table 6.6** and **Figure 6.6**) which may be due to the presence of O_2 environment in the reaction.

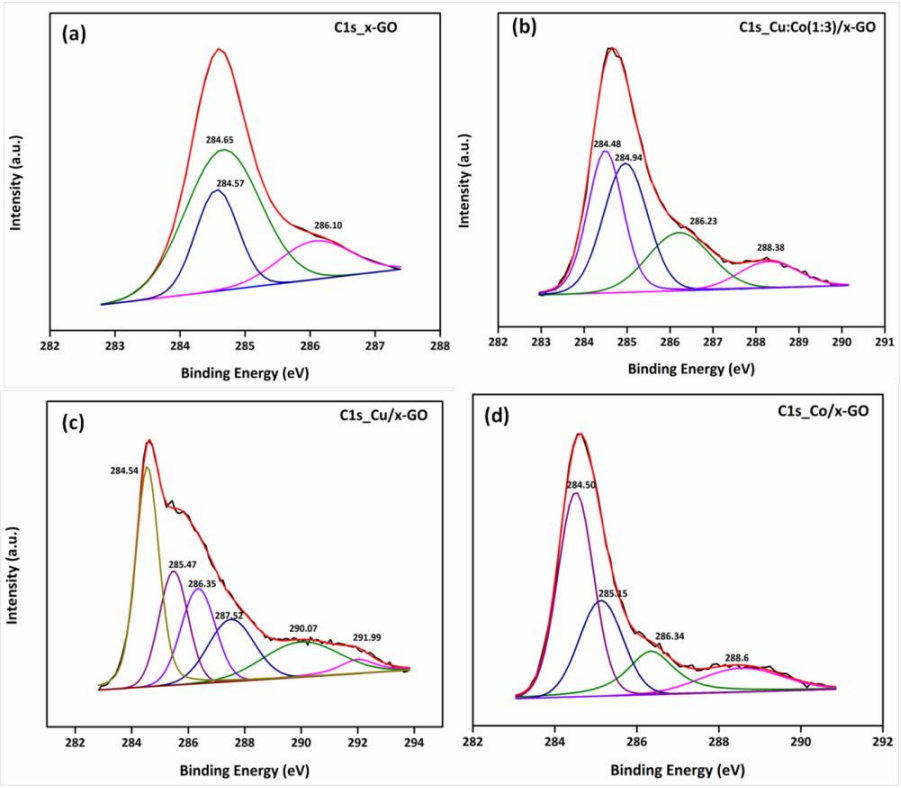

Figure 6.6: XPS deconvolution pattern of C1s (a) x-GO (b) Cu:Co(1:3)/x-GO (c) Cu/x-GO and (d) Co/x-GO

Since all the catalysts were supported on the exfoliated Graphene Oxide (x-GO), we also conducted the XPS deconvolution of C1s to expose the nature of x-GO surface as shown in **Figure 6.6**. Three peaks at BEs of 284.65, 284.57 and 286.10 eV were observed in x-GO for C1s corresponding to sp^3 -C-C- backbone, sp^2 C=C and surface –C=O groups (**Figure 6.6.a**) [54].

Table 6.4: XPS Peak intensity calculation in Cu:Co(1:3)/x-GO

Species	**B. E.**	**FWHM**	**Area%**
Cu 2p3/2	930.86	1.05	16
	932.50	1.86	20
	933.92	1.67	18

	934.99	2.65	17
	939.79	1.0	3
	941.01	1.78	9
	943.44	2.73	17
Co 2p3/2	779.54	1.54	18
	780.52	2.08	29
	782.09	3.49	36
	786.08	3.76	9
	789.80	3.33	8
C 1s	284.48	0.96	33
	284.94	1.2	35
	286.23	1.71	22
	288.38	1.61	10
O 1s	529.75	1.19	40
	530.53	2.09	15
	531.41	1.64	18
	533.50	2.69	27

Graphitic saturated –C-C- backbone was most intense peak with almost 60% relative amount in x-GO. Supported Cu showed additional impressions at BEs of 287.52 eV for –C-O, 290.07 eV for –COOH and 291.99 eV for π-π* shakeup transition suggesting presence of small amount of surface oxides (**Figure 6.6.c** and **Table 6.5**) [(55)]. Co/x-GO showed a broad satellite peak at BE of 288.6 eV which may be due to the interaction of surface hydroxide species of Co and x-GO which could be the reason of its high selectivity to FDCA (**Figure 6.6.d**) [(56)].

Table 6.5: XPS Peak intensity calculation for x-GO

Species	**B. E.**	**FWHM**	**Area%**
	284.57	0.77	25
	284.65	1.35	59
	286.10	1.31	16
O 1s	531.56	2.01	32
	533.32	1.74	36
	534.22	1.80	24
	535.48	2.05	8

These observations remained constant in most suitable Cu:Co(1:3)/x-GO also where sp^3 -C-C- skeleton was prominent with almost 36% followed by graphitic unsaturation (33%) and –C=O (22%) (**Table 6.4**). Here also interaction between metallic and surface –OH groups were observed which can also be the reason of its higher activity facilitated by its substrate adsorption capacity of surface (**Figure 6.6.b**). On comparing the scan survey profile of fresh and used Cu:Co(1:3)/-GO, significant quantitative increment of 17% for C was observed which may be because of the deposition of reaction crude on the surface of catalyst (**Table 6.7**). The same was also evident by the presence of peaks at BE of 289.31 eV (>C=O) and 288.20 eV (-OH bonding with reaction crude alcoholic species). This can also be the reason of decline in the catalytic activity of catalyst after each recycle. Moreover, presence of reaction intermediates on the surface was also evident by the appearance of sharp peak at very lower BE of 284.16 eV which is attributed to the 5 membered rings [(57)].

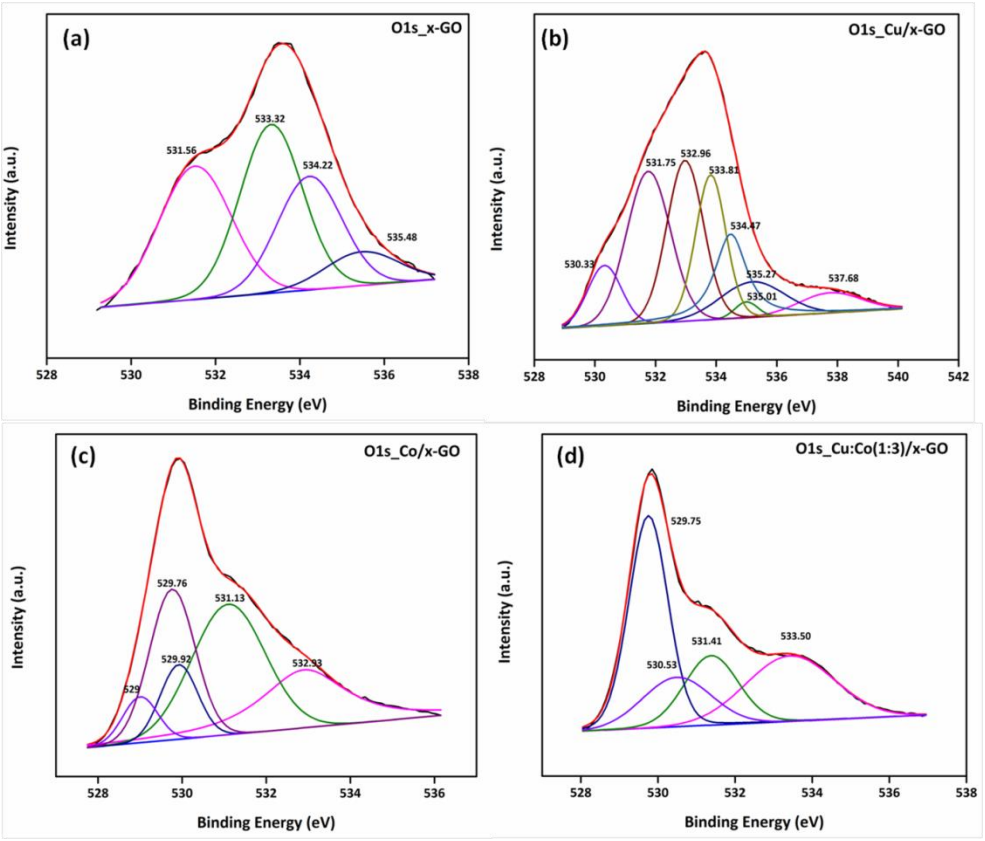

Figure 6.7: Nature of oxygen species of catalysts determined by deconvolution of O1s in (a) x-GO (b) Cu/x-GO, (c) Co/x-GO and (d) Cu:Co(1:3)/x-GO

The surface oxide species were analysed by XPS pattern of O1s in all the catalysts as shown in **Figure 6.7**. Multimodal asymmetric XPS pattern were observed in all the catalysts. The binding energy decreased a bit on supporting the metal which can be the due to the support surface interactions with metallic species. A peak at BE of 531.56 eV in x-GO represent surface oxide species like –OH/O_2/O^- which can be related aromatic carbon with –C=O or O=C-OH groups present on the surface (**Figure 6.7.a**) [58].

Table 6.6: XPS Peak intensity calculation in Cu:Co(1:3)/x-GO-Spent

Species	**B. E.**	**FWHM**	**Area%**
Cu 2p3/2	930.49	1.24	11
	932.65	1.63	27

	933.48	2.02	17
	934.83	2.66	24
	941.01	2.82	9
	943.66	2.32	12
Co 2p3/2	779.66	1.75	35
	780.98	1.75	22
	782.35	2.24	17
	784.65	3.52	12
	788.45	4.71	14
C 1s	284.16	1.11	23
	284.59	0.94	21
	285.59	1.11	23
	286.22	1.24	18
	287.26	1.26	6
	288.20	1.31	8
	289.31	1.19	1
O1s	529.51	1.18	22
	529.82	1.02	21
	531.12	1.62	29
	532.17	1.73	15
	533.53	2.12	13

Most intense peak was observed at BE of 533.32 eV with almost 36% relative amount and can be ascribed for aromatic =C-OH species of surface (**Table 6.5**) [(59)]. Oxygen species

connected to saturated sp3 C was also detected at the binding energy of 534.22 eV [(60)]. Intercalated aquatic content in x-GO was identified by an impression at BE of 535.48 eV in x-GO which can be due to chemisorption [(61)]. Aforementioned the binding energy was shifted towards lower side on the loading the metal same was observed in Cu/x-Go and Co/x-Go where lattice oxygen peaks appeared at BEs of 530.33 and 529 eV, respectively whereas surface active oxygen peaks were located at BEs of 531.75 and 531.13 eV, respectively (**Figures 6.7.b** and **6.7.c**). Oxygen attached to aliphatic carbon was observed at BE of 532.96 eV in Cu/x-GO whereas it was at 532.93 eV for Co/x-GO. Relative quantitative determination of oxygen species suggests that surface active oxygen was more in the case of Co (34%) than that in Cu (25%) which can be due to the autoredox nature of Co_3O_4 (**Table 6.2 and 6.3**)[(62)]. Two peaks were observed in close proximity for Co/x-GO at BEs of 529.76 and 529.92 eV which can be related to Co^{3+} (O) and Co^{2+} (O) of spinel Co_3O_4 due to presence in nearby different chemical environment [(63)]. Various terminal oxide peaks were also observed in Cu/x-GO at BEs of 535.27 and 537.68 eV which can be due to the metal-support hydroxyl group interactions or Lewis acid centre on surface of catalyst [(64)]. 4 peaks were observed in bimetallic Cu:Co(1:3)/x-GO at BEs of 529.75 (Co-O), 530.53 (Cu-O), 531.41 eV corresponding to surface active oxygen and a peak at BE of 533.50 eV for =C-OH nature of surface. Bimodal asymmetry of O1s was consistent in the used Cu:Co(1:3)/x-GO also as clearly evident by **Figure 6.7.d**.

Table 6.7: XPS Scan survey Profile Comparison for fresh and spent Cu:Co(1:3)/x-GO

Element	**Cu:Co(1:3)/x-GO_Fresh (%)**	**Cu:Co(1:3)/x-GO_Spent (%)**
Cu	2.61	7.06
Co	6.7	3.79

C	28.38	44.69
O	42.43	39.69
Co/Cu	2.56	1.86

Negative shift in the binding energy was observed in the O1s spectra of used catalyst which may be due to the loosely bounded oxygen species with surface adsorbed oxygenated reaction crude. Hence presence of $CuCo_2O_4$, CuO and Co_3O_4 on x-GO with plausible interaction capacities was established by detailed XPS study.

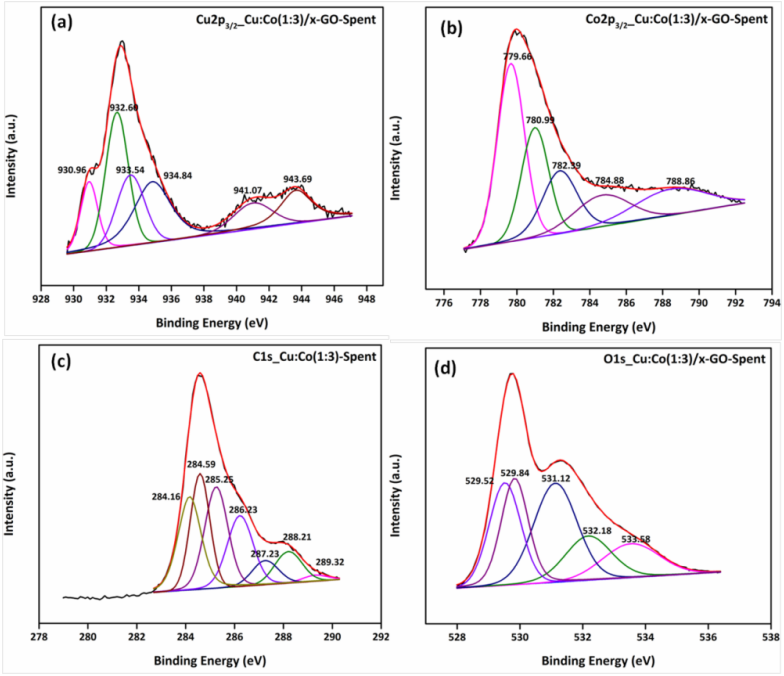

Figure 6.8: XPS deconvolution spectra of (a) Cu2p3/2, (b) Co2p3/2 (c) C1s and (d) O1s in spent Cu:Co(1:3)/x-GO catalyst

6.3.2.4. FE-SEM

To understand the distribution pattern and morphology of metallic component and support FE-SEM was conducted. FE-SEM images of spent Cu:Co(1:3) catalyst showed clear presence of larger spheres of almost 150-300 nm embedded in graphene oxide sheet (**Figures 6.9.a** and **6.9.b**).Wrinkled sheet shape irregular morphology of x-GO was observed as shown

in **Figure 6.10.a**. Small spherical particles in the range of 13-22 nm were also observed as shown in **Figure 6.10.b** which may be metallic components.

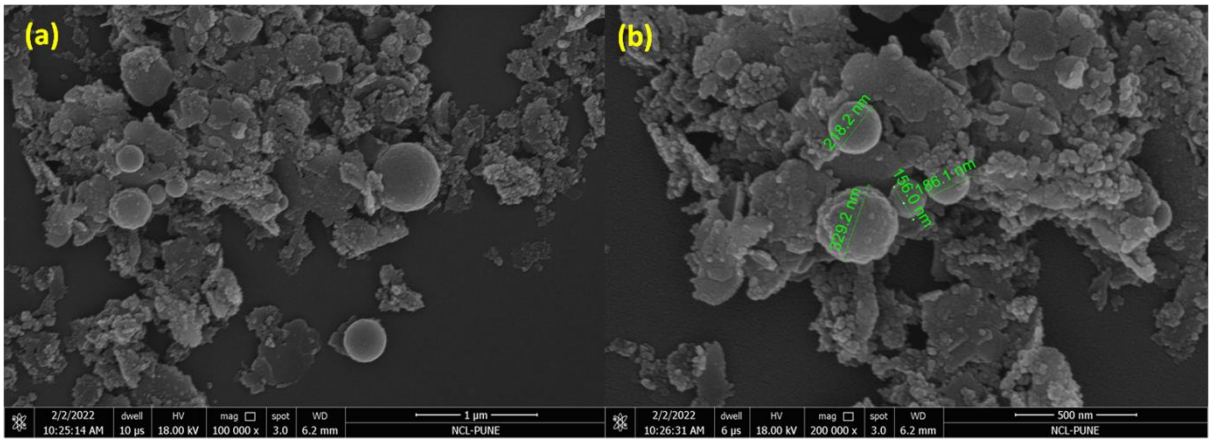

Figure 6.9: FE-SEM images of Spent Cu:Co(1:3)/x-GO at a scale of (a) 1 µm and (b) 500 nm

Elemental mapping was also conducted to bet the idea of position and distribution of Cu and Co on the surface of support. **Figure 6.10.c and 6.10.d** represents the elemental mapping of Cu and Co respectively. On careful investigation of elemental mapping, Cu and Co were found to be arranged in a specific array *i.e.* Cu was in line array mostly of 2/3 particle in a row whereas Co was more inclined to cluster formation. The EDX pattern of catalyst was also in the agreement of our theoretical calculation of Cu:Co(1:3) (**Figure 6.10.e**).

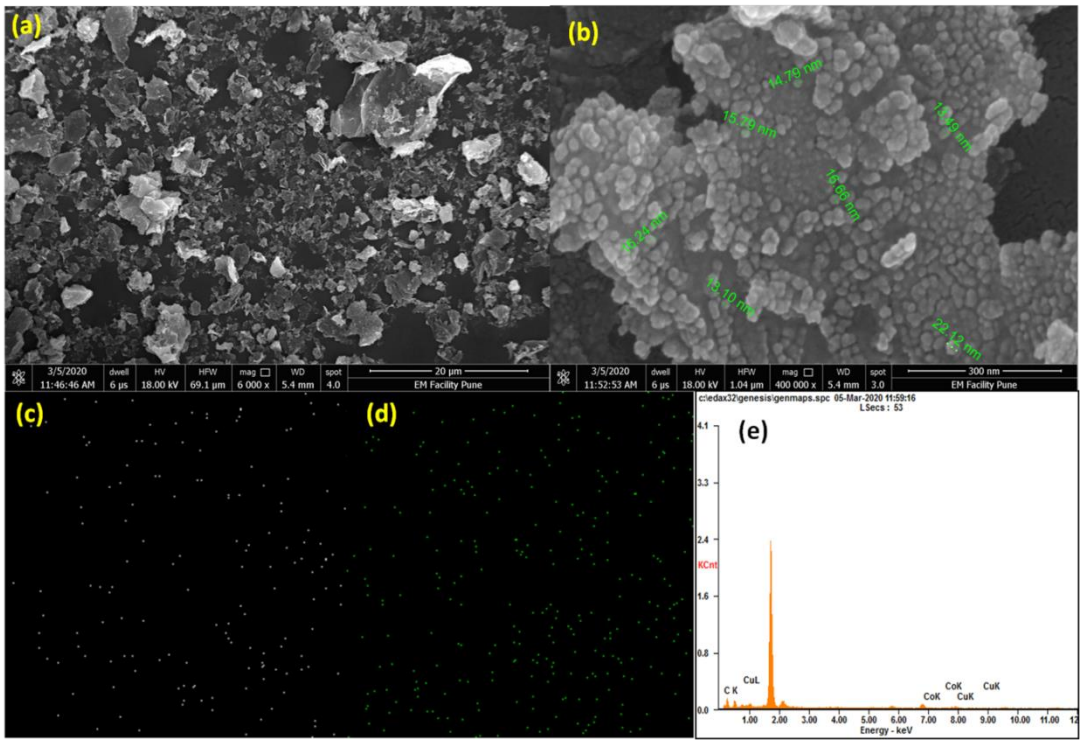

Figure 6.10: FE-SEM imaging of Cu:Co(1:3)/x-GO for (a) at the scale of 20µm (b) at the scale of 300 nm (c) elemental mapping of Cu in Cu:Co(1:3)/x-GO (d) elemental mapping of Co in Cu:Co(1:3)/x-GO and (e) EDX pattern of Cu:Co(1:3)/x-GO

6.3.2.5 TEM

Particle size, shape and distribution pattern was also analysed by TEM imaging. Large cubes shaped morphology of Co was observed among small sized round nanoparticles of Cu supported on x-GO with good distribution. Overlapping of some cubical lattices with same periodicity was observed which led to the appearance of Moiré fringe pattern as shown in **Figures 6.11.c** and **6.11.d**. These observations reaffirmed the elemental mapping findings about cluster formation of Co. After calculation of 200 nanoparticles, the average particle size was found to be between 3.64-5.38 nm whereas cube shaped particles showed a range of 7.50-8.75 nm. Three lattice fringes patterns were observed at 'd' spacing values of 0.216 nm, 0.259 nm and 0.477 nm corresponding to (400), (222) and (111) planes of spinel $CuCo_2O_4$.

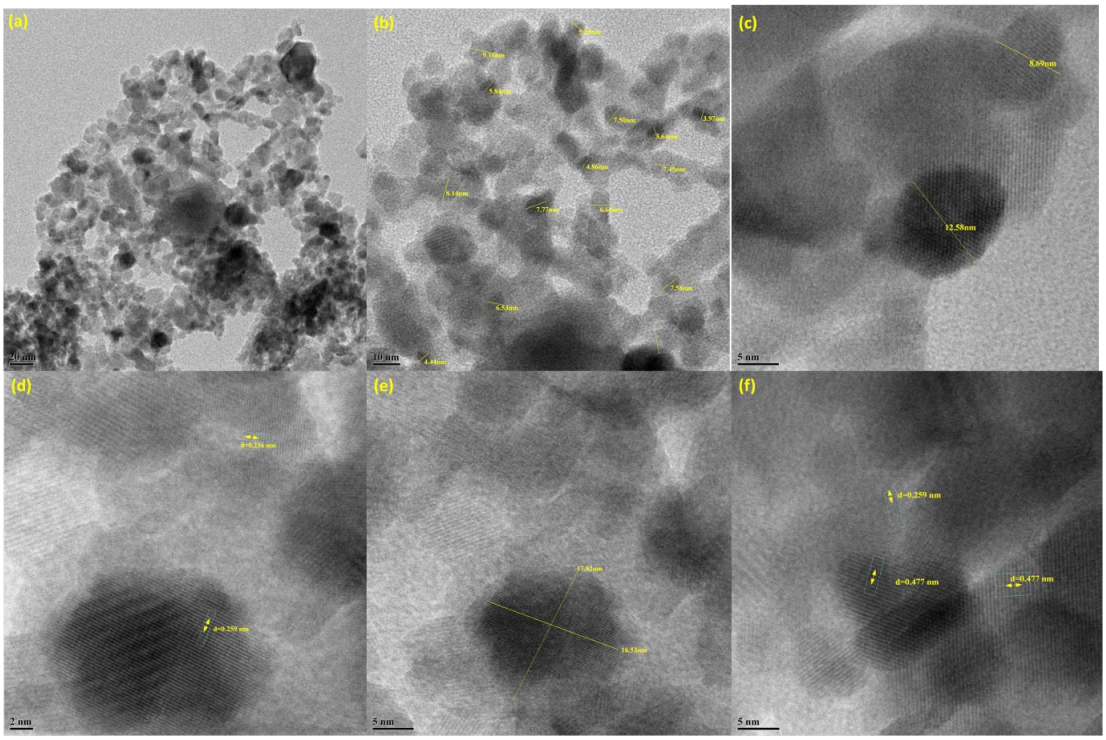

Figure 6.11: TEM imaging of Cu:Co(1:3)/x-GO at various scale (a) Distribution of particle on the scale of 20 nm (b) Particle size at the scale of 10 nm (c) at the scale of 5 nm (d) Fringe pattern (scale 2 nm) (e) Overlapped particle (scale 5 nm) and (f) Various d spacing observed (scale 5 nm)

6.3.2.6 HR-TEM

The particle distribution pattern and particle morphology was further analysed by HR-TEM. Due to translational movement of graphene oxide layers, Moiré patterns were observed which were also seen in TEM images [(65)]. Hexagonal sheets were overlapped on each other creating honey comb like Moiré pattern with 'd' spacing value of 0.358 nm with respect to (002) plane (2θ=23.92°) as shown in **Figure 6.12.a**. Additionally, 'd ' spacing of 0.1852 nm was observed for (202) plane of oval shaped Cu nanoparticles (2θ=44.58°) (**Figure 6.12.b**). Spinel phase of $CuCo_2O_4$ was reaffirmed by interplananr distances of 0.217 nm (400) and 0.477 nm (111) corresponding to 2θ values of 44.53° and 18.75° (**Figure 6.12.c and d**).

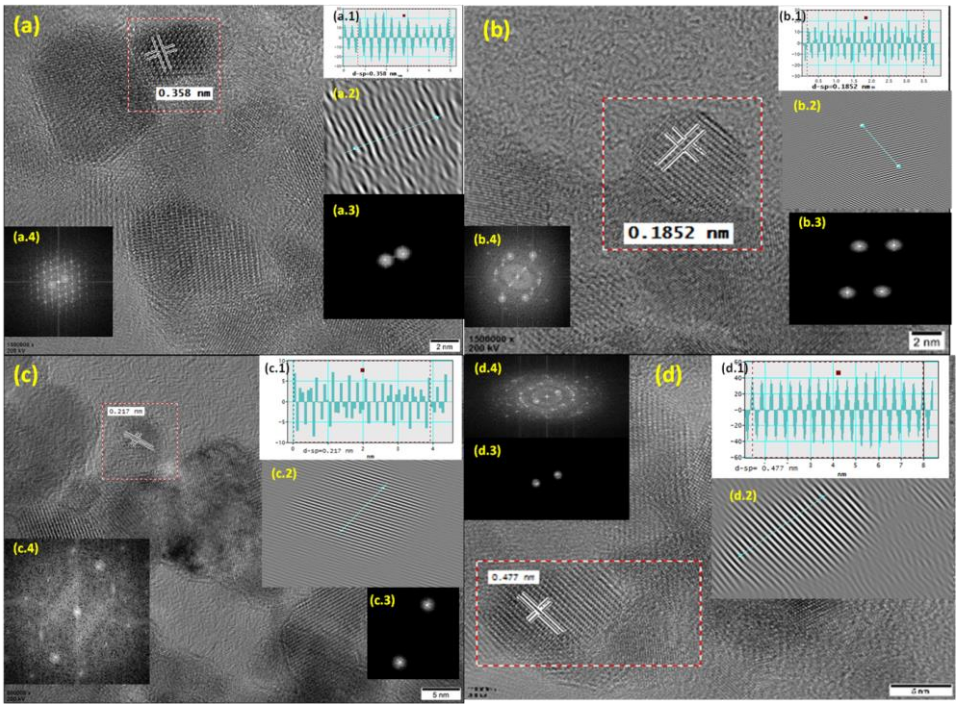

Figure 6.12: HR-TEM imaging of Cu:Co(1:3)/x-GO with their interpretation (a) d= 0.358 nm (b) d= 0.1852 nm (c) d= 0.217 nm and (d) d= 0.477 nm. The subsection of every image showed x.1 as IFFT profile, x.2 as IFFT profile, x.3 as FFT of selected area and x.4 as masking of selected plane where x is a-d.

6.3.2.7 FTIR

To reveal more about the catalytic surface, FTIR spectral studies were conducted as shown in **Figure 6.13**. Bare exfoliated graphene oxide showed a prominent peak around 1041 cm^{-1} along with slight glitch at 970 cm^{-1} which can be related to structural vibration of primary alkoxy –C-O group and epoxy/peroxide group of the surface, respectively [(66)]. Some other spikes of oxygenic groups were observed at 1182 cm^{-1}, 1374 cm^{-1} and 1719 cm^{-1} for epoxy (C-O-C), phenolic –OH and –C=O of acidic -COOH functional groups suggesting their presence on the exfoliated GO [(67-68)]. A sharp peak was also observed at 1580 cm^{-1} corresponding to typical -C-C- backbone vibration of graphene sheets [(69)]. A well defined

trough was observed at 2095 cm^{-1} which reduced as we loaded metals over x-GO and can be assigned for the unsaturated aromatic species present on the graphene oxide surface [70].

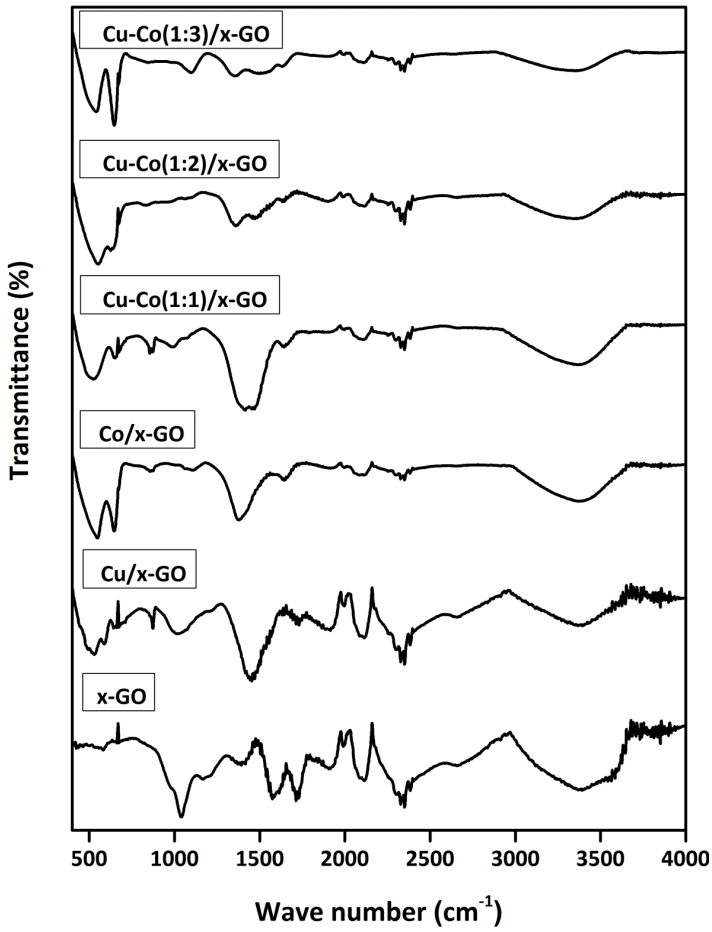

Figure 6.13: FTIR spectra of all x-GO and supported Cu and Co variants

These bands remain constant with Cu/x-Go also but with reduced intensity. The bands at 484 and 527 cm^{-1} assigned for stretching vibrations of Cu-O in monoclinic CuO [71]. A sharp band appeared at 1450 cm^{-1} which can be of C-O stretching mode of carbonate species of Cu which was also observed by XPS pattern earlier. Similar observations were observed for Co/x-GO where metallic bands were observed at 516 cm^{-1} and 635 cm^{-1} corresponding to stretching vibrations of Co-O and O-Co-O bridging vibrations [72]. Phenolic vibration were also observed with intense spike at 1386 cm^{-1} whereas a tiny impression at 1655 cm^{-1} suggested the restoration of π-π conjugated carbon backbone of GO [73]. In all the samples,

broad hump appeared starting from 2900 cm^{-1} and ending at 3600 cm^{-1} for characteristic symmetric and asymmetric –OH bond vibration of carbonic material though, its intensity reduced as the amount of metal loaded increased [(74)]. Finger print region of spinel oxides is 500-700 cm^{-1} in FTIR and sharp bands at 548 cm^{-1} and 655 cm^{-1} were observed to be elevated from their monometallic variants suggesting successful interaction with x-GO surface. A band at 548 cm^{-1} was assigned to the stretching vibrations of Co^{3+}-O^{2-} present in octahedral region whereas another band at 655 cm^{-1} was attributed to that of Cu^{2+}-O^{2-} located in tetrahedral region of spinel $CuCo_2O_4$ [(75)]. All the oxygenic peaks of the surface were also found reduced with increased amount of metal loading.

6.3.2.8 Py-IR

The type of surface acidity and their quantitative determination were carried out by FTIR using pyridine as a probe molecule as shown in **Figure 6.14**.

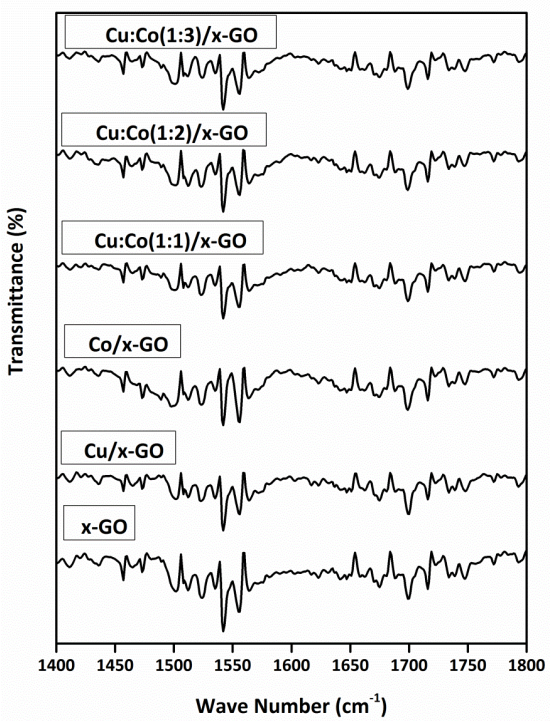

Figure 6.14: Pyridine IR analysis of x-GO supported metal oxides for 5-HMF oxidation

The pyridine IR results revealed about the carbocatalysis of x-GO which was evident by taking it as catalyst for 5-HMF oxidation (**Table 6.9, entry 7, 8**). X-GO showed significant amount of Brönsted acidity by corresponding peaks at 1542 and 1698 cm^{-1}. In fact, it was second most Brönsted acidic sites containing catalyst among all the variants as shown in **Table 6.8, entry 1**. The surface Brönsted acidity of GO was reported by many researchers for various multicomponent reactions including oxidation [(76-77)]. These sites may arise due to the oxygenated groups present on the edges of x-GO. Even low amount of Lewis acidity was also shown by x-GO surface as evident by **Table 6.8**. Cu/x-GO showed the most intense peaks for Lewis acidity at 1450 cm^{-1} and 1555 cm^{-1} which were due to interaction of pyridine molecule with Lewis acid site of the surface whereas Co/x-GO possessed significant amount of Brönsted acid sites (**Table 6.8, entry 2**) [(78)]. The quantitative amount of both these acid sites was found to increase in bimetallic catalysts. Combined Brönsted and Lewis acidity was observed by an impression at 1490 cm^{-1} which was continuous in all the monometallic as well as bimetallic variants. The overall order of Total Brönsted Acidity (TBA)/Total Lewis Acidity (TLA) was Cu:Co(1:1)/x-GO> Cu:Co(1:3)/x-GO > x-GO > Co/x-GO > Cu:Co(1:2)/x-GO > Cu/x-GO suggesting need of balanced acidic sites for selective oxidation of FDCA.

Table 6.8: Quantitative determination of total Brönsted and Total Lewis acidity

Sr. No.	**Catalyst**	**Type of acidity (mmol/g)**		**TBA/TLA**
		TBA	**TLA**	
1	x-GO	0.2585	0.1174	2.20
2	Cu/x-GO	0.2176	0.2041	1.07
3	Co/x-GO	0.2278	0.1078	2.11
4	Cu:Co(1:1)/x-GO	0.2227	0.0924	2.41

5	Cu:Co(1:2)/x-GO	0.2508	0.1271	1.97
6	Cu:Co(1:3)/x-GO	0.2592	0.1132	2.29

6.3.2.9 H_2-TPR

The reducibility of the catalytic domain was studied by their H_2 TPR profile as shown in **Figure 6.15**. A broad single peak was observed at 226°C which can be assigned for the reduction of CuO into metallic Cu. The onset was started at 153°C suggesting a small asymmetry in 226°C peak which may be due to different size of metallic nanoparticles [79].

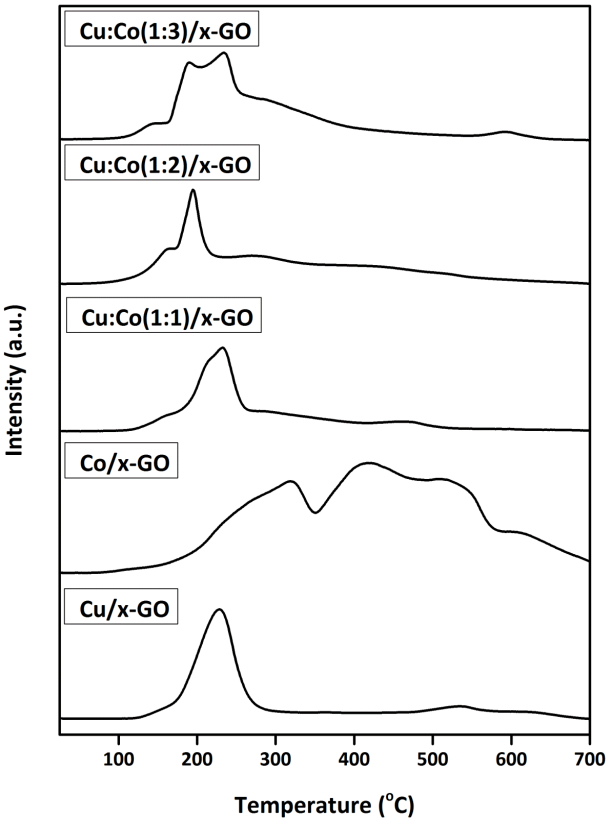

Figure 6.15: H_2 TPR of x–GO supported Cu, Co and its different variant designed for 5-HMF oxidation

A small broad peak was also observed at 534°C which could be because of presence of small amount of Cu^+ ions [80]. A broad profile with no symmetry was observed for Co/x-GO

locating at 316°C, 417°C and 538°C. Co_3O_4 contain two types of oxygen ion which are connected to Co^{n+} in two different manners leading to the formation of local crystal field sites. While one oxygen atom is bounded with single Co^{2+} and single Co^{3+} ions leading to the formation of weaker local crystal sites the stronger local crystal sites are generated by another oxygen atom bounded to three Co^{3+} ions [(81)]. The weaker local crystal filed was responsible for reduction at lower temperature (230°C embedded in 316°C peak). The peak at 316°C was assigned to reduction of Co_3O_4 to CoO which was again reduced to Co(0) at 417°C [(82)]. A broad continuation of satellite peak was also observed at 538°C which may be due to the generation of CH_4 on the surface of x-GO as mentioned elsewhere [(83)]. The higher reductive temperature was also indicating about the stronger interaction between the surface of Co and x-GO. When both metals were supported in co-precipitated manner on x-GO the reduction temperature decreased significantly suggesting confirmed mutual interaction and formation of new phases. In Cu:Co(1:1)/x-GO the reduction temperature decreased to 163°C and 232°C whereas for Cu:Co(1:2)/x-GO it further reduced to 161°C and 193°C suggesting reduction of spinel $CuCo_2O_4$ to metallic Cu and Co [(84)]. Similar trends were also observed in Cu:Co(1:3)/x-GO where first reduction temperature was at 143° followed by 189°C (Cu^{2+} to Cu^0), 232°C (overlapping of Cu^{2+} to Cu^0 and Co^{3+} to Co^{2+}) and 292°C (fractional reduction for Co^{3+} to Co^{2+}) whereas a reduction hump at higher temperature of 598°C could because of strong interaction of Cu-Co which may arise due to the close contact and uniform dispersion among them [(85)].

6.3.3 Catalytic activity evaluation

Various transition metals (Cu, Co, Fe and Mn) were screened for the oxidation of 5-HMF to FDCA as shown in **Table 6.9**. Out of these, best conversion was observed on CoO_x (57%) followed by Cu, Mn and Fe with 45%, 31% and 22%, respectively. Though conversion of 5-

HMF was highest for CoO_x the selectivity to FDCA was best shown by CuO_x followed by CoO_x whereas Mn and Fe were more selective towards DFF.

Table 6.9: Catalysts screening for selective oxidation of 5-HMF to FDCA, **Reaction Conditions:** 5-HMF= 100 mg, 5-HMF/NaOH=4, H_2O=25 g, Catalyst= 50 mg, T=90°C, P_{air} = 50 psig, t=1 h, Agitation speed= 1000 rpm. *Run was taken without base.

Sr. No.	**Catalyst**	**Conversion (%)**	**Selectivity (%)**					
			HMFCA	**FFCA**	**DFF**	**FDCA**	**BHMF**	**UnK**
1*	Blank run	0	0	0	0	0	0	0
2	Blank run	40	2	0	0	0	5	0
3	CoOx	57	30	24	5	33	8	0
4	CuOx	45	14	15	19	40	12	0
5	FeOx	22	15	10	53	8	14	0
6	MnOx	31	8	32	40	18	2	0
7*	x-GO	10	35	1	27	0	34	3
8	x-GO	66	39	5	26	1	28	1
9	Cu/x-Go	54	15	20	2	58	5	0
10	Co/x-GO	68	21	20	6	50	3	0
11	Cu-Co(1:1)/x-GO	75	10	16	8	65	1	0
12	Cu-Co(2:1)/x-GO	87	7	23	10	60	0	0
13	Cu-	100	5	10	17	68	0	0

	Co(3:1)/x-GO							
14	Cu-Co(1:2)/x-GO	100	4	16	5	75	0	0
15	Cu-Co(1:3)/x-GO	100	1	1	0	98	0	0

Based on these observations, our further study was focused on Cu and Co metals. Various combinations of Cu and Co were tried as shown in **Table 6.11** and it was observed that the highest conversion achieved was upto 70% with 51 % selectivity to FDCA on bare bimetallic oxides (**Table 6.11, entry 4**). Different supports were screened for finding out best suitable catalyst (**Table 6.10**) and it was observed that while CeO_2 and Al_2O_3 showed poor conversion with almost no FDCA, ZrO_2 and SiO_2 supported catalysts were very active with good conversions of 65% and 92% (**Table 6.10, entries 1-4**). Selectivity to FDCA was also good on the SiO_2 (60%). The loading which was on these supports was Cu:Co(1:3) as seen from the best results for 5-HMF oxidation in bare metallic oxide studies. The chitosan and x-GO were only two supports which marked complete conversion of 5-HMF and selectivity to FDCA was also very good *i.e.* 89% and 98%, respectively (**Table 6.10, entries 5 and 6**). Considering all these points Cu:Co(1:3)/x-GO was finalised as the catalyst of choice for 5-HMF oxidation and conducted all our further parameters optimization study using the same.

Table 6.10: Screening of various support for selective oxidation of 5-HMF to FDCA, **Reaction Conditions:** 5-HMF= 100 mg, 5-HMF/NaOH=4, H_2O=25 g, Catalyst= 50 mg, T=90°C, P_{air} = 50 psig, t=1 h, Agitation speed= 1000 rpm

Sr. No.	Support	C (%)	Selectivity (%)					
			HMFCA	FFCA	DFF	FDCA	BHMF	UnK
1	Cu:Co(1:3)/CeO_2	27	46	20	3	5	33	0
2	Cu:Co(1:3)/Al_2O_3	48	29	47	1	9	14	0
3	Cu:Co(1:3)/ZrO_2	65	17	52	1	23	7	0
4	Cu:Co(1:3)/SiO_2	92	11	26	1	60	2	0
5	Cu:Co(1:3)/Chitosan	100	3	7	1	89	0	0
6	Cu:Co(1:3)/x-GO	100	1	1	0	98	0	0

The activity of x-GO was seen by taking test runs as shown in **Table 6.9, entry 8**. To our pleasant surprise x-GO showed 66% conversion with HMFCA (39%) as the major product. These results indicated about the carbocatalytic property of x-GO which can be due to its surface oxygenated groups [(86)]. The same was also reaffirmed by the pyridine IR studies as demonstrated earlier. To further get the clear idea a fresh run devoid of base was conducted by taking x-GO as catalyst (**Table 6.9, entry 7**). This led to the competitive production of HMFCA (35%) and BHMF (34%) with only 10% conversion. A good amount of DFF (27%) was also observed which can be attributed to the high amount of textural Brönsted acidic sites of x-GO as mentioned earlier. Activity of metal oxides significantly increased after loading, as shown in **Table 6.9, entries 9 and 10**. Cu/x-GO and Co/x-Go marked a good increment in their conversion of 54% and 68% and selectivity to FDCA as 58% and 50%, respectively.

Encouraged by these results and bare metal oxide investigations, various combinations of Cu and Co were prepared on x-GO and screened (**Table 6.9, entries 11-15**). A significant increase in the activity was observed for the catalysts with bimetallic combinations loaded on x-GO. The conversion for equimolar Cu:Co(1:1)/x-GO jumped to 75% with 60% selectivity to FDCA (**Table 6.9, entry 11**). It was observed that when Cu was in excess, amount the appearance of DFF indicated the competitive oxidative dehydrogenation taking place on its surface due to which selectivity to FDCA was not increasing (**Table 6.9, entries 12, 13**). But when Co was taken as excess metal in an increment in selectivity of FDCA to 75% for Cu:Co(1:2)/x-GO and 98% for Cu:Co(1:3)/x-GO (**Table 6.9, entry 14, 15**) was observed. Further parameters optimization studies was therefore carried out on Cu:Co(1:3)/x-GO catalyst.

Table 6.11: Effect of bare bimetallic Cu-Co oxide on 5-HMF oxidation, **Reaction Conditions:** 5-HMF= 100 mg, 5-HMF/NaOH=4, H_2O=25 g, Catalyst= 50 mg, T=90°C, P_{air} = 50 psig, t=1 h, Agitation speed= 1000rpm

Sr. No.	Catalyst	Conversion (%)	Selectivity (%)					
			HMFCA	FFCA	DFF	FDCA	BHMF	UnK
1	Cu-Co(1:1)	56	19	21	16	37	7	0
2	Cu-Co(1:2)	66	13	16	20	43	8	0
3	Cu-Co(2:1)	60	15	10	35	30	10	0
4	Cu-Co(1:3)	70	14	16	11	51	8	0
5	Cu-Co(3:1)	68	10	8	45	28	9	0

6.3.4 Parameters Optimisation

6.3.4.1 Temperature effect

5-HMF oxidation to FDCA on Cu:Co(1:3)/x-GO was monitored in the temperature range of 45°C to 120°C as shown in **Figure 6.16**. Good conversion was observed even at lower temperature suggesting higher activity of catalyst though major product at 45°C was HMFCA with 35% selectivity. AS the temperature was increased the conversion as well as selectivity to FDCA increased exponentially. Best suitable reaction temperature was 90°C which led to complete conversion of HMF with excellent 98% selectivity to FDCA. It was observed that increase in temperature led to marginal decline in the selectivity of FDCA which may be due to the formation of condensation products of alcoholic and acidic intermediate in alkaline medium.

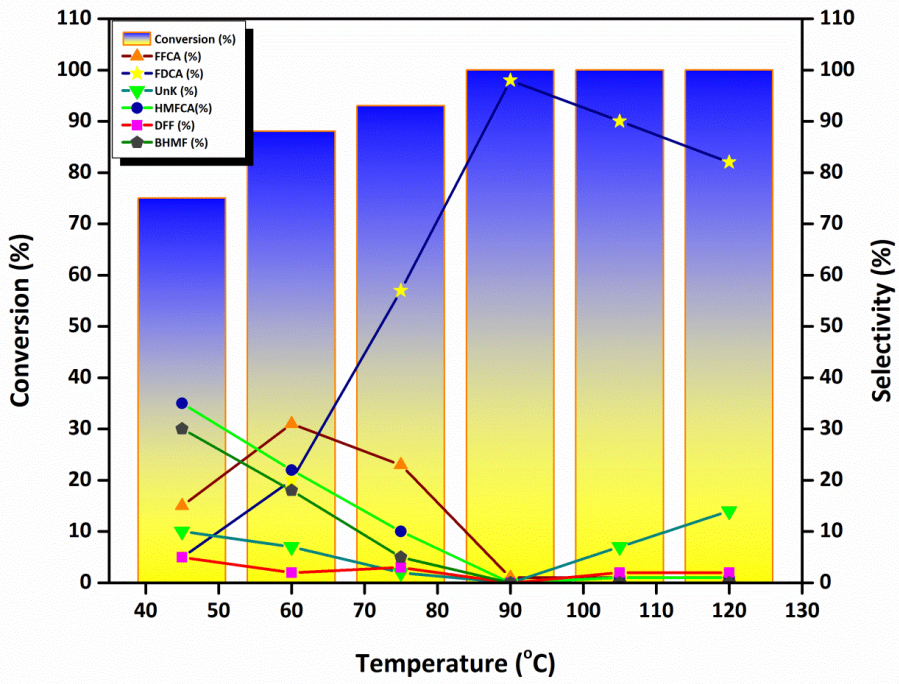

Figure 6.16: Effect of temperature on oxidation of 5-HMF to FDCA, **Reaction Conditions:** 5-HMF= 100 mg, 5-HMF/NaOH=4, H_2O=25 g, Catalyst= 50 mg, P_{air} = 50 psig, t=1 h, Agitation speed= 1000 rpm

6.3.4.2 Pressure effect

Since external air was used as an oxidising agent, its effect on reaction coordinates was monitored in the range of 25-100 psig. Optimum pressure range for the best results was found to be 50 psig with complete conversion of 5-HMF. Lower pressure conditions were more selective towards first oxidative intermediate *i.e.* HMFCA (37%). Significant amount of BHMF generated at 25 psig suggesting the parallel Canizarro reaction at mild conditions in presence of alkaline solution [87]. Higher pressure range showed marginal drop in the selectivity of FDCA which may be due to the more degradation of 5-HMF at higher pressure conditions as demonstrated in **Figure 6.17**.

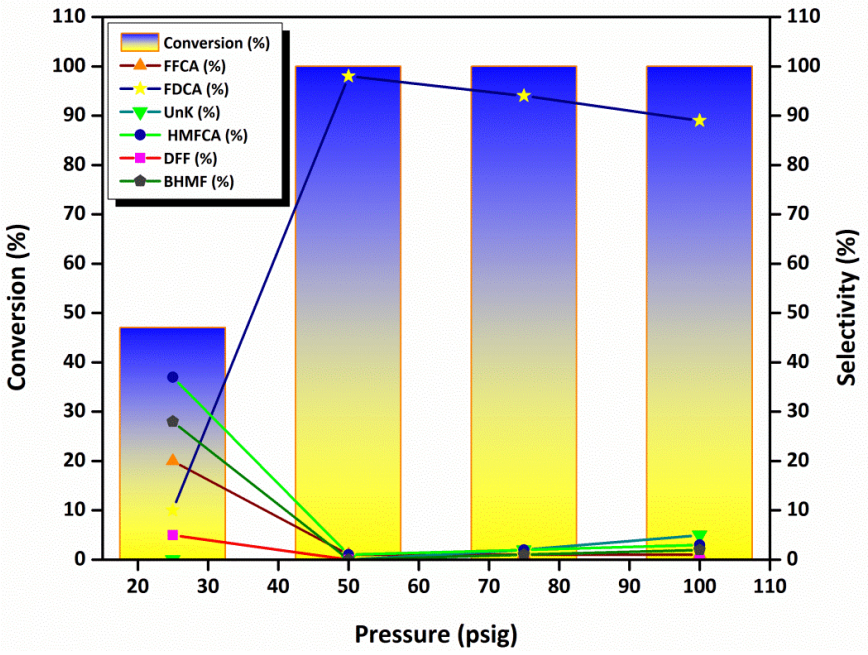

Figure 6.17: Effect of pressure on 5-HMF oxidation to FDCA, **Reaction Conditions:** 5-HMF= 100 mg, 5-HMF/NaOH=4, H_2O=25 g, Catalyst= 50 mg, T=90°C, t=1 h, Agitation speed= 1000 rpm

6.3.4.3 Catalyst loading effect

Catalyst loading studies were also taken for 5-HMF oxidation in order to find out the correct catalytic amount for the substrate in the range of 10-100 mg (**Figure 6.18**). Lower catalyst

concentration (10 mg) marked the FFCA (49%) as major product suggesting the arrest of reaction at FFCA. Further oxidation of FFCA to FDCA was not occurred efficiently due to the unavailability of catalytically active sites. Best results were obtained for 25 mg of the catalyst where complete conversion was observed with 98% selectivity to FDCA. The selectivity of FDCA remained 96% with 40 mg of the catalyst. Slight decline was observed due to the presence of trace amount of side products. Higher catalyst loading (55-100 mg) showed further decline in the selectivity of FDCA due to formation of condensation products which enhanced due to availability of higher catalytic sites.

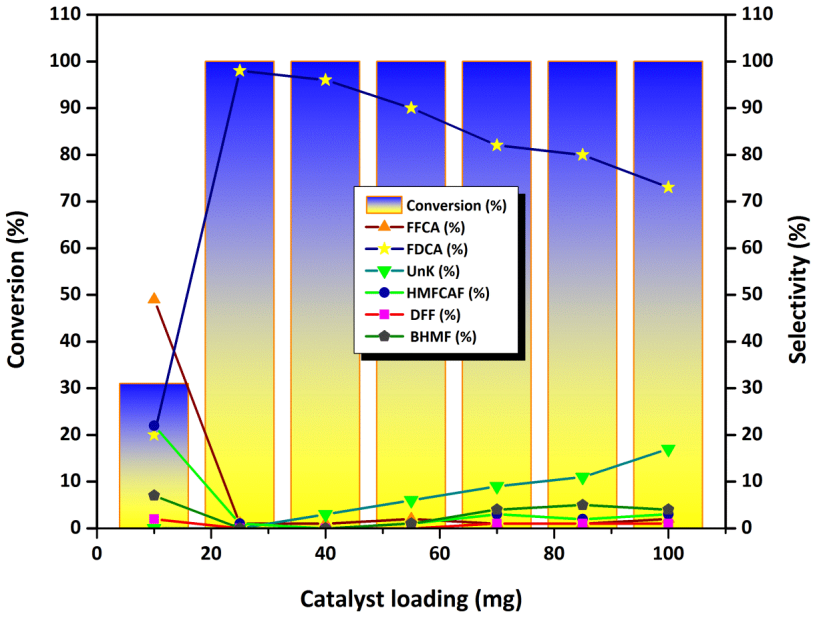

Figure 6.18: Effect of catalyst loading on 5-HMF oxidation to FDCA, **Reaction Conditions:** 5-HMF= 100 mg, 5-HMF/NaOH=4, H_2O=25 g, T=90°C, P_{air} = 50 psig, t=1 h, Agitation speed= 1000 rpm

6.3.4.4 Substrate loading effect

In order to assess the effect of 5-HMF concentration on conversion and selectivity to FDCA, its concentration was varied in the range of 100 to 300 mg (**Figure 6.19**). It was observed that as soon as the concentration increased from 100 mg, the selectivity to FDCA decreased

significantly due to less available active sites on the surface. Initially at higher concentration, Canizarro reaction operated in a significant amount leading to the formation of BHMF but later on this trend reversed and HMFCA was the major product.

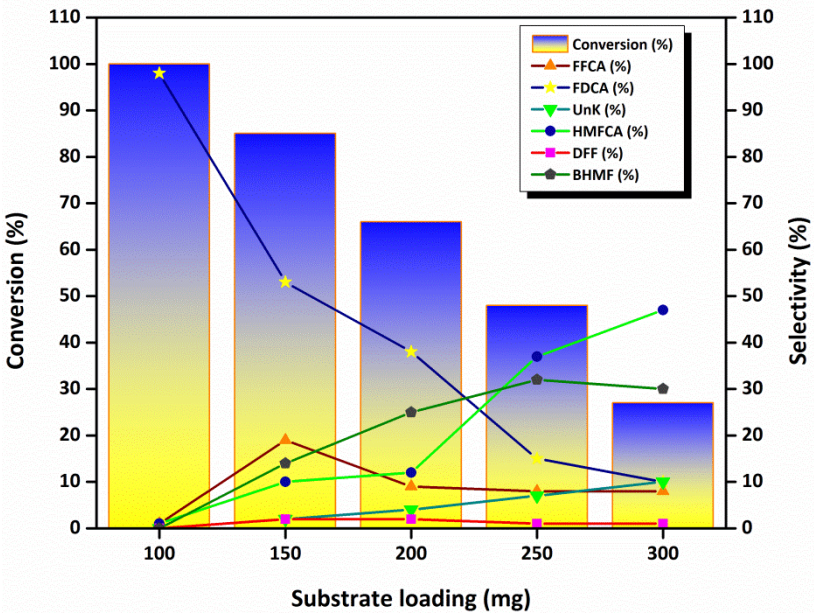

Figure 6.19: Effect of substrate loading on 5-HMF oxidation to FDCA, **Reaction Conditions:** 5-HMF/NaOH=4, H_2O=25 g, Catalyst= 50 mg, T=90°C, P_{air} = 50psig, t=1 h, Agitation speed= 1000 rpm

6.3.4.5 Effect of Base

The catalytic oxidation of 5-HMF highly depends on the alkaline medium so effect of basic medium was seen by taking various types of bases (**Figure 6.20.a**). While best results were obtained for NaOH only 10% decline in the activity was observed in the presence of KOH which may be due to the initial degradation of 5-HMF. The carbonates were proved inefficient for the selectivity to FDCA irrespective of their alkali counterparts. 59% selectivity to FDCA was observed for Na_2CO_3 whereas, only 64% was marked for K_2CO_3. Organic bases like imidazole was also screened which formed DFF suggesting operation of oxidative dehydrogenation reaction over oxidation. NaOH was also monitored with different

concentrations for this reaction and it was observed that higher amount of NaOH was required to catalyse the oxidation of intermediates like HMFCA. Equimolar concentration of NaOH led to formation of 76% HMFCA followed by FFCA. As the molar concentration of NaOH increased the appearance of FDCA started in the reaction aliquots. A detail account stating effect of amount of base on 5-HMF oxidation is also shown in **Figure 6.20.b**. Higher amount of base is also required for the separating the acidic counterpart from the catalytic sites and 4 mole of NaOH per mole of 5-HMF was required for our proposed results.

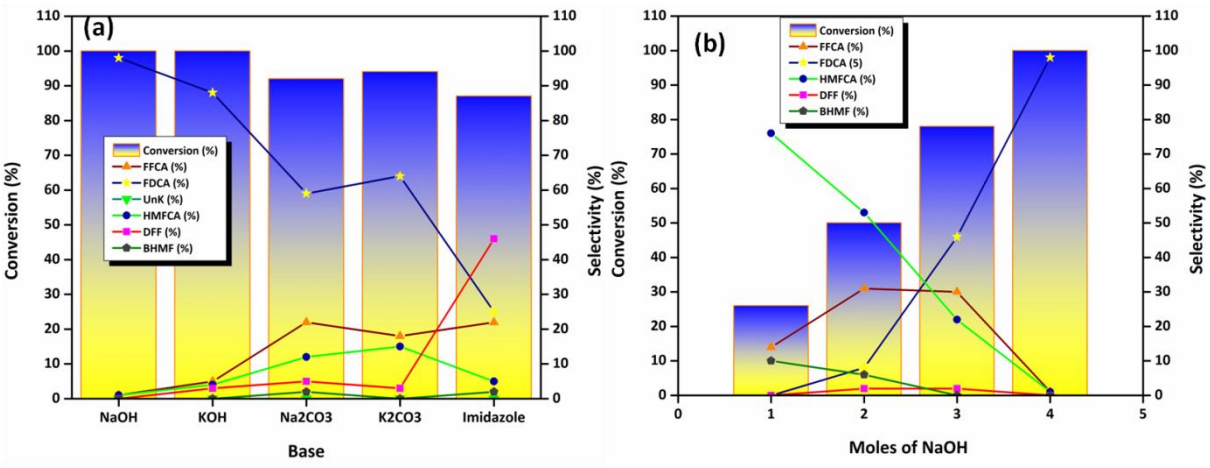

Figure 6.20: Effect of addition of **(a)** various base and **(b)** different moles of NaOH for the oxidation of 5-HMF into FDCA, **Reaction Conditions:** 5-HMF= 100 mg, 5-HMF/base=4, H_2O=25 g, Catalyst= 50 mg, T=90°C, P_{air} = 50 psig, t=1 h, Agitation speed= 1000 rpm

6.3.4.6 C-t Profile

To find out the due course of 5-HMF oxidation, the progress of the reaction was monitored till 1 h of reaction time as shown in **Figure 6.21**. The conversion was always on higher side even in initial sample taken after 0.25 h (53%) due to higher activity of catalyst and alkaline medium. The major product was HMFCA (44%) in the starting of the reaction with only 25% selectivity to FDCA. Further oxidation of HMFCA to FFCA and FDCA was observed in the 0.5h where the selectivity to FDCA was enhanced to 47% with second major product as FFCA (31%). The HMFA reduced to 18% suggesting the forward shift in the equilibrium of

the reaction with the reaction time. After 0.75 h of the reaction FFCA started to decline significantly as FDCA appeared as major product with 71% conversion and no side product was observed. The reaction completed with 100% conversion in 1 h of reaction time with 98% selectivity to FDCA with trace amount of HMFCA and FFCA which remained when reaction was screened for further time also. After 1.75 h of the reaction the selectivity decreased marginally which may be due to the appearance of condensation products in reaction media.

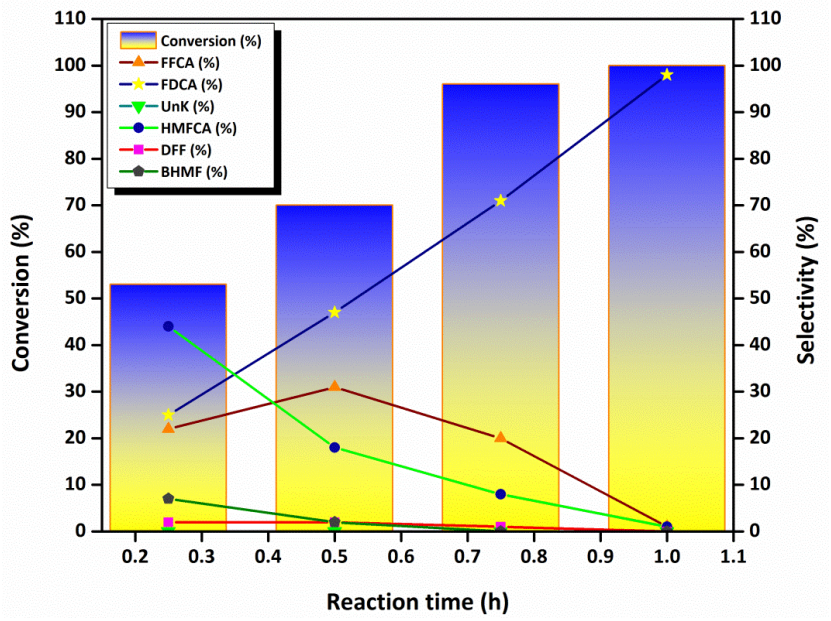

Figure 6.21: C-t profile of 5-HMF oxidation to FDCA, **Reaction Conditions:** 5-HMF= 100 mg, 5-HMF/NaOH=4, H_2O=25 g, Catalyst= 50 mg, T=90°C, P_{air} = 50 psig, t=1 h, Agitation speed= 1000 rpm

6.3.4.7 Recyclability test

The catalyst was tested in multiple reaction cycles to prove its reusability and it was observed that it was efficient till 4th recycle run. In first recycle run no deviation was found from the results of fresh catalyst suggesting no catalytic activity loss. But after that 6% decline in the selectivity of FDCA was observed though conversion was still 100%. The other

products were HMFCA and FFCA. Conversion also started to decline (97%) in 3rd recycle with marginal decrease in the selectivity of FDCA (90%) suggesting loss of active sites. FDCA reduced to 84% in 4th recycle run with 92% conversion. Second major product was FFCA with 14% of selectivity which indicate towards inability of the catalyst to further oxidise the aldehyde group due to the deposition of carbonaceous matter. Sharp decline in the catalytic activity was observed in the successive recycles where the selectivity of FDCA reduced to just 42% only. The reusability of the catalyst over several recycle is shown in **Figure 6.22**.

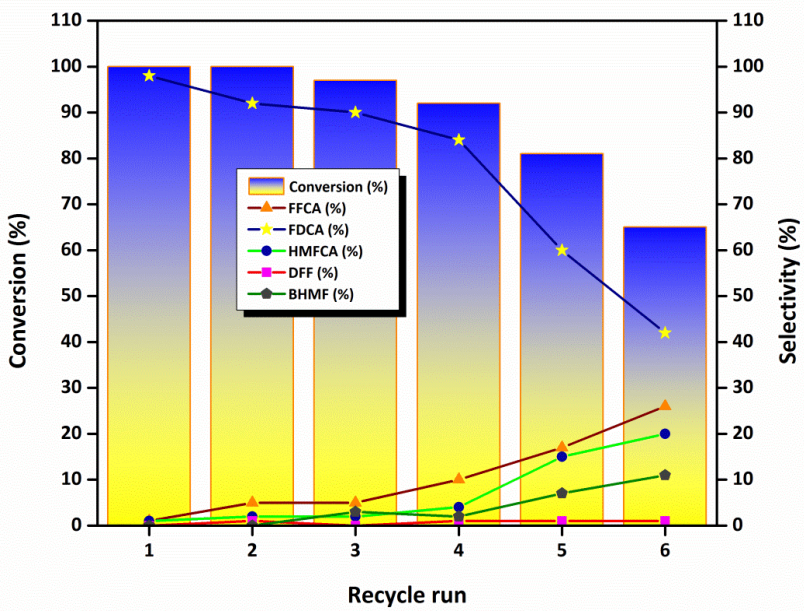

Figure 6.22: The recycle study of the catalyst, **Reaction Conditions:** 5-HMF= 100 mg, 5-HMF/NaOH=4, H_2O=25 g, Catalyst= 50 mg, T=90°C, P_{air} = 50 psig, t=1 h, Agitation speed= 1000 rpm

6.4 Reaction Pathway

Controlled experiments were conducted to find out the reaction pathway of 5-HMF oxidation by varying the substrate material. HMFCA when taken as a substrate, it led to the immediate formation of FFCA in 0.25 h of the reaction. Further oxidation of FFCA was slow and after

0.75 h of the reaction complete conversion was observed with FDCA was the only product. FFCA was also taken as reactant molecule and within 0.5 h the reaction completed with complete conversion. DFF was also seen our reaction samples in trace amount and when reaction was conducted by taking it as a substrate FFCA and FDCA were formed. Hence it can be proposed that in presence of alkaline medium and Cu:Co(1:3)/x-GO, the –OH group of 5-HMF undergoes dehydrogenation and froms FFCA after forming HMFCA easily in the reaction. The presence of DFF can be attributed to the first attack on –OH of 5-HMF rather than –C=O group. FFCA was further oxidised to FDCA as shown in **Reaction Scheme 6.2**.

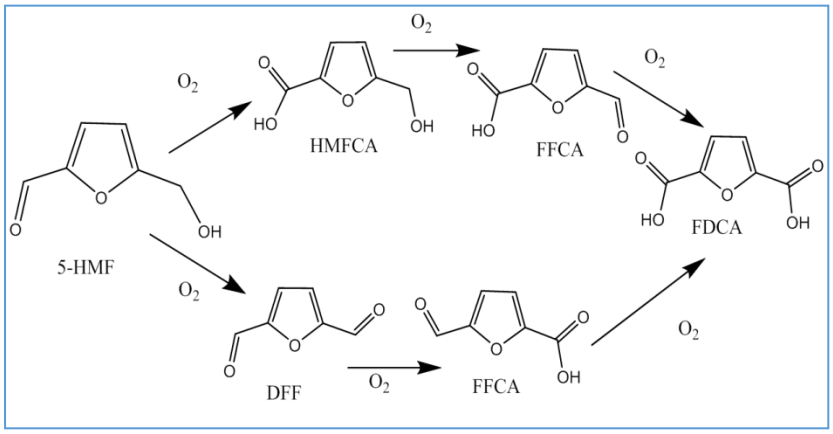

Reaction Scheme 6.2: Plausible reaction pathway for the selective oxidation of 5-HMF to FDCA

6.5 Plausible reaction mechanism

Based on catalytic study and observed parameter optimization pattern a plausible mechanism for 5-HMF oxidation to FDCA was proposed as shown in **Reaction Scheme 6.3**.

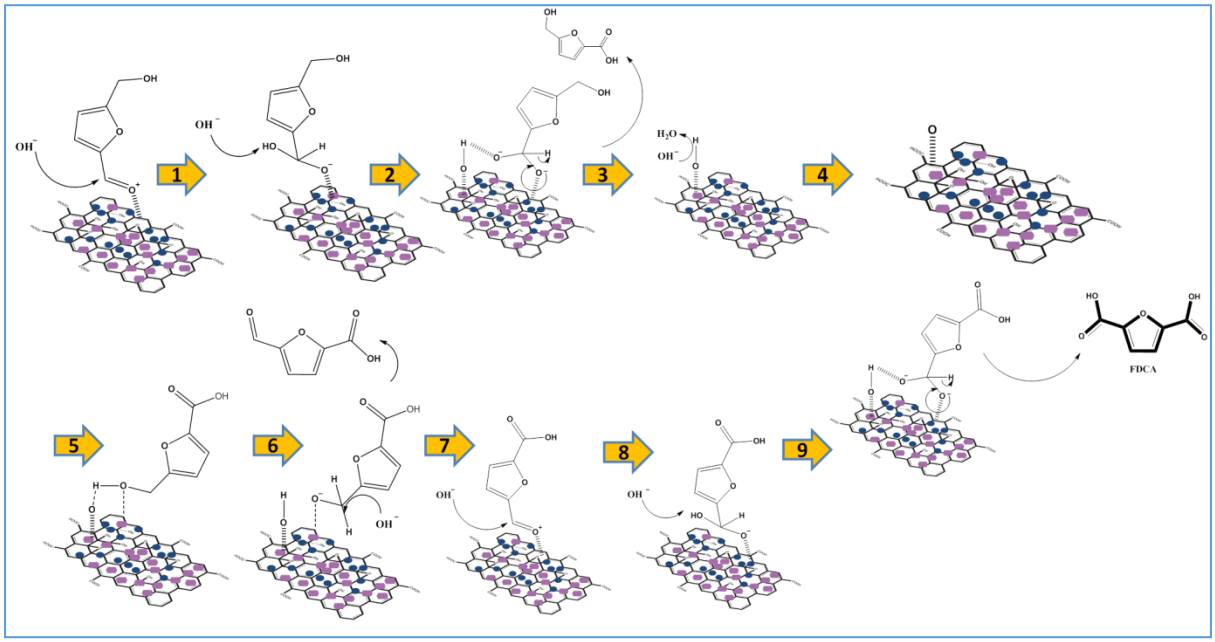

Reaction Scheme 6.3: Plausible reaction mechanism for complete oxidation of 5-HMF to FDCA

The Lewis acidic sites rich surface of x-GO catalyse the adsorption and activation of –CHO group of 5-HMF on the catalytic surface which undergo formation of HMFCA *via* hemiacetal formation in the presence of NaOH [88]. The hemiacetal derivative of 5-HMF is converted into HMFCA by removal of two hydrides on the surface of the metal which can be converted into water by active Oxygen ion. The desorption of HMFCA is facilitated by the hydrolysis reaction on the catalytic surface. Further oxidation of HMFCA takes place *via* the formation of metal-alcoholate intermediate species due to textural Brönsted acidity of $CuCo_2O_4$ [89]. In the presence of alkaline medium β-hydride elimination takes place along with metal-alcoholate bond cleavage leading to the formation of FFCA. Reaction equilibrium is more aligned towards β-hydride elimination than metal-alcoholate bond cleavage which increases the concentration of FFCA in reaction media [90]. Finally the formyl group of FFCA undergoes further oxidation and form the desired product FDCA *via* hemiacetal intermediate like first step.

6.6 Conclusion

Efficient oxidation of 5-HMF to FDCA was conducted on the bimetallic Cu:Co(1:3)/x-GO catalyst with complete conversion. The high catalytic activity of the catalyst was attributed to its well dispersed metal nanoparticles on x-GO having very high surface area and mesoporosity. New spinel phase was detected in by XPS, XRD and FTIR which led to the increase in the redox nature of catalysts. The decline in the binding energy after bimetallic combination was observed suggesting mutual synergism and high oxygen mobility. A $CoCu_2O_4/Co_3O_4$ nanopair was found on the surface which enhanced the conversion selectivity profile of the reaction by reorganised textural properties. High Lewis acidity was observed in Cu/x-Go whereas combined Lewis and Brönsted acidity was seen on Co/x-GO surface which redistributed in the bimetallic catalyst. Optimum reaction conditions were found by detail reaction parameter optimization studies which led to 98% selectivity at T=90°C, pressure of external air= 50 psig, 5-HMF/catalyst= 2, NaOH/5-HMF= 4 in 25 mL of water and 1 h of reaction time.

Reference

1. Y. Roman-Leshkov, J.N. Chheda and J.A. Dumesic, *Science,* **2006,** 312, 1933–1937

2. C. Christodoulou, D. Grimekis, K. D. Panopoulos, D. Vamvuka, S. Karellas and E. Kakaras, *Fuel,* **2014,** 132, 71−81

3. M. Besson, P. Gallezot and C. Pinel, *Chem. Rev.*, **2014,** 114, 1827−1870.

4. D. R. Dodds and R. A. Gross, *Science*, **2007,** 318, 1250–1251.

5. A. Boisen, T. B. Christensen, W. Fu, Y. Y. Gorbanev, T. S. Hansen, J. S. Jensen, K. S. Klitgaard, S. Pedersen, A. Riisager, T. Stáhlberg and J. M. Woodley, *Chem. Eng. Res. Des.,* **2009**, 87, 1318–1327.

6. A. Demirbas, *Energy Convers. Manage.*, **2001,** 42, 1357–1378.

7. G.W. Huber, S. Iborra and A. Corma, *Chem. Rev.,* **2006,** 106, 4044–4098.

8. A. Corma, S. Iborra and A. Velty, *Chem. Rev.,* **2007,** 107, 2411–2502.

9. S.P. Simeonov, J.A.S. Coelho and C.A.M. Afonso, *ChemSusChem,* **2012,** 5, 1388–1391.

10. A. A. Hengne, S. B. Kamble and C. V. Rode, *Green Chem.,* **2013,** 15, 2540–2547.

11. P. Verdeguer, N. Merat and A. Gaset, *J. Mol. Catal.*, **1993,** 85, 327–344.

12. H. Mehdi, V. Fábos, R. Tuba, A. Bodor, L. T. Mika and I. T. Horváth, *Top. Catal.,* **2008,** 48, 49–54.

13. T. Werpy, G. Peterson, Top Value Added Chemicals from Biomass, U.S. Department of Energy (DOE), Springfield, VA, **2004,** pp. 22161

14. R. Geyer, J. R. Jambeck and K. L. Law, *Sci. Adv.,* **2017,** 3, 1700782

15. B. Geyer, G. Lorenz and A. Kandelbauer, *eXPRESS Polym. Lett.,* **2016,** 10, 559-586.

16. R. Wei and W. Zimmermann, *Microb. Biotechnol.*, **2017,** 10, 1308-1322.

17. S. Yoshida, K. Hiraga, T. Takehana, I. Taniguchi, H. Yamaji, Y. Maeda, K. Toyohara, K. Miyamoto, Y. Kimura and K. Oda, *Science*, **2016,** 351, 1196–1199.

18. J. G. van Berkel, N. Guigo, J. J. Kolstad, L. Sipos, B. Wang, M. A. Dam, N. Sbirrazzuoli, *Macromol. Mater. Eng.*, **2015,** 300, 466-474.

19. T. S. Hansen, I. Sádaba, E. J. García-Suárez and A. Riisager, *Appl. Catal. A: Gen.*, **2013,** 456, 44–50.

20. K. F. Wang, C. L. Liu, K. Y. Sui, C. Guo and C. Z. Liu, *ChemBioChem,* **2018,** 19, 654–65.

21. W. Partenheimer and V. V. Grushin, *Adv. Synth. Catal.*, **2001,** 343, 102–111.

22. B. Saha, S. Dutta and M. M. Abu-Omar, *Catal. Sci. Technol.*, **2012,** 2, 79–81.

23. C. A. Antonyraj, N. T. T. Huynh, S. K. Park, S. Shin, Y. J. Kim, S. Kim, K. Y. Lee and J. K. Chuo, *Appl.Catal. A: Gen.*, **2017,** 547, 230-236.

24. H. A. Rass, N. Essayem and M. Besson, *Green Chem.*, **2013,** 15, 2240–2251.

25. G. Yi, S. P. Teong and Y. Zhang, *Green Chem.*, **2016,** 18, 979-983.

26. S. Albonetti, A. Lolli, V. Morandi, A, Migliori, C. Lucarelli and F. Cavani, *Applied Catalysis B: Environ.*, **2015,** 163, 520–530.

27. K. Gupta, R. K. Rai, A. D. Dwivedi and S. K. Singh, *ChemCatChem,* **2017,** 9, 2760 – 2767.

28. O. Casanova, S. Iborra and A. Corma, *ChemSusChem,* **2009,** 2, 1138 – 1144.

29. B. Saha, D. Gupta, M. M. Abu-Omar, A. Modak and A. Bhaumik, *J. Catal.,* **2013,** 299, 316–320.

30. S. Wang, Z, Zhang and B. Liu, *ACS Sustainable Chem. Eng.,* **2015,** 3, 406−412.

31. F. Neatu, R. S. Marin, M. Florea, N. Petrea, O. D. Pavel and V. I. Pârvulescu, *Appl. Catal. B: Environ.,* **2016,** 180, 751–757.

32. E. Hayashi, T. Komanoya, K. Kamata and M. Hara, *ChemSusChem,* **2017,** 10, 654 – 658.

33. M. Ventura, F. Nocito, E. de Giglio, S. Cometa, A. Altomare and A. Dibenedetto, *Green Chem.,* **2018,** 20, 3921–3926

34. D. Yan, J. Xin, C. Shi, X. Lu, L. Ni, G. Wang and S. Zhang, *Chemical Engineering Journal,* **2017,** 323, 473-482.

35. A. Jha, S. H. Patil, B. P. Solanki, A. P. C. Rebeiro, C. A. N. Castro, K. R. Patil, A. Coronas and C. V. Rode, *Chempluschem,* **2015,** 80, 1164-1169.

36. Y. Hou, J. Qi, J. Hu, Y. Xiang, L. Xin and X. Wei, *Processes,* **2020,** 8, 488-518.

37. M. Sharma, B. Das, M. Sharma, B. K. Deka, Y. B. Park, S. K. Bhargava and K. K. Bania, *ACS Appl. Mater. Interfaces,* **2017,** 9, 3453–3462.

38. L. Shahhriary and A. A. Athawale, *Int. J. Renew. Energy Environ. Eng.,* 2014, **2,** 58–63.

39. T.P. Teng, W.P. Wang and Y.C. Hsu, *Nanoscale Res. Lett.,* 2016, **11,** 288-301.

40. S. Pei and S. M. Cheng, *Carbon,* **2012,** 50, 3210-3228.

41. M. Mauro, V. Cipolletti, M. Galimberti, P. Longo and G. Guerra, *J. Phys. Chem. C,* **2012,** 116, 24809−24813.

42. Y. Hsu, T. Hsu, C. Sun, Y. Nien, N. Pu, M. Ger, *Electrochim. Acta,* **2012,** 82, 152–157.

43. A. Jha. D. Mahamane, A. Suryawanshi, S. M. Joshi, P. Shaikh, N. Biradar, S. C. Ogale and C. V. Rode, *Catal. Sci. Technol.,* **2014,** 4, 1771-1778.

44. K. Petrov, K. Krezhov and P. Konstantinov, *J. Phys. Chem. Solids,* **1989,** 50, 577-581.

45. Y. Sharma, N. Sharma, G. S. Rao and B. Chowdari, *J. Power Sources,* **2007,** 173, 495 501.

46. H. Sohn, I. I. Soykal, S. Zhang, J. Shan, F. Tao, J. T. Miller, U. S. Ozkan, *J. Phys. Chem. C,* **2016,** 120, 14631−14642.

47. A. Rokicińska, P. Natkański, B. Dudek, M. Drozdek, L. Lityńska-Dobrzyńska, P. Kuśtrowski, *Appl. Catal. B: Environ.,* **2016,** 195, 59−68.

48. B. Tan, K. J. Klabunde and P. M. A. Sherwood, *J. Am. Chem. Soc.*,**1991,** 113, 855– 861.

49. A. Han, H. Zhang, R. Yuan, H. Ji and P. du, *ACS Appl Mater Interfaces,* **2017,** 9, 2240–2248.

50. M. Silambarasan, N. Padmanathan, P. S. Ramesh and D. Geetha, *Mater Res Express,* **2016,** 3, 95021-95030.

51. J. P. Espinós, J. Morales, A. Barranco, A. Caballero, J. P. Holgado and A. R. González-Elipe, *J. Phys. Chem. B,* **2002,** 106, 6921–6929.

52. C. Drouet, C. Laberty, J. L. G. Fierro, P. Alphonse, A. Rousset, *International Journal of Inorganic Materials,* **2000,** 2, 419-426.

53. V. A. M. Brabers and F. Van Setten, *J Phys D: Appl Phys,* **1983,** 16, L169.

54. A. M. Soliman, S. A. A. Elsuccary, I. M. Ali and A. I. Ayesh, *Journal of Water Process Engineering,* **2017,** 17, 245–255.

55. J. Ederer, P. Janoš, P. Ecorchard, J. Tolsaz, V. Štengl, H. Beneš, M. Perchacz and O. P. Georgievski, *RSC Adv.,* **2017,** 7, 12464–12473.

56. Y. Liu, N. Zheng, C. Yu, L. Jiao and J. Chen, *Nano lett.,* **2016,** 16, 3321-3328.

57. M. S.· L. Scudiero, J. Espinal, J-S. McEwen and M. Garcia-Perez, *Carbon,* **2016,** 110, 155-171

58. A. Bagri, C. Mattevi, M. Acik, Y. J. Chabal, M. Chhowalla and V. B. Shenoy, *Nature Chem.,* **2010,** 2, 581–587.

59. D. Yang, A. Velamakanni, G. Bozoklu, S. Park, M, Stoller, R. D. Piner, S. Stankovich, I. Jung, D. A. Field, C. A. Ventrice Jr. and R. S. Ruoff, *Carbon,* **2009,** 47, 145-152.

60. H. C. Schniepp, J. L. Li, M. J. McAllister, H. Sai, M. Herrera-Alonso, D. H. Adamson, R. K. Prud'homme, R. Car, D. A. Saville, I. A. Aksay, *J. Phys. Chem. B,* **2006,** 110, 8535-8539.

61. O. Akhavan, *Carbon,* **2010,** 48, 509-519.

62. C. Yang, L. Fu, R. Zhu and Z. Liu, *Phys. Chem. Chem. Phys.,* **2016,** 18, 4635–4642.

63. P.H. Shi, X.F. Dai, H.G. Zheng, D.X. Li, W.F. Yao and C.Y. Hu, *Chem. Eng. J.,* **2014,** 240, 264-270.

64. G. Greczynski and L. Hultman, *Progress in Materials Science,* **2020,** 107, 100591-100636.

65. V. Luchnikov, A. Kondyurin, P. Formanek, A. Hannes Lichte and M. Stamm, *Nano Lett.,* **2007,** 7, 3628–3632.

66. Y. Zhang and C. Pan, *J. Mater. Sci.,* **2011,** 46, 2622–2626.

67. J. Shi, X. Li, G. He, L. Zhang and M. Li, *J. Mater. Chem. A*, **2015,** 3, 20619–20626

68. W. Zhang, Z. Zhou, X. Shan, R. Xu, Q. Chen, G. He, X. Sun and H. Chen, *New J. Chem.*, **2016,** 40, 4769-4774.

69. A. V. Murugan, T. Muraliganth and A. Manthiram, *Chem Mater*, **2009,** 21, 5004–5006.

70. D. Cuhadaroglu and O. A. Oygun, *Afr. J. Biotechnol.*, **2008,** 7, 3703-3710

71. U. Gulati, U. C. Rajesh and D. S. Rawat, *ACS Sustainable Chem. Eng.*, **2018,** 6, 8, 10039–10051

72. Y. Mussa, F. Ahmed, H. Abuhimd, M. Arsalan and E. Alsharaeh, *Sci. Rep.*, **2019,** 9, 44-53

73. D. Li, M. B. Muller, S. Gilje, R. B. Kaner and G. G. Wallace, *Nat. Nanotechnol.*, **2008,** 3, 101–105.

74. P. Liang, F. Wang and Z. Hu, *Chemical Engineering Journal*, **2018,** 350, 627–636.

75. G. Sivashanmugam, K. Lakshmi, B. Preethi, S. Nelson, and M. Sathiyaseelan, *J Mater Sci: Mater Electron*, **2021,** 32, 27148–27158.

76. T. A. J. Siddiqui, B. G. Ghule, S. Shaikh, P. V. Shonde, K. C. Gunturu, P. K. Zubaidha, J. M. Yun, C. O'Dwyer, R. S. Mane and K. H. Kim, *RSC Adv.*, **2018,** 8, 17373–17379.

77. S. Bhattacharya, P. Ghosh, and B. Basu, *Tetrahedron Lett.*, **2018,** 59, 899–903.

78. A. Corma, M. E. Domine and S. Valencia, *J. Catal.*, **2003,** 215, 294-304.

79. G. Delahay, B. Coq, L. Broussous, *Applied Catalysis B: Environmental*, **1997,** 12, 49-59.

80. E. A. Urquitea-González, L. Martin, R. P. S. Peguin and M. S. Batista, *Material Research*, 2002, 5, 321-327.

81. S. K. Mahammadunnisa, T. Akanksha, K. Krushnamurty and C. H. Subrahmanyam, *J. Chem. Sci.,* **2016,** 128, 1795–1804.

82. J. B. Li, Z. Q. Jiang, K. Qian and W. X. Huang, *Chin. J. Chem. Phys.,* **2012,** 25, 103-109.

83. F. Yang, J. Mao, S. Li, J. Yin, J. Zhou and W. Liu, *Catal. Sci. Technol.,* **2019,** 9, 1329-1333.

84. H. Song, Z. Li, G. Xu, C. Zhang, X. Ma, L. Zhang, and D. Jia, *RSC Adv.,* **2018,** 8, 24805-24811.

85. G. Fierro, M. Lo Jacono, M. Inversi, R. Dragone and P. Porta, *Top. Catal.*, **2000,** 10, 39–48.

86. C. Su and K. P. Loh, *Account of Chemical Research*, **2013,** 46, 2275-2285.

87. E.S. Kang, D. W. Chae, B. Kim and Y. G. Kim, *J. Ind. Eng. Chem.*, **2012,** 18, 174.

88. Y. C. Li, L. Wang, R. Y. Yan, J. X. Han and S. J. Zhang, *Catal. Sci. Technol.*, **2015,** 5, 3682–3692

89. A. Abad, A. Corma and H. García, *Chem. Eur. J.,* **2008,** 14, 212 – 222.

90. K. Yamaguchi and N. Mizuno, *Angew. Chem., Int. Ed.,* **2002,** 41, 4538−4542.

Chapter 7

Conclusion, Summary and Future Scope

Conclusion, Summary and Future Scope

This work represents the detail account of two different strategies for value addition of biomass derived C6 platform molecule 5-HMF, viz. catalytic hydrogenation of 5-HMF to DMF and catalytic oxidation of 5-HMF to DFF and FDCA. Versatile catalysts were synthesized and screened for their applications in both these strategies for catalytic valorization of 5-HMF. Catalytic hydrogenation of 5-HMF led to the formation of a potential fuel additive DMF which resonates with the fuel properties of gasoline. Keeping account of these facts, supported noble metal catalyst were first tested and conceptual learning from the study was implemented in the generation of economically viable non-noble bare metal-metal oxide combination with high efficiency for catalytic hydrogenation of 5-HMF to DMF. The chemoselective catalytic oxidation of 5-HMF generates DFF and its further complete oxidation to FDCA which is a monomeric unit for polyurethane. Synthesis of industrially important utility chemicals like FDCA and DFF serves the purpose of biorefinery. Alkali doped metal catalysts were synthesized and their potential was explored for chemoselective oxidation of 5-HMF to DFF. Immediate challenges in the area of investigation were identified by detailed literature survey and considering the outcomes supported metal oxide was developed for complete oxidation of 5-HMF to FDCA. Detailed characterization studies were carried out along with extensive parameter optimization which helped to establish a logical structure-activity correlation in our investigation. The major conclusions are summarised below:

- Supported noble metal catalysts (Pd, Ir, Rh, Ru etc) were prepared by wet impregnation method and screened for catalytic hydrodeoxygenation of 5-HMF. Pd/C with optimum metal loading of 3% catalyst was found to be the most efficient. Formation of Pd/PdO interface, complex mutual dπ-pπ electronic

interaction, uniformly distributed fine nanoparticles having size in the range of 2.6-3.0 nm and surface acidity led to complete conversion of 5-HMF with 99% selectivity to DMF. The parameter optimization studies were conducted and at 170°C, 300 psig external pressure of H_2, 5-HMF/catalyst=10 and in 2-propanol as reaction medium, highest activity of 3% Pd/C to DMF was observed in 4 h of reaction time.

- After initial results obtained over noble metal catalysts, the concept was applied on economically viable non-noble metal catalyst. Magnetically recoverable Cu(0)-$CuFe_2O_4$ was developed by co-precipitation method and specific reduction protocol for hydrodeoxygenation of 5-HMF. The oxophilic nature and Lewis acidity (0.5294) shown by Fe, high affinity of Cu towards -C=O bond and its surface Brönsted acidic sites (6.8226) led to generation of highly efficient nanohybrid with a size range of 15-17 nm. Magnetic recoverability, high reusability and active site regeneration served the economic sustainability aspect of green chemistry. Detail account of deactivation and plausible reaction mechanism was also proposed
- Chemoselective oxidation of 5-HMF to DFF was attempted on alkali and alkaline doped transition metals like Mn, Cu, Fe and Co. Out of them, Cs doped Mn proved highly useful with good catalytic activity. Due to higher oxygen mobility, enhanced lattice oxygen, enhanced surface basicity, active Brönsted basic sites, lattice oxygen defect and reduced work function Mn-Cs(80:20) was a standalone catalyst for oxidative dehydrogenation of 5-HMF. The reaction proceed via Mars van Krevelen mechanism which was supported by XPS where 17% increase in lattice oxygen species was identified after doping and Mn^{4+}

reduced to 39% from 60% suggesting operation of Mars van Krevelen mechanism on surface in presence of external O_2.

- Complete oxidation of 5-HMF was achieved on Cu:Co(1:3)/x-GO which was designed by the combination of modified Hummer's method and co-precipitation. Formation of spinel phase $CuCo_2O_4$, high surface area, uniformly distributed metallic nanoparticles and high reducibility altogether formed a highly efficient catalyst for complete oxidation of 5-HMF in FDCA under very mild condition of 90°C, 50 psig external air, 5-HMF/catalyst=2 in aqueous solvent within 1 h of reaction time. The high selectivity towards FDCA (98%) can be attributed to the reorganised surface acidity and enhanced redox nature due to formation of $CuCo_2O_4$-Co_3O_4 nanopair on the surface of x-GO with strong interaction.

The work done in the thesis pave the way for further scope in the field of value addition of 5-HMF. Synthesis of non-noble metal catalysts with high TON and TOF should be attempted. The ring hydrogenation product of 5-HMF, DMTHF is a saturated analogue of DMF which is easy to transport due to its saturated ring. Ring hydrogenation of 5-HMF requires noble metal catalysts and extremely harsh reaction conditions which should be countered by designing novel and environmentally benign catalysts. The base free oxidation of 5-HMF is a big challenge which need to be addressed to avoid the waste generation during the purification of FDCA. This will also add the green aspect to the process generation and can be immense contribution to this field. Further understanding of the catalytic properties in determining the driving force of the forward reaction can be achieved using cyclic voltammetry and modified temperature programmed desorption studies.

ABSTRACT

Name of the Student: Bhanupratap Singh Solanki **Registration No. : 10CC14A26024**
Faculty of Study: Chemical Science **Year of Submission: 2022**
AcSIR academic centre/CSIR Lab: NCL, Pune **Name of the Supervisor(s):**
Dr. Santosh B Mhaske (admin)
Dr. Chandrashekhar V Rode

Title of the thesis: Valorization of biomass derived platform molecule *via* catalytic hydrogenation and oxidation

The current work presented under the heading of "**Valorization of biomass derived platform molecule *via* catalytic hydrogenation and oxidation"** is divided into 7 chapters. This is a brief overview of the results obtained by conducting the various catalytic transformations on 5-HMF. **Chapter 1** present the introductory remarks on the formation of 5-HMF from lignocellulosic biomass. It also highlights the concept of catalyst and its role in biorefinery. **Chapter 2** deals with the experimental, characterization and methodology which was followed during the process protocol. **Chapter 3** describes the use of noble metal *viz.* Pd/C for the efficient hydrogenation of 5-HMF into fuel additive 2, 5-DMF. Complete conversion of 5-HMF and >99% selectivity of DMF was obtained. The excellent catalytic activity of Pd/C is explained by various characterization techniques. **Chapter 4** deals with the designing of non-noble, magnetically retrievable, Cu-Fe bimetallic catalyst for catalytic hydrodeoxygenation of 5-HMF. 97% conversion of 5-HMF along with 93% selectivity to DMF was achieved. In **Chapter 5**, alkali doped Mn (Mn-Cs) catalyst was developed for selective oxidation of 5-HMF into DFF. Dual morphology, catalytically active interfacial sites, enhanced redox properties, higher oxygen mobility and basicity led to 91% conversion of 5-HMF with 98% selectivity to DFF. **Chapter 6** explains formation of exfoliated graphene oxide based Cu-Co bimetallic catalyst for complete oxidation of 5-HMF to FDCA at very mild conditions due to surface redox properties and mutual synergism of Co, Cu and x-GO. **Chapter 7** enlists the conclusion summary and future scope of current research theme.

List of publication(s) in SCI Journal(s) (published & accepted) emanating from the thesis work

1. **B S Solanki** and C V Rode, Selective hydrogenolysis of 5-(hydroxymethyl) furfural over Pd/C catalyst to 2, 5-dimethylfuran, *Journal of Saudi Chemical Society*, **2019**, 23, 439-451

   https://www.sciencedirect.com/science/article/pii/S1319610318301017?via%3Dihub

2. **B S Solanki** and C V Rode, Selective hydrogenation of 5-HMF to 2, 5-DMF over a magnetically recoverable non-noble metal catalyst, *Green Chem*, **2019**, 21, 6390-6406

   https://pubs.rsc.org/en/content/articlelanding/2019/GC/C9GC03091C#!divAbstract

List of Papers with abstract presented (oral/poster) at national/international conferences/seminars with complete details

1. **NCLRF- AGNIMITRA Memorial Best Poster Award 2017,** organised by CSIR-NCL, Pune on 23-24 February 2017
2. **1st Runners up of NFCFA-ACS Poster contest 2019,** in **3rd National conference on "New Frontiers in Chemistry –from Fundamentals to Applications"** organised by Department of chemistry BITS Pilani K K Birla Goa Campus
3. **B S Solanki** " Hydrogenolysis of 5-HMF into DMF via non-noble bimetallic Cu-Fe catalyst, poster at **The 8th Tokyo Conference on Advanced Catalytic Science and Technology (TOCAT8)** held in Yokohama from 5th-10th August 2018
4. Poster at **CATSYMP22** organised by The Catalysis Society of India and CSIR-CSMCRI on 7-9 January 2015 in Bhavnagar, Gujarat
5. Poster at **International Conference on Sustainable Chemistry and Engineering (SusChemE)** organised by ICT Mumbai on 8-9 October 2015
6. Poster at **17th National Workshop on Challenges in Catalysis Science and Technology (CCST-2016)** organised by CSIR-IICT and Catalysis Society of India held at Hyderabad on 23-25th June 2016

7. Poster at **International Conference on Sustainable Development for Energy and Environment (ICSDEE-2017)** organised by Indian Institute of Chemical Engineers on 16-17th January 2017 at CSIR-NCL

Journal of Saudi Chemical Society (2019) **23**, 439–451

King Saud University

Journal of Saudi Chemical Society

www.ksu.edu.sa
www.sciencedirect.com

ORIGINAL ARTICLE

Selective hydrogenolysis of 5-(hydroxymethyl) furfural over Pd/C catalyst to 2,5-dimethylfuran

Bhanupratap S. Solanki, C.V. Rode *

Chemical Engineering and Process Development Division, CSIR-National Chemical Laboratory, Dr. Homi Bhabha Road, Pune 411008, India
Academy of Scientific and Innovative Research (ACSIR), Ghaziabad-201002, India

Received 5 May 2018; revised 18 August 2018; accepted 19 August 2018
Available online 3 September 2018

KEYWORDS

Hydrogenolysis;
Fuel additive;
Biomass;
Palladium;
Heterogeneous catalysis

Abstract Several metal supported catalysts were prepared and evaluated for 5-(hydroxymethyl) furfural (5-HMF) hydrogenolysis to 2,5-dimethylfuran (2,5-DMF) which is a renewable potential fuel additive. Among the prepared catalysts, 3%Pd/C showed excellent performance in terms of complete conversion of 5-HMF along with the highest selectivity of 99% to 2,5-DMF. Detailed physico-chemical characterisation was done in order to understand structure-activity correlation. Uniformly dispersed Pd nanoparticles on activated carbon provided the adsorption surface to enhance the hydrogenation of 5-HMF. Reaction was well optimised and established by extensive study of different reaction parameters like temperature, pressure, reaction time, stirring effect, substrate loading and metal loading.

1. Introduction

Worldwide diminishing of non-renewable energy resources and unpredictable fluctuating global oil economy, renewable and green alternatives are sought after in energy sector [1–5]. Around 200 billion metric tons of biomass is produced by photosynthesis having energy storage of 3×10^{18} KJ annually [6]. Lignocellulosic biomass is basically composed of cellulose (40–50%), hemicelluloses (25–35%) and lignin (15–20%) [7]. It is estimated that about 1/3rd fuel requirement of developed countries like USA can be fulfilled by lignocellulosic biomass as well as a wide variety of commodity chemicals can be also produced by this abundant renewable resource [8,9]. 5-(hydroxymethyl) furfural (5-HMF) obtained by triple dehydration of hexoses is of great industrial prospective as it can produce biofuels like 2,5-dimethylfuran (DMF), 2,5-dimethyltetrahydrofuran (DMTHF), and fuel additives like γ-valerolactone (GVL) and different 6-carbon monomers like 2,5-bis(hydroxymethyl)furan (BHMF) and 2,5-bis(hydroxymethyl)tetrahydrofuran (BHTHF) for the synthesis of artificial fibres, drugs and crown ethers [10–13]. Among these, DMF can play an important role in carbon neutral oil economy due to its higher energy density, ideal boiling point and higher octane number as compared to current market leading alternatives of gasoline like bio-ethanol and butanol [14]. More importantly, DMF being immiscible with water, the distillation cost in a refinery can be totally cut off [15]. Literature survey reveals that supported noble metals are used for the

* Corresponding author.
E-mail address: cv.rode@ncl.res.in (C.V. Rode).
Peer review under responsibility of King Saud University.

Production and hosting by Elsevier

https://doi.org/10.1016/j.jscs.2018.08.009
1319-6103

conversion of HMF to DMF. There are few reports on conversion of carbohydrates into DMF involving multiple steps. Roman-Leshkov et al., reported two steps synthesis of DMF from fructose and its subsequent hydrogenolysis to DMF over CuRu/C catalyst in 1-butanol giving 76–79% yield of DMF [16]. Under similar conditions Binder et al., achieved 49% yield of DMF from crude HMF which was obtained from hydrolysis-dehydration of corn stover [17]. Hydrogenolysis of DMF over Pd/C catalyst under very high H_2 pressure (900 psi) has been reported to give $<32\%$ yield of 2,5-DMF [18]. A very high yield of DMF (95%) was achieved in one-pot synthesis from fructose using H_2SO_4, formic acid and Pd/C however, the catalyst system could not be recycled due to the deactivation of Pd/C in acidic medium [19]. Whereas, Upare et al. achieved overall 92% yield of DMF from fructose in 1-butanol by a combination of dehydration over Amberlyst-15 and vapour phase hydrogenolysis of as obtained 5-HMF over the Ru-Sn/ZnO [20]. Higher DMF yields have been reported over Ru as well as Au based catalysts under different sets of reaction conditions. [21–24]. Mitra et al explained different approach for 5-HMF hydrogenation with hydrodeoxygenation and decarbonylation on the Pd/C catalyst. In the case of hydrodeoxygenation they used formic acid as the hydrogenation promoter and with 30 psi of external hydrogen pressure at 393 K they achieved 85% DMF after 15 h of the reaction. Although reaction conditions were quite mild but corrosive nature of formic acid and very long reaction time pose a serious concern [25]. Attempts were also made for the transfer hydrogenolysis of 5-HMF various solvents such as 2-propanol, supercritical methanol, etc. over noble as well as non-noble catalysts [26,27].

Although, there have been several reports on hydrogenolysis of HMF using various catalysts systems, but use of harsh reaction conditions like high temperature (473 K) [21], high metal loading (50%) [23], high pressure (as high as 900 psi) [18], long reaction time (15 h) [25], involvement of mineral acids (H_2SO_4) [19], etc. are the major drawbacks which necessitates scope for improved catalyst systems. In the present work, we report 3% Pd/C catalyst for the conversion of HMF to DMF at 443 K under 300 psi H_2 pressure in 4 h of reaction time to give 99.5% HMF conversion with 99% DMF selectivity. Various parameter effects such as pressure, temperature, stirring effect, reaction time, substrate loading, support study and metal loading on HMF conversion as well as DMF selectivity were studied in batch reactor.

2. Experimental

2.1. Materials

5-(hydroxymethyl)furfural (99.98%), 5-methyl furfural (98%), 2,5-dimethyl furan (98.5%) were purchased from Sigma–Aldrich, Bangalore, India. 2-propanol (99.7%), NaOH (97.5%) and $NaBH_4$ (96%) were purchased from Thomas Bakers. $PdCl_2$ was purchased from chemlab-India. Activated charcoal was purchased from Sigma–Aldrich, Bangalore, India. Hydrogen of high purity (99.99%) was obtained from Inox-India.

2.2. Catalyst preparation

Pd/C was prepared by modified wet impregnation method [28]. In a typical synthesis of 3% Pd/C calculated amount of $PdCl_2$ was dissolved in minimum amount of diluted HCl. In this homogeneous solution, 2 g aqueous slurry of activated charcoal was added. This mixture was vigorously stirred for 2 h at room temperature. After 2 h, 10 M solution of NaOH was added to maintain the *pH* of the solution in the range of 8–9 and the stirring was again continued for 0.5 h. After that $NaBH_4$ was added as reducing agent to the solution. The reaction mixture was further stirred for 0.5 h. After that as obtained slurry was washed with deionised water till the *pH* of the mother liquor becomes neutral and dried at 383 K for 24 h. Similarly, other Pt, Ir, Ru, and Re supported catalysts were prepared. The prepared catalysts were nominated as 3%M/C where M stands for metals. Catalysts on different support systems like ZrO_2, CeO_2 and Al_2O_3 were also synthesised by the same method.

2.3. Characterisation methodology

BET surface area of all the samples was measured on Chemisorb 2720 Micromeritics instrument by means of N_2 adsorption at 77 K. X-ray diffraction (XRD) patterns were recorded on a PAnalytical PXRD system (Model X-Pert PRO-1712), using Ni filtered Cu Kα radiation ($\lambda = 0.154$ nm) as a source (current intensity, 30 mA; voltage, 40 kV) and X-celerator detector. The samples were scanned in the 2θ range of 10–80° having step size of $2\theta = 0.008°$ and counter time of 15 min with 5°/min rate. The metal phases of the catalyst were identified by their characteristic 2θ values. The software program X-Pert High Score Plus was used to subtract the contribution of the Cu Kα_2 line prior to data analysis. The photoelectron spectra of the samples were recorded with a custom built ambient pressure photoelectron spectrometer (APPES) (Prevac, Poland) at CSIR-NCL Pune. The instrument sis equipped with a VG Scienta R3000HP analyser and MX650 monochromator. Monochromatic Al Kα X-rays were generated at 200 W and used for measuring the X-ray photoelectron spectrum (XPS) of the catalysts. Base pressure in the analysis chamber was maintained in the range of 10^{-10} mbar. The energy resolution of the spectrometer was set at 0.5 eV at pass energy of 50 eV. Binding energy (BE) was calibrated with respect to Au $4f_{7/2}$ core level at 84.0 eV.

Particle size and particle distributions were studied using transmission electron microscope (HR-TEM), model JEOL 1200 EX. A small amount of the solid sample was sonicated in 2-propanol for 1 min. A drop of prepared suspension was deposited on a Cu grid coated with a carbon layer, and the grid was then dried at room temperature before analysis. Particle morphology and elemental composition were studied by Scanning Electron Microscope (SEM) and Energy Dispersive X-rays Analysis (EDAX) respectively. Analysis was performed on LEO-LEICA STEREOSCAN 440 at various magnifications by Bruker detector. FT-IR spectra of the prepared catalysts were recorded on a Perkin Elmer 2000 FTIR spectrometer in the 4000–400 cm^{-1} wave number ranges using the KBr pellet technique. In order to evaluate the acidity of the catalysts,

NH_3–TPD measurements were carried out using Micromeritics ChemiSorb 2720 (ChemisoftTPx) instrument, by (i) pre-treating the samples from room temperature to 200 °C under helium flow rate of 25 mL/min. (ii) adsorption of ammonia at 50 °C (iii) desorption of ammonia with a heating rate of 10 °C/min starting from the adsorption temperature of 25–700 °C.

2.4. Catalyst activity test

The hydrogenation of HMF was carried out in 300 mL capacity autoclave supplied by Parr Instruments Co. USA at an agitation speed of 1000 rpm. The typical hydrogenation conditions were: temperature, 443 K, H_2 pressure, 300 psi, HMF, 0.1 g, solvent, 2-propanol, 20 g and catalyst loading, 0.01 g. The reproducibility of results was confirmed by repeating three times. Liquid samples were withdrawn after specific time interval. The aliquots taken during the reaction were analysed using a Trace GC 700 series GC System (Thermo SCINTIFIC) coupled with FID detector and capillary column (HP-5 capillary column, 30 m length × 0.32 mm id). The following temperature program method was used for GC analysis: 40 °C (3 min), 1 °C/min, 45 °C (1 min), 10 °C/min, 60 °C (0 min), 20 °C/min, and 250 °C (1 min). The mass balance calculated by gas chromatogram calibration was found 96.17%. The catalytic parameter like conversion, selectivity, Turn Over Number (TON) and Turn Over Frequency (TOF) were calculated and defined as follows:

$$(\%)\ Conversion = \frac{Initial\ conc.\ of\ HMF - Final\ Conc\ of\ HMF}{Initial\ conc.\ of\ HMF} \times 100 \quad (1)$$

$$(\%)\ Selectivity = \frac{Moles\ of\ desired\ product\ formed}{\sum moles\ of\ all\ products\ formed} \times 100 \quad (2)$$

$$Turn\ Over\ Number\ (TON) = \frac{Moles\ of\ substrate\ consumed}{Catalytic\ active\ sites\ (Pd)\ in\ moles} \quad (3)$$

$$Turn\ Over\ Frequeny\ (TOF) = \frac{Moles\ of\ substrate\ consumed}{Catalytic\ active\ sites\ (Pd)\ in\ moles * Reaction\ time\ (h)} \quad (4)$$

3. Results and discussions

Major objective of this work was (i) to reduce the harsh conditions like longer reaction time high pressure and temperature (ii) extensive study of reaction parameters for the Pd/C catalyst (iii) to find out the structure–activity correlation by in depth study of catalyst characterisation.

3.1. Catalyst characterisation

3.1.1. BET analysis

Textural properties of various metal supported carbon catalysts are presented in Tables 1 and 2. The surface area of the prepared catalysts was found to decrease in order of Pd/C (826 m^2/g) > Ru/C (546 m^2/g) > Ir/C (364 m^2/g) > Rh/C (359 m^2/g) > Re/C (291 m^2/g). The surface areas of all the metal supported catalyst was decreased as compared to bare activated carbon which confirmed the successful metal loading over the support material. Decrease in surface area, among all the catalyst might be due to agglomerisation which was also evidenced by TEM image, as discussed later. On the other hand, sizes of parent metal also influenced surface area of catalyst.

Table 1 BET surface area of prepared catalysts.

Sr. no.	Catalyst	Surface area m^2/g
1	Activated Carbon	954
2	3%Pd/C	826
3	3%Ir/C	364
4	3%Rh/C	359
5	3%Ru/C	546
6	3%Re/C	291

Table 2 BET surface area of prepared catalysts.

Sr. no.	Catalyst	Surface area m^2/g
1	3% Pd/C	826
2	3% Pd/Al_2O_3	208
3	3% Pd/ZrO_2	101
4	3% Pd/CeO_2	67

Similarly, Pd was also loaded on different supports to find out different comparative analysis. The surface area was found to vary according to the nature of supports as shown in Table 2.

The N_2 adsorption isotherm (Fig. 1) of fresh and used 3% Pd/C showed type-I isotherm which reveals that the catalyst possess microporous nature [29]. The pore volume decreased from 0.32 cc/g of fresh catalyst to used catalyst 0.21 cc/g. The average pore diameter was found be almost equal (5.1 Å) in both the cases.

3.1.2. XRDxxx

XRD patterns of fresh and used carbon supported Pd catalysts are shown in Fig. 2. The peaks observed at 2θ = 24.21°, 79.33°

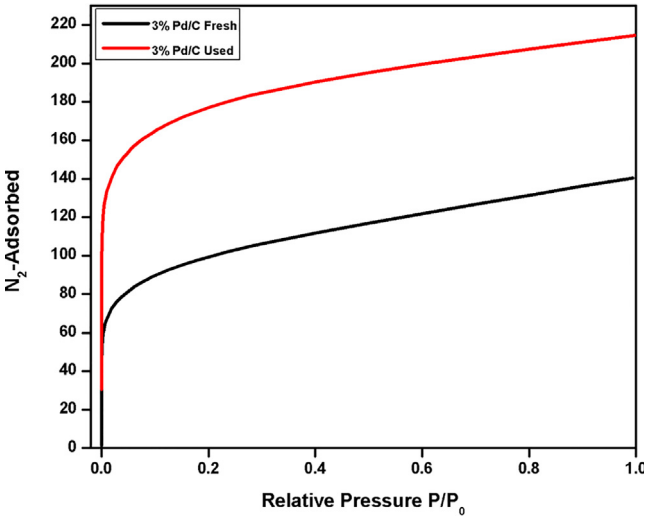

Fig. 1 N_2-adsorption isotherm of Pd/C fresh and used catalyst.

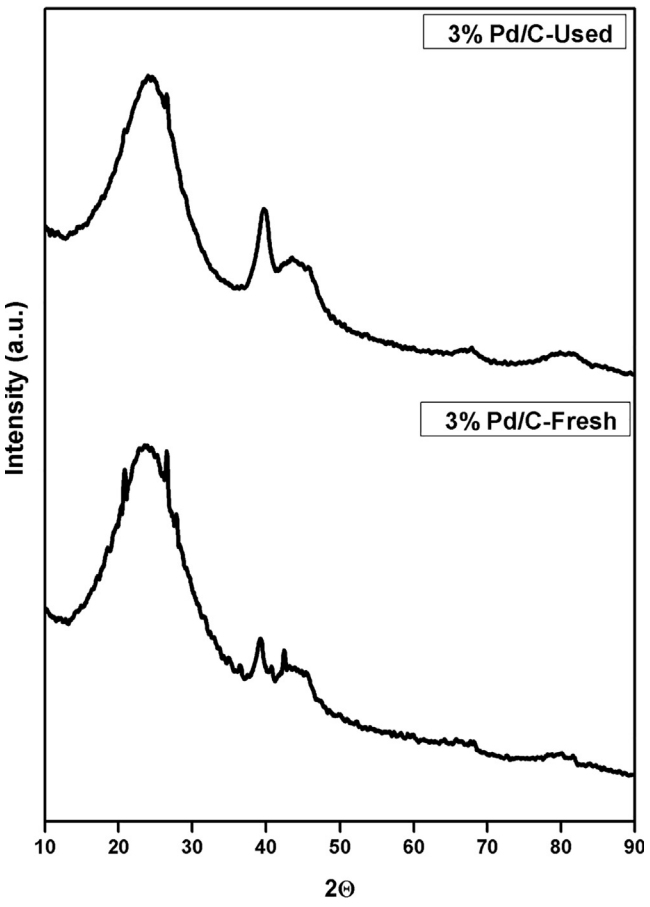

Fig. 2 XRD images of Fresh and used 3% Pd/C.

and 43.70° corresponded to graphitic carbon which is in well agreement with previous literature [30,31].

After impregnating Pd, the parent structure of carbon diminished with rise in characteristic XRD peaks of Pd at 2θ = 39.10° and 68.33° corresponding to (1 1 1) and (2 2 0) planes, respectively (JCPDS No #461043). For others metals (Ru, Rh, Pt, Ir), no any reflections corresponding to respective metals except Pt where Pt impressions were observed at 2θ = 39.71°, 46.66° and 67.99° corresponding to its (1 1 1), (2 0 0) and (2 2 0) plane. Rest of the metals didn't show any specific peaks which might be due to either overlapping of peaks with carbon or by formation of fine layer over carbon support (Fig. S1). In a similar way, after impregnation of Pd on various supports, no characteristic peaks of Pd were also observed (Fig. S2). In the XRD analysis of 3%Pd/Al_2O_3 characteristic peaks of ϒ-Al_2O_3 were observed at 2θ = 37.55°, 39.85°, 45.95°, 67.04, and 84.85°. Different phases of Pd which may be located at 40° and 46° could not be highlighted because of overlapping of different phases of ϒ-Al_2O_3. Similarly in case of CeO_2, characteristic peaks of fluorite structure of CeO_2 were observed at 2θ = 28.60°, 33.7°, 47.55°, 56.29° along with other small peaks at 2θ values of 59.59°, 69.59°, 76.78°, 79.08° and 88.32° lacking any specific information of Pd phases. Also in XRD pattern of 3% Pd/ZrO_2 monoclinic nature of ZrO_2 revealed irrespective of metal loading. In case of 3% Pd/C used catalyst; almost similar peaks corresponding to Pd were observed at the same 2θ values with negligible change in d spacing value (0.349 nm) of carbon confirming the catalyst stability under reaction conditions.

3.1.3. XPSxxx

Fig. 3 represents the XPS of both (a) fresh and (b) used 3% Pd/C. After deconvolution, four peaks were observed with $Pd3d_{3/2}$ and $Pd3d_{5/2}$. Intense peaks at 340.70 eV ($Pd3d_{3/2}$) and 335.3 eV ($Pd3d_{5/2}$) corresponded to metallic Pd, whereas the less intense peaks at 337 eV and 342 eV denote Pd^{+2} (PdO) oxidation state.

In order to differentiate between metallic and oxide states of Pd, the relative intensities of Pd^0 and PdO are presented in Table 4.

It was observed after these calculations that Pd/PdO ratio in various energy levels *i.e.* in Pd $3d_{3/2}$ is higher (2.55) than $Pd3d_{5/2}$ (1.87). The detailed XPS spectrum of O 1 s was also deconvoluted and it reveals information about the type of O present in the catalyst (Fig. 4). The PdO band was present at 530.13 eV, 531.72 eV is assigned for O-H bond whereas another peak at 533.14 eV is observed for C—O band [32]. In the spent 3%Pd/C, O 1s XPS spectra reveals only C—O and O—H bond characteristic. These observations reveal the presence of Pd-PdO nanohybrid in the catalyst. Although the major active sites is metallic Pd, the presence of PdO can enhance the activity of the catalyst due to the complex mutual electron interaction between Pd and PdO and also it is known that hydrogenation reactions proceed smoothly on the phase boundary of Pd-PdO rather than alone Pd [33]. The XPS analysis of used 3% Pd/C in Fig. 3b revealed the disappearance of Pd^{+2} peaks indicating its complete reduction to metallic Pd. The peak positions of the Pd $3d_{5/2}$ in fresh samples

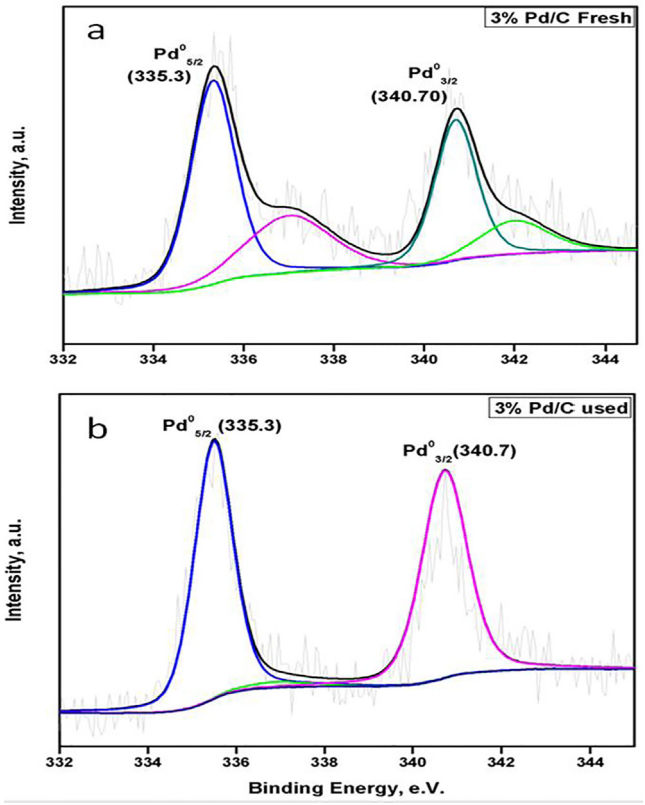

Fig. 3 XPS pattern of (a) Fresh 3%Pd/C (b) Used 3%Pd/C.

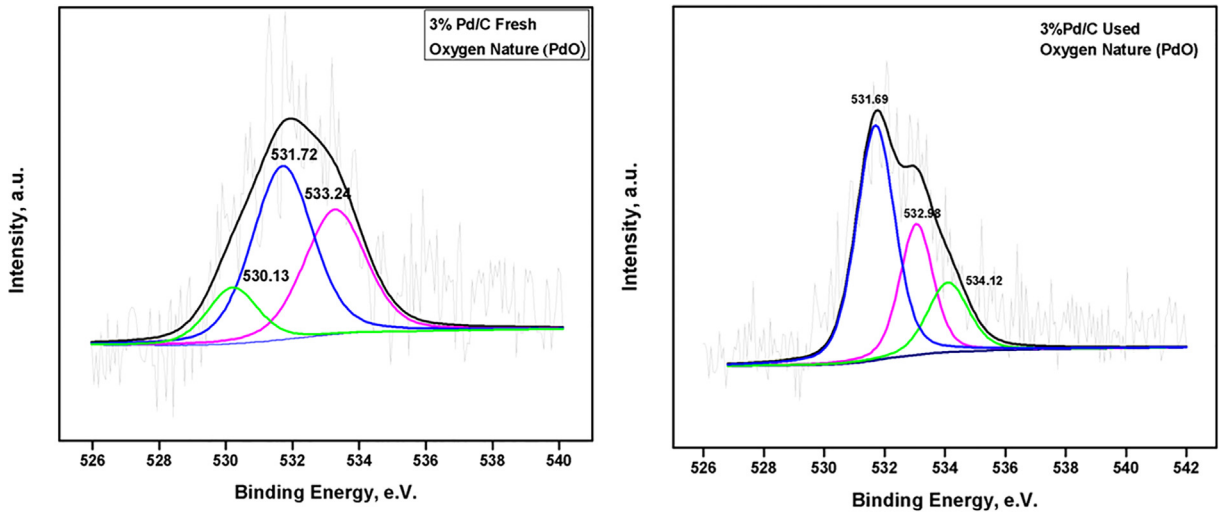

Fig. 4 Nature of Oxygen *via* O1s spectra in Fresh and used 3%Pd/C.

(BE: 335.3, and 340.70 eV, respectively) were in good agreement with the reported values for Pd^0 [34–36].

3.1.4. SEM and TEM

The morphology, metal dispersion and particle size of most active catalyst 3%Pd/C were determined by HR-TEM analysis (Fig. 5a, b).

In case of fresh 3% Pd/C catalyst, well dispersion of metal (Pd) over the surface of carbon support was observed, whereas used catalyst sample showed agglomeration of metal particles after repetitive use (Fig. 5c) which was also evidenced by SEM images (Fig. 6b). The average particle size of the Pd measured from counting 50 individual particles was found to be in the range of 2.6–3.0 nm (Fig. 5d).

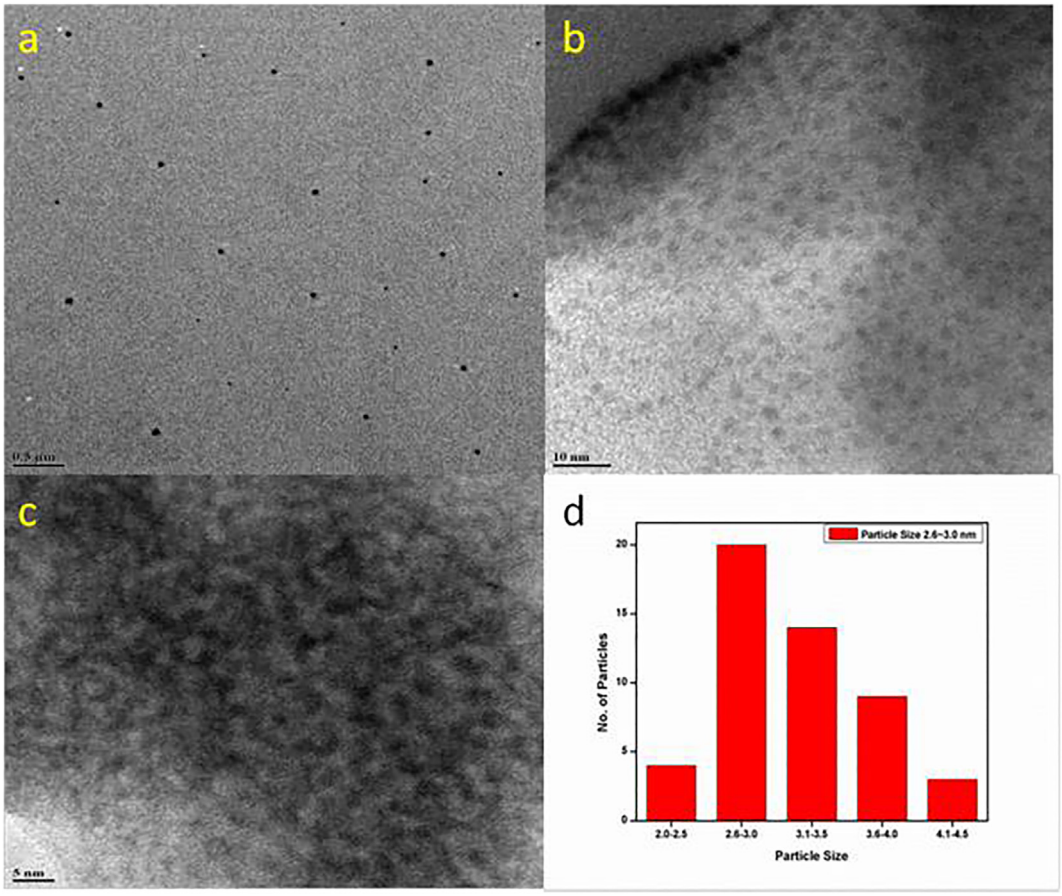

Fig. 5 TEM images of (a,b) Fresh 3%Pd/C (c) Used 3%Pd/C (d) Particle size distribution for fresh 3%Pd/C.

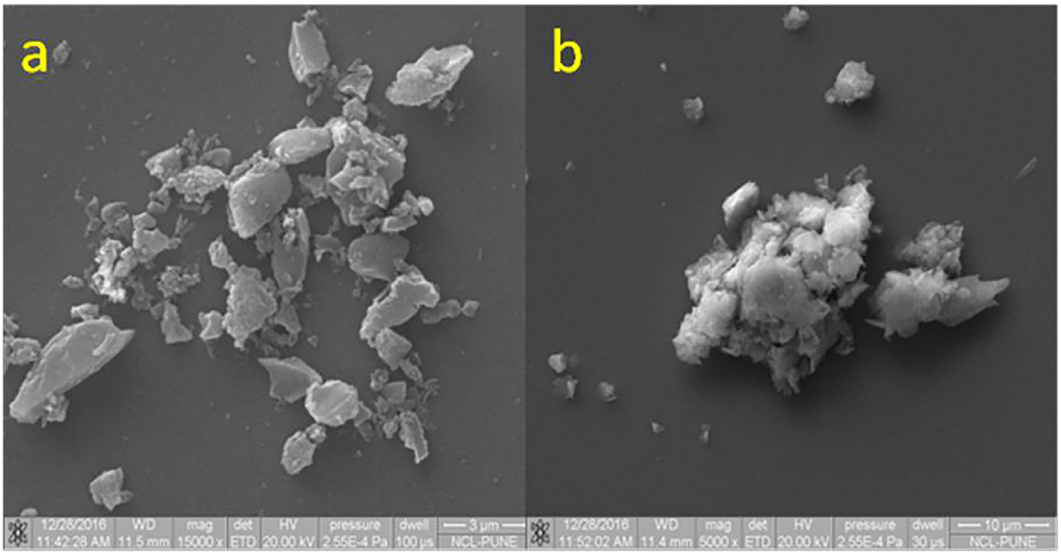

Fig. 6 (a) SEM images of Fresh 3%Pd/C and (b) used 3%Pd/C.

EDAX of fresh and spent catalyst samples shown in Fig. 7 confirmed that the actual Pd on activated C was approximately the same (2.80%) as used for the preparation. Fig. 7 shows that the Pd loading for the spent catalyst was nearly same as that of fresh 3%Pd/C (2.58%). These results are in well agreement with our hot filtration test which reveals that no any metal leaching was observed under the reaction conditions.

3.1.5. FTIRxxx

Fresh and spent catalyst samples were analysed by FTIR to find out the nature of carbonaceous matter deposited on the catalyst. A major IR band was observed at 1738 cm^{-1} (θ) which was assigned with to DMF (confirmed with standard FTIR of DMF and reaction crude after reaction, Figs. S3 and S4, respectively). Literature suggests a spike on 2860 cm^{-1} (μ) for the C—H stretching vibration of a —CHO group (5-HMF) [37].

Our analysis (Fig. 8) shows a tiny band in 4th hour suggesting almost complete conversion of 5-HMF (99.5%). Perturbation is also observed at 1572 cm^{-1} (α) in the first h of reaction which can be ascribed for C═C bands in highly conjugated structure (5-HMF) [38]. This band almost vanished in the 4th hour. A spike can be seen around 2973 cm^{-1} (η) which stands for the aliphatic C—H bands of asymmetric and symmetric —CH_2 and —CH_3 stretching mode. The peaks near 1369 cm^{-1} (β) and 1225 cm^{-1} (ω) are attributed to C—H deformation modes whereas a small band near 1020 cm^{-1} (ϕ) is claiming a minute presence of hydrogenated furan ring oligomer in the system [39]. A clear trough was seen at 3410 cm^{-1}(τ) in first hour of analysis which is associated with —OH group of 5-HMF. This trough was not observed in fourth hour which strengthens almost complete conversion of 5-HMF. A perturbed area was seen at 2347 cm^{-1} (Π) in FTIR spectra of catalyst which can be assigned to O—H stretching of the reaction media *i.e.* 2-propanol. FTIR study evidenced that there was complete conversion of 5-HMF and high selectivity of DMF is also justified.

3.2. Activity testing

3.2.1. Catalysts screening

All the prepared catalysts were screened for the hydrogenolysis of HMF to DMF and results are presented in Table 3. Bare carbon support showed very low HMF conversion of 10% with no formation of DMF (Table 3, entry1). Only 12% BHMF and 2% MFAL were due to the surface acidity of bare activated carbon and high temperature, respectively [26]. Total acidity in terms of NH_3-desorped per unit weight of activated carbon was found to be 1.1356 mmol/g. For comparison purpose NH_3-TPD of Pd/C was also taken (Fig. SI.5). Among all the screened catalysts, Pd, Ru, Rh and Pt showed higher conversion in the range of 90–99% although selectivity varied from moderate (70%) to excellent (99%) (Table 3, entries 2, 3 and 5). 3%Pd/C was found to be the most active catalyst in terms of complete HMF conversion with almost 99% selectivity to 2,5-DMF (Table 3, entry 2). Excellent performance of 3% Pd/C catalyst for 5-HMF hydrogenation might be due to combined outcome of excellent dispersion of Pd nanoparticles on the surface, mild acidity of the catalyst and Pd-PdO synergism in hydrodeoxygenation mechanism which makes it extremely efficient as well as the selective catalyst for 5-HMF hydrogenation. The main reason of activity of Pd can be referred to an association between the surface of Pd and furanic ring of HMF in which —C═O functional group of furan ring is bonded to Pd surface *via* both of its C and O atoms which leads to the formation of η^2 intermediate [40,41]. Formation of this η^2 intermediate enhances the hydrogenation route. Also it was reported that decarbonylation would occur at higher temperature when there is a formation of η^1 complex of carbon of —C═O group and Pd surface [42]. Since we have observed MFFR in trace amount in our reaction, it eliminated the probability of decarbonylation route. 5-HMF also contains —CH_2OH group on fifth position, besides —C═O group. It is also possible that the Pd forms an intermediate complex with this —OH group which might result in sideways or flat adsorption of 5-HMF over Pd surface. Such surface geometry of the

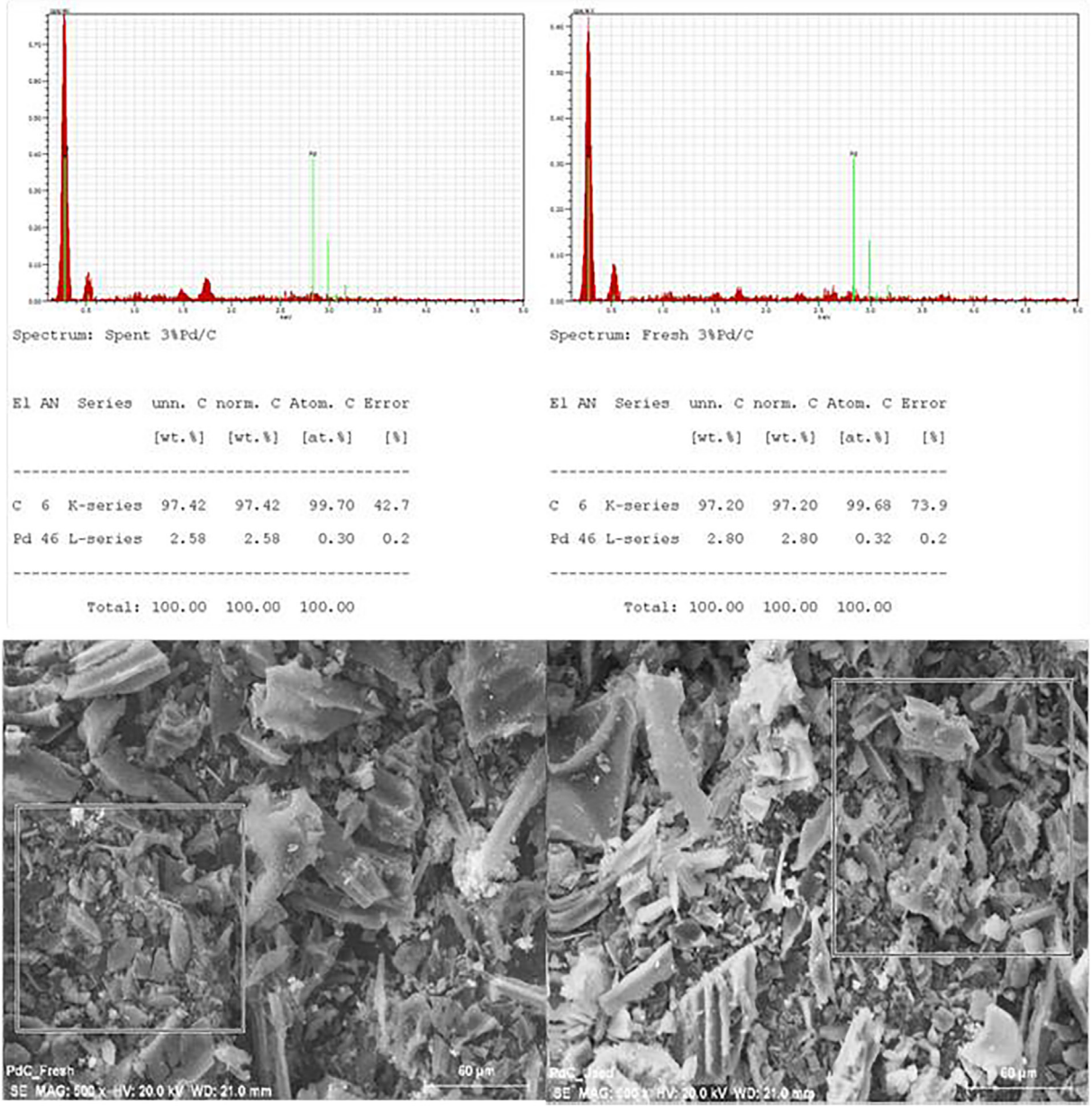

Fig. 7 EDAX pattern of 3%Pd/C.

adsorbed 5-HMF molecule can lead to dΠ–PΠ interaction between the conjugated furan ring and vacant d-orbitals of Pd. Different metal loadings of Pd were also tested as shown in Fig. 9.

It was observed that 5-HMF conversion and selectivity to DMF increased as the Pd loading increased. 1% and 2% Pd/C showed lower 47% and 69% conversion, respectively compared to 3% Pd/C which showed almost complete conversion of 5-HMF. Higher Pd loadings of 4% and 5% also showed complete conversion of HMF. Although the conversion was less for lower metal loading but selectivity towards DMF was always high *i.e.* 61% and 73%. Almost complete selectivity to DMF was observed for 3% Pd/C while further increase in metal loading (>3%) led to ring hydrogenation due to increased catalytic sites of Pd encourages formation of other products like DMTHF and ether dimers of HMF and IPA. Different support systems like ZrO_2, Al_2O_3 and CeO_2 were also studied with Pd but none was found to be as efficient as was Pd/C because of poor distribution of Pd over lower surface area of other supports. The activity order for the screened support was found to be Pd/C > Pd/Al_2O_3 > Pd/ZrO_2 > Pd/CeO_2. The catalysts with other metals like Rh and Ir showed lower 5-HMF conversion although their selectivity towards DMF was moderate. The order of activity among them was found to be Pd/C > Pt/C > Rh/C > Ru/C > Ir/C.

3.2.2. *Effect of temperature*

Fig. 10 shows the effect of temperature in the range of 353–443 K on 5-HMF conversion and DMF selectivity. At lower temperature of 353 K, conversion was very low (2%) whereas the selectivity towards DMF was 15% only. Here, major

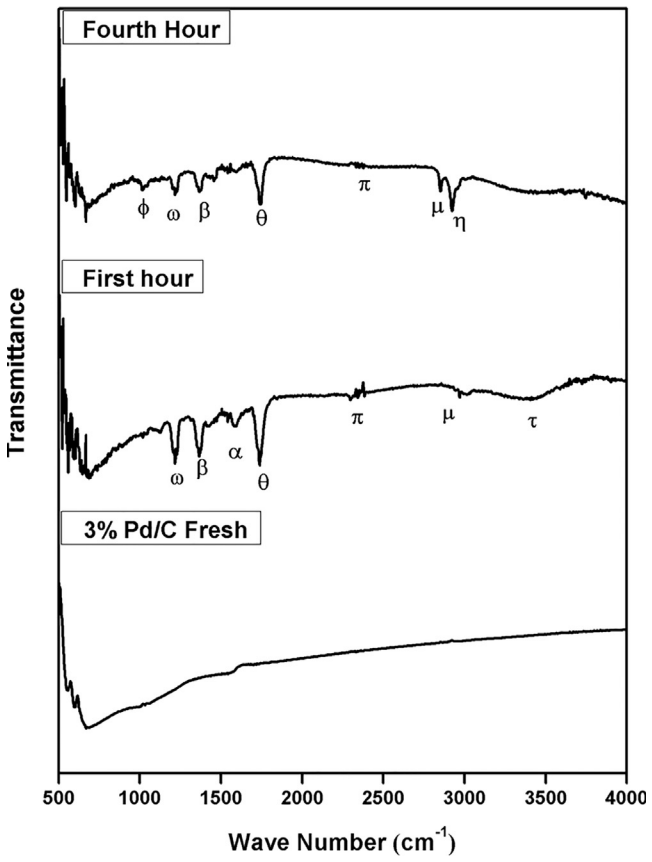

Fig. 8 FTIR Analysis of reaction progress over Pd/C.

product was BHMF with 23% of selectivity. Even at 383 K, HMF conversion was still at a lower level of 13% with 32% selectivity to DMF. Here also significant formation (30%) of BHMF was observed. Further rise in temperature up to 413 K, conversion drastically enhanced up to 75% from 13% with subsequent increase in DMF selectivity from 32% to 72% with a decrease in BHMF selectivity to 16% from 30%. At a higher temperature of 443 K, complete 5-HMF conversion and 99% selectivity to DMF could be achieved. Hence, optimum reaction temperature was 443 K and further study was done at this temperature.

Table 4 Relative peak intensity of Pd/PdO.

Catalyst	3%Pd/C-Fresh	3%Pd/C-Spent
Phase / Peaks	Pd/PdO	Pd/PdO
$3d_{3/2}$	2.55	212611
$3d_{5/2}$	1.87	24.88

3.2.3. Effect of H_2 pressure

Results of effect of H_2 pressure at 443 K, on HMF conversion and DMF selectivity are shown in Fig. 11. At a lower hydrogen pressure (100 psi) selectivity to DMF was 63% with 68% conversion of 5-HMF. When H_2 pressure increased from 100 psi to 200 psi, the conversion of HMF increased to 77% with 81% selectivity to DMF. It was observed that in both the above cases 17% and 6% BHMF was obtained in the first hour of reaction which later reduced to negligible amount suggesting that hydrogenation is readily followed by hydrogenolysis. It was further proved by appearance of MFAL in reaction crude. With further increase in H_2 pressure up to 300 psi, DMF selectivity enhanced to >99.5% with complete conversion of HMF. Still higher H_2 pressures of 400 and 500 psi favoured further ring hydrogenation producing byproducts at the cost of reduced selectivity to DMF *i.e.* (88% and 82% for 400 psi and 500 psi, respectively).

3.2.4. Effect of catalyst loading

The standard reaction was operated with an amount of 10 mg of 3% Pd/C. As can be seen from Fig. 12, enhancing the amount of catalyst to 50 mg DMF selectivity decreased to

Table 3 Hydrogenolysis of HMF over different catalysts.

Entry	Catalyst	Conversion (%)	Selectivity (%)				
			DMF	MFAL	MFFR	BHMF	UnK
1	Activated carbon	10	0	2	0	12	86
2	3%Pd/C	99.9	99	0.3	0	0.7	0
3	3%Pt/C	87	70	7	6	15	2
4	3%Ir/C	30	87	4	3	6	0
5	3%Ru/C	88	89	3	2	6	0
6	3%Rh/C	60	84	6	2	2	6
7	3% Pd/Al_2O_3	53	47	13	16	21	3
8	3%Pd/ZrO_2	42	41	10	13	30	6
9	3%Pd/CeO_2	25	32	22	18	18	10

Reaction conditions: HMF = 100 mg, IPA = 20 g, catalyst = 10 mg, T = 443 K P = 300 psi, agitation = 1000 rpm, t = 4 h.

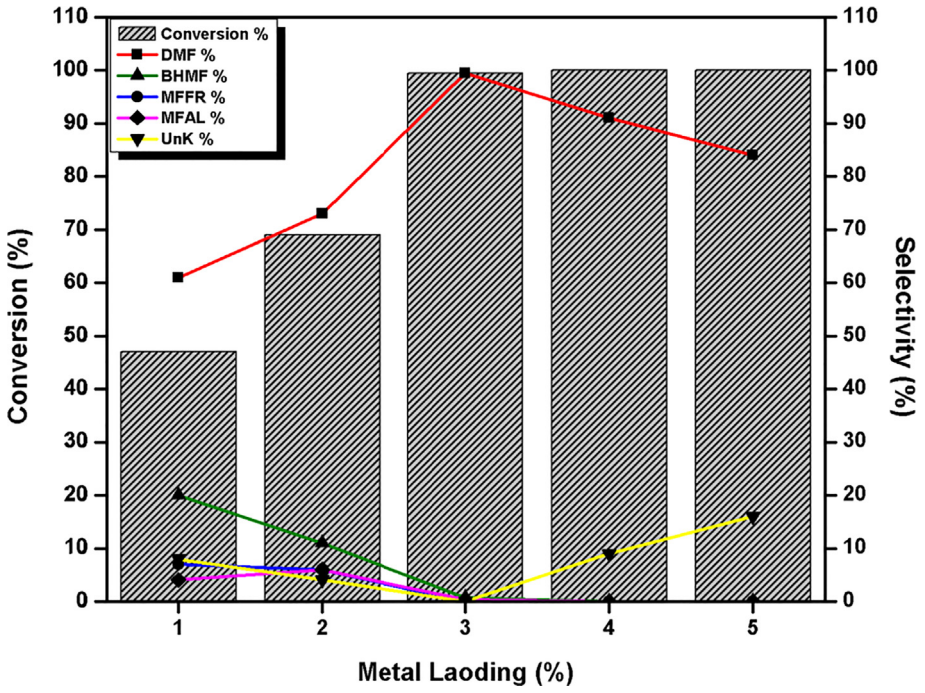

Fig. 9 Metal loading study of 5-HMF hydrogenation (Reaction Conditions: HMF = 100 mg, IPA = 20 g, catalyst = 10 mg, T = 443 K, P = 300 psi, t = 4 h, Agitation = 1000 rpm).

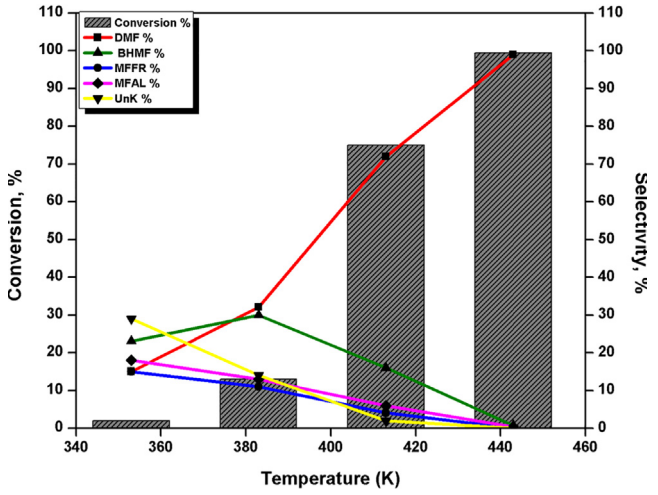

Fig. 10 Temperature effect on hydrogenolysis of HMF. (Reaction Conditions: HMF = 100 mg, IPA = 20 g, catalyst = 10 mg, P = 300 psi, t = 4 h, Agitation = 1000 rpm).

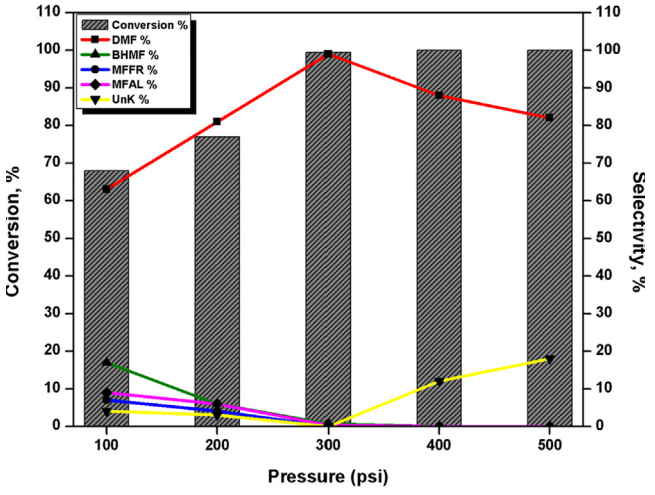

Fig. 11 Pressure effect on hydrogenolysis of HMF. (Reaction Conditions: HMF = 100 mg, IPA = 20 g, catalyst = 10 mg, T = 443 K, t = 4 h, Agitation = 1000 rpm).

71% because of production of dimer of HMF, etherified combination of IPA and reactant and ring hydrogenated products like DMTHF and BHMTHF.

3.2.5. Effect of substrate loading

Substrate loading effect was studied by increasing the amount of 5-HMF and keeping the catalyst concentration constant (Fig. 13). It was observed that as the initial concentration of 5-HMF increased, the conversion and selectivity decreased significantly. An increase in 5-HMF concentration from 0.8 mmol to 1.60 mmol led to a decrease in conversion up to 10 mol% whereas selectivity to DMF reduced to 16 mol%. This decline in conversion and selectivity continued with a further increase in 5-HMF concentration to 2.40 mmol. In this case the conversion of 5-HMF decreased up to 16 mol% whereas 24 mol% drop in selectivity of DMF than the original one was observed. When the initial concentration of 5-HMF was increased up to 3.20 mmol this decline in conversion-selectivity reached to 22 mol% and 26 mol% than that of original value. A further increase in 5-HMF concentration to 4 mmol caused steep decline in conversion form 55 mol% to 22 mol% whereas the selectivity decreased to 30 mol% with

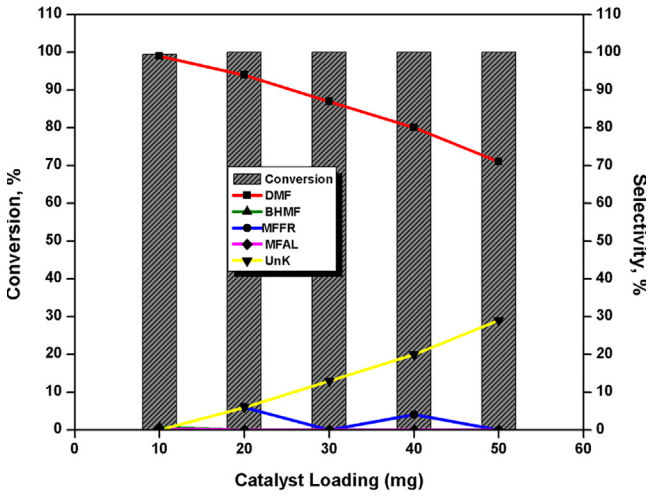

Fig. 12 Effects of catalyst loading on hydrogenolysis of HMF. (Reaction Conditions: HMF = 100 mg, IPA = 20 g, T = 443 K, P = 300 Psi, t = 4 h).

respect to 0.8 mmol concentration of 5-HMF. Hence it was observed that a 5 fold increase in the 5-HMF concentration leads to 55 mol% less conversion and 30% less DMF generation than the original amount. Hence after analysing all the results we concluded that 0.8mmole (100 mg) is the suitable amount for optimum catalyst concentration (10 mg). It was also observed that with an increase in the concentration of HMF selectivity to other products like MFFR, BHMF, MFAL also increased. Significant amount of dimer of HMF was detected in GC–MS analysis of the reaction crude.

3.2.6. Solvent study

Different solvents like H_2O, 1-butanol and CH_3OH along with IPA were screened for the catalytic hydrogenation of 5-HMF and the results are shown in Fig. 14. The excellent efficiency of 2-propanol can be attributed to its low dielectric constant. Solvent having low dielectric constant have higher solubility of hydrogen [43]. The order of dielectric constant is 2-propanol ~ 1-butanol < CH_3OH < H_2O. It suggests that among all these solvents 2-propanol is most efficient solvent. Although 2-propanol and 1-butanol has almost similar hydrogen solubility but still the selectivity for DMF in 1-butanol was very poor. This can be explained by solvation effect [44]. As we stated earlier, the reaction proceeds *via* Pd-η^2 acyl complex to give rise to BHMF. This BHMF is a polar compound which interacts with 1-butanol and could not access to metal surface.

Although 2-propanol has almost same relative polarity its high activity can be attributed to its ability to donate Hydrogen [45]. This was investigated by carrying a run in 2-propanol without any external Hydrogen. We obtained 48% conversion of 5-HMF along with 22% DMF selectivity. In case of CH_3OH, DMF obtained was only 38%. 1-butanol proved very poor solvent in terms of DMF selectivity although conversion was good (89%). Only 16% DMF was detected and here major product was BHMF with 67% selectivity. The efficiency was considerably high when solvent was H_2O which gave 92% conversion of 5-HMF with DMF selectivity of 70%. Second major product here was BHMF (27%). Overall study of various solvents as the reaction medium concluded that best suitable solvent for hydrogenation of 5-HMF was 2-propanol.

3.2.7. C-t profile

Since, as synthesised 3% Pd/C catalyst showed best results with complete conversion of HMF along with complete selectivity to DMF selectivity *v/s* time profile was also obtained to understand the reaction pathway.

Fig. 15 presents c-t profile of hydrogenolysis of HMF over 3% Pd/C catalyst. Initially, at 1st hour, 41% HMF conversion was achieved with 45% selectivity to DMF along with 29% BHMF and 14% MFFR. 5-HMF conversion enhanced from 41% to 66% in the second hour followed by 87% in third hour. This suggests that reaction proceeds with subsequent hydrogenation of HMF into BHMF which on hydrogenolysis forms MFAL. This MFAL is a hydrogenation product of

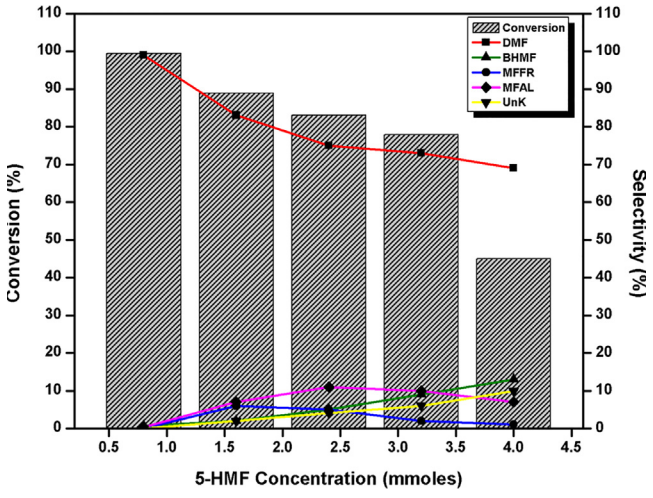

Fig. 13 Effects of substrate loading on hydrogenolysis of HMF. (Reaction Conditions: IPA = 20 g, Catalyst = 10 mg, T = 443 K, P = 300 Psi, t = 4 h).

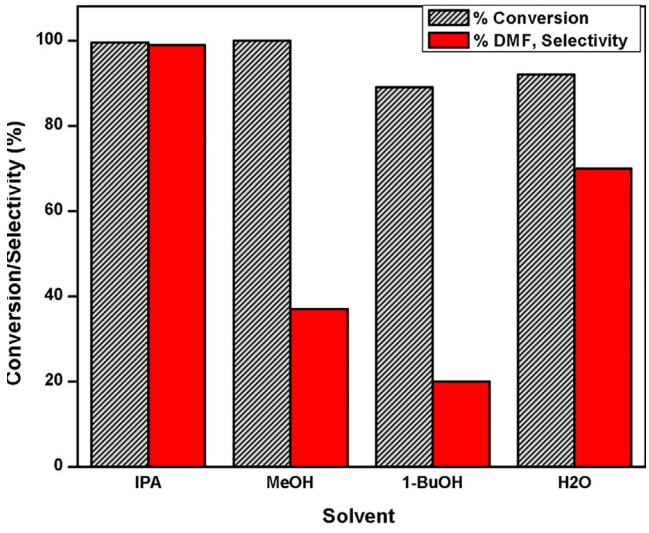

Fig. 14 Solvent study of HMF hydrogenation (Reaction Conditions: HMF = 100 mg, Solvent = 20 g, catalyst = 10 mg, T = 443 K, P = 300 psi, t = 4 h, Agitation = 1000 rpm).

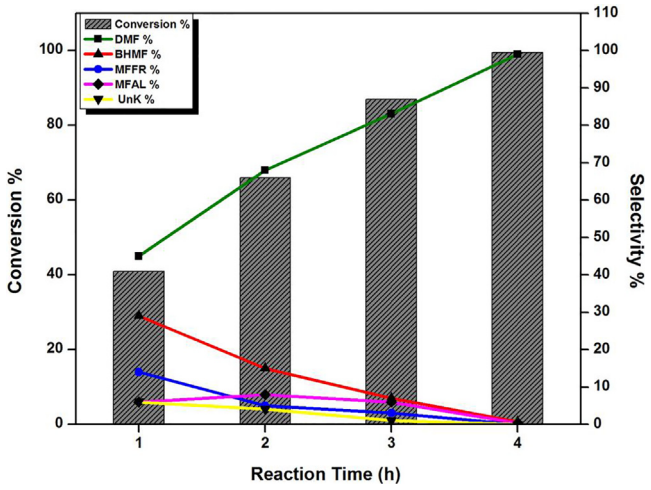

Fig. 15 C-t Profile of hydrogenolysis of HMF via 3% Pd/C (Reaction Conditions: HMF = 100 mg, IPA = 20 g, catalyst = 10 mg, T = 443 K, P = 300 psi, t = 4 h, Agitation = 1000 rpm.

MFFR also while, MFFR appears in significant amount in starting of reaction as stated earlier. At the end of 4th hour, almost complete conversion of 5-HMF was achieved with selective formation of DMF (99%), suppressing formation of other by products. In order to find exact reaction pathway, various control experiments were carried out taking intermediates as the starting materials and the reaction pathway of HMF hydrogenolysis is depicted in Scheme 1.

MFFR was taken as substrate and converted into DMF in optimised conditions. It was observed that within 2 h of reaction complete conversion was obtained. The selectivity to DMF was 94% in the second hour. After 2 h, DMF started to convert into DMTHF. When MFAL was taken as a substrate, within 1 h of the reaction itself, DMF was observed (98%). These observations were in well accordance with our previous work in which strong activity of Pd was attributed to the interaction of Π electrons of furan ring and Pd metal [46].

3.2.8. Catalyst recycle study

In order to study the stability of the catalyst, catalyst recycle reactions were carried out and the results are shown in Fig. 16.

Since after 4th hour the conversion was always near to 100%, reusability of the catalyst was studied for a partial conversion at 1.5 h. After the first reaction, catalyst was collected by filtration of reaction crude, dried at 383 K and reused for next reaction. The catalyst could be reused for 4 times using

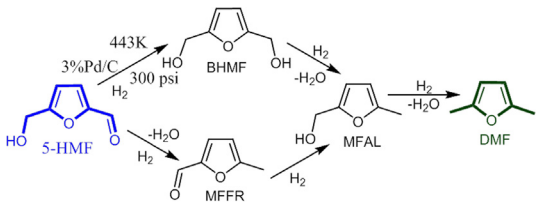

Scheme 1 Pathways for hydrogenolysis of 5-HMF into 2,5-DMF.

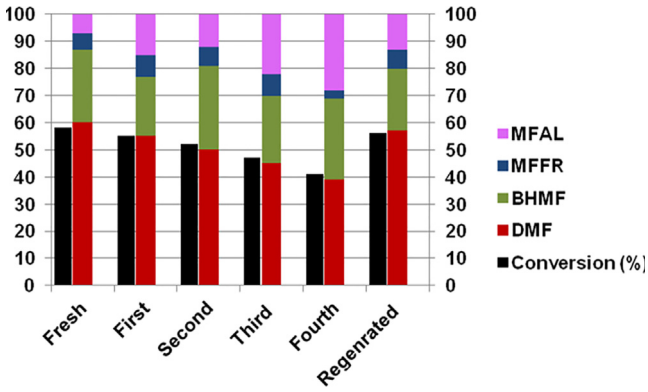

Fig. 16 Recycle study of 3% Pd/C for hydrogenolysis of HMF. (Reaction Conditions: HMF = 100 mg, IPA = 20 g, catalyst = 10 mg, T = 443 K, P = 300 psi, t = 1.5 h, Agitation = 1000 rpm).

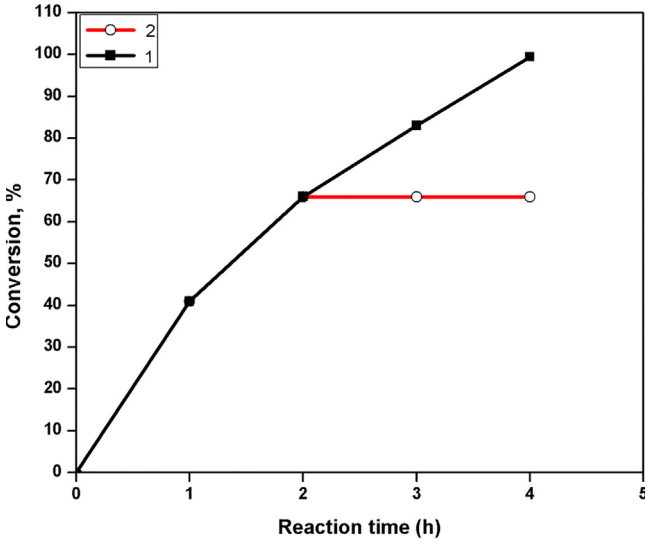

Fig. 17 Hot filtration test. (Reaction Conditions: HMF = 100 mg, IPA = 20 g, catalyst = 10 mg, T = 443 K, P = 300 psi, t = 4 h, Agitation = 1000 rpm). (1) With Catalyst (2) Without catalyst after 2 h.

the same procedure which showed complete conversion of HMF till 4th recycle with a marginal drop in selectivity to DMF. In first recycle study, the conversion remain as high as 55% with 53% selectivity to DMF. In 2nd and 3rd recycle study conversion remained almost constant (52% and 47% respectively) with DMF selectivity of 50% and 45%, respectively. After 4th recycle activity of catalyst decreased as conversion of HMF reduced to 41% and selectivity to DMF also declined to 39%. After 4th run the used catalyst was heated at 383 K and treated to reduction protocol at 523 K with H_2 flow of 3.0 mL/min till 2 h. This reduction treatment leads to regeneration of activity of 3%Pd/C. The activity of regenerated catalyst was almost same as that of fresh 3%Pd/C *i.e.* 56% conversion and 57% selectivity to DMF.

Catalyst leaching was also tested by performing the hot filtration test (Fig. 17). The reaction was terminated after 2 h and

the catalyst was separated from mother liquor by filtration and reactor was further charged with reaction crude without the catalyst. The reaction was carried out till 4 h and conversion was observed to be constant for further reaction time revealing no Pd leaching occurred under the conditions of the present work.

4. Conclusions

Selective hydrogenation of HMF to DMF was successfully achieved over highly efficient 3%Pd/C catalyst, showing almost complete conversion of 5-HMF in 4 h. Catalyst was extensively characterised and well recycled till 4 times. Due to well dispersed nature of Pd on carbon no crystalline phase was observed in the XRD. Pd-PdO nanohybrid synergism was revealed form XPS analysis. TEM studies also revealed the excellent dispersion of the metal with narrow particle size in the range of 2.5–3.5 nm. All these properties cumulatively make 3%Pd/C superior catalyst over the earlier reports in terms of efficiency, reaction time (energy consumption) and recyclability without addition of any other reagent like formic acid, hence which was also environment friendly. TON and TOF of 3%Pd/C for 5-HMF hydrogenolysis were found to be 280.42 and 70.10 h^{-1} respectively. Various parameters of reaction aspect like temperature, pressure and metal loading were studied thoroughly based on which reaction was optimised. It was observed that increase in both temperature and pressure leads to reach almost complete conversion (99%) whereas temperature played predominant role for tuning the selectivity from HMF to DMF.

Acknowledgements

One of the authors Bhanupratap S. Solanki acknowledges Council of Scientific and Industrial Research, New Delhi, UGC for the award of JRF.

Appendix A. Supplementary material

Supplementary data associated with this article can be found, in the online version, at https://doi.org/10.1016/j.jscs.2018.08.009.

References

[1] J.C. Serrano, R. Luque, A. Sepulveda-Escribano, Transformations of biomass-derived platform molecules: from high added-value chemicals to fuels via aqueous-phase processing, Chem. Soc. Rev. 40 (2011) 5266–5281.
[2] J.M.R. Gallo, D.M. Alonso, M.A. Mellmer, J.A. Dumesic, Production and upgrading of 5-hydroxymethylfurfural using heterogeneous catalysts and biomass-derived solvents, Green Chem. 15 (2012) 85–90.
[3] J. Deng, T. Pan, Q. Xu, M.Y. Chen, Y. Zhang, Q.X. Guo, Y. Fu, Linked strategy for the production of fuels via formose reaction, Sci. Rep. 3 (2013) 1244–1250.
[4] G.W. Huber, S. Iborra, A. Corma, Synthesis of transportation fuels from biomass chemistry, catalysts, and engineering, Chem. Rev. 106 (2006) 4044–4098.
[5] B. Kamm, Production of platform chemicals and synthesis gas from biomass, Angew. Chem. Int. Ed. 46 (2007) 5056–5058.
[6] A. Demirbas, Biomass resource facilities and biomass conversion processing for fuels and chemicals, Energy Convers. Manage. 42 (2001) 1357–1378.
[7] D.M. Alonso, J.Q. Bond, J.A. Dumesic, Catalytic conversion of biomass to biofuels, Green Chem. 12 (2010) 1493–1513.
[8] P. Szuromi, B. Jasny, D. Clery, J. Austin, B. Hanson, Special issue on sustainability and energy, Science 315 (2007) 781.
[9] P. Gallezot, Conversion of biomass to selected chemical products, Chem. Soc. Rev. 41 (2012) 1538–1558.
[10] L. Deng, J. Li, D.M. Lai, Y. Fu, Q.X. Guo, Catalytic conversion of biomass-derived carbohydrates into gamma-valerolactone without using an external H_2 supply, Angew. Chem. Int. Ed. 48 (2009) 6529–6532.
[11] J.Q. Bond, D.M. Alonso, D. Wang, R.M. West, J.A. Dumesic, Integrated catalytic conversion of gamma-valerolactone to liquid alkenes for transportation fuels, Science 327 (2010) 1110–1114.
[12] I.T. Horváth, J. Mehdi, V. Fábos, L. Boda, L.T. Mika, γ-Valerolactone- a sustainable liquid for energy and carbon-based chemicals, Green Chem. 10 (2008) 238–242.
[13] J.P. Lange, W.D. van de Graaf, R.J. Haan, Conversion of furfuryl alcohol into ethyl levulinate using solid acid catalysts, ChemSusChem 2 (2009) 437–441.
[14] H.B. Nisbet, The blending octane numbers of 2,5-dimethylfuran, J. Inst. Petrol. 32 (1946) 162–166.
[15] J.M. Simmie, J. Wurmel, Harmonising production, properties and environmental consequences of liquid transport fuels from biomass 2,5-dimethylfuran as a case study, ChemSusChem 6 (2013) 36–41.
[16] Y. Roman-Leshkov, C.J. Barrett, Z.Y. Liu, J.A. Dumesic, Production of dimethylfuran for liquid fuels from biomass-derived carbohydrates, Nature 447 (2007) 982–986.
[17] J.B. Binder, R.T. Raines, Simple chemical transformation of lignocellulosic biomass into furans for fuels and chemicals, J. Am. Chem. Soc. 131 (2009) 1979–1985.
[18] M. Chidambaram, A.T. Bell, A two-step approach for the catalytic conversion of glucose to 2,5-dimethylfuran in ionic liquids, Green Chem. 12 (2010) 1253–1262.
[19] T. Thananatthanachon, T.B. Rauchfuss, Efficient production of the liquid fuel 2,5-dimethylfuran from fructose using formic acid as a reagent, Angew. Chem., Int. Ed. 49 (2010) 6616–6618.
[20] P.P. Upare, D.W. Hwang, Y.K. Hwang, U.H. Lee, D.Y. Honga, J.S. Chang, An integrated process for the production of 2,5-dimethylfuran from fructose, Green Chem. 17 (2015) 3310–3313.
[21] L. Hu, X. Tang, J.X. Xu, Z. Wu, L. Lin, S.J. Liu, Selective transformation of 5-hydroxymethylfurfural into the liquid fuel 2,5- dimethylfuran over carbon-supported ruthenium, Ind. Eng. Chem. Res. 53 (2014) 3056–3064.
[22] Y.H. Zu, P.P. Yang, J.J. Wang, X.H. Liu, J.W. Ren, G.Z. Lu, Y.Q. Wang, Efficient production of the liquid fuel 2,5-dimethylfuran from 5-hydroxymethylfurfural over Ru/Co_3O_4 catalyst, Appl. Catal., B 146 (2014) 244–248.
[23] S. Nishimura, N. Ikeda, K. Ebitani, Selective hydrogenation of biomass-derived 5 hydroxymethylfurfural (HMF) to 2,5-dimethylfuran (DMF) under atmospheric hydrogen pressure over carbon supported PdAu bimetallic catalyst, Catal. Today 232 (2014) 89–98.
[24] X. Kong, R. Zheng, Y. Zhu, G. Ding, Y. Zhu, Y.W. Lia, Rational design of Ni-based catalysts derived from hydrotalcite for selective hydrogenation of 5-hydroxymethylfurfural, Green Chem. 17 (2015) 2504–2514.
[25] J. Mitra, X. Zhou, T. Rauchfuss, Pd/C-catalyzed reactions of HMF: decarbonylation, hydrogenation, and hydrogenolysis, Green Chem. 17 (2015) 307–313.
[26] J. Jae, W. Zheng, R.F. Lobo, D.G. Vlachos, Production of dimethylfuran from hydroxymethylfurfural through catalytic transfer hydrogenation with ruthenium supported on carbon, ChemSusChem 6 (2013) 1158–1162.

[27] T.S. Hansen, K. Barta, P.T. Anastas, P.C. Ford, A. Riisager, One-pot reduction of 5-hydroxymethylfurfural via hydrogen transfer from supercritical methanol, Green Chem. 14 (2012) 2457–2461.
[28] N.S. Biradar, A.A. Hengne, S.N. Birajdar, R. Swami, C.V. Rode, Tailoring the product distribution with batch and continuous process options in catalytic hydrogenation of furfural, Org. Process Res. Dev. 18 (2014) 1434–1442.
[29] H. Zhang, B. Dai, X. Wang, W. Li, Y. Han, J. Gu, J. Zhnag, Non-mercury catalytic acetylene hydrochlorination over bimetallic Au-Co(III)/SAC catalysts for vinyl chloride monomer production, Green Chem. 15 (2013) 829–836.
[30] X. Li, Y. Wang, L. Kang, M. Zhu, B. Dai, A novel, non-metallic graphitic carbon nitride catalyst for acetylene hydrochlorination, J. Catal. 311 (2014) 288–294.
[31] N.S. Date, N.S. Biradar, R.C. Chikate, C.V. Rode, Effect of reduction protocol of Pd catalysts on product distribution in furfural hydrogenation, Chem. Sel. 2 (2017) 24–32.
[32] M. Korzec, P. Bartczak, A. Niemczyk, J. Szade, M. Kapkowski, P. Zenderowska, K. Balin, J. Lelatko, J. Polanski, Bimetallic nano-Pd/PdO/Cu system as a highly effective catalyst for Sonogashira reaction, J. Catal. 313 (2014) 1–8.
[33] C. Wang, F. Yang, W. Yang, L. Ren, Y. Zhang, X. Jia, L. Zhang, Y. Li, PdO nanoparticles enhancing the catalytic activity of Pd/carbon nanotubes for 4-nitrophenol reaction, RSC Adv. 15 (2015) 27526–27532.
[34] K.S. Kim, A.F. Gossmann, N. Winograd, X-ray photoelectron spectroscopic studies of palladium oxides and the palladium-oxygen electrode, Anal. Chem. 146 (1974) 197.
[35] F. Bozon-Verduraz, A. Omar, J. Escard, B. Pontvianne, Chemical state and reactivity of supported palladium: I. Characterization by XPS and UV-visible spectroscopy, J. Catal. 53 (1978) 126–134.
[36] A.M. Venezia, A. Rossi, D. Duca, A. Martorana, G. Deganello, Particle size and metal-support interaction effects in pumice supported palladium catalysts, Appl. Catal. A: Gen. 125 (1995) 113–128.
[37] J.R. McManus, J.M. Vohs, Deoxygenation of glycolaldehyde and furfural on Mo_2C/Mo(100), Surf. Sci. 630 (2014) 16–23.
[38] J. Ryczkowski, IR spectroscopy in catalysis, Catal. Today 8 (2001) 263–381.
[39] S. Barsberg, L.G. Thygesen, Poly(furfuryl alcohol) formation in neat furfuryl alcohol and in cymene studied by ATR-IR spectroscopy and density functional theory (B3LYP) prediction of vibrational bands, Vib. Spectrosc. 49 (2009) 52–63.
[40] R. Shekhar, R.V. Plank, J.M. Vohs, M.A. Barteau, Adsorption and reaction of aldehydes on Pd Surfaces, J. Phys. Chem. B 101 (1997) 7939–7951.
[41] J.L. Davis, M.A. Barteau, Polymerisation and decarbonylation reaction of aldehydes on the Pd(111) surface, J. Am. Chem. Soc. 111 (1989) 1782–1792.
[42] S. Sitthisa, D.E. Resasco, Hydrodeoxygenation of furfural over supported metal catalyst: a comparative study Cu, Pd and Ni, Catal. Lett. 141 (2011) 784–791.
[43] N.S. Biradar, A.M. Hengne, S.S. Sakate, et al, Single pot transfer hydrogenation and aldolization of furfural over metal oxide catalysts, Catal. Lett. 146 (2016) 1611–1619.
[44] E. Toukoniitty, J. Kuusisto, V. Nieminen, M. Hotokka, T. Salmi, Solvent effects in enantioselective hydrogenation of 1-phenyl-1,2-propanedione, J. Mol. Catal. A 192 (2003) 135–151.
[45] R.L. Augustine, P. Techasauvapak, Heterogeneous catalysis in organic synthesis. Part 9. Specific site solvent effects in catalytic hydrogenations, J. Mol. Catal. 87 (1994) 95–105.
[46] N.S. Biradar, A.M. Hengne, S.N. Birajdar, P.S. Niphadkar, P. N. Joshi, C.V. Rode, Single-pot formation of THFAL via catalytic hydrogenation of FFR over Pd/MFI catalyst ACS sustainable, Chem. Eng. 2 (2014) 272–281.

Green Chemistry

PAPER

View Article Online
View Journal | View Issue

Cite this: *Green Chem.*, 2019, **21**, 6390

Selective hydrogenation of 5-HMF to 2,5-DMF over a magnetically recoverable non-noble metal catalyst†

Bhanupratap Singh Solanki [a,b] and Chandrashekhar V. Rode *[a,b]

Received 2nd September 2019,
Accepted 11th October 2019

DOI: 10.1039/c9gc03091c

rsc.li/greenchem

A non-noble bimetallic catalyst Cu–Fe (1 : 2) was magnetically recoverable, highly selective and efficient for 5-(hydroxymethyl) furfural (5-HMF) hydrogenation to 2,5-dimethyl furan (DMF). The structure–activity correlation was established by characterising the prepared catalyst by XRD, XPS, TEM, ESEM, BET surface area, N_2-adsorption, NH_3-TPD, pyridine-IR and H_2-TPR measurements. The high catalytic efficiency was attributed to the oxophilic nature and Lewis acidity of Fe, whereas the selectivity towards DMF was attributed to the Brønsted acidity of CuO and its affinity towards the C–O bond which was further confirmed by NH_3-TPD and Py-IR analyses. XPS and XRD revealed the presence of Cu/$CuFe_2O_4$ species which catalyzed the hydrogenolysis pathway. TEM and SEM images evidenced the presence of a Cu–Fe nanomorph in which Cu/$CuFe_2O_4$ was present. The size of the Cu–Fe nanomorph was found to be between 15.4–17.6 nm. Under the optimised reaction conditions, the highest conversion of 97% and selectivity of 93% were achieved.

Introduction

A major global challenge for the scientific community is to develop sustainable alternatives for rapidly shrinking conventional resources of fossil fuels.[1–3] Naturally available biomass feedstock can be one of the practical solutions to counter this problem.[4] Biomass derived molecules can be converted into numerous potential fuel options such as 2,5-dimethyl furan (DMF), 2,5-dimethyl tetrahydrofuran (DMTHF), γ-valerolactone (GVL), 2-methyl tetrahydrofuran (Me-THF), tetrahydrofuran (THF) *etc*. They can also be helpful in obtaining fine chemicals such as 2,5-furandicarboxyllic acid (FDCA), 2,5-diformyl furan (DFF), 2,5-bis(hydroxymethyl) furan (BHMF), 2,5-bis(hydroxymethyl) tetrahydrofuran (BHMTHF) *etc*. which can shift the direction of the market of their respective sectors such as polymers, perfumery, pharmaceutics *etc*.[5–10] Since biomass derived molecules are invariably multi-oxygenates, it is necessary to selectively deoxygenate such molecules to obtain the desired products.[11] Cellulosic biomass on hydrolysis generates sugars such as glucose and fructose which on acidic dehydration give an important platform molecule such as 5-HMF.[12] Hydrogenation of 5-HMF gives 2,5-DMF which is a useful fuel additive. There are several advantages of 2,5-DMF over bio-ethanol and bio-butanol which are considered as front runners, as an alternative to gasoline. For example, 2,5-DMF has a higher boiling point (93 °C) than bio-ethanol (77 °C) which is helpful in suppressing the vapour lock in an inlet.[13] Its boiling point being lower than that of bio-butanol (117.25 °C) also facilitates its cold starting performance at low ambient temperature.[14] In order to qualify as a fuel additive, it should be immiscible with water and in this context, the solubility of 2,5-DMF is much less (0.26% at 20 °C) than that of bio-ethanol (7.7% at 20 °C) which makes it more suitable than bio-ethanol.[15] Another positive aspect of 2,5-DMF is that it has a lower kinematic viscosity (0.57 cSt at 20 °C) than bio-ethanol (1.5 cSt at 20 °C) and bio-butanol (3.6 cSt at 20 °C) but almost similar to gasoline (0.37–0.44 cSt at 20 °C).[16] It not only is helpful in establishing the injection pressure but also protects its movement in engine components. 2,5-DMF has a high Lower Heating Value (LHV) and consumes less fuel.[17] Its higher research octane number (119) makes it superior to bio-ethanol and bio-butanol and even gasoline having RON of 110, 98, and 100, respectively.[18]

Noble metal catalysis is a much exploited approach for 5-HMF hydrogenation where the use of Ru, Pd, Pt, Au *etc*. over different supports has been studied.[19–26] 5-HMF hydrogenation to 2,5-DMF over non-noble metals is a less explored reaction. Among non-noble metals, hydrogenation of 5-HMF has been reported mostly over Ni and Cu metals. Ni, in particular, is attractive as it has a strong tendency to break the C–O bond.[27] Ni was supported on perovskite $LaFeO_3$ by Chen *et al.*

[a]CEPD Division, CSIR-National Chemical Laboratory, Pune-411008, India. E-mail: cv.rode@ncl.res.in
[b]Academy of Scientific and Innovative Research (AcSIR), Ghaziabad-201002, India

†Electronic supplementary information (ESI) available. See DOI: 10.1039/c9gc03091c

where 98.3% selectivity to 2,5-DMF was achieved in ethanol after 6 h of reaction under very harsh conditions of 503 K temperature and 725 psig of external H_2 pressure.[28] Ni was also tested with Co_3O_4 by Wang *et al.*, which after 24 h of reaction time gave 76% of 2,5-DMF with complete conversion of 5-HMF.[29] A bimetallic combination of Ni and Fe supported on CNT was screened for tunable synthesis of 2,5-DMF and 2,5-BHMF in butanol.[30] At a lower temperature of 383 K and after 18 h, 96.1% of 2,5-BHMF was obtained, whereas, at a higher temperature of 473 K, 91.3% of 2,5-DMF was obtained. Recently, 18.2% Ni supported on ZrP (phosphate zirconia) has been reported to yield 68.2% of 2,5-DMF under very harsh conditions such as 513 K and 725 psig external H_2 pressure for a long reaction time of 20 h in THF as a solvent.[31] Apart from Ni, Cu in combination with porous mesoporous oxide (PMO) was also examined by Hansen *et al.* for 5-HMF hydrogenation under very high temperature (533 K) conditions.[32] They used supercritical methanol for *in situ* generation of H_2 and in 3 h, 48% yield of 2,5-DMF was achieved. Cu–Zn alloy NPs were designed to obtain 2,5-DMF and 2,5-BHMF using cyclopentyl methyl ether (CPME) as a solvent under harsh reaction conditions (T = 493 K, P = 435 psig, 6 h) forming 2,5-DMTHF along with 2,5-DMF, whereas mild conditions favoured the formation of 2,5-BHMF.[33] Cu-ZnO derived from the malachite mineral catalyzed the hydrogenolysis of 5-HMF to form 2,5-BHMF and 2,5-DMF under a H_2 pressure of 220 psig and 373 K in 1 h, giving 99% of 2,5-BHMF with 84% conversion, whereas at a higher temperature of 493 K and a higher reaction time of 5 h, 92% of 2,5-DMF was obtained.[34] Reduced Co_3O_4 was also tested by Liu *et al.* under relatively milder conditions *i.e.* 443 K and 145 psig external H_2 pressure in 1,4-dioxane; however, longer reaction time (12 h) was required giving a low selectivity (83.3%) of the desired product.[35]

Herein, we report an efficient, recoverable and reusable Cu–Fe catalytic system for 5-HMF hydrogenation. Various ratios of the Cu–Fe catalyst were screened and Cu–Fe (1 : 2) was found to be an excellent catalyst to achieve 97% conversion and an excellent selectivity of 93% to DMF. In order to understand the role of different species, the catalyst was characterised thoroughly using different techniques such as XPS, XRD, TEM, SEM, BET, CO_2-TPD and NH_3-TPD. The Cu–Fe bimetallic combination could be recycled up to 5 times and regeneration of the catalytic sites was also attempted. A possible reaction mechanism was also proposed for the hydrogenolysis of 5-HMF.

Experimental

Materials

$Cu(NO_3)_2{\cdot}3H_2O$ (95%), $Fe(NO_3)_3{\cdot}9H_2O$ (97%), $Co(NO_3)_2{\cdot}6H_2O$ (99%), iso-propyl alcohol (IPA) (98%) and NaOH (98%) were purchased from Thomas Baker. Hydrogen of high purity (99.99%) was obtained from Inox-India. 5-HMF (99.98%) and 2,5-DMTHF (96%) were purchased from Sigma Aldrich, India, whereas 5-methyl furfural (MFFR) (98%) and 2,5-DMF (99%) were obtained from TCI Ltd.

Catalyst preparation

A bimetallic Cu–Fe catalyst was prepared by a co-precipitation method. Calculated amounts of Cu and Fe precursors (100 ml each) in different ratios were taken in a 500 ml three neck round bottom flask along with 2 M solution of NaOH. All three solutions were mixed dropwise with continuous stirring. The stirring was continued for 10 h. The as-obtained precipitate was washed with deionised H_2O until the pH became 7. This cake was dried at 383 K and calcined at 723 K for 4 h with a rate of 10 °C min^{-1}. The calcined catalyst was activated using hydrogen at 523 K for 3 h with a rate of 2 °C min^{-1}. The flow of hydrogen was maintained at 2 ml min^{-1}. All the metal catalysts were prepared by the same method.

Characterization methodology

The BET surface area of all the samples was measured on a Chemisorb 2720 Micromeritics instrument by means of N_2 adsorption at 77 K. X-ray diffraction (XRD) patterns were recorded on a PAnalytical PXRD system (Model X-Pert PRO-1712), using Ni filtered Cu Kα radiation (λ = 0.154 nm) as a source (current intensity, 30 mA; voltage, 40 kV) and X-celerator detector. The samples were scanned in the 2θ range of 10°–80°. The metal phases of the catalysts were identified by their characteristic 2θ values. The software program X-Pert High Score Plus was used to subtract the contribution of the Cu $K\alpha_2$ line prior to data analysis. X-ray photoelectron spectra were recorded using an ESCA-3000 (VG Scientific, Ltd, England) with a 9-channeltron CLAM4 analyzer under vacuum greater than 1×10^{-8} Torr, using Mg Kα radiation (1253.6 eV) and a constant pass energy of 50 eV. The binding energy values were charge-corrected to the C_{1s} signal (284.6 eV). Particle size and distribution were studied using a transmission electron microscope (HR-TEM), model JEOL 1200 EX. A small amount of the solid sample was sonicated in 2-propanol for 1 min. A drop of the prepared suspension was deposited on a Cu grid coated with a carbon layer, and the grid was then dried at room temperature before analysis. The particle morphology and elemental composition were studied by Scanning Electron Microscopy (SEM) and Energy Dispersive X-ray Analysis (EDAX), respectively. The analysis was performed on LEO-LEICA STEREOSCAN 440 at various magnifications using a Bruker detector. NH_3-TPD experiments were carried out on a Micromeritics-2720 (Chemisoft TPx) instrument. In order to evaluate the acidity of the catalysts, ammonia TPD measurements were carried out by: (i) pre-treating the samples from room temperature to 200 °C under a helium flow rate of 25 mL min^{-1}, (ii) adsorption of ammonia at 40 °C and (iii) desorption of ammonia with a heating rate of 10 °C min^{-1} starting from the adsorption temperature to 700 °C. CO_2-TPD experiments were also carried out on a Micromeritics-2720 (Chemisoft TPx) instrument. In order to evaluate the surface basicity of the catalysts, CO_2-TPD measurements were carried out by: (i) pre-treating the samples from room temperature to 200 °C under a helium flow rate of 25 mL min^{-1}, (ii) adsorption of CO_2 at 40 °C and (iii) desorption of CO_2 with a heating rate of 10 °C min^{-1} starting from the

adsorption temperature to 700 °C. Pyridine-IR spectra of all the prepared catalysts were recorded on a PerkinElmer 2000 FTIR spectrometer in the wave number range of 4000–400 cm^{-1} using the KBr pellet technique. 20 μL of pyridine was injected step by step and scans were performed in the temperature range of 25–170 °C. H_2-TPR studies of the catalysts were carried out using a Micromeritics Autochem-2920 instrument in the temperature range of 50–750 °C at a heating rate of 5 °C min^{-1} using 5% H_2 in He as the probe gas. The H_2 consumption in the TPR study was estimated quantitatively with a thermal conductivity detector that was calibrated before the TPR study. The Raman spectra of the samples were recorded on a Horiba JY Lab RAM HR800 micro-Raman spectrometer with 17 mW, 632.8 nm laser excitation. DTA/TGA-MS curves were obtained on a Simultaneous thermal analyzer SDT-Q600 Discovery series MS by heating the samples from room temperature to 600 °C under a N_2 atmosphere with a ramping rate of 10 °C min^{-1}.

Catalyst activity test

The hydrogenation of HMF was carried out in a 45 mL capacity autoclave supplied by Parr Instruments Co. USA, at an agitation speed of 1000 rpm. The typical hydrogenation conditions were as follows: temperature: 443 K, H_2 pressure: 300 psig, 5-HMF: 100 mg, solvent, 2-propanol: 20 g and catalyst loading: 50 mg. Liquid samples were withdrawn after a specific time interval. The aliquots taken during the reaction were analysed using a Trace GC 700 series GC System (Thermo Scientific) coupled with an FID detector and capillary column (HP-5 capillary column, 30 m length × 0.32 mm id). The following temperature program method was used for GC analysis: 40 °C (3 min), 1 °C min^{-1}, 45 °C (1 min), 10 °C min^{-1}, 60 °C (0 min), 20 °C min^{-1}, and 250 °C (1 min). The conversion and selectivity were calculated and defined as follows:

$$(\%)\text{Conversion} = \frac{(\text{initial conc. of HMF} - \text{final conc. of HMF})}{(\text{initial conc. of HMF})} \times 100 \quad (1)$$

$$(\%)\text{Selectivity} = \frac{(\text{moles of desired product formed})}{(\text{moles of 5-HMF consumed})} \times 100 \quad (2)$$

Results and discussion

The major objectives of this work were to (1) design a non-noble metal, efficient, reusable and recoverable metal catalyst and (2) understand the structure–activity correlation to explain the observed catalytic activity performance.

Catalyst characterization

BET surface area. Table 1 presents the BET surface area and N_2-adsorption isotherm results of all the catalysts. The BJH studies revealed that the nature of the material is mesoporous since all the catalysts showed type IV N_2 adsorption isotherms.

Table 1 Surface area analysis and crystallite sizes by XRD for all the components of catalysts used in this work

Sr. no.	Catalysts	Surface area (m^2 g^{-1})	BJH pore size diameter (nm)	Pore volume (cc g^{-1})	Crystallite size (nm) from XRD
1	CuO_x	65	3.38	0.136	56.4
2	FeO_x	137	9.88	0.238	45.3
3	Cu–Fe (1 : 1)	85	10.16	0.192	63.4
4	Cu–Fe (2 : 1)	61	9.50	0.145	25.2
5	Cu–Fe (1 : 2)	109	11.40	0.147	42.8

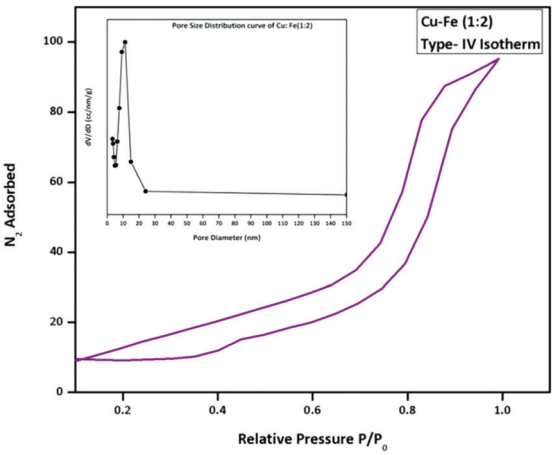

Fig. 1 N_2 adsorption isotherm of Cu–Fe (1 : 2). Inset: pore size distribution of Cu–Fe (1 : 2).

Fig. 1 shows the N_2-adsorption isotherm for Cu–Fe (1 : 2) as it is the most efficient catalyst. Fig. 1 shows a H4 type of low pressure hysteresis loop which appears well before a P/P_0 value of 0.4. This can be due to the unstable meniscus of liquid N_2 inside the narrow slit shaped pores.[36] The highest surface area was observed for FeO_x (Table 1, entry 2) *i.e.* 137 m^2 g^{-1} while Cu–Fe (1 : 2) (Table 1 entry 5) had a surface area of 109 m^2 g^{-1}. The pore diameter of Cu–Fe (1 : 2) was found to be 11.4 nm (Table 1, entry 5) from BJH analysis.

TGA analysis. Fig. 2 presents the TGA of Cu–Fe (1 : 2) with one endothermic peak from 30 °C to 182 °C which can be due to the loss of water or the hydroxyl group from the lattice as shown by an m/z of 18 in Fig. SI 6.†[37] In this temperature window, the total weight loss was found to be 4.65%. It continues to move downwards in the range of 200–800 °C which results in 1.22% weight loss which may account for the phase transition of $CuFe_2O_4$ and loss of nitrate residues from the surface which is further confirmed by a mass fragment of 30 as shown in Fig. SI 6.†[38] After 800 °C, a steep weight loss of 2.4% was observed that may be because of the loss of lattice oxygen.

XRD analysis. Fig. 3 shows XRD patterns of the activated samples of all the catalysts including monometallic Cu and Fe. It was observed that Cu was present mainly in metallic and +2 oxidation states in the form of CuO. XRD peaks at 2θ = 43.70° (111), 50.64° (211) and 74.23° (220) having JCPDF# 85-1326

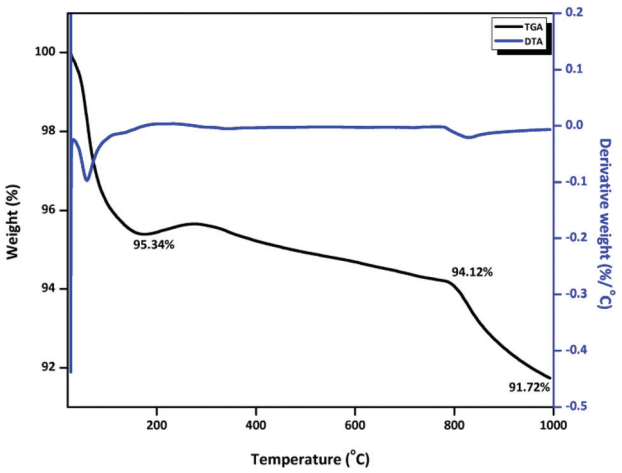

Fig. 2 TGA-DTA analysis of Cu–Fe (1 : 2).

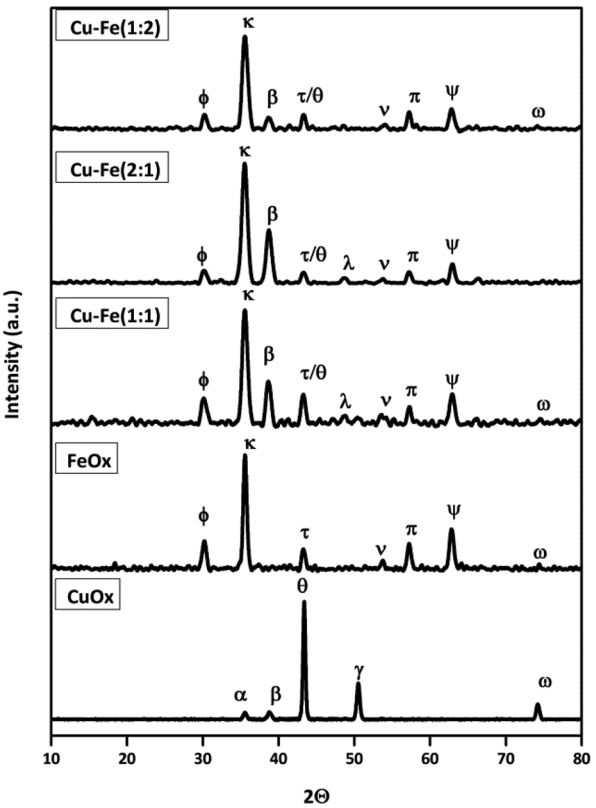

Fig. 3 XRD patterns of all the screened catalysts: α = 35.25°, β = 38.60, θ = 43.70°, γ = 50.64°, ω = 74.23°, φ = 30.11°, κ = 35.76°, τ = 43.45°, ν = 53.95°, π = 57.54°, Ψ = 62.69°, λ = 48.71° (τ/θ are overlapped).

were assigned to Cu(0), whereas those at 2θ = 35.25° and 38.60° could be attributed to the monoclinic CuO phase of Cu with JCPDF# 01-1242.[39,40] The presence of CuO was attributed to its thermodynamic stability over metastable $Cu(OH)_2$ which could be formed before calcination.[41] In the case of FeO_x, various peaks at 2θ = 35.76° (220), 62.69° (440) and 53.95° (422) represent the magnetite Fe_3O_4 phase.[42] The presence of the haematite phase (α-Fe_2O_3) was evidenced by a couple of peaks at 2θ = 57.54° (511) and 43.45° (400).[43] Similarly, the FeO (wustite) phase was confirmed by the appearance of a peak at 2θ = 30.11° (220).[44] In bimetallic Cu–Fe catalysts, peaks at 2θ = 35.50° (311) and 38.85° (222) represented spinel $CuFe_2O_4$ (JCPDF # 77-0010) in Cu–Fe (1 : 1), Cu–Fe (2 : 1) and Cu–Fe (1 : 2) samples, respectively. Metallic Cu was also evidenced by a peak at 2θ = 43.20°. The peak at 2θ = 30.11° represented FeO of $CuFe_2O_4$ and those at 2θ = 57.54° and 62.94° could be attributed to α-Fe_2O_3 and Fe_3O_4, respectively.[45,46] The crystallite sizes of all the catalysts calculated using the Scherer equation are given in Table 1. These XRD studies evidenced that the bimetallic catalyst comprised Cu(0), $CuFe_2O_4$, Fe_3O_4 and α-Fe_2O_3. It also suggests bimetallic synergism between Cu and Fe which is further investigated by XPS analysis.

The presence of Cu–$CuFe_2O_4$ pair can play a significant role in increasing the selectivity of DMF since Cu is known for its activity towards C–O bond cleavage. The above results revealed that Fe atoms were arranged in a BCC lattice, whereas Cu was present in an FCC lattice and the oxides of Fe became indispensible to prevent sintering of Cu(0) due to their inclusion.[43] The stability of Cu–Fe (1 : 2) was evidenced by the XRD analysis of the catalyst sample after its first and fifth recycle runs and it was found that CuO (2θ = 35.50° and 38.85°) existed in all three catalysts. It was observed that in the fresh catalyst, the largest peak was that of CuO at 2θ = 35.50° but after successive recycles, the metallic phase observed at 2θ = 30.11° became more intense. It was also observed that the metallic phase shifted towards a lower value in the fifth recycle, appearing at 2θ = 28.51°. The catalyst sample after the 5th recycle shows the presence of a new peak at 2θ = 24.01° (Fig. 4) due to the formation of a different phase of the mixed oxide. These studies led to the conclusion that the catalyst suffers deposition of a carbonaceous material during the course of the reaction.

HR-TEM. Fig. 5 shows TEM images of Cu–Fe (1 : 2) (Fig. 5a). The fringe pattern revealed the interplanar spacing of both Cu (0.239 nm) and its ferrites (0.476 nm) with respect to planes (222) and (311), respectively (Fig. 5d and b, respectively). The SAED pattern of the catalyst shows well-arranged planes (Fig. SI 1†). After studying 100 nanoparticles, the average particle size of Cu–Fe (1 : 2) was found to be in the range of 15.4–17.6 nm (Fig. 5c).

SEM-EDX analysis and elemental mapping. The morphology of the catalysts was studied by their epitaxial scanning in SEM. Fig. 6b reveals that Cu metallic particles were dispersed near irregularly shaped larger $CuFe_2O_4$. To find out the position of Cu on the Fe surface, elemental mapping analysis was done (Fig. 7). The images of elemental mapping revealed the dispersion patterns of Cu, Fe and O. Cu was shown in green, whereas Fe was shown in pink colour. The oxygen species of both the metals are represented in blue colour. The EDAX pattern (Fig. 6a and c) revealed that Cu was almost 26% and Fe was around 51% by weight, while oxygen was found to be around 23% by weight.

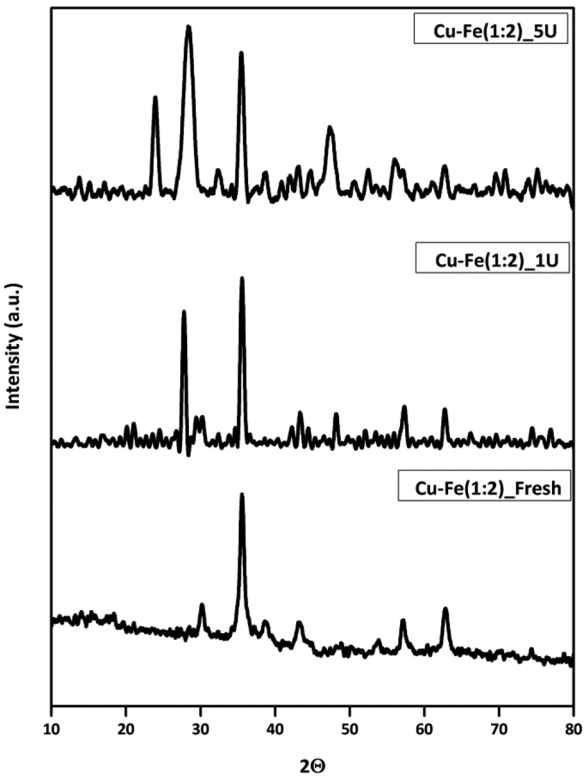

Fig. 4 Comparative XRD analysis of the textural properties of fresh and spent Cu–Fe (1 : 2) catalysts.

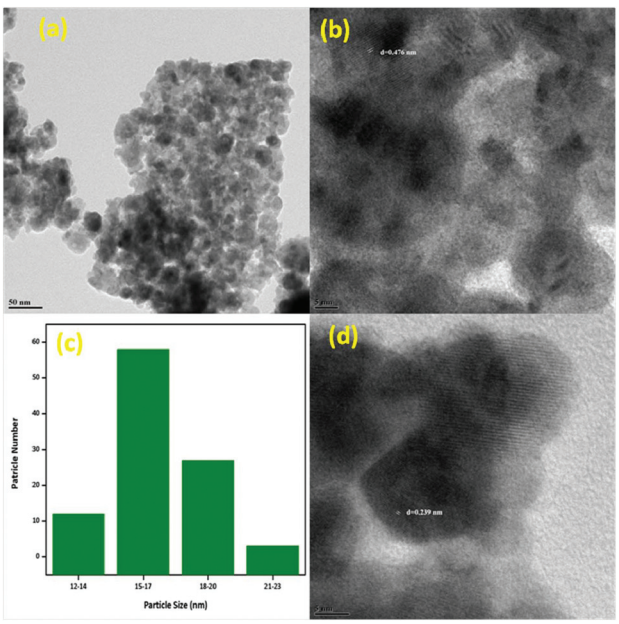

Fig. 5 HR-TEM analysis of (a) the distribution of Cu–Fe (1 : 2) at a 50 nm scale. (b) Fringe width of Fe. (c) Particle size distribution. (d) Fringe width of Cu.

XPS analysis. XPS analysis was performed to know the oxidation states of Cu and Fe. Fig. 8 presents the XPS survey scan profiles of Cu and Fe in monometallic and bimetallic catalysts.

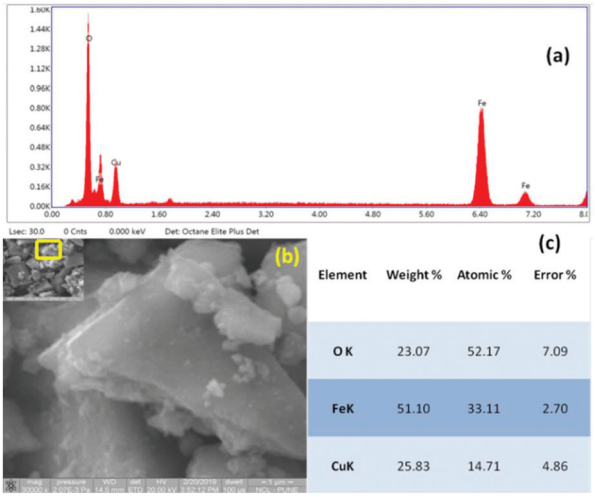

Fig. 6 SEM of Cu–Fe (1 : 2) (a) EDAX pattern of Cu–Fe (1 : 2). (b) Morphology of Cu–Fe (1 : 2). (c) Elemental % of Cu, Fe and O in Cu–Fe (1 : 2).

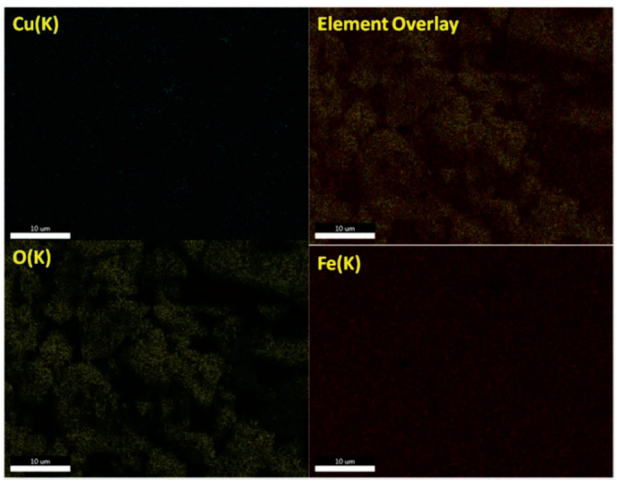

Fig. 7 Elemental mapping of Cu, Fe and O in Cu–Fe (1 : 2).

Fig. 8a presents the $2p_{1/2}$ and $2p_{3/2}$ peaks of Cu. Cu $2p_{3/2}$ core level spectra evidenced the presence of metallic Cu and CuO by the peaks in the range of B.E. of 933.20 to 933.74 eV, consistently in all the catalysts. Strong shake up peaks in a B.E. range of 943.32–943.74 eV suggested the presence of CuO.[47] If this satellite peak would have been weak it could be assigned to the presence of Cu_2O which was not the case in our catalyst.[48] The Cu $2p_{1/2}$ core level peak is located in a B.E. range of 953.05–953.84 eV in all the catalysts. The strong Cu^{2+} satellite peak around a B.E. range of 961.71–962.50 eV confirmed the presence of CuO.[49]

Similarly, the surface composition and valence state of Fe were also analysed by its XPS survey scan. Fig. 8b shows the cumulative XPS of Fe in all the catalysts including that of bare monometallic FeO_x. The peak for core level Fe $2p_{3/2}$ was located in a B.E. range of 710.37–711.04 eV, whereas the Fe

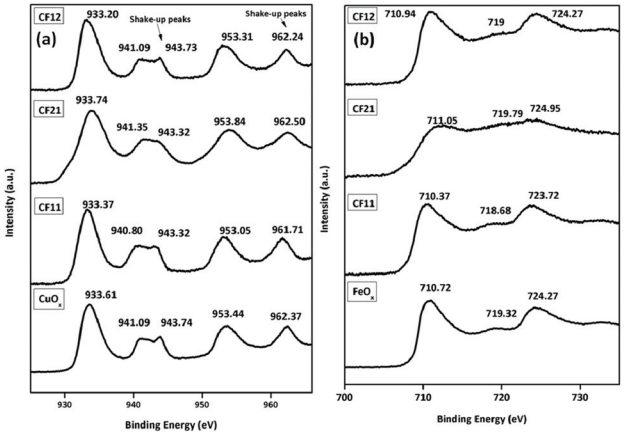

Fig. 8 XPS scan survey profiles of (a) Cu and (b) Fe.

$2p_{1/2}$ peak showed its presence in a B.E. range of 723.72–724.95 eV. A satellite peak was also observed at around a B.E. range of 718.68–719.79 eV with much lower intensity which indicates the presence of α-Fe_2O_3.[50] Fe $2p_{3/2}$ peaks at B.E. of 710.72 eV and 710.94 eV showed the presence of α-Fe_2O_3 and Fe_3O_4 in the case of monometallic FeO_x and Cu–Fe (1 : 2), respectively, which was also confirmed by XRD studies. A slightly higher shift in the XPS peak of Cu–Fe (2 : 1) was attributed to the FeO phase.[51] All the Fe survey profiles contained a tiny satellite peak in the B.E. range of 718.68–719.79 eV. These satellite peaks strongly evidenced the presence of Fe^{3+}.[52] The composition of each metal in the catalyst and its oxidation state were also determined by deconvoluting the survey scan profiles of Cu $2p_{3/2}$ and Fe $2p_{3/2}$.

As shown in Fig. 9, the Cu compositions in both monometallic and bimetallic catalysts were compared by analyzing the Cu $2p_{3/2}$ peak. The CuO_x species in the monometallic (Fig. 9a)

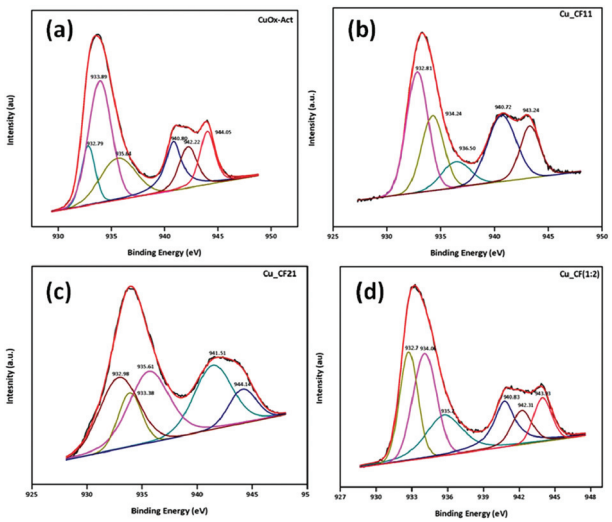

Fig. 9 Phases of Cu determined by XPS analysis in all the screened catalysts: (a) Cu in CuO_x-Act, (b) Cu in Cu–Fe (1 : 1), (c) Cu in Cu–Fe (2 : 1) and (d) Cu in Cu–Fe (1 : 2).

catalyst showed the major peaks at B.E. of 933.89, 932.79 and 935.64 eV with satellite peaks in the range of 942–945 eV. The major peak at a B.E. of 933.89 eV was assigned to the Cu^{2+} oxidation state due to the formation of CuO, whereas the peak at a B.E. of 932.79 eV was assigned to metallic Cu. Although it could be due to the presence of Cu^{1+} since the binding energies of Cu(0) and Cu^{1+} are indistinguishable, the presence of satellite peaks was another supporting factor for the presence of Cu(0).[53,54] A broad peak at a higher binding energy of 935.64 eV suggested the presence of Cu(+2) in different chemical environments as reported elsewhere.[55] The satellite peaks at B.E. of 940.80, 942.22 and 944.05 eV represented different oxide peaks of Cu.

These characteristic peaks of Cu were observed with other bimetallic catalysts also. In an equimolar Cu–Fe catalyst *i.e.* Cu–Fe (1 : 1) (Fig. 9b), a slight shift towards higher binding energy was observed which clearly indicates the interaction of Cu with Fe. A major peak at a B.E. of 932.81 eV was that of Cu (0) which suggested that the reduction protocol in a H_2 environment at 523 K was successful followed by two other oxide peaks which were located at B.E. of 934.24 eV and 936.50 eV which shows that CuO was present in two different chemical environments. The peak at 934.24 eV was assigned to octahedral CuO, whereas the other peak at the higher binding energy of 936.50 eV could be assigned to tetrahedral Cu(+2) present in $CuFe_2O_4$ spinel ferrite.[56,57] The satellite peaks ranging between B.E. of 940 and 945 eV were also observed with other bimetallic catalysts with varying Cu and Fe contents. In the case of Cu–Fe (2 : 1) with an excess of Cu, almost equal amounts of Cu(0) and Cu(+2) of $CuFe_2O_4$ were observed with a slight edge over the latter one (Fig. 9c). Another minor peak observed at a B.E. of 933.38 eV interfered with the metallic peak which was octahedrally coordinated CuO of spinel ferrite. Shake up peaks at B.E. of 941.51 and 944.14 eV were assigned to various oxides of Cu. These results were consistent with those of our most efficient catalysts *i.e.* Cu–Fe (1 : 2) (Fig. 9d). Here also sharp peaks were observed at B.E. of 932.7 eV and 934.06 eV for the combination of Cu(0)-$CuFe_2O_4$ along with a peak at a B.E. of 935.7 eV assigned to tetrahedral CuO of $CuFe_2O_4$. This detailed XPS analysis showed that there was the formation of very strong Cu–$CuFe_2O_4$ pairs in all the catalysts which could be responsible for the excellent catalytic activity in the hydrogenation of 5-HMF. These results also revealed that interactions existed between Fe and Cu which could lead to the synergism between the two metals. Hence, analysis of the metallic surface of Fe becomes very important. In all the catalysts, only the oxide form of Fe was detected and metallic Fe species were absent. In bare FeO_x (Fig. 10a), the peaks at B.E. of 711.27 and 710.76 eV could be assigned to haematite and magnetite forms of iron; however, a tiny satellite peak at a B.E. of 719 eV supported the presence of haematite *i.e.* α-Fe_2O_3 also. The presence of the Fe(+2) species was also observed at a B.E. of 709.85 eV which could be assigned to FeO. A broad hump was detected at a higher binding energy of 712.98 eV which could be assigned to Fe_3O_4.[58,59] These results remained consistent with those of all

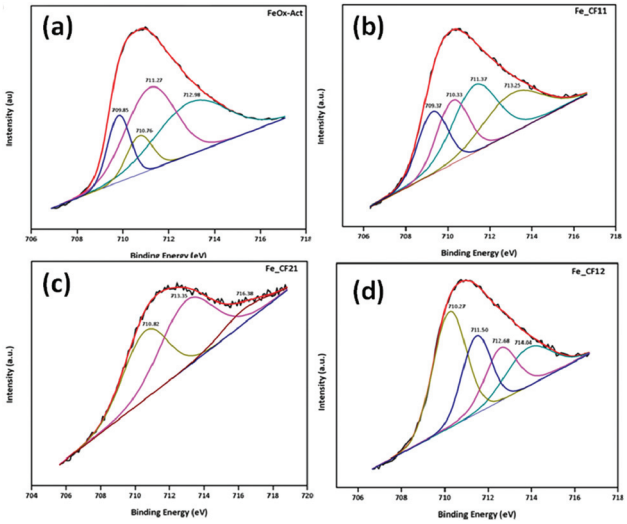

Fig. 10 XPS analysis of different Fe phases in all the screened catalysts: (a) Fe in FeO_x, (b) Fe in Cu–Fe (1 : 1), (c) Fe in Cu–Fe (2 : 1) and (d) Fe in Cu–Fe (1 : 2).

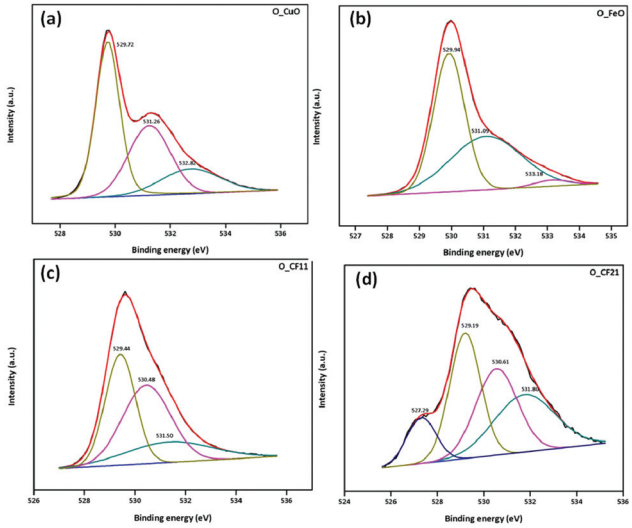

Fig. 11 Nature of oxygen in all screened catalysts as determined by XPS analysis: (a) O in CuO_x, (b) O in FeO_x, (c) O in Cu–Fe (1 : 1) and (d) O in Cu–Fe (2 : 1).

the bimetallic catalysts with a substantial shift towards higher binding energy indicating a strong interaction with other metallic species.[60] Four peaks were observed in the equimolar Cu–Fe (1 : 1) catalyst at B.E. of 709.37, 710.33, 711.37 and 713.25 eV, which were assigned to FeO, α-Fe_2O_3 and Fe_3O_4 as discussed earlier (Fig. 10b). The shift of the peak due to Fe_3O_4 towards higher binding energy (713.25 eV) was indicative of the formation of spinel $CuFe_2O_4$.[61] All these peaks were also observed in the Cu–Fe (2 : 1) and Cu–Fe (1 : 2) catalysts, except for the FeO species. The α-Fe_2O_3 species was very much dominant in all the catalysts evident from the peaks at a B.E. of 710.82 eV in Cu–Fe (2 : 1), and 710.27 eV and 711.50 eV in Cu–Fe (1 : 2). Our most efficient catalyst Cu–Fe (1 : 2) also showed the presence of Fe_3O_4 at a B.E. of 712.68 eV. Two higher binding energy peaks appearing at a B.E. of 716.38 eV in Cu–Fe (2 : 1) (Fig. 10c) and 714.04 eV in Cu–Fe (1 : 2) (Fig. 10d) could be assigned to the oxide species of Fe (FeO, Fe_3O_4) present in $CuFe_2O_4$, thus confirming the presence of interactions between Cu and Fe.[62] Since oxides of both the metals were present, the nature of the oxygen species can reveal significant information related to the nanohybrid pair and Fe species and their respective roles in the hydrogenation of 5-HMF to DMF. Fig. 11 presents O 1s curve fitting XPS spectra for different catalysts. In all the catalysts, except Cu–Fe (2 : 1), three peaks were observed after deconvolution at B.E. of 529.94, 531.09 and 533.18 eV (Fig. 11b) which could be assigned to FeO_x. The major peak at a B.E. of 529.94 eV represented the O^{2-} state of lattice oxygen of Fe, whereas the one at a B.E. of 531.09 eV was assigned to the lateral peak of O 1s. The lateral O 1s peak could be due to the oxygen species coordinated differently in different chemical environments and subsurface oxygen of the lattice.[63] A satellite broad peak at a B.E. of 533.18 eV could be assigned to the adsorbed oxygen.[64] Similar peaks were also observed in the O 1s spectrum of monometallic CuO_x (Fig. 11a) at B.E. of 529.72, 531.6 and 533.82 eV for the Cu–Fe (1 : 1) sample (Fig. 11c) at 529.44, 530.48 and 531.50 eV and in Cu–Fe (1 : 2) (Fig. 11d) at 529.93, 531.16 and 532.20 eV. All these observations revealed that the nature of oxygen in the Cu and Fe lattice was similar even in bimetallic cases. The O 1s spectra of bimetallic catalysts showed three peaks located at close B.E. of 529.44, 530.48 and 531.50 eV. However, the Cu–Fe (2 : 1) sample showed an additional peak at 527.29 eV (Fig. 11d) which was a low binding energy spike and was attributed to the surface oxide defects of Cu–Fe (2 : 1) and would be the reason for its excellent activity in 5-HMF conversion.[65] Thus, the Cu/$CuFe_2O_4$ pairs evidenced in XPS studies have an excellent synergism including different oxide defects on the surface that strongly accelerated 5-HMF hydrogenation to 2,5-DMF. All these results were also commensurate with our XRD analysis. Since Cu played a significant role in enhancing the selectivity to DMF, the quantitative composition of each phase of Cu in each catalyst based on the relative peak intensity is also given in Table 2.

Table 2 Relative intensity ratio of metallic Cu and CuO

Sr. no.	Catalysts	Cu/CuO
1	CuO_x	0.2052
2	Cu–Fe (1 : 1)	1.0911
3	Cu–Fe (2 : 1)	0.6210
4	Cu–Fe (1 : 2)	0.4720

XPS of the spent Cu–Fe (1 : 2) catalyst was also analysed to determine the changes that occurred in various species of the catalyst during the reaction (Fig. 12). The major peak observed in deconvolution of Cu is Cu(0) at a B.E. of 932.31 eV, whereas other oxide peaks at B.E. of 933.01 and 934.66 eV were also observed which were the same as those for the fresh Cu–Fe (1 : 2) sample (Fig. 12a). The satellite peaks at B.E. of 940.80

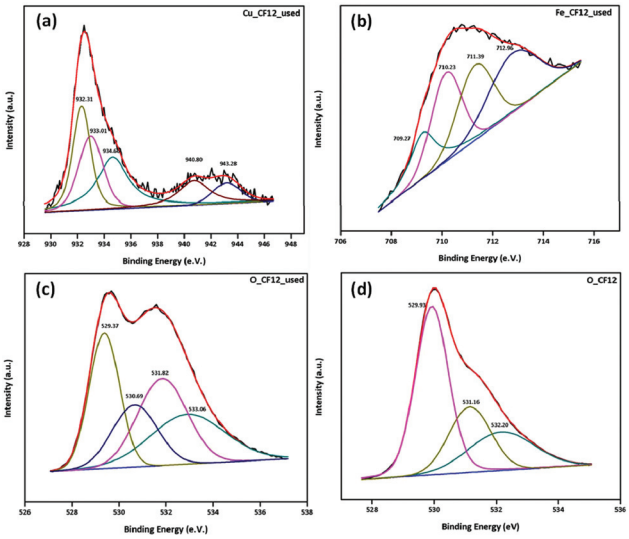

Fig. 12 XPS of spent Cu–Fe (1 : 2) and the nature of Cu, Fe and O: (a) Cu in Cu–Fe (1 : 2)-used, (b) Fe in Cu–Fe (1 : 2)-used, (c) O in Cu–Fe (1 : 2)-used and (d) O in Cu–Fe (1 : 2)-fresh.

and 943.28 eV were also present in the used catalyst sample but with less intensity which might be due to the continuous H_2 environment under reaction conditions. XPS curve fitting of Fe also revealed similar observation of the presence of α-Fe_2O_3, Fe_3O_4 and FeO to those observed in fresh Cu–Fe (1 : 2) at B.E. of 709.27, 710.23, 711.39 and 712.96 eV (Fig. 12b). The O 1s curve fitting profile showed the presence of 4 different peaks in the range of B.E. of 529–533 eV. The most intense peak at a B.E. of 529.37 eV could be related to lattice oxygen of Cu–Fe (1 : 2), whereas the second intense peak present at a B. E. of 531.82 eV was assigned to ether derivatives of the solvent and the one at a B.E. of 530.69 eV was assigned to oxygen of the –OH group (Fig. 12c).[66] A broad peak at a B.E. of 533.06 eV evidenced the presence of carbonaceous matter adsorbed on the catalyst surface in the form of –C═O groups of the reaction crude which was further proved by the appearance of a peak at higher B.E. of 286.57 eV and 288.85 eV corresponding to –C–O and –C–OH in the carbon XPS profile of the used Cu–Fe (1 : 2) sample (Fig. SI 1†).[67] These broad peaks at higher binding energies for oxygen were absent in all the fresh catalysts.

CO_2-TPD. The basicity of the catalyst was estimated by CO_2-TPD analysis which was important because the excess Cu content is known to provide more basic sites, whereas the higher acidic sites are obtained when the Fe content is higher in the bimetallic catalyst.[68] This also justifies our selection of the excess Fe containing Cu–Fe (1 : 2) catalyst since acidity played an important role in 5-HMF hydrogenation. The acid strength and type of acid site were further assessed by NH_3-TPD and Py-IR studies. This can also be the probable reason why a highly basic catalyst such as CoO_x remains inactive in our reaction. Fig. SI 3 and Table S.1† present the CO_2-TPD of all the Cu and Fe catalysts screened in this work.

NH_3-TPD and Py-IR analyses. Fig. 13 and Table 3 present the total amount of NH_3 desorbed by various Cu–Fe catalysts. It

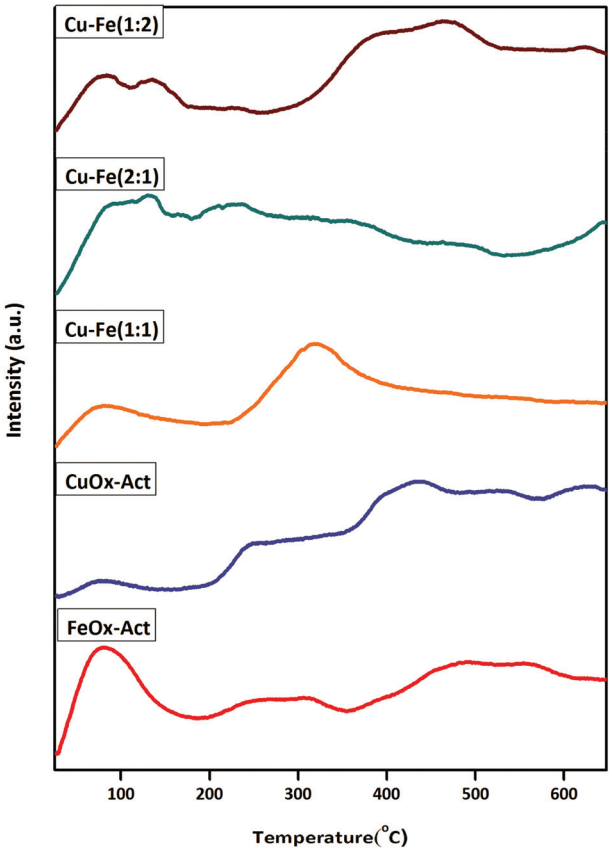

Fig. 13 NH_3-TPD profiles of all the screened catalysts.

Table 3 Acidity by NH_3-TPD analysis

Sr. no.	Catalysts	Temperature range (°C) 25–200	200–400	400–750	Total NH_3 desorbed (mmol g^{-1})
1	CuO_x	0.0280	0.1640	0.0203	0.2123
2	FeO_x	0.3788	0.0228	0.0752	0.4768
3	Cu–Fe (1 : 1)	0.2495	0.5149	0.0457	0.8101
4	Cu–Fe (2 : 1)	0.0429	0.0679	0.0783	0.1891
5	Cu–Fe (1 : 2)	0.1126	0.0563	0.0765	0.2454

was observed that on increasing any of the metal content, the amount of NH_3-desorbed decreased. A maximum acidity of 0.8101 mmol g^{-1} was observed for Cu–Fe (1 : 1), while a minimum acidity of 0.1891 mmol g^{-1} was observed for Cu–Fe (2 : 1) (Table 3, entries 3 and 4, respectively). This implies that a particular amount of a well dispersed acid is only required rather than highly acidic conditions for 5-HMF hydrogenation.

Distinction between the Lewis and Brönsted acid sites was done by Py-IR (Table 4). It was observed that while Fe possessed mainly Lewis acidity, Cu had Brönsted acidity as clearly confirmed by the BA/LA ratio for Fe of 0.5294, while for Cu it was very high, 6.82 (Table 4, entries 2 and 1, respectively), although the values of the Brönsted acidity of both CuO_x and FeO_x were found to be almost similar *i.e.* 0.2347 and 0.2511, respectively (Table 4).

Table 4 BA/LA of all the catalysts by Py-IR analysis

Sr. no.	Catalysts	Types of acidity: Total Lewis acidity (TLA)	Total Brönsted acidity (TBA)	TBA/TLA
1	CuO_x	0.0344	0.2347	6.8226
2	FeO_x	0.4743	0.2511	0.5294
3	Cu–Fe (1 : 1)	0.0196	0.0656	3.3469
4	Cu–Fe (2 : 1)	0.1519	0.3268	2.1514
5	Cu–Fe (1 : 2)	0.3195	0.2337	0.7314

When both the metals interacted, BA/LA decreased as shown by the order: Cu–Fe (1 : 1) > Cu–Fe (1 : 2) > Cu–Fe (2 : 1) (Table 4, entries 3–6). Despite having a higher Cu content, Cu–Fe (2 : 1) showed a lower BA/LA ratio suggesting that there was certainly some interaction occurring between Cu and Fe to form $CuFe_2O_4$ as evidenced by XPS and XRD studies. Similar observations were made in the case of Cu–Fe (1 : 2) in which excess Brönsted acid sites were observed. Since Cu–Fe (1 : 2) was found to be the most efficient catalyst, its py-IR studies were carried out at different temperatures as shown in Fig. 14. It shows two major peaks at 1540 cm^{-1} and 1698 cm^{-1} which could be attributed to Brönsted and (Brönsted + Lewis) acidity, respectively.[69] On fine deconvolution, it was observed that a peak at 1455 cm^{-1} due to Lewis acidity was embedded in a broad hump at 1540 cm^{-1}, whereas the peak at 1640 cm^{-1} (Brönsted acidity) is seen in a hump at 1698 cm^{-1}.[70] A comparative Py-IR study of both monometallic and Cu–Fe (1 : 2) catalysts is shown in Fig. SI 4.† It clearly shows that Lewis acidity peaks at 1440 cm^{-1} and 1630 cm^{-1} are present in FeO_x. In monometallic CuO_x, Brönsted acidity was observed at 1540 cm^{-1}. The Lewis acid centre of the Cu–Fe catalyst can activate the –C=O group of 5-HMF which further can lead to sideways binding between the catalytic surface and electron rich oxygen of the carbonyl group which enhances the synthesis of BHMF and neutralises the decarbonylation activity of Cu, whereas the Brönsted acidity of the Cu–Fe catalyst enhances the dehydration of BHMF which proves decisive in determining the selectivity of the hydrogenolysis pathway.[71,72] Hence, both the acidic properties play an important role in the hydrogenation and the dehydration step of the reaction mechanism as discussed later.

H_2-TPR. The reducibility of the catalyst was determined by H_2-TPR studies. As can be seen from Fig. 15, monometallic CuO_x shows a broad peak at around 234 °C with a bifurcation around 195 °C. This could be correlated with the reduction of CuO into Cu(0).[73] The shoulder peak at higher temperature was because of different sizes of nanoparticles of Cu on crystalline CuO. The absence of any other maxima at higher temperature indicates the absence of the Cu_2O phase in our catalyst. This is also in accordance with the fact that the reduction of Cu(+1) to Cu(0) requires very high temperature and that pow-

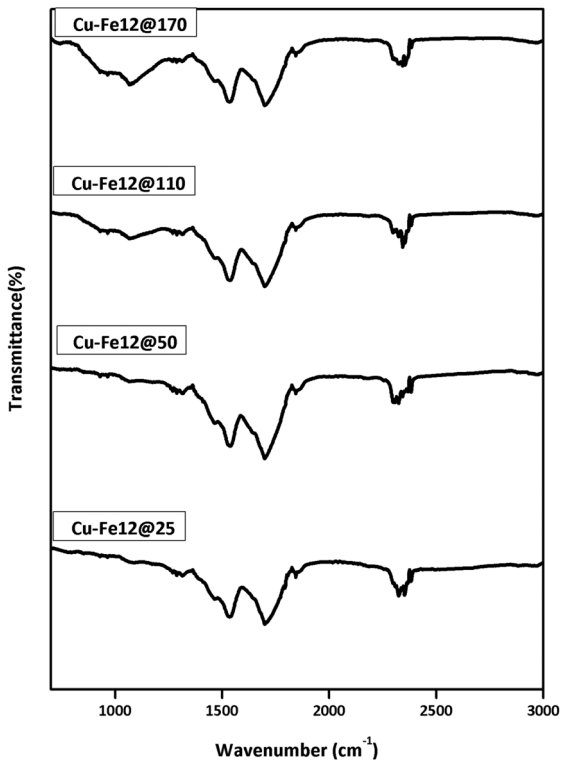

Fig. 14 Determination of different acidic sites by Py-IR.

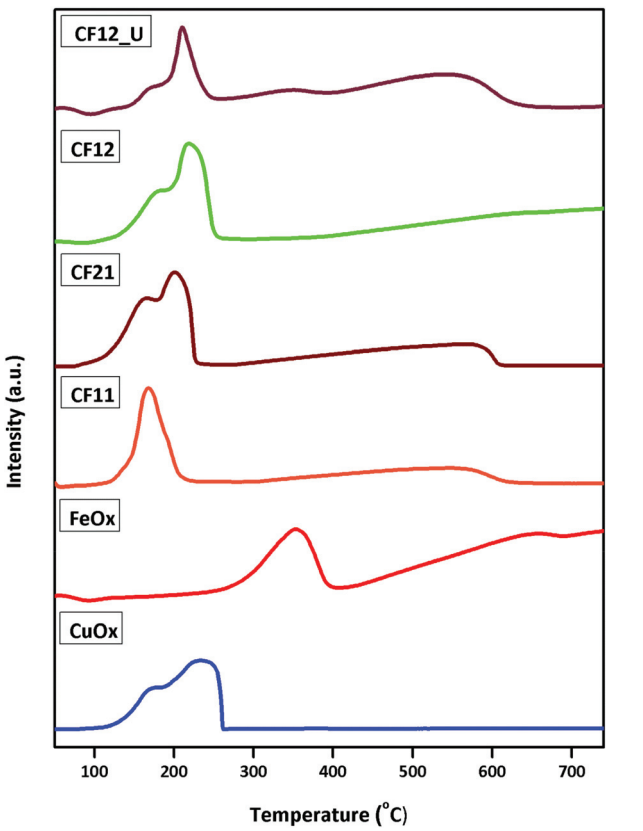

Fig. 15 H_2-TPR of the screened catalysts: Cu–Fe (1 : 1) is represented as CF11, Cu–Fe (1 : 2) as CF12, Cu–Fe (2 : 1) as CF21 and spent Cu–Fe (1 : 2) as CF12_U.

dered CuO_x tends to reduce directly into metallic Cu instead of any kind of intermediate phases such as Cu_2O or Cu_4O_3.[74] In FeO_x samples, three peaks at 301.47 °C, 552.68 °C and 698.16 °C were deconvoluted which clearly indicate the sequential reduction of Fe(+3) into Fe(0) in a lower to higher temperature range. The peak at 301.47 °C is related to the conversion of α-Fe_2O_3 into Fe_3O_4 which at high temperature (552.68 °C) reduced to the FeO phase which finally reduced to metallic Fe at a still higher temperature of 698.16 °C.[75] In the case of all the bimetallic Cu–Fe catalysts, two common maxima were observed, first at around 170–230 °C and second at a higher temperature around 500–600 °C. The equimolar Cu–Fe bimetallic catalyst represented as CF-11 in the TPR profile showed a difference in terms of the appearance of lower temperature maxima. In the cases of CF-12 and CF-21 lower temperature maxima were clearly observed as bifurcation due to different sizes of the particles and clearly indicating the interaction between Cu and Fe. The lower temperature peaks were because of the reduction of $CuFe_2O_4$ into metallic Cu and α-Fe_2O_3, whereas the higher temperature peaks could be assigned to the sequential reduction of α-Fe_2O_3 into FeO and Fe as described earlier.[76] To reveal the nature and reducibility of the spent Cu–Fe (1 : 2) catalyst, its TPR was performed and two shoulder peaks were observed unlike the fresh Cu–Fe (1 : 2) sample, which could be attributed to the carbonaceous oxygen on the CuO surface which was further confirmed by XPS and XRD of the used catalyst. One small reduction maximum was also observed at 458.86 °C which could be related to the oxide state of Fe again due to carbonaceous matter formed under reaction conditions.[77] Another usual peak at higher temperature was related to complete reduction of Fe. First reduction of all the catalysts occurred at relatively lower temperatures of 170–230 °C and was due to their mesoporous nature which was in accordance with our BET surface area results. The mesoporous nature is known to cause reduction of the T_m in the case of copper ferrites.[78]

Activity evaluation

Different catalysts were screened for 5-HMF hydrogenolysis and the results are shown in Table 5.

The as-prepared CoO_x-NP enabled 47% conversion but no hydrogenation product was obtained. This showed that cobalt was unsuitable for this reaction. Bare CuO_x-NP and FeO_x-NP were also tested and it was observed that with CuO_x-NP excellent conversion of 80% was achieved and the major product obtained was DMF with 59% selectivity and considerable amounts of other reduction intermediates such as BHMF (6%), MFFR (6%) and MFAL (10%) were also formed. Surprisingly, Cu-NP gave 2-methyl furan (17%) and furfuryl alcohol (FAL) (2%) which suggests that in the presence of Cu, hydrogenation and decarbonylation were the competitive reactions. In the presence of FeO_x-NP, the conversion was quite low *i.e.* 39% but all the reaction intermediates were formed in moderate amounts. The major product was BHMF with 38%

Table 5 Catalyst screened for 5-HMF hydrogenation into DMF; reaction conditions: 5-HMF = 100 mg; solvent (IPA) = 20 g; catalyst = 50 mg; temperature = 443 K; H_2 pressure = 300 psig; reaction time = 4 h; agitation speed = 1000 rpm

			Selectivity (%)				
Sr. no.	Catalysts	Conv. (%)	DMF	BHMF	MFFR	MFAL	2-MF + FAL
1	CoO_x-NP	47	0	0	0	0	0
2	CuO_x-NP	80	59	6	6	10	19
3	FeO_x-NP	39	16	38	10	25	0
4	Cu–Fe (1 : 1)	85	72	8	3	7	10
5	Cu–Fe (2 : 1)	95	84	3	1	1	11
6	Cu–Fe (1 : 2)	97	93	4	1	2	0

selectivity along with 10% MFFR and 25% MFAL. Only 16% DMF was observed but the decarbonylation route was completely absent unlike in the case of CuO_x-NP. Bimetallic Cu–Fe catalysts in different molar ratios were prepared and screened for 5-HMF hydrogenolysis. With equimolar concentrations of Cu and Fe *i.e.* Cu–Fe (1 : 1), the conversion and DMF selectivity increased significantly to 85% and 72%, respectively, which clearly indicated the synergism between Cu and Fe. Other intermediates such as 4% FAL, 6% 2-MF, BHMF (8%), MFFR (3%) and MFAL (7%) were also formed. For a Cu/Fe ratio of 2, an increase in the decarbonylation products *i.e.* 2-MF (8%) and FAL (3%) was observed, which could be attributed to the excess of the Cu content in the catalyst. In the case of Cu–Fe (2 : 1), 95% conversion of 5-HMF was observed with DMF as a major product with 84% selectivity and other reaction intermediates were obtained in much lower amounts *i.e.* BHMF (3%), MFFR (1%) and MFAL (1%). To suppress the decarbonylation, Cu–Fe (1 : 2) with Fe in excess was evaluated and, as expected, there was no 2-MF observed under similar reaction conditions. The Cu–Fe (1 : 2) catalyst proved to be highly efficient among all the screened catalysts, enabling 97% conversion along with very high (93%) selectivity to DMF. The other products included 4% BHMF along with 1% MFFR and 2% MFAL. The formation of 4% BHMF revealed that the hydrogenation route of 5-HMF was initiated *via* hydrogenation of the –C=O group (Scheme 1). This may be attributed to the oxophilic nature of Fe. The excellent conversion of BHMF into DMF is because of the C–O hydrogenation nature of Cu. So, Cu and Fe were tuned to an appropriate ratio in order to achieve the efficient nature of the catalyst.

Temperature effect

The reaction temperature studies (Fig. 16) revealed that the reaction was feasible even at a low temperature of 363 K, although the conversion was only 21% with the major product formed being BHMF (30%) and DMF was obtained in a much lower amount (17%). The hydrogenolysis activity of Cu/$CuFe_2O_4$ at lower temperature was also visible by the formation of MFFR (27%) and MFAL (26%) at 363 K. These trends changed dramatically at higher temperature and, at 383 K, DMF selectivity steadily increased to 33% whereas the other major products were BHMF and MFFR with 25% selectivity.

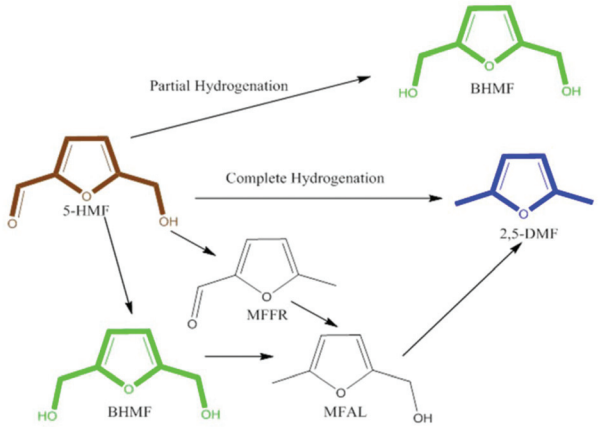

Scheme 1 Reaction pathway of 5-HMF hydrogenation.

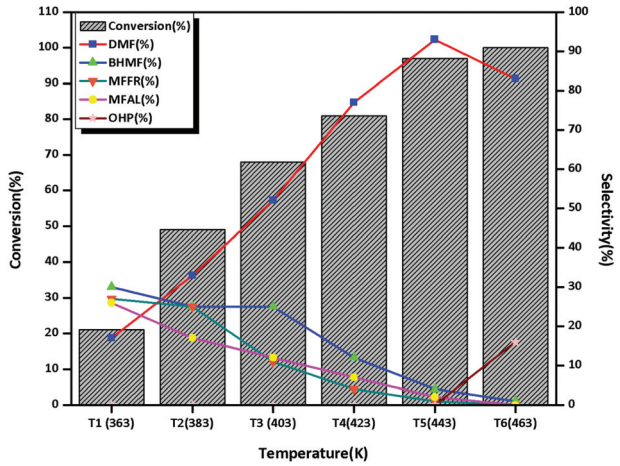

Fig. 16 Temperature effect on 5-HMF hydrogenation; reaction conditions: 5-HMF = 100 mg; catalyst = 50 mg; solvent (IPA) = 20 g; H_2 pressure = 300 psig; reaction time = 4 h; agitation speed = 1000 rpm.

The conversion of 5-HMF also increased significantly to 49%. On further increasing the temperature to 403 K, a sharp increase in both the conversion of 5-HMF (from 49% to 68%) and DMF selectivity (52%) was observed. At 423 K, the selectivity towards BHMF was the same as that at 403 K. This fact supports that the first step in the hydrogenation pathway (Scheme 1) of 5-HMF is its partial hydrogenation. The 5-HMF conversion achieved was 81% at 423 K with 77% selectivity towards DMF and 12% towards BHMF as a second major product. MFFR and MFAL appeared in very minute amounts *i.e.* 4% and 7%, respectively, at 423 K. On further increasing the temperature to 443 K, 5-HMF conversion achieved was 97% with selectivity to DMF as high as 93%. Further rise in temperature led to ring hydrogenation products *i.e.* BHMTHF and DMTHF as the DMF selectivity decreased to 83% from 93%.

H_2 pressure effect

The 5-HMF hydrogenolysis was performed over various pressure conditions and 300 psig was found to be the best

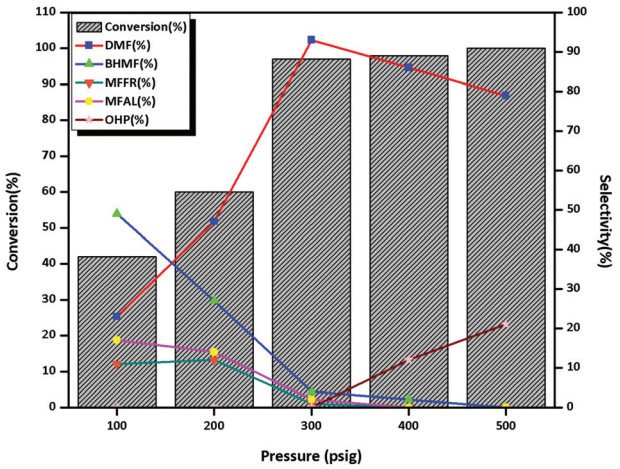

Fig. 17 Effect of H_2 pressure on the hydrogenation of 5-HMF; reaction conditions: 5-HMF = 100 mg; catalyst = 50 mg; solvent (IPA) = 20 g; temperature = 443 K; reaction time = 4 h; agitation speed = 1000 rpm.

suited pressure. Fig. 17 shows that at a H_2 pressure of 100 psig, the major product formed was BHMF (49%) indicating the partial hydrogenation of 5-HMF taking place at lower pressure.

As the pressure was increased to 200 psig, the conversion of BHMF into DMF increased (47% from 23%). This trend continued as the pressure increased to 300 psig where DMF selectivity reached the highest value of 93%. When the H_2 pressure was further increased to 400 psig, overhydrogenated products such as BHMTHF, DMTHF and an ether derivative of 5-HMF were observed. Their formation increased from 12% to 21% when the pressure was further increased to 500 psig. At this pressure, ring opening products of 5-HMF such as 2,5-hexandiol were also detected. Thus, beyond 300 psig, the selectivity to DMF decreased sharply due to further hydrogenation of the furan ring and its etherification.

Catalyst loading effect

In order to find the optimum amount of the catalyst for efficient hydrogenation of 5-HMF, a range of catalyst loading was screened (Fig. 18) and the most suitable catalyst loading was found to be 50 mg. For the lowest catalyst loading of 25 mg, 5-HMF conversion achieved was only 59% although the major product formed was DMF with 51% selectivity. Other products formed were BHMF (38%), MFFR (4%) and MFAL (7%). With an increase in catalyst loading to 50 mg, the highest conversion of 5-HMF was achieved (93%) with the highest selectivity of 97% towards DMF. On increasing the catalyst loading further to 75 mg, DMTHF was observed as the second major product with 14% selectivity with complete conversion of 5-HMF. With further increase in the catalyst loading to 100 mg, the selectivity to overhydrogenated products increased to 33%.

Agitation speed effect

The effect of agitation speed on 5-HMF conversion and product distribution was also studied and the results are

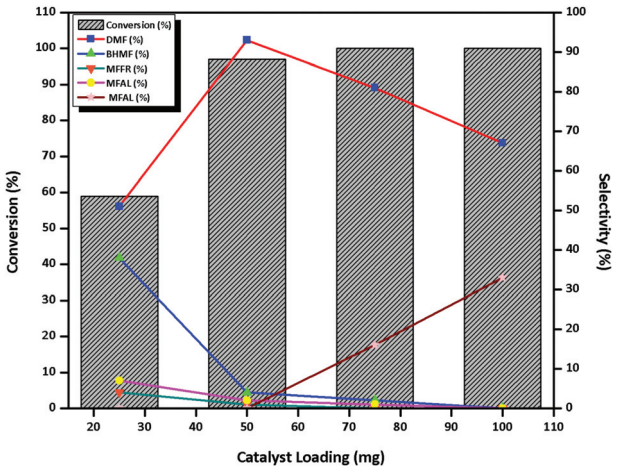

Fig. 18 Effect of catalyst loading on 5-HMF hydrogenation; reaction conditions: 5-HMF = 100 mg; solvent (IPA) = 20 g; temperature = 443 K; H_2 pressure = 300 psig; reaction time = 4 h; agitation speed = 1000 rpm.

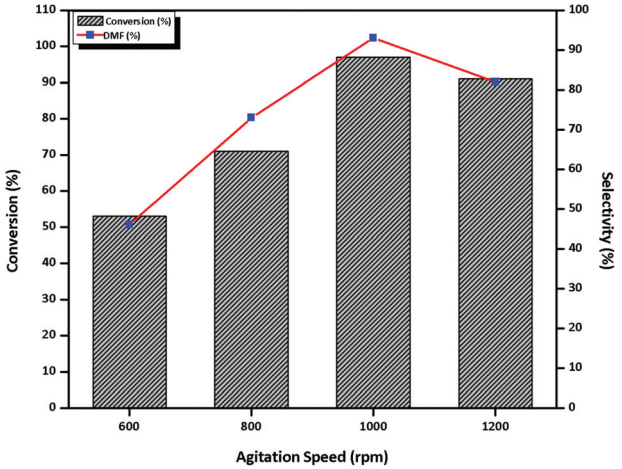

Fig. 19 Effect of agitation speed on 5-HMF hydrogenation; reaction conditions: 5-HMF = 100 mg; catalyst = 50 mg; solvent (IPA) = 20 g; temperature = 443 K; H_2 pressure = 300 psig; reaction time = 4 h.

shown in Fig. 19. At a lower agitation speed of 800 rpm, the 5-HMF conversion achieved was 71% with 73% selectivity to DMF. On further slowing down the agitation speed to 600 rpm, the conversion of HMF decreased to 53% along with a selectivity lowering to 46% to DMF. This decrease in conversion and selectivity at lower agitation speeds was due to less catalyst–substrate contact which obviously led to less adsorption of the reactants on the catalytic surface.[79]

Solvent effect

Since the solubility of both 5-HMF and hydrogen would significantly influence the 5-HMF conversion and DMF selectivity, studies on solvent screening were also carried out and the results are shown in Fig. 20. Among the screened solvents, IPA (iso-propyl alcohol) proved to be highly efficient which was

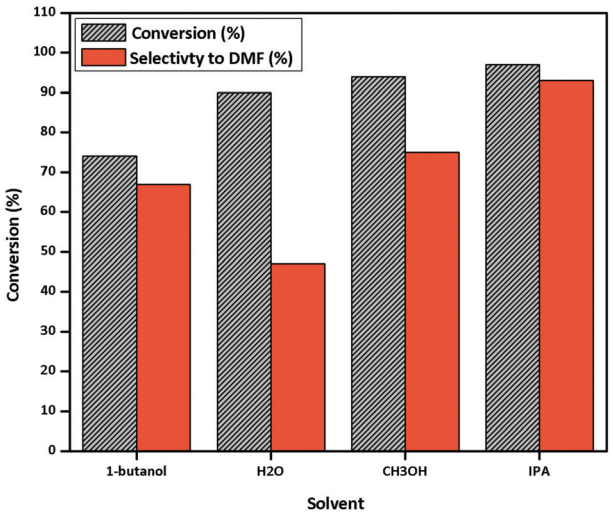

Fig. 20 Effect of the solvent on 5-HMF hydrogenation; reaction conditions: 5-HMF = 100 mg; catalyst = 50 mg; solvent = 20 g; temperature = 443 K; H_2 pressure = 300 psig; reaction time = 4 h; agitation speed = 1000 rpm.

due to its tendency to donate hydrogen, moderate boiling point, lower polarity, low dielectric constant and less bulky nature.[80] When 1-butanol was used as the reaction medium, the conversion of 5-HMF was only 74% with a lower selectivity of 67% to DMF. This might be due to the lower solubility of both 5-HMF and hydrogen and also its bulky nature which can cause steric hindrance to reaction intermediates.[81]

The reaction was also attempted in H_2O in which a sharp decrease in the selectivity to DMF (47%) was observed. In this case, the other major product formed was BHMF with 32% selectivity. The lower conversion could be obviously due to lower hydrogen solubility in water. However, the higher BHMF selectivity could be due to the solvolysis effect of water.[82] The reaction was also performed in methanol in which 94% conversion of 5-HMF was achieved but the selectivity to DMF was only 75%. Lower alcohols are known for the etherification reaction and hemiketal formation at higher temperatures with other alcoholic counterparts.[83] Here also we observed some methoxy ethers of 5-HMF and BHMF during GC-MS analysis which can be responsible for its low efficiency as reaction medium for 5-HMF hydrogenation.

Time effect

Fig. 21 presents the effect of reaction time on 5-HMF hydrogenation. The reaction was monitored for a maximum of 8 h. For longer reaction durations, higher extents of overhydrogenated products were formed. After 8 h, the selectivity to DMF decreased considerably to 66% and the formation of DMTHF (34%) was observed. Similarly for 6 h, a 19% mixture of BHMTHF and DMTHF was observed. During the initial 2 h reaction time, C–O bond hydrogenation was in progress and a total of 33% (15% MFFR and 18% MFAL) hydrogenolysis products were observed. The most suitable reaction time was

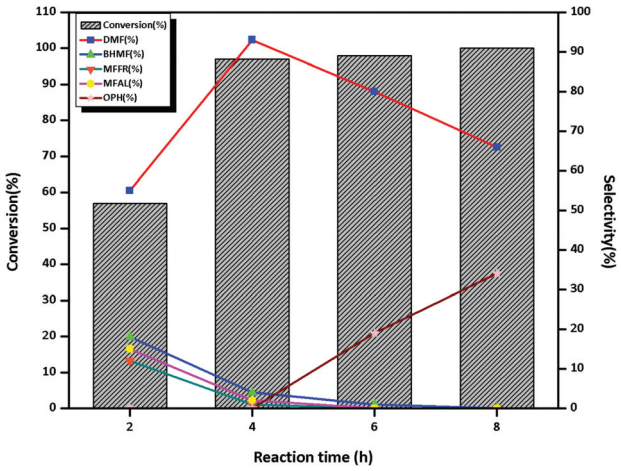

Fig. 21 Effect of reaction time on 5-HMF hydrogenation; reaction conditions: 5-HMF = 100 mg; catalyst = 50 mg; solvent (IPA) = 20 g; temperature = 443 K; H_2 pressure = 300 psig; agitation speed = 1000 rpm.

found to be 4 h for 5-HMF hydrogenation to give DMF with high selectivity.

C–t profile

Conversion/selectivity as a function of time was studied and this profile is shown in Fig. 22. In the first hour of reaction, 38% conversion of 5-HMF occurred and the first step hydrogenation product BHMF was the major product initially with 33% selectivity, whereas DMF and MFAL selectivities were 32% and 22%, respectively. A lower selectivity of 13% was achieved towards MFFR indicating that the hydrogenation was the initial step rather than hydrogenolysis of 5-HMF. In second hour of reaction, DMF appeared as a major product with 55% selectivity with decrease in selectivity to other products such as BHMF (18%), MFAL (15%) and MFFR (12%). A significant increase in the conversion of 5-HMF form 38 to 57% was observed. Similar trends were observed in the third hour of reaction where 74% conversion of 5-HMF took place with 79% selectivity to DMF. With the progress in reaction time, BHMF started getting further hydrogenated to form DMF. Hence a major product other than DMF was MFAL, whereas BHMF and MFFR were present in equal amounts. In the fourth hour of reaction, 97% conversion of 5-HMF was achieved with the all-time best 93% selectivity to DMF. Here MFAL reduced to 2% and only 1% MFFR remained in the reaction crude.

Catalyst stability

In order to rule out the possibility of any metal leaching from the catalyst, the hot filtration test was conducted. After continuing the reaction for 2 h, the catalyst was filtered out from the reaction crude and the reaction was further continued for 4 h devoid of the catalyst (Fig. 23). No further increase in conversion was observed proving that no active metal leaching took place during the 5-HMF hydrogenation reaction. These observations were further supported by the SEM-EDAX profile of the used Cu–Fe (1 : 2) where both the metals were present in almost same concentrations as in fresh Cu–Fe (1 : 2).

Fig. 24 shows that the catalyst was magnetically retrievable from the reaction crude due to the presence of Fe. The stability of our catalyst was also confirmed by its reusable efficiency. Fig. 25 shows that Cu–Fe (1 : 2) could be efficiently recycled up to the 4th run. In the first recycle run, no change in conversion of 5-HMF was observed but the selectivity towards DMF reduced to 90%. In the second and third recycle runs, conversions were 95% and 92% but the selectivity decreased to 87% and then 83%, respectively. Both conversion and selectivity started to decrease significantly in the 4th recycle run, while in the 5th recycle run although the conversion remained at 78%, the selectivity was just 68%. This loss in

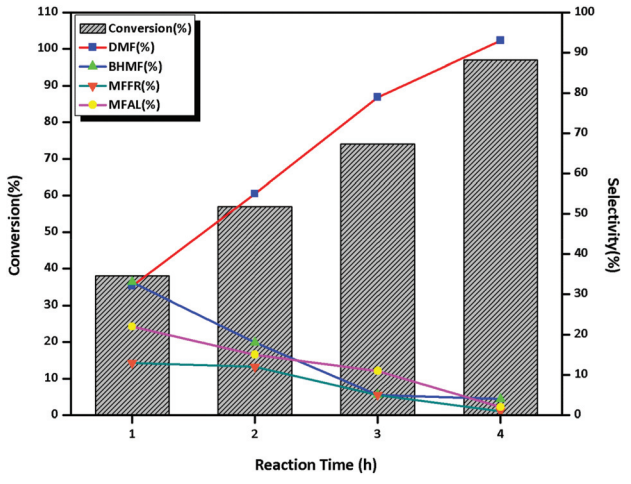

Fig. 22 *C–t* profile of 5-HMF hydrogenation; reaction conditions: 5-HMF = 100 mg; catalyst = 50 mg; solvent (IPA) = 20 g; temperature = 443 K; H_2 pressure = 300 psig; reaction time = 4 h; agitation speed = 1000 rpm.

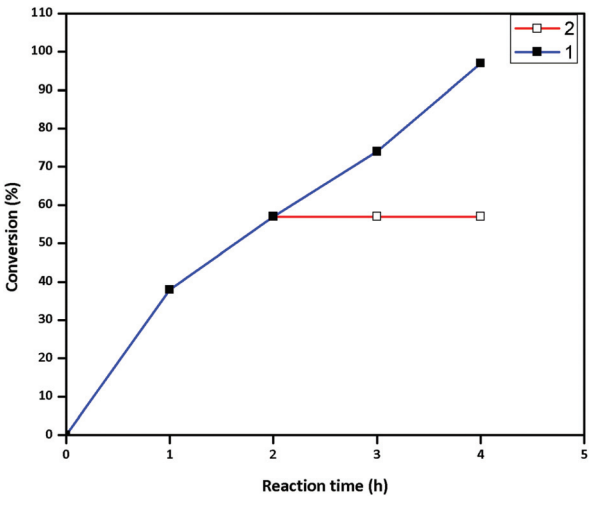

Fig. 23 Metal leaching study of 5-HMF hydrogenation; reaction conditions: 5-HMF = 100 mg; catalyst = 50 mg; solvent = 20 g; temperature = 443 K; pressure = 300 psig; reaction time = 4 h; agitation speed = 1000 rpm; (1) with Cu–Fe (1 : 2) and (2) without Cu–Fe (1 : 2).

Fig. 24 Magnetic recoverability of Cu–Fe (1 : 2).

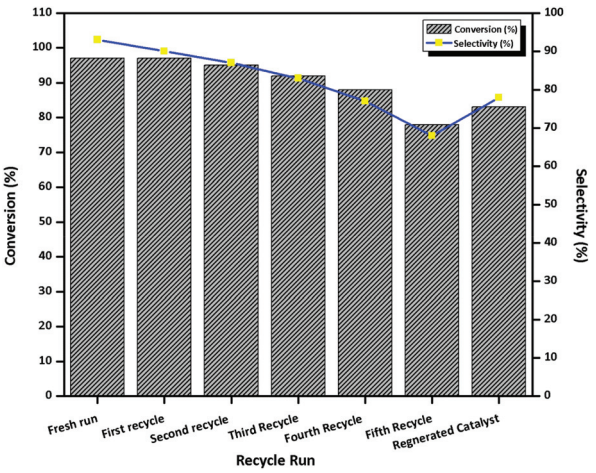

Fig. 25 Catalyst recycling study of 5-HMF hydrogenation; reaction conditions: 5-HMF = 100 mg; catalyst = 50 mg; solvent = 20 g; temperature = 443 K; pressure = 300 psig; reaction time = 4 h; agitation speed = 1000 rpm.

catalytic activity can be attributed to the deposition of carbonaceous matter on the catalytic surface which results in covering of the active sites and it was also visible from the colour change of the catalyst (Fig. SI 5†). Raman spectroscopy (Fig. 26) of the fresh catalyst compared well with that of the spent catalyst. The peaks at 226 cm^{-1}, 411 cm^{-1}, and 508 cm^{-1} were for the F_{2g} phonon while those at 606 cm^{-1} and 693 cm^{-1} were for the A_{1g} phonon and a single peak at 290 cm^{-1} was for the E_{1g} phonon of fresh Cu–Fe (1 : 2).[84] These results indicated the cubical inverse spinel phase of $CuFe_2O_4$ in which the peak at 411 cm^{-1} revealed the octahedral position of the metal cation, whereas the peak at 606 cm^{-1} could be attributed to

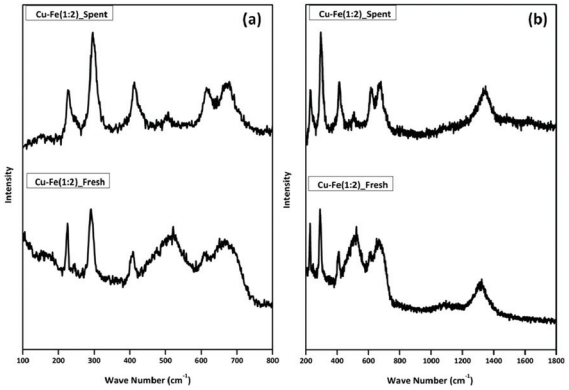

Fig. 26 Raman spectra of fresh and spent Cu–Fe (1 : 2) ranging between (a) 100–800 cm^{-1} and (b) 200–1800 cm^{-1}.

the intrinsic stretching vibration of the tetrahedral occupancy of the metal cation. The broad natured hump at 508 cm^{-1} could be assigned to a mixture of different peaks which are related to the secondary phase of haematite (Fig. 26b) with a peak at 1312 cm^{-1}.[85] This pattern was repeated in the Cu–Fe (1 : 2) spent catalyst with obvious shifting of the Raman peak because of biomass char deposition. Fig. 26b shows peaks at 1622 cm^{-1} and 1347 cm^{-1} which are related to the G peaks of disordered coke and sp^2 C–C skeleton bands associated with the carbonaceous material of organic nature.[31,86] The broadness of the peak at 1347 cm^{-1} was attributed to its overlapping with the haematite peak. This fact was also checked by TEM of the spent catalysts. In the first recycle of the catalyst, deposition of carbonaceous matter was seen (Fig. 27a and b), whereas in the 5th recycle, growth of branched chain organic matter was clearly observed which indicates the continuous

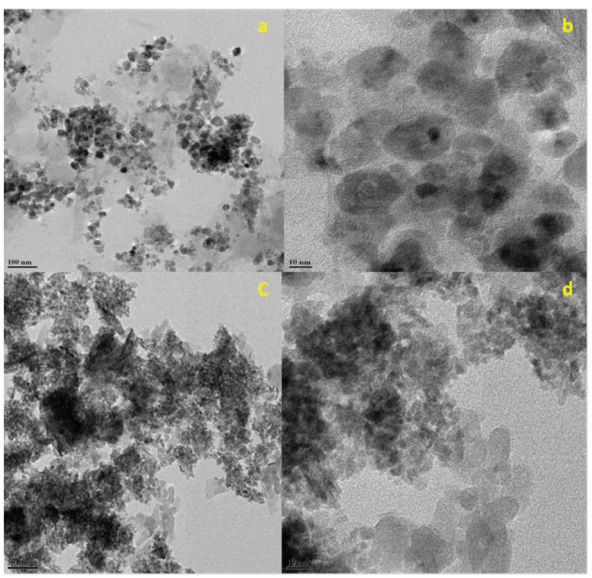

Fig. 27 TEM pattern of spent Cu–Fe (1 : 2): (a) Cu–Fe (1 : 2)_1U at 100 nm; (b) Cu–Fe (1 : 2)_1U at 10 nm; (c) Cu–Fe (1 : 2)_5U at 50 nm and (d) Cu–Fe (1 : 2)_5U at 10 nm.

deposition of carbon on the catalytic surface leading to the inability of the reactant to access catalytically active sites (Fig. 27c and d). An attempt to revive the activity of the spent catalyst was made by subjecting it to the standard reduction protocol. The reaction with the regenerated catalyst resulted in 83% conversion of 5-HMF with 78% DMF selectivity (Fig. 25).

Plausible reaction pathway

A plausible reaction pathway for 5-HMF hydrogenation is proposed in Scheme 2. The initial activation of 5-HMF occurs through the –C═O group by the Lewis acidity and oxophilic nature of Fe by attacking its electron rich oxygen.[87] As a result of this, the H_2 molecule which dissociates on the metallic Cu of the Cu–$CuFe_2O_4$ nanomorph attacks the electrophilic carbon of the –C═O group giving BHMF as an initial reaction intermediate. This enhances the rapid dehydration of BHMF into DMF *via* MFAL. The oxygen of Cu and Fe shows an O–H nature which was further proved by XPS analysis. This can be the reason why Cu and Fe show Brönsted acidity as further analysed by Py-IR and NH_3-TPD. The combined Brönsted acidity of Cu and Fe species activates the hydroxymethyl group of BHMF for dehydration as shown in Scheme 2. This leads to the formation of 2,5-dimethylfuran (DMF) as the sole product. Some control experiments were also performed to deduce the reaction pathway for 5-HMF hydrogenation. For example, when BHMF was used as a substrate, within 2 h, complete conversion of BHMF took place to give DMF. On further continuation of the reaction, the presence of MFAL and traces of BHMTHF and DMTHF was also observed indicating ring hydrogenation of DMF. MFFR as a substrate showed complete conversion and selectivity towards DMF in about 2.5 h. This indicates that the initial hydrogenation step of –C═O is slower while the further step of hydration is very fast. When MFAL was taken as a starting material, within just 1 h complete conversion into DMF was observed.

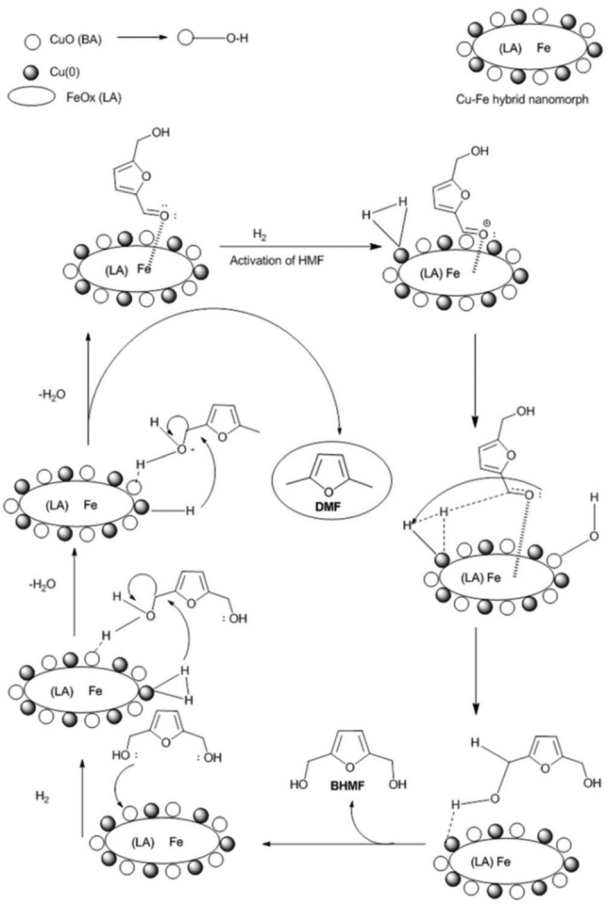

Scheme 2 Plausible reaction mechanism of 5-HMF hydrogenation.

Conclusions

The magnetically retrievable bimetallic Cu–Fe (1 : 2) catalyst was found to be highly selective (93%) for 5-HMF hydrogenation to DMF because of its specific structural properties in the form of a hybrid nanomorph which was confirmed by XRD and SEM. It was found that the Lewis acidity of Fe activates the 5-HMF for hydrogenation, whereas the combined Brönsted acidity of Cu and Fe species catalyzed the dehydration of BHMF and MFAL which was responsible for the higher selectivity to DMF. Studies of various reaction parameters were conducted to determine the appropriate reaction conditions for efficient catalytic activity. It was found that at 443 K temperature and 300 psig H_2 pressure, 97% conversion of 5-HMF took place within 4 h of reaction time. Based on our experimental work we can say that due to the high affinity of Cu towards the C–O bond and the oxophilic nature of Fe, 5-HMF was efficiently converted into DMF.

Conflicts of interest

There are no conflicts to declare in this work.

Acknowledgements

Bhanupratap Singh Solanki is grateful to the UGC for the award of JRF and ACSIR for providing the research facility to conduct this research work.

References

1 J. C. Serrano-Ruiz and J. A. Dumesic, *Energy Environ. Sci.*, 2011, **4**, 83–99.
2 G. W. Huber, S. Iborra and A. Corma, *Chem. Rev.*, 2006, **106**, 4044–4098.
3 P. Gallezot, *Chem. Soc. Rev.*, 2012, **41**, 1538–1558.
4 K. Barta and P. C. Ford, *Acc. Chem. Res.*, 2014, **47**, 1503–1512.
5 Y. Roman-Leshkov, C. J. Barrett, Z. Y. Liu and J. A. Dumesic, *Nature*, 2007, **447**, 982–985.

6 A. A. Hengne, S. B. Kamble and C. V. Rode, *Green Chem.*, 2013, **15**, 2540–2547.
7 L. Hu, G. Zhao, W. Hao, X. Tang, Y. Sun, L. Lin and S. Liu, *RSC Adv.*, 2012, **2**, 11184–11206.
8 P. Verdeguer, N. Merat and A. Gaset, *J. Mol. Catal.*, 1993, **85**, 327–344.
9 H. Mehdi, V. Fábos, R. Tuba, A. Bodor, L. T. Mika and I. T. Horváth, *Top. Catal.*, 2008, **48**, 49–54.
10 Y. Nakagawa, K. Takada, M. Tamura and K. Tomishige, *ACS Catal.*, 2014, **4**, 2718–2726.
11 N. Yan, C. Zhao, P. J. Dyson, C. Wang, L. T. Liu and Y. Kou, *ChemSusChem*, 2008, **1**, 626–629.
12 B. Saha and M. M. A. Omar, *Green Chem.*, 2014, **16**, 24–38.
13 B. Saha and M. M. A. Omar, *ChemSusChem*, 2015, **8**, 1133–1142.
14 J. B. Binder and R. T. Raines, *J. Am. Chem. Soc.*, 2009, **131**, 1979–1985.
15 S. H. Zhong, H. M. Xu and P. Richards, *Energy Fuels*, 2010, **24**, 2891–2899.
16 J. L. da Silva and M. Aznar, *Fuel*, 2014, **136**, 316–325.
17 Y. Qian, L. F. Zhu, Y. Wang and X. C. Lu, *Renewable Sustainable Energy Rev.*, 2015, **41**, 633–646.
18 L. Hu, Y. Sun and L. Lin, *Prog. Chem.*, 2011, **23**, 2079–2084.
19 M. Chidambaram and A. T. Bell, *Green Chem.*, 2010, **12**, 1253–1262.
20 T. Thananatthanachon and T. B. Rauchfuss, *Angew. Chem., Int. Ed.*, 2010, **49**, 6616–6618.
21 P. P. Upare, D. W. Hwang, Y. K. Hwang, U. H. Lee, D. Y. Honga and J. S. Chang, *Green Chem.*, 2015, **17**, 3310–3313.
22 L. Hu, X. Tang, J. X. Xu, Z. Wu, L. Lin and S. J. Liu, *Ind. Eng. Chem. Res.*, 2014, **53**, 3056–3064.
23 Y. H. Zu, P. P. Yang, J. J. Wang, X. H. Liu, J. W. Ren, G. Z. Lu and Y. Q. Wang, *Appl. Catal., B*, 2014, **146**, 244–248.
24 S. Nishimura, N. Ikeda and K. Ebitani, *Catal. Today*, 2014, **232**, 89–98.
25 J. Jae, W. Zheng, R. F. Lobo and D. G. Vlachos, *ChemSusChem*, 2013, **6**, 1158–1162.
26 Y. Yang, Q. Liu, D. Li, J. Tan, Q. Zhang, C. Wang and L. Ma, *RSC Adv.*, 2017, **7**, 16311–16318.
27 X. Kong, R. Zheng, Y. Zhu, G. Ding, Y. Zhu and Y. W. Lia, *Green Chem.*, 2015, **17**, 2504–2514.
28 M. Y. Chen, C. B. Chen, B. Zada and Y. Fu, *Green Chem.*, 2016, **18**, 3858–3866.
29 P. Yang, Q. Cui, Y. Zu, X. Liu, G. Lu and Y. Wang, *Catal. Commun.*, 2015, **66**, 55–59.
30 L. Yu, L. He, J. Chen, J. Zheng, L. Ye, H. Lin and Y. Yuan, *ChemCatChem*, 2015, **7**, 1701–1707.
31 C. Zhu, Q. Liu, D. Li, H. Wang, C. Zhang, C. Cui, L. Chen, C. Cai and L. Ma, *ACS Omega*, 2018, **3**, 7407–7417.
32 T. S. Hansen, K. Barta, P. T. Anastas, P. C. Ford and A. Riisager, *Green Chem.*, 2012, **14**, 2457–2461.
33 G. Bottari, A. J. Kumalaputri, K. K. Krawczyk, B. L. Feringa, H. J. Heeres and K. Barta, *ChemSusChem*, 2015, **8**, 1323–1327.
34 Y. Zhu, X. Kong, H. Zheng, G. Ding, Y. Zhu and Y.-W. Lia, *Catal. Sci. Technol.*, 2015, **5**, 4208–4217.
35 D. Li, Q. Liu, C. Zhu, H. Wang, C. Cui, C. Wang and L. Ma, *J. Energy Chem.*, 2019, **30**, 34–41.
36 M. Sharma, B. Das, M. Sharma, B. K. Deka, Y. B. Park, S. K. Bhargava and K. K. Bania, *ACS Appl. Mater. Interfaces*, 2017, **9**, 3453–3462.
37 R. B. Mane, S. E. Kondawar, P. S. Niphadkar, P. N. Joshi, K. R. Patil and C. V. Rode, *Catal. Today*, 2012, **198**, 321–329.
38 E. Agouriane, B. Rabi, A. Essoumhi, A. Razouk, M. Sahlaoui, B. F. O. Costa and M. Sajeiddin, *J. Mater. Environ. Sci.*, 2016, **7**, 4116–4120.
39 R. B. Mane, A. A. Hengne, A. A. Ghalwadkar, S. Vijayanand, P. H. Mohite, H. S. Potdar and C. V. Rode, *Catal. Lett.*, 2010, **135**, 141–147.
40 R. B. Mane and C. V. Rode, *Green Chem.*, 2012, **14**, 2780–2789.
41 Y. Cudennec and A. Lecerf, *Solid State Sci.*, 2003, **5**, 1471–1474.
42 Y. Deng, D. Qi, C. Deng, X. Zhang and D. Zhao, *J. Am. Chem. Soc.*, 2008, **130**, 28–29.
43 R. Han, W. Li, W. Pan, M. Zhu, D. Zhou and F. S. Li, *Sci. Rep.*, 2014, **4**, 7493–7497.
44 K. Faungnawakij, Y. Tanaka, N. Shimoda, T. Fukunaga, R. Kikuchi and K. Eguchi, *Appl. Catal., B*, 2007, **74**, 144–151.
45 K. Yan, X. Wu, X. An and X. M. Xie, *J. Alloys Compd.*, 2013, **552**, 405–408.
46 K. Yan and A. Chen, *Fuel*, 2014, **115**, 101–108.
47 G. Avgouropoulos and T. Ioannides, *Appl. Catal., A*, 2003, **244**, 155–167.
48 X. M. Liu, W. D. Yin, S. B. Miao and B. M. Ji, *Mater. Chem. Phys.*, 2009, **113**, 518–522.
49 R. B. Mane, S. E. Kondawar, P. S. Niphadkar, P. N. Joshi, K. R. Patil and C. V. Rode, *Catal. Today*, 2012, **198**, 321–329.
50 B. J. Tan, K. J. Klabunde and P. A. Sherwood, *Chem. Mater.*, 1990, **2**, 186–191.
51 P. Mills and J. L. Sullivan, *J. Phys. D: Appl. Phys.*, 1983, **16**, 723–732.
52 T. Yamashita and P. Hayes, *Appl. Surf. Sci.*, 2008, **254**, 2441–2449.
53 C. C. Chusuei, M. A. Brookshier and D. W. Goodman, *Langmuir*, 1999, **15**, 2806–2808.
54 J. Ghijsen, L. H. Tjeng, J. van Elp, H. Eskes, J. Westerink, G. A. Sawatzky and M. T. Czyzyk, *Phys. Rev. B: Condens. Matter Mater. Phys*, 1988, **38**, 11322–11330.
55 J. P. Espinós, J. Morales, A. Barranco, A. Caballero, J. P. Holgado and A. R. González-Elipe, *J. Phys. Chem. B*, 2002, **106**, 6921–6929.
56 C. Reitz, C. Suchomski, J. Haetge, T. Leichtwiess, Z. Jagličić, I. Djerdj and T. Brezesinski, *Chem. Commun.*, 2012, **48**, 4471–4473.
57 J. L. Cao, Y. Wang, X. L. Yu, S. R. Wang, S. H. Wu and Z. Y. Yuan, *Appl. Catal., B*, 2008, **79**, 26–34.
58 L. Dong, Z. Liu, Y. Hu, B. Xu and Y. Chen, *J. Chem. Soc., Faraday Trans.*, 1998, **94**, 3033–3038.

59 S. J. Roosendaal, B. V. Asselen, J. W. Elsenaar, A. M. Vredenberg and F. H. P. M. Habraken, *Surf. Sci.*, 1999, **442**, 329–337.
60 L. He, X. Li, W. Lin, W. Lia, H. Cheng, Y. Yu, S. I. Fujit, M. Arai and F. Zhao, *J. Mol. Catal. A: Chem.*, 2014, **392**, 143–149.
61 T. Schedeniedrig, W. Weiss and R. Schlogl, *Phys. Rev. B: Condens. Matter Mater. Phys*, 1995, **52**, 17449–17460.
62 M. C. Biesinger, B. P. Payne, A. P. Grosvenor, L. W. M. Lau, A. R. Gerson and R. Smart, *Appl. Surf. Sci.*, 2011, **257**, 2717–2730.
63 A. P. Grosvenor, B. A. Kobe and N. S. McIntyre, *Surf. Sci.*, 2004, **572**, 217–227.
64 C. R. Brundle, T. J. Chuang and K. Wandelt, *Surf. Sci.*, 1977, **68**, 459–468.
65 B. R. Strohmeier, D. E. Levden, R. S. Field and D. M. Hercules, *J. Catal.*, 1985, **94**, 514–530.
66 N. S. Date, A. M. Hengne, K. W. Huang, R. C. Chikate and C. V. Rode, *Green Chem.*, 2018, **20**, 2027–2037.
67 A. Jha, D. W. Jeong, J. O. Shim, W. J. Jang, Y. L. Lee, C. V. Rode and H. S. Roh, *Catal. Sci. Technol.*, 2015, **5**, 2752–2760.
68 Y. Zhou, S. Wang, M. Xiao, D. Han, Y. Lu and Y. Meng, *RSC Adv.*, 2012, **2**, 6831–6837.
69 T. Mathew, B. B. Tope, N. R. Shiju, S. G. Hegde, B. S. Rao and C. S. Gopinath, *Phys. Chem. Chem. Phys.*, 2002, **4**, 4260–4267.
70 K. Cheng, W. Song, Y. Cheng, H. Zheng, L. Wang, J. Liu, Z. Zhao and Y. Wei, *RSC Adv.*, 2018, **8**, 19301–19309.
71 H. Li, H. Luo, L. Zhuang, W. Dai and M. Qiao, *J. Mol. Catal. A: Chem.*, 2003, **203**, 267–275.
72 H. Y. Zheng, Y. L. Zhu, L. Huang, Z. Y. Zeng, H. J. Wan and Y. W. Li, *Catal. Commun.*, 2008, **9**, 342–348.
73 H. Tan, M. N. Hedhill, Y. Wang, J. Zhang, K. Li, S. Sioud, Z. A. A. Talla, M. H. Amad, T. Zhan, O. E. Talla and Y. Han, *Catal. Sci. Technol.*, 2013, **3**, 3360–3370.
74 J. Y. Kim, J. A. Rodriguez, J. C. Hanson, A. I. Frenkel and P. L. Lee, *J. Am. Chem. Soc.*, 2003, **125**, 10684–10692.
75 G. Neri, A. M. Visco, S. Galvagno, A. Donato and M. Panzalorto, *Thermochim. Acta*, 1999, **329**, 39–46.
76 K. Faungnawakij, Y. Tanaka, N. Shimoda, T. Fukunaga, R. Kikuchi and K. Eguchi, *Appl. Catal., B*, 2007, **74**, 144–151.
77 K. Faungnawakij, R. Kikuchi, T. Fukunaga and K. Eguchi, *Catal. Today*, 2008, **138**, 157–161.
78 Y. Wang, H. Zhao, M. Li, J. Fan and G. Zhao, *Appl. Catal., B*, 2014, **147**, 543–545.
79 L. Hu, X. Tang, J. Xu, Z. Wu, L. Lin and S. Liu, *Ind. Eng. Chem. Res.*, 2014, **53**, 3056–3064.
80 N. S. Biradar, A. A. Hengne, S. S. Sakate, R. K. Swami and C. V. Rode, *Catal. Lett.*, 2016, **146**, 1611–1619.
81 E. Toukoniitty, J. Kuusisto, V. Nieminen, M. Hotokka and T. Salmi, *J. Mol. Catal. A: Chem.*, 2003, **192**, 135–151.
82 R. L. Augustine, R. W. Warner and M. J. Melnick, *J. Org. Chem.*, 1984, **49**, 4853–4856.
83 B. Minder, T. Mallat, P. Skrabal and A. Baiker, *Catal. Lett.*, 1994, **29**, 115–124.
84 B. J. Rani, B. Saravanakumar, G. Ravi, V. Ganesh, S. Ravichandran and R. Yuvakkumar, *J. Mater. Sci.: Mater. Electron.*, 2018, **29**, 1975–1984.
85 B. K. Chatterjee, K. Bhattacharjee, A. Dey, C. K. Ghosh and K. K. Chattopadhyay, *Dalton Trans.*, 2014, **43**, 7930–7944.
86 A. Milani, M. Tommasini, V. Russo, A. L. Bassi, A. Lucotti, F. Cataldo and C. S. Casari, *Beilstein J. Nanotechnol.*, 2015, **6**, 480–491.
87 H. Li, H. Luo, L. Zhuang, W. Dai and M. Qiao, *J. Mol. Catal. A: Chem.*, 2003, **203**, 267–275.

